

IMPROVING DUCTILITY AND SHEAR CAPACITY OF REINFORCED
CONCRETE COLUMNS WITH CARBON FIBER REINFORCED POLYMER

A THESIS SUBMITTED TO
THE GRADUATE SCHOOL OF NATURAL AND APPLIED SCIENCE
OF
MIDDLE EAST TECHNICAL UNIVERSITY

BY

OKAN ÖZCAN

IN PARTIAL FULFILLMENT OF THE REQUIREMENTS
FOR
THE DEGREE OF DOCTOR OF PHILOSOPHY
IN
CIVIL ENGINEERING

DECEMBER 2009

Approval of the thesis:

**IMPROVING DUCTILITY AND SHEAR CAPACITY OF REINFORCED
CONCRETE COLUMNS WITH CARBON FIBER REINFORCED
POLYMER**

submitted by **OKAN ÖZCAN** in partial fulfillment of the requirements for the degree of **Doctor of Philosophy in Civil Engineering Department, Middle East Technical University** by,

Prof. Dr. Canan Özgen
Dean, Graduate School of **Natural and Applied Sciences**

Prof. Dr. Güney Özcebe
Head of Department, **Civil Engineering**

Prof. Dr. Güney Özcebe
Supervisor, **Civil Engineering Dept., METU**

Assoc. Prof. Dr. Barış Binici
Co-Supervisor, **Civil Engineering Dept., METU**

Examining Committee Members:

Prof. Dr. Uğur Ersoy
Civil Engineering Dept., BOUN

Prof. Dr. Güney Özcebe
Civil Engineering Dept., METU

Prof. Dr. Sinan Altın
Civil Engineering Dept., Gazi University

Assoc. Prof. Dr. Ahmet Yakut
Civil Engineering Dept., METU

Assoc. Prof. Dr. Erdem Canbay
Civil Engineering Dept., METU

Date: December 16, 2009

I hereby declare that all information in this document has been obtained and presented in accordance with academic rules and ethical conduct. I also declare that, as required by these rules and conduct, I have fully cited and referenced all material and results that are not original to this work.

Name, Last name: Okan Özcan

Signature:

ABSTRACT

IMPROVING DUCTILITY AND SHEAR CAPACITY OF REINFORCED CONCRETE COLUMNS WITH CARBON FIBER REINFORCED POLYMER

Özcan, Okan

PhD. Department of Civil Engineering

Supervisor: Prof. Dr. Güney Özcebe

Co-Supervisor: Assoc. Prof. Dr. Barış Binici

December 2009, 279 pages

The performance of reinforced concrete (RC) columns during recent earthquakes has clearly demonstrated the possible failures associated with inadequate confining reinforcement. The confinement reinforcement requirements of older codes were less stringent than present standards. Many studies were conducted by applying different retrofitting techniques for RC columns that have inadequate confinement reinforcement. A new retrofitting technique by means of Carbon Fiber Reinforced Polymer (CFRP) was developed and tested in many countries in the last decade. This technique is performed by CFRP wrapping the critical region of columns. The effectiveness of CFRP retrofitting technique was shown in many studies conducted worldwide. In Turkey, the frame members are considerably deficient from the seismic detailing point of view. Therefore, in order to use the CFRP retrofitting technique effectively in Turkey, experimental evidence is needed. This study investigates the performance of CFRP retrofitted RC columns with deficient confining steel and low concrete strength. It was concluded by experimental and analytical results that the CFRP retrofitting method can be implemented to seismically deficient columns. Moreover, two design approaches were proposed for CFRP retrofit design of columns considering safe design regulations.

Keywords: Carbon Fiber Reinforced Polymer (CFRP), rectangular columns, confinement, analytical method, design-oriented method

ÖZ

BETONARME KOLONLARIN SÜNEKLİĞİNİN VE KESME KAPASİTESİNİN KARBON FİBER LİFLİ POLİMER İLE İYİLEŞTİRİLMESİ

Özcan, Okan

Doktora, İnşaat Mühendisliği Bölümü

Tez Yöneticisi: Prof. Dr. Güney Özcebe

Ortak Tez Yöneticisi: Doç. Dr. Barış Binici

Aralık 2009, 279 sayfa

Son yıllarda yaşanan depremlerde betonarme (BA) kolonların performansı, yetersiz sargı donatısı ile ilişkili olası kusurları açıkça göstermiştir. Eski yönetmeliklerdeki sargı donatısı gereksinimleri, günümüz standartlarını karşılamaktan uzaktır. Yeterli sargı donatısı olmayan BA kolonlarda farklı güçlendirme teknikleri uygulanarak çeşitli çalışmalar yapılmıştır. Yeni bir güçlendirme tekniği olan Karbon Lifli Polimer (CFRP) ile güçlendirme sistemi son on yılda birçok ülke tarafından test edilerek geliştirilmiştir. Bu teknik kolonların kritik bölgelerininin CFRP ile sarılmasıyla gerçekleştirilmektedir. CFRP güçlendirme tekniğinin etkisi dünya çapında yapılan birçok uygulamada gösterilmiştir. Türkiye’de çerçeve elemanları, sismik detaylandırma açısından önemli ölçüde yetersizdir. Bu nedenle, CFRP ile güçlendirme tekniğinin Türkiye’de etkili bir şekilde uygulanması için deneysel kanıtlar gerekmektedir. Bu çalışma, yetersiz sargı donatılı ve düşük beton dayanımlı CFRP sargılı BA kolonların performansını incelemektedir. Yapılan deneysel ve analitik çalışmalarda, CFRP güçlendirme metodunun sismik açıdan yetersiz kolonlara uygulanabilirliği gösterilmiştir. Ayrıca, kolonların CFRP güçlendirme tasarımı için güvenli tasarımı dikkate alan iki tasarım yaklaşımı öne sürülmüştür.

Anahtar Kelimeler: Karbon Fiber Lifli Polimer (CFRP), dikdörtgen kolonlar, sargı etkisi, analitik metot, tasarım metodu

Dedicated to My Parents

ACKNOWLEDGEMENTS

I would like to express my gratitude to my thesis supervisor, Prof. Dr. Güney Özcebe for his continuous support and guidance throughout the thesis with his patience and knowledge. It is an honor for me to work with him.

I would also like to convey my deepest appreciation to my thesis co-supervisor, Assoc. Prof. Dr. Barış Binici without whose knowledge, support and encouragement this thesis would not be completed.

Also, I would like to extend my acknowledgement to all faculty and my friends for their friendship and support throughout my academic studies.

I am grateful to METU Structural Mechanics Laboratory staff, especially Burhan Avcı and Hasan Metin for their valuable help and collaboration during this study.

I wish to express my gratitude to my parents and brother for their continuous encouragement, support and love during the years of my studies.

TABLE OF CONTENTS

ABSTRACT.....	iv
ÖZ	v
ACKNOWLEDGEMENTS	vii
TABLE OF CONTENTS	viii
LIST OF TABLES	xi
LIST OF FIGURES	xii
CHAPTERS	
1. INTRODUCTION.....	1
1.1. General	1
1.2. Retrofit Needs	3
1.3. Seismic Retrofitting	4
1.4. Literature Survey.....	6
1.4.1. Columns under Axial Compression	7
1.4.2. Columns under Cyclic Displacement Excursions.....	12
1.4.3. FRP Design Guidelines for Columns.....	22
1.4.3.1. ACI440.2R	23
1.4.3.2. Turkish Earthquake Code.....	24
1.5. Objective and Scope.....	26
2. EXPERIMENTAL PROGRAM	28
2.1. General	28
2.2. Material Properties	28
2.2.1. Concrete	28
2.2.2. Steel.....	29
2.2.3. Carbon Fiber Reinforced Polymer (CFRP).....	30
2.3. Test Specimens and Preparation	30
2.3.1. Test Specimens	34
2.3.2. Preparation of Test Specimens.....	35
2.3.3. CFRP Implementation.....	40
2.4. Test Setup and Instrumentation.....	43
2.5. Correction of Lateral Load.....	50

2.6. Experimental Observations and Test Results.....	51
2.6.1. Series 1	53
2.6.2. Series 2	69
2.6.3. Series 3	86
2.7. Examination of Test Results	102
2.7.1. Envelope Response Comparisons	102
2.7.2. Rotation and Deflection Components	123
2.7.3. Deflection Profiles	143
2.7.4. Energy Dissipation Comparisons.....	147
2.7.5. Stiffness Degradation Comparisons.....	150
2.8. Discussion of Test Results	153
2.8.1. Effect of CFRP Layers	153
2.8.2. Effect of Axial Load during Strengthening and Repairing	154
2.8.3. Effect of Plain Bars	155
2.8.4. Effect of Column Corner Rounding Radius.....	156
2.8.5. Effect of Column Section Aspect Ratio	157
2.8.6. Effect of CFRP Anchor Dowels and Anchor Dowel Configurations	157
3. ANALYTICAL STUDIES.....	159
3.1. General	159
3.2. Constitutive Models for Materials	159
3.2.1. Unconfined Concrete Model	160
3.2.2. FRP Confined Concrete Model.....	161
3.2.3. Steel Model	163
3.3. Bond Slip Model	165
3.4. Tip Displacement Calculations	168
3.5. Program Outputs and Experimental Comparisons.....	169
3.5.1. Series 1	169
3.5.2. Series 2	170
3.5.3. Series 3	171
3.6. Parametric Study	171
3.6.1. Effect of CFRP Thickness.....	172
3.6.2. Effect of Column Corner Rounding Radius.....	173
3.6.3. Effect of Axial Load.....	175

4. DESIGN-ORIENTED STUDIES	178
4.1. Introduction.....	178
4.2. Previous Research	178
4.3. Proposed Design Procedure	181
4.3.1. Ultimate Drift Based: Method I	181
4.3.2. Ultimate Compressive Strain Based: Method II	191
4.3.3. Database Comparison and Code Recommendations	205
5. CONCLUSIONS AND FUTURE RECOMMENDATIONS.....	207
REFERENCES.....	212
APPENDICES	
A. BASE ROTATION CALCULATIONS AND MEMBER STABILITY	
CHECKS	220
B. UNEXPECTED FAILURE MODES	224
C. HYSTERETIC STRAIN PLOTS	240
D. CURVATURE DISTRIBUTION TABLES	257
E. THE PROGRAM NAKO	263
F. DESIGN EXAMPLE OF CFRP COLUMN RETROFITTING	274
CURRICULUM VITAE	278

LIST OF TABLES

Table 2.1 Concrete mixture properties for different target nominal 28-day concrete compressive strengths.	29
Table 2.2 Mechanical properties of reinforcing bars for column and stub	29
Table 2.3 Specimen Properties.....	31
Table 2.4 Analytical yield and peak responses with standard section analysis	51
Table 2.5 Specimen Responses	52
Table 4.1 Results for the used database	184
Table 4.2 Results for the experimental study.....	185
Table 4.3 The experimental and obtained results using TEC07	193
Table 4.4 The obtained results for database using simplified models	194
Table 4.5 The obtained results for experimental study using simplified models.....	195
Table D.1 Curvature distribution for S-L-0-00.....	257
Table D.2 Curvature distribution for S-L-1-00	257
Table D.3 Curvature distribution for S-L-1-34	258
Table D.4 Curvature distribution for S-L-2-00	258
Table D.5 Curvature distribution for S-L-2-32	259
Table D.6 Curvature distribution for S-H-0-00.....	259
Table D.7 Curvature distribution for S-H-1-00.....	259
Table D.8 Curvature distribution for S-HC-1-00.....	260
Table D.9 Curvature distribution for S-HD-1-00.....	260
Table D.10 Curvature distribution for S-HD-1-27.....	261
Table D.11 Curvature distribution for R-NC-0-00	261
Table D.12 Curvature distribution for R-HC-1-16P	261
Table D.13 Curvature distribution for R-MC-1-16P.....	262
Table D.14 Curvature distribution for R-MC-1-8P.....	262
Table D.15 Curvature distribution for R-MC-1-NP.....	262

LIST OF FIGURES

Figure 1.1 Seismic rehabilitation strategies	5
Figure 1.2 Typical seismic strengthening methods.....	5
Figure 2.1 The stress-strain relationships for the plain bars used in the specimens ..	30
Figure 2.2 CFRP anchor dowel configurations.....	33
Figure 2.3 Reinforcing cage for square columns	36
Figure 2.4 Reinforcing cage for rectangular columns.....	37
Figure 2.5 A typical footing formwork with reinforcement placed inside	38
Figure 2.6 (a) First, (b) Second, (c) and (d) Last phase of specimen casting	39
Figure 2.7 Strengthened and repaired column preparation during CFRP application	41
Figure 2.8 CFRP anchor dowel implementation.....	42
Figure 2.9 CFRP strengthened and repaired columns ready for the test.....	42
Figure 2.10 Test Setup: Front View	44
Figure 2.11 Test Setup: Profile	45
Figure 2.12 Test Setup: Top View	48
Figure 2.13 Instrumentation: 3D View	48
Figure 2.14 Instrumentation: 3D-Close-up View.....	48
Figure 2.15 12-Bit Data Acquisition System	49
Figure 2.16 Loading Program	49
Figure 2.17 Restraining effect of axial load and moment correction.....	50
Figure 2.18 Columns at the end of testing (a) S-L-0-00, (b) S-L-1-00, (c) S-L-1-34, (d) S-L-2-00, (e) S-L-2-32	54
Figure 2.19 Lateral Load (P) – Deflection (Δ) response for S-L-0-00.....	56
Figure 2.20 Lateral Load (P) – Deflection (Δ) response for S-L-1-00.....	57
Figure 2.21 Lateral Load (P) – Deflection (Δ) response for S-L-1-34.....	57
Figure 2.22 Lateral Load (P) – Deflection (Δ) response for S-L-2-00.....	58
Figure 2.23 Lateral Load (P) – Deflection (Δ) response for S-L-2-32.....	58
Figure 2.24 Moment (M) – Average Curvature (K) responses of S-L-0-00: Relative to (a) 50 mm height and (b) Base.....	59

Figure 2.25 Moment (M) – Average Curvature (K) responses of S-L-1-00: Relative to (a) 50 mm height and (b) Base.....	60
Figure 2.26 Moment (M) – Average Curvature (K) responses of S-L-1-34: Relative to (a) 50 mm height and (b) Base.....	61
Figure 2.27 Moment (M) – Average Curvature (K) responses of S-L-2-00: Relative to (a) 50 mm height and (b) Base.....	62
Figure 2.28 Moment (M) – Average Curvature (K) responses of S-L-2-32: Relative to (a) 50 mm height and (b) Base.....	63
Figure 2.29 Moment (M) – Fixed End Rotation (FER) response of S-L-0-00	64
Figure 2.30 Moment (M) – Fixed End Rotation (FER) response of S-L-1-00	64
Figure 2.31 Moment (M) – Fixed End Rotation (FER) response of S-L-1-34	65
Figure 2.32 Moment (M) – Fixed End Rotation (FER) response of S-L-2-00	65
Figure 2.33 Moment (M) – Fixed End Rotation (FER) response of S-L-2-32	66
Figure 2.34 Strain – Drift responses for S-L-0-00	66
Figure 2.35 Strain – Drift responses for S-L-1-00	67
Figure 2.36 Strain – Drift responses for S-L-1-34	67
Figure 2.37 Strain – Drift responses for S-L-2-00	68
Figure 2.38 Strain – Drift responses for S-L-2-32	68
Figure 2.39 Columns at the end of testing (a) S-H-0-00, (b) S-H-1-00, (c) S-HD-1-00, (d) S-HD-1-27, (e) S-HC-1-00.....	71
Figure 2.40 Lateral Load (P) – Deflection (Δ) response for S-H-0-00	72
Figure 2.41 Lateral Load (P) – Deflection (Δ) response for S-H-1-00	73
Figure 2.42 Lateral Load (P) – Deflection (Δ) response for S-HD-1-00	73
Figure 2.43 Lateral Load (P) – Deflection (Δ) response for S-HD-1-27	74
Figure 2.44 Lateral Load (P) – Deflection (Δ) response for S-HC-1-00	74
Figure 2.45 Moment (M) – Average Curvature (K) responses of S-H-0-00: Relative to (a) 50 mm height and (b) Base.....	75
Figure 2.46 Moment (M) – Average Curvature (K) responses of S-H-1-00: Relative to (a) 50 mm height and (b) Base.....	76
Figure 2.47 Moment (M) – Average Curvature (K) response of S-HD-1-00: Relative to (a) 50 mm height and (b) Base.....	77

Figure 2.48 Moment (M) – Average Curvature (K) response of S-HD-1-27: Relative to (a) 50 mm height and (b) Base.....	78
Figure 2.49 Moment (M) – Average Curvature (K) response of S-HC-1-00: Relative to (a) 50 mm height and (b) Base.....	79
Figure 2.50 Moment (M) – Fixed End Rotation (FER) response of S-H-0-00.....	80
Figure 2.51 Moment (M) – Fixed End Rotation (FER) response of S-H-1-00.....	80
Figure 2.52 Moment (M) – Fixed End Rotation (FER) response of S-HD-1-00.....	81
Figure 2.53 Moment (M) – Fixed End Rotation (FER) response of S-HD-1-27.....	81
Figure 2.54 Moment (M) – Fixed End Rotation (FER) response of S-HC-1-00.....	82
Figure 2.55 Strain – Drift responses for S-H-0-00.....	82
Figure 2.56 Strain – Drift responses for S-H-1-00.....	83
Figure 2.57 Strain – Drift responses for S-HD-1-00: Damage cycles	83
Figure 2.58 Strain – Drift responses for S-HD-1-00.....	84
Figure 2.59 Strain – Drift responses for S-HD-1-27: Damage cycles	84
Figure 2.60 Strain – Drift responses for S-HD-1-27.....	85
Figure 2.61 Strain – Drift responses for S-HC-1-00.....	85
Figure 2.62 Columns at the end of testing (a) R-NC-0-00, (b) R-MC-1-16P, (c) R-MC-1-8P, (d) R-MC-1-NP, (e) R-HC-1-16P	87
Figure 2.63 Lateral Load (P) – Deflection (Δ) response for R-NC-0-00.....	89
Figure 2.64 Lateral Load (P) – Deflection (Δ) response for R-MC-1-16P	90
Figure 2.65 Lateral Load (P) – Deflection (Δ) response for R-MC-1-8P	90
Figure 2.66 Lateral Load (P) – Deflection (Δ) response for R-MC-1-NP	91
Figure 2.67 Lateral Load (P) – Deflection (Δ) response for R-HC-1-16P.....	91
Figure 2.68 Moment (M) – Average Curvature (K) response of R-NC-0-00: Relative to (a) 50 mm height and (b) Base.....	92
Figure 2.69 Moment (M) – Average Curvature (K) response of R-MC-1-16P: Relative to (a) 50 mm height and (b) Base	93
Figure 2.70 Moment (M) – Average Curvature (K) response of R-MC-1-8P: Relative to (a) 50 mm height and (b) Base.....	94
Figure 2.71 Moment (M) – Average Curvature (K) response of R-MC-1-NP: Relative to (a) 50 mm height and (b) Base	95

Figure 2.72 Moment (M) – Average Curvature (K) response of R-HC-1-16P: Relative to (a) 50 mm height and (b) Base	96
Figure 2.73 Moment (M) – Fixed End Rotation (FER) response of R-NC-0-00.....	97
Figure 2.74 Moment (M) – Fixed End Rotation (FER) response of R-MC-1-16P....	97
Figure 2.75 Moment (M) – Fixed End Rotation (FER) response of R-MC-1-8P.....	98
Figure 2.76 Moment (M) – Fixed End Rotation (FER) response of R-MC-1-NP.....	98
Figure 2.77 Moment (M) – Fixed End Rotation (FER) response of R-HC-1-16P	99
Figure 2.78 Strain – Drift responses for R-NC-0-00	99
Figure 2.79 Strain – Drift responses for R-MC-1-16P.....	100
Figure 2.80 Strain – Drift responses for R-MC-1-8P.....	100
Figure 2.81 Strain – Drift responses for R-MC-1-NP.....	101
Figure 2.82 Strain – Drift responses for R-HC-1-16P	101
Figure 2.83 Normalized Lateral Load (P/Py) – Drift comparisons for S-L-0-00, S-L-1-00 and S-L-2-00	103
Figure 2.84 Normalized Lateral Load (P/Py) – Drift comparisons for S-L-0-00, S-L-1-00 and S-L-1-34.....	104
Figure 2.85 Normalized Lateral Load (P/Py) – Drift comparisons for S-L-0-00, S-L-2-00 and S-L-2-32	104
Figure 2.86 Normalized Moment (M/My) – Curvature comparisons for S-L-0-00, S-L-1-00 and S-L-2-00: at location (a) 350 – 0 and (b) 350 – 50 mm	105
Figure 2.87 Normalized Moment (M/My) – Curvature comparisons for S-L-0-00, S-L-1-00 and S-L-1-34: at location (a) 350 – 0 and (b) 350 – 50 mm	106
Figure 2.88 Normalized Moment (M/My) – Curvature comparisons for S-L-0-00, S-L-2-00 and S-L-2-32: at location (a) 350 – 0 and (b) 350 – 50 mm	107
Figure 2.89 Normalized Moment (M/My) – Fixed End Rotation comparisons for S-L-0-00, S-L-1-00 and S-L-2-00.....	108
Figure 2.90 Normalized Moment (M/My) – Fixed End Rotation comparisons for S-L-0-00, S-L-1-00 and S-L-1-34.....	108
Figure 2.91 Normalized Moment (M/My) – Fixed End Rotation comparisons for S-L-0-00, S-L-2-00 and S-L-2-32.....	109
Figure 2.92 Lateral Load (P) – Drift comparisons for S-H-0-00, S-H-1-00 and S-HC-1-00	110

Figure 2.93 Lateral Load (P) – Drift comparisons for S-H-0-00, S-HD-1-00 and S-HD-1-27	111
Figure 2.94 Lateral Load (P) – Drift comparisons for S-H-0-00, S-H-1-00 and S-HD-1-00	111
Figure 2.95 Moment (M) – Curvature comparisons for S-H-0-00, S-H-1-00 and S-HC-1-00: at location (a) 350 – 0 and (b) 350 – 50 mm.....	112
Figure 2.96 Moment (M) – Curvature comparisons for S-H-0-00, S-HD-1-00 and S-HD-1-27: at location (a) 350 – 0 and (b) 350 – 50 mm	113
Figure 2.97 Moment (M) – Curvature comparisons for S-H-0-00, S-H-1-00 and S-HD-1-00: at location (a) 350 – 0 and (b) 350 – 50 mm	114
Figure 2.98 Moment (M) – Fixed End Rotation comparisons for S-H-0-00, S-H-1-00 and S-HC-1-00	115
Figure 2.99 Moment (M) – Fixed End Rotation comparisons for S-H-0-00, S-HD-1-00 and S-HD-1-27	115
Figure 2.100 Moment (M) – Fixed End Rotation comparisons for S-H-0-00, S-H-1-00 and S-HD-1-00	116
Figure 2.101 Normalized Lateral Load (P/Py) – Drift comparisons for R-NC-0-00, R-HC-1-16P and R-MC-1-16P	117
Figure 2.102 Normalized Lateral Load (P/Py) – Drift comparisons for R-NC-0-00, R-MC-1-8P and R-MC-1-NP.....	118
Figure 2.103 Normalized Lateral Load (P/Py) – Drift comparisons for R-NC-0-00, R-MC-1-8P and R-MC-1-16P	118
Figure 2.104 Normalized Moment (M/My) – Curvature comparisons for R-NC-0-00, R-HC-1-16P and R-MC-1-16P: at location (a) 350 – 0 and (b) 350 – 50 mm	119
Figure 2.105 Normalized Moment (M/My) – Curvature comparisons for R-NC-0-00, R-MC-1-8P and R-MC-1-NP: at location (a) 350 – 0 and (b) 350 – 50 mm.....	120
Figure 2.106 Normalized Moment (M/My) – Curvature comparisons for R-NC-0-00, R-MC-1-8P and R-MC-1-16P: at location (a) 350 – 0 and (b) 350 – 50 mm.....	121
Figure 2.107 Normalized Moment (M/My) – Fixed End Rotation comparisons for R-NC-0-00, R-HC-1-16P and R-MC-1-16P	122
Figure 2.108 Normalized Moment (M/My) – Fixed End Rotation comparisons for R-NC-0-00, R-MC-1-8P and R-MC-1-NP.....	122

Figure 2.109 Normalized Moment (M/My) – Fixed End Rotation comparisons for R-NC-0-00, R-MC-1-8P and R-MC-1-16P.....	123
Figure 2.110 (a) Rotation and (b) Deflection Components for S-L-0-00	125
Figure 2.111 (a) Rotation and (b) Deflection Components for S-L-1-00	126
Figure 2.112 (a) Rotation and (b) Deflection Components for S-L-1-34	127
Figure 2.113 (a) Rotation and (b) Deflection Components for S-L-2-00	128
Figure 2.114 (a) Rotation and (b) Deflection Components for S-L-2-32	129
Figure 2.115 (a) Rotation and (b) Deflection Components for S-H-0-00.....	131
Figure 2.116 (a) Rotation and (b) Deflection Components for S-H-1-00.....	132
Figure 2.117 (a) Rotation and (b) Deflection Components for S-HD-1-00 (damage)	133
Figure 2.118 (a) Rotation and (b) Deflection Components for S-HD-1-00.....	134
Figure 2.119 (a) Rotation and (b) Deflection Components for S-HD-1-27 (damage)	135
Figure 2.120 (a) Rotation and (b) Deflection Components for S-HD-1-27.....	136
Figure 2.121 (a) Rotation and (b) Deflection Components for S-HC-1-00	137
Figure 2.122 (a) Rotation and (b) Deflection Components for R-NC-0-00.....	138
Figure 2.123 (a) Rotation and (b) Deflection Components for R-MC-1-16P.....	139
Figure 2.124 (a) Rotation and (b) Deflection Components for R-MC-1-8P.....	140
Figure 2.125 (a) Rotation and (b) Deflection Components for R-MC-1-NP.....	141
Figure 2.126 (a) Rotation and (b) Deflection Components for R-HC-1-16P	142
Figure 2.127 Deflection Profiles for Series 1.....	144
Figure 2.128 Deflection Profiles for Series 2.....	145
Figure 2.129 Deflection Profiles for Series 3.....	146
Figure 2.130 Cumulative Dissipated Energy (CDE) calculation method.....	147
Figure 2.131 Normalized Cumulative Dissipated Energy (CDE) – Cumulative Drift Ratio (CDR) graph for Series 1 columns	149
Figure 2.132 Normalized Cumulative Dissipated Energy (CDE) – Cumulative Drift Ratio (CDR) graph for Series 2 columns	149
Figure 2.133 Normalized Cumulative Dissipated Energy (CDE) – Cumulative Drift Ratio (CDR) graph for Series 3 columns	150
Figure 2.134 Normalized secant stiffness degradation curves for Series 1	152
Figure 2.135 Normalized secant stiffness degradation curves for Series 2	152

Figure 2.136 Normalized secant stiffness degradation curves for Series 3	153
Figure 2.137 Ultimate Drift (DR_u) – Confinement Ratio comparisons for Series 3	158
Figure 3.1 The constitutive models for (a) Unconfined concrete, (b) Steel, (c) Confined concrete – softening and (d) Confined concrete – hardening.....	160
Figure 3.2 The bond-slip model	166
Figure 3.3 The plastic hinging model	169
Figure 3.4 Effect of CFRP layers on (a) Lateral Load (P)-Tip Deflection (Δ), (b) Moment (M) - Curvature (K) and (c) Moment (M) - Fixed-end Rotation (FER)....	173
Figure 3.5 Effect of corner-rounding radius on (a) Lateral Load (P) – Tip Deflection (Δ), (b) Moment (M) – Curvature (K) and (c) Moment (M) – Fixed-end Rotation (FER) responses	174
Figure 3.6 Effect of axial load on (a) Lateral Load (P) – Tip Deflection (Δ), (b) Moment (M) – Curvature (K) and (c) Moment (M) – Fixed - End Rotation (FER)	175
Figure 3.7 Effect of longitudinal bar buckling on (a) Lateral Load (P) – Tip Deflection (Δ), (b) Moment (M) – Curvature (K) and (c) Moment (M) – Fixed-end Rotation (FER) responses	177
Figure 4.1 Best-fit drift equation compared with experimental data in confinement ratio basis for constant (a) longitudinal reinforcement ratio and (b) axial load.....	186
Figure 4.2 Best-fit drift equation compared with experimental data in axial load basis for constant (a) confinement ratio and (b) longitudinal reinforcement ratio.	187
Figure 4.3 Best-fit drift equation compared with experimental data in longitudinal reinforcement ratio basis for constant (a) confinement ratio and (b) axial load.	188
Figure 4.4 Predicted results by nonlinear regression analysis for CSA S806-02 equation	189
Figure 4.5 Predicted results by nonlinear regression analysis for proposed best-fit equation	189
Figure 4.6 Predicted results by nonlinear regression analysis for proposed design equation	190
Figure 4.7 TEC07 models for (a) Concrete, (b) Steel and simplified proposed models for (c) Concrete and (d) Steel.....	192
Figure 4.8 Regression results considering best-fit equation	197
Figure 4.9 Regression results considering design equation	197
Figure 4.10 Experimental and design comparison for the specimen S-L-0-00.....	198

Figure 4.11 Experimental and design comparison for the specimen S-L-1-00.....	198
Figure 4.12 Experimental and design comparison for the specimen S-L-1-34.....	199
Figure 4.13 Experimental and design comparison for the specimen S-L-2-00.....	199
Figure 4.14 Experimental and design comparison for the specimen S-L-2-32.....	200
Figure 4.15 Experimental and design comparison for the specimen S-H-0-00	200
Figure 4.16 Experimental and design comparison for the specimen S-H-1-00	201
Figure 4.17 Experimental and design comparison for the specimen S-HC-1-00	201
Figure 4.18 Experimental and design comparison for the specimen R-NC-0-00	202
Figure 4.19 Experimental and design comparison for the specimen R-MC-1-16P .	202
Figure 4.20 Experimental and design comparison for the specimen R-MC-1-8P ...	203
Figure 4.21 Experimental and design comparison for the specimen R-MC-1-NP ..	203
Figure 4.22 Experimental and design comparison for the specimen R-HC-1-16P ..	204
Figure A.1 The forces acting on the specimen for the worst case scenario	220
Figure A.2 Elastic Stiffness and member response for specimen S-L-0-00	222
Figure A.3 Elastic Stiffness and member response for specimen S-H-0-00.....	222
Figure A.4 Elastic Stiffness and member response for specimen R-NC-0-00.....	223
Figure B.1 U1 at the end of test (a) Full view and (b) Close-up view	225
Figure B.2 The Lateral Force (P) – Tip Deflection (Δ) response for U1	225
Figure B.3 Moment-Curvature response for U1: (a) 350-0 and (b) 350-50 mm	226
Figure B.4 The Moment (M) – Fixed End Rotation (FER) response for U1	227
Figure B.5 The Deflection profile for U1	227
Figure B.6 (a) Rotation and (b) Deflection Components for U1	228
Figure B.7 Drift – Strain (ϵ) response for U1	229
Figure B.8 U2 at the end of test (a) Full view and (b) Close-up view	230
Figure B.9 The Lateral Force (P) – Tip Deflection (Δ) response for U2.....	230
Figure B.10 Moment-Curvature response for U2: (a) 350-0 and (b) 350-50 mm ...	231
Figure B.11 The Moment (M) – Fixed End Rotation (FER) response for U2.....	232
Figure B.12 The Deflection profile for U2	232
Figure B.13 (a) Rotation and (b) Deflection Components for U2	233
Figure B.14 Drift – Strain (ϵ) response for U2	234
Figure B.15 C1 at the end of test	235
Figure B.16 The Lateral Force (P) – Tip Deflection (Δ) response for C1	235
Figure B.17 Moment-Curvature response for C1: (a) 350-0 and (b) 350-50 mm....	236

Figure B.18 The Moment (M) – Fixed End Rotation (FER) response for C1	237
Figure B.19 The Deflection profile for C1	237
Figure B.20 (a) Rotation and (b) Deflection Components for C1.....	238
Figure B.21 Drift – Strain (ϵ) response for C1.....	239
Figure C.1 Strain gage responses for specimen S-L-0-00.....	240
Figure C.2 Strain gage responses for specimen S-L-1-00.....	241
Figure C.3 Strain gage responses for specimen S-L-1-34.....	242
Figure C.4 Strain gage responses for specimen S-L-2-00.....	243
Figure C.5 Strain gage responses for specimen S-L-2-32.....	244
Figure C.6 Strain gage responses for specimen S-H-0-00	245
Figure C.7 Strain gage responses for specimen S-H-1-00	246
Figure C.8 Strain gage responses for specimen S-HD-1-00: Damage cycles.....	247
Figure C.10 Strain gage responses for specimen S-HD-1-27: Damage cycles.....	249
Figure C.11 Strain gage responses for specimen S-HD-1-27: Cycles after repairing	250
Figure C.12 Strain gage responses for specimen S-HC-1-00	251
Figure C.13 Strain gage responses for specimen R-NC-0-00.....	252
Figure C.14 Strain gage responses for specimen R-MC-1-16P	253
Figure C.15 Strain gage responses for specimen R-MC-1-8P	254
Figure C.16 Strain gage responses for specimen R-MC-1-NP	255
Figure C.17 Strain gage responses for specimen R-HC-1-16P.....	256
Figure F.1 Determining the spectral acceleration and displacement values for the design example.....	275

CHAPTER 1

INTRODUCTION

1.1. General

The seismic activity in Turkey's faults and the tectonic characteristic of this region engendered many major earthquakes that hit Turkey several times. Regarding the earthquakes occurred after 1990, the ones having highest magnitude (M_s), life loss and hazard are Erzincan (1992), Dinar (1995), Ceyhan (1998), İzmit (1999), Düzce (1999) and Bingöl (2003) earthquakes.

During the Erzincan earthquake in 1992, it was reported by the site investigators [1-3] that many buildings were damaged or demolished owing to the lack of seismic detailing in structural elements. In addition, the researchers revealed that most of these buildings collapsed or were seriously damaged due to the poor detailing of columns. In most of these buildings, inadequate confinement reinforcement was observed and the structural failure of columns was preceded by reinforcement buckling and concrete crushing. It was demonstrated by the site investigations that the column reinforcement consisted of plain bars with 90-degree hooks placed at approximately 200 mm to as high as 500 mm spacing. Besides, the use of plain reinforcing bars for longitudinal reinforcement with no crossties was typical in most of the cases in the region.

In 1995, the city of Dinar was hit by an earthquake that caused extensive damage not only in Dinar but also in nearby towns and villages. As stated in the official reports [4, 5], the destroyed buildings were about 40-50% of the entire building stock in the region. Design and construction errors such as insufficiently confined structural elements (beams, columns and beam-column joints), low concrete quality and lack of inspection during construction were reported to provoke severe damaging and even collapsing of the buildings.

The earthquake that occurred in Adana-Ceyhan in 1998 caused extensive damage in many reinforced concrete (RC) buildings. The researchers [6, 7] pointed out that these buildings suffered from inappropriate selection of the structural system and design insufficiencies such as asymmetric and irregular structural designs. In addition, building failures due to lateral monolithic toppling over of the upper stories as a result of crushing and plastic hinging at the ground storey columns were majorly reported. Insufficient confinement detailing was commonly surveyed in the seismic area such as wide stirrup spacing, 90-degree hooks that triggered premature bar buckling in columns.

The devastating Kocaeli and Düzce earthquakes caused extensive damage in Southern and South-Eastern Marmara region. In Kocaeli, the buildings with 4 to 6 floors suffered the heaviest damage inflicting most of the casualties as declared by the researchers [8-15]. The predominantly used structural system in the region was reported as reinforced concrete frame with masonry infills. It was stated that the frame systems were predominantly designed for gravity loads and consequently many buildings collapsed by performing inelastic cycles during seismic excitations without providing stipulated drift demands. Extra masses above the ground storey imposed excessive amounts of base shear and deformation demands on ground storey columns. Consequently, these columns experienced heavy damage because of the insufficient confinement reinforcement and lack of seismic detailing. According to the researchers stated above, the most common practice encountered was transverse reinforcement including 8 mm diameter plain bars placed at 300 mm or wider spacing with 90-degree hooks that resulted in compression crushing or diagonal tension failures in columns.

On May 1 2003, an earthquake on Eastern Anatolian Fault (EAF) struck eastern Anatolia, Bingöl causing damage to hundreds of reinforced concrete and masonry buildings in the city and surrounding villages. The official reports [16-20] indicated that the present structures in the city were reinforced concrete buildings up to five or six stories, unreinforced masonry structures and himis (buildings that were composed of timber frames and braces with adobe infills). Most of the newly constructed reinforced concrete structures, particularly after 1999, were observed to be collapsed

or heavily damaged since it was stated by the site investigators that the code requirements were not abided. Thus, the code compliancy of confinement detailing in frame members determined the performance of the buildings during the seismic action. Moreover, it was denoted that heavy masonry infills above the ground storey increased the overall mass of the structure and put the burden of energy dissipation primarily on the first storey columns. The collapse of these buildings was attributed to the increased drift demands and insufficient deformation capacities of columns. The confinement reinforcement detailing that was inspected after the earthquake consisted of widely spaced plain reinforcing bars that were bent 90-degrees. Inadequate transverse detailing was reported to cause excessive shear cracking and trigger longitudinal bar buckling due to the insufficiency of confinement in columns.

1.2. Retrofit Needs

The apparent damage distribution observed in aforementioned earthquakes that struck Turkey emphasized the necessity of structural retrofitting in buildings having light to moderate damage. In addition, newly built structures in seismic regions should be investigated concerning the earthquake code compliancy.

According to the previous research report by METU research team [20], the damage observed in reinforced concrete structures was primarily due to inappropriate selection of the structural system. In addition, structural deficiencies such as discontinuous lateral load carrying system, abruptly changing lateral stiffness/strength (that yields the formation of weak/soft stories), overhangs, captive columns and deviated plan/elevation were shown to be responsible for the observed damage during earthquakes. The additional factors that induced structural damage were pointed out as inappropriate and non-seismic structural detailing in design and construction. It was also declared that the non code-compliant design circumstances in terms of member strength and ductility were exacerbated by poor workmanship and inadequate inspection during construction. Herein, poorly detailed and inadequate lateral reinforcement in structural members was reported to be one of the major shortcomings that led to severe damage in structures. Further, the major deficiencies observed in structures were summarized under the headlines of non

code-compliant member design, poor material quality, abruptly changing structural system and poor construction practice. Considering these frequently observed inadequacies in RC structures during a ground motion, rapid retrofit methods should be implemented especially in framed systems in order to make structures sustain the required deformation demands.

1.3. Seismic Retrofitting

The evaluation of existing RC structures located at seismically active regions has been found to be a critical issue. Hence, the seismic rehabilitation strategies namely, recovering/upgrading original structural performance and reducing the seismic response in order to reduce seismic vulnerability of the building, can be accepted as summarized by Sugano [21]. As shown in Figure 1.1, recovering the original performance of a structure can be achieved by repairing or replacing the damaged parts of the structure. For performance upgrading, several methods can be applied by means of strengthening and stiffening. The structural irregularities in terms of stiffness and strength distribution can be resolved by changing the structural configuration. Another task in rehabilitation was indicated as using energy dissipation devices that will improve the damping characteristics of the building and will lead to lower structural seismic demands. Additionally, the fundamental period of structures can be increased by implementing ground isolation and increasing masses to reduce seismic response.

Since the vulnerability of the buildings in Turkey revealed the major deficiencies in the structural members after the earthquakes as shown by post-earthquake reports [1-20], the most proper rehabilitation strategy can be accepted as upgrading original performance by means of strengthening of existing structures. This strategy suits the retrofit needs of Turkey due to its rapidity in implementation and economic reasons. For long-term, different strategies can be applied as pointed in Figure 1.1. Fukuyama et al. [22] investigated the details under the heading of seismic strengthening task that was introduced by the previous study of Sugano [21].

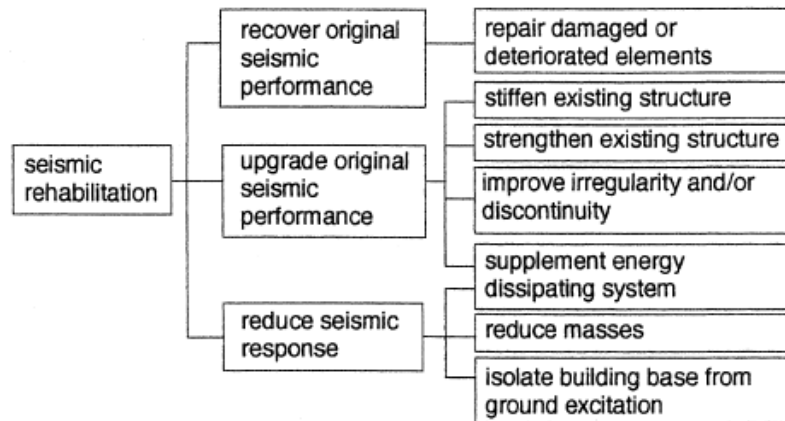


Figure 1.1 Seismic rehabilitation strategies [21]

In this study, typical seismic strengthening methods were outlined in three main sections: (a) increasing strength, (b) increasing strength and ductility and (c) increasing ductility. Among various strategies summarized in Figure 1.2, the newest methods were shown as member jacketing strategies using steel, concrete and fibers. Herein, instead of using traditional techniques of concrete or steel jacketing, rapid and simpler methods should be selected as addressed in Figure 1.2.

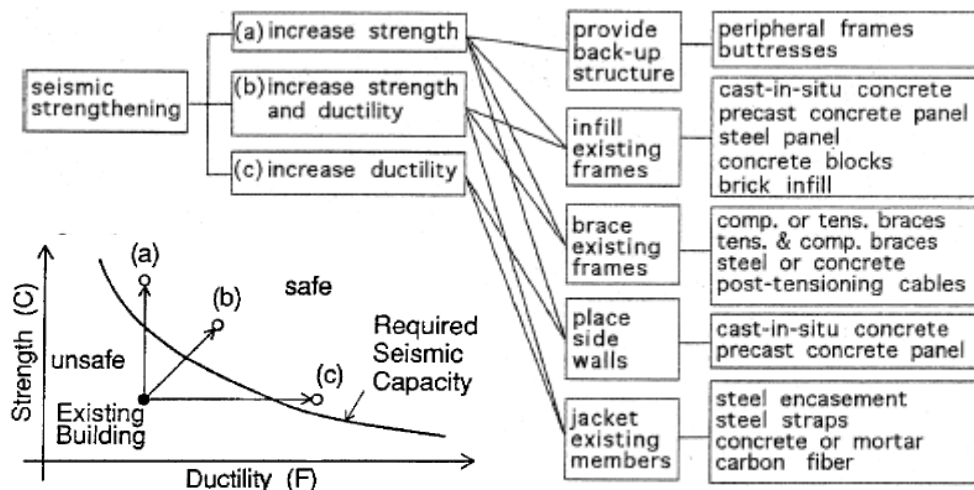


Figure 1.2 Typical seismic strengthening methods [22]

Thus, FRP jacketing method to increase ductility can be utilized in structural members easily by its high construction workability in addition to its anti-corrosion, high strength and lightweight characteristics. For construction works, the use of FRP was reported as beneficial owing to its enhanced characteristics of durability, abrasion, fatigue, elevated temperature resistance, strength to weight ratio and service life [23]. However, interrelated with these factors, the disadvantages of FRP systems were indicated as its high implementation cost, low resistance to alkalis, radiation, moisture and inconsistent material properties with other materials. As reported by ACI Committee 440 [23], FRP composite products were first used for the construction of RC structures in FRP reinforcing bar applications in concrete. Furthermore, FRPs were developed for special needs in RC construction such as nonmagnetic properties and the structural members under chemical attack. The major development in FRP technology for civil engineering applications was indicated as externally bonded FRP for strengthening and repairing of RC structures. Since many of the structures were built and rehabilitated around the world with FRP, the utilization of FRP-based systems has gained attraction due to the aforementioned advantages in pre and post-construction processes. The structural applications of FRP include retrofitting of beams, columns, beam-column joints, shear walls and slabs. ACI440 also states new application areas of FRP such as reinforcing bars, grids and tendons for concrete confinement in addition to prestressed FRP tendons. The main areas that are being explored for the FRP research are concrete repair and reinforcement, bridge deck repair and new installation.

1.4. Literature Survey

The efficiency of FRP based rehabilitation techniques in structural and non-structural members has proven that the improvements in FRP retrofitting technology can be successfully applied to the structures and can be used in structural design. Accordingly, considering the vertical and lateral load transferring mechanism in a building between the structural members, the most vulnerable structural elements are columns. Since any successive failure in columns can result in total collapsing of the structure, the design of the columns should be done vigilantly

In order to implement FRP retrofitting in structural members such as columns, the mechanism of FRP confinement in RC cross sections should be analyzed comprehensively taking the FRP material properties and FRP confinement characteristics into account. Mainly, FRP wrapping in fiber direction around the perimeter of the columns are used for enhancing confinement properties and shear capacities. Besides, the FRPs are used for flexural strength improvement purposes by utilizing fibers along the column axis.

In the literature, confinement properties and major characteristics of FRP retrofitted RC columns were studied by many researchers. Mainly, three FRP types were used in these studies namely carbon (CFRP), glass (GFRP) and aramid (ARFP). The FRP retrofitted columns were tested under axial compression and reversed cyclic lateral loading. The parameters under investigation were primarily corner round-off radius, column aspect ratio and the number of FRP layers wrapped around the column.

1.4.1. Columns under Axial Compression

The axial compression tests for the columns were conducted by many researchers and some of the leading studies are presented below. By these primary studies in FRP confined concrete under axial compression, the cyclic behavior and consequent seismic performance of the columns was obtained more accurately.

Demers and Neale (1994) [24] conducted an experimental series of small-scaled unreinforced columns with square or circular sections that were wrapped with unidirectional sheets of CFRP and GFRP. The specimens were wrapped with FRP providing a confining pressure of 5 MPa. Increase in axial capacity and ultimate strain was reported over the unjacketed specimens. The observed results of the tests revealed that FRP wrapping increased the strength and ductility of the unwrapped specimens. Demers observed the jacket rupture strains at strain levels of 0.005 to 0.01 formerly whereas the material tensile tests indicated a strain of 0.015. The researchers also examined few confinement models and concluded that the models overestimated the specimen capacity.

Demers et al. (1995) [25] studied the effects of different amounts of FRP materials wrapped around both circular and square specimens on the RC column performance. The circular and square specimens were reported to show different performances under axial loading. For the circular columns, the entire cross section was confined since the circular specimens were comprised of uniform confining pressure around the entire circumference. This case was not valid upon square specimens while the square columns had high confining pressures at the corners but little pressure at their flat sides. Hence, the entire section was not effectively confined that resulted in lower strength improvement. The un-rounded corners caused this shape effect due to the stress concentration at the corners.

Picher et al. (1996) [26] examined the effects of fiber orientation in concrete cylinders wrapped with CFRP and evaluated the application of CFRP on rectangular and square shaped short columns. Twenty-seven short columns were CFRP wrapped with different fiber orientations and with specimens of circular, square and rectangular columns. Picher et al. tested specimens with corner radius in range of 3.3 to 50% of the section width. According to the test results, the authors claimed that ductility and compressive strengths of the cylinders were improved by CFRP confinement. Increasing the wrapping orientation angle resulted in axial stiffness degradation however; ductility and failure modes did not vary with the change in orientation angle. Further, increasing the corner round-off radius caused the behavior of square and rectangular columns to behave gradually similar to circular columns.

Mirmiran et al. (1998) [27] primarily studied the effects of shape and length on FRP confined concrete. In the axial compression tests, square and cylindrical specimens were used in order to investigate the effects of cross section on FRP confined concrete. Concerning the results of the tests, the authors observed that the confinement effectiveness for square shaped columns was lower than circular columns and hence both the corner radius and column rectangularity affected the level of confinement in RC columns. CFRP wrapped circular columns have great enhancement in response whereas this enhancement is minimal for square columns. The effect of column length to diameter ratios was found to be insignificant in strength and ductility within the range of 2 to 5. There was no stiffness difference

observed in initial or secondary slopes of the comparable specimens of different lengths regarding the axial and transverse strains.

Chaallal et al. (2000, 2003) [28, 29] conducted an experimental study including uniaxial tests of short rectangular columns to investigate the behavior of CFRP wrapped columns. The parameters considered were the concrete strength, the aspect ratio and the number of CFRP layers. According to the tests, greater the number of CFRP layers, the higher the increase in compressive stresses regarding the reference columns. In addition, for a given number of CFRP layers, the increase in axial capacity of the columns with lower concrete strengths was greater than higher strength columns. The maximum strength gain for low strength columns with respect to the reference column was higher than its high strength companion column. The unexpected behavior of rectangular columns having higher ultimate strengths than square columns was attributed to the requirement of further investigations on aspect ratio and confining effect of the plates of the testing machine.

Rochette and Labossiere (2000) [30] conducted a research program that concentrated on the behavior of square, rectangular and circular small-scale columns, which were wrapped by either CFRP or AFRP. The test parameters under investigation were the shape of the section, the aspect ratio, the stiffness of confinement and the corner round-off radius. The specimens had varying cross sectional shapes of square, rectangular and circular types that were strengthened with several layers of either CFRP or AFRP by varying corner round-off radii. In the tests, it was determined that the number of FRP layers and column round-off radius had a pronounced effect on column behavior. Each addition of a confining layer increased the stiffness that can be evaluated by the slope of the second portion of their stress-strain curves. The authors also added that when rounding of corners for square sections cannot be increased, additional confinement could be achieved by additional FRP wraps and they suggested the investigation of angle-ply wrap configurations as a potential way of achieving more strength and ductility.

Pessiki et al. (2001) [31] studied the axial behavior of small and large-scale circular and square columns confined with FRP composite jackets subject to monotonic,

concentric axial loads. Factors influencing the behavior of FRP confined concrete such as transverse dilation, confinement efficiency and their relationships to jacket properties were identified. In order to observe the axial characteristics of columns confined with FRP jackets, an experimental research was conducted addressing the issues including the axial and transverse dilation behavior of FRP confined concrete. In addition, the effects of section shape and the efficiency of FRP jackets in terms of strength and deformation capacity of FRP material was investigated. The plain concrete column tests consisted of small-scale circular and square columns. Following these tests, full-scale RC circular and rectangular columns were tested to failure under monotonically increasing concentric axial load. The full-scale RC columns had 90-degree bent transverse ties that represented typical pre-1971 design practice. The authors claimed that all the small-scale specimens had very stiff FRP jackets relative to their section dimensions hence it should be practical to use jacket stiffness' proportional to the cross sections. The jacket rupture strains were observed to be comparable to circular full-scale and small-scale tests. The authors concluded that the axial stress-strain capacities of the columns enhanced with increasing FRP jacket strength and stiffness while the strength and stiffness were stated to be functions of the number of plies. In addition, the square sections were not confined as efficient as circular sections due to the presence of ineffectively confined areas in square sections. The in-situ jacket rupture strains were found to be lower than the tensile coupon tests and an efficiency factor was introduced. A need for further research was suggested concerning different section aspect ratios and jacket properties.

Tan (2002) [32] conducted an experimental study examining the case of rectangular RC columns that were typical construction of monolithic housing apartments. The specimens were tested to failure under concentric load to investigate the effects of fiber types, fiber configuration and fiber anchors on the strength enhancement of columns. The specimens were strengthened with various configurations of unidirectional FRP sheets in longitudinal and transverse directions. A constant corner-rounding radius was used for all the FRP strengthened specimens. The transverse fiber sheets contributed to strength enhancement by confining the concrete and provided higher compressive strengths however, the longitudinal fiber sheets

could withstand compression if and only if outward buckling could be inhibited by transverse fiber sheets. The assumed confinement shapes are termed in two models. For the first one, the internal links were assumed to provide additional anchor points and confinement effects whereas the other model assumed that only column corners acted as anchor points that led to lesser amount of confinement. Increasing the amount of longitudinal fiber sheets led to higher strength and ductility however, this argument was only valid in cases of using longitudinal and transverse sheets together. If the transverse sheets were used for strengthening, only the ductility was improved. The fiber anchors improved the efficiency of transverse sheets and the longitudinal sheets by restraining them from buckling. Additionally, delamination of fiber sheets was more likely to be observed in GFRP rather than in CFRP throughout the column length. Tan recommended further work for fiber anchors and columns with similar section aspect ratios.

Shehata et al. (2002) [33] conducted an experimental study investigated the gain in strength and ductility of CFRP confined concrete columns. The studied variables in tests were the section shape and the amount of confinement expressed in number of CFRP sheets. In order to examine the effects of CFRP confinement on column strength and ductility, the columns in circular, square and rectangular shape were tested under axial compression. The column corners were rounded before CFRP wrapping in order to prevent the breakage of CFRP sheets due to sharp bends. It was shown that the highest strain values were obtained for confined circular columns. The confinement effectiveness was found to be maximum for circular ones and minimum for rectangular ones. The test results revealed that the strength enhancement provided by confinement was very sensitive to the cross-section geometry and the rate of increase dropped sharply as the geometry deviated from the circular one.

Lam and Teng (2003) [34] described a simple design-oriented stress-strain model for FRP confined rectangular columns. The authors had an origin of shortage in previous studies about design-oriented models and they further improved the understanding of FRP confinement mechanism in rectangular columns. Column aspect ratio and corner rounding radius was inspected as primary factors affecting

FRP confinement. The majority of the existing test database was found to be for low confinement levels that did not cover a sufficient range of confinement levels desirable for existing theoretical models. In addition, the data of low confinement was interpreted to display a relatively large scatter introducing undesirable uncertainty in existing theoretical models. Consequently, an experimental research was accomplished including circular, square and rectangular specimens. The strengthened specimens were wrapped in fiber direction around the specimen perimeter by CFRP with different corner-rounding radii. The obtained results pointing out the influence of CFRP amount and corner-rounding radius contributed to the proposed stress-strain model that was based on new expressions for compressive strength and ultimate axial strain. In the proposed model, the effect of section shape was properly accounted for by the introduction of shape factors and the definition of an equivalent circular column. The enhancement factors of stress-strain were defined based on the observation that the increase in section aspect ratio resulted in reduced compressive strength but an increased ultimate axial strain. Good correlation between the proposed model and the experimental database was achieved.

1.4.2. Columns under Cyclic Displacement Excursions

Several investigations to understand the behavior of FRP wrapped rectangular columns under cyclic excitations were also conducted simultaneously with the columns that were tested under concentric compression. Ever since the innovations about fiber-based materials were made, further research about using these materials for structural retrofitting purposes had been conducted to observe the performance of RC columns under reversed cyclic lateral excitations as much as axial compression. Hence, RC columns were reverse-cyclically tested and their lateral capacities were evaluated in order to verify the sustainable drift demands of the structure. Some of the leading studies that cover the primary research in the area of concrete jacketing are also presented below.

Aksan et al. (1989) [35] conducted one of the leading studies in the area of concrete jacketing. The researchers tested five specimens in order to observe the effects of concrete strengthening and repairing on the seismic performance of the column. In

this study, the effect of axial load during strengthening and repairing was also evaluated. The repaired columns were first damaged to failure and then repaired to enlarged sections under the presence or absence of the axial load. All columns were tested under constant axial load and reversed lateral displacement cycles. According to the obtained results, strengthening with concrete jacket was found to be very effective where 80 to 90% of monolithic specimen's capacity could be reached. In addition, strengthening under the absence or presence of axial load yielded close results. For repairing, in the absence of axial load during repairing almost 80% of monolithic capacity could be attained. However, for the case of repairing under axial load, the capacity was found to be much lower and it was recommended by the authors that strength of the core concrete should be disregarded.

Suleiman et al. (1991) [36] investigated the behavior of strengthened and repaired columns by concrete jacketing under axial and monotonic/reversed cyclic lateral loading. The parameters under investigation were the damage level before jacketing and the loading type. Test results indicated that the strengthened columns by concrete jacketing showed a comparable performance as the monolithic specimen under both monotonic and reversed cyclic loading. However, for the repaired columns by concrete jacketing, the stiffness and strength were lower than the monolithic specimen.

Seible et al. (1995, 1997) [37, 38] developed and implemented a new retrofit system consisting of continuous CFRP tows wrapped around RC columns within the design models including retrofitting by using variable jacket thicknesses along the column heights. The authors stated that ductile behavior could be achieved through added confinement in the form of hoop or transverse reinforcement in new and external jacketing in existing columns. In order to determine the required jacket thicknesses for different column regions based on aforementioned failure types, design equations were derived by Seible et al. 1995 [37]. In order to validate this design approach, an experimental study was conducted in order to approve the performance of CFRP jacketing tests. The experimental objectives in this study were meeting or exceeding retrofit performance of comparable steel jacket retrofits in comparison with as-built and un-retrofitted test specimens. The shear retrofitting of rectangular column in

double bending was applied to convert brittle shear failure to ductile flexural failure considering the previously stated target column performances. In addition, flexural retrofitting of rectangular RC column was applied to achieve at least twice the unretrofitted displacement ductility level. It was demonstrated that CFRP jacketing systems could be just as effectively as conventional steel jacketing in improving the seismic response characteristics of substandard RC columns. The effectiveness and accuracy of established design models was validated by large-scale bridge column tests for column failure modes of shear and plastic hinge confinement. In addition, the CFRP retrofitting concepts and developed design guidelines were found to be ready for actual column retrofit applications since the design criteria provided sufficient structural effectiveness.

Saadatmanesh et al. (1997) [39, 40] conducted an experimental investigation to observe flexural behavior of earthquake damaged RC columns repaired with CFRP. Rectangular RC specimens were tested to failure under reversed inelastic cyclic loading. The design details such as inadequate transverse reinforcement and insufficient starter bar length were used to simulate the existing seismic deficiencies in RC columns. The major design parameter used in the study were column cross-section, longitudinal reinforcement ratio and reinforcement development details that extended into the footing. The spliced and continuous bars were used in design for the columns to investigate the bond failure mechanisms in the lapped region and longitudinal bar buckling during the test. According to the observed results in the tests, spliced columns failed due to debonding of the longitudinal reinforcing bars in the lapped region whereas the column having continuous reinforcement failed in shear with longitudinal bars separating from the core concrete. The repaired columns with continuous reinforcement exhibited relatively larger lateral displacements at low load levels compared to the reference columns due to the pre-existing damage in the form of bond deterioration between reinforcement and concrete with inducing cracks during the test. However, the lateral strength of increased compared to the reference column. The repaired column having lap-splice, showed small reduction in lateral capacity. Consequently, CFRP composite wraps were found to be effective in restoring the flexural strength and ductility capacity of pre-damaged rectangular RC columns.

Gergely et al. (1998) [41] performed the application of CFRP jackets for three columns, cap beam of an existing concrete bridge pier was and evaluated CFRP rehabilitated condition of the pier both analytically and experimentally. This bridge pier was selected for CFRP retrofitting owing to the main reasons of having inadequate seismic detailing and severe corrosion-related deterioration. Hence, the design procedures were developed for using the CFRPs to restore the use of it as close as to its original condition for gravity loads by enhancing the shear capacity of the columns, cap beam and joints and to improve the performance of the pier by enhancing the ductility of the pier. The strain-stress models for steel and CFRP confined concrete were used considering the stiffness and ductility reduction for CFRP confinement due to the square shape of the columns. The design of the columns was evaluated for both confinement enhancement effects and shear strength. The analytical data and experimental observations were found to be very close to each other and the enhancement in ductility was achieved by using CFRP retrofitting. The advantage of CFRP retrofitting was found to be a fast and non-intrusive since it did not increase the weight of the pier as compared to mantling techniques.

Pentelides et al. (1999) [42] conducted lateral in-situ tests of two bridge bents to determine the strength and ductility of an existing concrete bridge and the improvements was achieved by using CFRP retrofitting. The objectives of this study were to determine the capacity of the as-built bent and to determine the improvement in strength and ductility of the CFRP retrofitted bent that was designed to double the displacement ductility of the as-built condition. The CFRP retrofitting of column plastic hinges provided confinement of the core and prevented spalling of the cover that afforded the lateral stability of the longitudinal bars. The CFRP design layout was designed as a square jacket with twice the CFRP thickness required for an equivalent circular jacket. The conducted in-situ tests had shown that the CFRP retrofitting could greatly enhance the displacement ductility of the bridge bent. In the tests, it was observed that since the as-built bent had extensive diagonal cracks extended to cap beam, flexural cracks in the upper region of columns and radial cracks around the columns. Thus, the CFRP composite design that was based on doubling the ductility of the as-built bent was found to be successful.

Ghosh (2002) [43] investigated square RC columns detailed with poor lap-splices and inadequate transverse confinement at the plastic hinge region. The experimental study conducted herein was directed towards the effectiveness of CFRP laminates in strengthening and repair of columns under simulated earthquake loading. The parameters studied in the program were the effect of the presence of lap splices, effectiveness of CFRP, effects of axial load level, shape of column cross-section and confinement details. The columns were detailed as per the provisions of ACI codes. All the as-built columns exhibited considerable damage in the zone of maximum moment near the column-stub interface in the form of cracking and spalling of concrete and slippage/buckling of the rebars. The unretrofitted specimens developed an unstable response due to premature lap-splice failure between the longitudinal column bars and the starter bars. The columns tested under high levels of axial load suffered the most extensive damage due to considerable reduction in ductility along with buckling of the reinforcing bars. For the CFRP retrofitted columns, under low axial loads the failure was governed by the slippage of rebars due to gradual separation of the column from the stub without any rupture of CFRP. The confining pressure provided by CFRP wrapping helped to delay the initiation of internal cracking and hence prevented the splitting of the concrete around the spliced longitudinal rebars. In the columns under high axial load, although the failure was initiated by the slippage of rebars, rebar buckling occurred at higher deflection levels and this fact resulted in the rupture of CFRP in buckling region.

Ye et al. (2003) [44] investigated the seismic performance of RC columns that were strengthened and repaired with CFRP strips that were tested under constant axial load and lateral cyclic excitations. For the strengthened columns, CFRP implementation was done under sustained axial load to imitate strengthening under service conditions and the repaired columns were retrofitted by CFRP after pre-damaging the column to its yield level. The specimens square cross-section with a constant corner-rounding radius to avoid stress concentrations in CFRP sheets. The main parameters under investigation were the amount of CFRP, presence of sustained axial load during strengthening and the effects of repairing the column pre-damaged to the yield level. The observed results implied that the CFRP sheets prevented the columns fail in shear and the flexural capacities were held constant

with an increased ductility. As the flexural deformations increased, the expansion in the concrete compression zone increased and thus the CFRP strips were ruptured with the amplified stresses in the fibers. Hence, the specimens that were wrapped with highest amount of CFRP showed the best performance among all specimens. The expansion characteristic of the concrete had a tendency to increase by the amount of CFRP layers provided. For strengthened columns, the wrapped CFRP sheets contributed to shear and flexural capacities with the confinement effect of the strips. Moreover, when the flexural mode was dominated in columns, the CFRP strains were mainly caused by concrete expansion rather than shear deformations. The CFRP strengthened column under sustained axial load had CFRP strains lower than the specimens that were strengthened under the absence of axial load. This was explained by the authors that the expansion of concrete was initiated before wrapping of the CFRP strips. For the repaired specimens, a quicker development of CFRP strains was observed than strengthened columns due to the formation of larger shear deformations before repairing the column. However, the development of the CFRP strains in repaired columns showed a decreasing tendency after yielding as compared to strengthened columns.

Iacobucci et al. (2003) [45] studied the possible effects of strengthening and repairing square shaped RC columns by using CFRP and GFRP jackets. The main variables investigated in the study were the number of CFRP layers in the hinging zone, the presence of column damage and the level of applied axial load. All specimens were tested under constant axial load with reversed cyclic flexural and shear loads in order to simulate seismic loading conditions. The specimens represented seismically deficient columns with insufficient lateral reinforcement. While the strengthened specimens were wrapped with CFRP before the application of any load, the repaired specimens that were cycled until yielding of reinforcement initiated and cover spalling occurred, were repaired under axial load. It was concluded from this study that CFRP retrofitting increased the ductility and energy dissipation capacities of the columns, improving the seismic resistance in the process. It was observed that CFRP jackets provided extra confinement to critical sections and cyclic behavior improved through decreases in stiffness and strength degradation rates as the number of CFRP layers increased. For the repaired columns,

CFRP retrofitting enhanced the seismic behavior although this enhancement depended on the severity of the damage sustained. Thus, more CFRP layers were needed for highly degraded columns to achieve a performance similar to the strengthened columns. Moreover, higher axial loads degraded overall column response and put additional demands on CFRP jackets to restrain critical regions. Therefore, a larger amount of CFRP was required for columns subjected to higher axial load levels to realize similar performance to retrofitted columns under lower axial loads.

Harajli and Rteil (2004) [46] undertook an experimental investigation that evaluated the seismic performance of rectangular RC columns designed for gravity load and confined externally with CFRP sheets. The main parameters under investigation were the reinforcement ratio, the area of CFRP sheets and the volume fraction of CFRP sheets. This study contributed to revealing of the mechanism by which confinement reinforcement enhances the deformation capacities and ductility of the hinging regions of gravity load-designed columns under cyclic loading. For strengthening purposes, unidirectional CFRP sheets were implemented in one layer wide strip or one wide strip plus three equally wide strips. For the unstrengthened columns, significant loss in load resistance due to concrete crushing at the column base and extensive spalling of concrete was observed. The CFRP confinement in the hinging zone improved the bond resistance of the spliced columns and a more ductile and stable behavior was attained. No bond failure or CFRP fracture was observed. In steel fiber reinforced columns, the flexural and splitting cracks were inhibited in the hinging zone due to the improved bond performance of the reinforcing bars and less concrete spalling compared to the control specimens.

Bousias et al. (2004) [47] tested rectangular columns emulating older construction to investigate the effects of seismic retrofitting with FRP (carbon or glass) layers as well as the effects of reinforcing bar corrosion on the retrofitting effectiveness. Experimental results on the effectiveness of FRP wrapping were stated as abundant for circular columns, to a limited extent for square columns but scarce for columns with rectangular cross-sections where the effectiveness of FRP in confining the wide side for the section was questioned. Since the FRP retrofitting was used mainly for

upgrading undamaged columns, the authors pointed out the impact of previous damage on FRP rehabilitation effectiveness. The specimens were tested in strong and weak directions. The repaired specimens were wrapped with FRP after the pre-damage was induced by a preliminary cyclic test that carried the column beyond yielding. Although the strength of unretrofitted columns was reduced by corrosion, as it was controlled by the flexural capacity and affected by the loss in longitudinal steel area, hysteretic behavior and deformation capacity were not adversely affected by corrosion. For the repaired columns, more rapid strength degradation and lower deformation capacities was observed as compared to the unretrofitted columns. This behavior was attributed to the fact that, concrete had already experienced permanent lateral expansion in the absence of FRP jacket and reached its crushing strain with the lesser activation of the FRP wraps before the repairing process. This fact was observed to be much larger in the strong direction due to the presence of a narrower compression zone where the effects of FRP confinement were most significant. Using GFRP instead of CFRP layers for confinement by ensuring the same level of extensional stiffness led to the columns exhibit the same performance whereas provided slightly lower strength but a little improved deformation capacity

Sause et al. (2004) [48] carried out an experimental and partly analytical investigation that included the use of CFRP composite jackets as a method of retrofitting non-ductile square RC building columns. The effects of amount of CFRP layers on the RC column performance was observed concerning the design parameters of CFRP jacket transverse strain and ultimate concrete compressive stress. Although the conventional method of determining retrofitting jacket requirements is based on limiting the jacket strain, concrete compressive strain capacity will control the available curvature capacity before the jacket strain capacity is exhausted. Thus, concerning these limitations, the CFRP jacket design was carried out. The reversed cyclic lateral load was applied to the column that provided an axial-flexural column response and eventual failure. The results of this experimental and analytical study revealed that the use of CFRP jackets to confine the inelastic hinge region of non-ductile square building columns greatly enhanced the deformation capacities without significantly increasing their strength or lateral stiffness. The deformation capacity increased with increases in jacket thickness. The

authors also suggested that to achieve the desired retrofit column behavior, knowledge of the concrete axial strain capacity was required. The enhancement in the strain capacity was provided by sufficient confinement pressure while limiting the jacket transverse strains.

Haroun and Elsanadedy (2005) [49] conducted an inclusive testing program on scaled models of RC bridge columns with insufficient lap-splice length. Square columns were tested as a part of the study in flexure and axial loading as the test setup. In the experimental study, the effects of jacket thickness, design rupture strain and type on the behavior of RC columns were studied. The retrofitted columns were designed for a jacket strain of 0.001 to provide a minimum confinement pressure of 2.0 MPa in the lap-splice region and the required jacket thickness was increased by a factor of 1.5 as stated in Caltrans guidelines. However, in view of ductility constraints all columns failed to meet the design requirements. None of the square-jacketed columns failed due to extreme concrete crushing within the plastic hinge zones but rather due to lap-splice slippage at low ductility, as the composite jacket showed no signs of tensile failure due to concrete confinement. According to the test results, it was concluded that owing to the short lap-splice length and insufficient transverse reinforcement, the concrete cover started to spall prematurely and anchorage of the lapped bars degraded rapidly due to the splitting action under fully reversed cyclic loads. In addition, considering the shape of the rectangular sections the confining action could only induce near the corners of the jacket, as the pressure of the concrete against the sides of the jacket tended to bend them outward. Hence, composite jackets could not develop the strength necessary to inhibit lap-splice slippage in square columns and failed to satisfy the ductility requirements of design guidelines. Accordingly, circular or elliptical composite jackets were suggested to be more effective.

Galal et al. (2005) [50] conducted an experimental program that had the objective of evaluating the seismic response of FRP retrofitted (glass and carbon) RC columns having various transverse reinforcement ratios. The columns were tested under constant axial load and lateral cyclic excursions with double curvature. The first test series were compliant with Canadian Code however the second set of test specimens

were non code-compliant. The column retrofitting schemes were proposed in order to enhance their shear resistance and prevent the brittle shear failure ensuring plastic hinge formation. The parameters of anchorage by means of fibers, lateral reinforcement and FRP amount were selected in order to investigate the column performances by implementing proper retrofitting methods. The test results indicated that FRP anchoring could be used for enhancing the shear and energy dissipation capacities for RC short columns by improving confinement characteristics in terms of strain reduction in lateral steel and strain amplification in fibers. In addition, providing higher transverse reinforcement ratio was observed to reduce the FRP jacket strains and likewise increasing the CFRP layers decreased the transverse and FRP strains. The authors reported that carbon fiber anchors led to a more enhanced behavior in terms of lateral and energy dissipation capacities. Thus, CFRP wrapping along plastic hinging regions and providing extra confinement by CFRP anchors was recommended as the most proper retrofitting method for columns.

Chang and Tsai (2005) [51] investigated the performance of FRP wrapped rectangular full-scale RC columns. The specimens were tested under reversed cyclic loading. In order to confirm the effectiveness of FRP materials in RC columns, the specimens were designed according to either general design requirements having brittle performances or seismic design provisions with ductile detailing. Although CFRP had been used for strengthening in plate form as additional external bending reinforcement, its effects for shear strengthening was not fully established. The use of CFRP for shear strengthening had the disadvantages of anchorage and handling on site hence, the CFRP L-shaped plates were developed due to their lightweight and ease of application. The retrofit objective of this study was to provide additional lateral reinforcement so that the strengthened columns would have the same level of lateral confinement as the specimen having seismic detailing. The columns retrofitted either by CFRP or CFRP L-shaped plate, were observed to behave in a more ductile manner than the column that was designed according to the seismic provisions. The cyclic performances of the columns revealed that the specimens retrofitted with either CFRP or CFRP L-shaped plates showed similar behavior before the CFRP laminates delaminated. Since these tests were the first application of CFRP L-shaped plates, further research should be conducted to confirm the observed results.

Haroun and Elsanadedy (2005) [52] conducted experimental studies on scaled models of bridge columns strengthened and repaired with FRP (glass and carbon) jackets. Half-scaled rectangular columns were tested under fully reversed cyclic shear in a double bending configuration. It was concluded from this experimental study that inadequate transverse reinforcement and shear provisions, led to the columns to fail in a brittle manner involving severe stiffness, strength and physical degradation at very limited displacement ductility as the reference specimen. Contrary to the common assumption of 45-degree shear plane inclination, 30-degree inclination planes were observed in the tests. Accordingly, most of the codes were found to be conservative for estimating the shear capacity of RC columns. FRP retrofitting scheme was observed to enhance the shear strength of the columns by providing passive confinement within the hinging zone and hence the brittle failure mode in shear was changed to ductile flexural failure. The authors also noted that the composite jackets had shown their advantage over steel jackets since they did not alter column stiffness and consequently the dynamic characteristics were not affected for the bridges.

1.4.3. FRP Design Guidelines for Columns

RC elements having poor performance under lateral loads owing to the inadequate seismic detailing revealed the urgent need of a retrofitting code comprising the use of externally bonded FRP systems for structural members. The design guidelines were developed for strengthening structural or non-structural elements (beams, columns, beam-column joints, masonry walls etc.). The FRP based strengthening methods that were explained in the codes are alternatives of the previously implemented methods such as steel jacketing, steel plate bonding and concrete mantling. In order to illustrate the current design philosophy of externally bonded FRP systems in structures, the codes of ACI440.2R and the Turkish Earthquake Code Appendix-7E are explained below for the column retrofitting applications. Column rehabilitation techniques are explained thoroughly in the specified strengthening codes.

1.4.3.1. ACI440.2R

The code developed by ACI Committee 440 [53] considers the characteristics of FRP confined columns majorly dependent on the fiber reinforcement to concrete contact. In order to avoid local stress concentrations in the FRP wrapped region, flat or convex surfaces are recommended with a minimum 13 mm of corner round-off radius. In ACI440, axial capacity enhancement of concrete is unveiled by transversely wrapped FRP layers regarding the column longitudinal axis. The axial capacity and compressive strength of FRP confined concrete are calculated by Equations 1.1 and 1.2. The lateral pressure due to FRP confinement can be calculated by Equation 1.3 that is in linear proportion with the FRP rupture strain. Combination of compressive and shear forces acting on the structural members enforces a limitation on ultimate FRP strain that is presented in Equation 1.4. This limit should be employed for shear, axial and ductility enhancement.

$$\varphi P_n = 0.80\varphi \left(0.85\psi_f f_{cc}' (A_g - A_{st}) + f_y A_{st} \right) \quad (1.1)$$

$$f_{cc}' = f_c' \left[2.25 \sqrt{1 + 7.9 \frac{f_l}{f_c'}} - 2 \frac{f_l}{f_c'} - 1.25 \right] \quad (1.2)$$

$$f_l = \frac{\kappa_a \rho_f f_{fe}}{2} = \frac{\kappa_a \rho_f \varepsilon_{fe} E_f}{2} \quad (1.3)$$

$$\varepsilon_{fe} = 0.004 \leq 0.75 \varepsilon_{fu} \quad (1.4)$$

where f_{cc}' , f_c' and f_y are the confined, unconfined concrete strength and steel yield strength, respectively. f_l represents lateral confining pressure due to FRP. A_g and A_{st} are the gross and steel area in the cross section. ψ_f is the reduction factor. κ_a is the efficiency factor for FRP reinforcement, ρ_f is the FRP volumetric ratio, f_{fe} and ε_{fe} are the effective stress and strain in FRP, respectively. To enhance ductility, ACI440 denotes that concrete compressive strains should be developed by adequate FRP confinement regarding the displacement demands. For FRP wrapped members, maximum compressive strain can be calculated by Equation 1.5. In order to introduce member rectangularity, the FRP reinforcement ratio and shape efficiency factor can be calculated by Equations 1.6 and 1.7, respectively.

$$\varepsilon_{cc}' = \frac{1.71(5f_{cc}' - 4f_c')}{E_c} \quad (1.5)$$

$$\rho_f = \frac{2nt_f(b+h)}{bh} \quad (1.6)$$

$$\kappa_a = 1 - \frac{(b-2r)^2 + (h-2r)^2}{3bh(1-\rho_g)} \quad (1.7)$$

where b , h and r are the column dimensions with corner rounding radius, n represents the number of FRP plies and ρ_g is the longitudinal reinforcement ratio. In addition, for the members with column section aspect ratios greater than 1.5, FRP confinement should be regarded as insignificant.

1.4.3.2. Turkish Earthquake Code

The Turkish Earthquake Code [54] includes FRP based strengthening techniques in Appendix-7E that is primarily developed for retrofitting purposes. In order to improve the compressive strength of the columns using FRP wrapping, the section aspect ratio should not exceed 2. The column cross-sections may be modified by changing the section from rectangular to ellipse and the effectiveness of FRP will be improved. In the ellipse sections, the ratio of long to short side lengths should not exceed 3. While calculating the axial strength of a FRP wrapped column, the f_{cc} value should be used instead of f_{cm} as shown in Equation 1.8. The lateral pressure provided by FRP should be calculated in the form of Equation 1.9. The rupture strain of FRP, ε_f should be used in the form as shown in Equation 1.10. In Equation 1.9, b and h are the cross-section dimensions and r_c is the corner-rounding radius for square and rectangular columns. κ_a can be calculated by Equation 1.11 considering different cross sections.

$$f_{cc} = f_{cm} \left(1 + 2.4 \frac{f_l}{f_{cm}} \right) \geq 1.2 f_{cm} \quad (1.8)$$

$$f_l = \frac{1}{2} \kappa_a \rho_f \varepsilon_f E_f \quad (1.9)$$

$$\varepsilon_f \leq \begin{cases} 0.5\varepsilon_{fu} \\ 0.004 \end{cases} \quad (1.10)$$

$$\kappa_a = \begin{cases} 1 & \text{circular} \\ \left(\frac{b}{h}\right) & \text{ellipse} \\ 1 - \frac{(b-2r_c)^2 + (h-2r_c)^2}{3bh} & \text{rectangular} \end{cases} \quad (1.11)$$

where f_{cc} , f_{cm} and f_l are the confined, unconfined strengths of concrete and the lateral pressure provided by FRP, respectively. κ_a and ρ_f are the confinement efficiency factor and the volumetric ratio of FRP, respectively.

For ductility enhancement, the ultimate concrete strain corresponding to FRP-confined compressive strength can be obtained as shown in Equation 1.12. The value of f_l can be calculated as stated in Equation 1.9. In order to improve ductility by FRP wrapping, the minimum enhancement in concrete strength should be sustained as stated in Equation 1.8. While performing linear elastic analysis methods, if the value of ε_{cc} (Equation 1.12), is higher than 0.018, the column should be considered as confined. For other cases, the column can be considered as unconfined. For non-linear analyses, while calculating the moment-curvature responses, the idealization of bilinear stress-strain curve can be used for FRP-confined concrete. In this relationship, the values of concrete strength and 0.002 can be used for the bending point. The ultimate points in the stress-strain relationship can be derived using Equations 1.8 and 1.12.

$$\varepsilon_{cc} = 0.002 \left(1 + 15 \left(\frac{f_l}{f_{cm}} \right)^{0.75} \right) \quad (1.12)$$

1.5. Objective and Scope

The major objective of this research program includes improving the seismic performance of columns under dominant flexural effects by strengthening and repairing with CFRP wrapping. In addition, the objective also involves an analytical work to estimate envelope column response and design-oriented study to predict the ultimate performance of columns in terms of ultimate drift levels. For the experimental work, three series of square and rectangular columns were CFRP retrofitted and tested under constant axial load and reversed cyclic lateral excursions in order to simulate the behavior of a typical non code-compliant building column in as-built and retrofitted conditions. The columns with non-seismic details were used in the experimental program that had continuous plain bars and 90-degree hooks at tie ends. For all the test series, test results were evaluated in terms of Lateral Load (P) vs. Lateral Deflection (Δ), Moment (M) vs. Average Curvature (K_{avg}), Moment (M) vs. Fixed-end Rotation (FER), Strain (ϵ) vs. Drift Ratio (DR) vs., Cumulative Dissipated Energy (CDE) vs. Cumulative Drift Ratio (CDR) and Secant Stiffness (SS) vs. Cumulative Drift Ratio (CDR). In addition, deflection profiles that record each deflection level at various locations along the column height were assessed. Further, the column tip deflections were evaluated considering its flexural and fixed-end constituents.

The major parameters investigated in the first test series were the CFRP amount and the presence of the axial load during strengthening. The effect of CFRP amount on column performance was evaluated by wrapping either 1 or 2 layers of CFRP around the columns. Besides, the effect of the presence of axial load during strengthening was assessed by sustaining the axial load level on CFRP wrapped square columns. The second series focused on the effects of initial pre-damage, sustained axial load during CFRP repairing and corner rounding radius on the seismic performance of square RC columns. The specimens were first laterally loaded to introduce a moderate damage and then retrofitted with one layer of CFRP under both the presence and absence of the axial load. A reduced corner rounding radius was employed in order to simulate more rapid CFRP implementation conditions. In the last series, the effect of different CFRP anchor dowel configurations and CFRP

confinement level on the performance of CFRP strengthened rectangular columns was examined. All the specimens were loaded laterally in the direction of their strong axis and wrapped with one layer of CFRP considering two different CFRP anchor configurations in order to monitor the effects of confinement ratio on the column performance.

In addition, an analytical study was conducted to predict the behavior of as-built and retrofitted columns. In the analytical part of the research, the column performance was predicted using constitutive models of concrete, steel, bond-slip and plastic hinging and compared with the experimental data. Thus, a program that estimates the column Lateral Load (P) vs. Tip Deflection, Moment (M) vs. Curvature (K) and Moment (M) vs. Fixed-End Rotation (FER) responses was developed.

Furthermore, a design-oriented study was carried out in order to predict the seismic performance of FRP retrofitted RC columns having rectangular cross-section. The parameters of FRP confinement, axial load and longitudinal reinforcement ratio were selected as the key parameters of design. The ultimate drift performance of the columns was estimated by using two approaches that were based on ultimate drift and ultimate concrete strain. Simple design equations regarding the column database were proposed and both of the design – oriented methods were evaluated by their comparisons with the experimental data so that the designer can select the proper method to implement. Lastly, conclusions and further recommendations in the light of this study are given. Subsequent appendix chapters include member stability checks, unexpected failure modes, model calibration test, hysteretic strain plots, used analytical program and the design example.

CHAPTER 2

EXPERIMENTAL PROGRAM

2.1. General

Current study concentrates on investigating the behavior of CFRP confined RC columns that were non-seismically designed ignoring the seismic design regulations in Turkey. All the tests in this research were conducted at Middle East Technical University Structural Mechanics Laboratory (METU-SML). The experimental research consists of testing non-seismically designed 18 RC columns (13 square and 5 rectangular) under cyclic reversed displacement excursions and constant axial load. For each of the test series, one column was tested as control specimen and the remaining four columns were either CFRP strengthened or repaired along the height of its possible plastic hinging region. Hereafter, the material properties, steps of specimen construction with details and test observations with analyzed data were presented.

2.2. Material Properties

The specific properties of the materials used in the experimental program such as concrete, steel and CFRPs are defined and experimentally obtained values are listed. For CFRPs, the material properties were directly taken from the manufacturer.

2.2.1. Concrete

Each column was cast vertically at the same time with a column stub, using three batches of concrete by a hand mixer. The used concrete mixture had particle sizes having different compositions of 0-3 mm sand, 3-7 mm and 7-15 mm aggregates. The mixture properties of concrete for target 28-day nominal concrete compressive strengths of 10, 15 and 20 MPa are shown in Table 2.1. In order to measure the concrete compressive strength of the specimens, three 150×300 mm concrete cylinders were cast simultaneously with the specimen for each batch of the concrete

mixture. After removing the formwork, the specimen and the concrete cylinders were wrapped with wet burlaps to assure proper curing. Concrete cylinders were tested by a pressure controlled axial testing unit with a loading rate of approximately 2000 N/s to monitor the compressive strengths until the test day.

Table 2.1 Concrete mixture properties for different target nominal 28-day concrete compressive strengths.

Strength (MPa)	0-3 Sand (kg/batch)	3-7 Aggr. (kg/batch)	7-15 Aggr. (kg/batch)	Water, e (lt/batch)	Cement, c (kg/batch)	c/e
10	80	160	85	50	50	1.00
15	80	160	85	45	50	1.11
20	80	160	85	40	55	1.38

2.2.2. Steel

In order to form the steel cages for the column and the stub, plain and deformed bars were used, respectively. For the stub, deformed bars having diameter of 16 mm and 8 mm were used for longitudinal and transverse reinforcement, respectively. Additionally, the column reinforcement consisted of 18 and 22 mm diameter plain longitudinal bars for different test series and 10 mm diameter plain transverse ties. The average values of elasticity modulus (E_s), yield strength (f_y), ultimate strength (f_{su}) and corresponding strain levels of yield (ϵ_y), strain hardening (ϵ_{sh}) and ultimate (ϵ_{su}) were obtained by three direct tension tests for each type of steel with different diameter (Table 2.2). Stress-strain curves are presented in Figure 2.1.

Table 2.2 Mechanical properties of reinforcing bars for column and stub

Steel	Diameter (mm)	E_s (MPa)	f_y (MPa)	f_{su} (MPa)	ϵ_y	ϵ_{sh}	ϵ_{su}
Plain bars	10	200000	331	439	0.00166	0.0080	0.25
	18	200000	275	427	0.00137	0.0045	0.30
	22	200000	284	453	0.00142	0.0038	0.30
Deformed	8, 16	200000	420	650	0.00210	0.0040	0.10

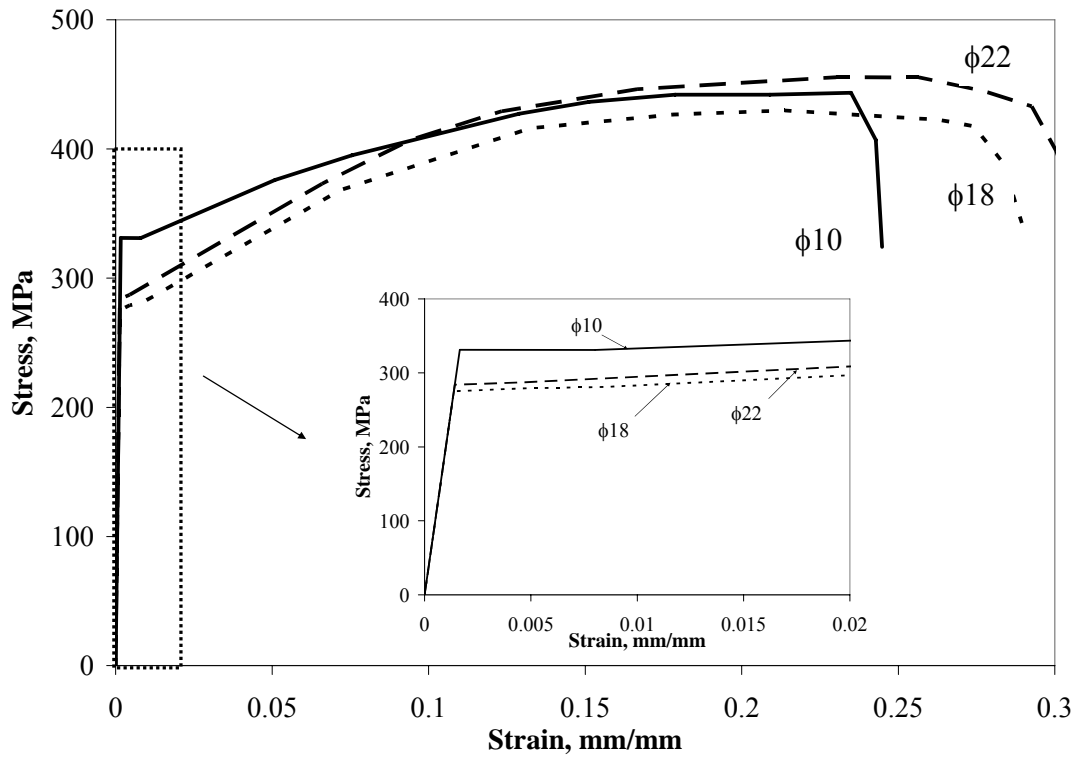


Figure 2.1 The stress-strain relationships for the plain bars used in the specimens

2.2.3. Carbon Fiber Reinforced Polymer (CFRP)

The unidirectional CFRP sheets of MBT-MBrace® C1-30 Fiber were used for retrofitting of columns and forming CFRP anchor dowels. According to the manufacturer, CFRP sheets had a thickness of 0.165 mm and an elasticity modulus of 230000 MPa with a rupture strain and tensile stress of 0.015 and 3430 MPa, respectively.

2.3. Test Specimens and Preparation

In the experimental part of this research, three series of tests were conducted in order to investigate the seismic behavior of flexure dominant RC columns simulating non-seismic Turkish design practice (Table 2.3). The columns were designed to

experience flexure-dominant behavior with and aspect ratio ($h / L =$ section depth / column height) of either 5 or 5.7 for square and rectangular columns, respectively.

Table 2.3 Specimen Properties

Name	Specimen Properties				Long Steel Ratio	Axial Load N/N_0 ***	CFRP Application	
	f'_c	f_y	Reinforcement				Ply No	Wrap
	MPa	MPa	Long.	Trans.				
S-L-0-00	14.0					34	0	Ref
S-L-1-00	19.4					27	1	S,NL*
S-L-1-34	14.0	275	8 ϕ 18mm (plain)		1.66	34	1	S,UL**
S-L-2-00	11.4					39	2	S,NL
S-L-2-32	15.6					32	2	S,UL
S-H-0-00	20.0						0	Ref
S-H-1-00	20.0						1	S,NL
S-HD-1-00	19.0	284	8 ϕ 22mm (plain)	$\phi=10$ mm at 200 (plain)	2.55	27	1	R,NL
S-HD-1-27	20.0						1	R,UL
S-HC-1-00	22.0						1	S,NL,C
R-NC-0-00	12.0						0	Ref
R-HC-1-16P	10.0						1	S,16-pin
R-MC-1-16P	15.5	275	8 ϕ 18mm (plain)		2.48	35	1	S,16-pin
R-MC-1-8P	10.5						1	S,8-pin
R-MC-1-NP	9.0						1	S, no-pin

* NL, UL: CFRP application was made under the absence-presence of axial load

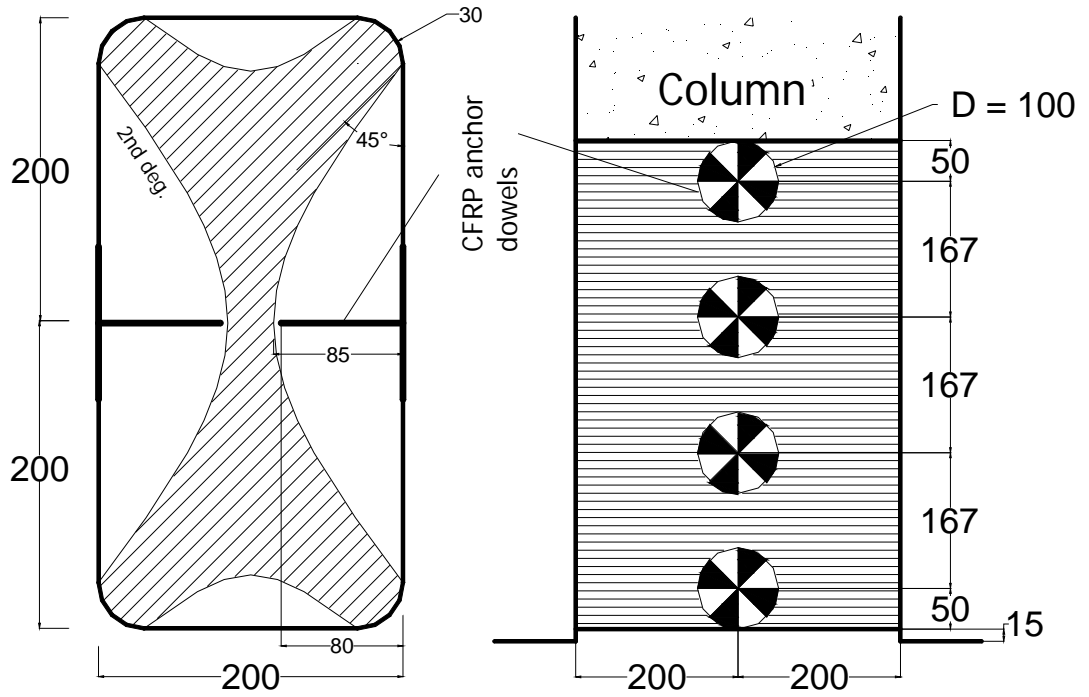
** S: Strengthening, R: Repair, C: Decreased column corner rounding radius

*** $N_0 = 0.85 f'_c A_g + A_{st} f_y$

For the first series, the specimens were categorized alphanumerically in a way that the first letter S, defines the cross-section shape as square (350×350 mm) and the second letter L denotes the longitudinal reinforcement as low (8 – 18 mm rebars: $\rho_l = 1.66$ %). The number in between the dashes specifies the number of CFRP layers that were wrapped around 500 mm of the column base and the last index shows the axial load level in percents under which the specimen was wrapped with CFRP. For the reference specimens and columns strengthened under the absence of axial load, the last index has the value of 00.

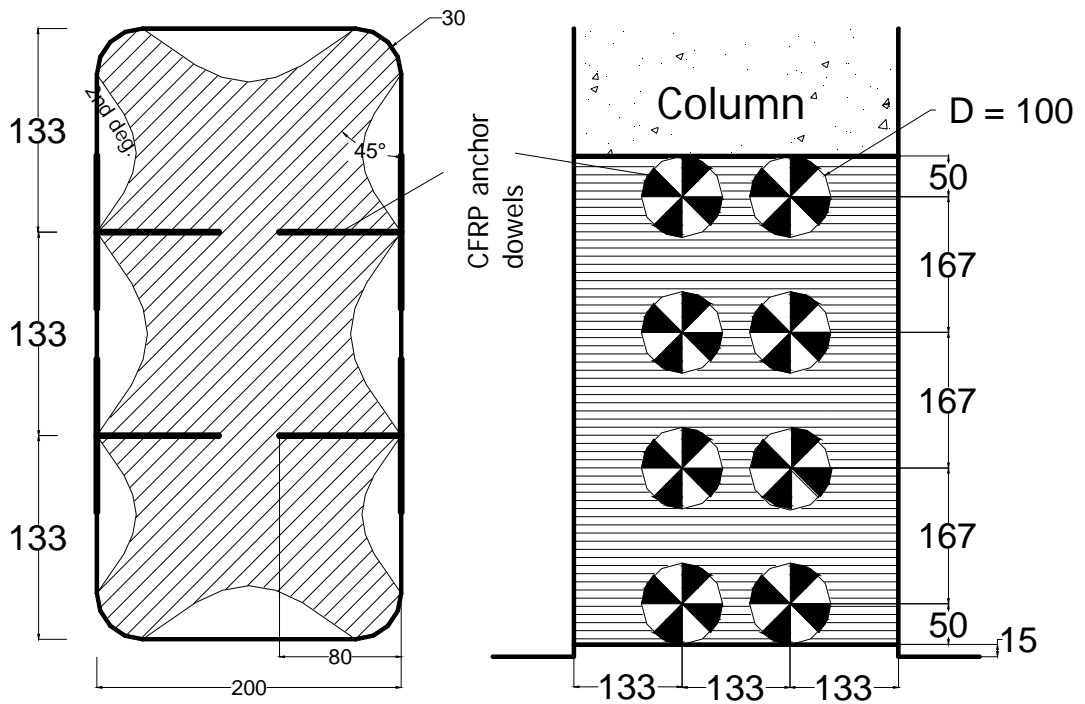
The columns in Series 2 were identified by using a similar notation with Series 1. The first letter, S in the specimen name represents the square cross-section with the same dimensions as Series 1 and the second letter after the dashes, H shows that the specimen has high longitudinal reinforcement ratio with eight 22 mm diameter rebars ($\rho_l = 2.55\%$). Additional letters for the second index, D or C points out that the specimen has previous moderate damage level of 2% drift or the corner-rounding radius is changed to 10 mm, respectively. For the moderate damage level of 2%, the specimen first experienced the damage, CFRP retrofitted and then re-tested. The following number shows the number of CFRP layers that are wrapped around the columns and the last index indicates the level of axial load level under which the column is CFRP retrofitted.

The columns in Series 3 were reinforced with 8 – 18 mm diameters rebars ($\rho_l = 2.48\%$) and the test specimens were classified regarding four identification parameters. The character R, in the first index identifies the cross-section as rectangular and the second index shows the degree of CFRP confinement that was moderate (MC) or high (HC). NC index is used for no confined reference columns. For the reference column, since there is no CFRP confinement the specimen name was identified as NC. The following number in between dashes shows the number of CFRP wraps wrapped and last index indicates the type of the CFRP anchor dowel configuration. The 16 and 8-pinned anchor dowel configurations are represented by the indices 16P and 8P respectively while the no-pinned specimen is specified by the NP index. The CFRP dowel configurations are shown in Figure 2.2.



All units in mm.

(a) 8 anchor dowels



All units in mm.

(b) 16 anchor dowels

Figure 2.2 CFRP anchor dowel configurations

2.3.1. Test Specimens

The first series of the experimental study consisted of five deficient RC columns with dimensions of $350 \times 350 \times 2000$ mm (width \times depth \times length) that were connected to a stub of $400 \times 500 \times 1350$ mm (width \times depth \times length). The main parameters under investigation were the number of CFRP layers and the presence/absence of axial load during strengthening. Regarding the control specimen S-L-0-00, two companion specimens, S-L-1-00 and S-L-2-00, were either wrapped with one and two layers of CFRP under the absence of axial load, respectively. However, for the specimens S-L-1-34 and S-L-2-32, CFRP implementation was done under an axial load of approximately 35% of column axial load carrying capacity ($N_0 = 0.85 f'_c A_g + A_{st} f_y$). For Series 1, the axial load level could not be maintained exactly at 35% of axial capacity since an unintended variation in concrete compressive strength (ranging from 11.4 MPa to 19.4 MPa) in columns was observed. For all the CFRP strengthened specimens in Series 1, three handmade CFRP anchors were used in only one side of the column between two longitudinal rebars at heights of 50, 250 and 450 mm from column base in order to prevent any bond failure between overlapping layers of CFRP.

The second part of the experimental study included square columns with cross-section dimensions of 350×350 mm that were connected to the same footing as Series 1. For the second series, the effects of previous damage, corner rounding radius and presence of axial load of about 27% of the capacity during repairing on the seismic performance of columns were investigated. The control specimen S-H-0-00 was non-seismically reinforced with plain bars and inadequate lateral steel. The strengthened specimen, S-H-1-00 was wrapped with one layer of CFRP along 500 mm height of the column, whereas the repaired specimen S-HD-1-00 was previously damaged to a moderate drift level of 2% and then the CFRP retrofitted along 650 mm of the column in order to prevent any failures outside the test region. In addition, the same CFRP anchoring scheme was used for Series 2 as in Series 1, whereas an additional CFRP anchor was placed at 600 mm from the base for additional safety. The concrete compressive strengths used for the columns in Series 2 were approximately 20 MPa.

The third series in the experimental program comprised of five specimens having a rectangular cross-section of 200×400 mm that were tested in column strong axis. The major parameters observed in Series 3 were the section aspect ratio and the confinement levels provided by means of CFRP anchor dowel configurations. The control specimen R-NC-0-00 was reinforced with non-seismic transverse detailing similar to the other test series. The columns R-MC-1-16P, R-MC-1-8P and R-MC-1-NP were constructed in order to observe the effects of anchor dowel configurations on the seismic behavior CFRP strengthened RC columns. Since the 80 mm-long CFRP anchor dowels were not penetrated into the borderline of the FRP confined region that was 85 mm away from the column edge, the confined region was assumed to have no change in shape (Figure 2.2a). The remaining specimen R-HC-1-16P was identical with its dowel configuration with R-MC-1-16P except its concrete compressive strength and the resultant confinement level. The CFRP anchor dowel configurations are illustrated in Figures 2.2a and 2.2b.

2.3.2. Preparation of Test Specimens

All the specimens were cast vertically at the same time with the stub by aluminum formworks. Firstly, the reinforcing cage of the stub was constructed by using four 16 mm diameter deformed bars at top and bottom. Further, for lateral steel, 8 mm deformed bars were placed at 200 mm spacing and all the connections for longitudinal and lateral steel were welded carefully in order to prevent any failure types in the footing rather than in the test region. Afterwards, 90-degree bent plain longitudinal rebars were inserted into the reinforcing cage of the stub and each bar was connected to the footing. The column stirrups were inserted through the longitudinal rebars with 200 mm spacing having 90-degree hooks at tie ends. The transverse bars were selected as 10 mm diameter in order to prevent shear failure. The reinforcement details for square and rectangular columns are shown in Figures 2.3 and 2.4. After forming the reinforcing cages, they were placed into the previously cleaned and greased formworks (Figure 2.5) and for each of the specimens, three batches of concrete were placed starting from the foundation level to the column's top level.

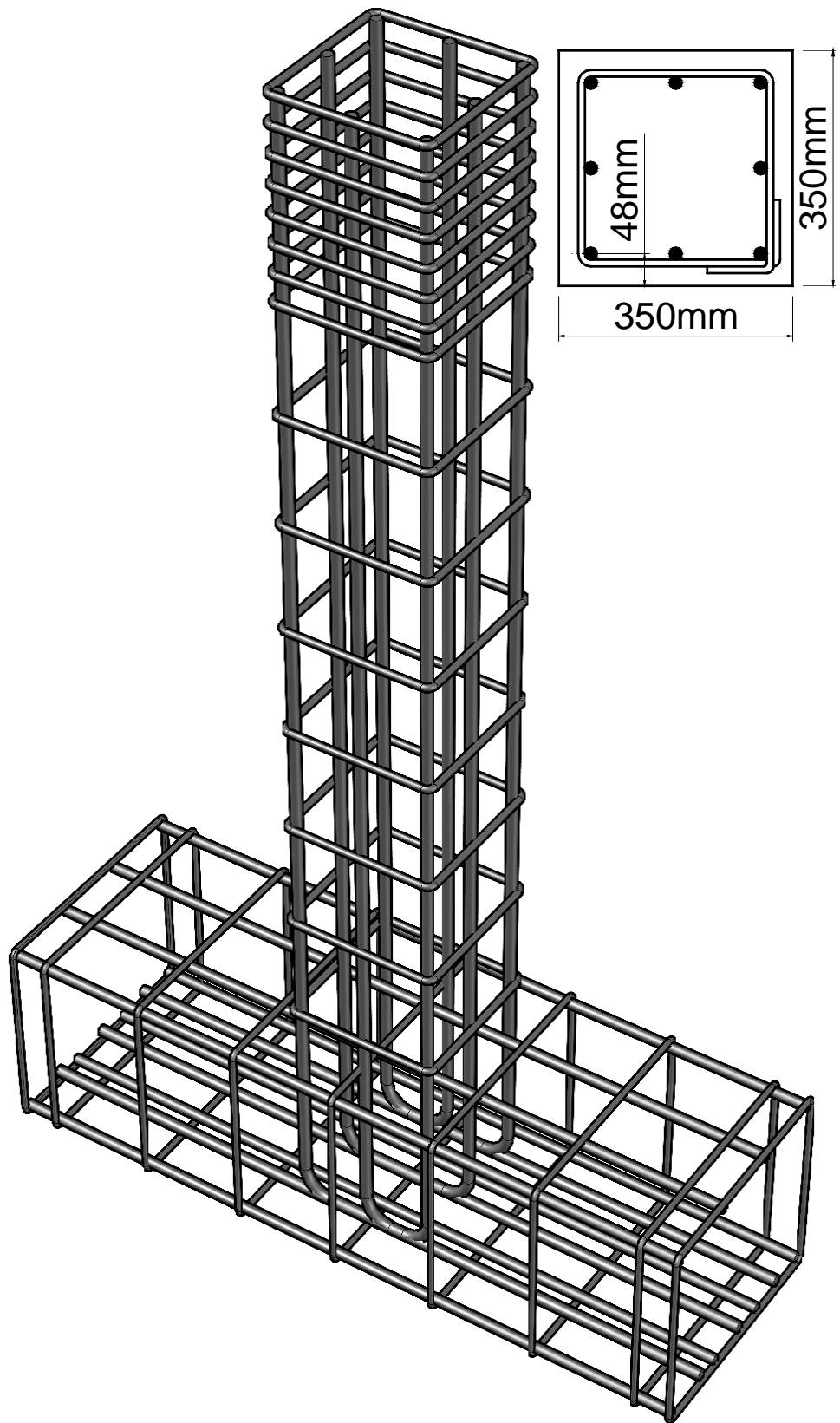


Figure 2.3 Reinforcing cage for square columns

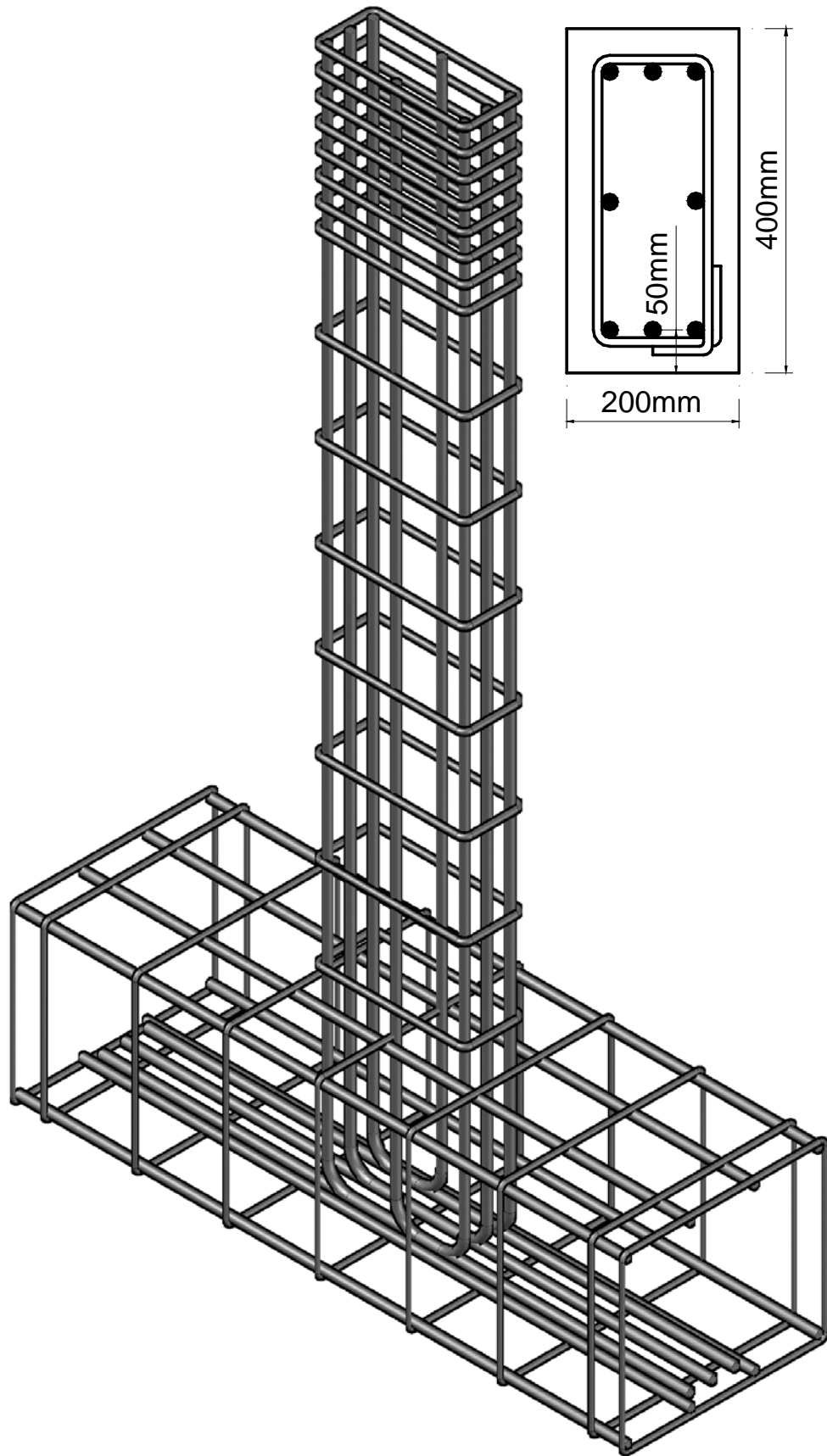


Figure 2.4 Reinforcing cage for rectangular columns



Figure 2.5 A typical footing formwork with reinforcement placed inside

In addition, there were eight cylindrical spacers in the footing placed parallel to the column axis that were further used to connect the specimen to the test setup. In the first phase of the casting process, a part of the foundation level was cast with the first batch of concrete (Figure 2.6a). Subsequently, the formwork of the upper part of the column was fixed during the preparation of the second batch (Figure 2.6b) and casting was finished by placing the last batch of concrete at the top of the column (Figures 2.6c and 2.6d). The vibrators were used at each stage of casting in order to provide proper placement of concrete in the formwork. At the top of each column, eight 24 mm diameter threaded bolts were cast invertedly with the specimen by which the column was connected to the steel head and consequently to lateral and axial loading units. After the casting process, the perpendicularity of the specimen was checked by a bubble level. Two weeks after casting, the formworks were removed and the specimens were wrapped with water-impregnated burlaps with nine concrete cylinders whose forms were also removed at the same time with the specimen. For as-built columns, the specimen was ready for testing after the concrete would have its 28-day nominal compressive strength. For the strengthened or repaired columns, CFRP was implemented in 3 or 4 weeks after casting regarding the type of the test.



(a)



(b)



(c)



(d)

Figure 2.6 (a) First, (b) Second, (c) and (d) Last phase of specimen casting

2.3.3. CFRP Implementation

At the first phase of CFRP implementation for the strengthened columns, the corners of each column were rounded to a radius of either 30 or 10 mm. After rounding off the corners, a thin layer of undercoat of MBT-MBrace® Primer was applied on the plastic hinge region of the column (bottommost 500-600 mm) using a brush by mixing 3 units of Component A and 1 unit of Component B in weight. Subsequently, the epoxy-based mortar of MBT-MBrace® Putty was applied by using the mixture of 3 units of Component A and 1 unit of Component B in weight (Figure 2.7a).

For the case of repaired columns, the putty was applied at the concrete sections that were spalled during the damage. After waiting for proper curing of the epoxy mortar, a thin layer of undercoat was applied again on the 650 mm of the column height and the putty application followed that step (Figure 2.7b). Then, FRP sheet was first impregnated into MBT-MBrace® Adesivo (Saturant) that was prepared by using the same mixture ratios. After, the test region of the column was wrapped by leaving a gap of 15 mm above the column-stub interface (Figure 2.7c) after waiting about 2-3 hours for proper curing of the putty.

To achieve a good connection between the column and the CFRP sheet, in-house fabricated CFRP anchorages were placed along the test region of the columns. In order to apply these carbon fiber anchor dowels, 12 mm diameter holes with a depth of 80 mm were drilled at different heights according to the specimen. The CFRP anchor dowels were formed from 120 × 130 mm carbon fiber strips as shown in Figure 2.8a. These strips were rolled in the fiber direction and tied with a string. After folding, 130 mm-long dowels were obtained and its 80 mm length was inserted into the previously cleaned and drilled holes (Figure 2.8b). The anchorages were placed both to prevent debonding of the overlap section of the CFRP sheet during the test and to provide seismic retrofitting of rectangular RC columns by FRP wrapping to enhance confinement efficiency, regarding the needs of the experiments. The strengthened specimens were tested one week after the CFRP application (Figure 2.9).



(a) Undercoat and epoxy mortar application for strengthened columns



(b) Undercoat and epoxy mortar application for repaired columns after damage

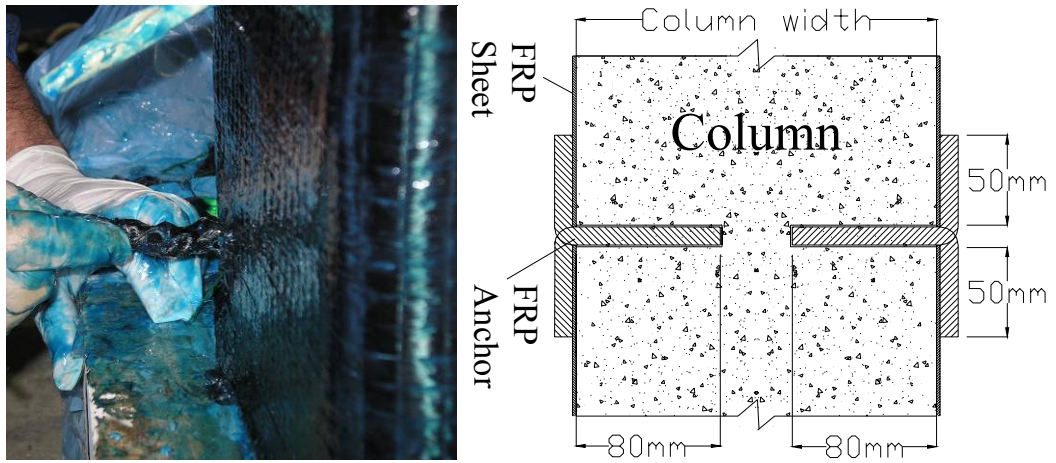


(c) CFRP wrapping

Figure 2.7 Strengthened and repaired column preparation during CFRP application



(a) CFRP anchor dowel preparation



(b) CFRP anchor dowel insertion

Figure 2.8 CFRP anchor dowel implementation



Figure 2.9 CFRP strengthened and repaired columns ready for the test

2.4. Test Setup and Instrumentation

The column test setup was designed and constructed in order to sustain an axial load of 800 kN simultaneously with a lateral load of 100 kN. For the axial loading unit, three 1350 mm long, box-shaped steel supporting frames were constructed to apply the axial load on the specimens. Two steel profiles were designed to share the design axial load of 800 kN that was applied on one steel supporting frame located at the top of the specimens as shown in Figures 2.10-2.12. The specimens were connected to the steel head by which the axial and lateral loading was applied on the columns at the same time. After connecting the column to the test setup, the distance between the lateral load application point and the column base was 2000 mm since the steel head was connected to the specimen and lateral load was applied by this rigid link. Thus, half-height of the steel head was added to the specimen height.

The lateral loading unit was connected to the steel head and included a 300/100 kN (Compression/Tension) capacity hydraulic jack with a stroke of 510 mm. The hydraulic jack had two circular joints at both ends one of which was connected to the steel head and the other end was connected to the strong wall. The axial load was applied by using two hydraulic jacks having compressive and tensile capacities of 600 kN and 100 kN, respectively. These hydraulic jacks were placed at the two sides of the upper steel frame and the applied axial load was transferred to the lower steel frames by high strength (HS) threaded rods that were connected to the lower frames by two square joints in order to prevent bending at the connections of HS rods and the bottom profiles. Furthermore, eight 48 mm diameter high strength bolts were used to connect the specimen to the main footing and additional four 48 mm diameter HS bolts were connected to bottom profiles in order to transfer the axial load to the strong floor. Since the axial load level varied during the application of lateral load during the load reversals, it was kept constant at various drift levels by pressure stabilizer, fine and a coarse pressure adjustment valves that were connected to the electrical hydraulic pump. During the tests, axial load was controlled with a separate system by a KYOWA UCAM-5B unit. In addition, during the tests that acquired the presence of axial load on the column for one week, a digital timer was used for intermittent hydraulic pumping.

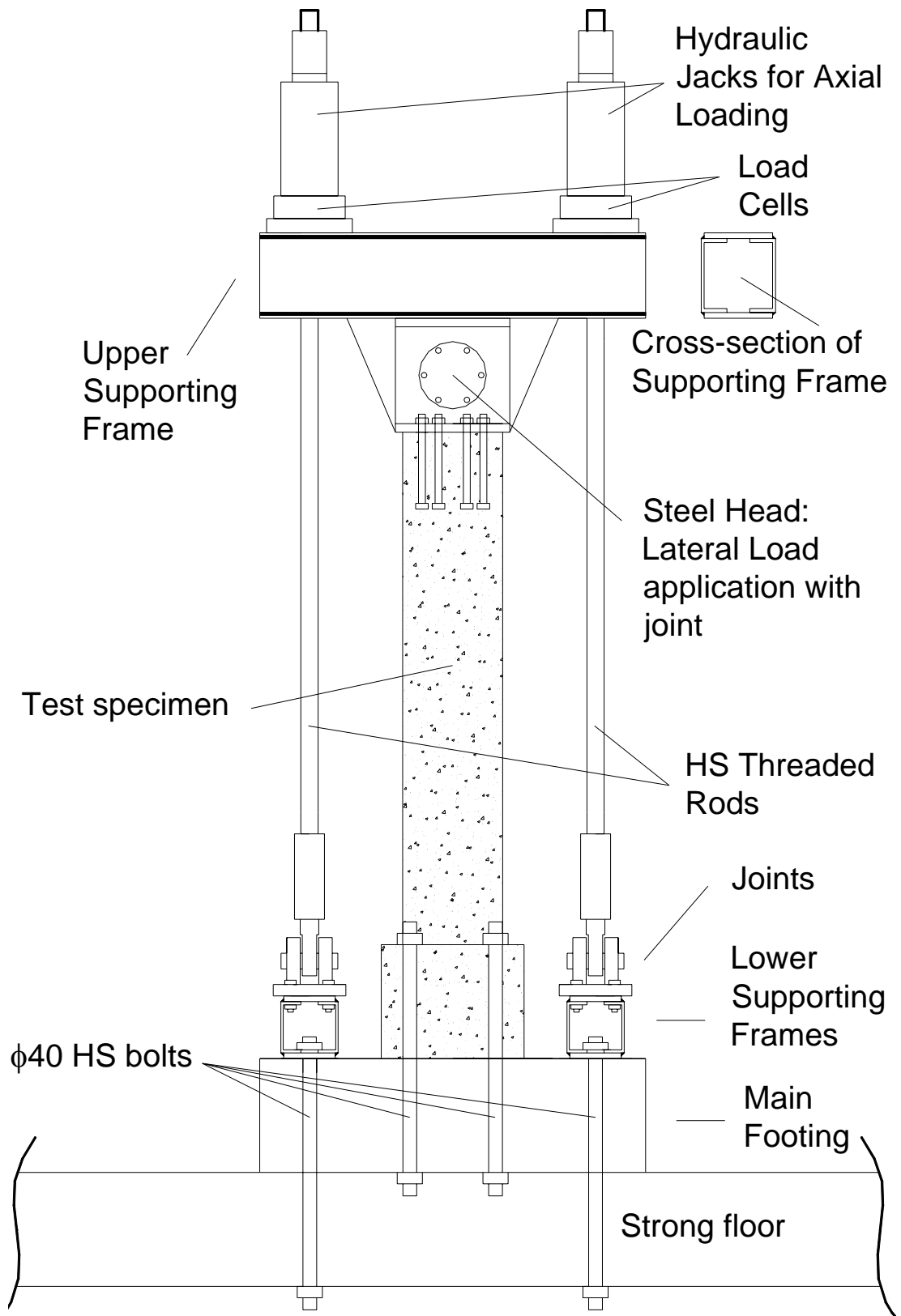


Figure 2.10 Test Setup: Front View

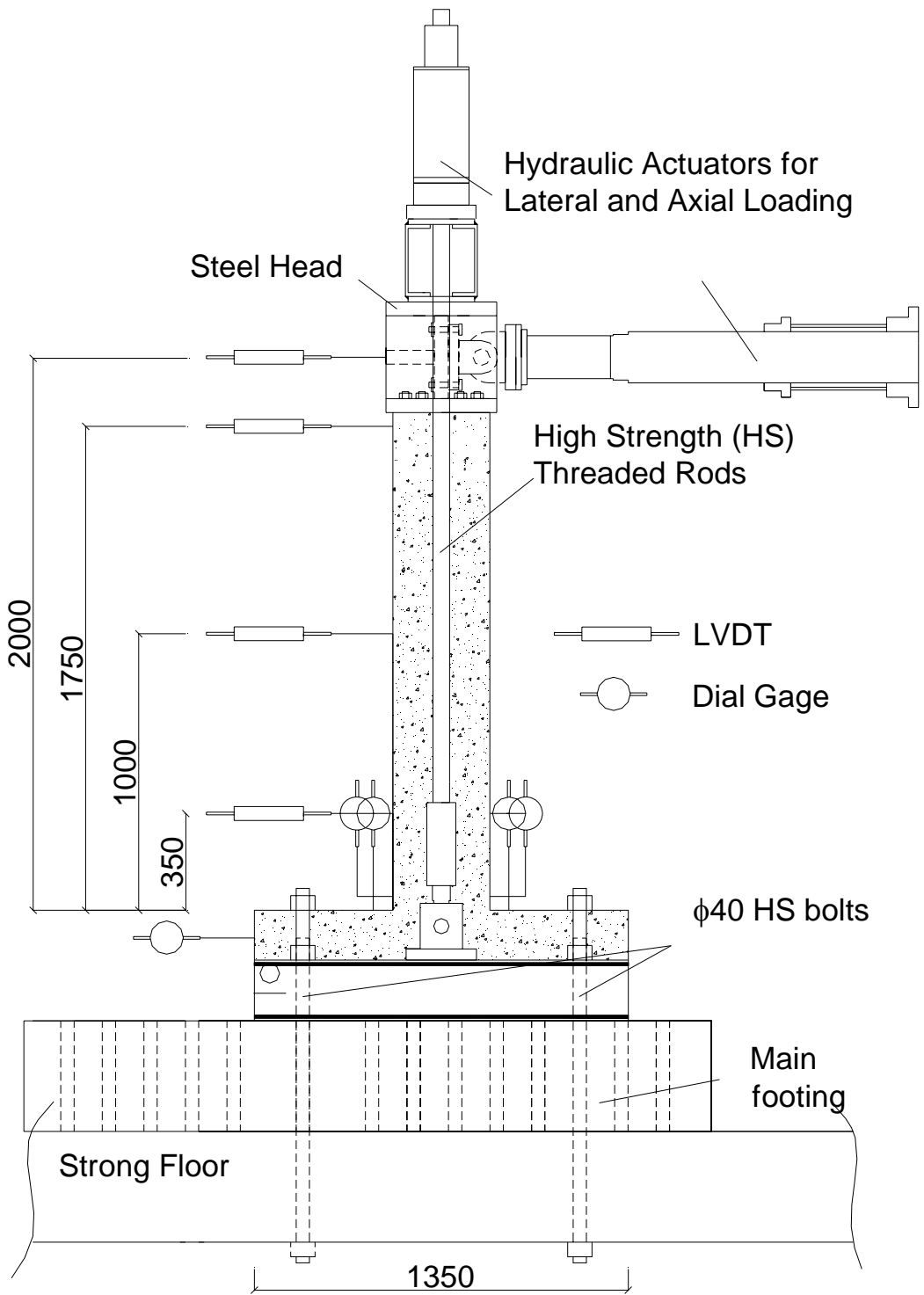


Figure 2.11 Test Setup: Profile

The specimens were carefully instrumented to obtain the required data at different deformation levels. Linear Variable Differential Transducers (LVDTs) were used to measure horizontal deflections. Rotations at critical regions were measured by using eight electronic dial gages. All specimens were instrumented to measure hinge region deformations using two sets of displacement readings on the two sides of the specimens. One set of dial gages were used to measure the displacement of the section located 350 mm away from the column base relative to a location 50 mm from the column base. These measurements were converted into average strains and were used to calculate column base curvatures within 300 mm. The other set of displacement readings were taken from 350 mm away from the column base relative to the column-footing interface. The concentrated deformations of the 50 mm region at the base of the column were accepted as the concentrated base rotations due to the slip of the column reinforcement. Columns were guided with 4 rollers between the guide rails to assure uniaxial bending in the plane of loading. The schematic illustrations of the instrumentation are shown in Figures 2.13 and 14.

Axial and lateral loading were controlled by three load cells. In addition, the specimens were guided with four rollers to assure bending in plane of lateral loading during the lateral displacement cycles. All the instruments were connected to a 12-bit Data Acquisition System as shown in Figure 2.15. The tests were started with the application of axial loading except the specimens that were tested under axial load. Firstly the axial load was applied and then the lateral load was increased from zero to failure. All the specimens were subjected to constant axial load and cyclic lateral displacement excursions. In the lateral loading program, the drift increment of 0.5% was used until 3% drift level having 3 cycles per drift level. Beyond 3% drift ratio, the number of cycles per drift level was decreased to 2 with a drift increment of 1% (Figure 2.16).

In addition, stability and base rotation checks were done in Appendix A and the base rotations were found to be insignificant under most unfavorable axial and lateral load combinations.

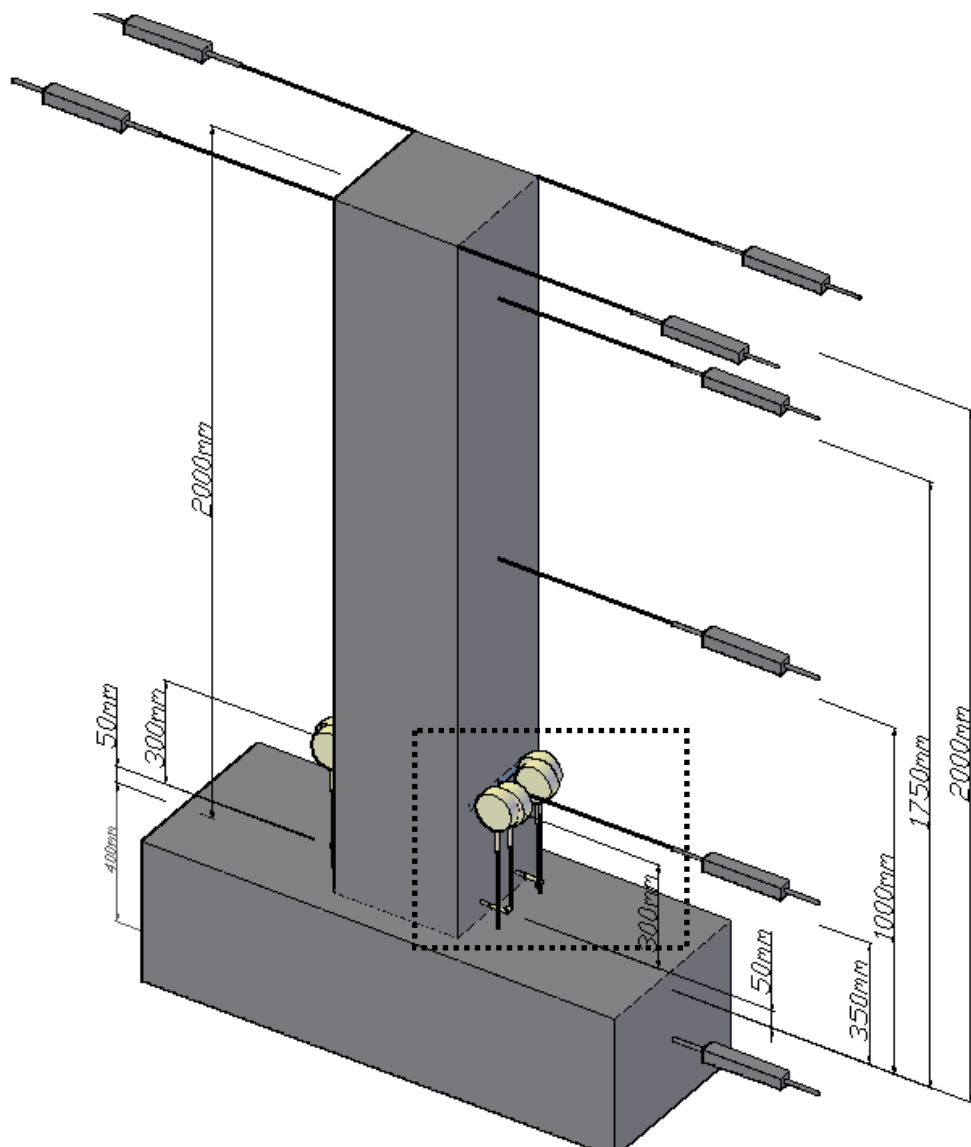


Figure 2.13 Instrumentation: 3D View

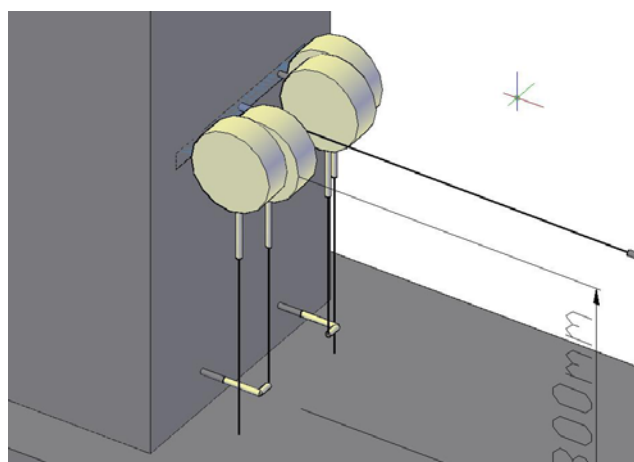


Figure 2.14 Instrumentation: 3D-Close-up View

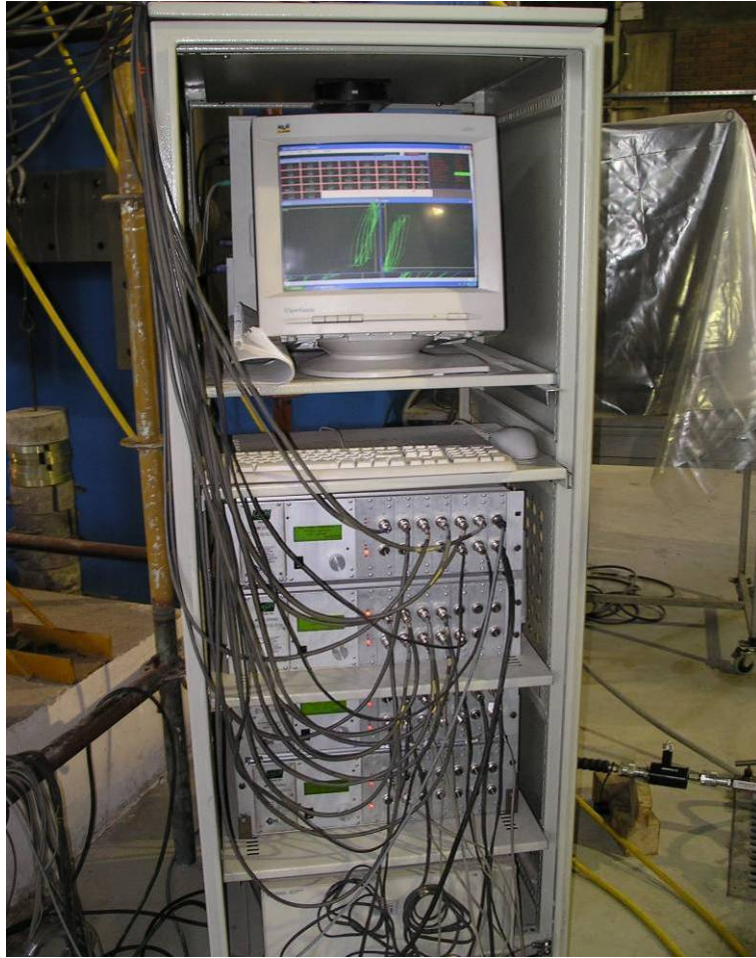


Figure 2.15 12-Bit Data Acquisition System

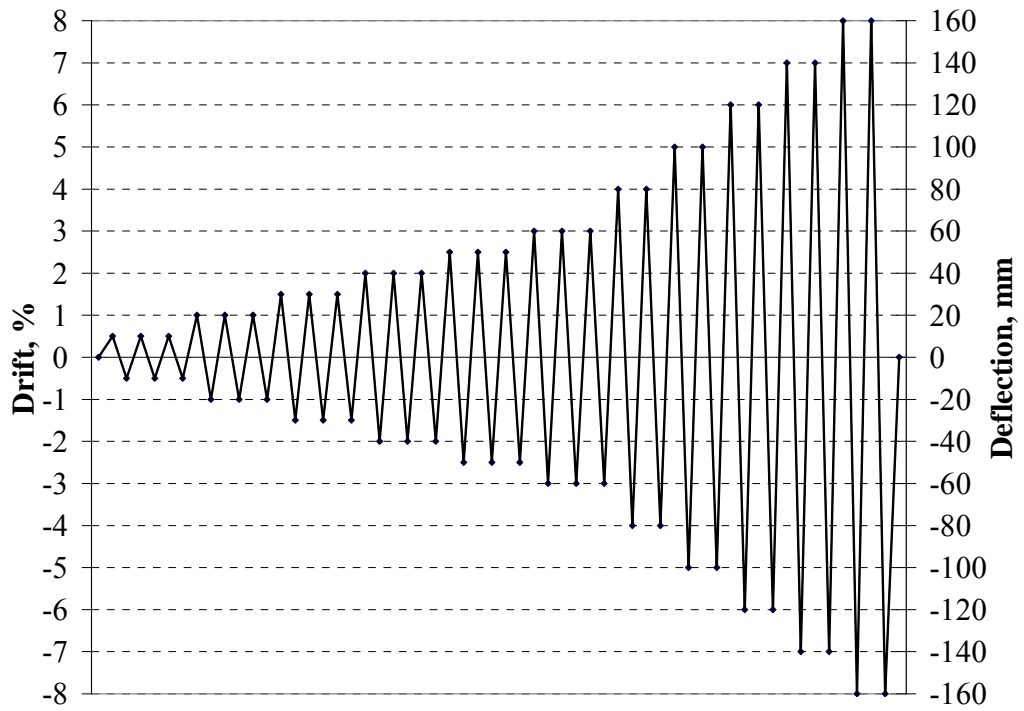


Figure 2.16 Loading Program

2.5. Correction of Lateral Load

The lateral force during the tests was modified according to the axial force at various drift levels. While the specimen underwent pre-specified drift levels, the restraining effect of axial load enforced the column remain at its original position. A schematic illustration is shown in Figure 2.17. The restraining effect of the axial load made the lateral load cell to measure higher lateral forces than the actual values. Hence, the recorded lateral forces were corrected regarding the attained drift levels and the present axial load on the specimen.

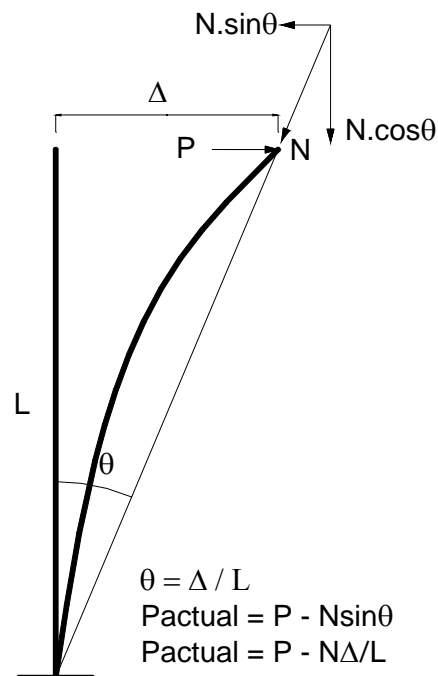


Figure 2.17 Restraining effect of axial load and moment correction

The actual lateral force acting on the column (P_{actual}) was obtained by subtracting the horizontal component of the axial load (N) while the column experienced a displacement level of Δ . The column length is defined as L and θ represents the chord rotation of the column. The significance of lateral load correction was observed while the drift levels increased. (i.e. for an axial load of 800 kN and drift ratio of 6%, 48 kN of lateral load correction should be considered.)

2.6. Experimental Observations and Test Results

The lateral response of each specimen was illustrated by Lateral load (P) – Tip Deflection (Δ) and Moment (M) – Average Curvature (K) graphs. Additional graphical representations of Moment (M) – Fixed End Rotation (FER) and Strain (ϵ) – Drift Ratio (DR) were demonstrated in order to elucidate bond, plastic hinging and longitudinal reinforcement behavior at the hinging region of the column. The yield and ultimate values of forces and moments that were obtained by standard section analysis are shown in Table 2.4. In addition, the ratios of yield and ultimate moments to the reference specimen in each series are also presented. All specimens exhibited flexural dominant response during the reversed cyclic displacement based loading program. The drift or deflection level corresponding to 20% drop in lateral capacity was regarded as the ultimate drift or deflection. In addition, concerning each loading cycle, the drift levels were recorded at which important events such as column-stub interface cracking, CFRP debonding, CFRP rupturing and 20% drop in lateral capacity was observed. The experimental results are shown for push (+) and pull (-) directions in Table 2.5.

Table 2.4 Analytical yield and peak responses with standard section analysis

Specimen	Yield		Peak		M_u/M_y	$M_y/M_{y, REF}$	$M_u/M_{u, REF}$
	P_y (kN)	M_y (kNm)	P_u (kN)	M_u (kNm)			
S-L-0-00	61.8	123.6	67.4	134.8	1.09	1.00	1.00
S-L-1-00	71.7	143.4	85.5	171.0	1.19	1.16	1.27
S-L-1-34	61.8	123.6	75.2	150.4	1.22	1.00	1.12
S-L-2-00	53.3	106.6	67.2	134.4	1.26	0.86	0.99
S-L-2-32	66.9	133.8	83.6	167.2	1.25	1.08	1.24
S-H-0-00	85.9	171.8	89.9	179.7	1.05	1.00	1.00
S-H-1-00	86.0	171.9	89.5	178.9	1.04	1.00	1.00
S-HD-1-00	84.9	169.8	87.8	175.6	1.03	0.99	0.98
S-HD-1-27	86.0	171.9	89.5	178.9	1.04	1.00	1.00
S-HC-1-00	87.3	174.6	93.2	186.3	1.07	1.02	1.04
R-NC-0-00	49.5	99.0	55.5	110.9	1.12	1.00	1.00
R-HC-1-16P	34.5	69.0	48.1	96.2	1.39	0.70	0.87
R-MC-1-16P	59.5	119.0	63.4	126.8	1.07	1.20	1.14
R-MC-1-8P	39.0	78.0	49.5	98.9	1.27	0.79	0.89
R-MC-1-NP	36.5	73.0	49.0	97.9	1.34	0.74	0.88

Table 2.5 Specimen Responses

Specimen	L _p mm	P _{peak} , kN			P _{yield} , kN			Δ _{yield} , mm			‡K _{u 350-50} , rad/km			§K _{u 350-BASE} , rad/km			FER _u , %			IC **	CFRP		BB	Drift, DR _u		
		†+	-	Avg.	+	-	Avg.	+	-	Avg.	+	-	Avg.	+	-	Avg.	+	-	Avg.		Debond	Rupture		+	-	Avg.
S-L-0-00	350	63.7	62.5	63.1	53.6	53.1	53.4	14.1	12.8	13.5	59.7	49.5	54.6	72.5	72.0	72.3	0.8	0.8	0.8	0.5	1.50 (crushing)		2.5	2.7	2.5	2.6
S-L-1-00	300	78.5	87.0	82.7	64.5	72.0	68.3	15.0	15.4	15.2	45.5	123.6	84.6	117.0	120.4	118.7	2.8	2.8	2.8	0.5	2.5	4.0	5.0	5.2	4.6	4.9
S-L-1-34	290	71.4	83.1	77.3	58.3	71.2	64.8	13.9	14.8	14.4	81.1	47.8	64.5	137.9	154.4	146.2	1.6	3.2	2.4	0.5	2.5	5.0	5.0	4.8	5.4	5.1
S-L-2-00	310	53.9	66.0	59.9	43.4	57.4	50.4	13.6	12.5	13.1	42.6	39.5	41.1	201.2	188.1	194.7	4.9	5.1	5.0	0.5	3.0	7.0	7.0	6.4	6.2	6.3
S-L-2-32	300	67.3	74.8	71.1	53.9	62.6	58.3	15.3	14.2	14.8	42.7	125.5	84.1	153.3	139.6	146.5	*	*	*	0.5	3.0	6.0	5.0	6.1	5.9	6.0
S-H-0-00	350	75.3	88.3	81.8	64.0	77.8	70.9	15.6	15.9	15.8	77.9	50.0	64.0	81.9	99.3	90.6	0.8	1.9	1.4	0.5	2.0 (crushing)		3.0	3.3	3.3	3.3
S-H-1-00	310	69.1	94.5	81.8	60.1	86.0	73.1	13.8	17.5	15.7	36.0	46.9	41.5	101.2	114.5	107.9	*	*	*	0.5	2.5	5.0	5.0	4.1	4.1	4.1
S-HD-1-00	300	79.3	87.0	83.2	65.5	69.4	67.5	35.1	34.5	34.8	93.7	182.3	138.0	128.7	129.6	129.2	*	*	*	0.5	2.0	5.0	5.0	5.3	5.1	5.2
S-HD-1-27	280	58.3	70.4	64.3	50.0	60.8	55.4	34.0	36.6	35.3	79.1	113.0	96.1	141.6	156.1	148.9	3.5	3.6	3.6	0.5	2.0	5.0	4.0	5.1	5.0	5.0
S-HC-1-00	350	80.5	76.3	78.4	69.4	64.8	67.1	15.3	16.1	15.7	38.9	*	38.9	68.4	95.9	82.2	3.8	3.3	3.6	0.5	2.0	5.0	5.0	3.1	4.2	3.6
R-NC-0-00	470	49.9	55.6	52.8	41.6	48.4	45.0	11.7	10.8	11.3	17.0	30.0	23.5	31.0	37.8	34.4	0.6	0.1	0.4	0.5	1.5 (crushing)		1.5	1.9	1.7	1.8
R-HC-1-16P	350	40.1	49.0	44.6	32.3	38.0	35.2	14.1	18.4	16.3	*	51.1	51.1	151.2	103.7	127.5	4.9	3.7	4.3	0.5	2.0	4.0	5.0	6.1	6.1	6.1
R-MC-1-16P	340	60.4	65.7	63.0	50.5	54.5	52.5	12.7	11.1	11.9	60.6	53.2	56.9	89.7	131.2	110.5	1.0	1.3	1.2	0.5	2.0	6.0	4.0	4.0	4.0	4.0
R-MC-1-8P	350	41.1	49.6	45.4	33.7	41.3	37.5	11.9	16.6	14.3	30.0	45.4	37.7	91.7	90.3	91.0	2.3	1.5	1.9	0.5	2.0	2.5	3.0	3.8	3.7	3.7
R-MC-1-NP	310	37.7	46.1	41.9	28.5	37.1	32.8	12.4	16.8	14.6	112.6	112.5	112.6	93.1	93.5	93.3	1.6	*	1.6	0.5	2.0	4.0	3.0	3.9	3.8	3.9

* Values could not be obtained, ‡ Average curvatures recorded between 350 and 50 mm height from the column base.

§ Average curvatures recorded between 350 mm and the column base, ** IC: Column-stub interface cracking, BB: Onset of bar buckling L_p: Plastic hinge length

† + and -: Push and pull directions, respectively. u: Ultimate values where the lateral capacity dropped 80% of peak.

2.6.1. Series 1

All of the test specimens experienced a similar failure mode in the column base namely flexural failure due to column plastic hinging. The pictures of plastic hinge regions of failed specimens are shown in Figure 2.18. (The analytical envelope lines that are shown on the hysteretic loops in all test series are going to be explained in Chapter 3 for comparison.) For the reference specimen S-L-0-00, the column-stub interface cracked at 0.5% drift and increasing displacement cycles forced the column to experience inelastic deformations. Evenly distributed horizontal flexural cracks developed at both faces of the column between 200 to 1000 mm from the column-stub interface. Owing to widening of the interface crack, slipping and extension of the reinforcement was augmented. The lateral load resistance started to degrade due to concrete crushing starting from the base along a height of approximately equal to the column section width (350 mm) at 1.5% drift. The utmost drift level at which the column could sustain subsequent steady three cycles without any significant strength loss was termed as the onset of rebar buckling for all test series. The onset of longitudinal bar buckling was pointed at a drift of 2.5%, afterwards the lateral load capacity decreased significantly below 80% of the peak load with a negative stiffness slope. The hysteretic behavior of S-L-0-00 is shown in Figure 2.19. In the cycles of 0.5% drift level of S-L-1-00, the initiation of visible flexural cracks at distances of 650 to 1000 mm from the column base and cracking of the column-stub interface was observed as pointed in hysteresis curves shown in Figure 2.20. The cracks developed above the wrapped region were closer to each other than those observed in the reference specimen. In the following cycles, the flexural cracks widened and lengthened above the wrapped region. At 2.5% drift, horizontal cracks along CFRP plies occurred at a height of approximately 300 mm from the column base. At the opposite face, CFRP sheet started to debond owing to compression-tension cycles imposed on it. The presence of the CFRP lamina prevented the rebars from buckling and thus, slippage of the reinforcement at the stub-column interface progressed. First rupture in CFRP occurred at 4% drift and the lateral load resistance started to decrease. The degrading behavior was observed until 5% drift ratio followed by an explosive rupture at the CFRP at the end of the test resulting in significant reduction of lateral load as can be seen in Figure 2.20.



(a)



(b)



(c)



(d)



(e)

Figure 2.18 Columns at the end of testing (a) S-L-0-00, (b) S-L-1-00, (c) S-L-1-34, (d) S-L-2-00, (e) S-L-2-32

Specimen S-L-1-34 experienced a similar behavior in terms of cracking and base rotations due to rebar slip. The drift ratio, at which the CFRP sheet ruptured, was higher than the S-L-1-00 but this change did not affect the ultimate deflection of the column. The resistance exhibited by both specimens dropped below 80% of their lateral load capacities at about 5% drift as pointed out in hysteretic curves shown in Figure 2.21. Specimen S-L-2-00, which was wrapped with two plies of CFRP, behaved in a similar manner with the specimen S-L-2-32. In earlier cycles, visible flexural cracks formed between distances 500 to 1000 mm from the column base. In both of the specimens, the column-stub interface cracking and CFRP debonding occurred at 0.5% and 3% drifts, respectively. In Figures 2.22 and 2.23, the formation interval of these events is plotted in hysteretic response of the specimens. Specimen S-L-2-32 had a very similar behavior considering crack locations and plastic hinge length. CFRP rupture took place at drifts of 7% and 6% for S-L-2-00 and S-L-2-32, respectively. 20% drop of column capacity occurred at approximately 6% for both of the specimens. Considering the Moment (M) – Average Curvature (K) values monitored between 350-0 and 350-50 mm above the column base, the curvature values corresponding to the 20% strength drop were approximately 70 and 50 rad/km for the reference (S-L-0-00), 130 and 70 rad/km for one layer CFRP wrapped specimens (S-L-1-00 and S-L-1-34) and 180 and 70 rad/km for two layer wrapped specimens (S-L-2-00 and S-L-2-32) as shown in Figures 2.24-2.26 (Table 2.5). For all the specimens, the ultimate value of the average curvature values monitored between 350-0 mm above the column base were observed to be higher than the curvatures measured between 350-50 mm (Figures 2.24-2.28). The readings recorded relative to the column base were greater since the opening of the interface crack enforced all damage to accumulate just above the column base and the interface crack. Thus, the readings relative to the column base included additional rotations due to rebar slip; rebar extension, concrete crushing and plastic hinging. As a result, the monitored data relative to 50 mm height were observed to be lower than the total rotation in between 350 mm height and the column base. As can be observed from the graphs, for both 1 layer CFRP wrapped specimens, the ultimate curvature values could reach approximately 130 rad/km regarding the gage readings relative to the column base. However, the monitored data relative to 50 mm above the column base indicated that the ultimate curvature values could reach about 70 rad/km. The

monitored fixed-end rotation data implied that the maximum rotation in the test region due to the extension and slipping of the plain reinforcing bars was 0.008 rad for the reference specimen, S-L-0-00 (Figure 2.29). However, for the one and two-layer CFRP wrapped columns, the fixed-end rotations were in levels of approximately 0.03 and could reach up to 0.05 rad for S-L-2-00, as shown in Figures 2.30-2.33. The strain gage readings for the reference specimen indicated that after the yielding of the longitudinal bars, the strains measured at 50 mm above the column base could not exceed the strain value of 0.004 regarding the buckling of the reinforcing bars in the compression zone (Figure 2.34). The observed maximum strain values for the one-layer wrapped specimens were approximately 0.005 (Figures 2.35 and 2.36) and this maximum strain value reached up to 0.008 for the two-layer wrapped specimens (Figures 2.37 and 2.38) owing to the prevention of reinforcement buckling by the wrapped CFRP sheets.

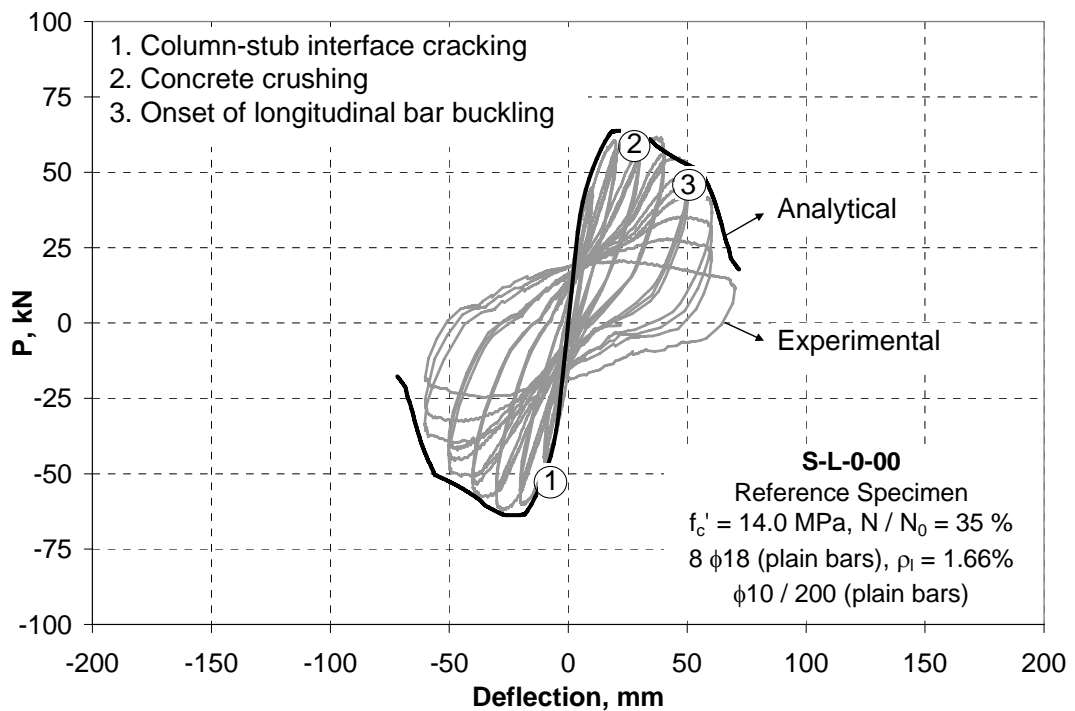


Figure 2.19 Lateral Load (P) – Deflection (Δ) response for S-L-0-00

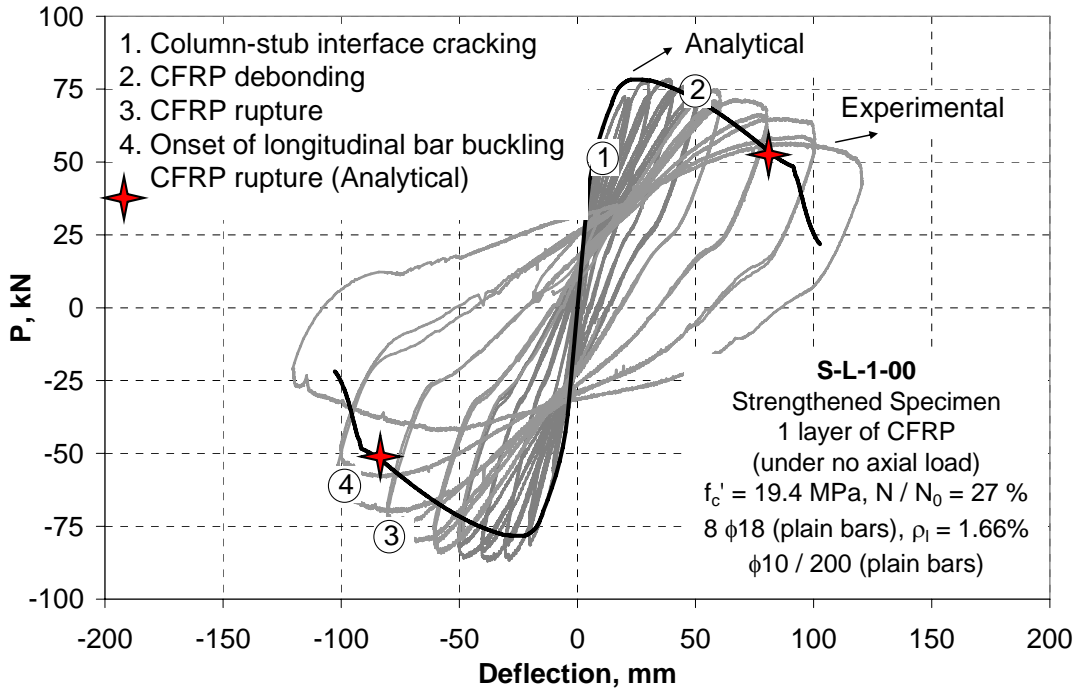


Figure 2.20 Lateral Load (P) – Deflection (Δ) response for S-L-1-00

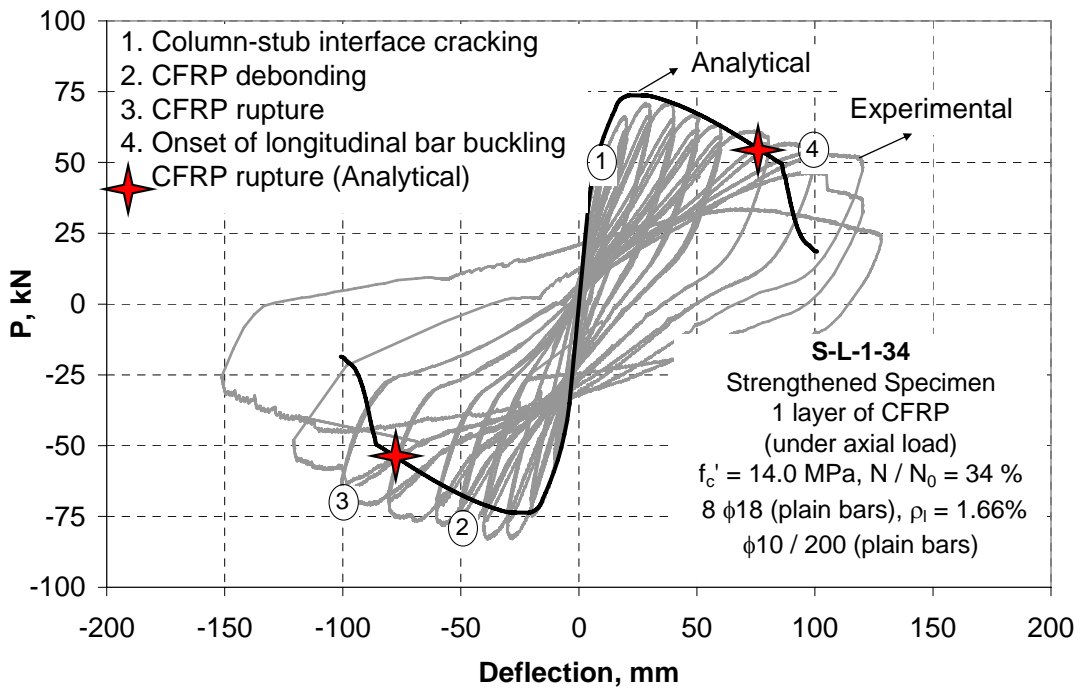


Figure 2.21 Lateral Load (P) – Deflection (Δ) response for S-L-1-34

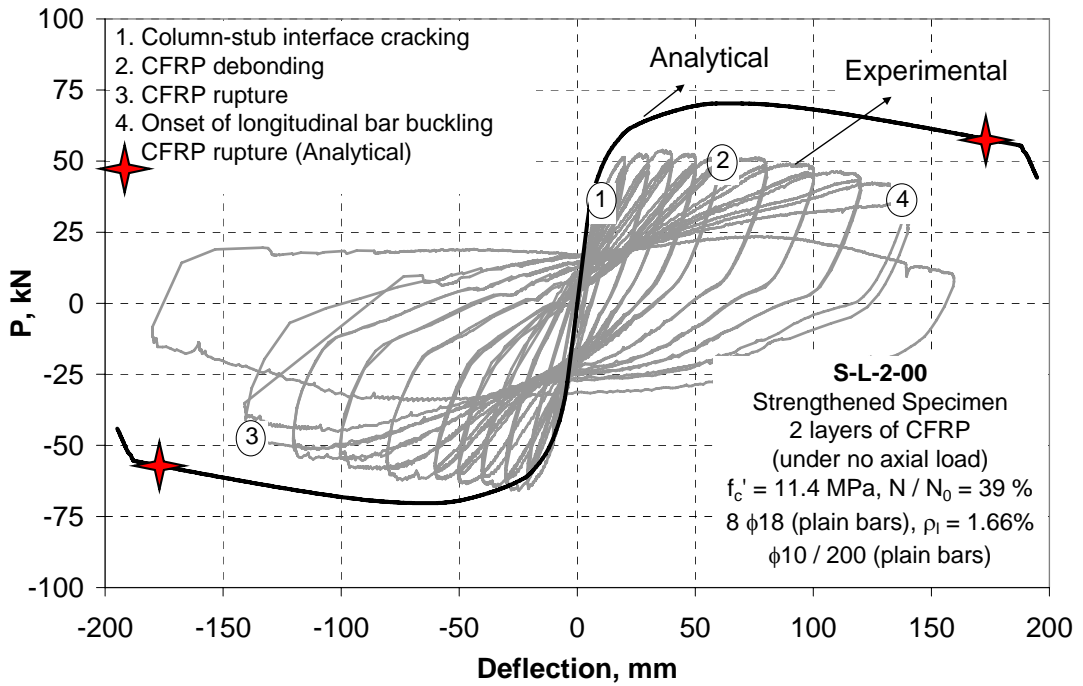


Figure 2.22 Lateral Load (P) – Deflection (Δ) response for S-L-2-00

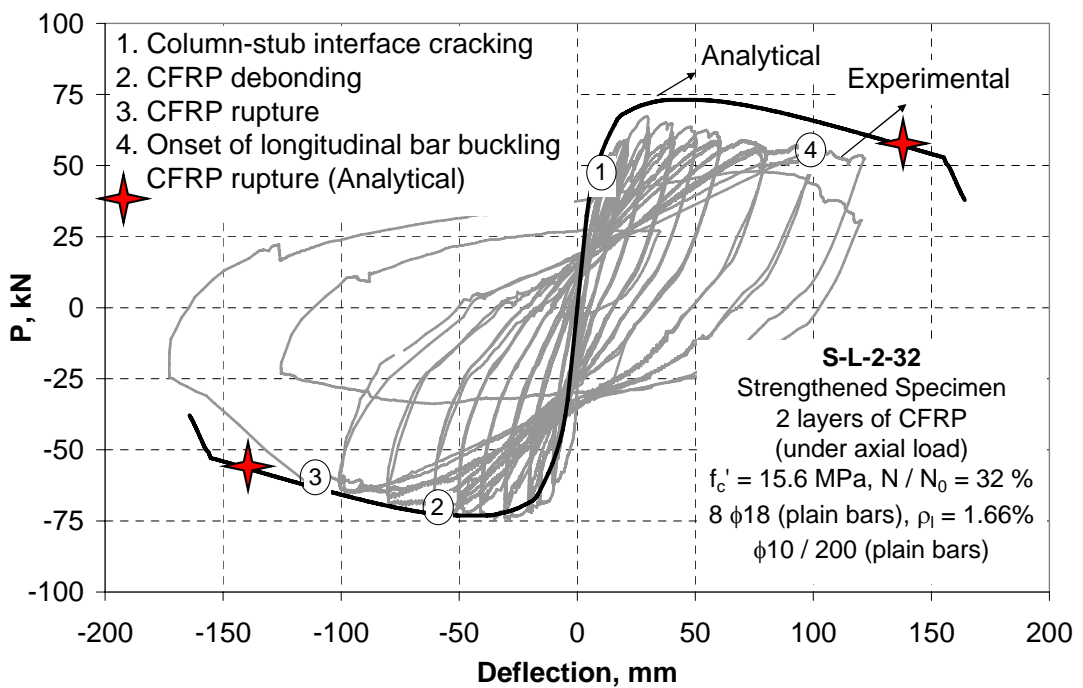
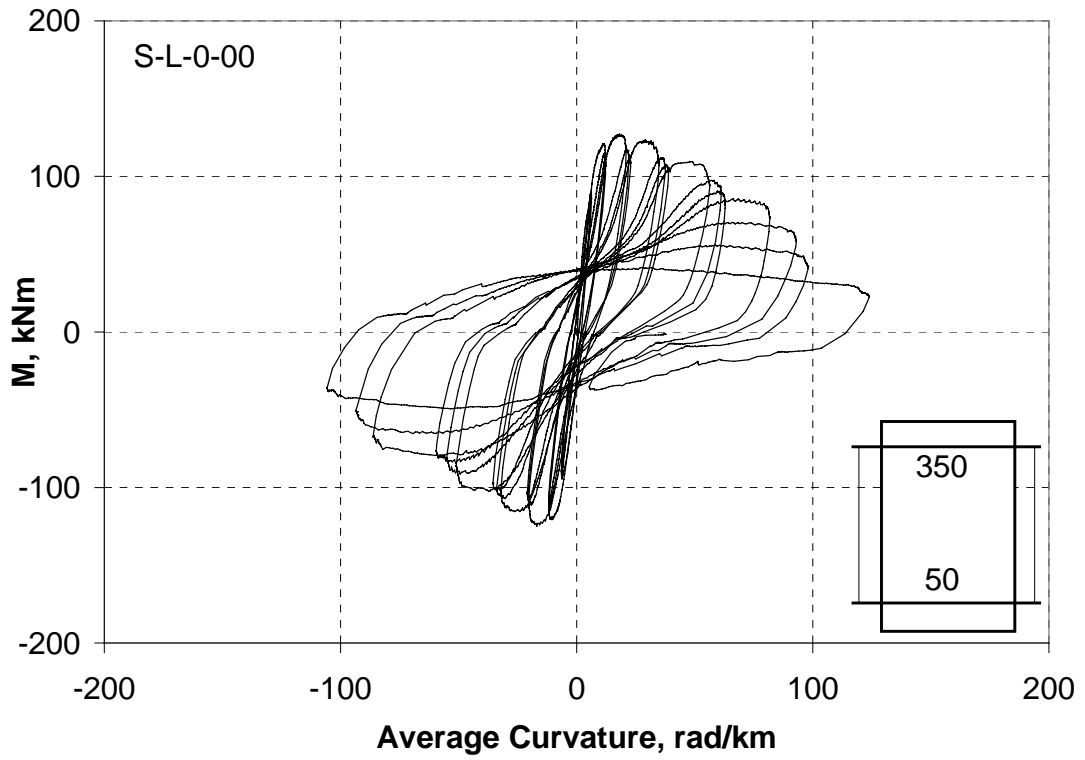
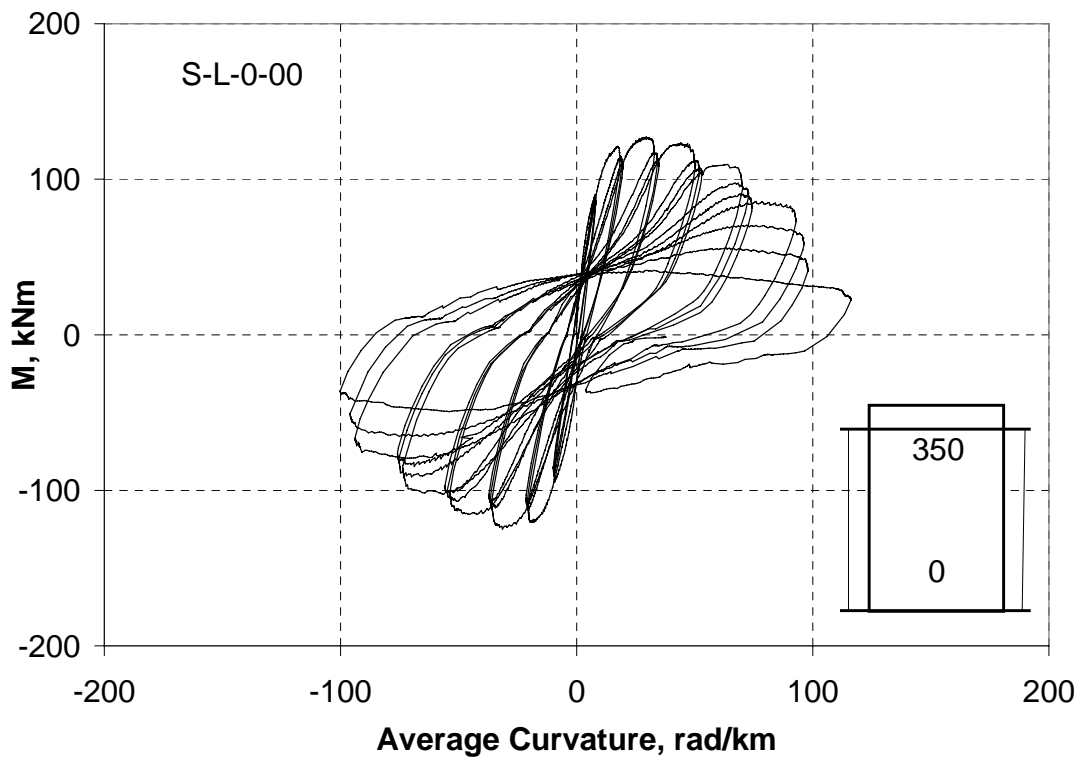


Figure 2.23 Lateral Load (P) – Deflection (Δ) response for S-L-2-32

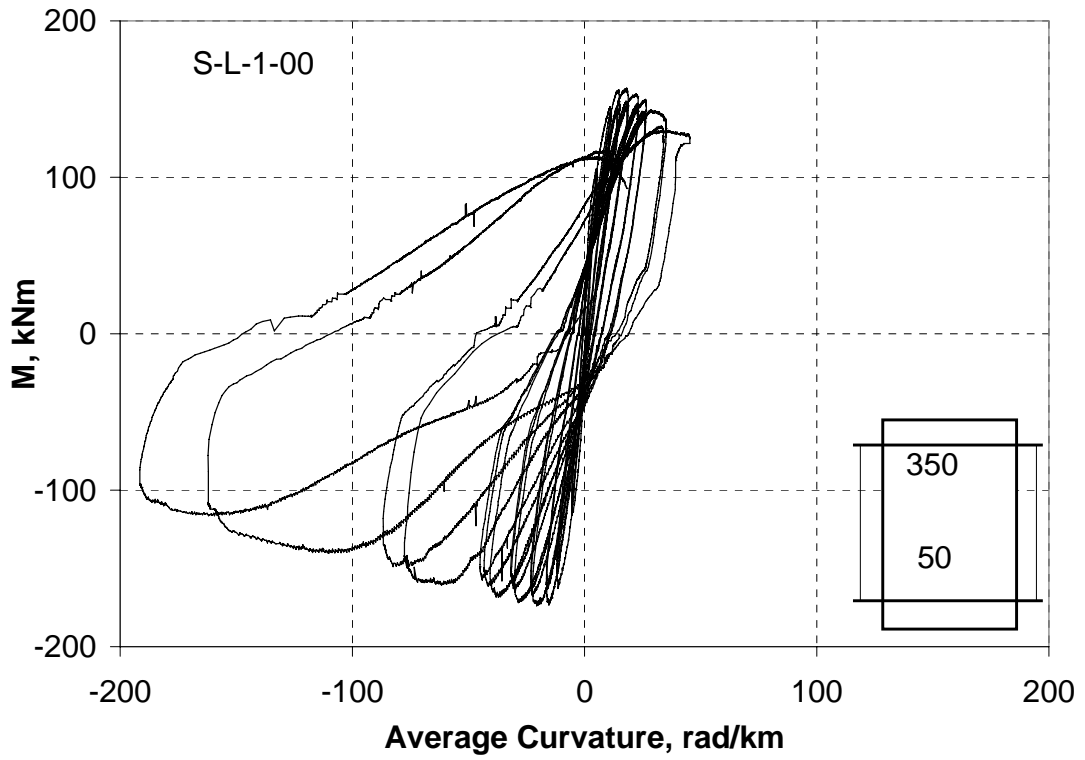


(a)

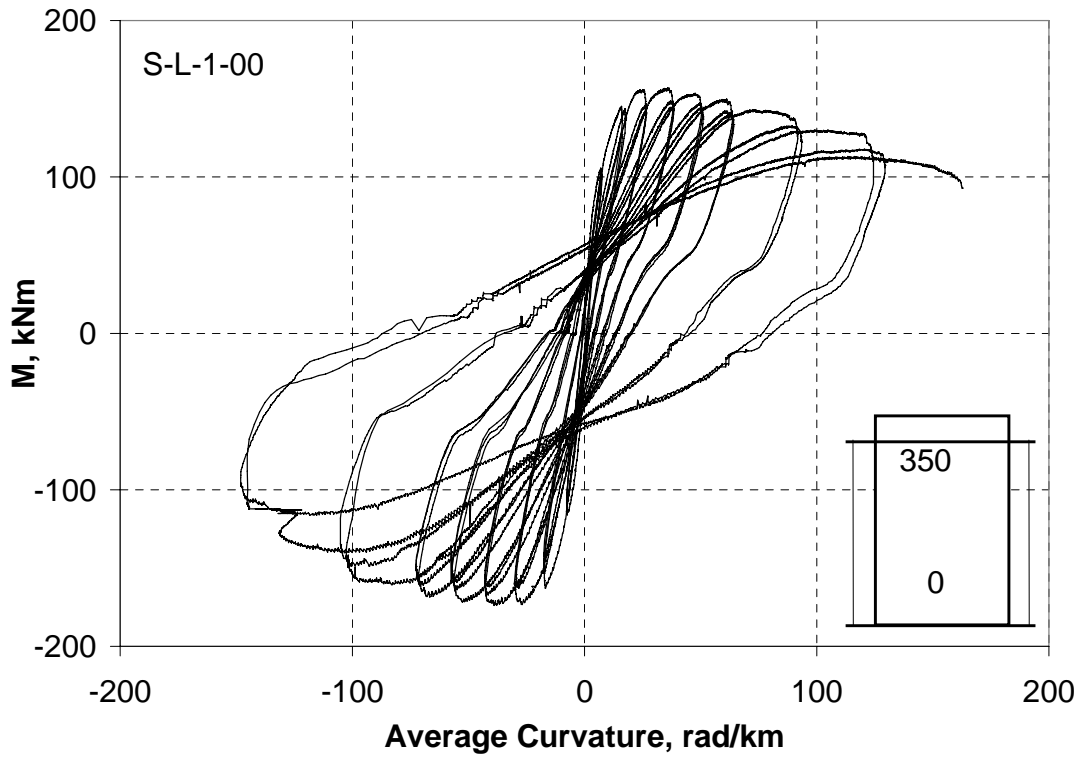


(b)

Figure 2.24 Moment (M) – Average Curvature (K) responses of S-L-0-00: Relative to (a) 50 mm height and (b) Base

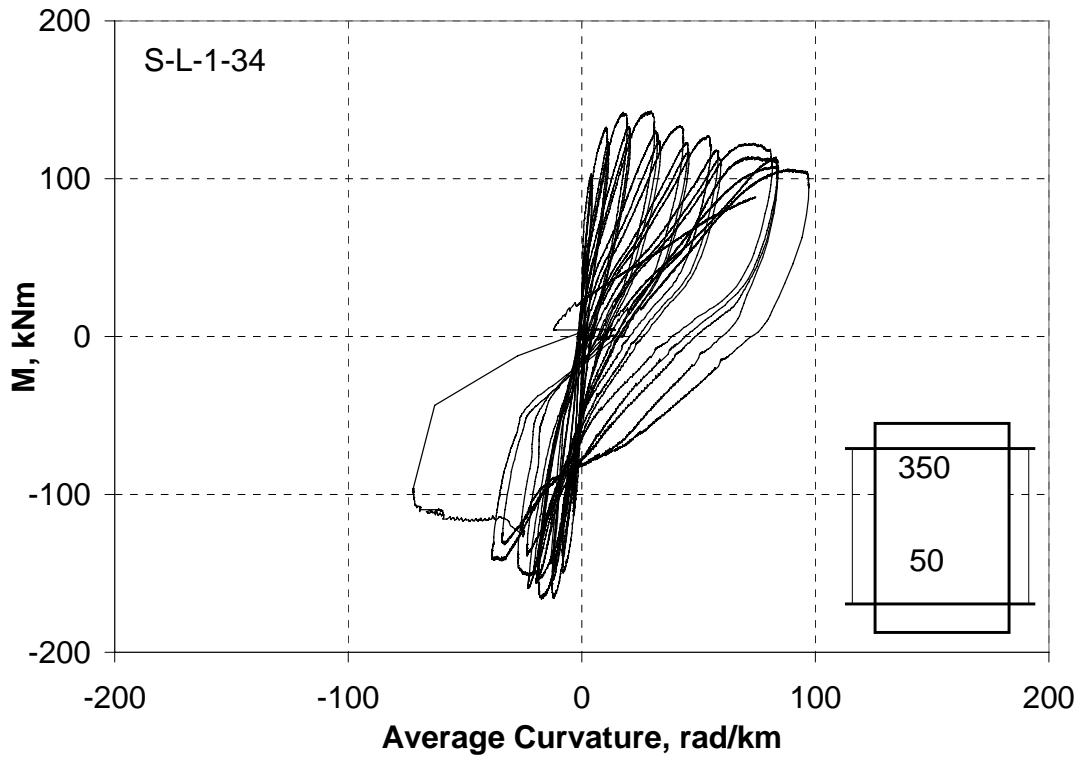


(a)

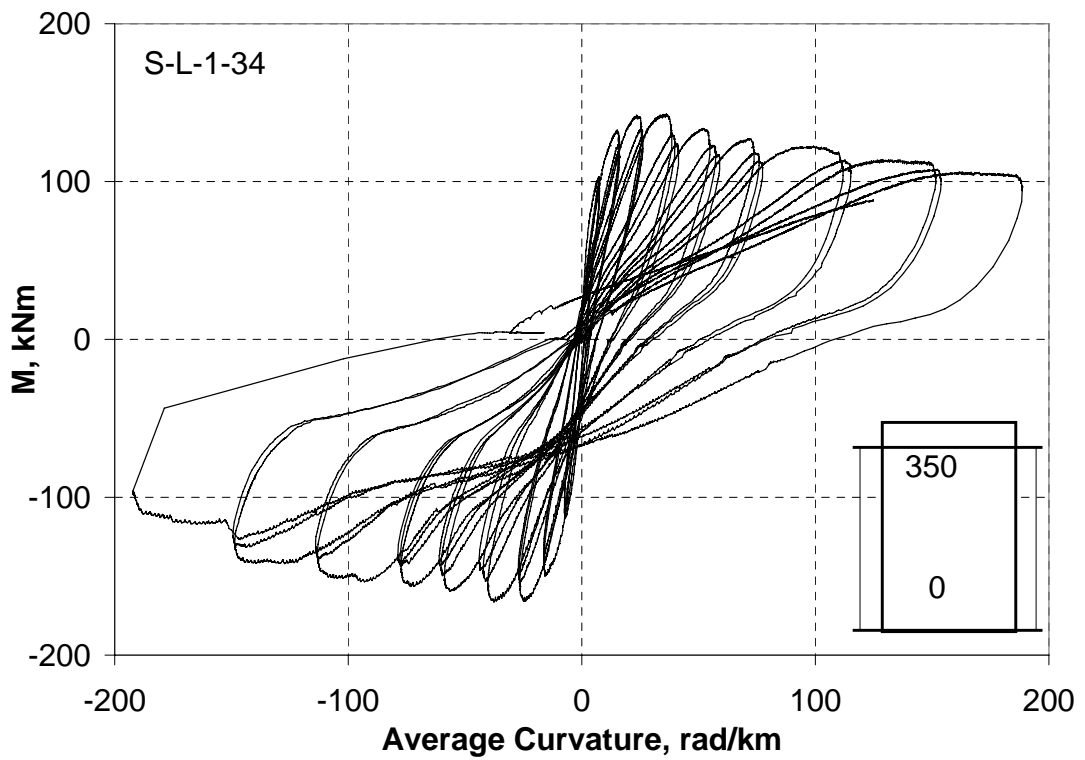


(b)

Figure 2.25 Moment (M) – Average Curvature (K) responses of S-L-1-00: Relative to (a) 50 mm height and (b) Base

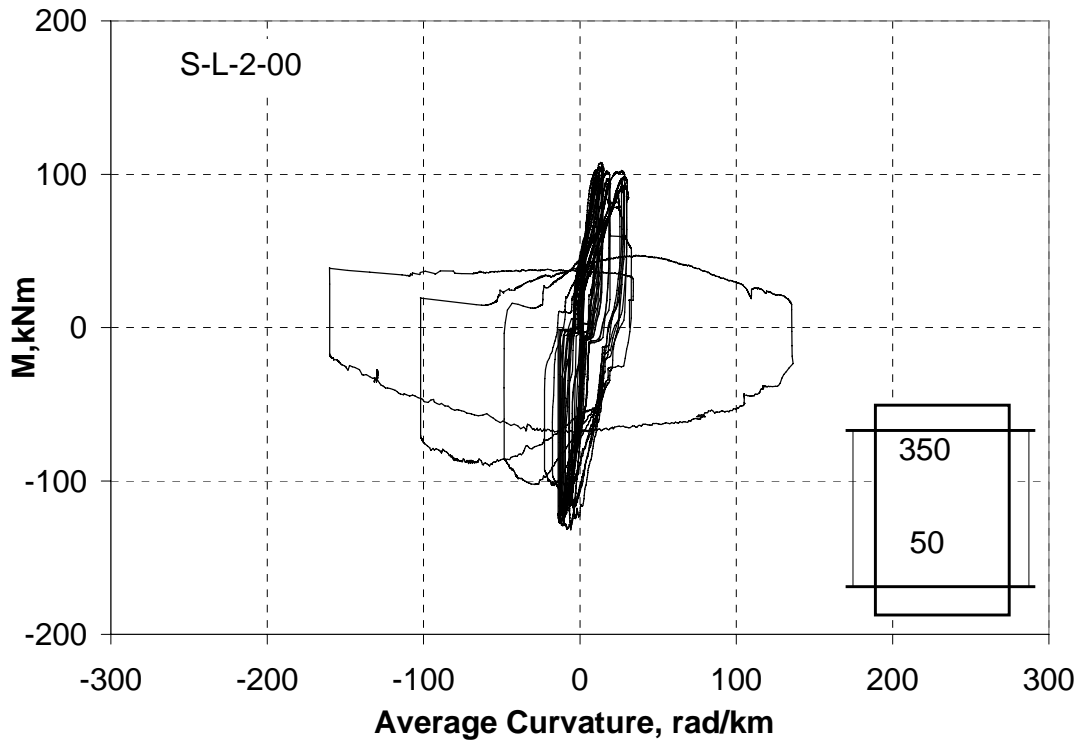


(a)

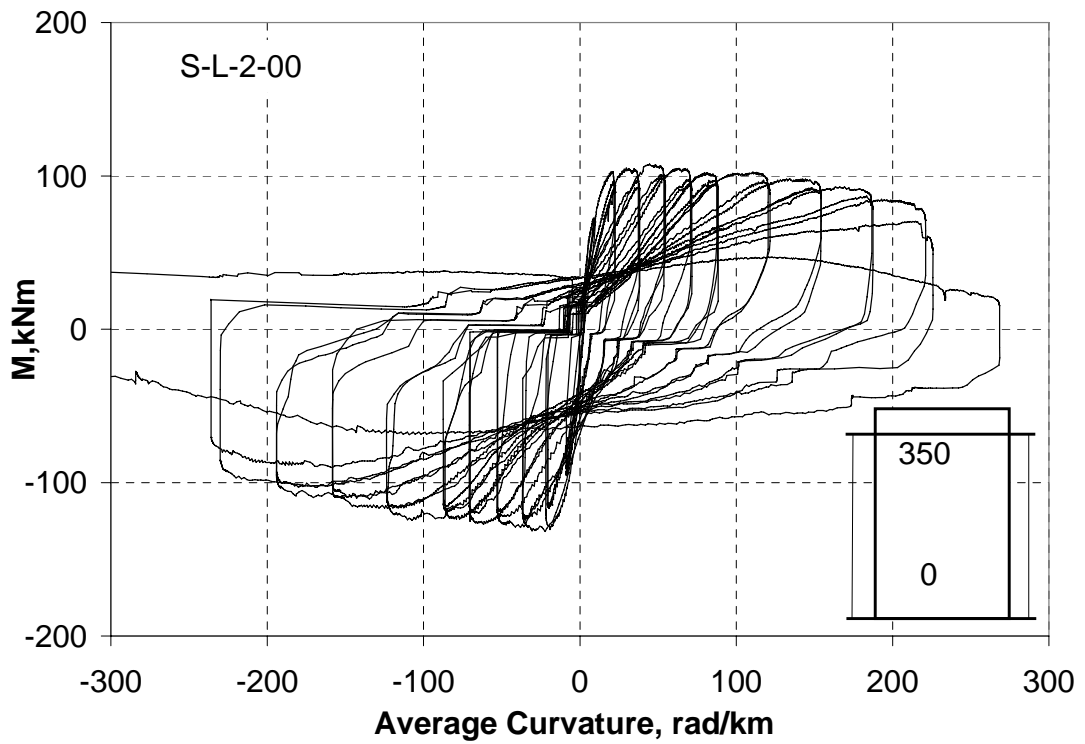


(b)

Figure 2.26 Moment (M) – Average Curvature (K) responses of S-L-1-34: Relative to (a) 50 mm height and (b) Base

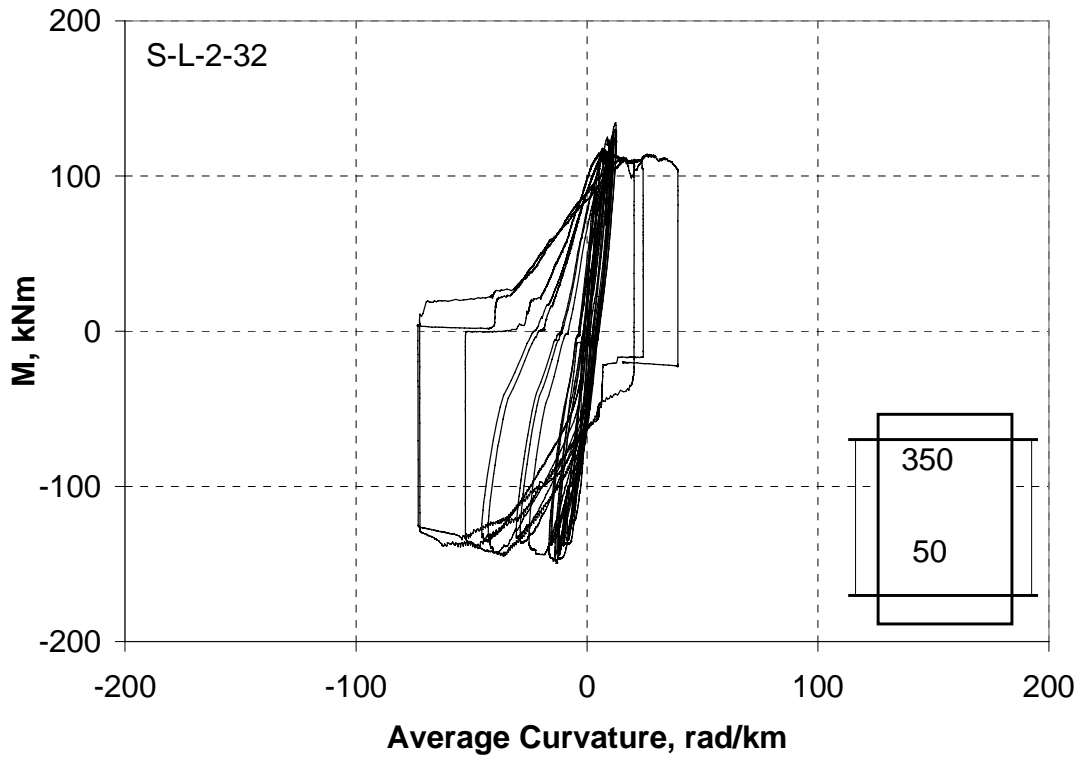


(a)

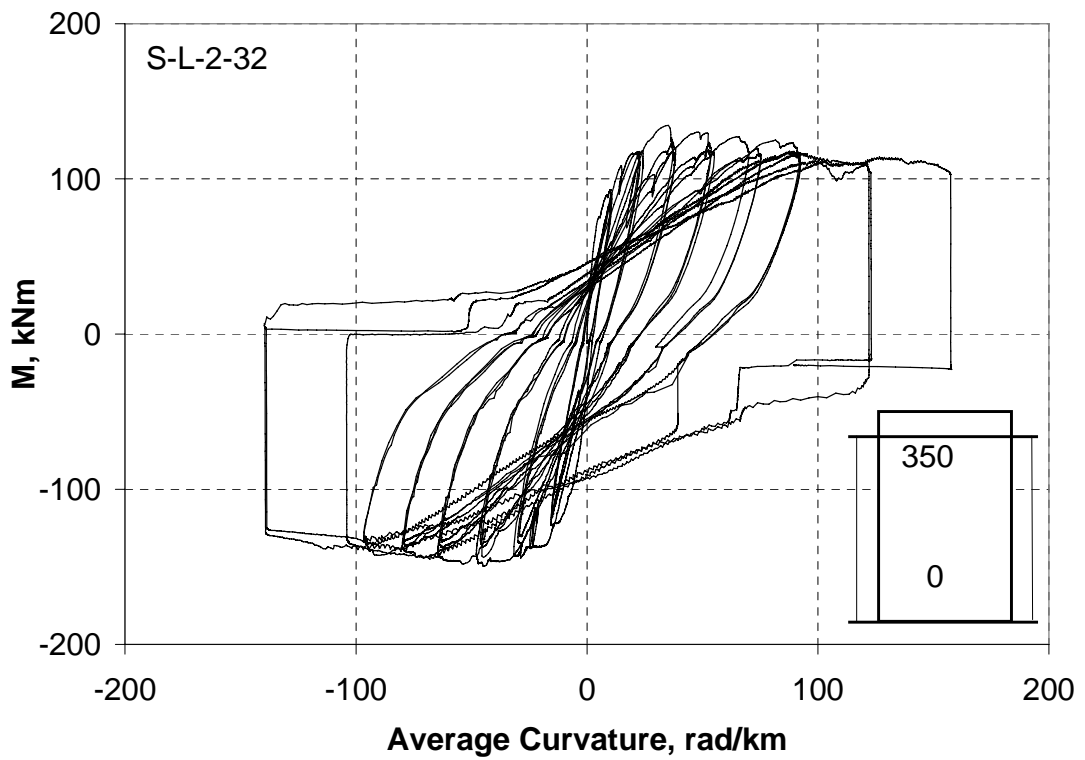


(b)

Figure 2.27 Moment (M) – Average Curvature (K) responses of S-L-2-00: Relative to (a) 50 mm height and (b) Base



(a)



(b)

Figure 2.28 Moment (M) – Average Curvature (K) responses of S-L-2-32: Relative to (a) 50 mm height and (b) Base

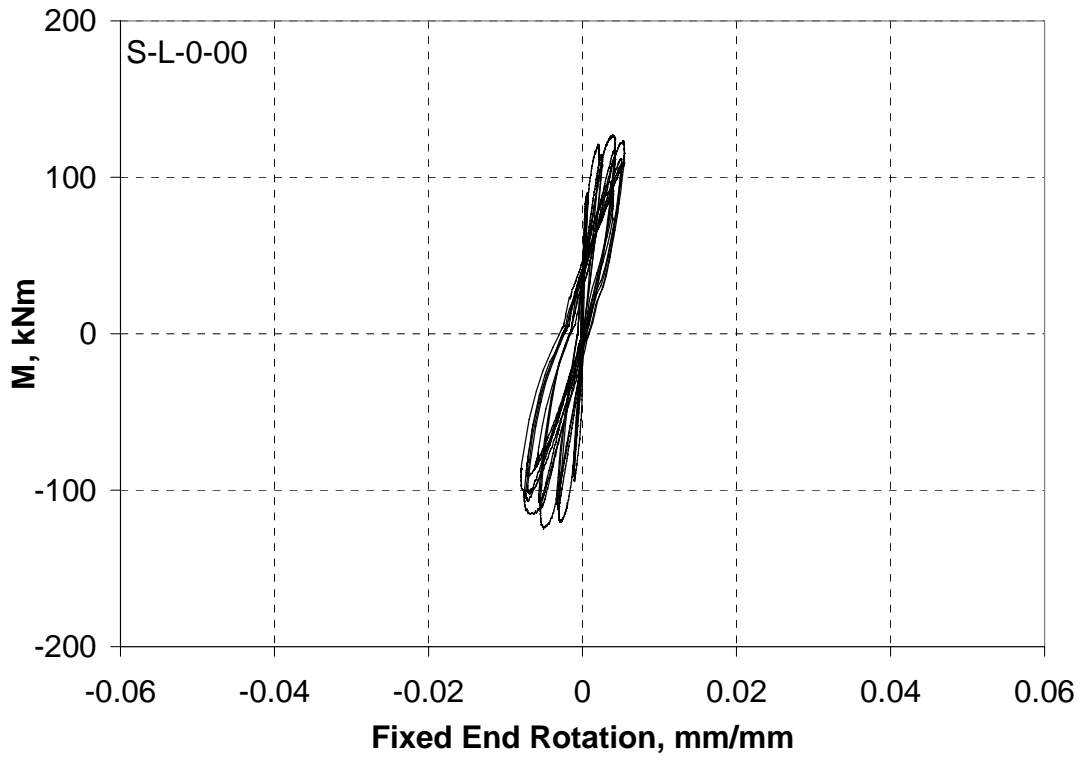


Figure 2.29 Moment (M) – Fixed End Rotation (FER) response of S-L-0-00

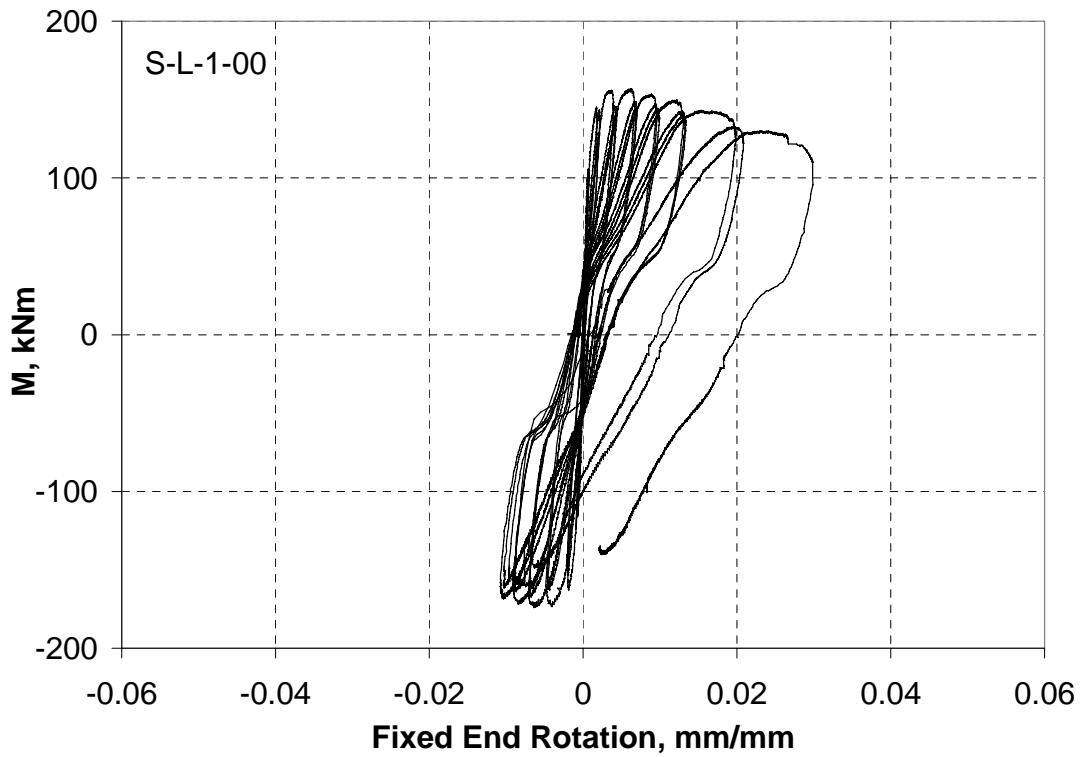


Figure 2.30 Moment (M) – Fixed End Rotation (FER) response of S-L-1-00

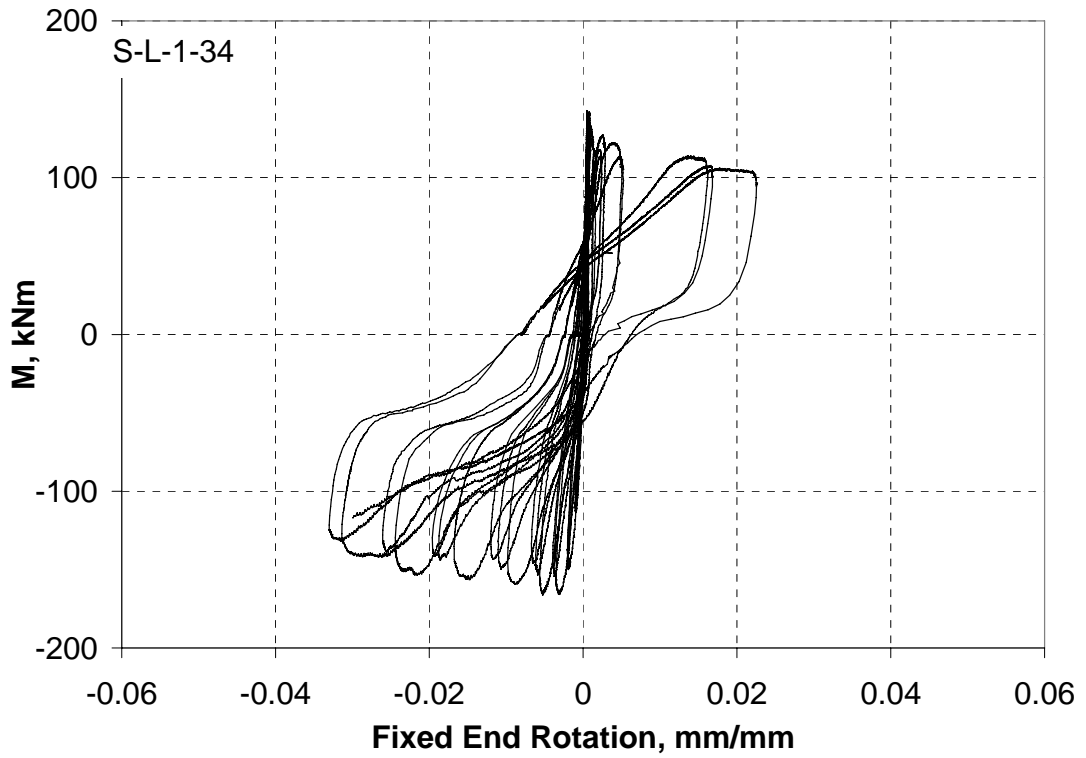


Figure 2.31 Moment (M) – Fixed End Rotation (FER) response of S-L-1-34

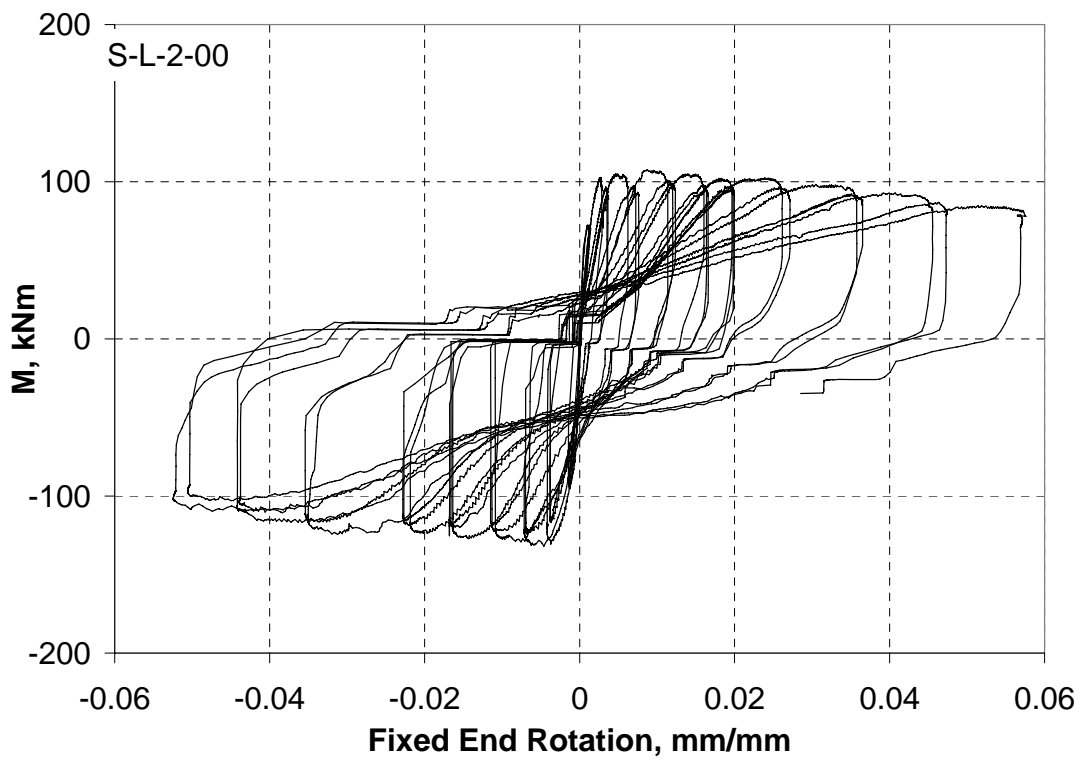


Figure 2.32 Moment (M) – Fixed End Rotation (FER) response of S-L-2-00

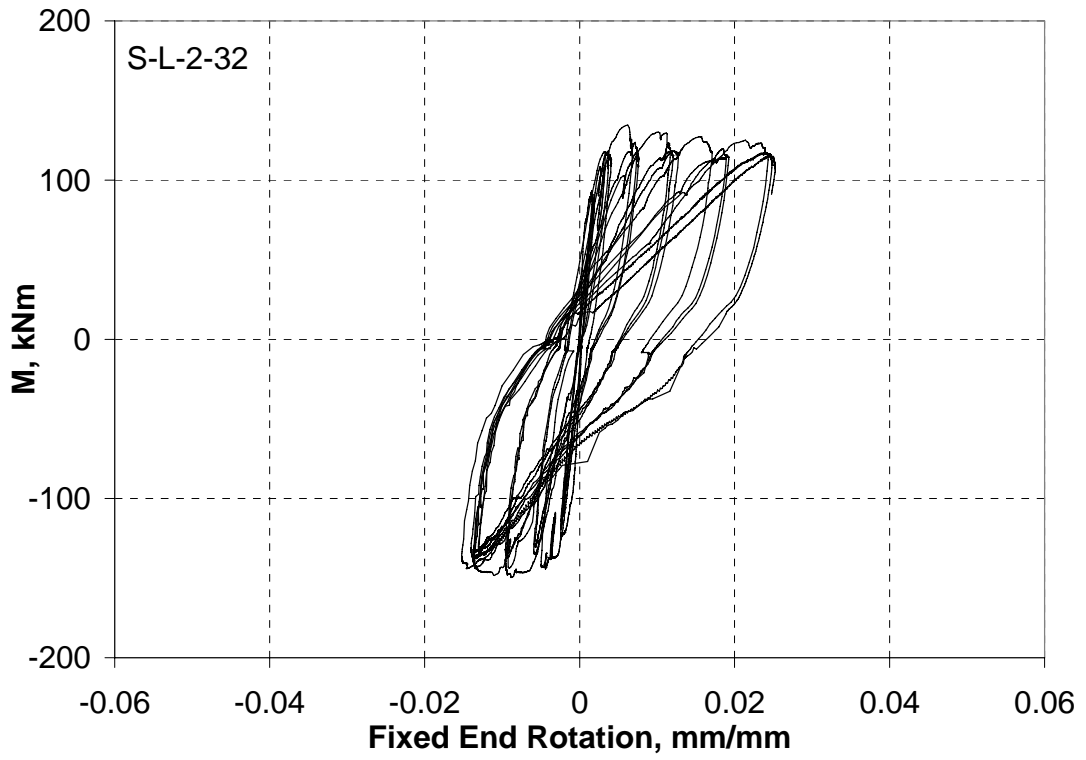


Figure 2.33 Moment (M) – Fixed End Rotation (FER) response of S-L-2-32

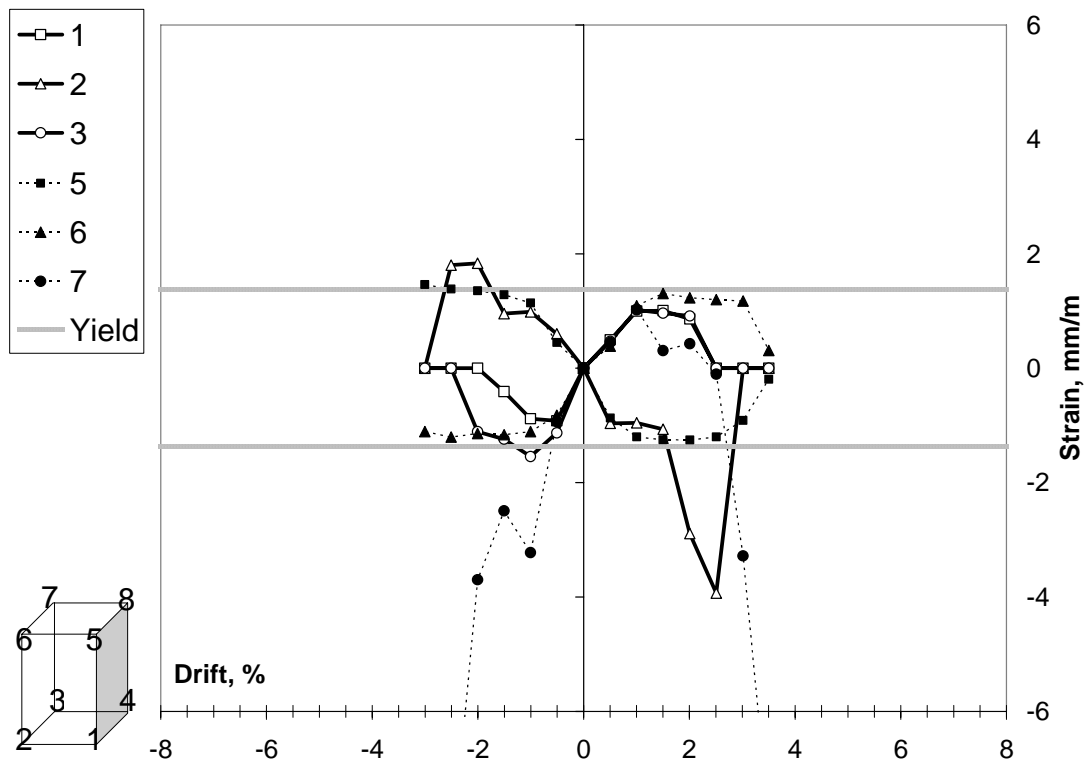


Figure 2.34 Strain – Drift responses for S-L-0-00

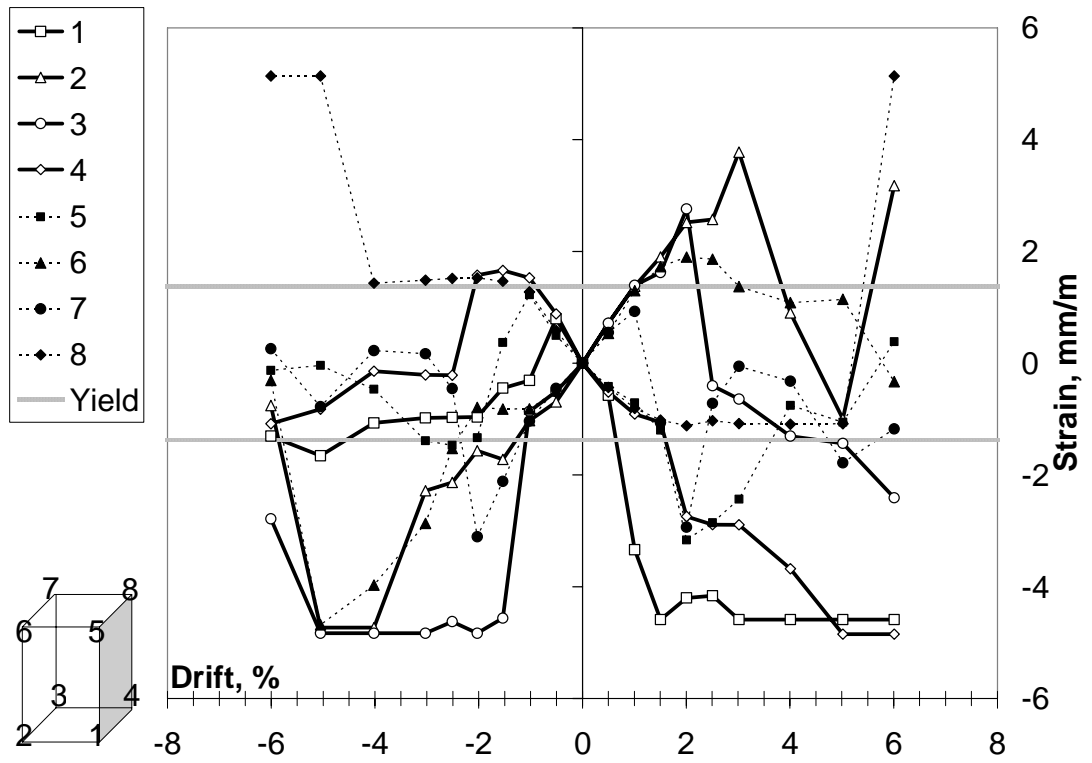


Figure 2.35 Strain – Drift responses for S-L-1-00

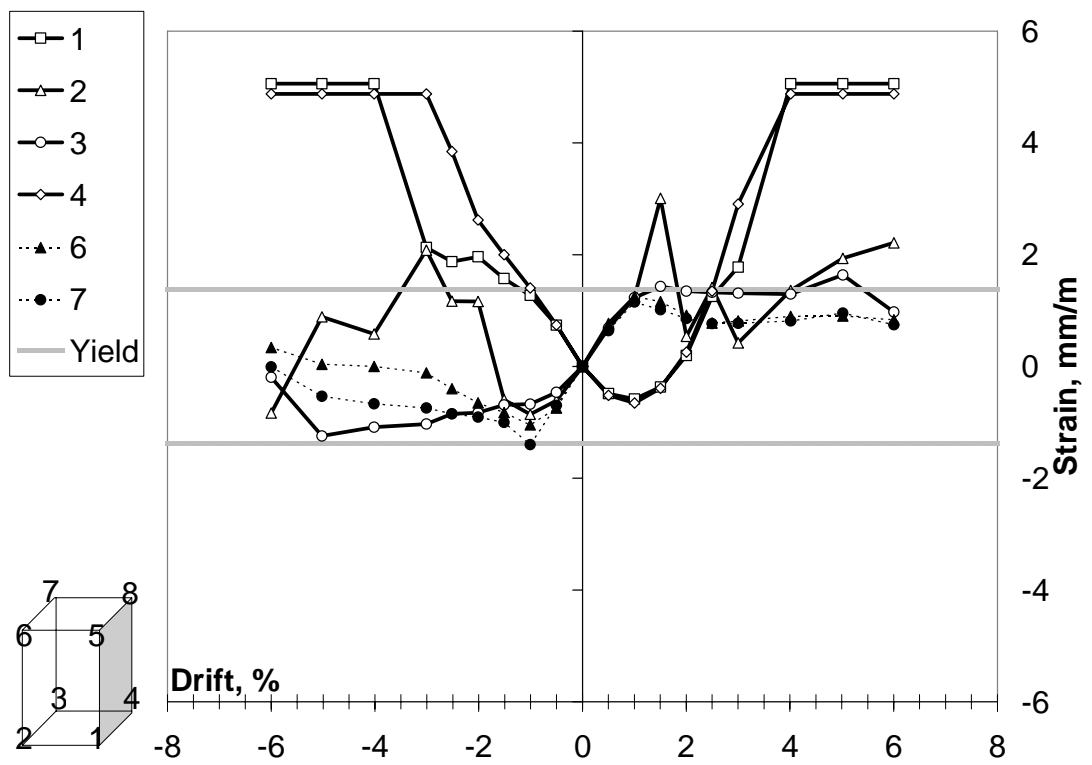


Figure 2.36 Strain – Drift responses for S-L-1-34

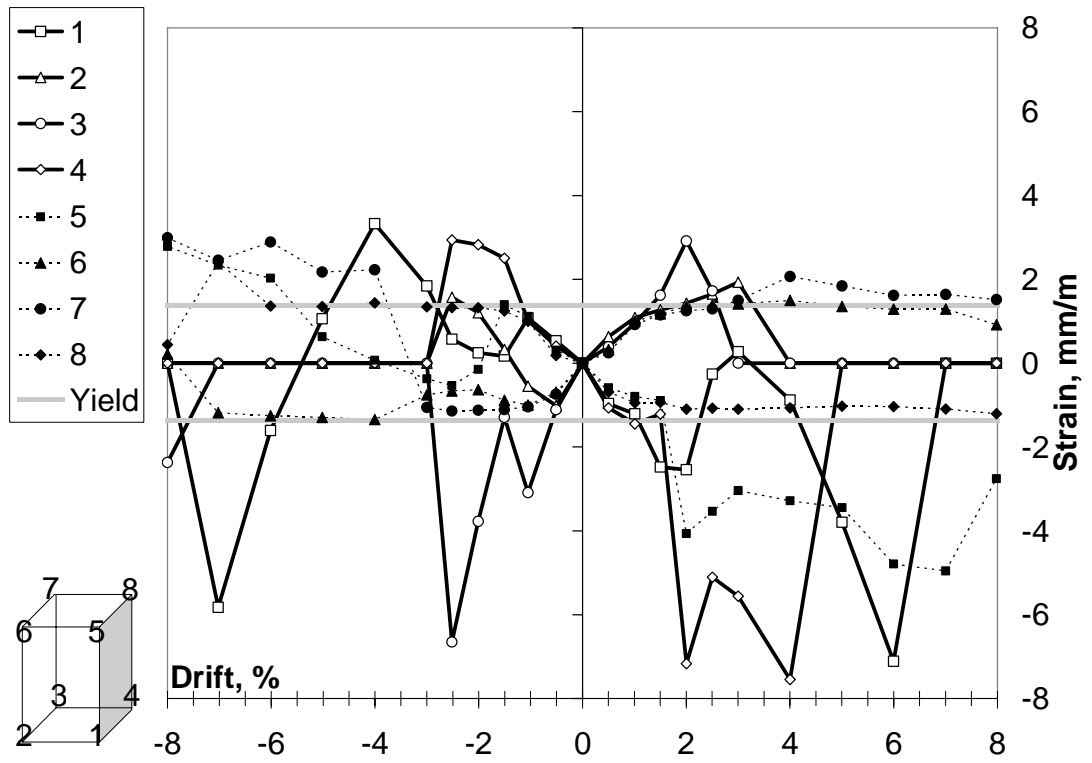


Figure 2.37 Strain – Drift responses for S-L-2-00

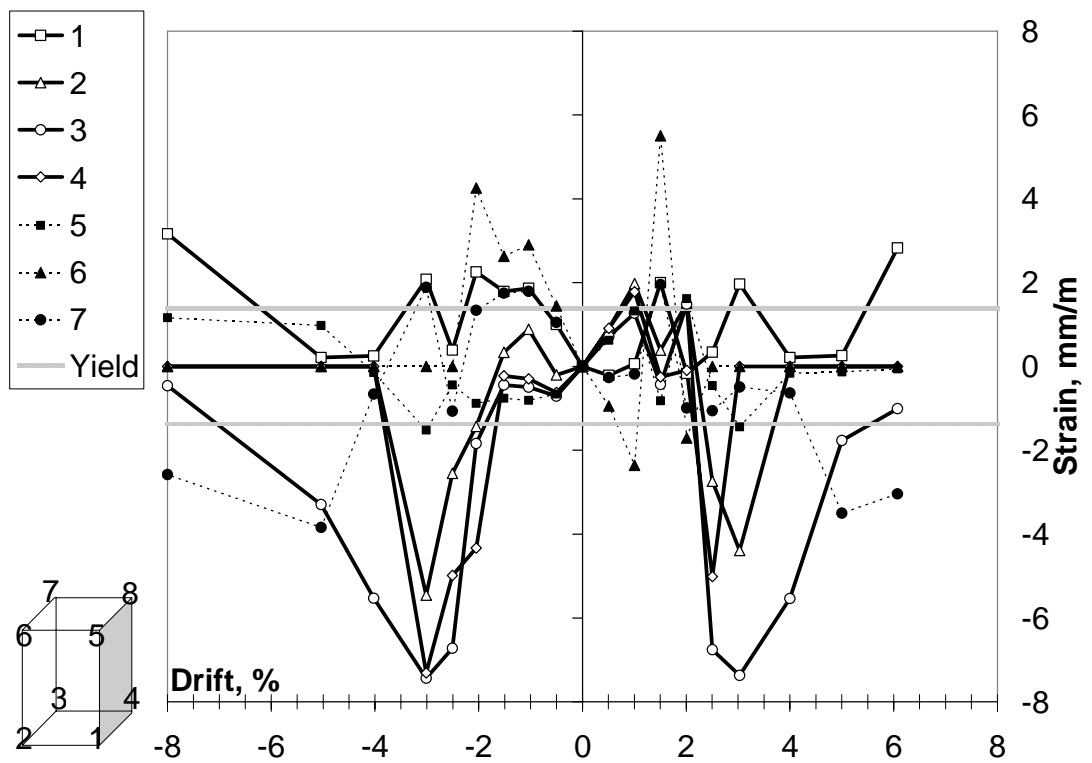


Figure 2.38 Strain – Drift responses for S-L-2-32

2.6.2. Series 2

All of the test specimens in Series 2 experienced a similar failure mode at the column base namely flexural failure due to column plastic hinging. The pictures of plastic hinge regions of failed specimens are shown in Figure 2.39. For the reference specimen S-H-0-00, the column-stub interface cracked at 0.5% drift level and as the column performed inelastic displacement cycles, slipping of the reinforcement increased due to widening of the interface crack. Furthermore, evenly distributed flexural cracks were observed at both faces of the column at heights from 50 to 1000 mm. First cover crushing was observed at the column base corners during the cycles of 2% drift level. Lateral load carrying capacity degraded below 80% of the capacity after onset of buckling of the longitudinal rebars at a drift level of 3%. The hysteretic behavior for the specimen S-H-0-00 is presented in Figure 2.40. All the retrofitted columns were wrapped with 1 layer of CFRP within 650 mm starting from 15 mm above the column base. In all columns, the column-stub interface cracking was observed at 0.5% drift level. In the strengthened column, S-H-1-00, the visible flexural cracks were developed at heights from 650 to 1000 mm from the base of the column at the initial cycles of displacement excursions. These cracks were closer to each other than those observed in the reference specimen. In the following cycles, the flexural cracks opened further and closed in the opposite cycles of deformations. Due to the horizontal CFRP cracks at 100 mm from the base, CFRP at the other face of the column started to debond at about 2.5% drift level. The confinement effect of CFRP helped in maintaining the lateral capacity constant and preventing longitudinal bar buckling. The interface crack (i.e. crack observed at column base stub interface) widened which resulted in increase of the longitudinal reinforcement slip at the column-stub interface and the drift ratio reached the ultimate at about 4% drift. The first rupture at the CFRP sheet occurred at 5% drift and the lateral load dropped below 80% of the capacity by onset of buckling of the longitudinal rebars as illustrated in Figure 2.41. The repaired columns, S-HD-1-00 and S-HD-1-27 exhibited similar deformation behavior. In the first phase of the tests, both of the repaired columns were subjected to a moderate damage level of 2% drift. Evenly distributed flexural cracks formed at heights from 50 to 1000 mm from the column base. The only difference was the presence of axial load during the repairing process,

which was about 27% of the axial capacity for the column S-HD-1-27. The flexural cracks that formed in the pre-damage state opened further and no new flexural cracks outside the strengthened region occurred in the retesting stage. The drift levels at which CFRP debonding, CFRP rupture and 20% drop in lateral capacity took place were identical for the three specimens (2%, 4% and 5% drift respectively) as shown in Figures 2.42-2.44. The lateral load capacity of the repaired column S-HD-1-27 did not change as compared to the capacity observed at the damage stage whereas for its companion column S-HD-1-00, the lateral capacity enhancement of about 15% was observed (Figures 2.42 and 2.43). For the repaired columns, the strength of the columns decreased compared to the strengthened column due to the initial damage. Furthermore, for the repaired columns, the initial stiffness degraded about half of the strengthened specimen owing to the previous damage cycles. The initial stiffness of the repaired columns reduced due to further opening of the pre-formed cracks at previously applied moderate damage cycles.

For the reference specimen, S-H-0-00, the average curvature at which the column lateral capacity dropped below 80% of the capacity was approximately 90 and 50 rad/km relative to column base and 50 mm height, respectively (Figure 2.45). The CFRP strengthened and repaired specimens experienced average curvature values beyond this level as much as 100 to 150 rad/km relative to the column base (Figures 2.45-2.49). However, the monitored curvature readings relative to 50 mm height was observed to be lower than the recorded data relative to the column base as similar to the curvature readings in Series 1. A similar behavior was observed for the strengthened columns in Series 2 due to damage accumulation just above the column base after the cracking of the column-stub interface.



(a)



(b)



(c)



(d)



(e)

Figure 2.39 Columns at the end of testing (a) S-H-0-00, (b) S-H-1-00, (c) S-HD-1-00, (d) S-HD-1-27, (e) S-HC-1-00

The same impact of CFRP wrapping on fixed-end rotations was observed upon comparing the 1-layer CFRP wrapped specimens with the reference specimen since the fixed-end rotations that the columns experienced were increased from 0.015 to 0.03 rad (Figures 2.50-2.54). The longitudinal reinforcement strains observed in the reference specimen S-H-0-00, increased up to the strain level of 0.004 and subsequently due to the buckling of the longitudinal rebars, the strain could not exceed that level owing to the wide spacing of the stirrups in the test region (Figure 2.55). The strengthened and repaired specimens experienced longitudinal strain values in the test region up to 0.005 since the confining effect of CFRP prevented premature buckling of the longitudinal rebars and made the columns sustain higher drift levels by enhancing the fixed-end rotation and curvature response of the columns (Figures 2.56-2.61). In addition, the strain levels during the damage cycles were observed to be very close to the yielding level as shown in Figures 2.57 and 2.59.

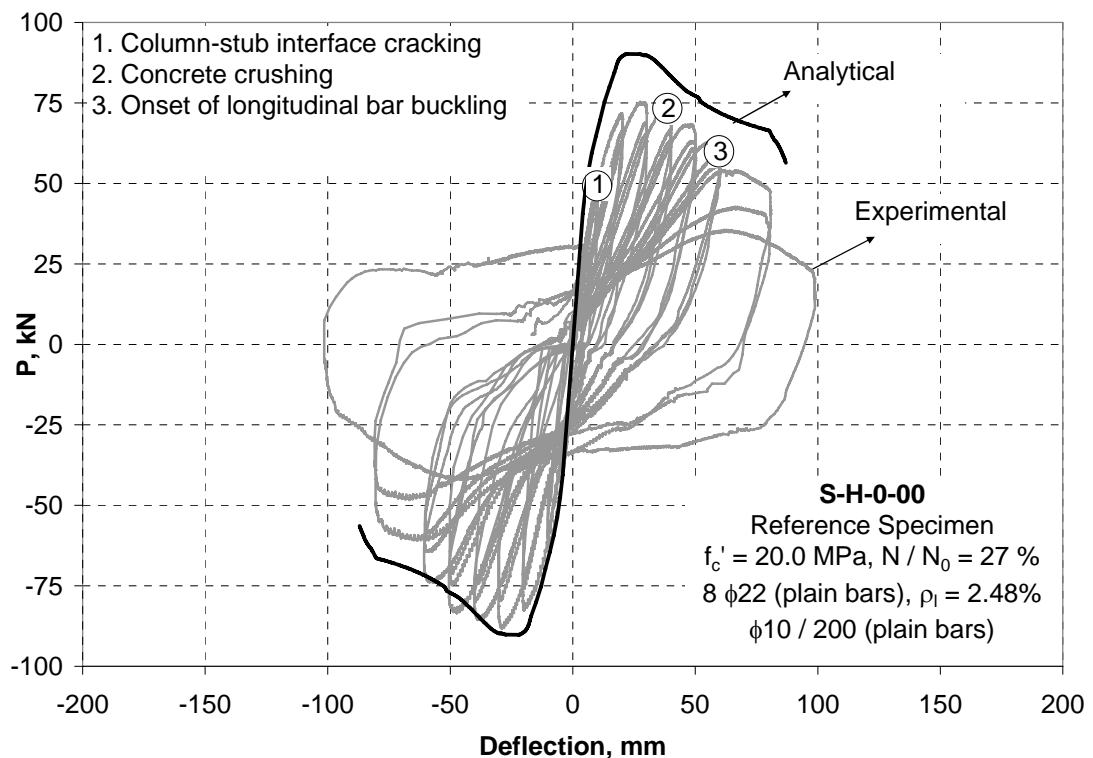


Figure 2.40 Lateral Load (P) – Deflection (Δ) response for S-H-0-00

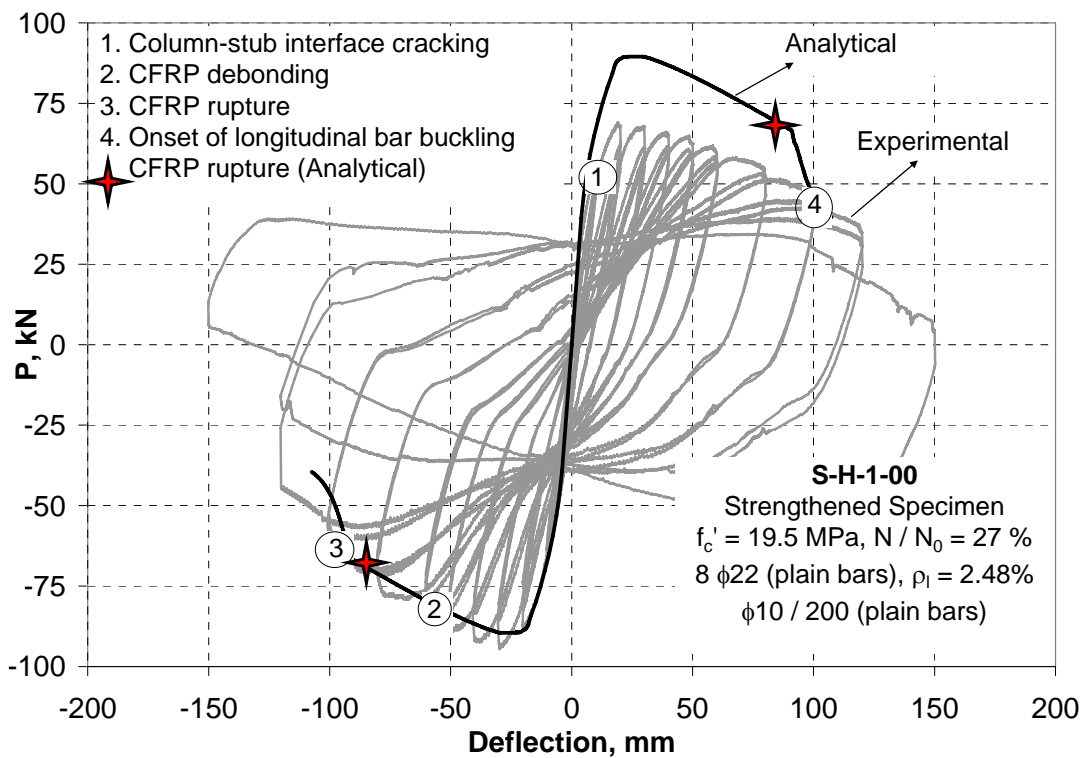


Figure 2.41 Lateral Load (P) – Deflection (Δ) response for S-H-1-00

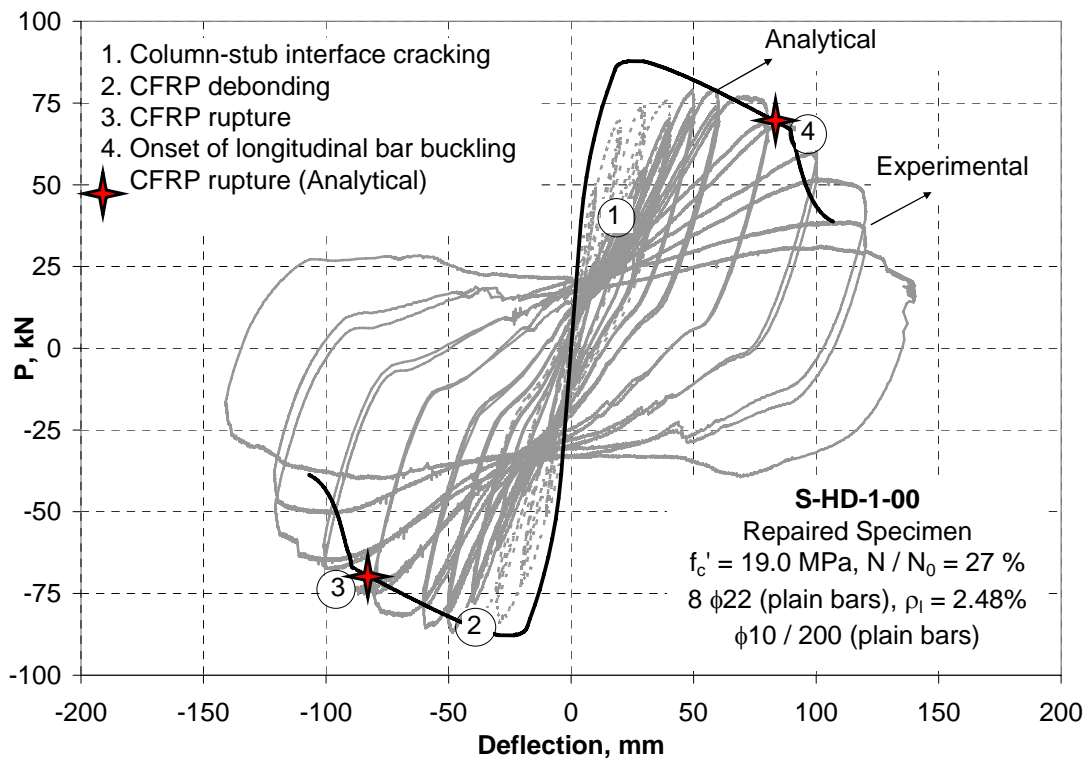


Figure 2.42 Lateral Load (P) – Deflection (Δ) response for S-HD-1-00

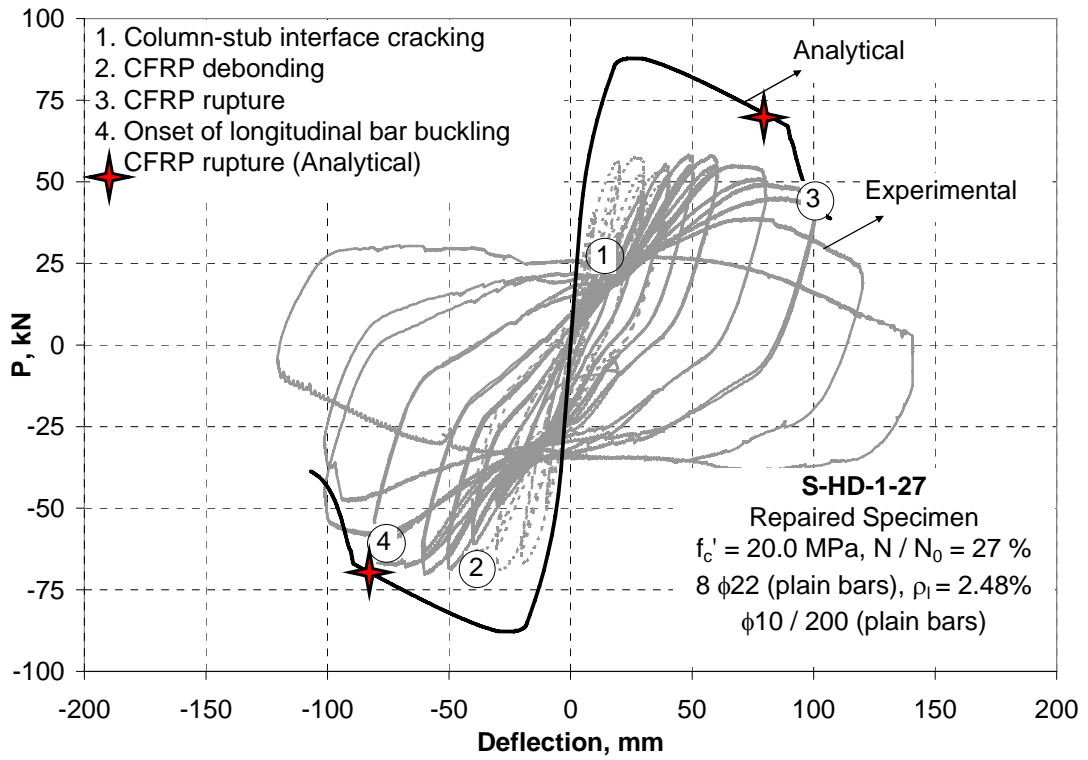


Figure 2.43 Lateral Load (P) – Deflection (Δ) response for S-HD-1-27

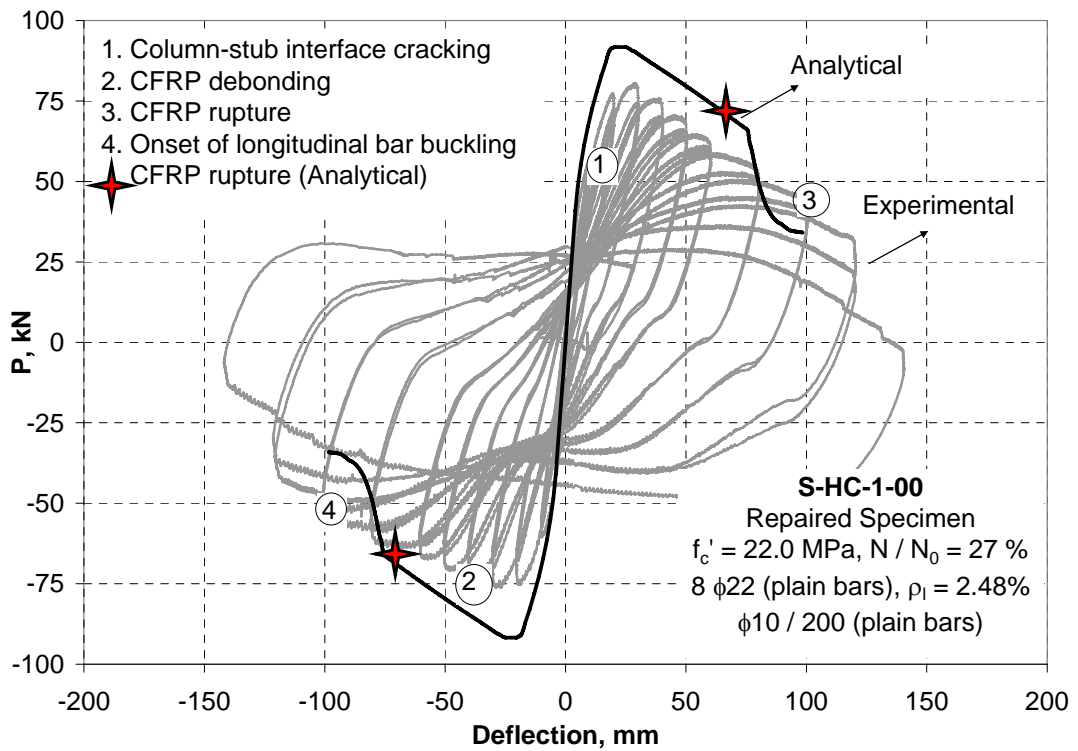
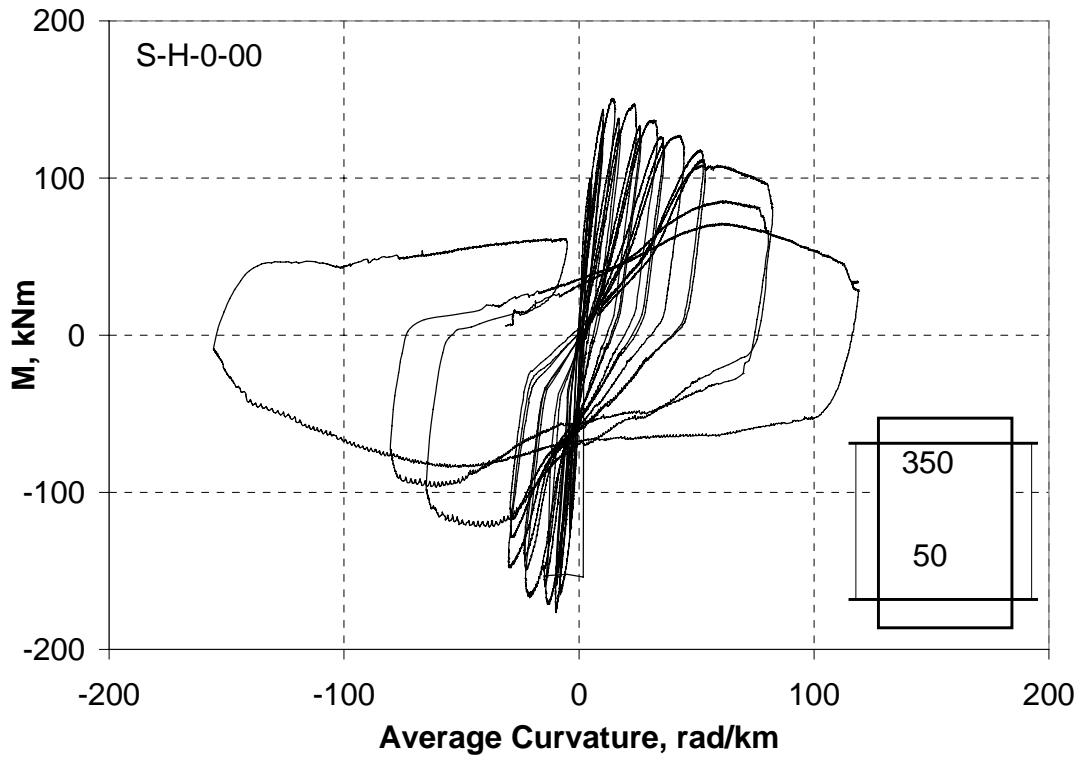
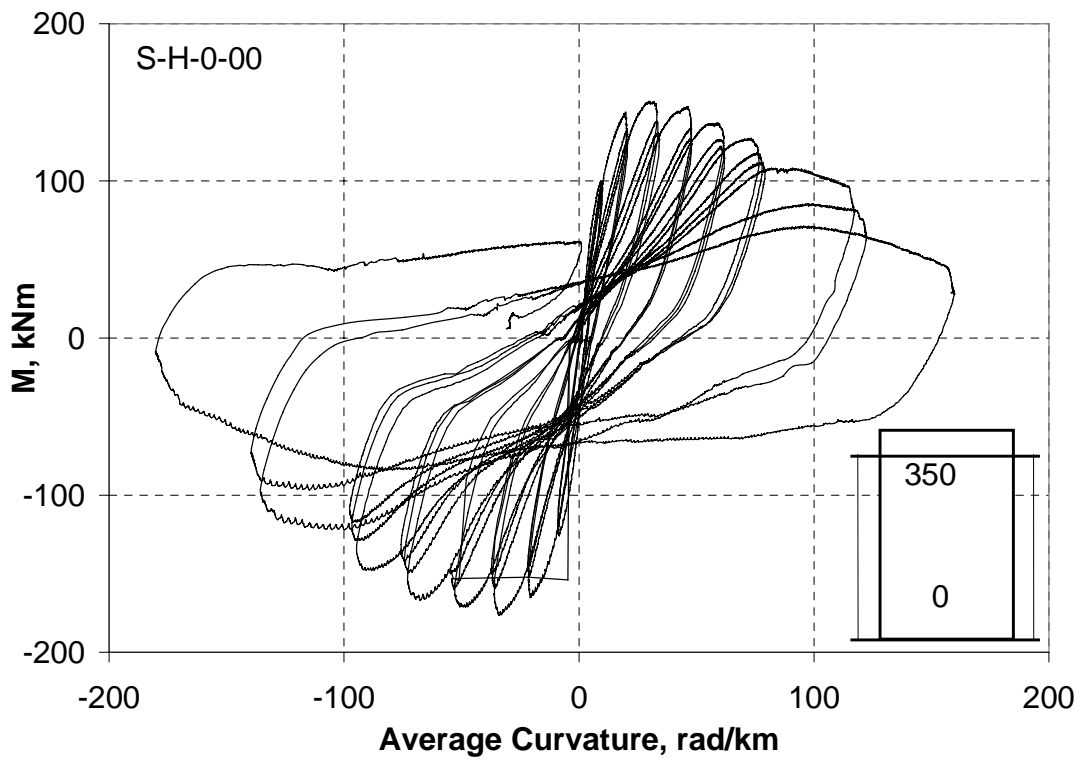


Figure 2.44 Lateral Load (P) – Deflection (Δ) response for S-HC-1-00

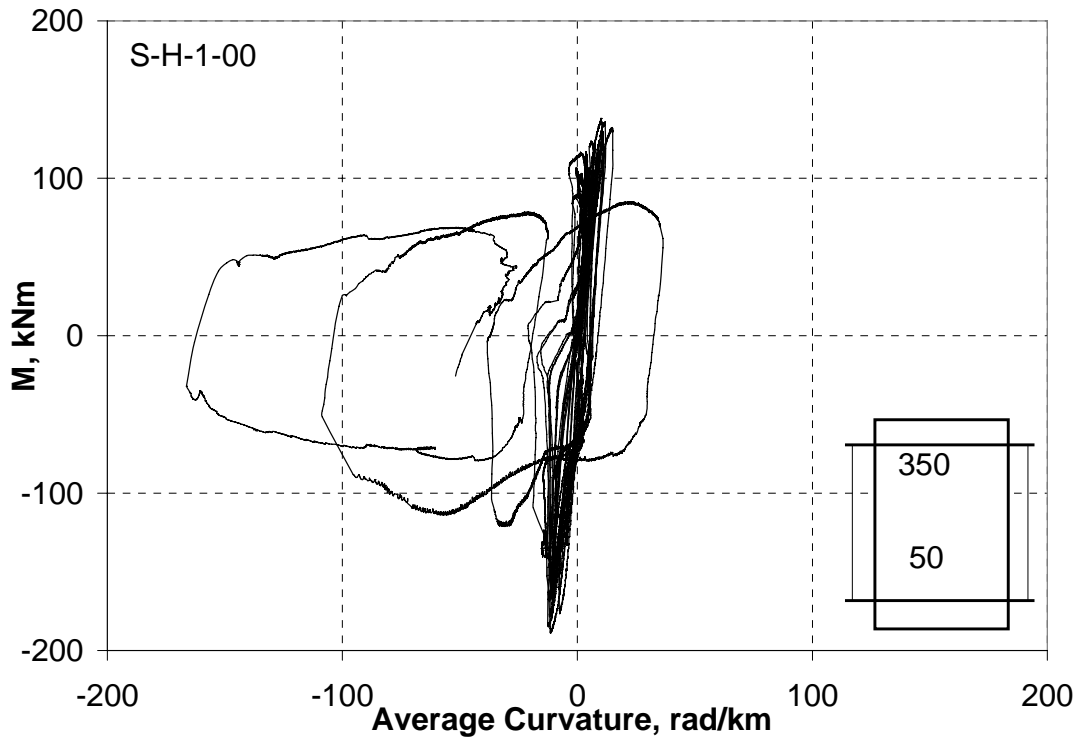


(a)

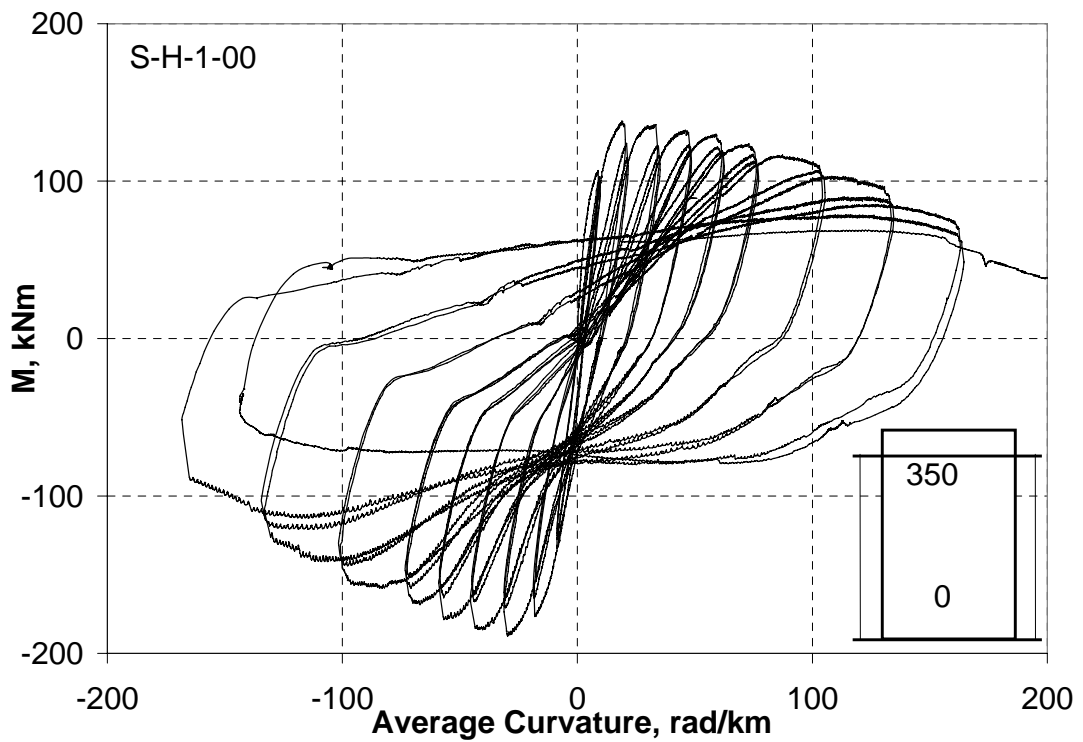


(b)

Figure 2.45 Moment (M) – Average Curvature (K) responses of S-H-0-00: Relative to (a) 50 mm height and (b) Base

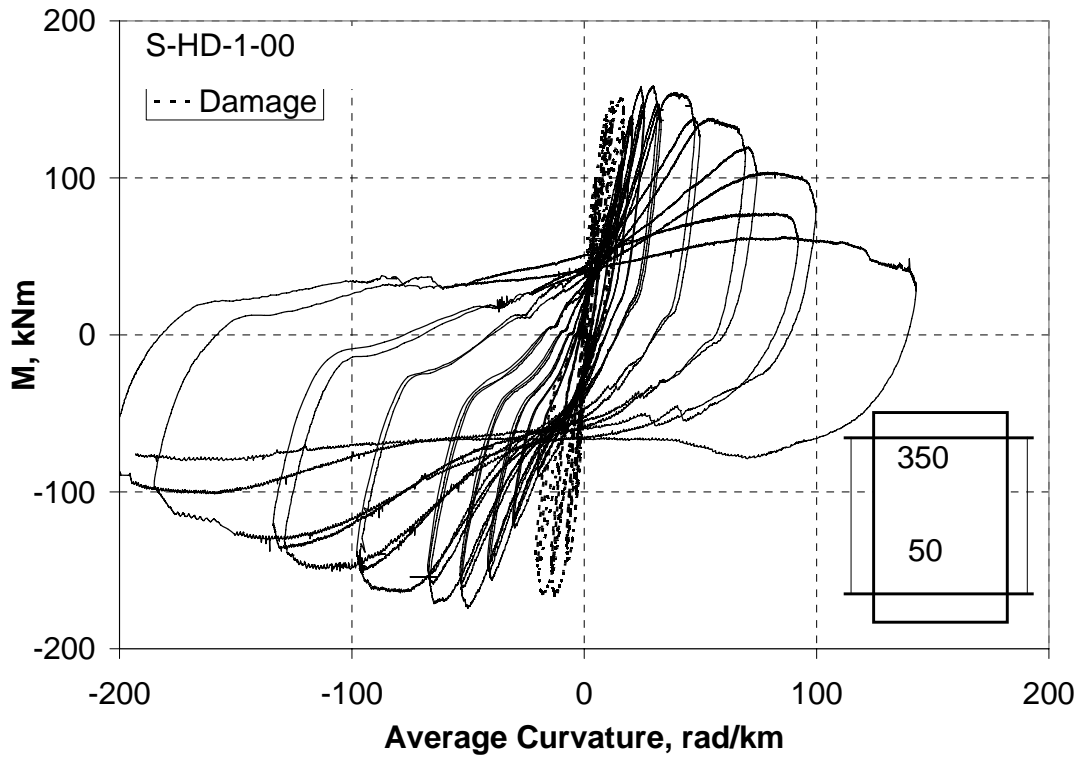


(a)

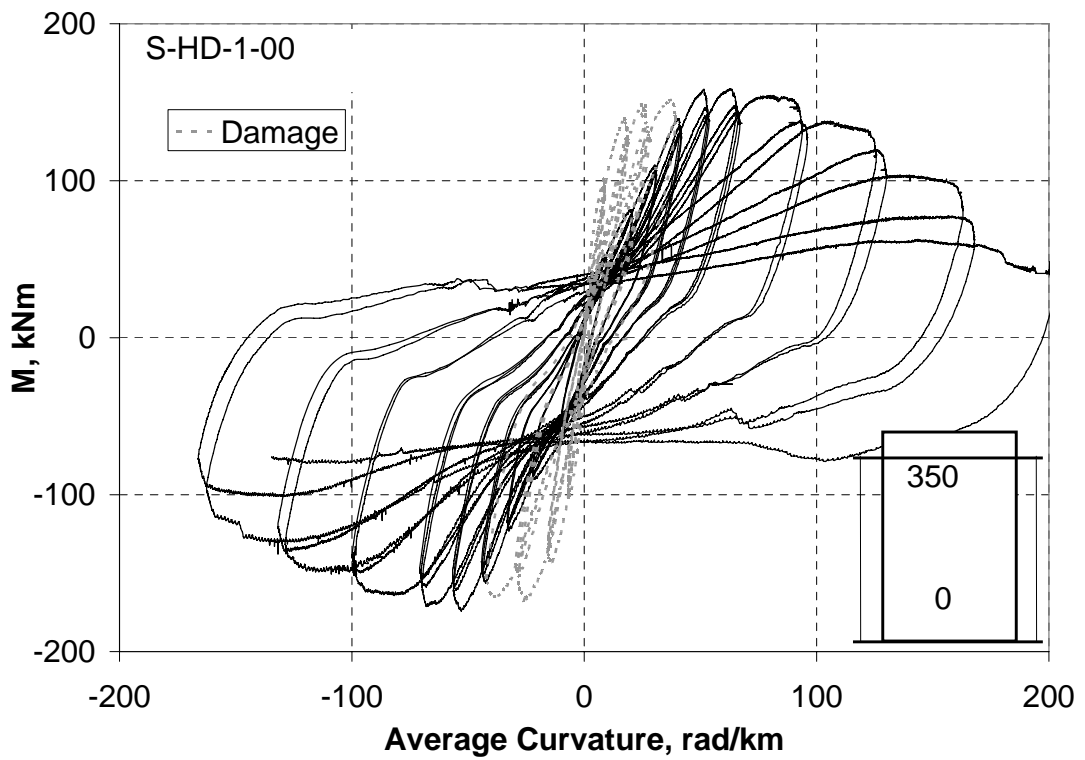


(b)

Figure 2.46 Moment (M) – Average Curvature (K) responses of S-H-1-00: Relative to (a) 50 mm height and (b) Base

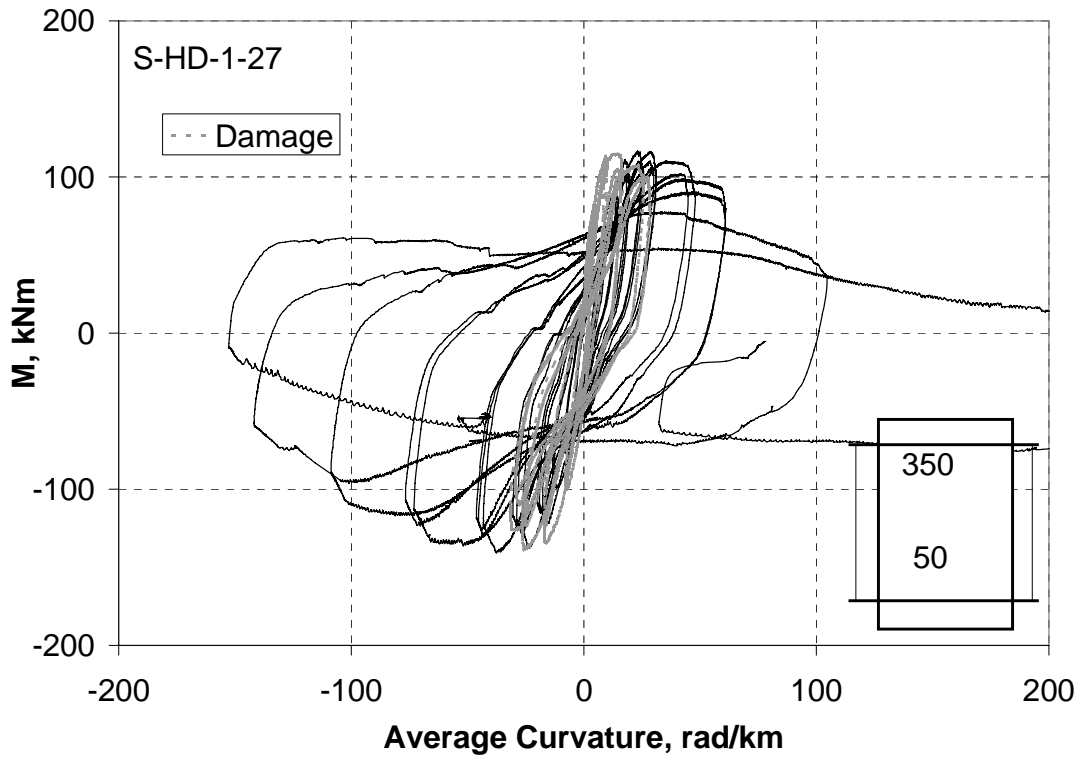


(a)

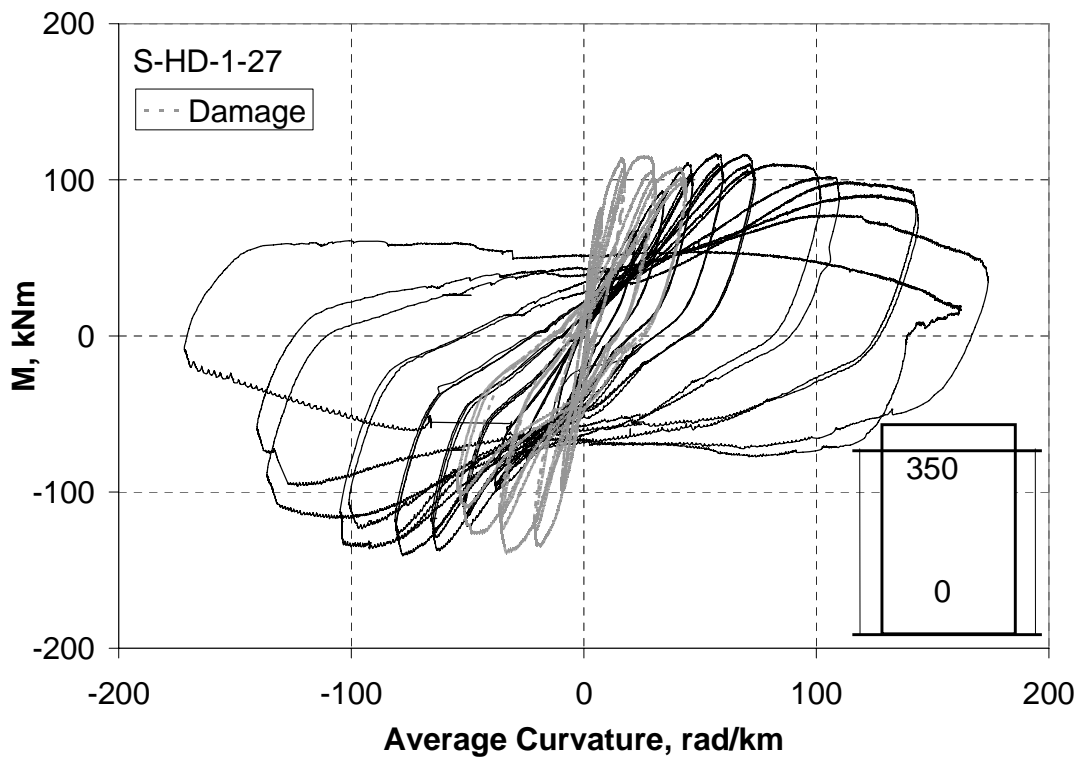


(b)

Figure 2.47 Moment (M) – Average Curvature (K) response of S-HD-1-00: Relative to (a) 50 mm height and (b) Base

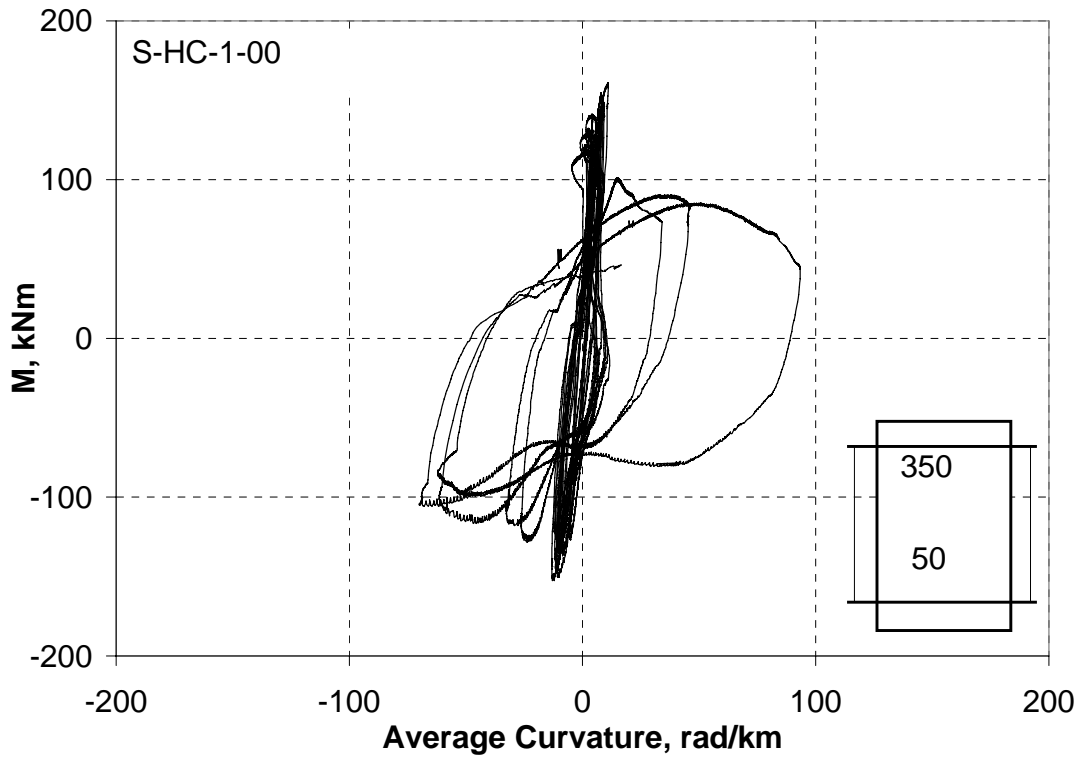


(a)

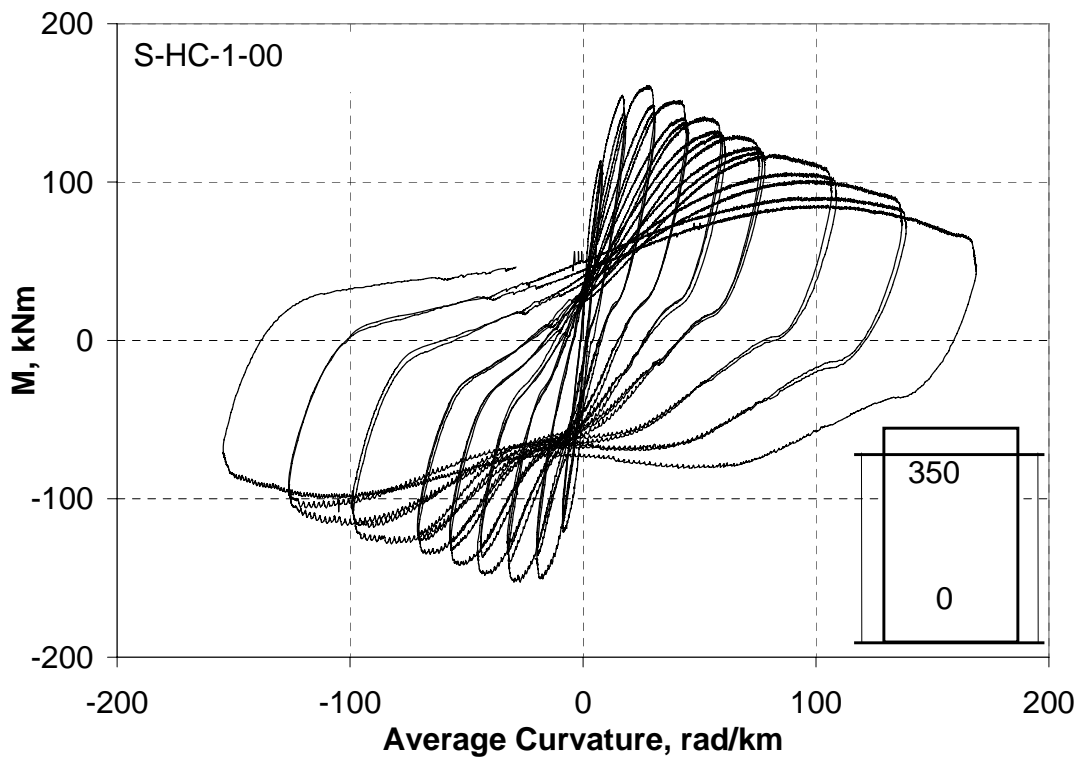


(b)

Figure 2.48 Moment (M) – Average Curvature (K) response of S-HD-1-27: Relative to (a) 50 mm height and (b) Base



(a)



(b)

Figure 2.49 Moment (M) – Average Curvature (K) response of S-HC-1-00: Relative to (a) 50 mm height and (b) Base

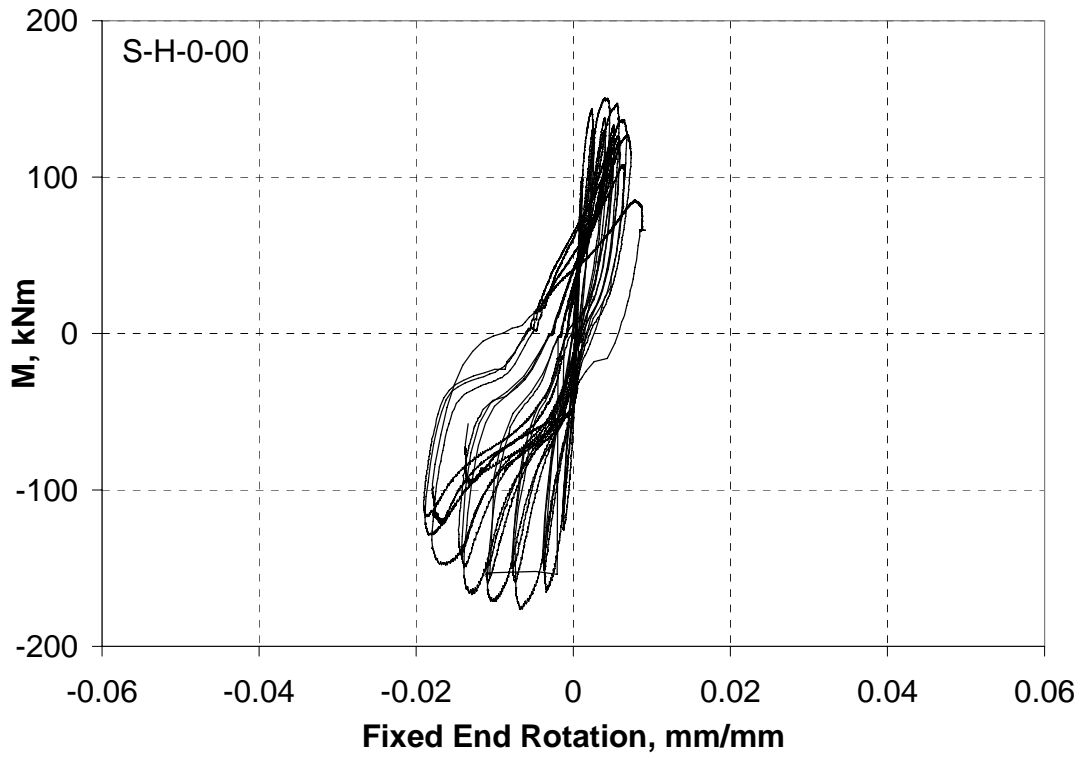


Figure 2.50 Moment (M) – Fixed End Rotation (FER) response of S-H-0-00

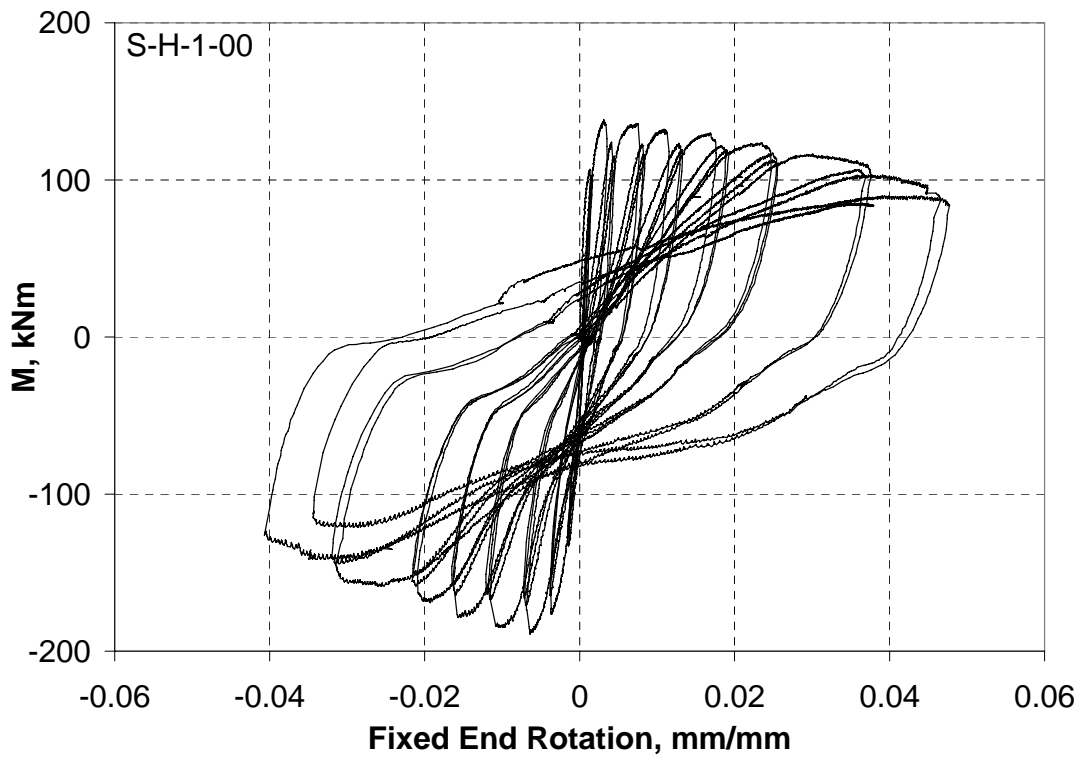


Figure 2.51 Moment (M) – Fixed End Rotation (FER) response of S-H-1-00

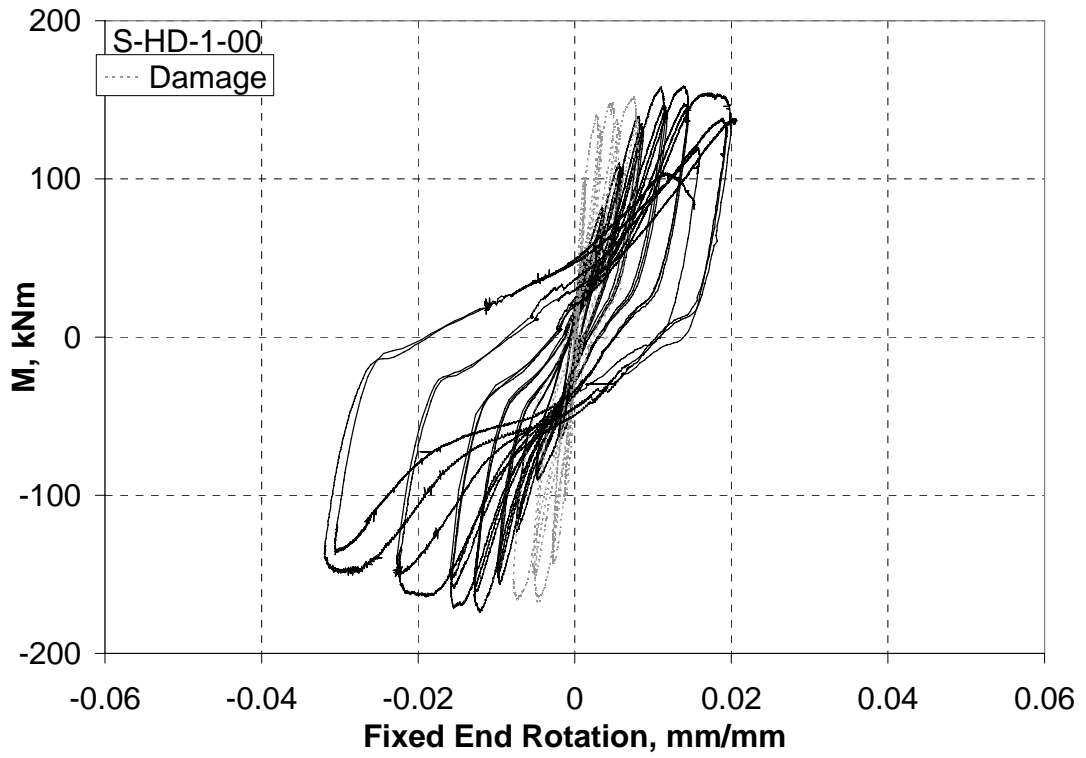


Figure 2.52 Moment (M) – Fixed End Rotation (FER) response of S-HD-1-00

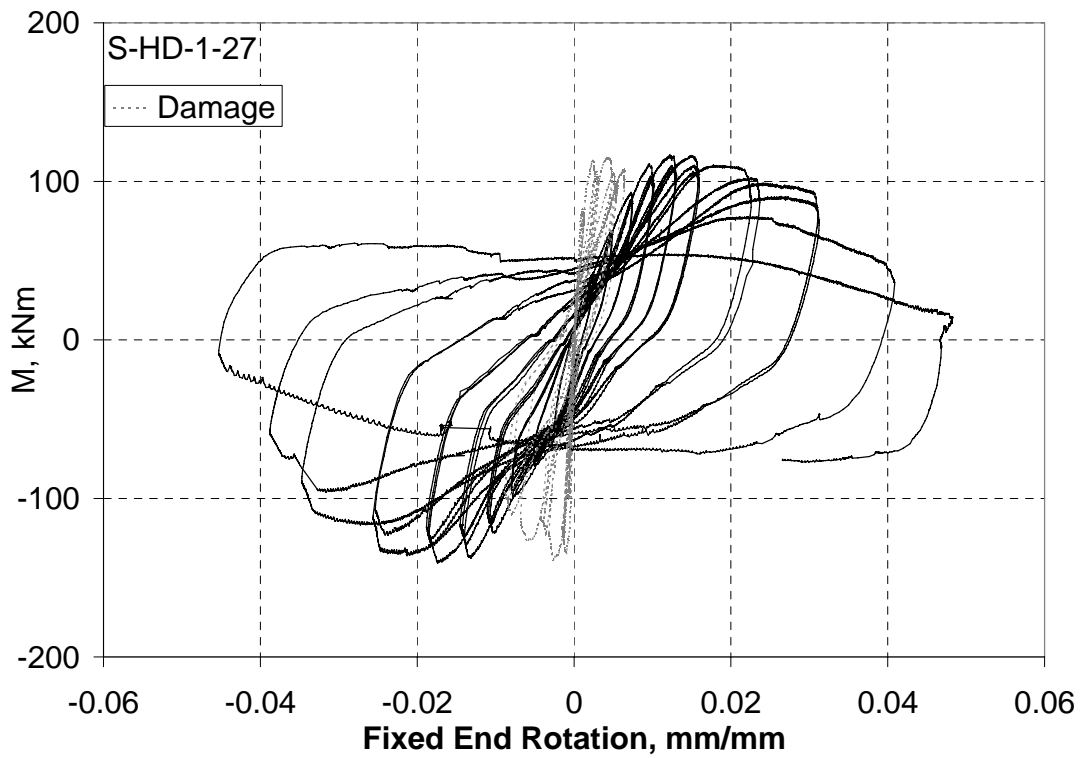


Figure 2.53 Moment (M) – Fixed End Rotation (FER) response of S-HD-1-27

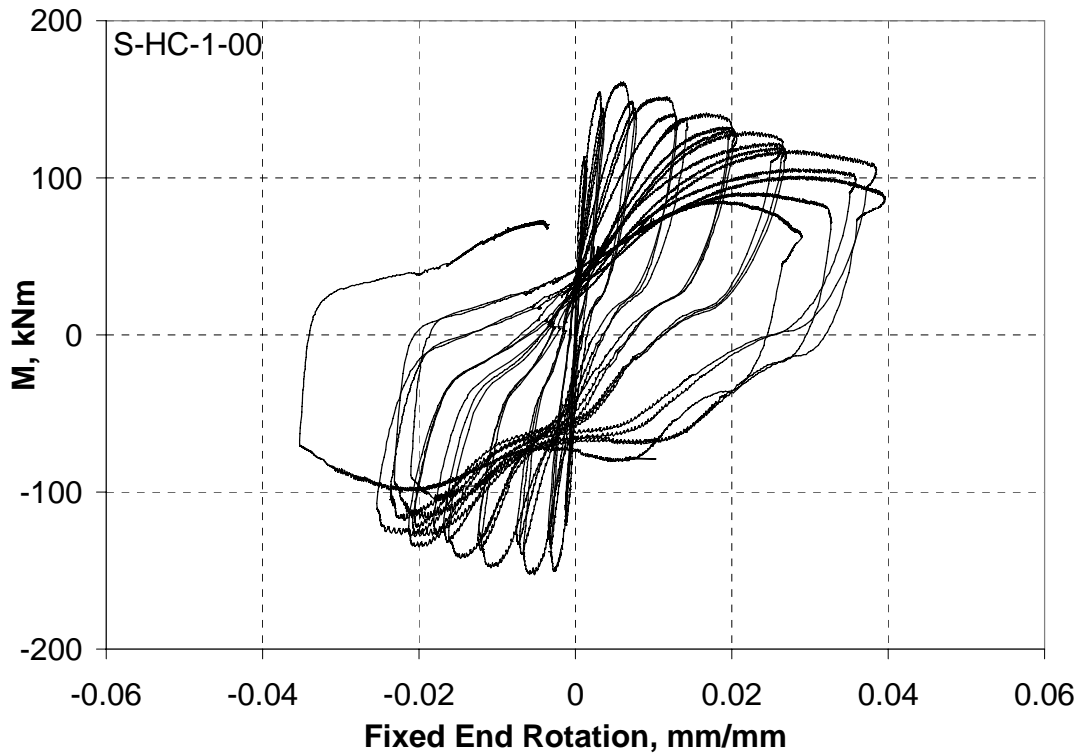


Figure 2.54 Moment (M) – Fixed End Rotation (FER) response of S-HC-1-00

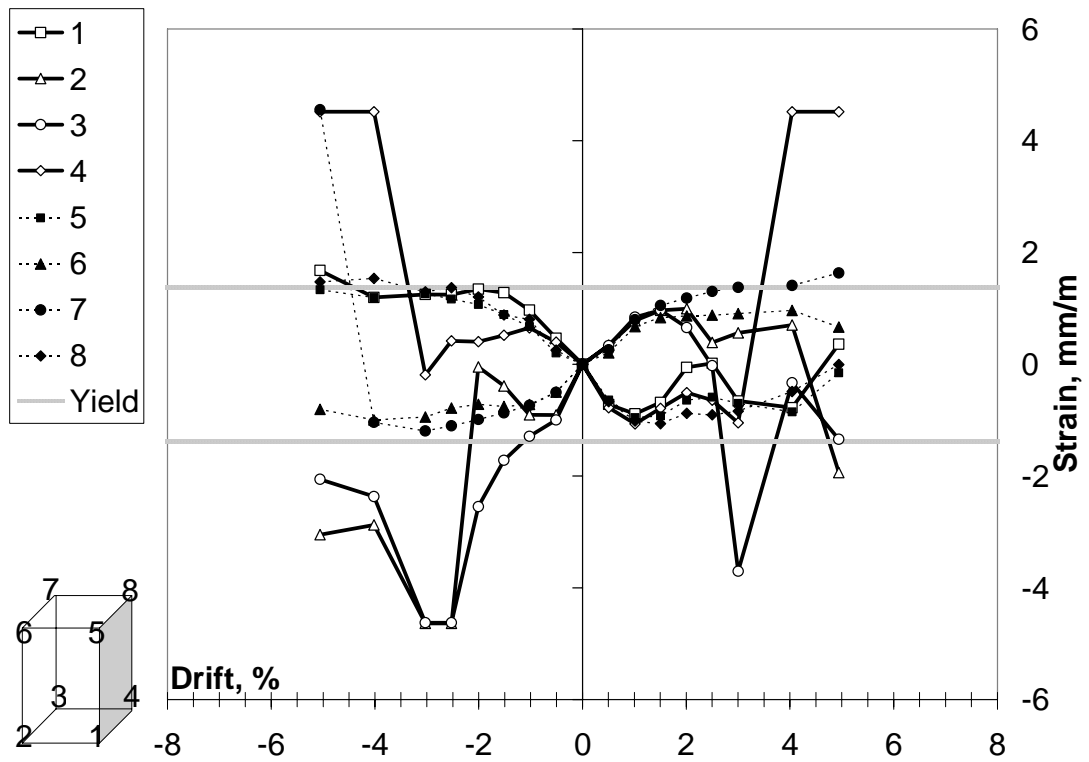


Figure 2.55 Strain – Drift responses for S-H-0-00

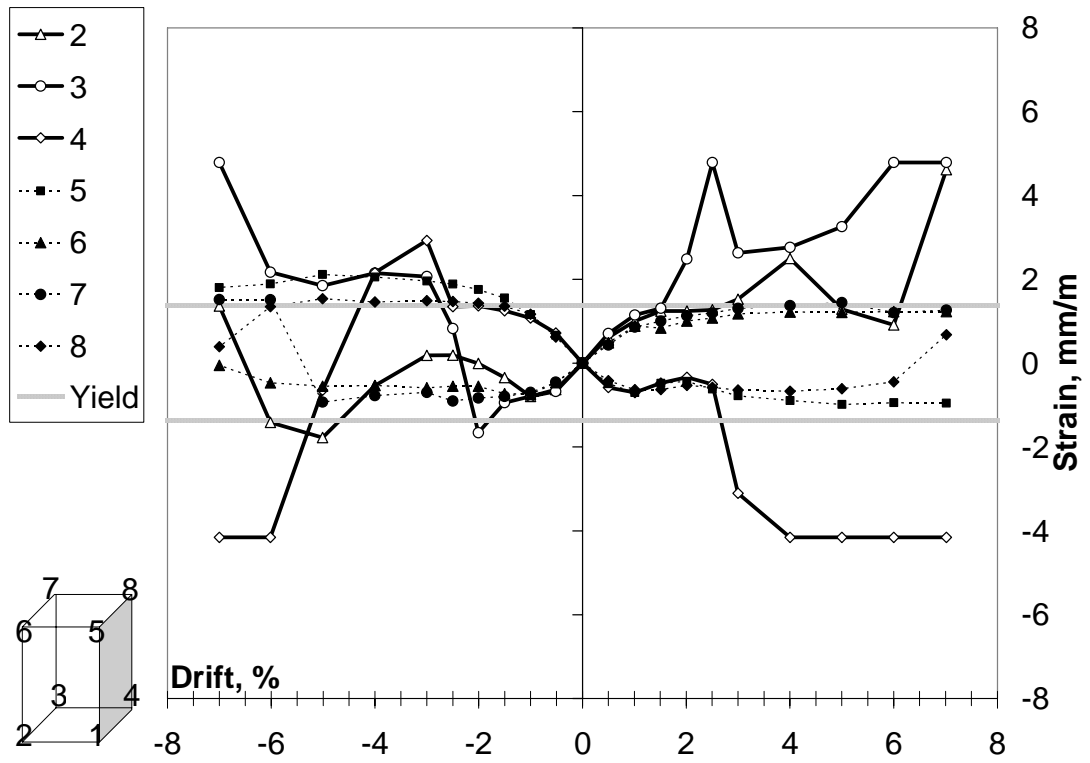


Figure 2.56 Strain – Drift responses for S-H-1-00

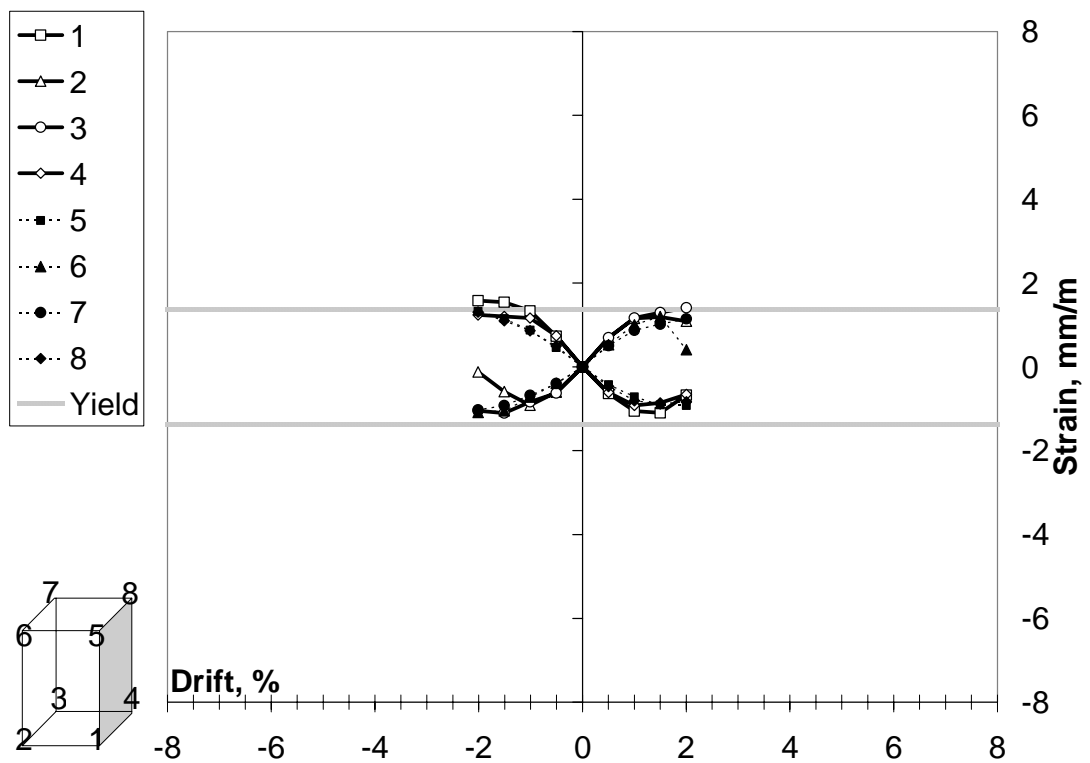


Figure 2.57 Strain – Drift responses for S-HD-1-00: Damage cycles

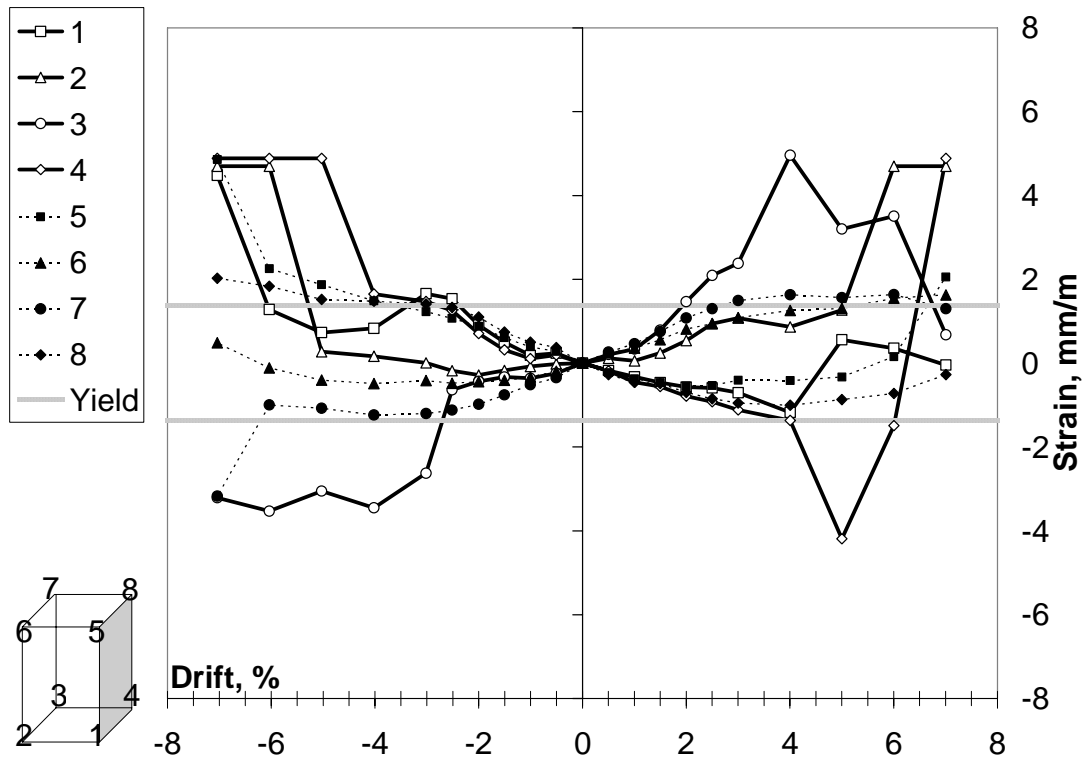


Figure 2.58 Strain – Drift responses for S-HD-1-00

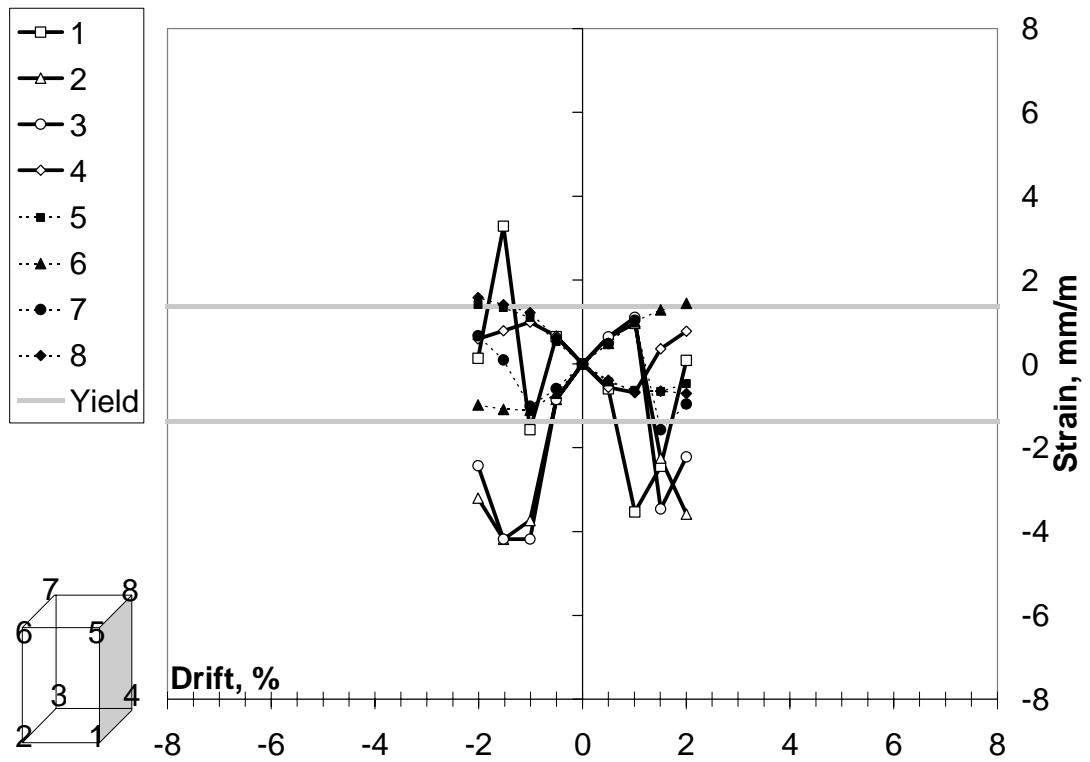


Figure 2.59 Strain – Drift responses for S-HD-1-27: Damage cycles

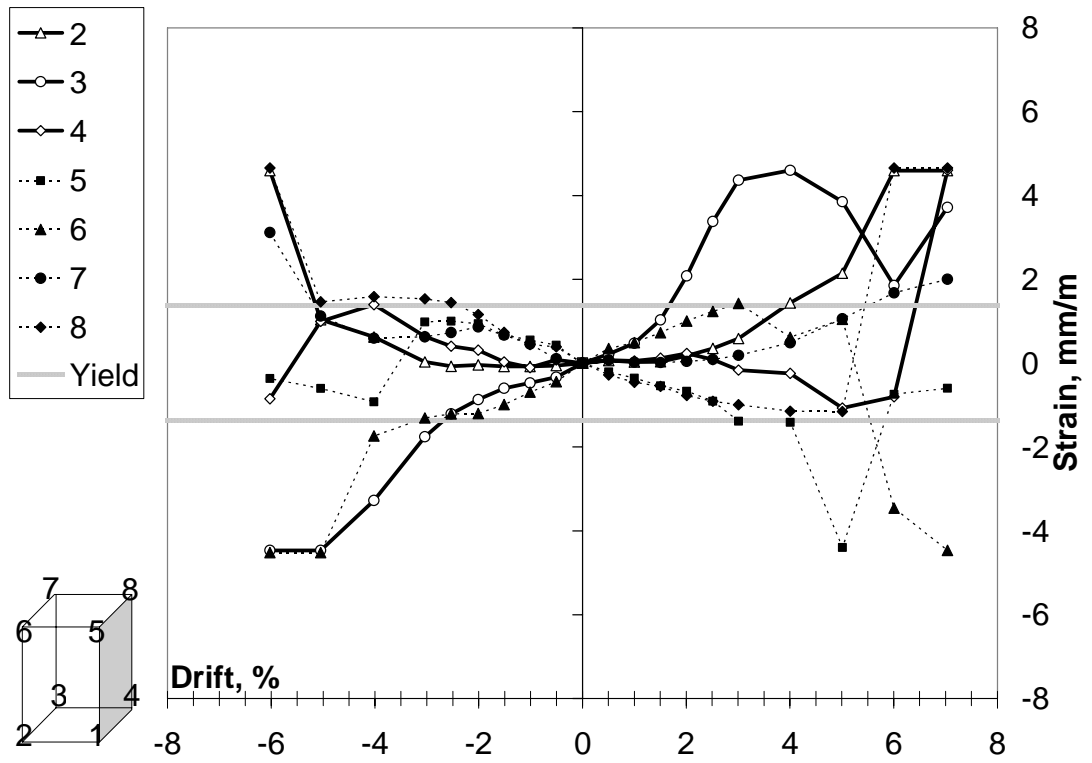


Figure 2.60 Strain – Drift responses for S-HD-1-27

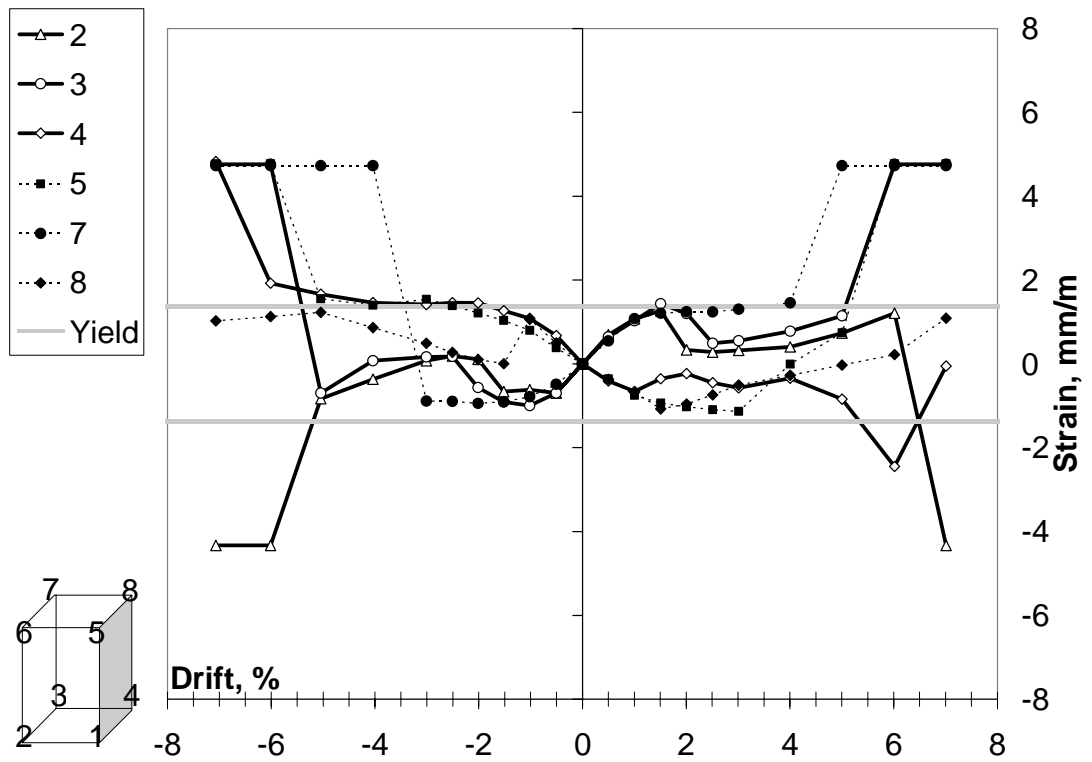


Figure 2.61 Strain – Drift responses for S-HC-1-00

2.6.3. Series 3

All of the test specimens in Series 3 experienced a similar failure mode in the column base namely flexural failure due to column plastic hinging. The pictures of plastic hinge regions of the failed specimens are shown in Figure 2.62. The reference specimen, R-NC-0-00, experienced first flexural cracks up to 900 mm height with an approximate spacing of 100 mm during the cycles of 0.5% drift level. The column-stub interface cracking also occurred at this drift level in both sides of the column and the amplified drift levels made this crack open further owing to the excessive slipping and elongation of the longitudinal rebars. In the cycles of 1% drift, a new crack formed at 1200 mm height and previously formed cracks opened further and lengthened in two adjacent faces of the column with an inclination angle of about 45 degrees. The tendency of the cracks to incline in about 45 degrees was due to the shear force acting on the column that was close to the critical shear-cracking load. As shown in Figure 2.63, the initial signs of concrete crushing and plastic hinging at the bottom of the column were observed during the cycles of 1% drift. Further, drift levels beyond 1% made the column experience more inelastic behavior owing to the spreading of the plastic hinge region over a height of about depth of the section, h that was approximately 470 mm in length. At 2% drift level, the onset of rebar buckling contributed to the strength degradation below 80% of the lateral capacity of the specimen and the specimen failed as both the axial and lateral capacities dropped to zero during the following cycles. In all the strengthened specimens, column-stub interface cracking occurred in the cycles of 0.5% drift. For the strengthened specimen, R-MC-1-16P, initial visible flexural cracks were observed above the CFRP wrapped region at heights of 700 to 1000 mm in the cycles of 0.5% drift level. The crack widths and lengths promoted until 2% drift level with the same crack inclination properties as the reference specimen. At 2% drift, first flexural cracks in CFRP appeared in the tension side and CFRP debonding occurred in compression side of the CFRP wrapped region. During the cycles of 4% drift ratio, first CFRP rupture and onset of rebar buckling took place.



(a)



(b)



(c)



(d)



(e)

Figure 2.62 Columns at the end of testing (a) R-NC-0-00, (b) R-MC-1-16P, (c) R-MC-1-8P, (d) R-MC-1-NP, (e) R-HC-1-16P

Subsequent cycles beyond 4% drift led to spreading of CFRP debonding over the plastic hinge region (~340 mm) in adjacent faces of the column except the perimeter of the CFRP anchors. After 5% drift, CFRP debonding occurred also in the perimeter of the CFRP anchorages at the base and further buckling of the reinforcing bars resulted in dropping of lateral capacity beyond 80% of the ultimate as illustrated on the hysteretic cycles in Figure 2.64. The specimens R-MC-1-8P and R-MC-1-NP experienced a similar behavior as R-MC-1-16P in terms of CFRP debonding, CFRP rupturing and onset of longitudinal bar buckling. The drift ratios belonging to these important events were identical however, for the specimen R-MC-1-8P, the first rupture in CFRP occurred at 2.5% of drift (Figures 2.65 and 2.66). The occurrence of CFRP rupturing at a lower level of drift for the specimen R-MC-1-8P can be due to an unexpected stress concentration at the column base level and consequential excessive stressing of CFRP. For 8-pinned CFRP anchor configuration, the CFRP rupture initiated at the shorter side and progression was along the longer side of the column. Adversely, the CFRP rupture mechanism was observed completely at the longer side of the column for no-pinned CFRP anchor detailing. The specimen R-HC-1-16P demonstrated better seismic behavior than R-MC-1-16P under the lateral cycles owing to its lower concrete strength and resultant higher confinement ratio. For R-HC-1-16P, CFRP debonding happened at the same drift level as the specimen R-MC-1-16P. However, the drift ratios at which CFRP rupturing and onset of longitudinal bar buckling occurred was improved to 6 and 5% drift (Figure 2.67), respectively regarding the enhancement in confining ratio. Besides, CFRP rupturing started and dispersed along the shorter sides of the column for 16-pinned configuration of CFRP anchors. According to the Moment (M) – Average Curvature (K) responses of the reference specimen R-NC-0-00, the ultimate curvature at which the lateral capacity dropped to 80% of the peak was approximately 40 and 25 rad/km that were measured relative to column base and 50 mm height, respectively (Figure 2.68). However, the moderately confined specimens (R-MC-1-16P, R-MC-1-8P and R-MC-1-NP), could attain ultimate curvature levels up to 50 and 100 rad/km (Figures 2.69-2.71). The average ultimate curvature levels increased up to 150 rad/km for R-HC-1-16P, considering the monitored curvatures relative to the column base (Figure 2.72 and Table 2.5). The ultimate fixed-end rotation values for the reference specimen R-NC-0-00 was up to levels of 0.6% (Figure 2.73) while that

level augmented to 2, 2.5 and 1.5% for the moderately confined specimens R-MC-1-16P, R-MC-1-8P and R-MC-1-NP (Figures 2.74-2.76). Increasing the confinement level, made the augmentation in fixed-end rotations to approximately 5%, since the increase in confinement prevented premature longitudinal rebar buckling in the test region (Figure 2.77). The recorded longitudinal strain values for the reference specimen implied that after yielding of the rebars at 0.00138 the specimen was failed owing to the unavoidable rebar buckling in the test region (Figure 2.78). For the moderately confined specimens R-MC-1-16P, R-MC-1-8P and R-MC-1-NP, the obtained longitudinal strain data showed that wrapping 1-layer of CFRP prevented buckling of the rebars to the strain levels of up to 0.004 (Figures 2.79-2.81). Lastly, the highly confined specimens R-HC-1-16P exhibited a better performance during the lateral cycles since the longitudinal strains reached to a level of approximately 0.005 as shown in Figure 2.82. Furthermore, unexpected failure modes namely, column failures outside the potential plastic hinging region are presented in Appendix B. The hysteretic strain plots are presented in Appendix C.

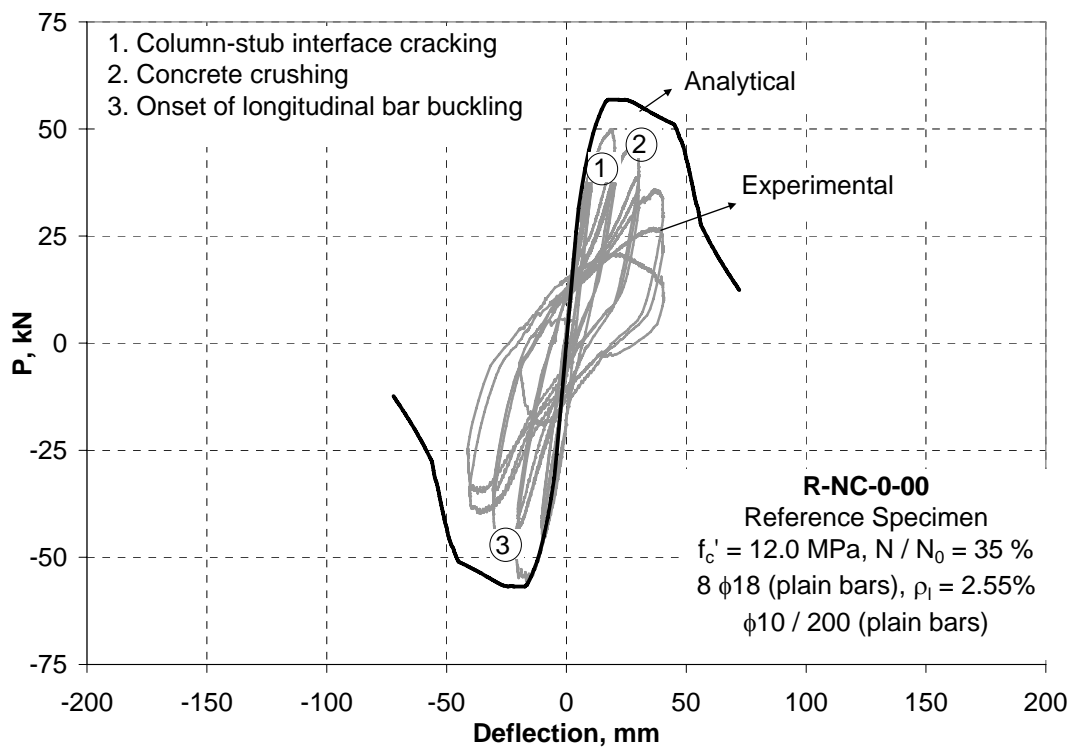


Figure 2.63 Lateral Load (P) – Deflection (Δ) response for R-NC-0-00

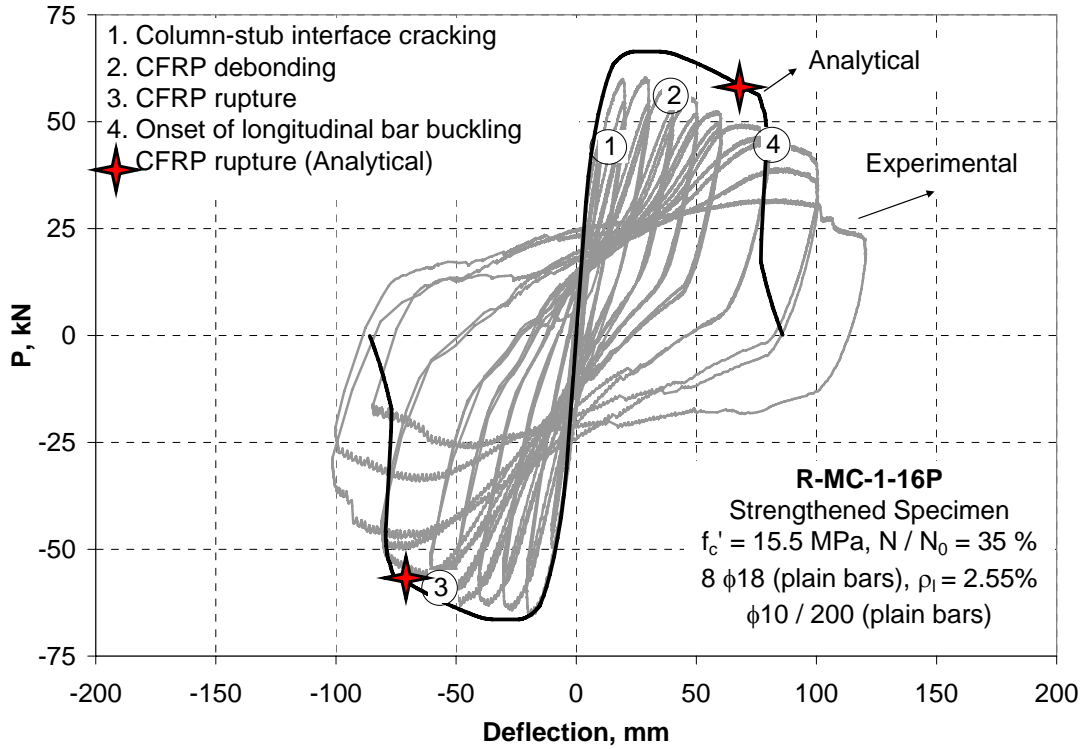


Figure 2.64 Lateral Load (P) – Deflection (Δ) response for R-MC-1-16P

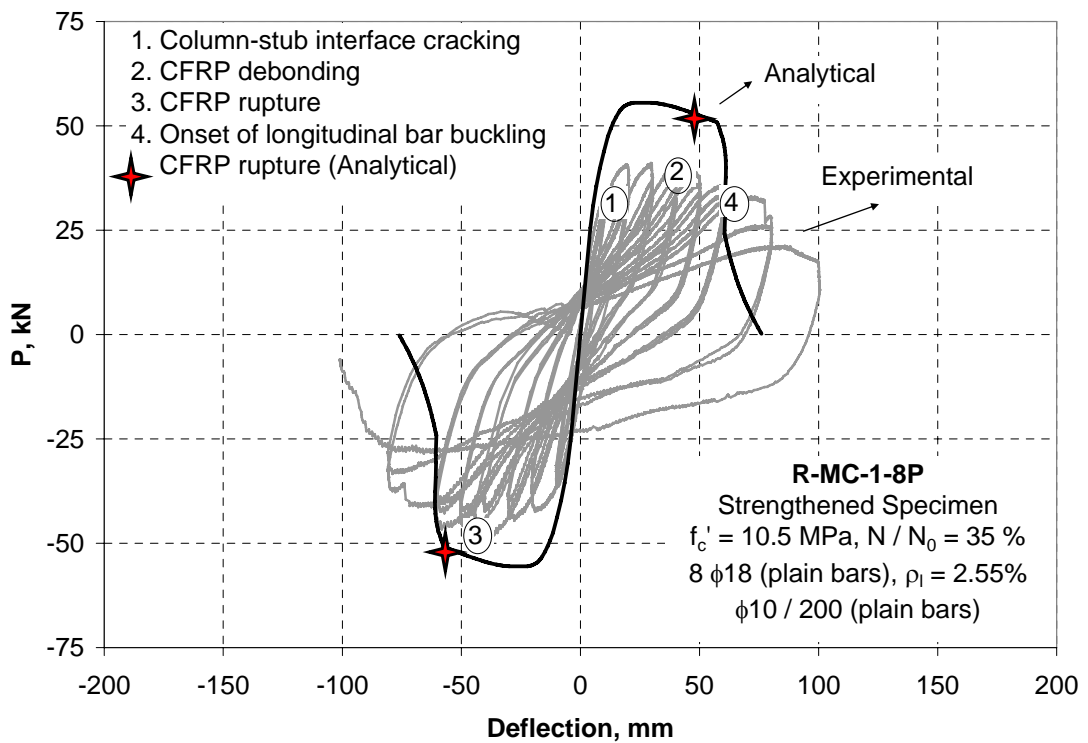


Figure 2.65 Lateral Load (P) – Deflection (Δ) response for R-MC-1-8P

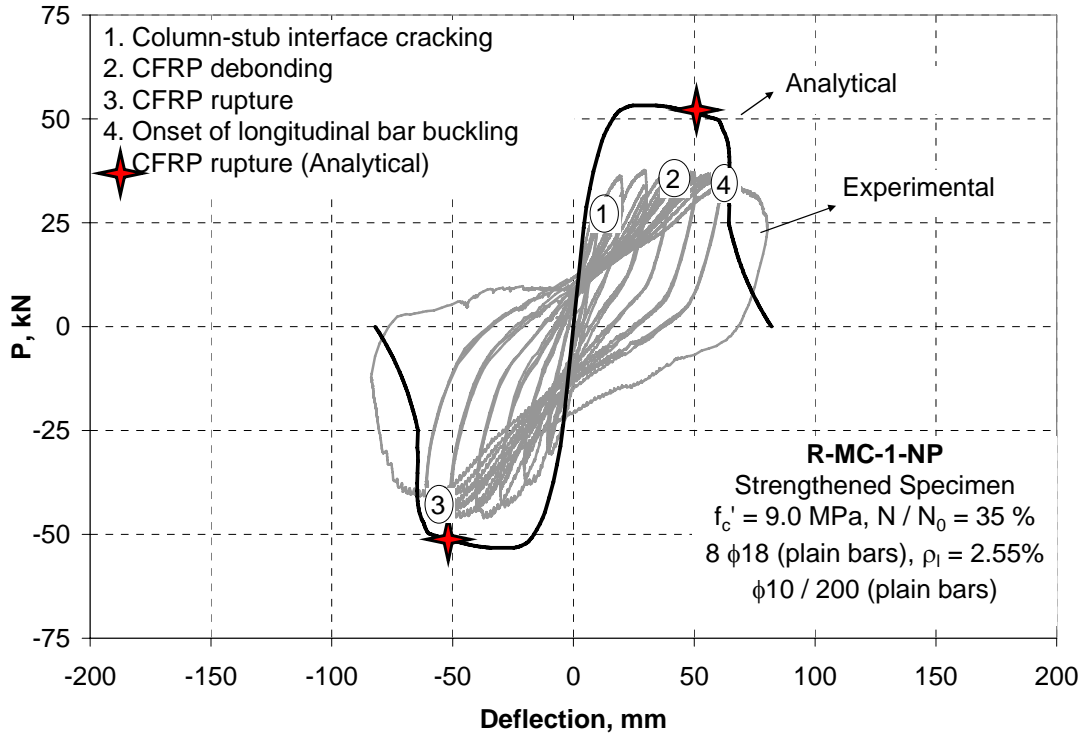


Figure 2.66 Lateral Load (P) – Deflection (Δ) response for R-MC-1-NP

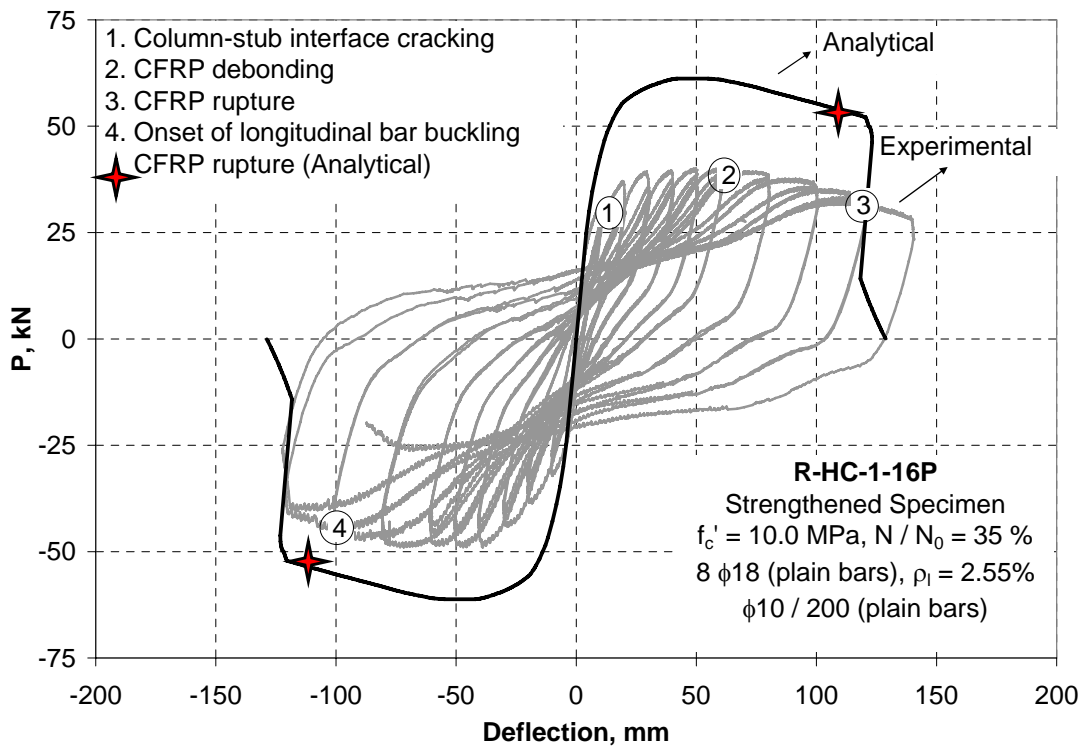
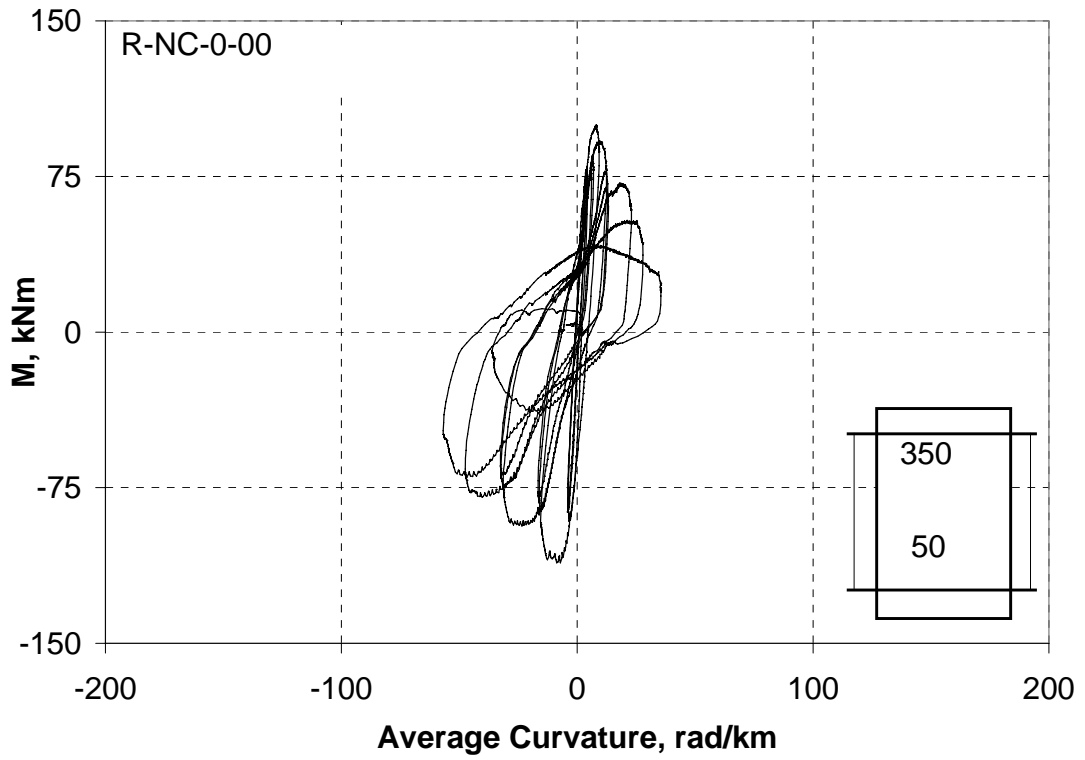
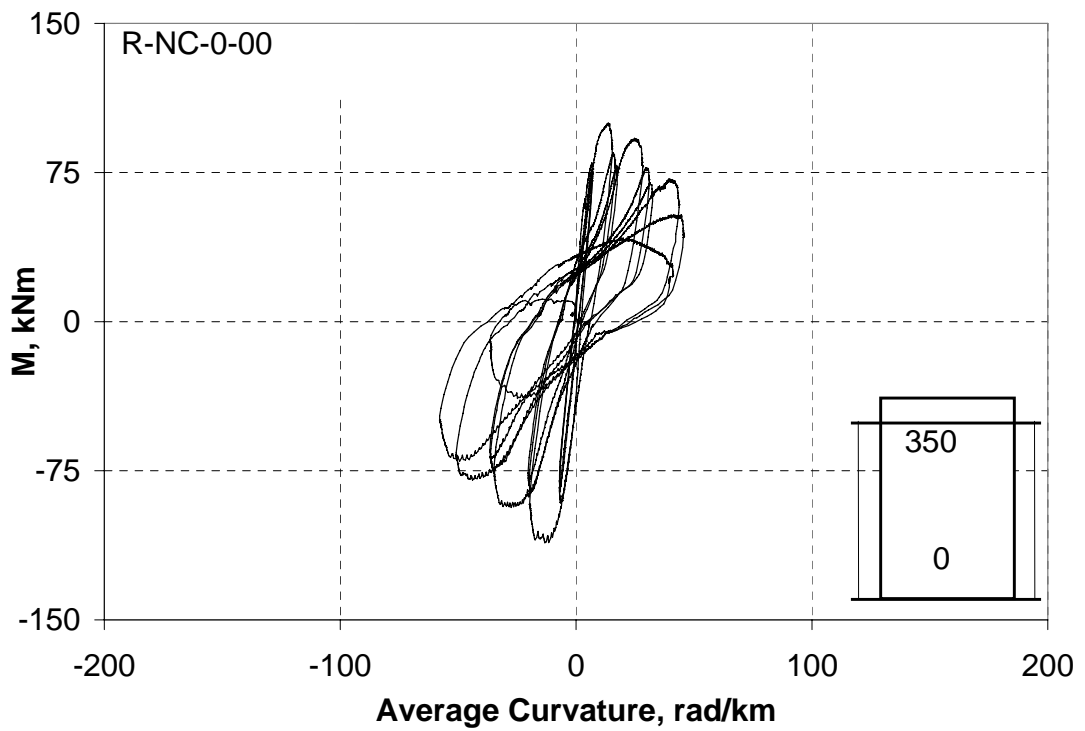


Figure 2.67 Lateral Load (P) – Deflection (Δ) response for R-HC-1-16P

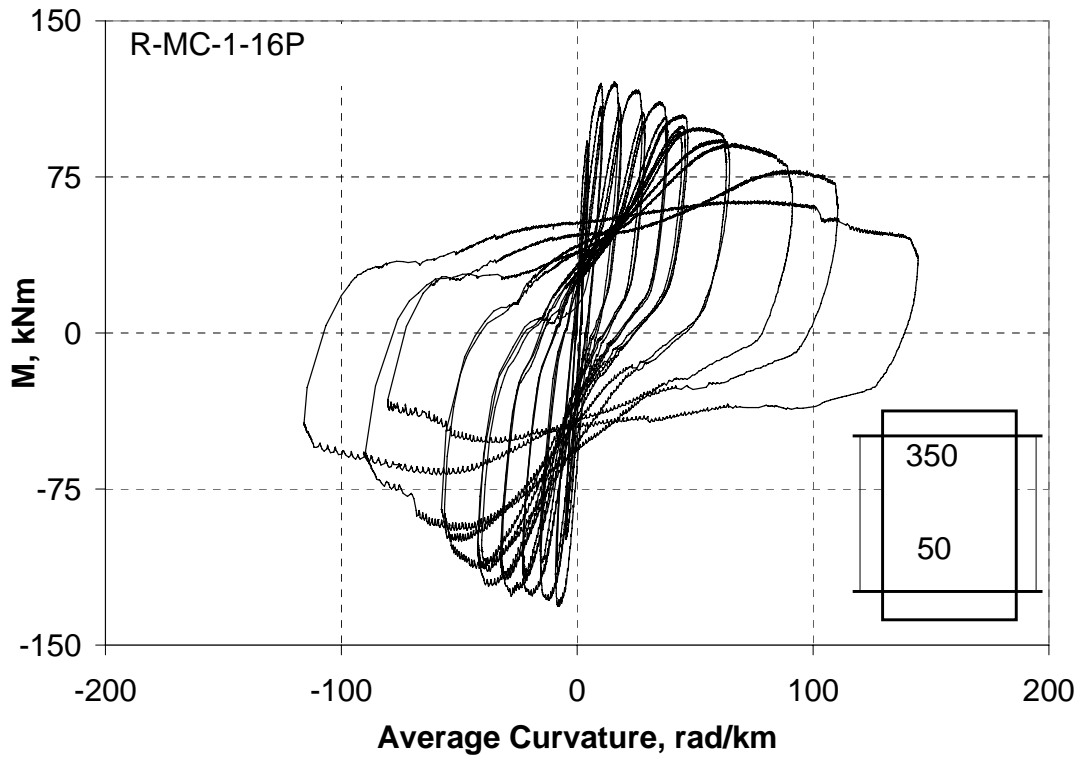


(a)

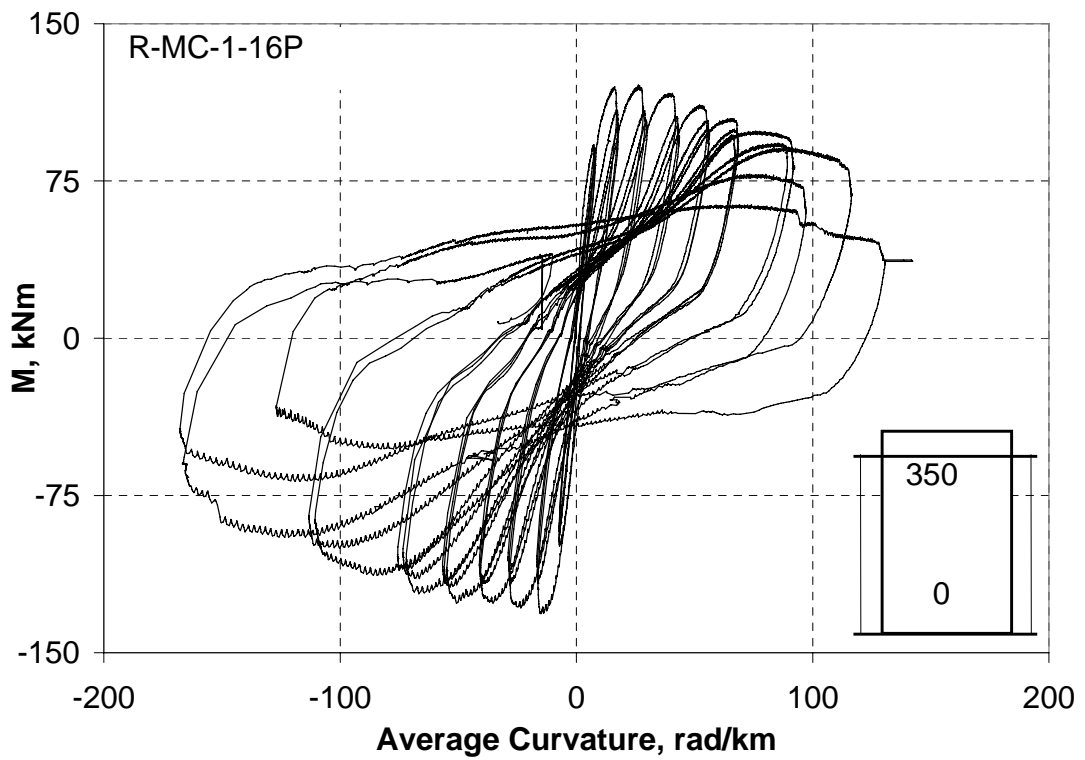


(b)

Figure 2.68 Moment (M) – Average Curvature (K) response of R-NC-0-00: Relative to (a) 50 mm height and (b) Base

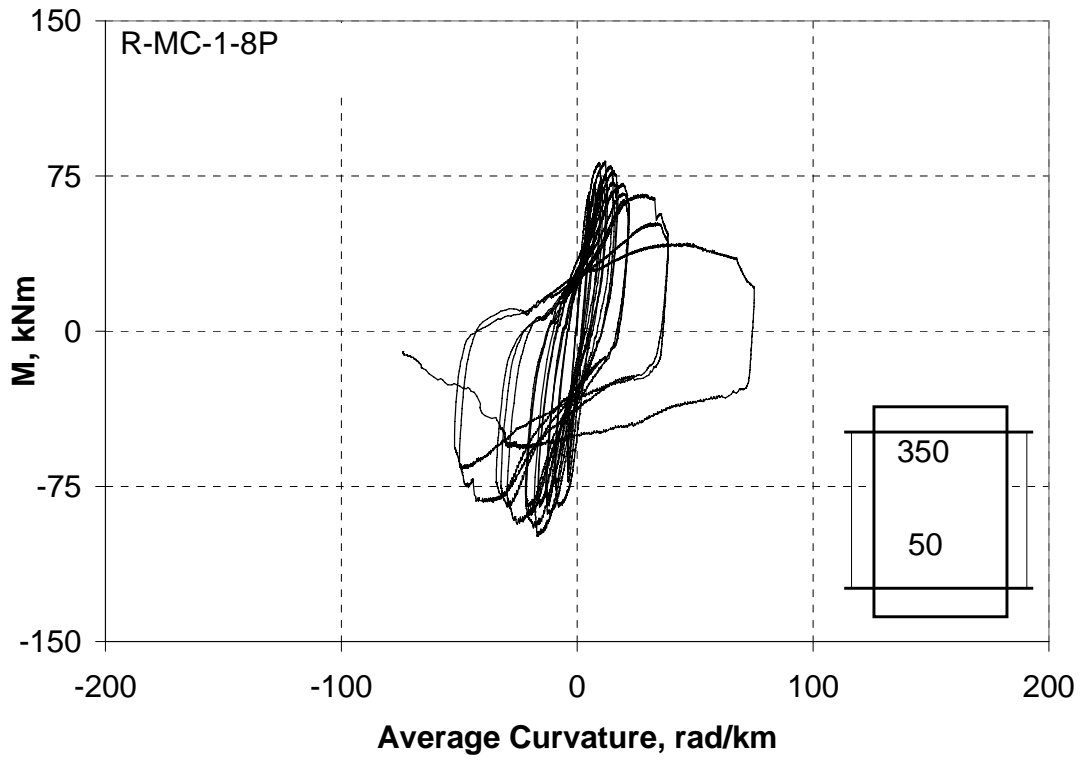


(a)

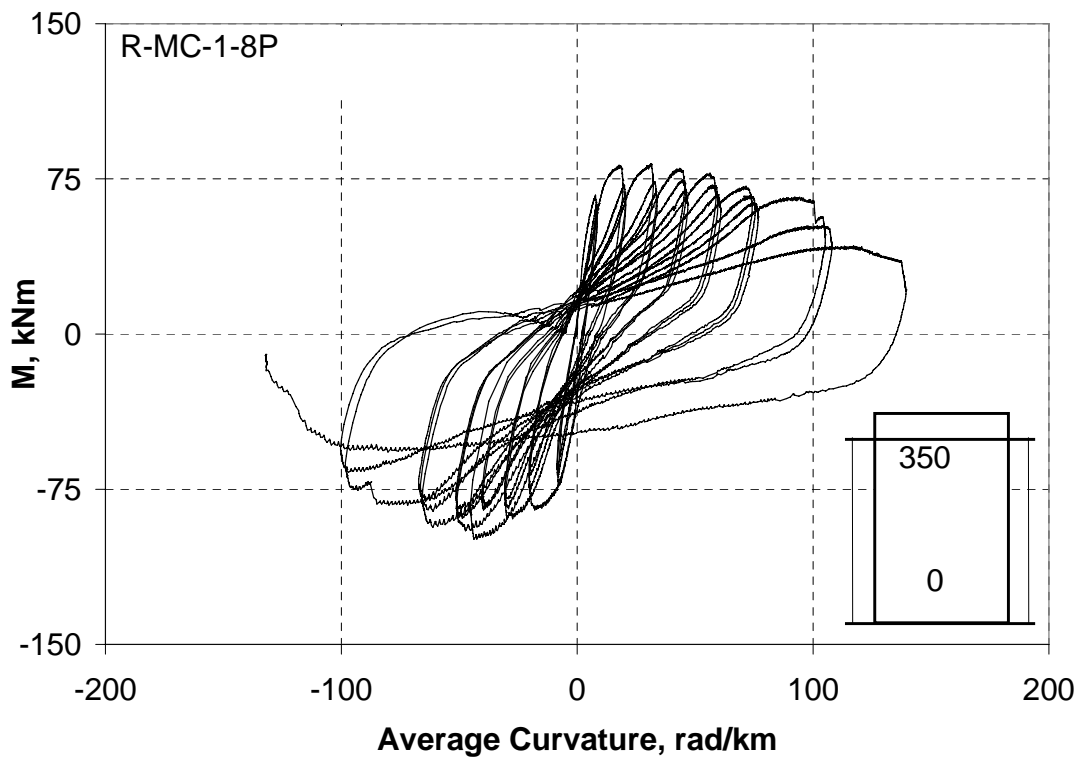


(b)

Figure 2.69 Moment (M) – Average Curvature (K) response of R-MC-1-16P: Relative to (a) 50 mm height and (b) Base

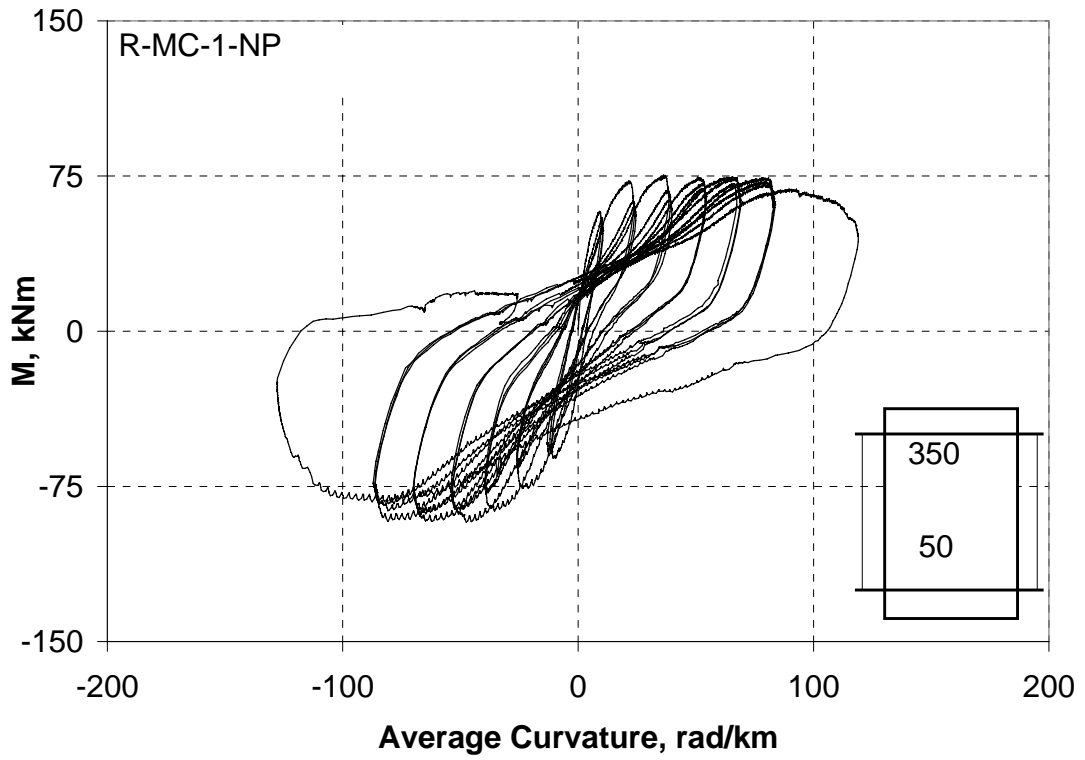


(a)

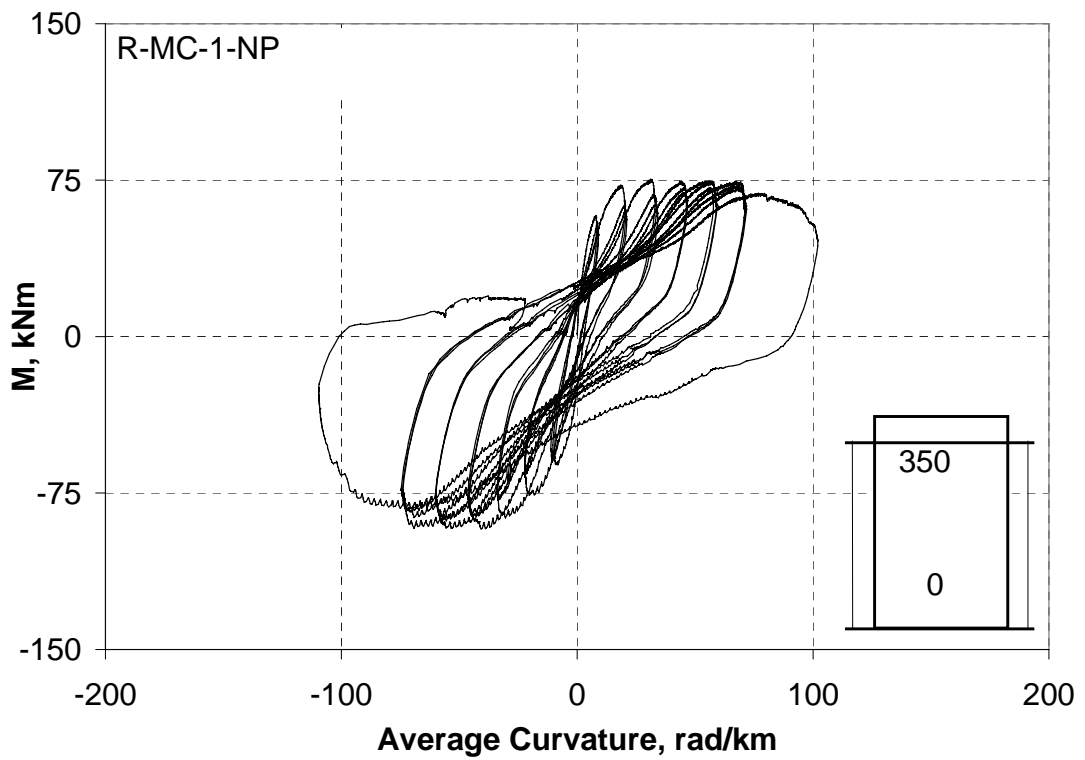


(b)

Figure 2.70 Moment (M) – Average Curvature (K) response of R-MC-1-8P: Relative to (a) 50 mm height and (b) Base

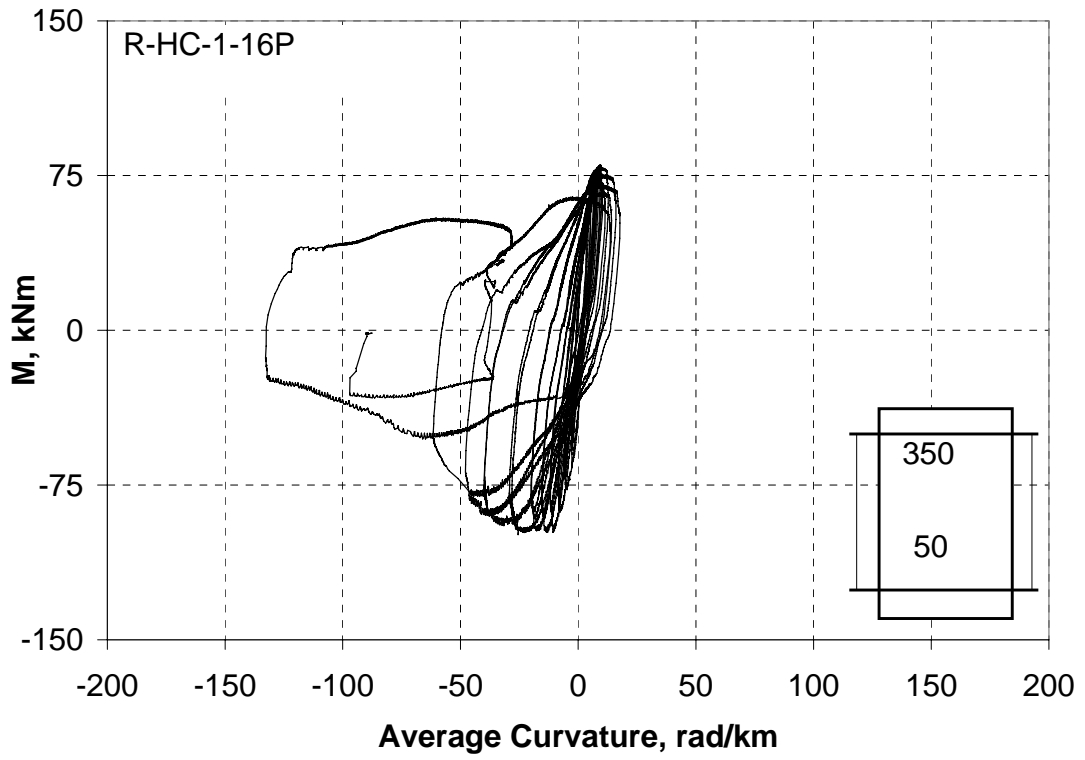


(a)

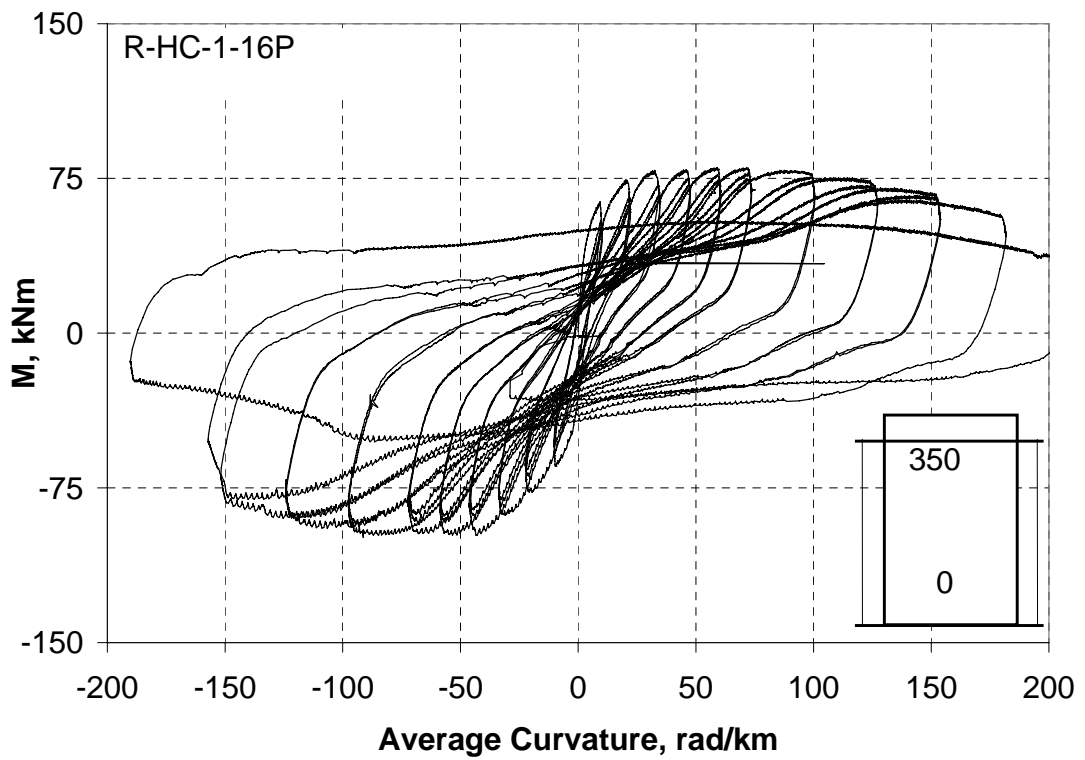


(b)

Figure 2.71 Moment (M) – Average Curvature (K) response of R-MC-1-NP: Relative to (a) 50 mm height and (b) Base



(a)



(b)

Figure 2.72 Moment (M) – Average Curvature (K) response of R-HC-1-16P: Relative to (a) 50 mm height and (b) Base

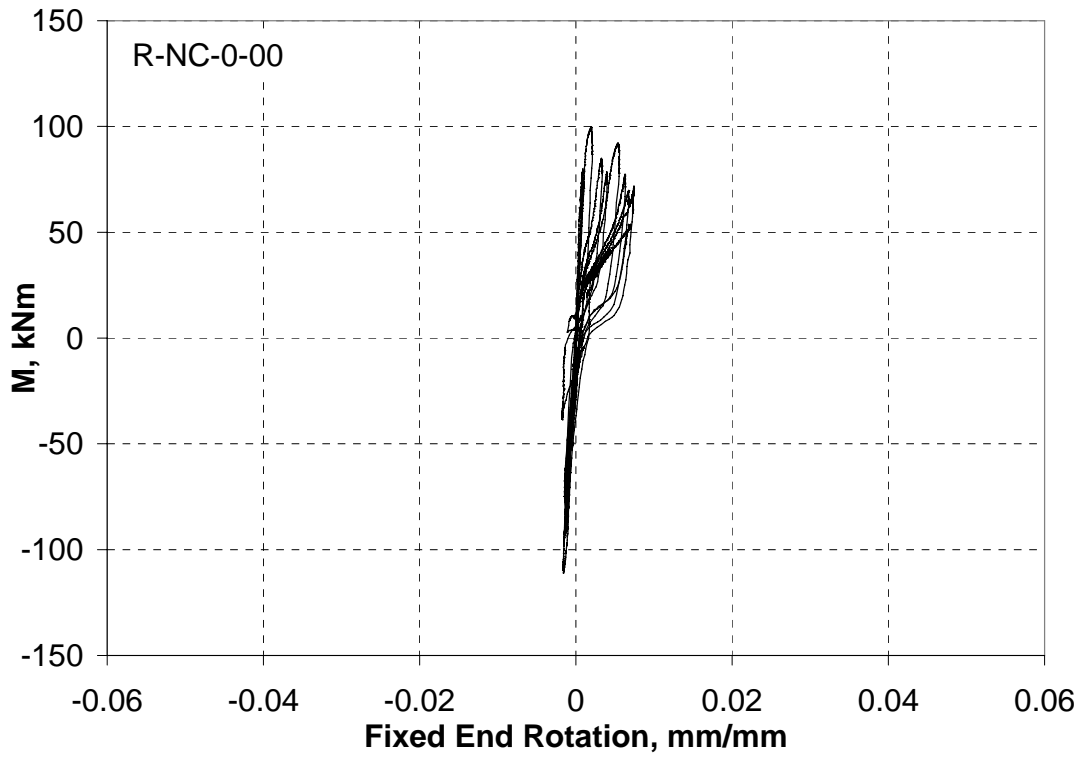


Figure 2.73 Moment (M) – Fixed End Rotation (FER) response of R-NC-0-00

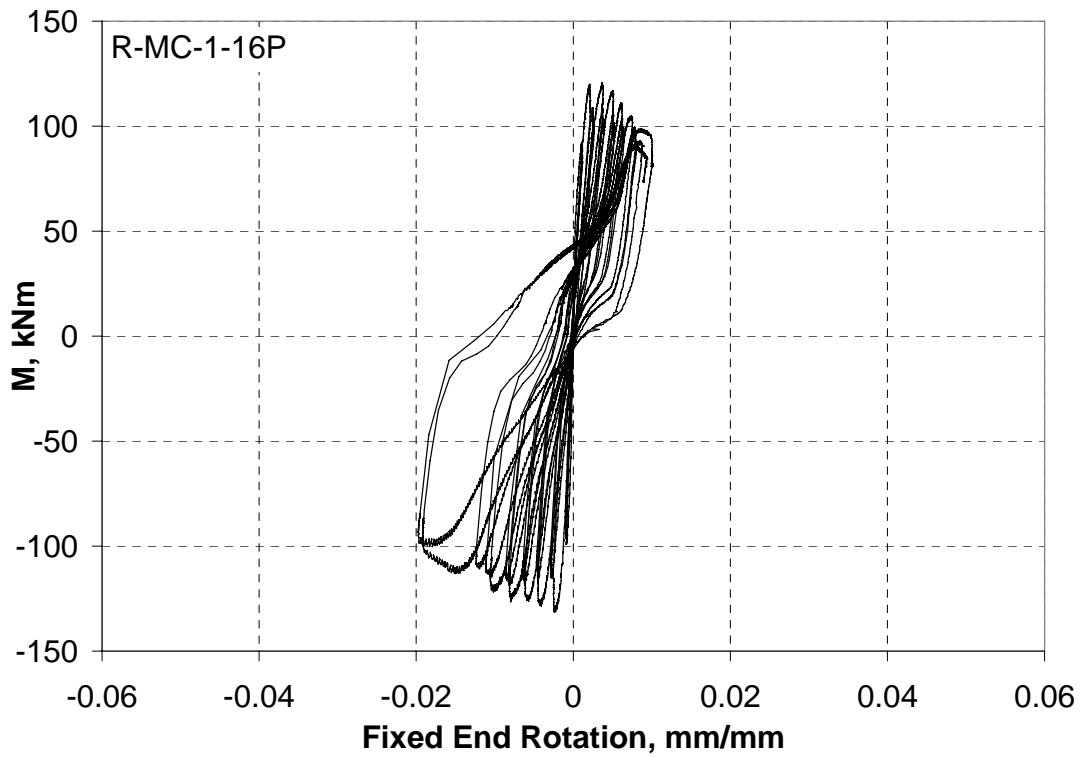


Figure 2.74 Moment (M) – Fixed End Rotation (FER) response of R-MC-1-16P

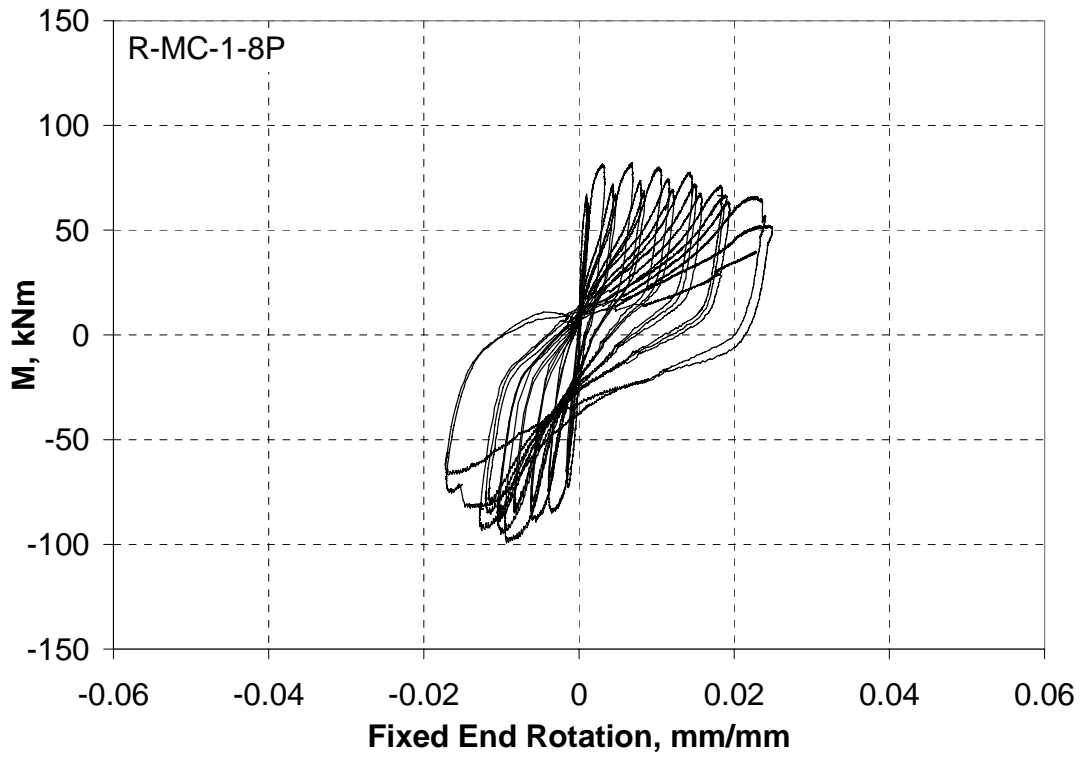


Figure 2.75 Moment (M) – Fixed End Rotation (FER) response of R-MC-1-8P

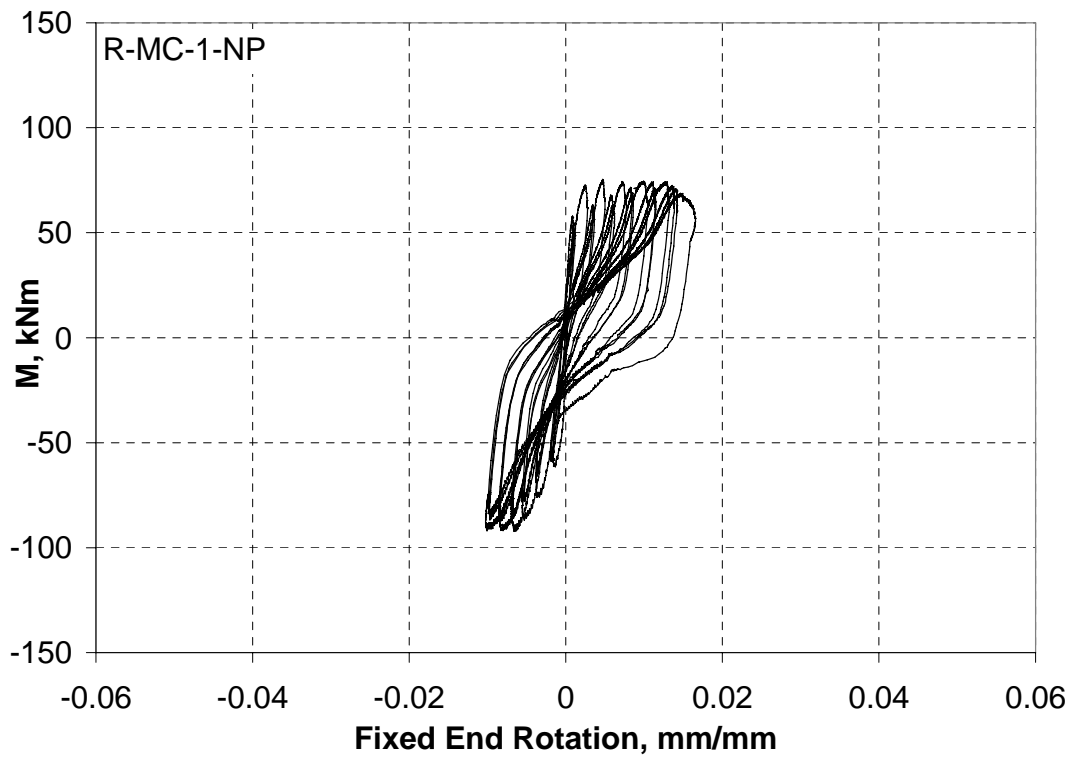


Figure 2.76 Moment (M) – Fixed End Rotation (FER) response of R-MC-1-NP

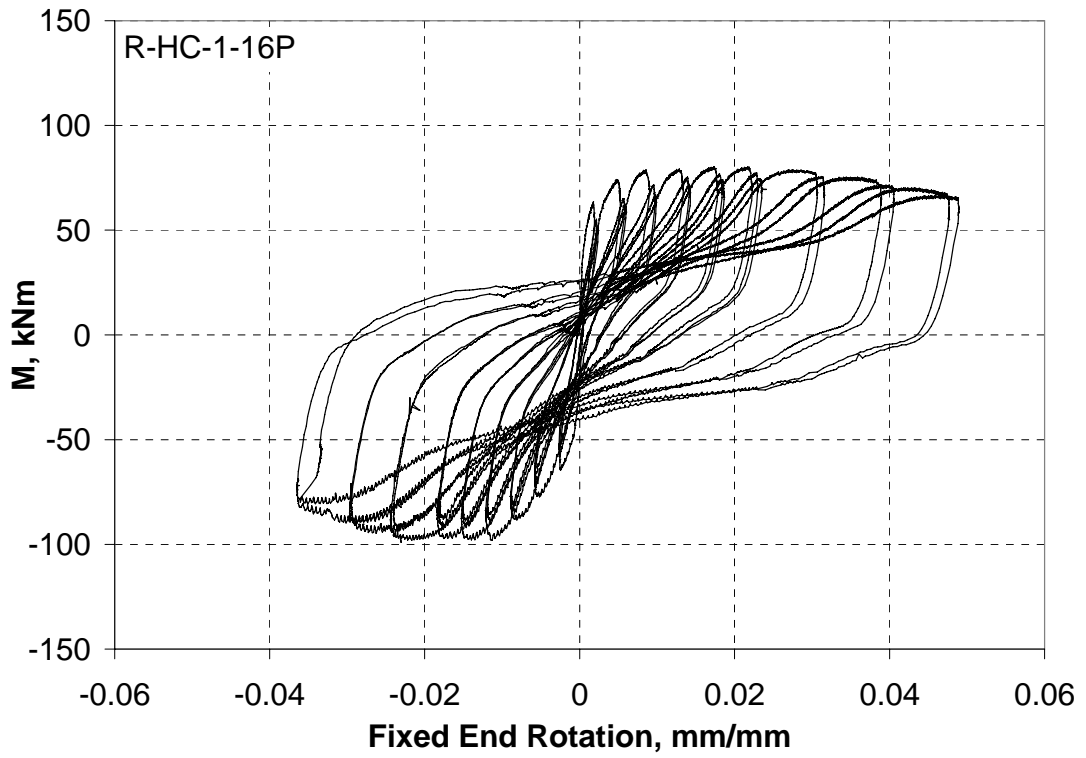


Figure 2.77 Moment (M) – Fixed End Rotation (FER) response of R-HC-1-16P

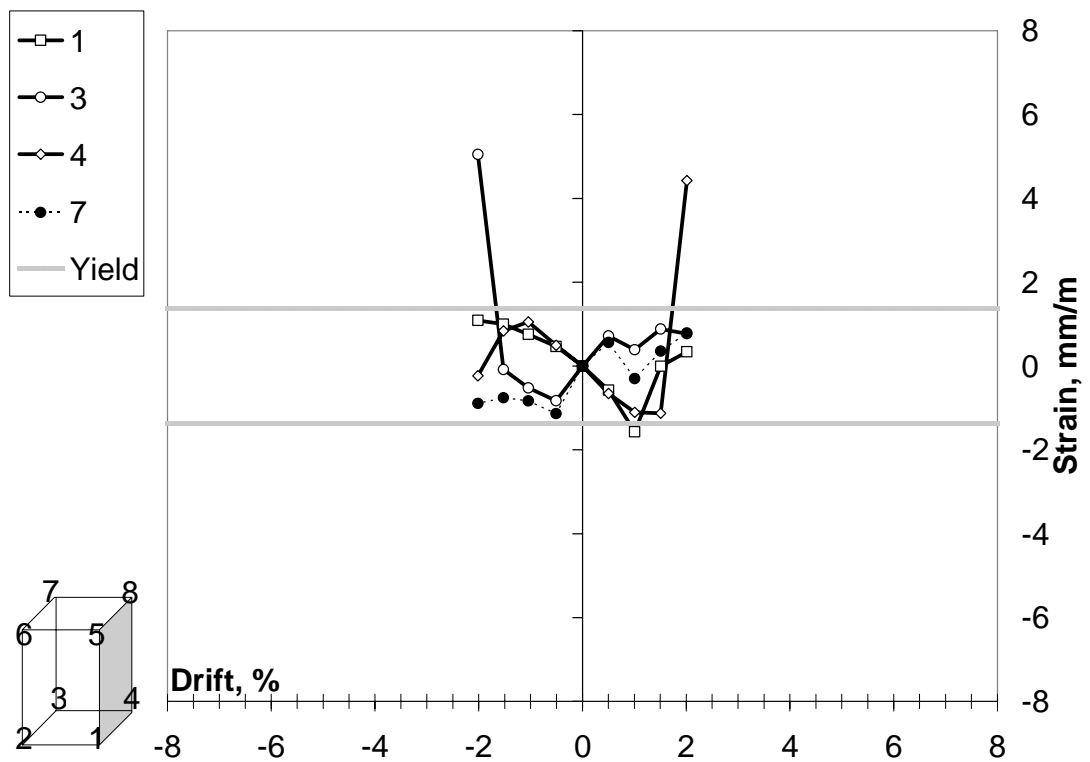


Figure 2.78 Strain – Drift responses for R-NC-0-00

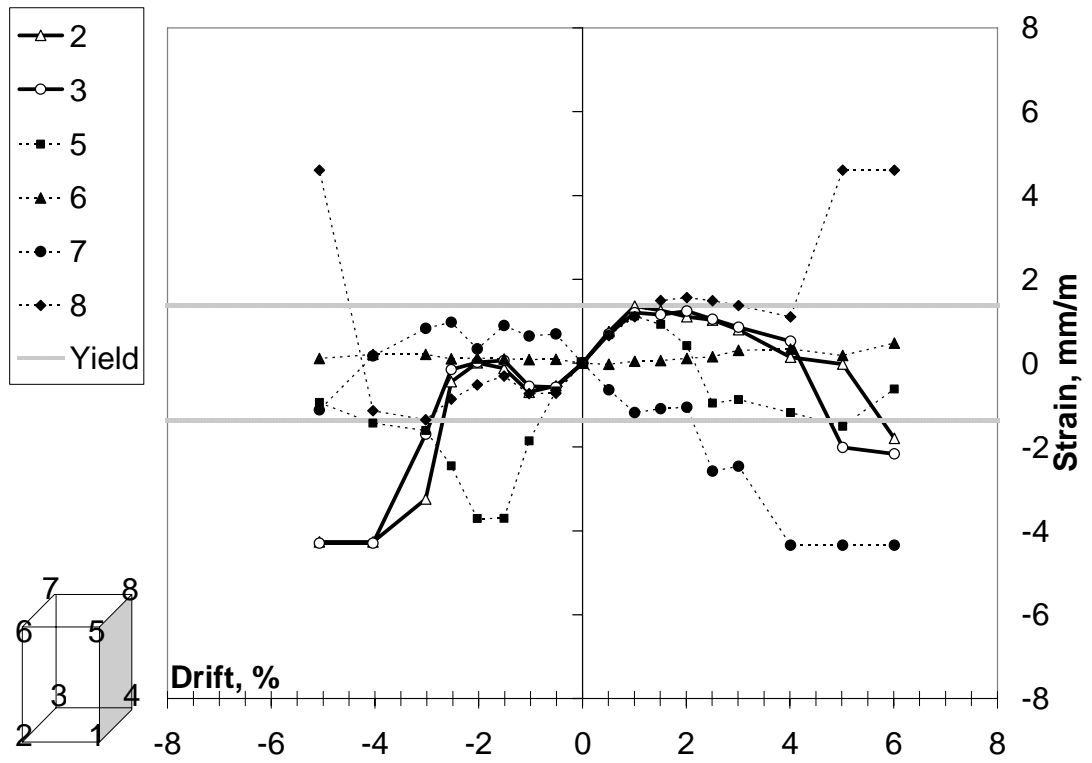


Figure 2.79 Strain – Drift responses for R-MC-1-16P

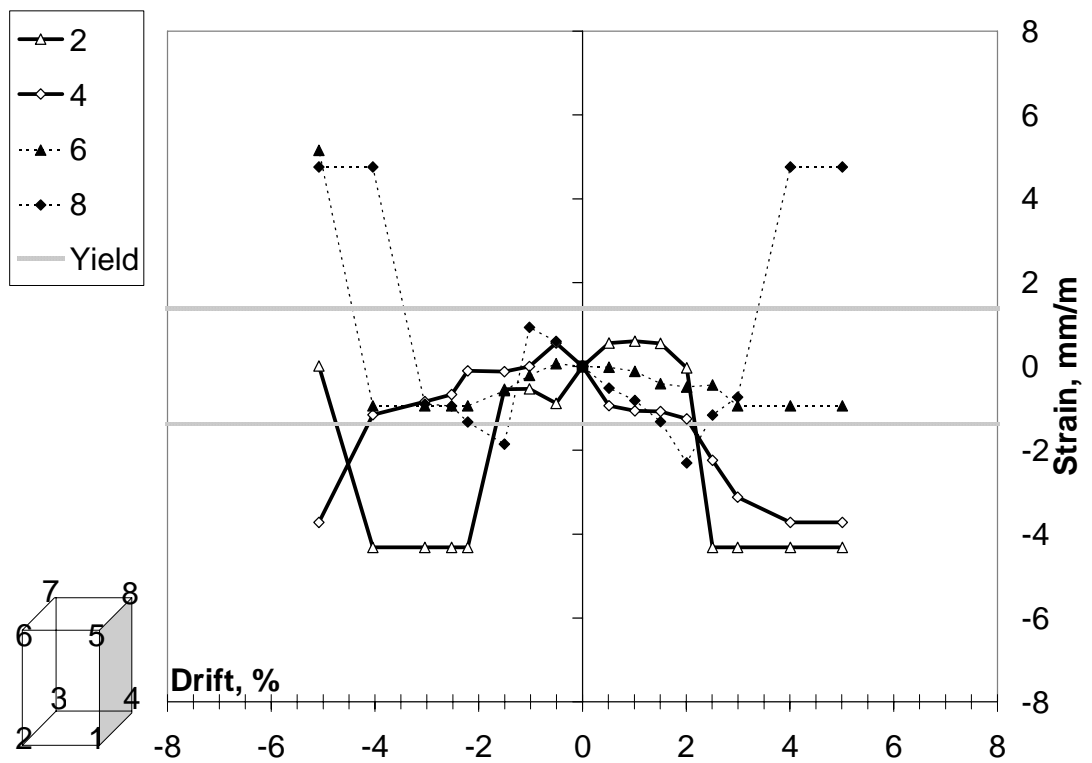


Figure 2.80 Strain – Drift responses for R-MC-1-8P

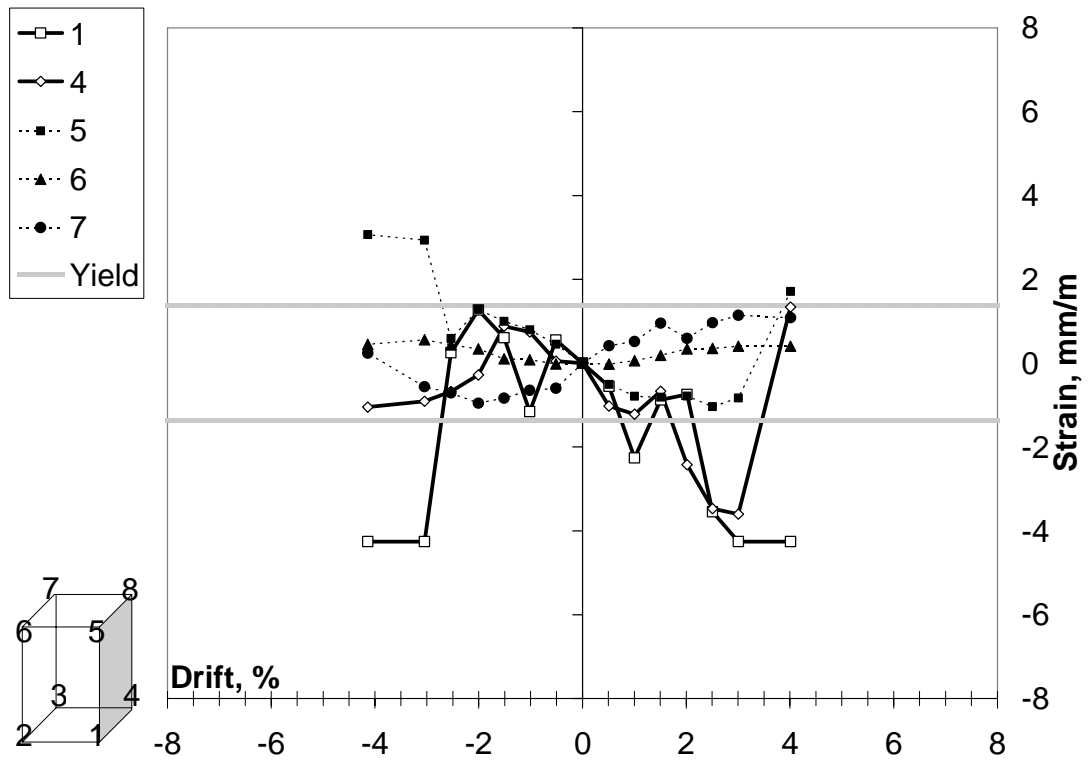


Figure 2.81 Strain – Drift responses for R-MC-1-NP

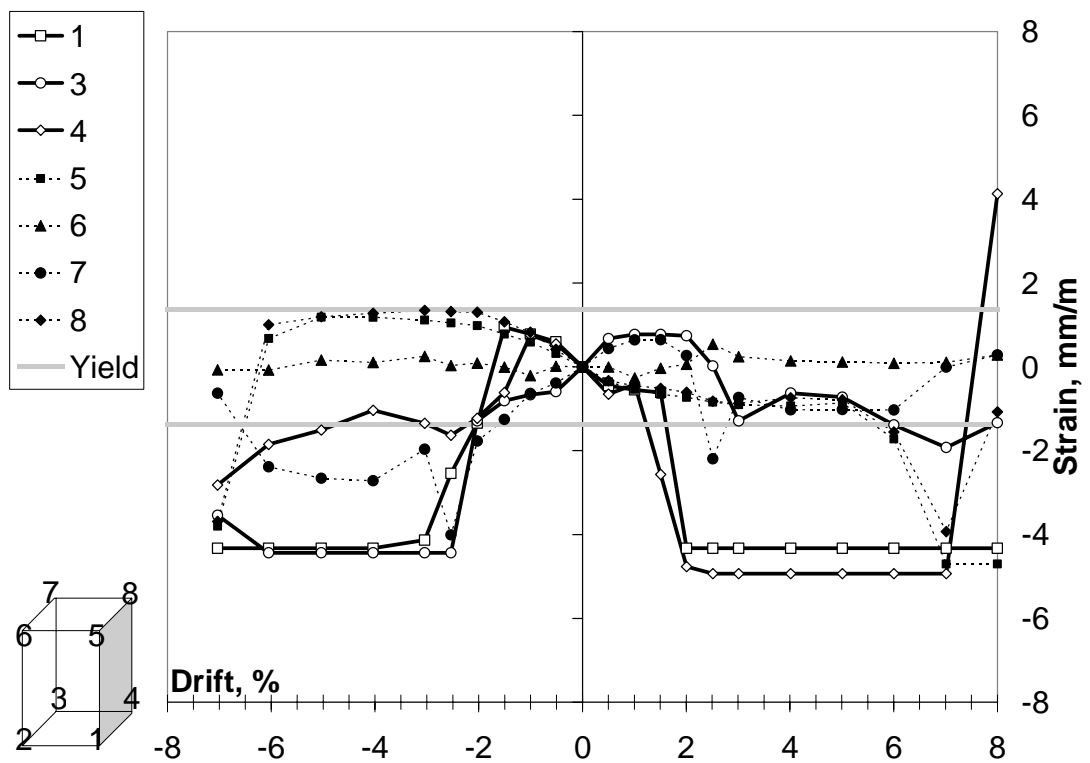


Figure 2.82 Strain – Drift responses for R-HC-1-16P

2.7. Examination of Test Results

In all test series, lateral loads and moments were normalized by dividing the lateral load values into the experimental yield load values (Table 2.5) except the Series 2 since all test specimens in Series 2 had concrete compressive strengths close to each other. Seismic behavior of each specimen was examined upon comparing the attained ultimate drift levels and curvatures, dissipated energy and strength degradation characteristics. Average curvatures were obtained and compared considering the rotations both relative to the column base and 50 mm height above the column base. Thereafter, fixed-end and flexural components of total rotation and tip deflection were shown on each drift level. Shear deformations were ignored in the data analyses since the behavior of the columns were flexural dominant with an aspect ratio (column height/section depth) of about 5.7 for square and 5.0 for rectangular columns.

2.7.1. Envelope Response Comparisons

The normalized graphs implied that wrapping 1 and 2 layers of CFRP around the column improved attained ultimate drifts level from 2.6% to 5% and 6.2%, respectively (Figure 2.83, Table 2.5) for Series 1. Upon comparing the CFRP strengthened columns under axial load of about 35% of capacity, both columns with 1 layer or 2 layers CFRP wrapping had approximately the same level of ultimate drift, i.e. 5% and 6.2%, respectively (Figures 2.84- 2.85). Besides, a strength increase of approximately 15% was observed for the CFRP strengthened specimens due to the confining effect of the CFRP. By wrapping 1 and 2 layers of CFRP, average ultimate curvatures measured relative to 50 mm height above the column base, increased up to 100 rad/km in comparison with the reference specimen that failed at an ultimate curvature of about 50 rad/km. However, as shown in Figures 2.86-2.88, the inconsistency of the average curvatures relative to 50 mm height for 1 and 2 CFRP layers (i.e. 40 rad/km for S-L-2-00 and 85 rad/km for S-L-1-00) can be interpreted due to damage accumulation along 50 mm above the column-stub interface. Thus, higher average curvatures were obtained relative to column base rather than the readings relative to 50 mm height above the column base as shown in Figures 2.86a

and 2.86b. Figures 2.87a and 2.88a indicate that the average curvatures relative to the column base showed a similar behavior with the hysteretic lateral load – drift behavior. However, the curvature readings relative to 50 mm height were observed to be lower since the damage was accumulated in a zone of 50 mm above the column base (Figures 2.87b, 2.88b). Further, the curvature distribution along the test region at heights of 25 and 200 mm for the columns in Series 1 is presented in Appendix D. The monitored data demonstrated the accumulation of damage in a zone of 50 mm above the column base while augmented levels of curvatures at 25 mm height were observed during various drift levels until the failure of the columns. In addition, since the fixed-end rotations at the ultimate point where the lateral capacity dropped 80% of the peak were about 0.008 rad for the reference specimen, it was improved to 0.03 and 0.05 rad for 1 and 2-layer CFRP wrapped columns as shown in Figure 2.89. A comparable performance was investigated for the companion one (S-L-1-00, S-L-1-34) and two-layer (S-L-2-00, S-L-2-32) CFRP strengthened specimens while the fixed-end rotations were in a very close agreement (Figures 2.90, 2.91). It shows the trivial effect of strengthening under axial load of approximately 35% of capacity.

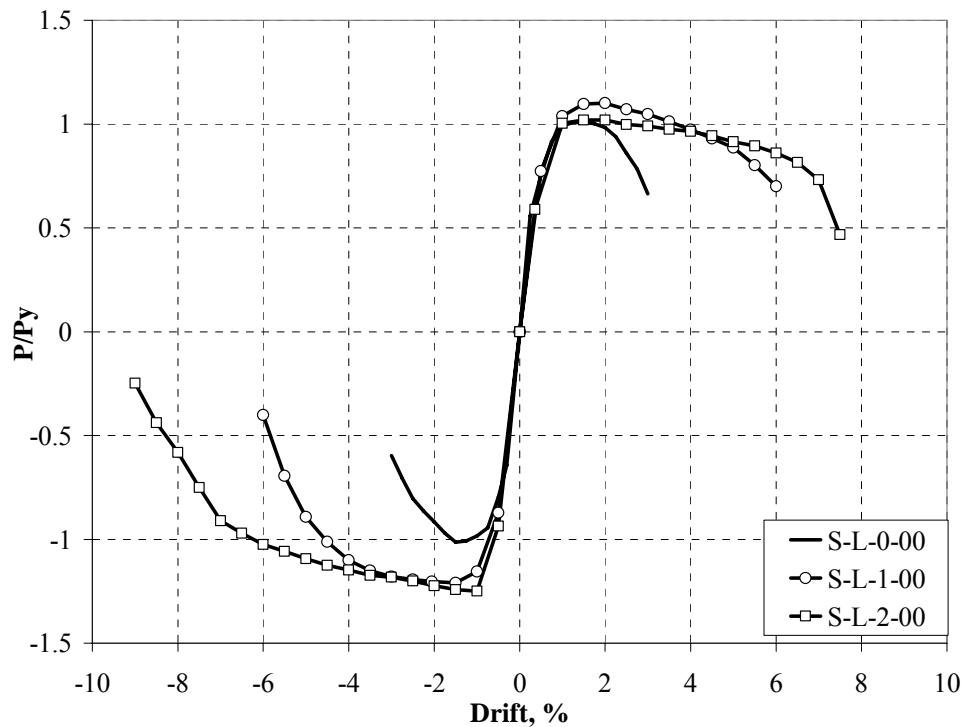


Figure 2.83 Normalized Lateral Load (P/P_y) – Drift comparisons for S-L-0-00, S-L-1-00 and S-L-2-00

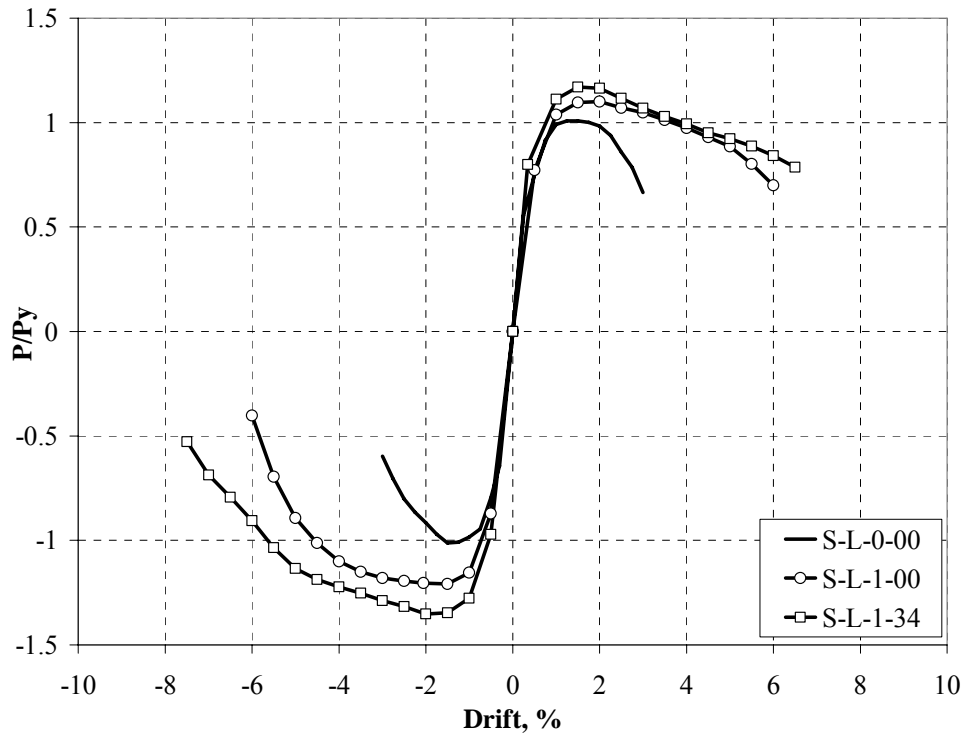


Figure 2.84 Normalized Lateral Load (P/Py) – Drift comparisons for S-L-0-00, S-L-1-00 and S-L-1-34

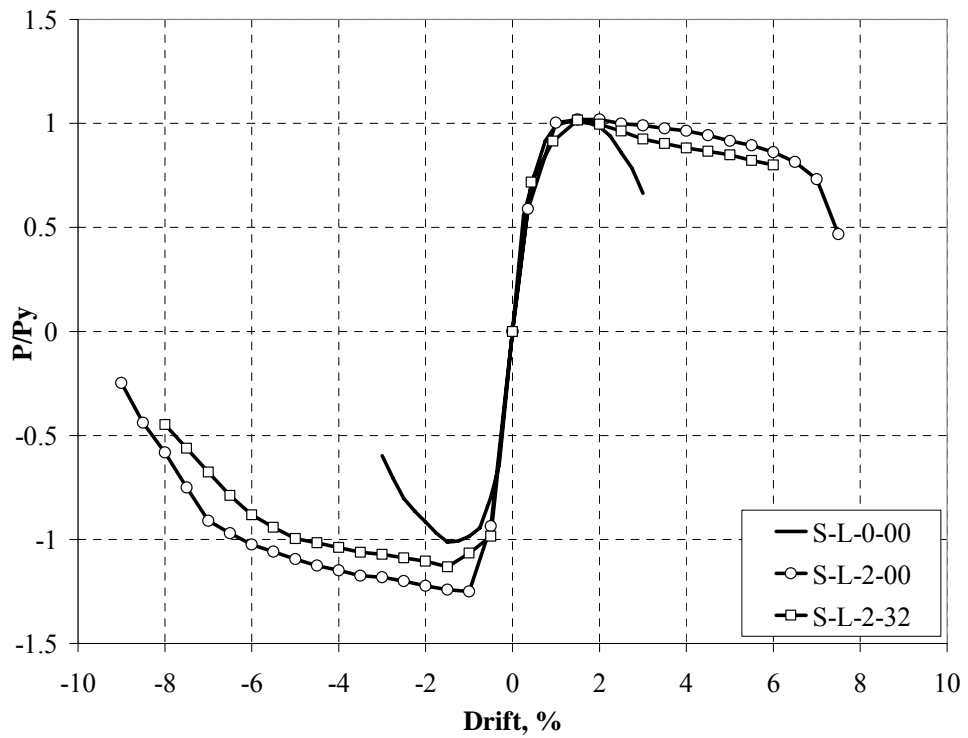
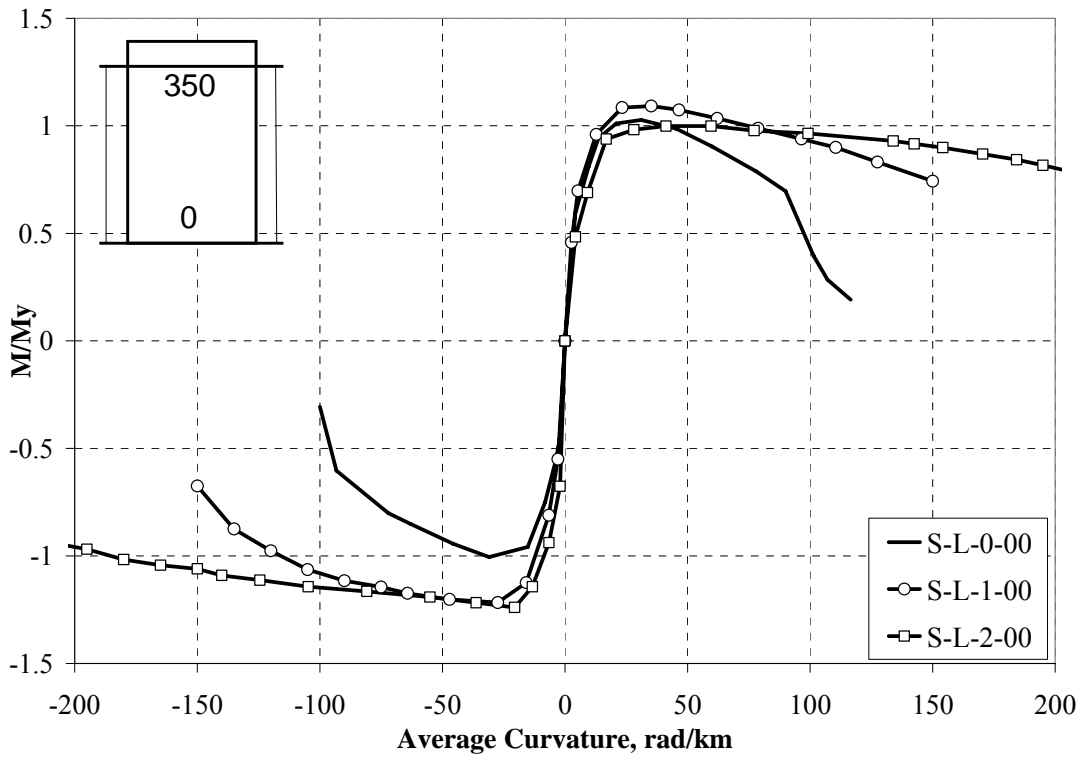
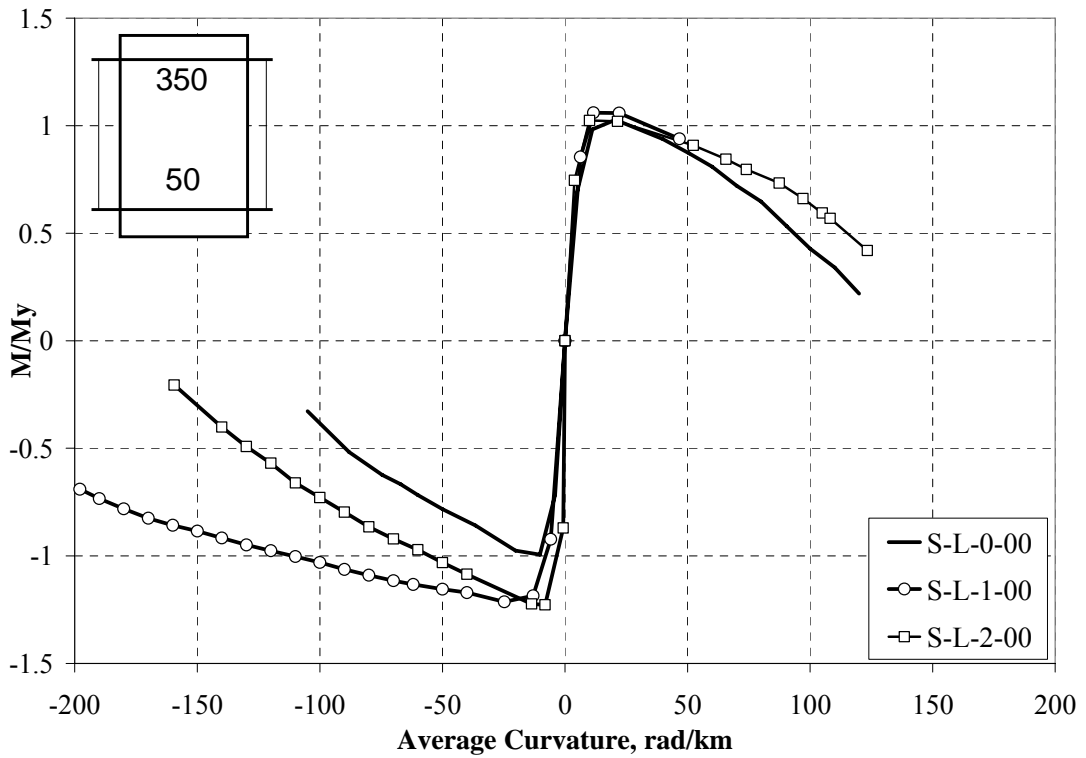


Figure 2.85 Normalized Lateral Load (P/Py) – Drift comparisons for S-L-0-00, S-L-2-00 and S-L-2-32

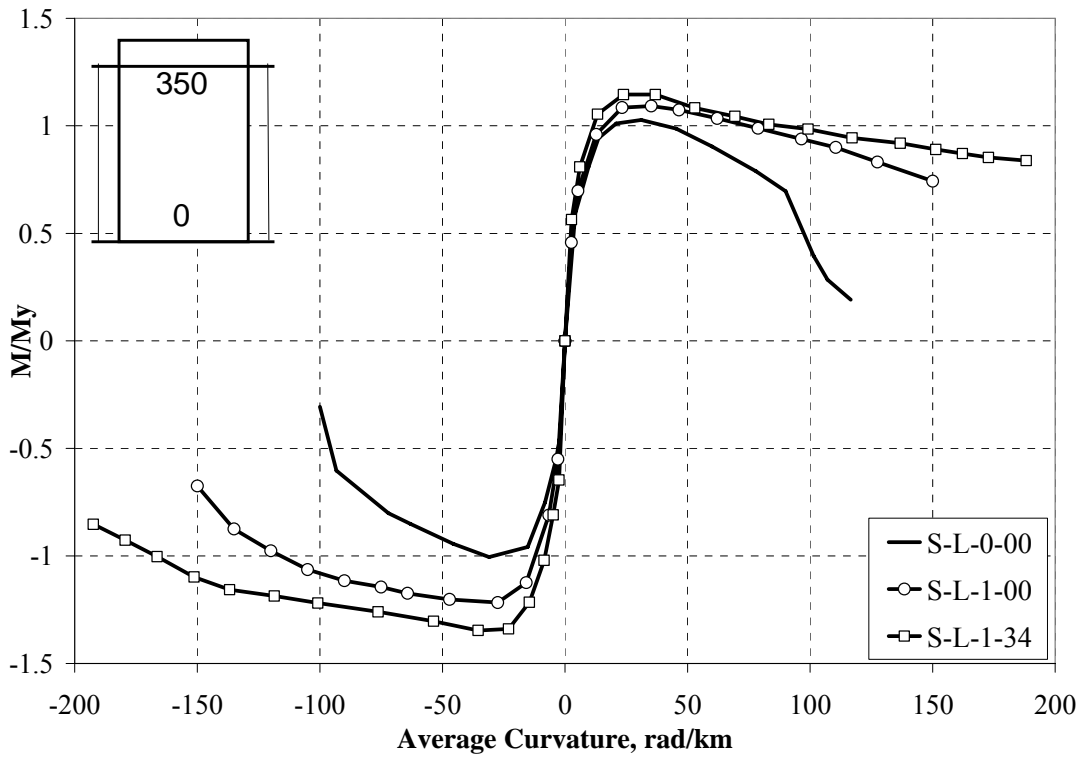


(a)

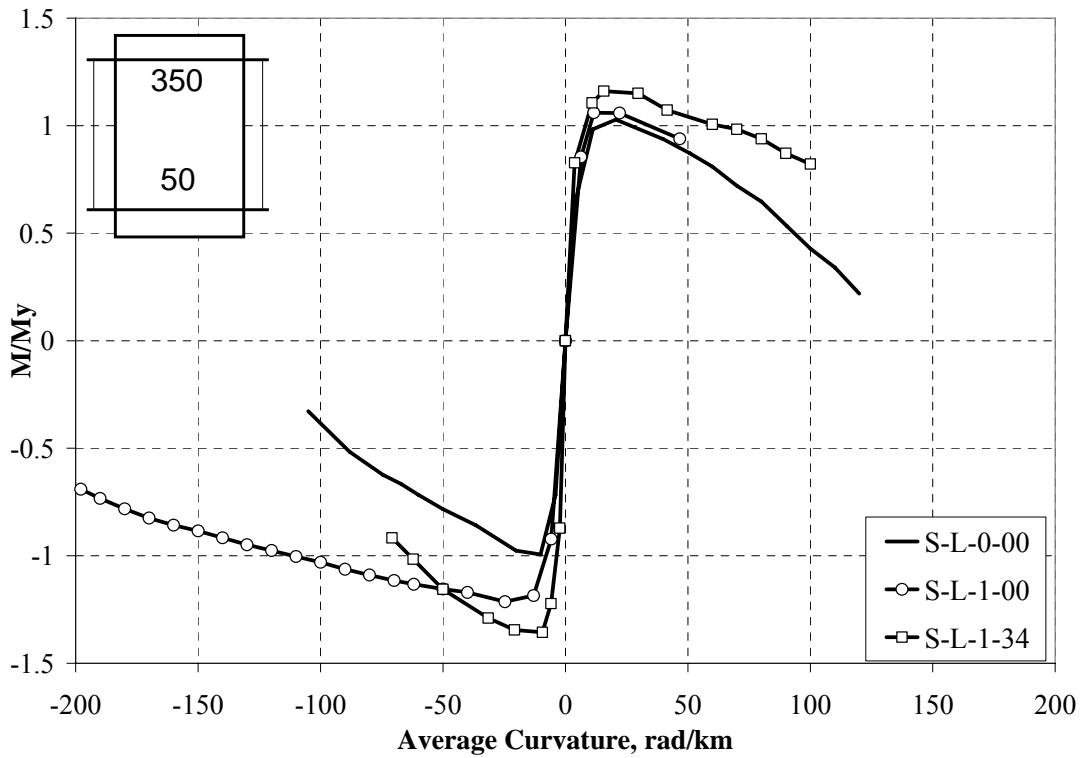


(b)

Figure 2.86 Normalized Moment (M/M_y) – Curvature comparisons for S-L-0-00, S-L-1-00 and S-L-2-00: at location (a) 350 – 0 and (b) 350 – 50 mm

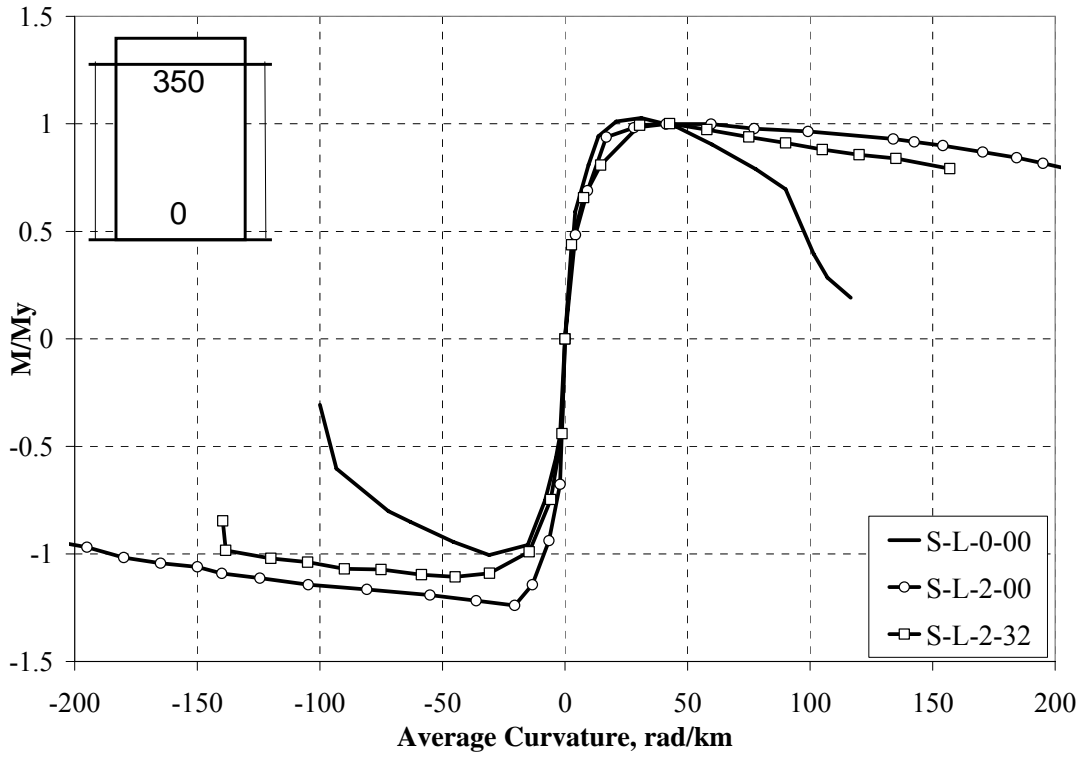


(a)

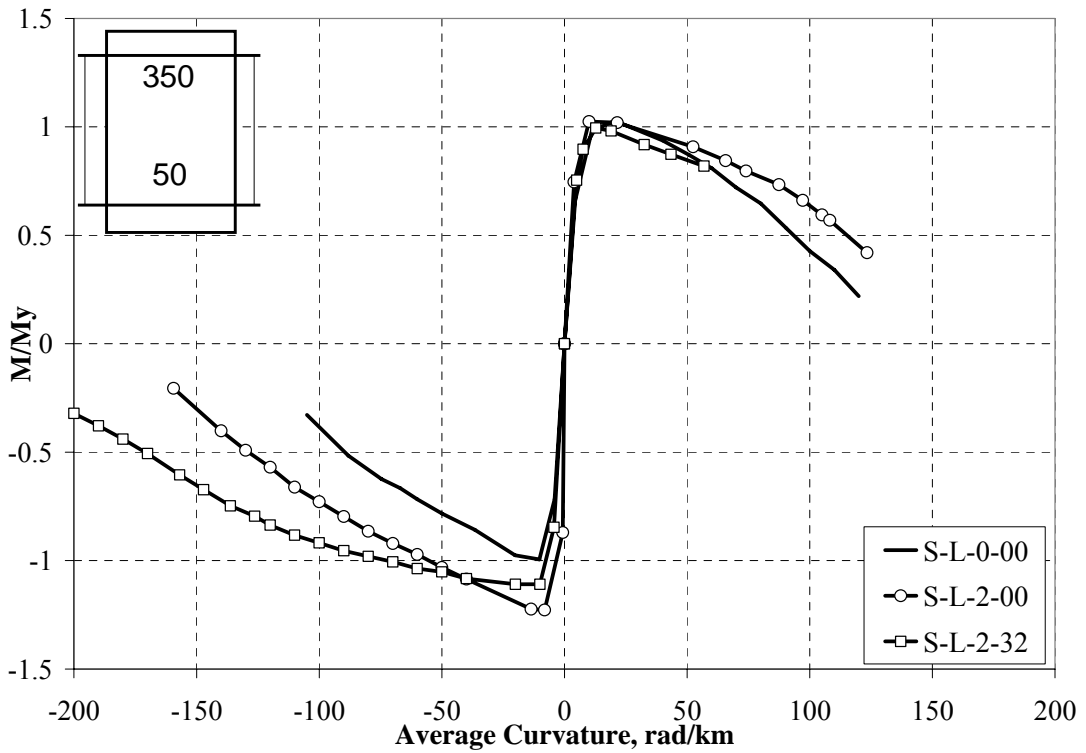


(b)

Figure 2.87 Normalized Moment (M/M_y) – Curvature comparisons for S-L-0-00, S-L-1-00 and S-L-1-34: at location (a) 350 – 0 and (b) 350 – 50 mm



(a)



(b)

Figure 2.88 Normalized Moment (M/M_y) – Curvature comparisons for S-L-0-00, S-L-2-00 and S-L-2-32: at location (a) 350 – 0 and (b) 350 – 50 mm

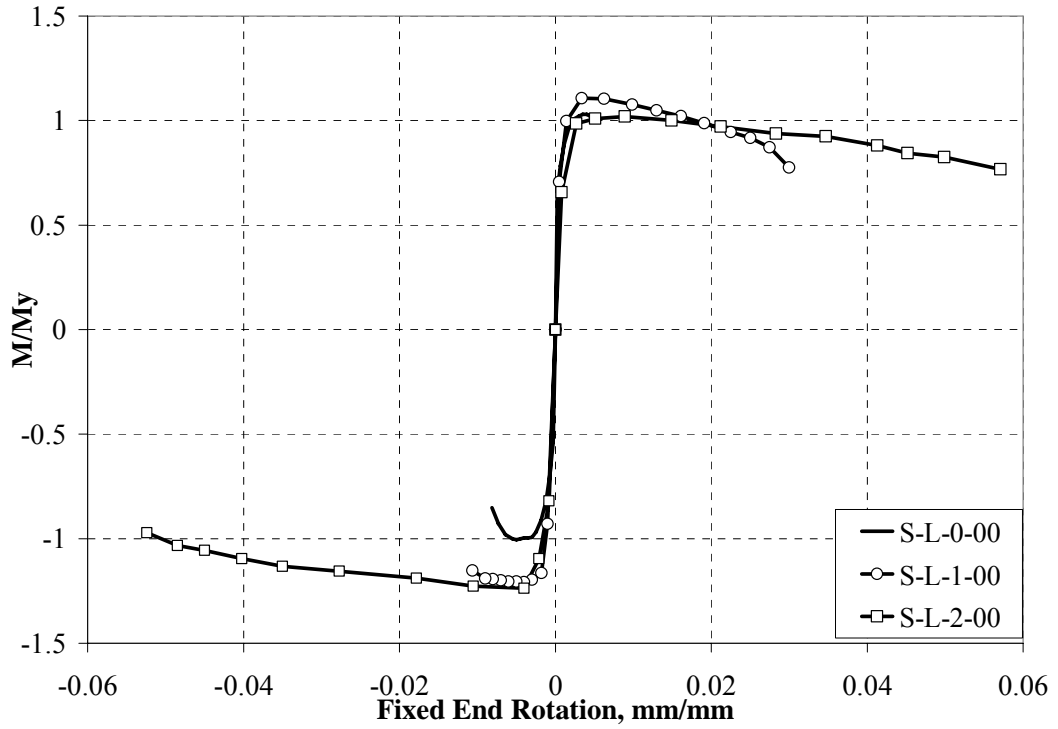


Figure 2.89 Normalized Moment (M/My) – Fixed End Rotation comparisons for S-L-0-00, S-L-1-00 and S-L-2-00

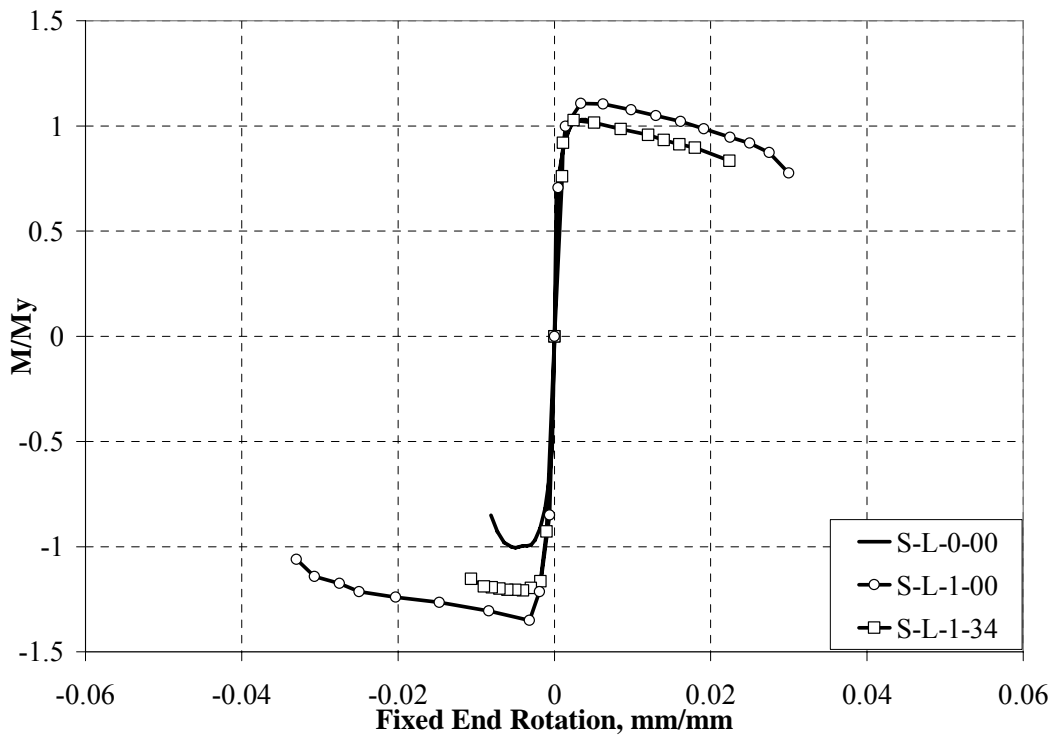


Figure 2.90 Normalized Moment (M/My) – Fixed End Rotation comparisons for S-L-0-00, S-L-1-00 and S-L-1-34

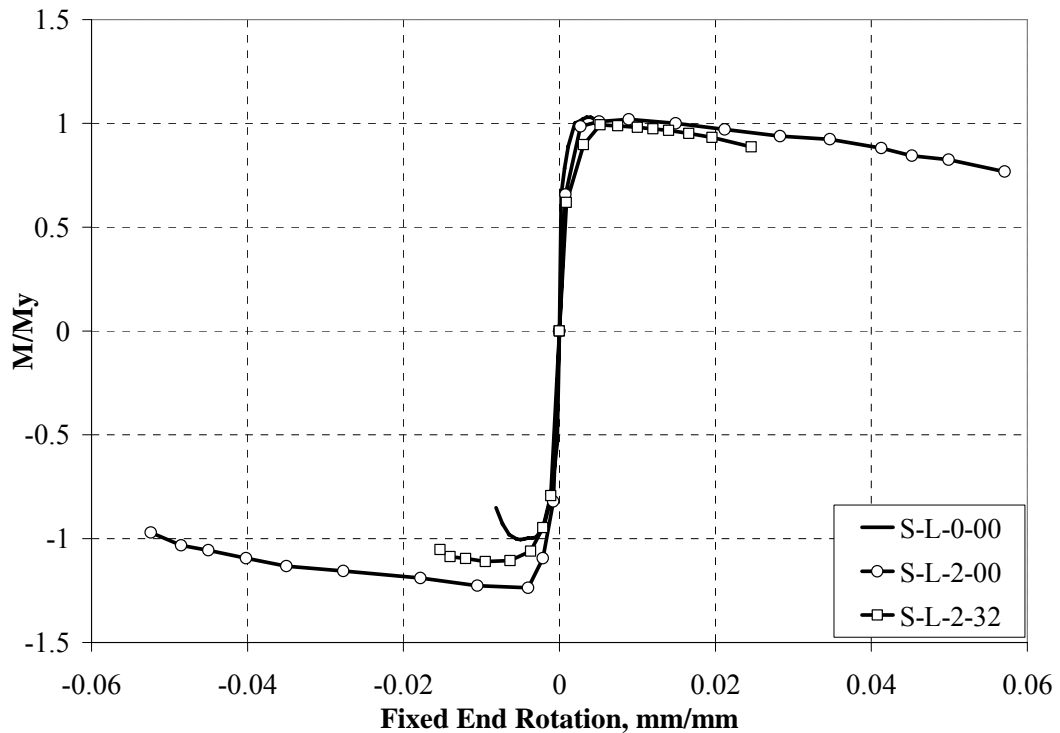


Figure 2.91 Normalized Moment (M/My) – Fixed End Rotation comparisons for S-L-0-00, S-L-2-00 and S-L-2-32

For Series 2, the ultimate drift levels improved from 3.3% to 4.1 and 5.1% for strengthened and repaired columns, respectively. However, decreasing the corner-rounding radius to 10 mm had a pronounced effect on the column behavior since 1 layer CFRP strengthening improved the attained drift level to only 3.6% (Figure 2.92). The observed strength gain for the strengthened specimens was in the limits of 15-20% due to the confining effect of CFRP. In addition, CFRP repairing of columns under an axial load of about 27% of the capacity had no significant improvement in lateral strength whereas if the CFRP repairing process was implemented before the axial load was maintained constant, the strength gain was observed to be about 20% (Figure 2.93). This behavior can be explained by high compressive strength of the epoxy mortar that was used in repairing and replacing the spalled concrete cover after the column experienced a moderate level of damage. For the column that was repaired under axial load, high strength epoxy-based repair mortar having compressive strength of approximately 70 MPa, did not contribute to the lateral strength due to the existing axial load on the column during the repairing process.

This behavior was not valid for its companion specimen since the axial load was applied after repairing the spalled concrete and hence the replaced parts could carry additional lateral and axial loads (Figure 2.94). Similar results were acquired by comparing the Moment – Average Curvature behavior of the columns that were measured relative to the column base. For S-H-0-00, the ultimate average curvature relative to 50 mm height was about 50 rad/km however; for the strengthened and repaired columns, sustained ultimate curvature levels were recorded as approximately 30 and 90 rad/km, respectively (Figures 2.95-2.97). However, similar to the damage accumulation phenomenon along 50 mm height observed in Series 1, the average curvature readings relative to the column base were monitored to be higher. Thus, the average curvatures increased approximately to 100 and 150 rad/km from 90 rad/km for strengthened, repaired and reference specimens, respectively. The curvature distribution shown in Appendix D demonstrates the damage accumulation in terms of curvatures for Series 2. The ultimate fixed-end rotations were 0.014 and 0.037 rad for the reference and retrofitted columns, respectively. (Figures 2.98-2.100).

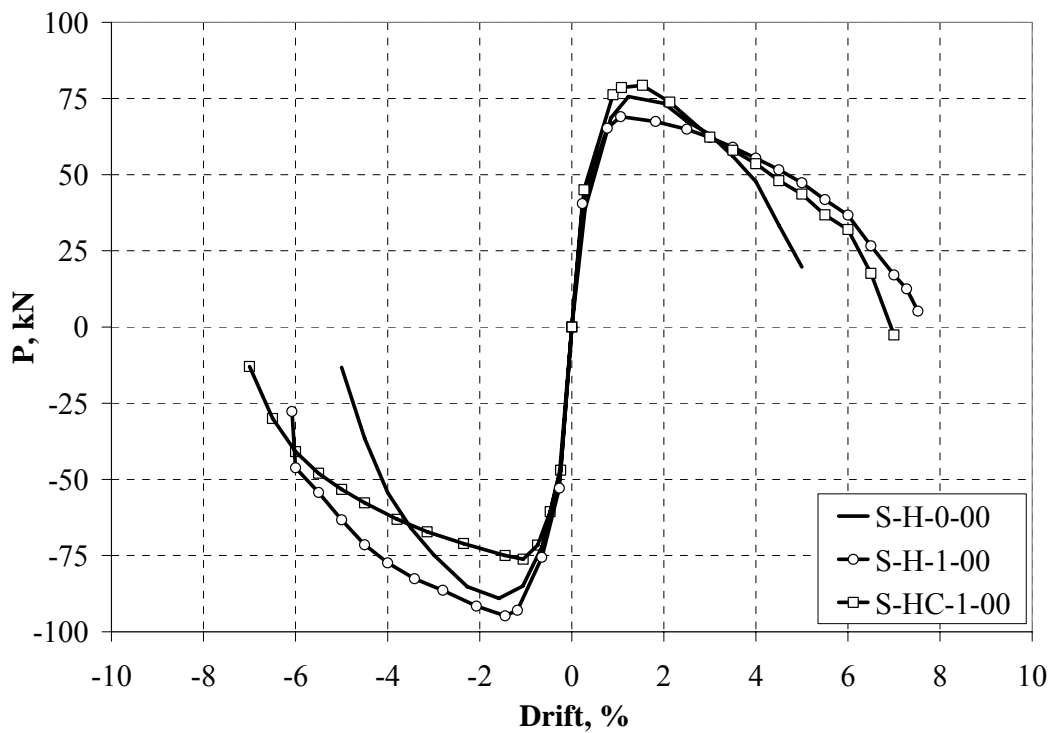


Figure 2.92 Lateral Load (P) – Drift comparisons for S-H-0-00, S-H-1-00 and S-HC-1-00

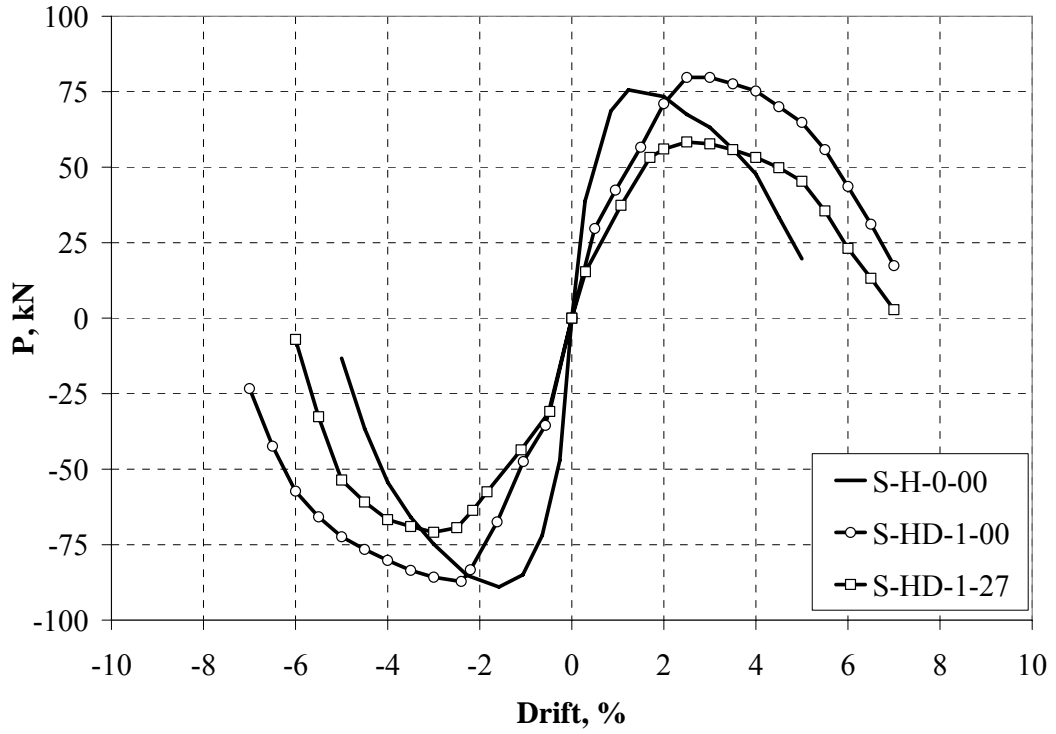


Figure 2.93 Lateral Load (P) – Drift comparisons for S-H-0-00, S-HD-1-00 and S-HD-1-27

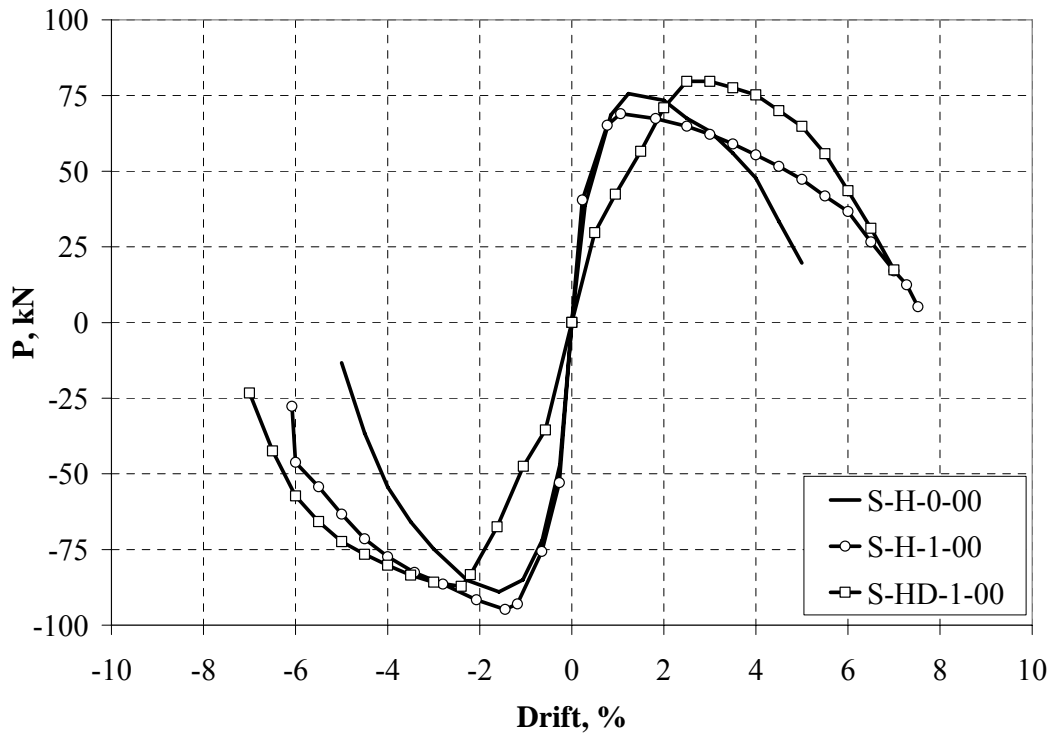
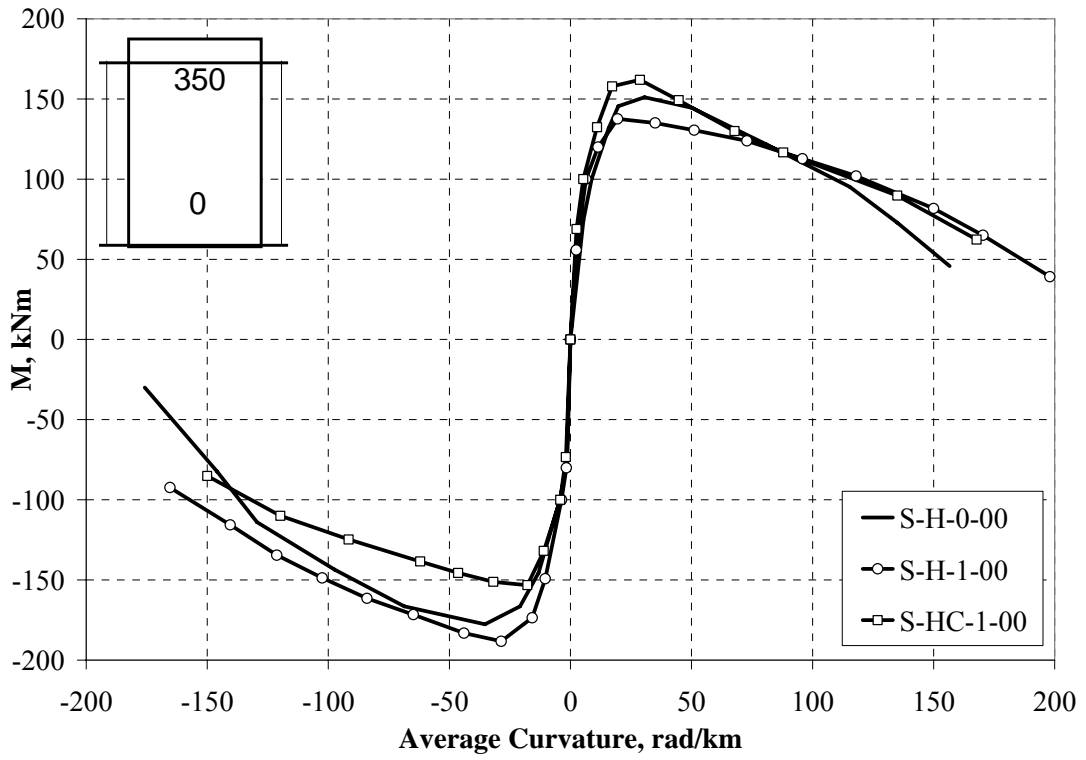
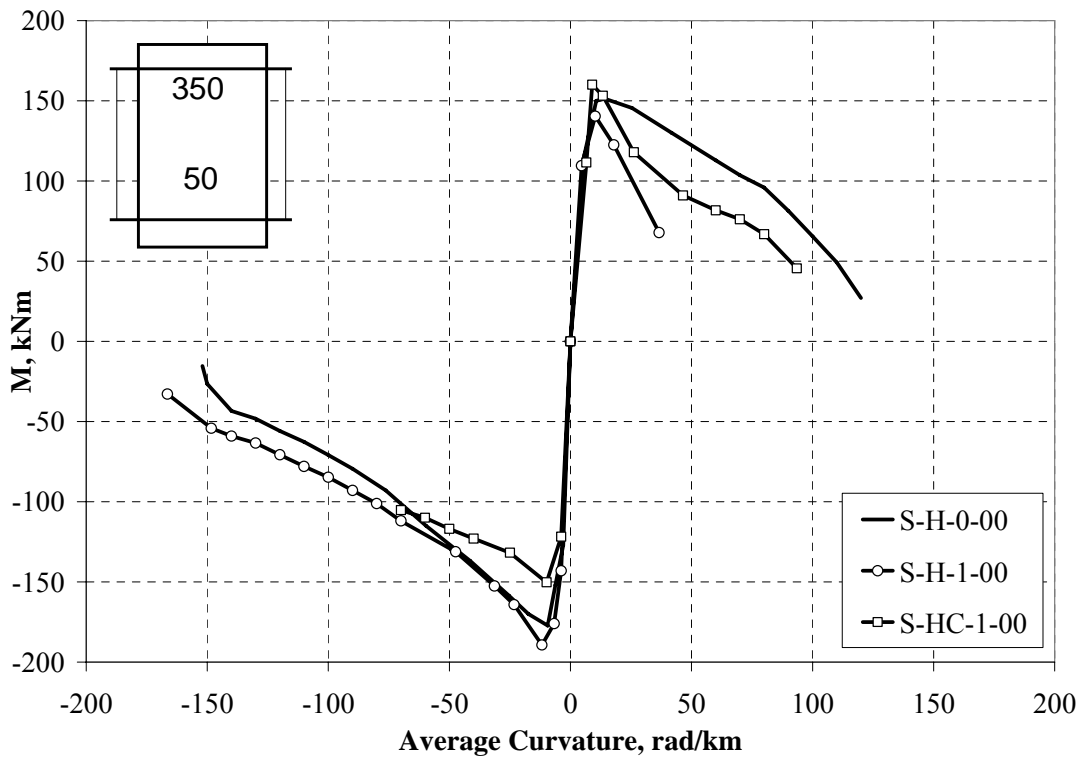


Figure 2.94 Lateral Load (P) – Drift comparisons for S-H-0-00, S-H-1-00 and S-HD-1-00

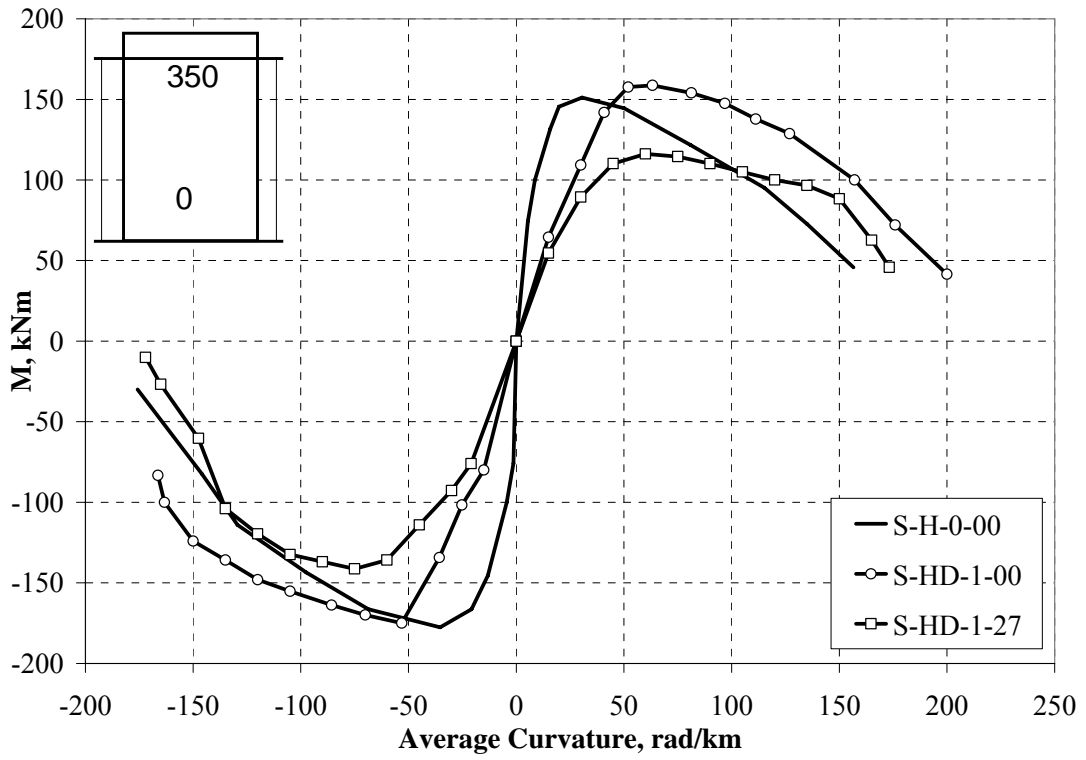


(a)

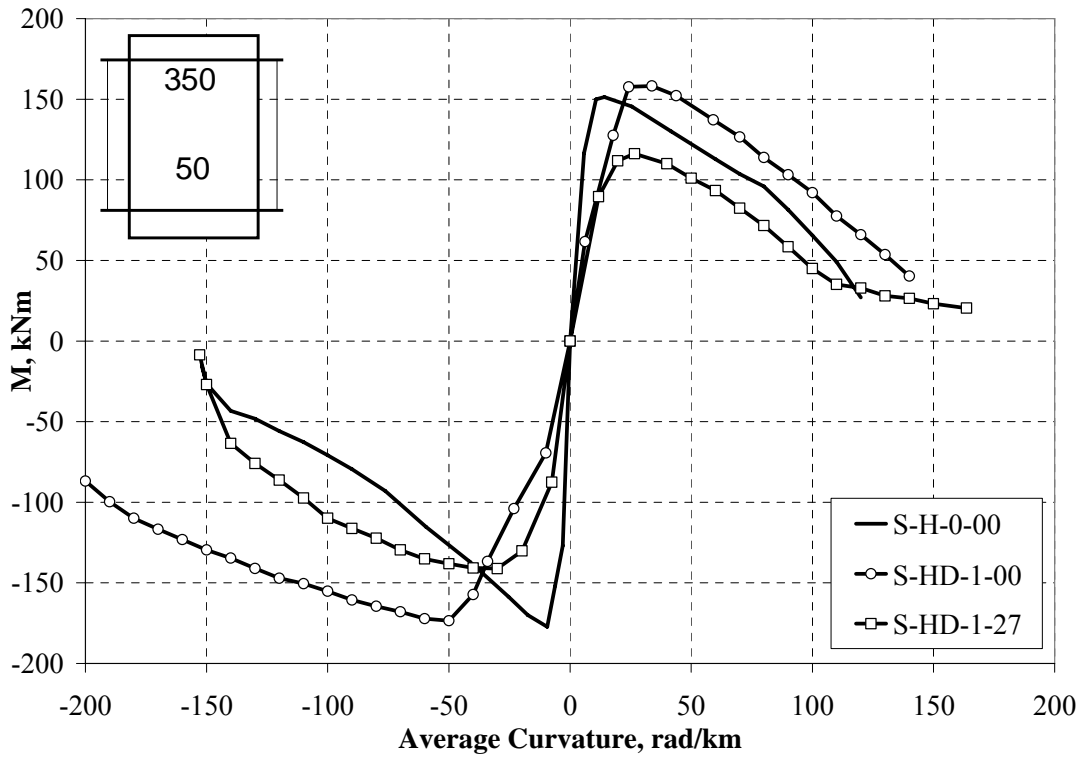


(b)

Figure 2.95 Moment (M) – Curvature comparisons for S-H-0-00, S-H-1-00 and S-HC-1-00: at location (a) 350 – 0 and (b) 350 – 50 mm

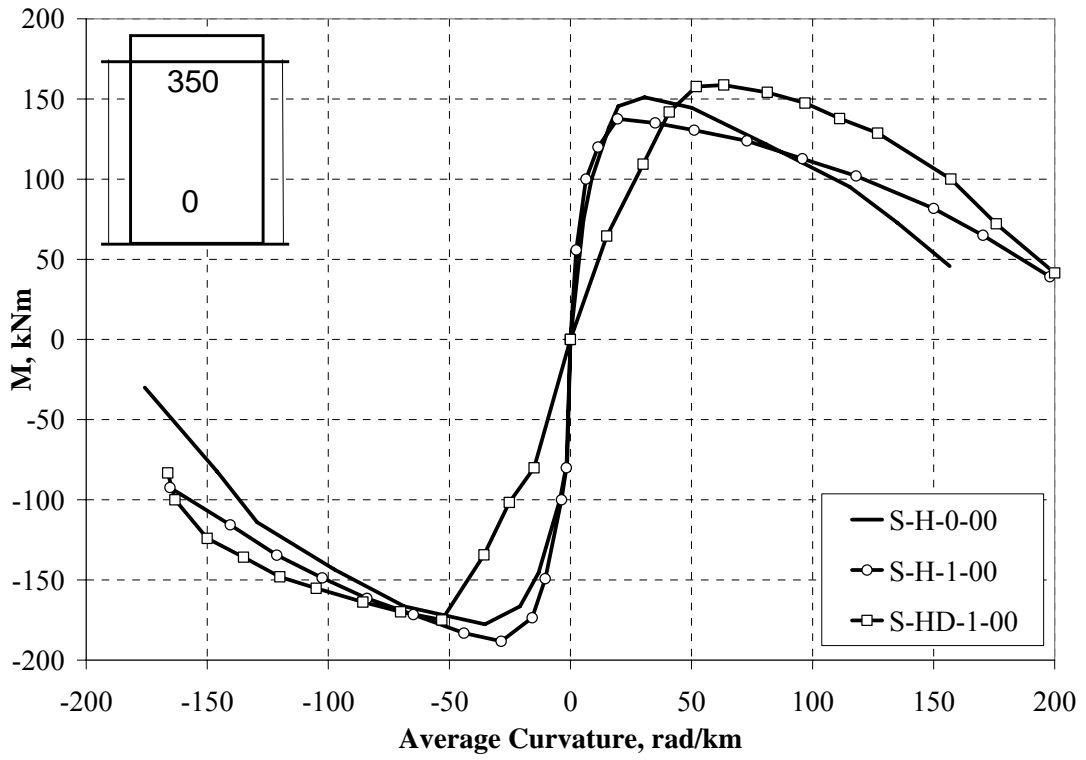


(a)

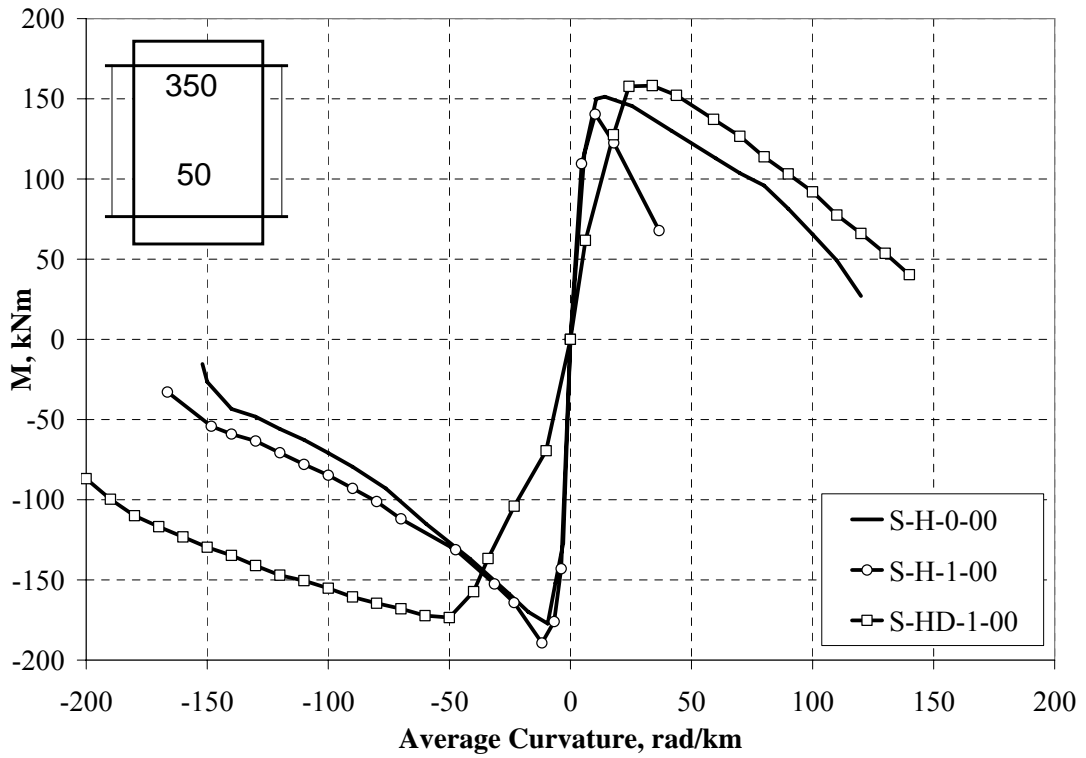


(b)

Figure 2.96 Moment (M) – Curvature comparisons for S-H-0-00, S-HD-1-00 and S-HD-1-27: at location (a) 350 – 0 and (b) 350 – 50 mm



(b)



(b)

Figure 2.97 Moment (M) – Curvature comparisons for S-H-0-00, S-H-1-00 and S-HD-1-00: at location (a) 350 – 0 and (b) 350 – 50 mm

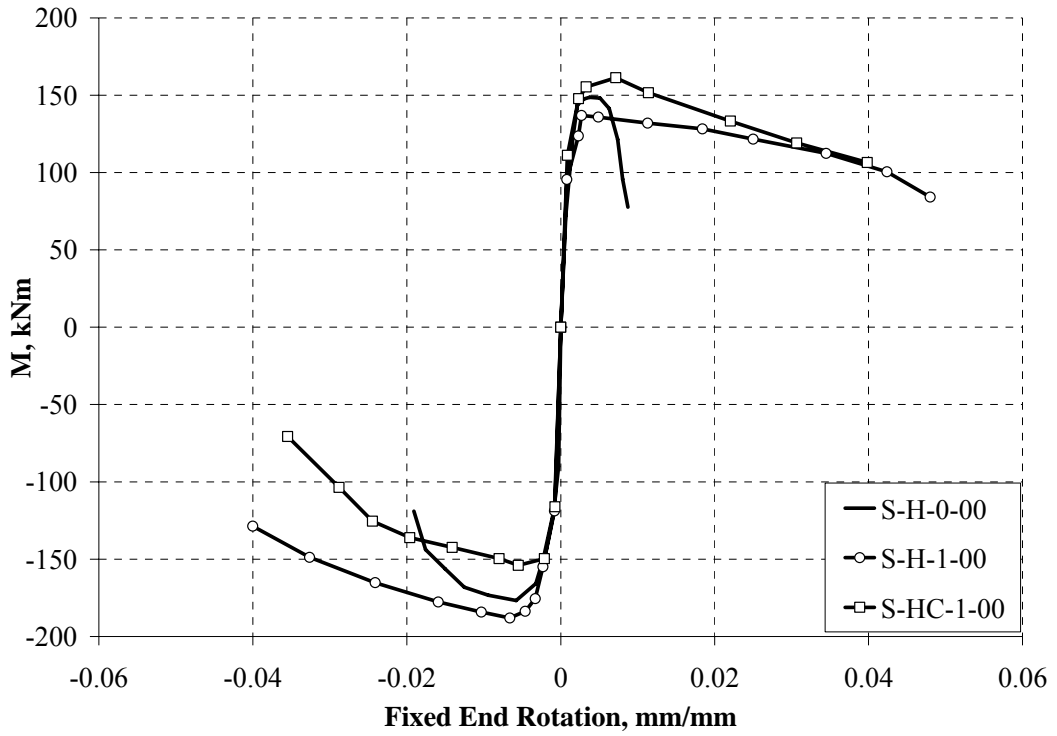


Figure 2.98 Moment (M) – Fixed End Rotation comparisons for S-H-0-00, S-H-1-00 and S-HC-1-00

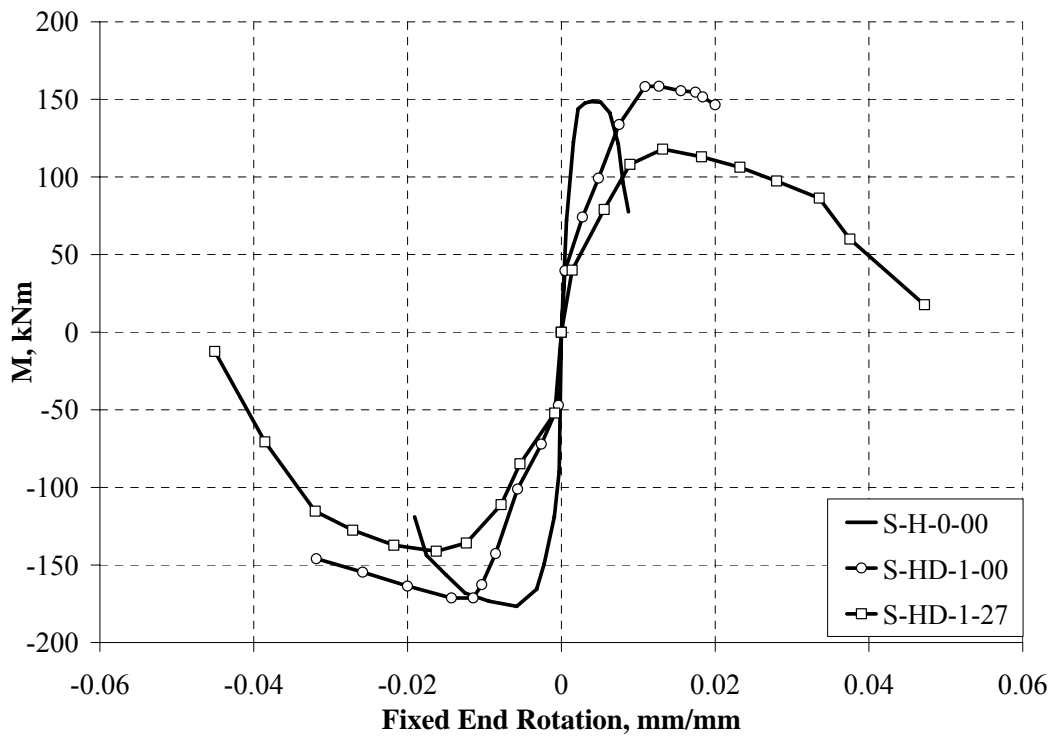


Figure 2.99 Moment (M) – Fixed End Rotation comparisons for S-H-0-00, S-HD-1-00 and S-HD-1-27

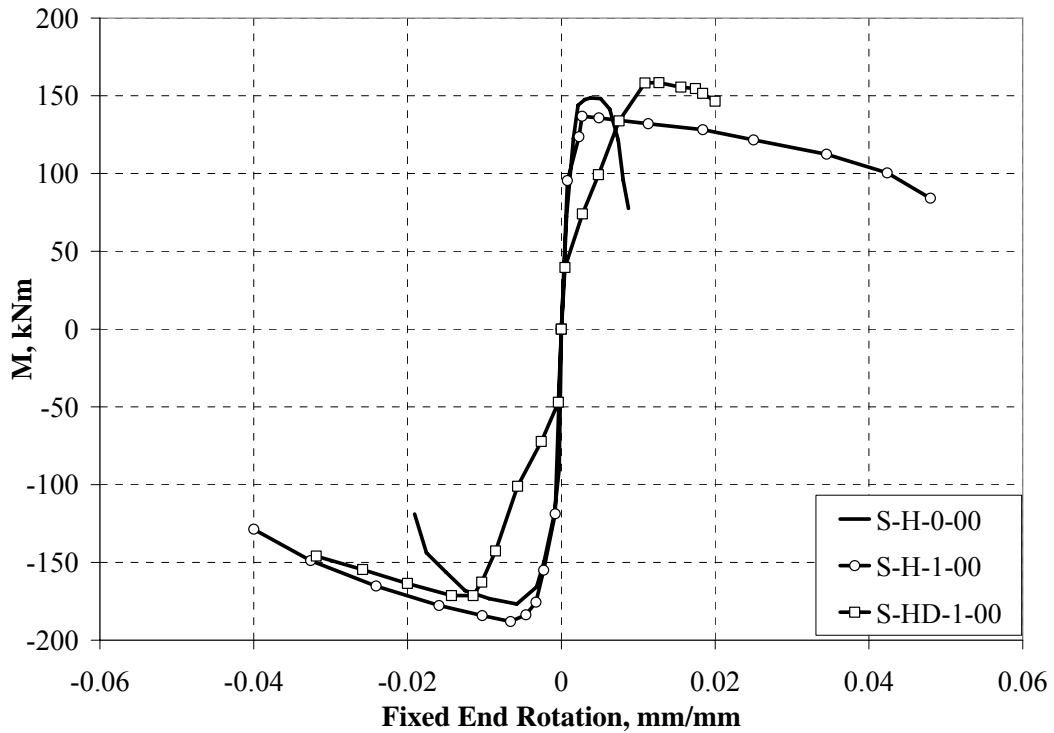


Figure 2.100 Moment (M) – Fixed End Rotation comparisons for S-H-0-00, S-H-1-00 and S-HD-1-00

For Series 3, the ultimate drift levels for the 16-pinned specimens having high and moderate confinement levels were 6.1% and 4.0%, respectively (Figure 2.101). This fact presented the beneficial effect of CFRP confinement by CFRP anchor dowels regarding the reference specimen that failed at 1.8% of drift level. Using 8-pinned or no-pinned anchor configuration had an insignificant effect on the column behavior since the acquired ultimate drift level for the specimens R-MC-1-8P and R-MC-1-NP was about 4%. Since the 80 mm-long CFRP anchor dowels did not fully penetrate into the borderline of CFRP confined region that was 85 mm inside the column long side, it had no influence on the column behavior and it had the same effect as the column having no CFRP anchor dowels used (Figure 2.102). The confining effect of CFRP anchor dowels changed only the behavior of the 16-pinned specimen by increasing the confined area of its cross-section and made the column attain similar drift levels (Figure 2.103). The ultimate average curvatures monitored relative to 50 mm height, were approximately 25 rad/km for the reference specimen R-NC-0-00

and reached about 50 rad/km for the 16-pinned specimens R-HC-1-16P and R-MC-1-16P (Figure 2.104). While the specimen R-MC-1-8P failed with an ultimate curvature of about 40 rad/km, 110 rad/km of ultimate curvature was monitored for the specimen R-MC-1-NP (Figures 2.105 and 2.106). However, according to the curvature readings relative to the column base, the average ultimate curvature levels were observed to be augmented to approximately 35 and 100 rad/km for the reference and strengthened specimens due to the damage accumulation along 50 mm height from the column base. In addition, the curvature distributions at various drift levels are presented in Appendix D that establish the damage accumulation phenomenon for the specimens tested in Series 3. The ultimate fixed-end rotation for the reference specimen was about 0.004 rad regarding the 16-pinned specimens R-HC-1-16P and R-MC-1-16P having ultimate fixed-end rotations of 0.04 and 0.02 rad, respectively (Figure 2.107). The column R-HC-1-16P possessed a superlative behavior over its moderately confined companion column R-MC-1-16P, while decreasing confinement level led to a decrease in fixed-end rotations. (Figures 2.108 and 2.109).

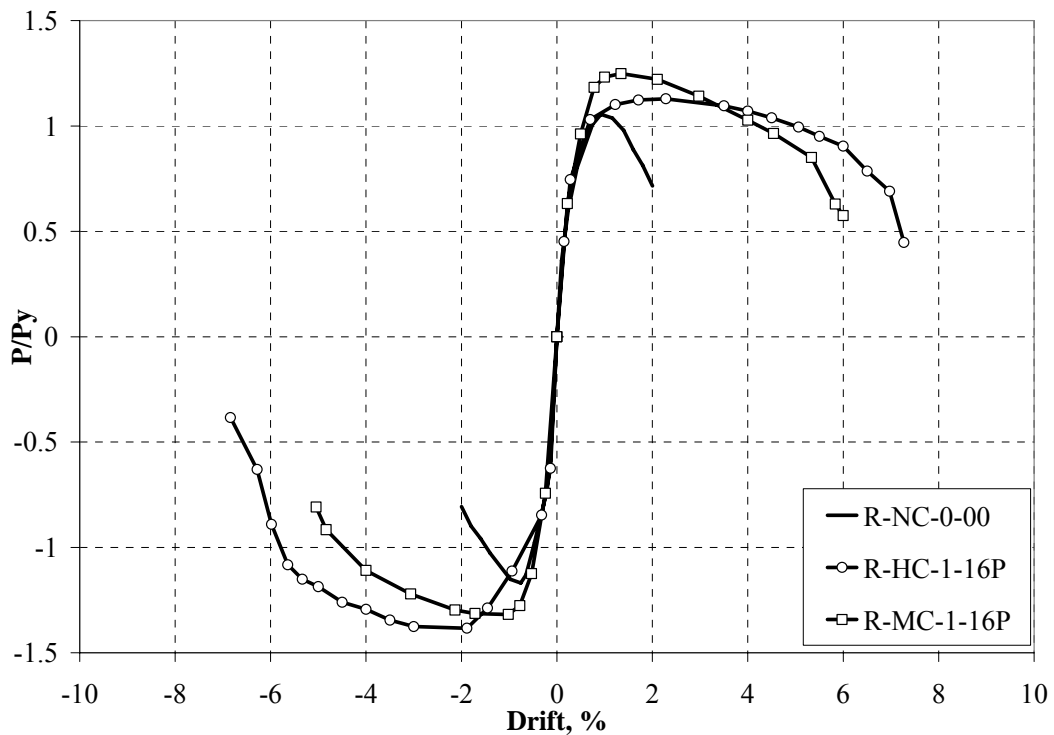


Figure 2.101 Normalized Lateral Load (P/P_y) – Drift comparisons for R-NC-0-00, R-HC-1-16P and R-MC-1-16P

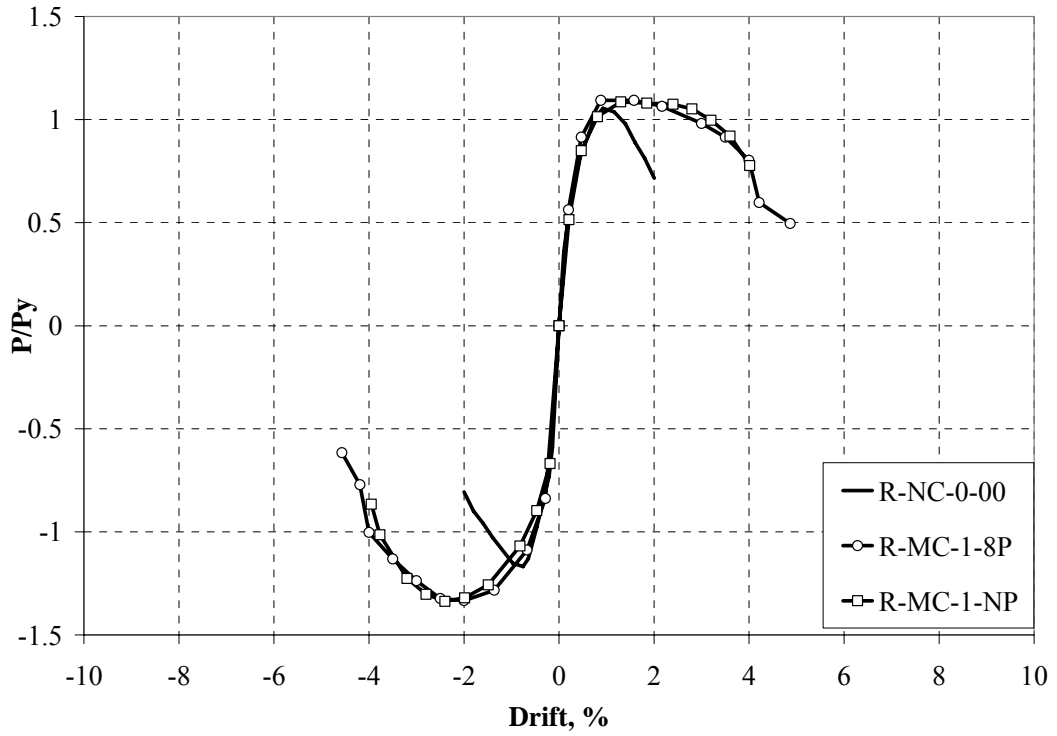


Figure 2.102 Normalized Lateral Load (P/P_y) – Drift comparisons for R-NC-0-00, R-MC-1-8P and R-MC-1-NP

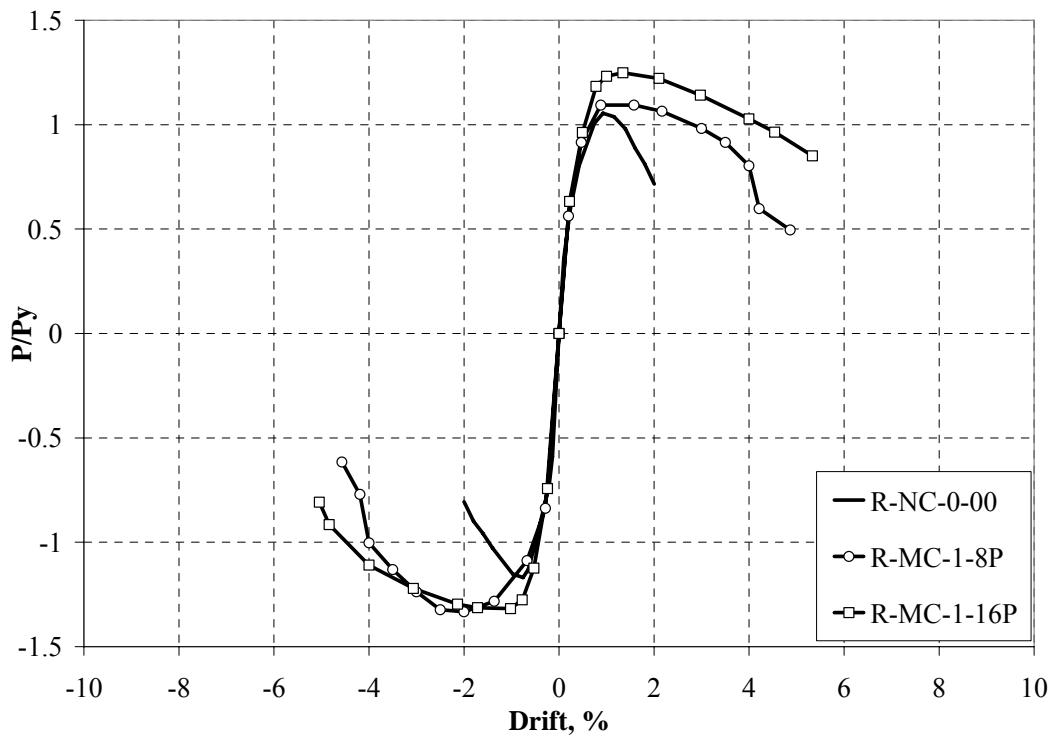
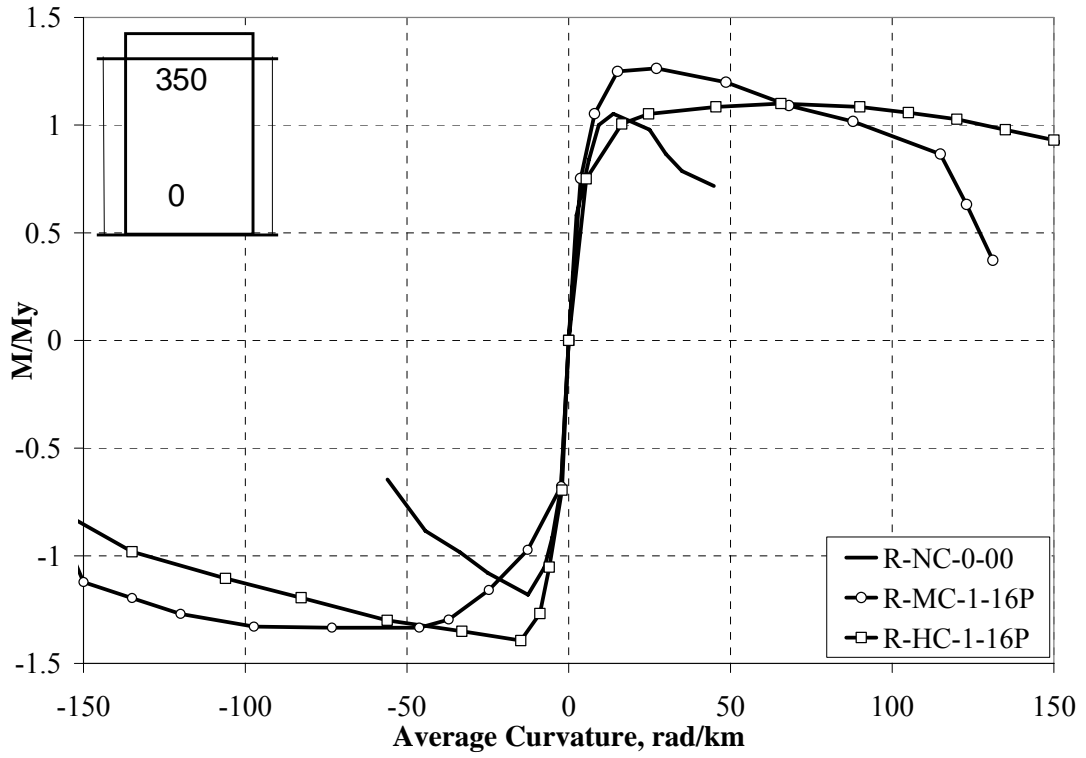
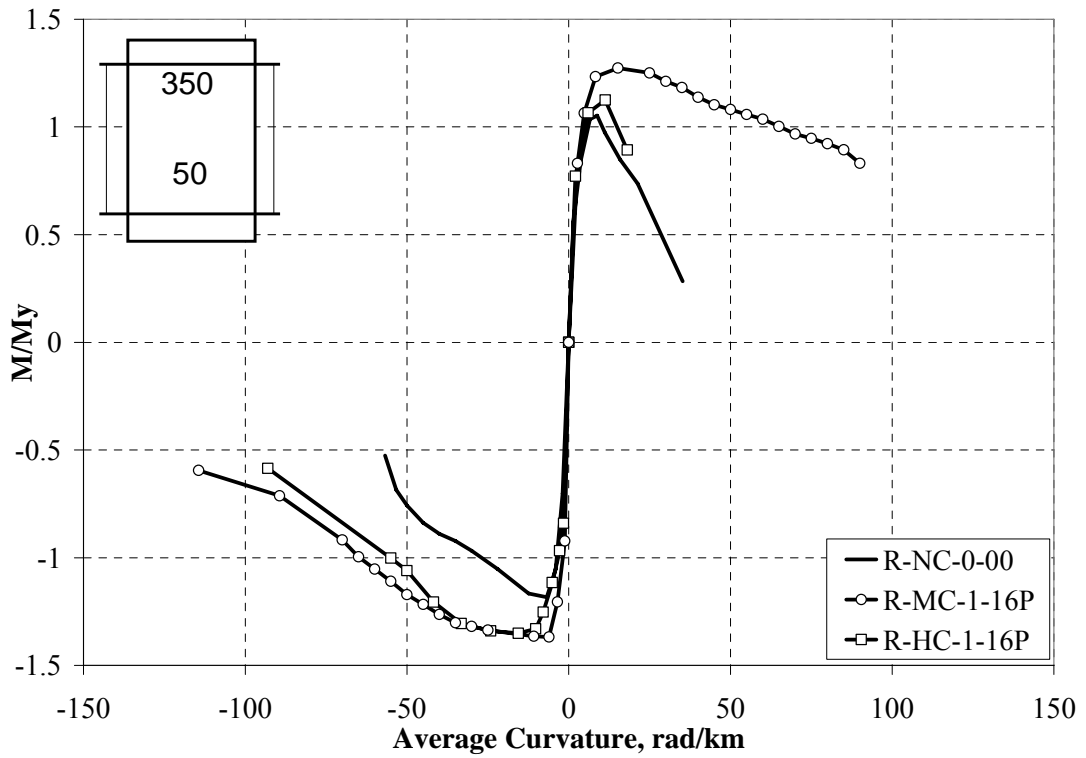


Figure 2.103 Normalized Lateral Load (P/P_y) – Drift comparisons for R-NC-0-00, R-MC-1-8P and R-MC-1-16P

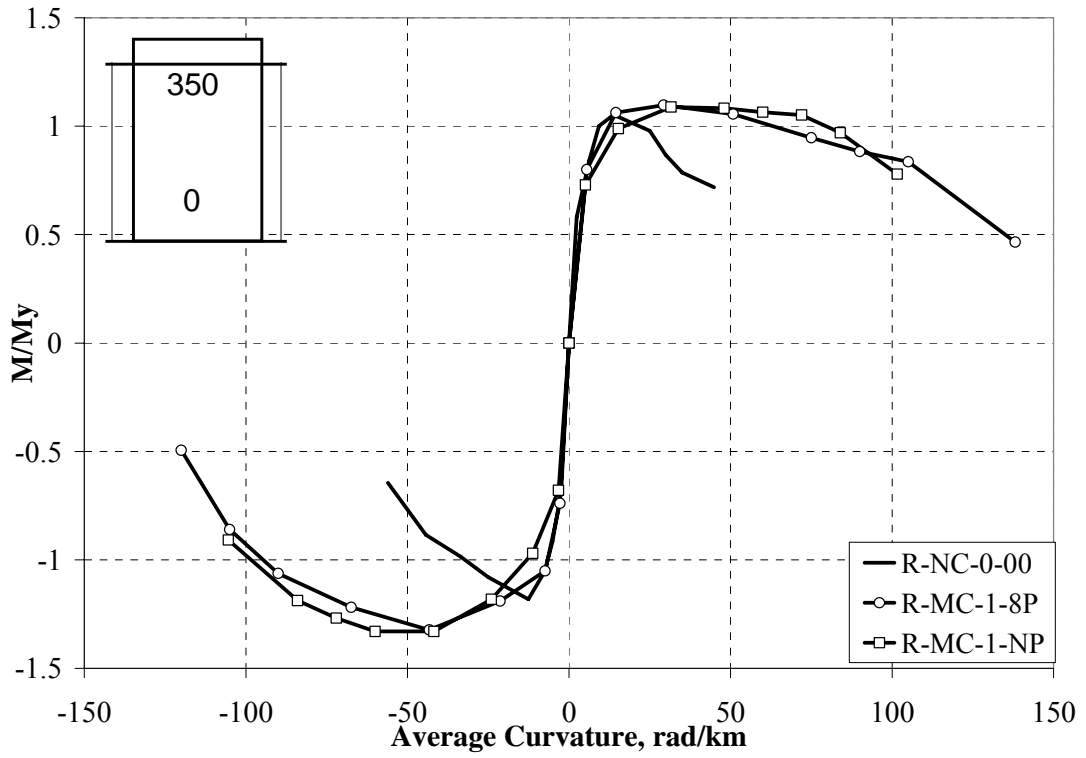


(a)

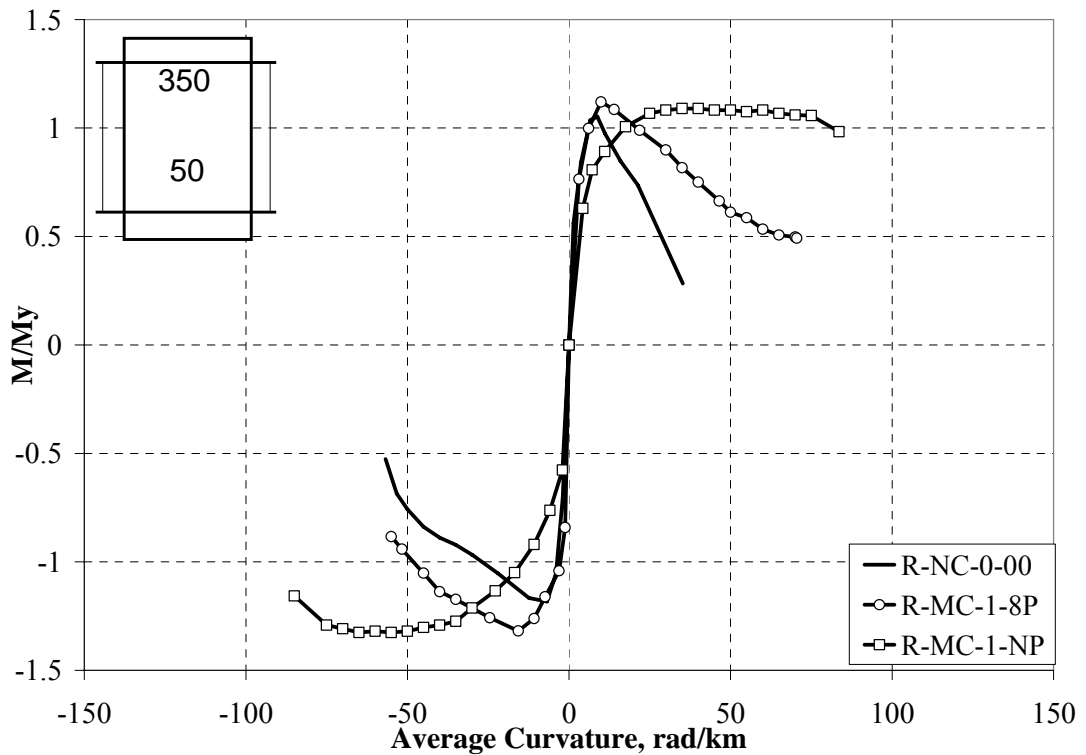


(b)

Figure 2.104 Normalized Moment (M/M_y) – Curvature comparisons for R-NC-0-00, R-HC-1-16P and R-MC-1-16P: at location (a) 350 – 0 and (b) 350 – 50 mm

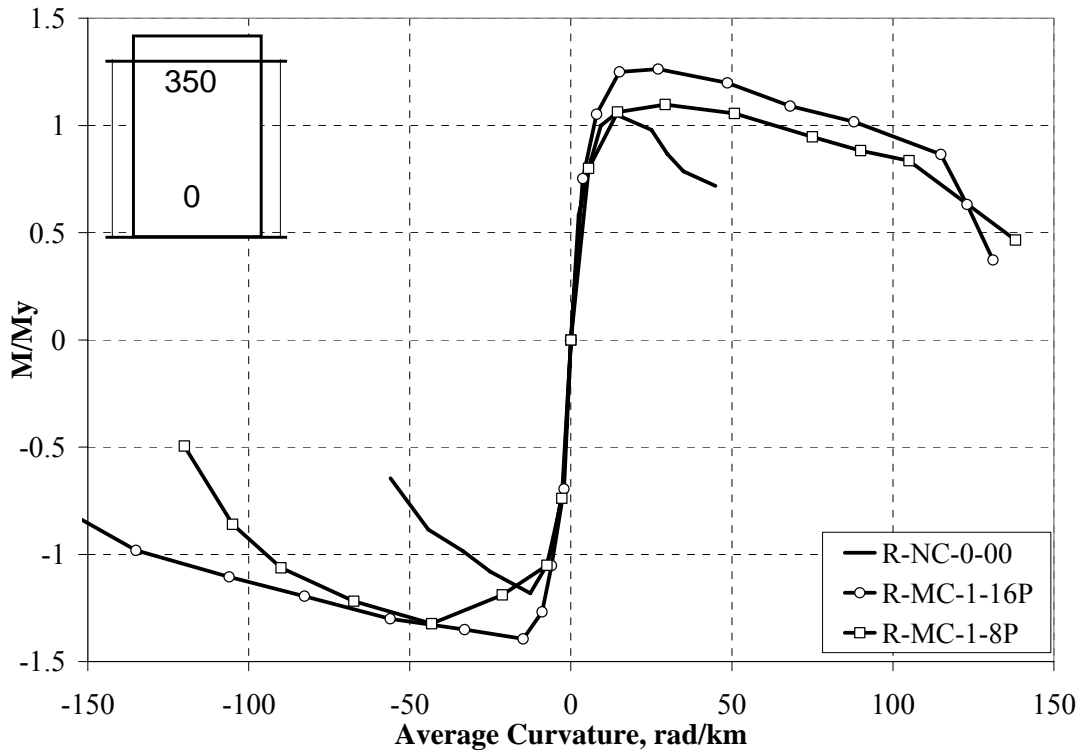


(a)

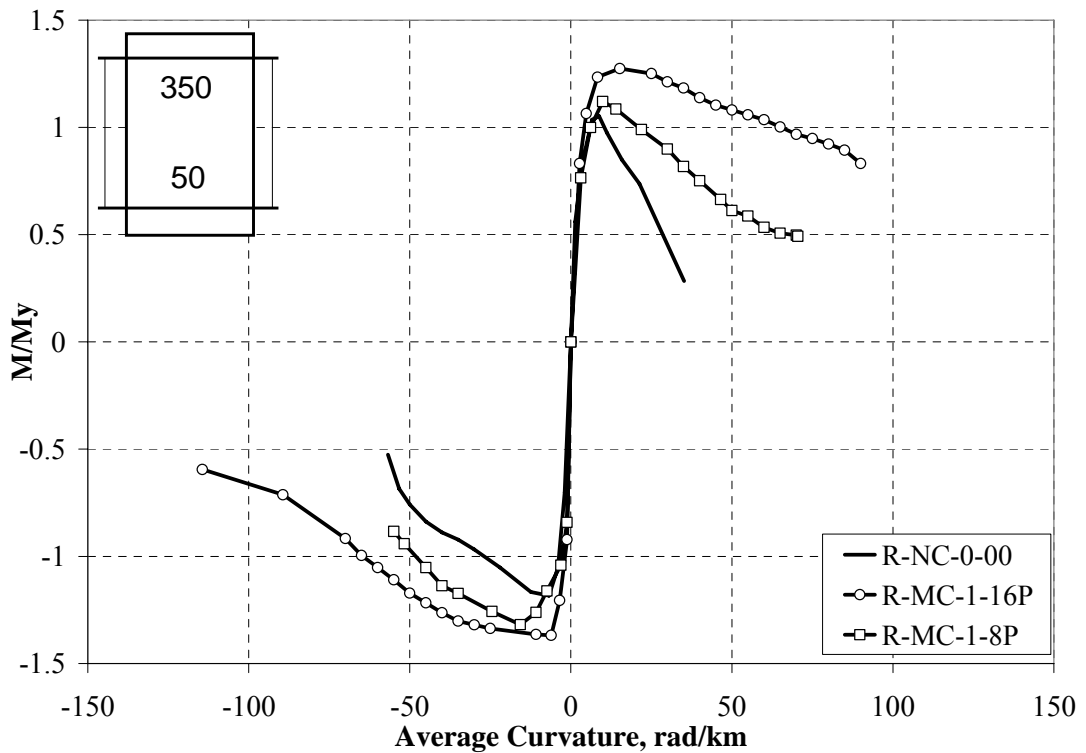


(b)

Figure 2.105 Normalized Moment (M/M_y) – Curvature comparisons for R-NC-0-00, R-MC-1-8P and R-MC-1-NP: at location (a) 350 – 0 and (b) 350 – 50 mm



(a)



(b)

Figure 2.106 Normalized Moment (M/M_y) – Curvature comparisons for R-NC-0-00, R-MC-1-8P and R-MC-1-16P: at location (a) 350 – 0 and (b) 350 – 50 mm

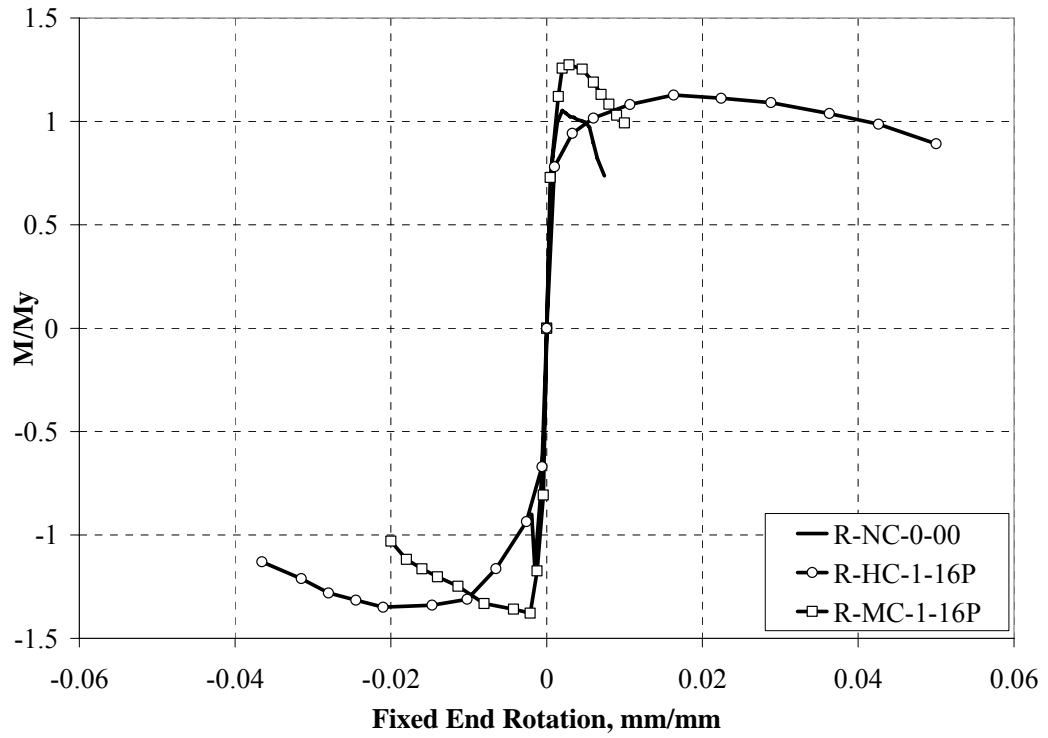


Figure 2.107 Normalized Moment (M/My) – Fixed End Rotation comparisons for R-NC-0-00, R-HC-1-16P and R-MC-1-16P

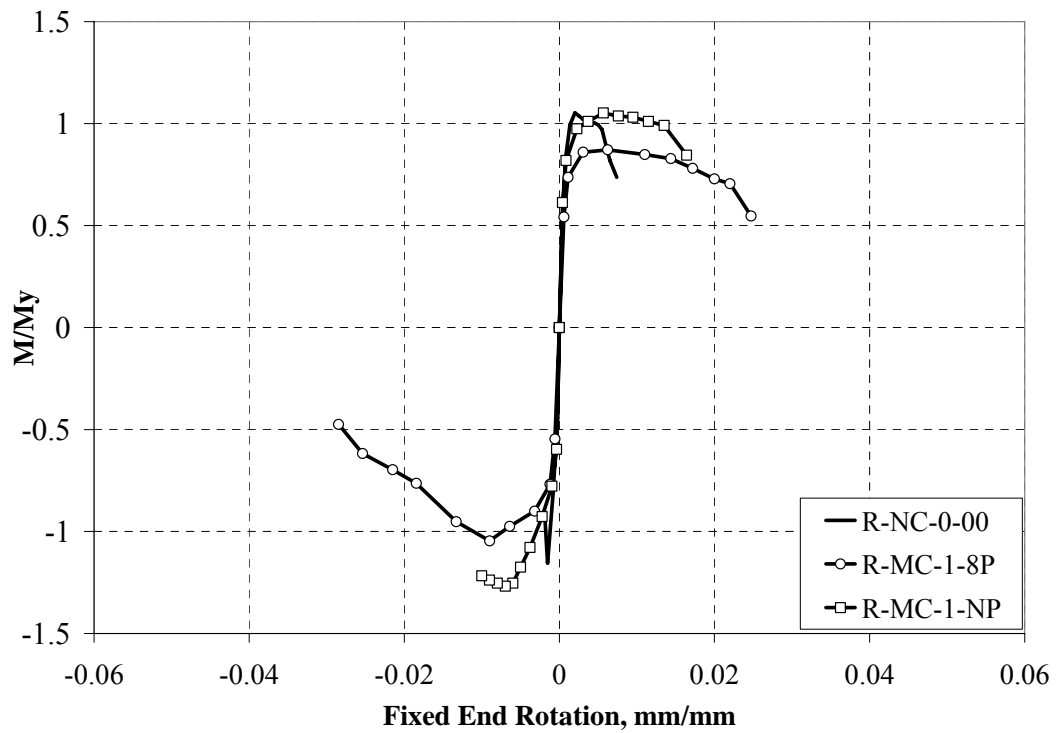


Figure 2.108 Normalized Moment (M/My) – Fixed End Rotation comparisons for R-NC-0-00, R-MC-1-8P and R-MC-1-NP

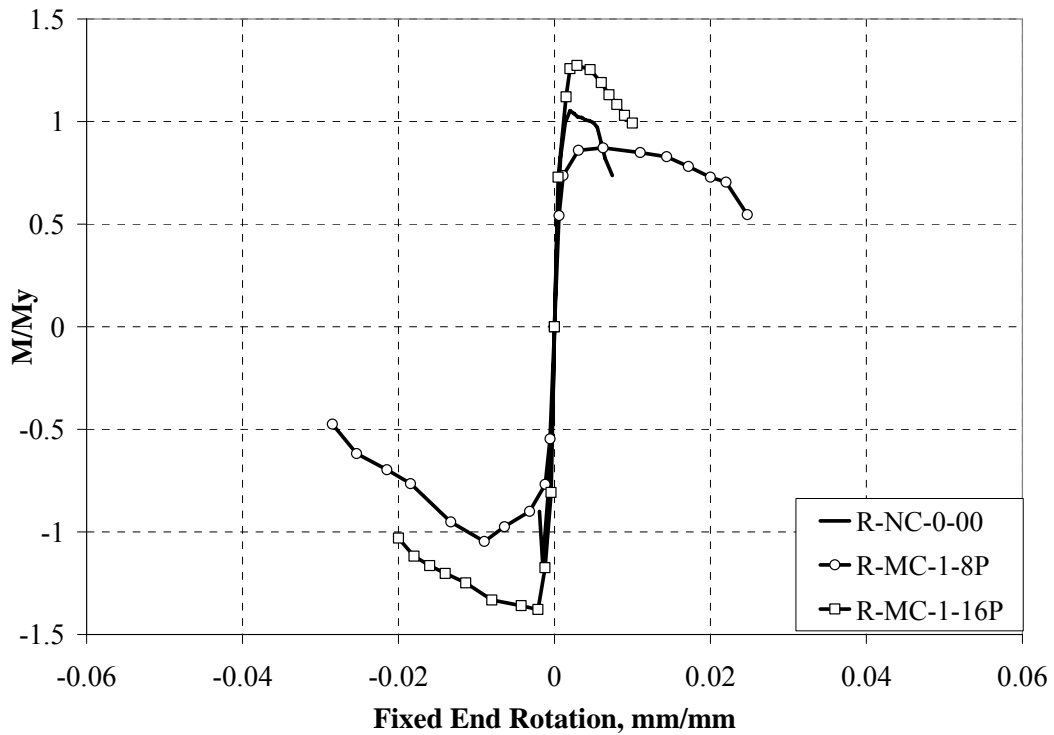


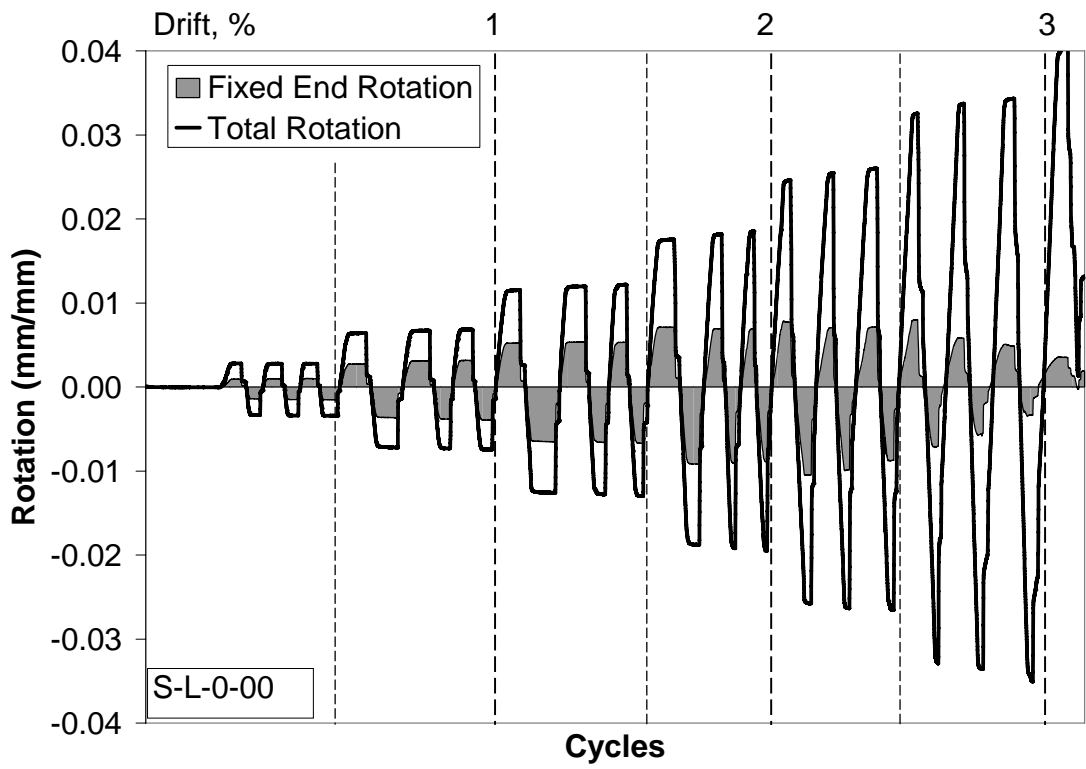
Figure 2.109 Normalized Moment (M/My) – Fixed End Rotation comparisons for R-NC-0-00, R-MC-1-8P and R-MC-1-16P

2.7.2. Rotation and Deflection Components

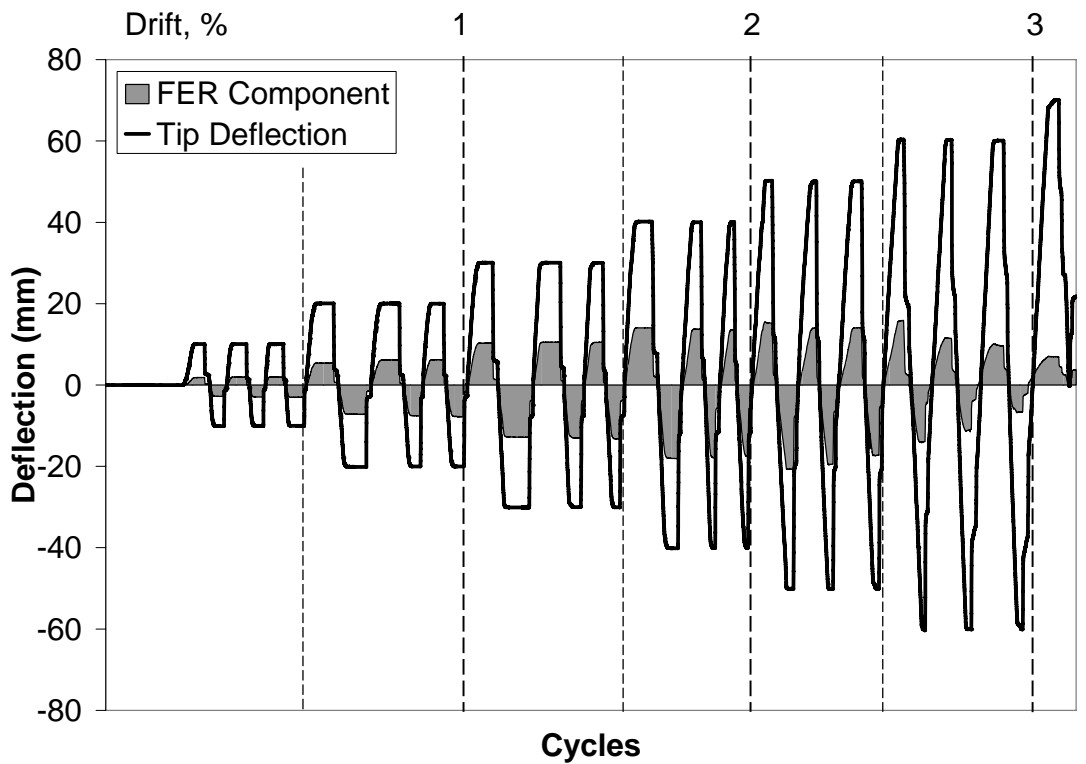
The fixed-end and flexural rotation components were evaluated concerning the recorded data in the plastic hinging region of the column. The relative dial gage readings that were recorded between 350 to 50 mm height from the column base were used to obtain flexural rotations and average curvatures in the test region. The difference between the readings relative to column base and 50 mm over the base was attributed as fixed-end rotation components. Since the dial gages could be placed at most 50 mm close to the column base, the exact curvature at the base of the column could not be determined accurately since the current instrumentation could not record any data closer than 50 mm to the column base. However, it can be stated that the average curvatures in 50 mm cannot be lower than the average curvatures in the testing region. Thus, the average curvatures monitored in 50 mm were multiplied by the distance of 50 mm to acquire the average rotation of this section. Accordingly, this rotation was added to the flexural rotation and subtracted from the fixed-end

rotation components in the plastic hinging region. This correction was essential to acquire the rotation or deflection components at relatively higher drift levels. In order to obtain deflection components, fixed-end rotations were multiplied by the column height since the column was assumed to rotate rigidly from the base by the slip and extension of the longitudinal rebars. The remaining component of the deflection was considered as flexural displacement that was the result of the integrated curvature distribution over the column height while the shear deformations were neglected in all the test series.

For Series 1, while the reference specimen S-L-0-00 had fixed-end rotation (FER) components that were about 40% of the total rotations (Figure 2.110), wrapping 1 and 2 layers of CFRP increased the FER components to levels of about 60 (Figures 2.111 and 2.112) and 80% (Figures 2.113 and 2.114), respectively. Herein, the confining effect of CFRP layers prevented premature buckling of the longitudinal rebars and thus, the column could withstand larger drift levels. Increasing the number of CFRP layers from 1 to 2, improved the confinement level and led to higher levels of ultimate drift. For the reference specimen, the further cycles beyond ultimate drift ratios, led to a decrease in fixed-end rotations since the longitudinal reinforcement started to buckle and due to opening of the cracks further increased the flexural rotations in the plastic hinging region of the column. For the strengthened columns, this decrease in fixed-end rotations was monitored at further cycles than the reference column since the ultimate drift ratios were improved by means of enhanced confinement levels due to FRP wrapping. As presented in Figures 2.111 and 2.114, baseline shifting of the fixed-end rotations was monitored since the cracks formed in the testing region affected the monitored data and led to unsymmetrical results with regard to the zero-axis. Besides, the presence of axial load about 35% of axial capacity during strengthening was observed to have an insignificant effect on FER responses for rotation and deflection components. Figures 2.112 and 2.114 clarify these observations.

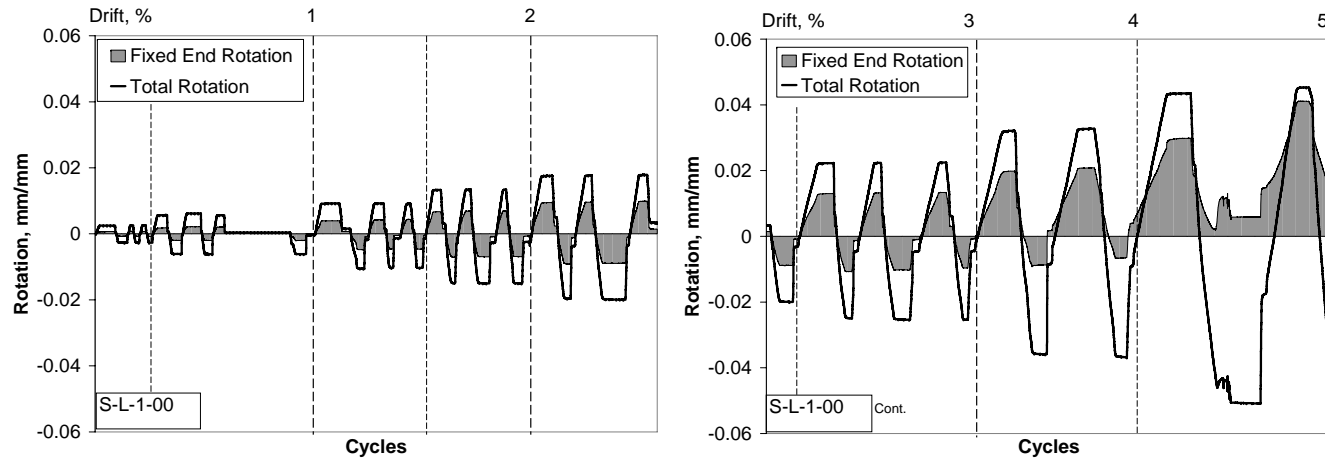


(a)

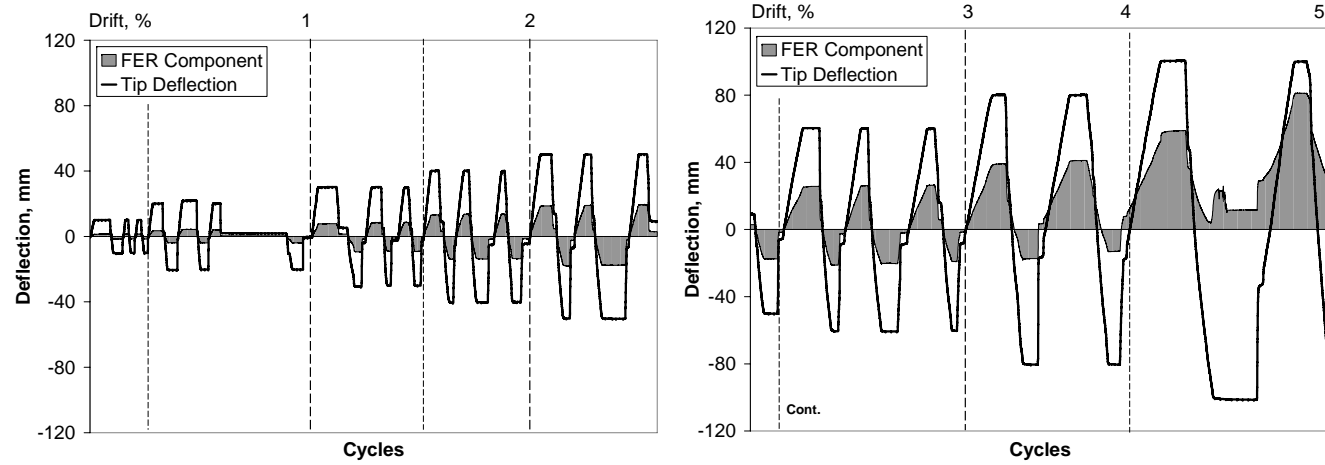


(b)

Figure 2.110 (a) Rotation and (b) Deflection Components for S-L-0-00



(a)



(b)

Figure 2.111 (a) Rotation and (b) Deflection Components for S-L-1-00

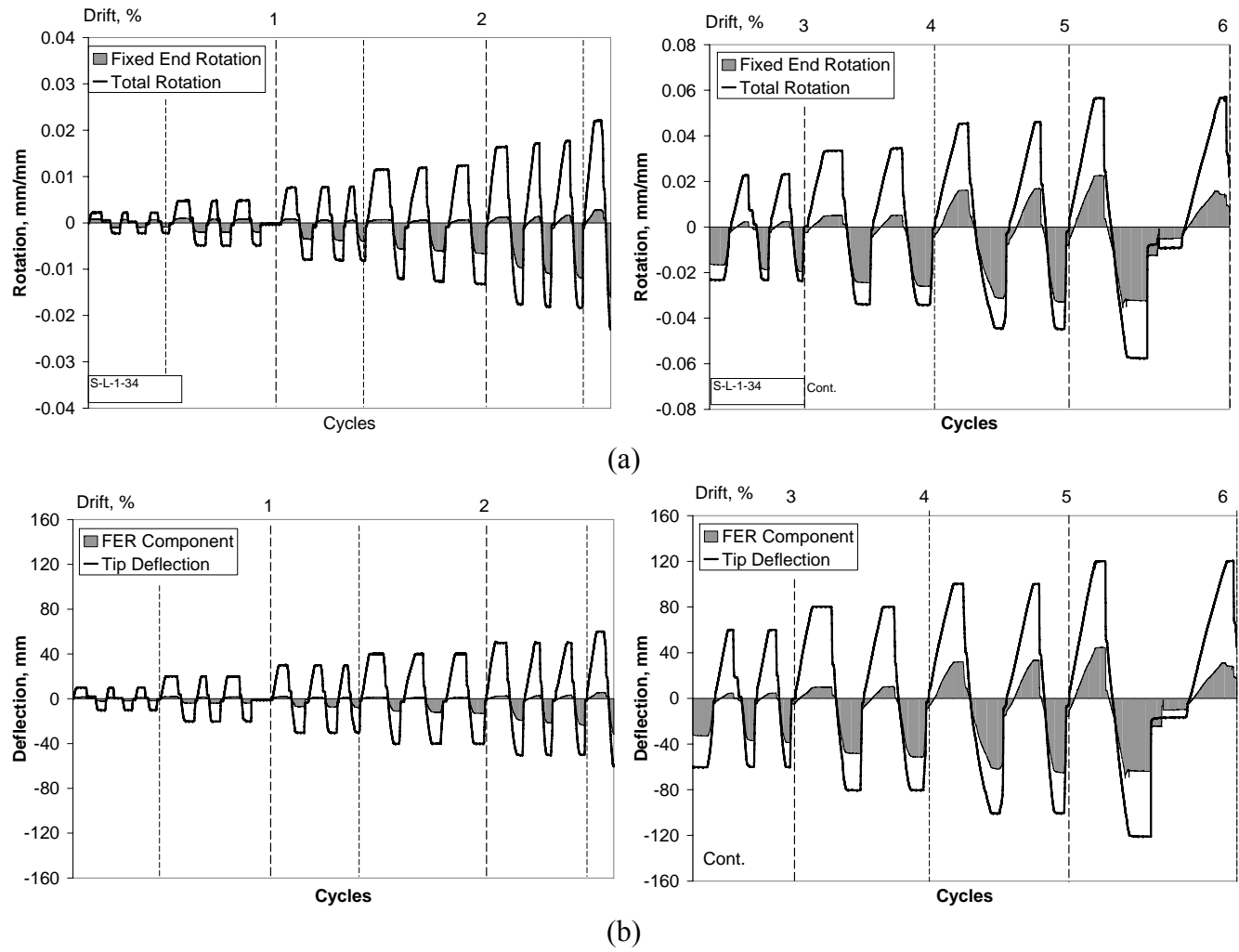
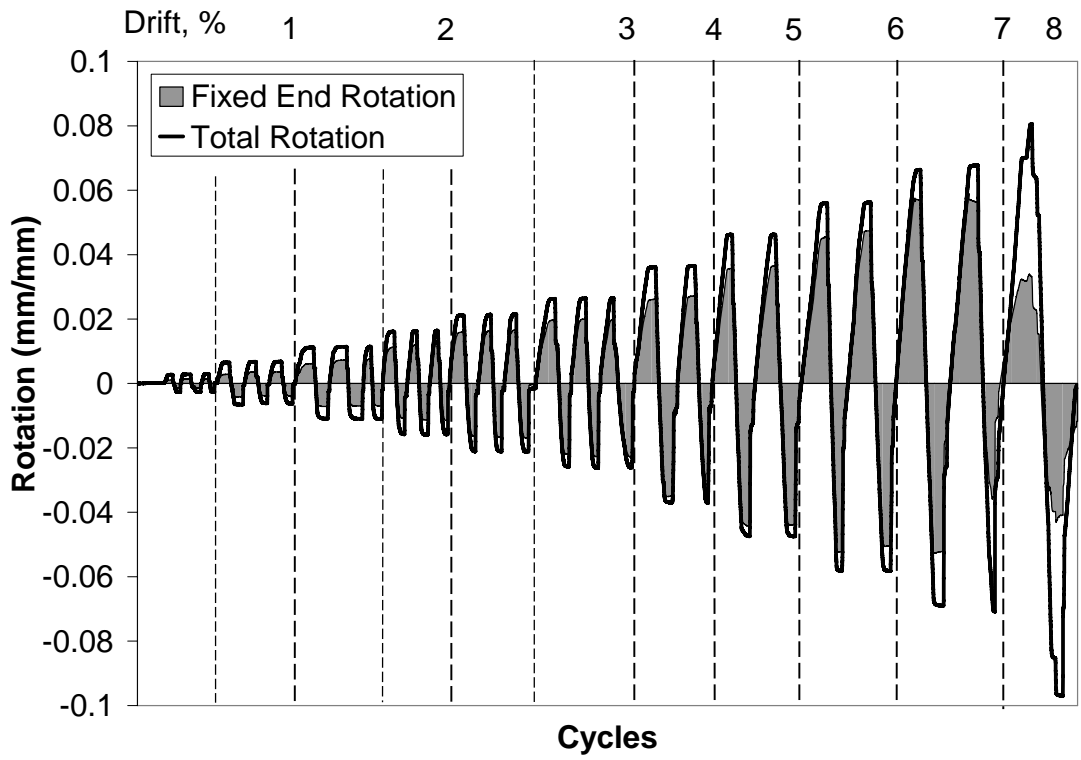
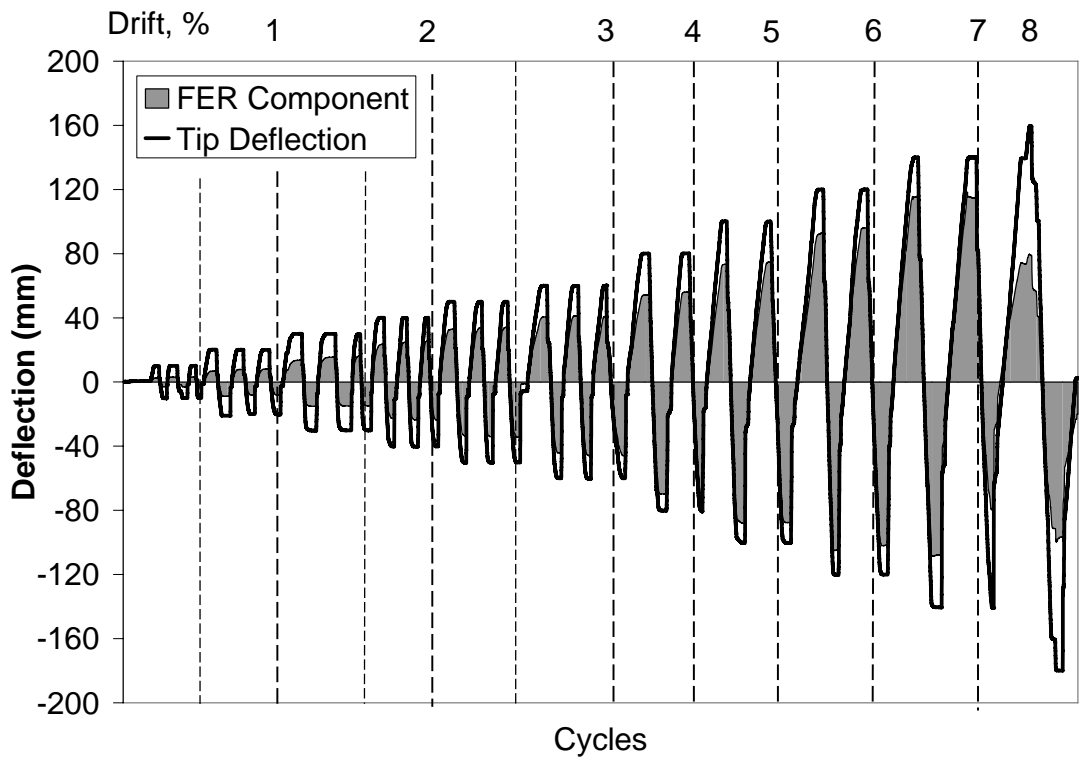


Figure 2.112 (a) Rotation and (b) Deflection Components for S-L-1-34

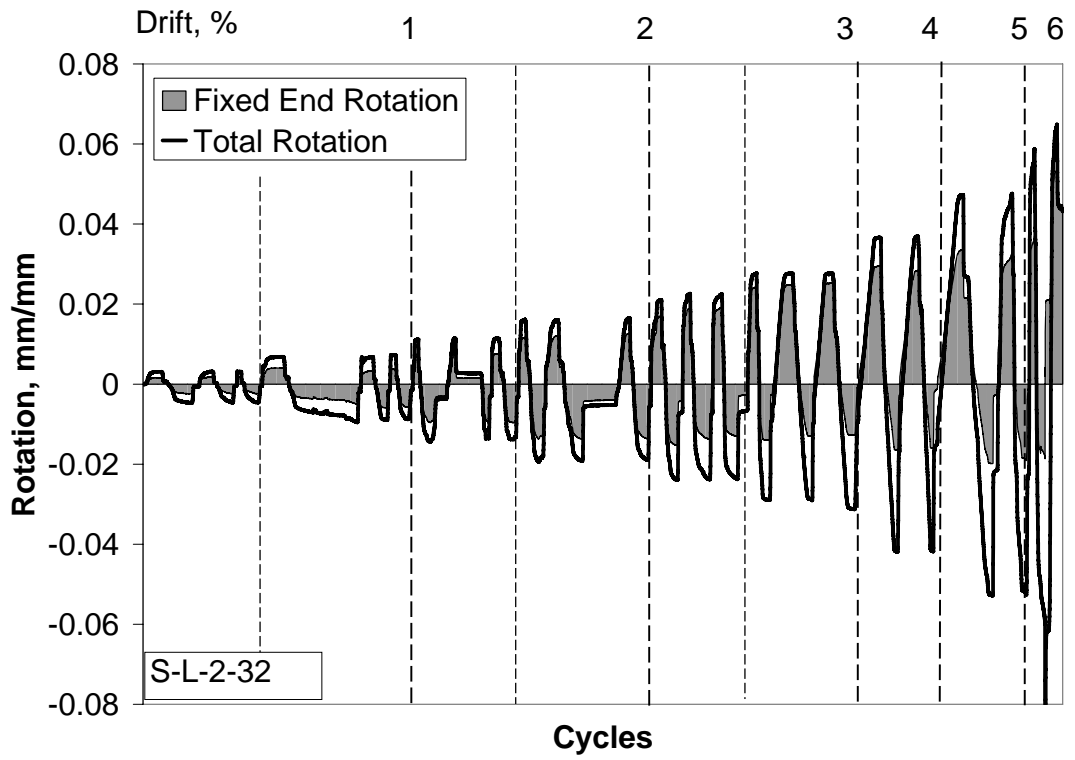


(a)

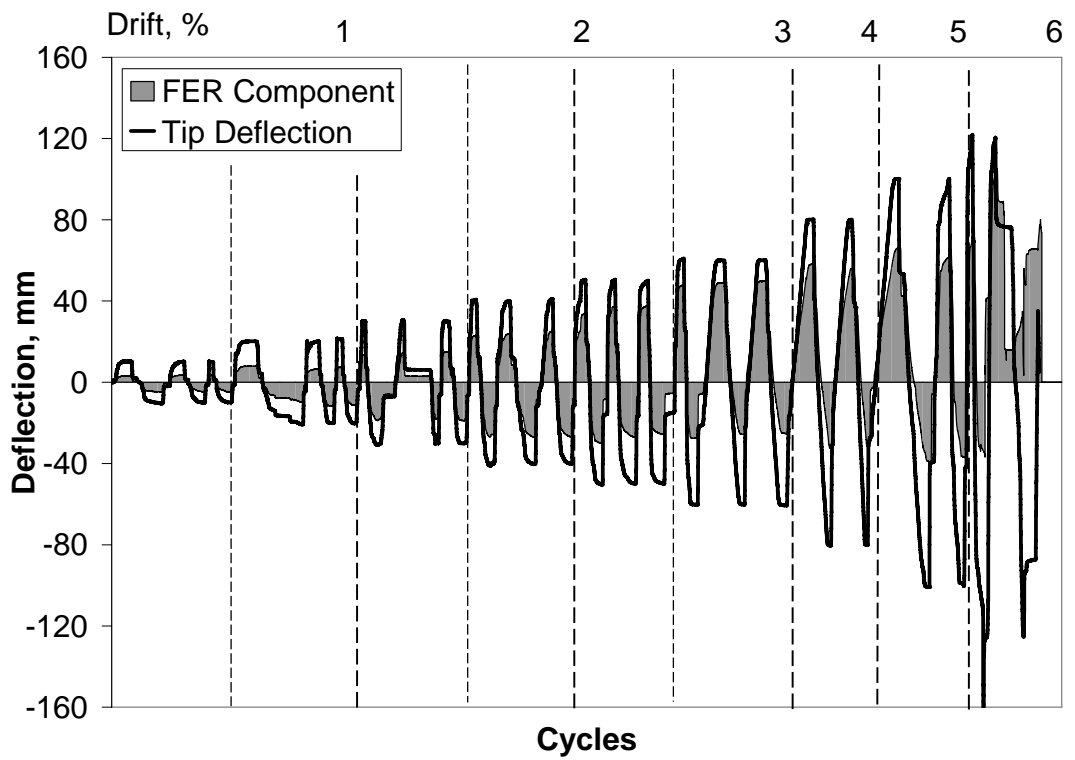


(b)

Figure 2.113 (a) Rotation and (b) Deflection Components for S-L-2-00



(a)

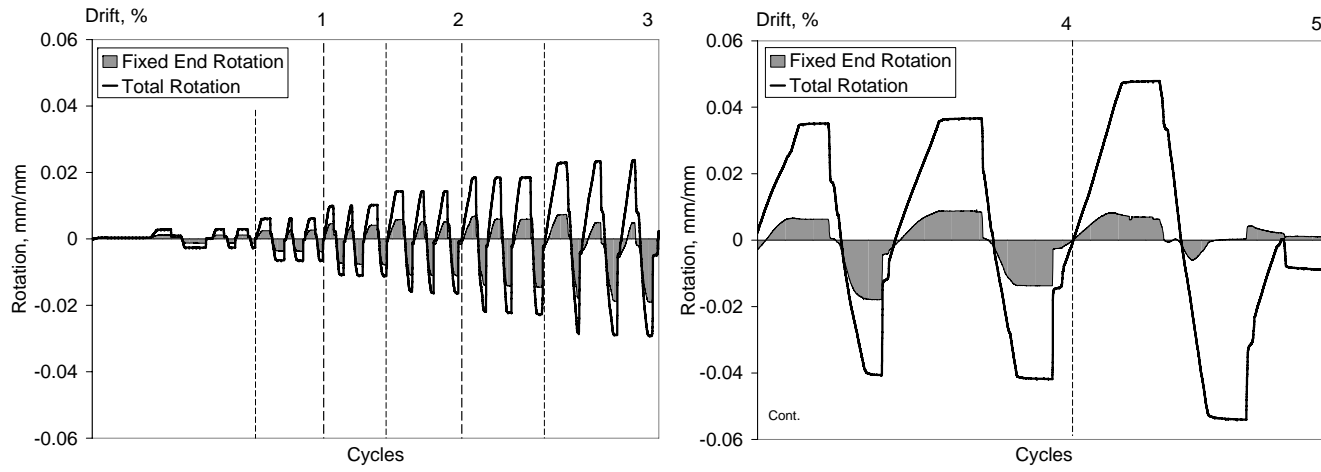


(b)

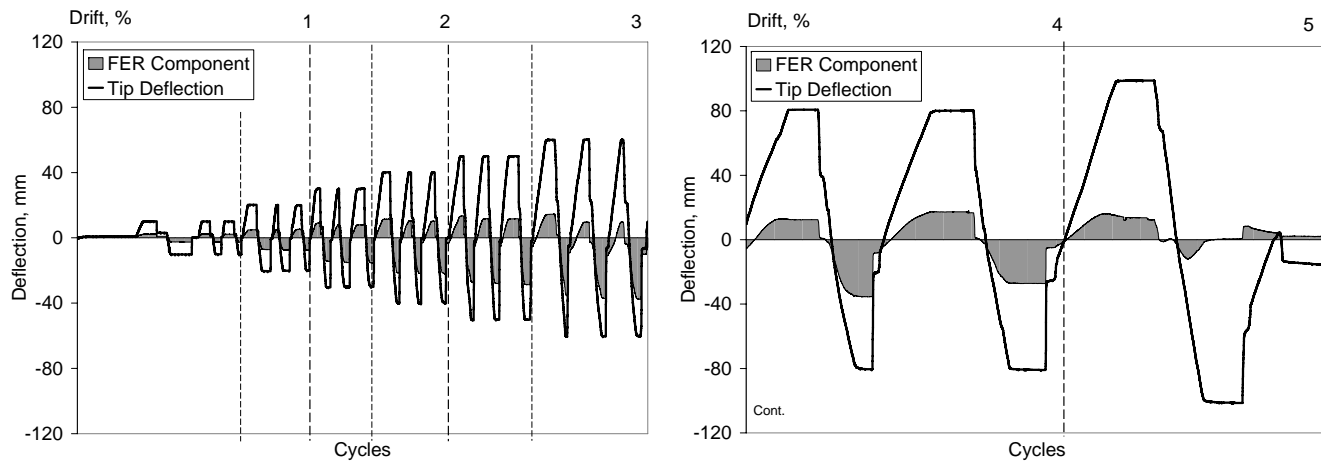
Figure 2.114 (a) Rotation and (b) Deflection Components for S-L-2-32

The same effects of CFRP confinement were also monitored in Series 2 columns. For the reference specimen S-H-0-00, the contribution of FER to total rotation and tip deflection was about 40% as illustrated in Figure 2.115. The FER contribution for strengthened columns S-H-1-00 and S-HC-1-00 were approximately 80% of the total rotation and deflection whereas only 60% of FER contribution was observed in the repaired specimens S-HD-1-00 and S-HD-1-27 (Figures 2.116-2.121). The increase in FER components up to levels of 80% can be interpreted due to the increase in the bar diameter and consequently in the slipping surface throughout the embedment length. For the repaired specimens, the increase in FER components were relatively lower than the strengthened columns, since the moderate damage level on the specimens made the longitudinal reinforcement persist the same level of slip and extension as in the damaged condition without CFRP wrapping. The FER components were able to augment to the levels of 60% for both cases of repairing under the presence or absence of the axial load (Figures 2.118 and 2.120).

The specimens in the last series exhibited a proportional increase in FER components with the confinement level. The reference specimen R-NC-0-00 had FER components up to 40% of the total rotations and tip deflections (Figure 2.122). However, using moderate level of confinement by 16, 8 and no-pinned CFRP anchor dowels, the FER contribution increased to up to 60% as shown in Figures 2.123-2.125. Using high confinement level by 16-pinned CFRP anchor dowel configuration having relatively low concrete compressive strength made the column sustain about 80% of FER components by the help of the increase in confining level and the prevention of premature longitudinal bar buckling as shown in Figure 2.126. The confining effect of CFRP can be seen in the specimens of Series 3 by increasing the FER contribution for the total rotation and tip deflection responses.

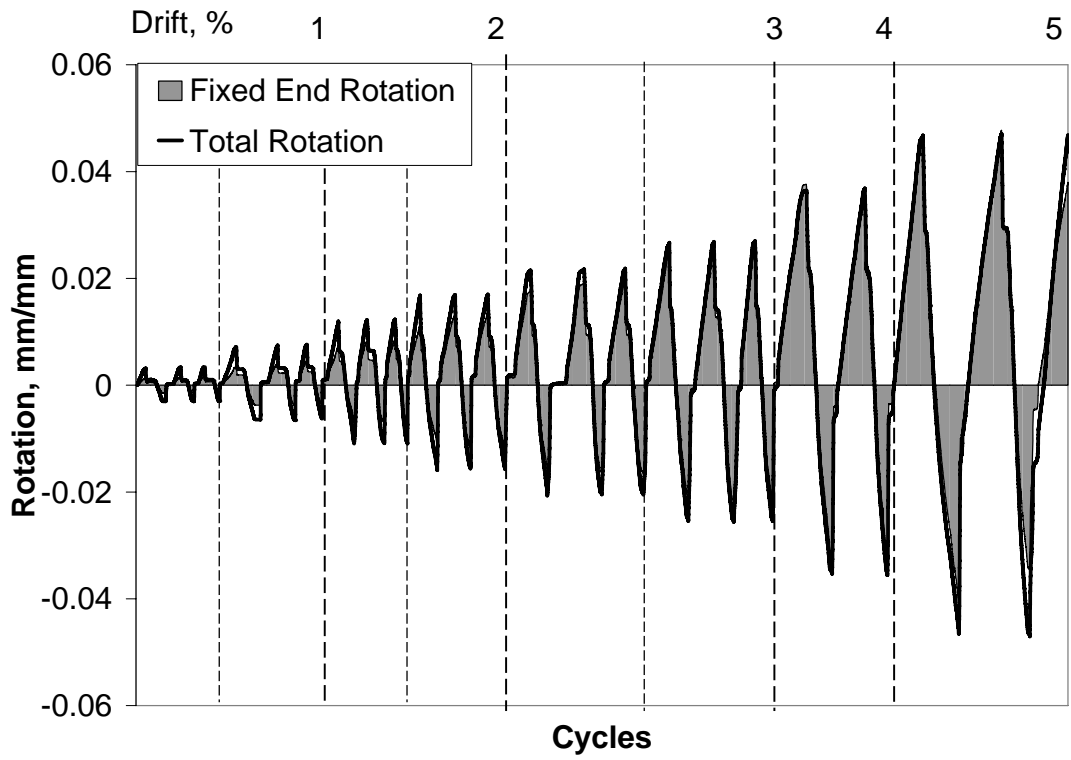


(a)

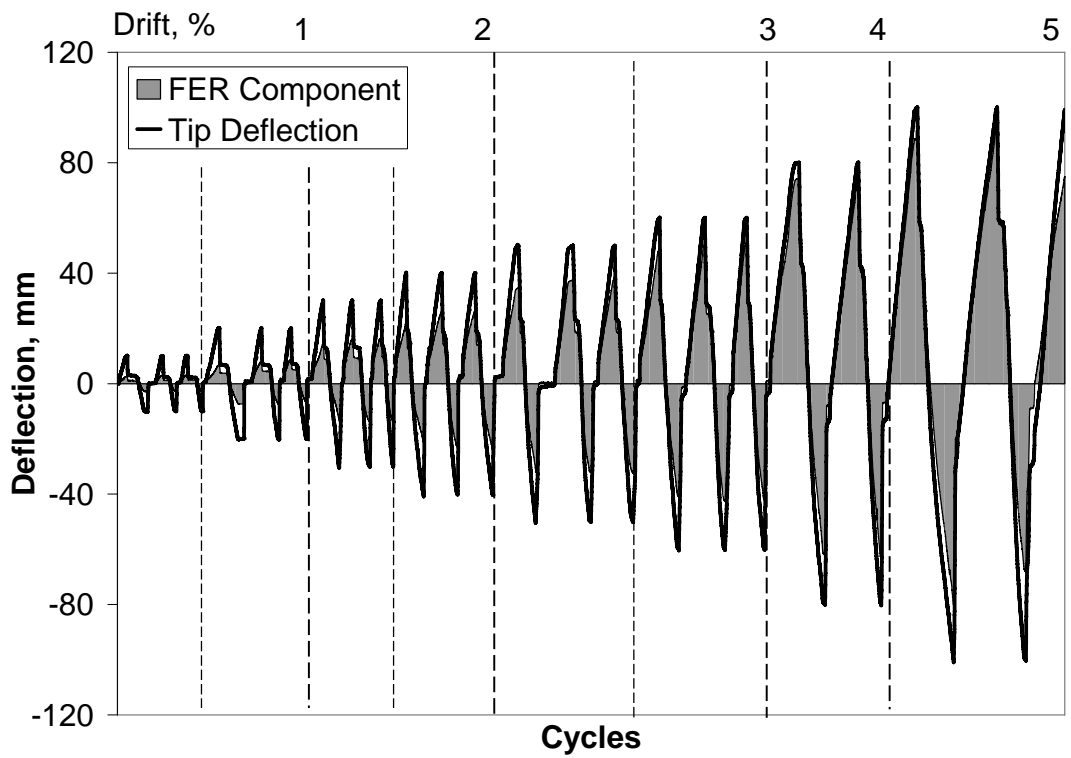


(b)

Figure 2.115 (a) Rotation and (b) Deflection Components for S-H-0-00

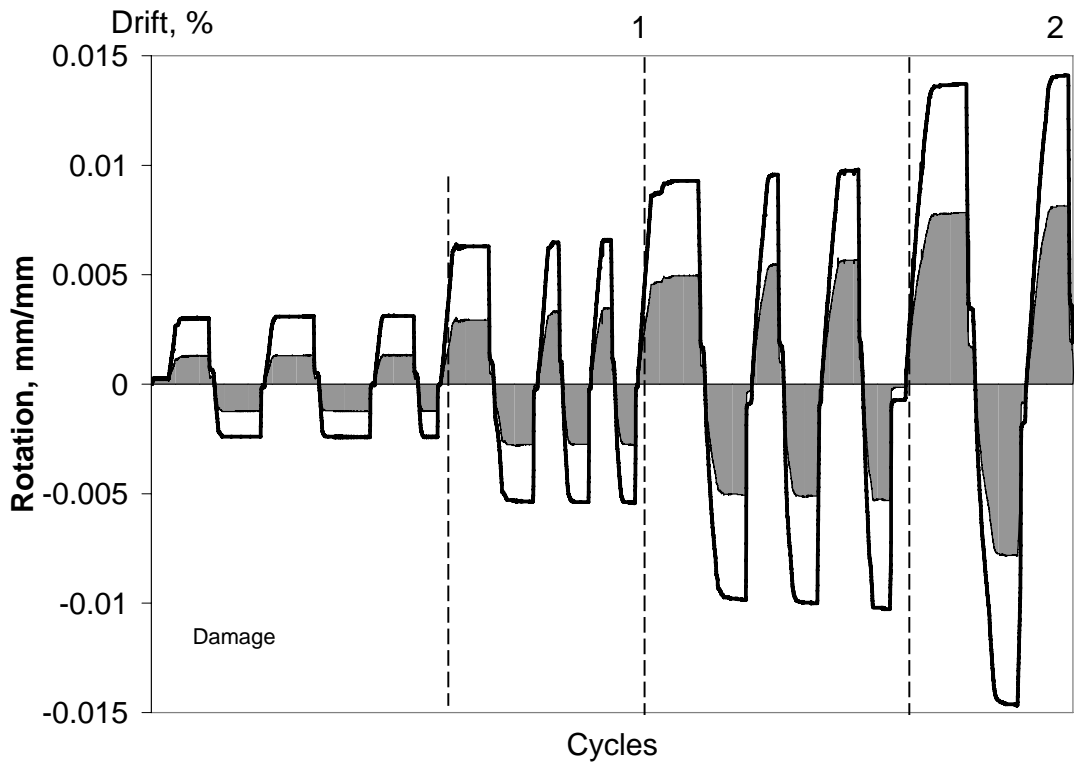


(a)

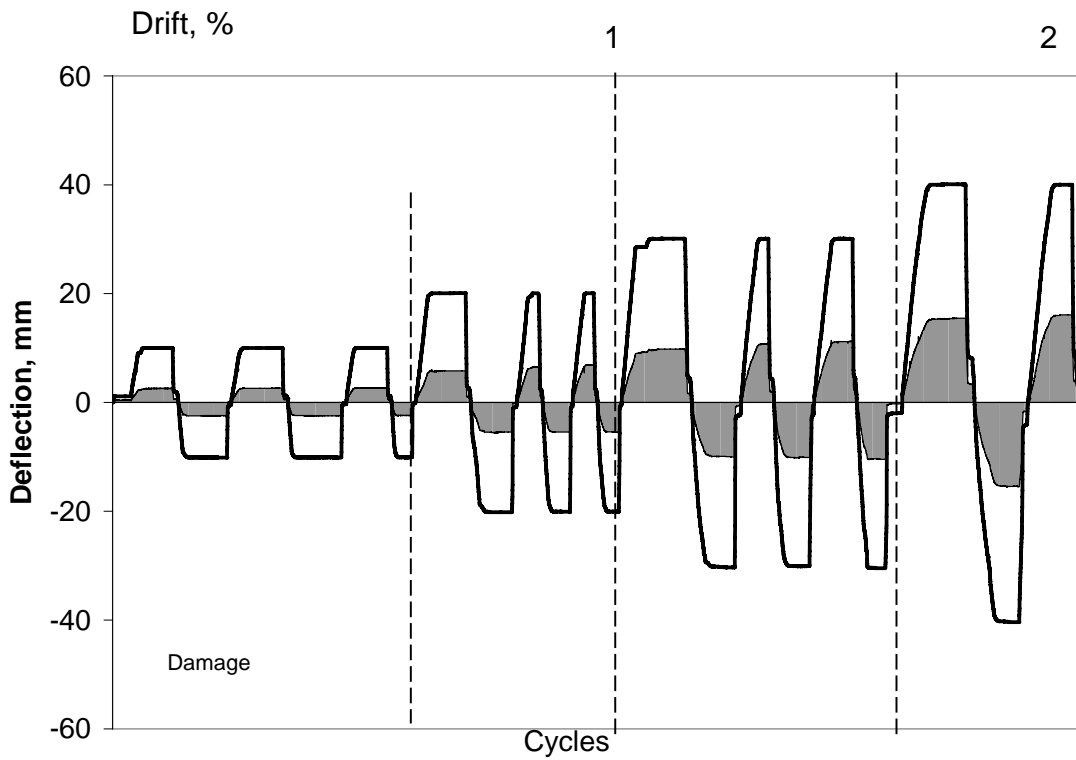


(b)

Figure 2.116 (a) Rotation and (b) Deflection Components for S-H-1-00

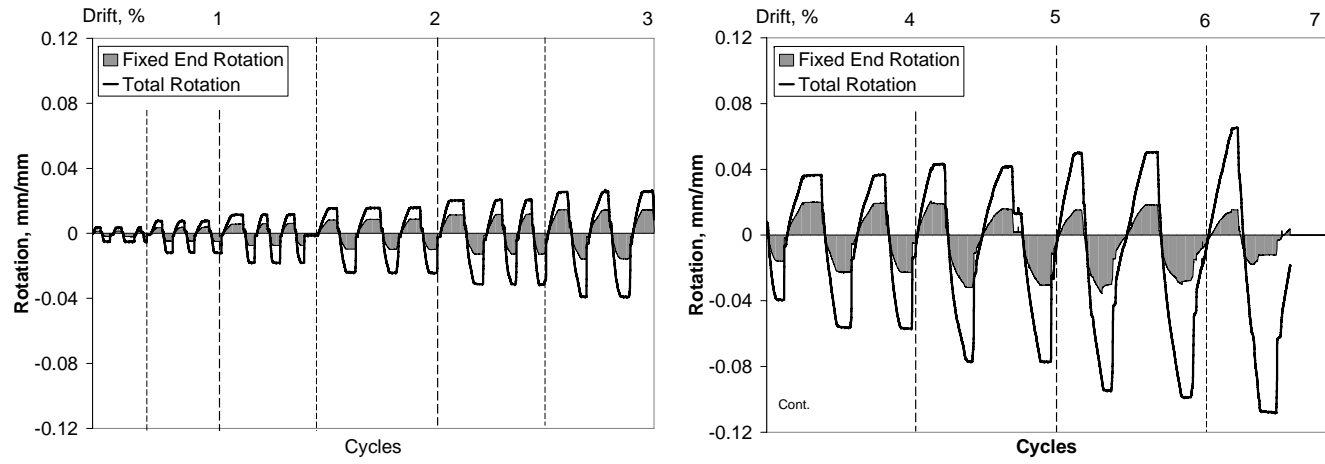


(a)

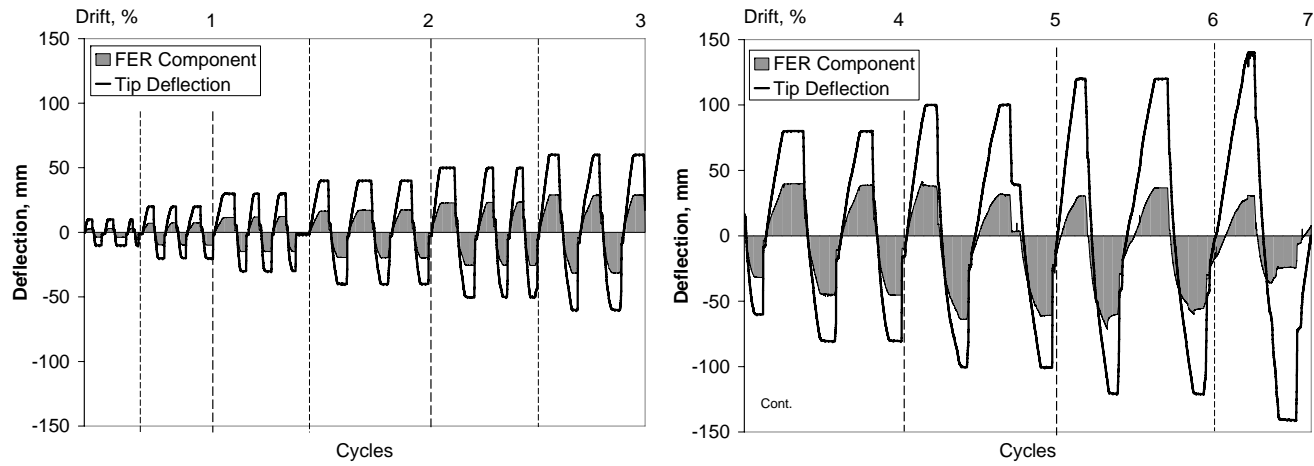


(b)

Figure 2.117 (a) Rotation and (b) Deflection Components for S-HD-1-00 (damage)

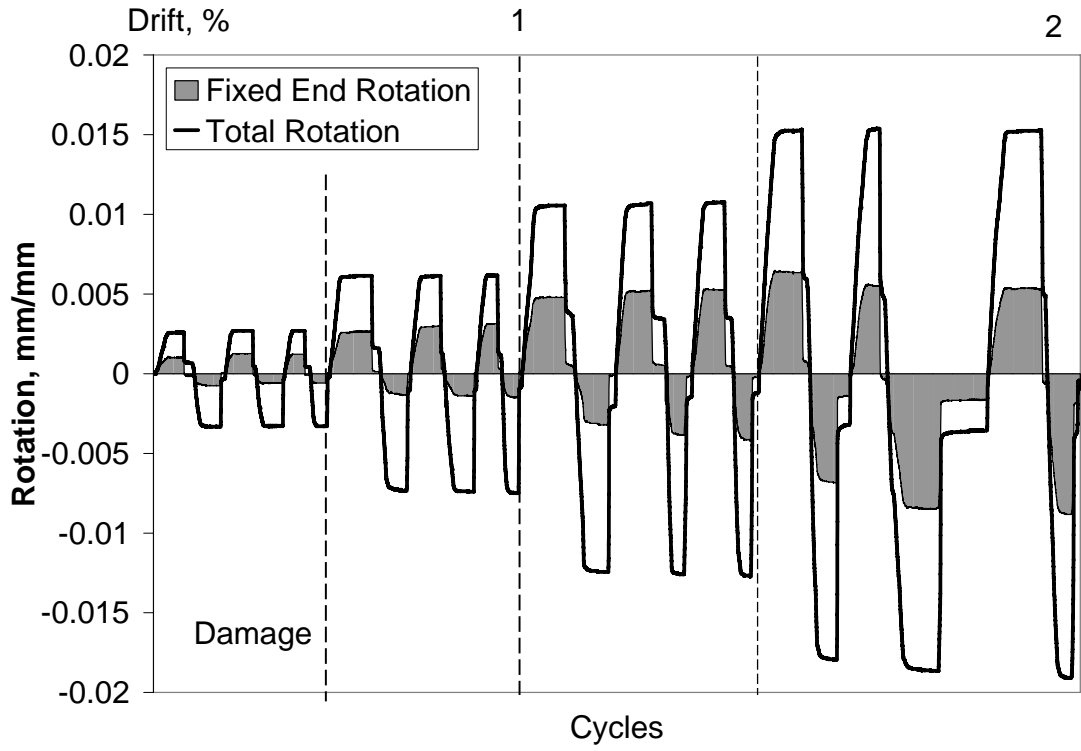


(a)

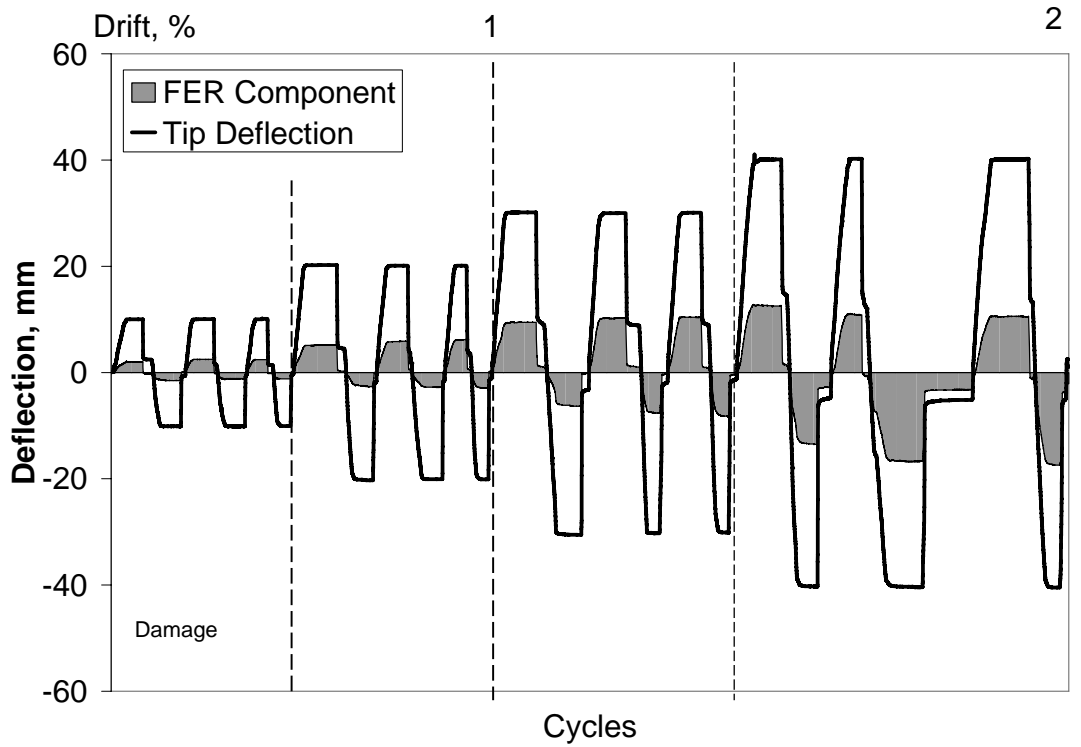


(b)

Figure 2.118 (a) Rotation and (b) Deflection Components for S-HD-1-00

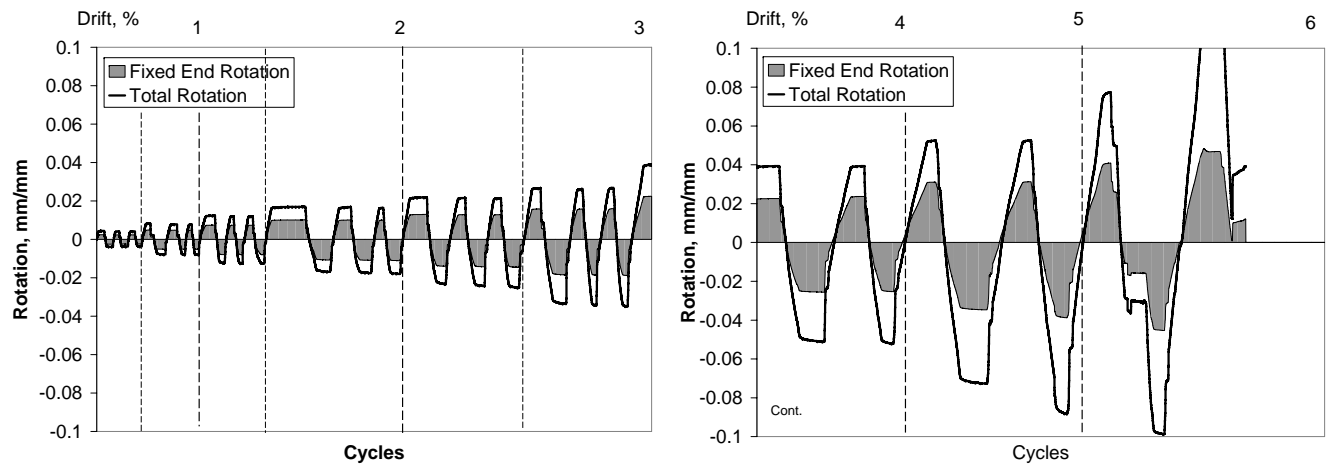


(a)

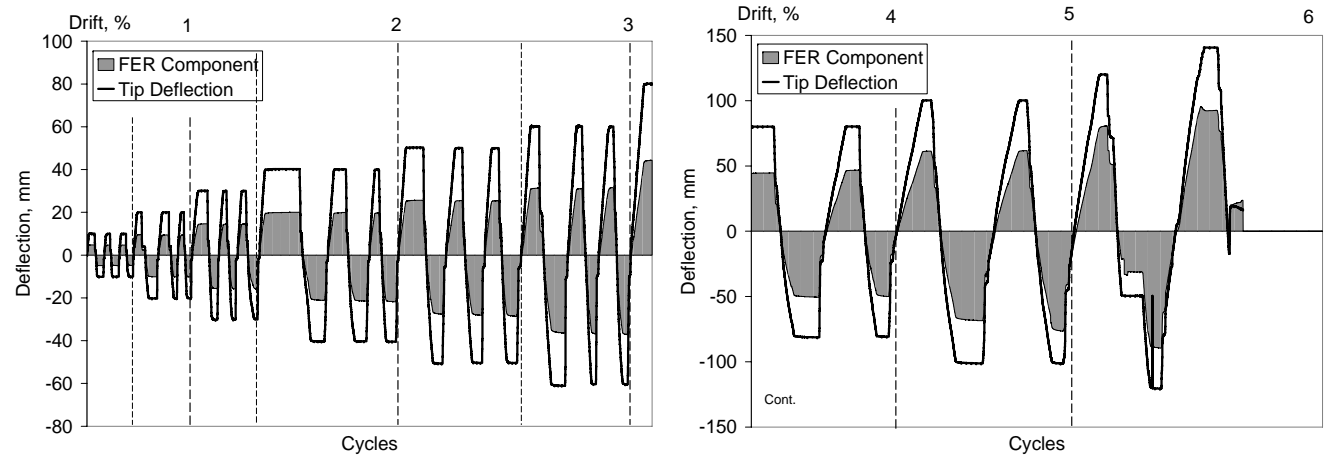


(b)

Figure 2.119 (a) Rotation and (b) Deflection Components for S-HD-1-27 (damage)

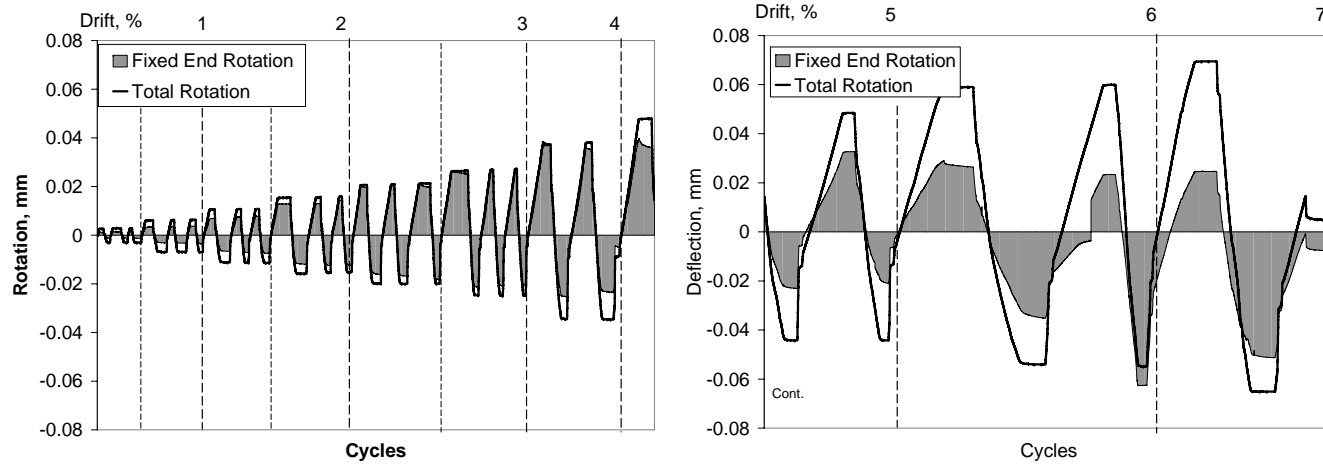


(a)

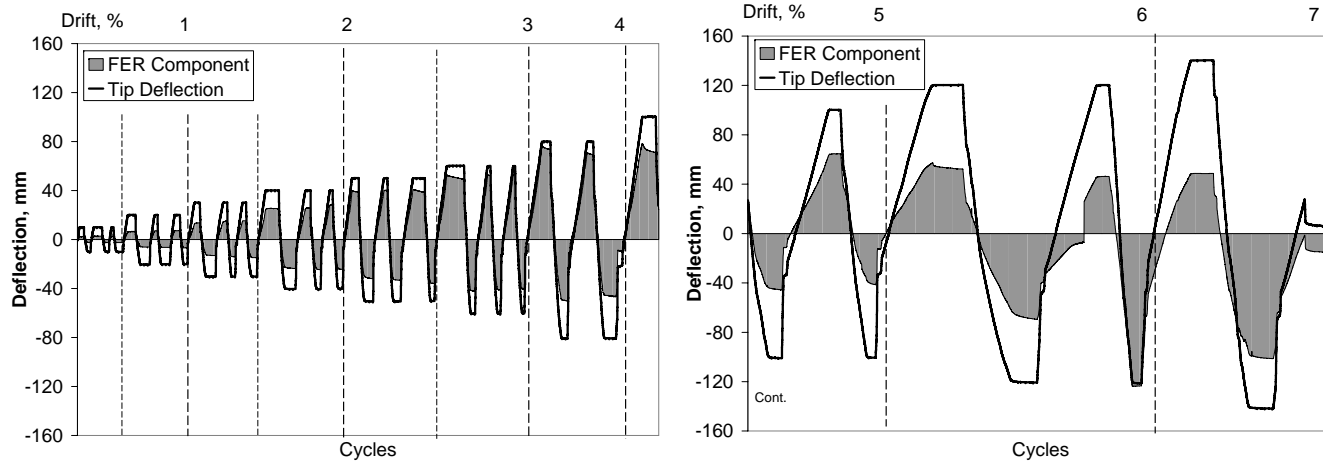


(b)

Figure 2.120 (a) Rotation and (b) Deflection Components for S-HD-1-27

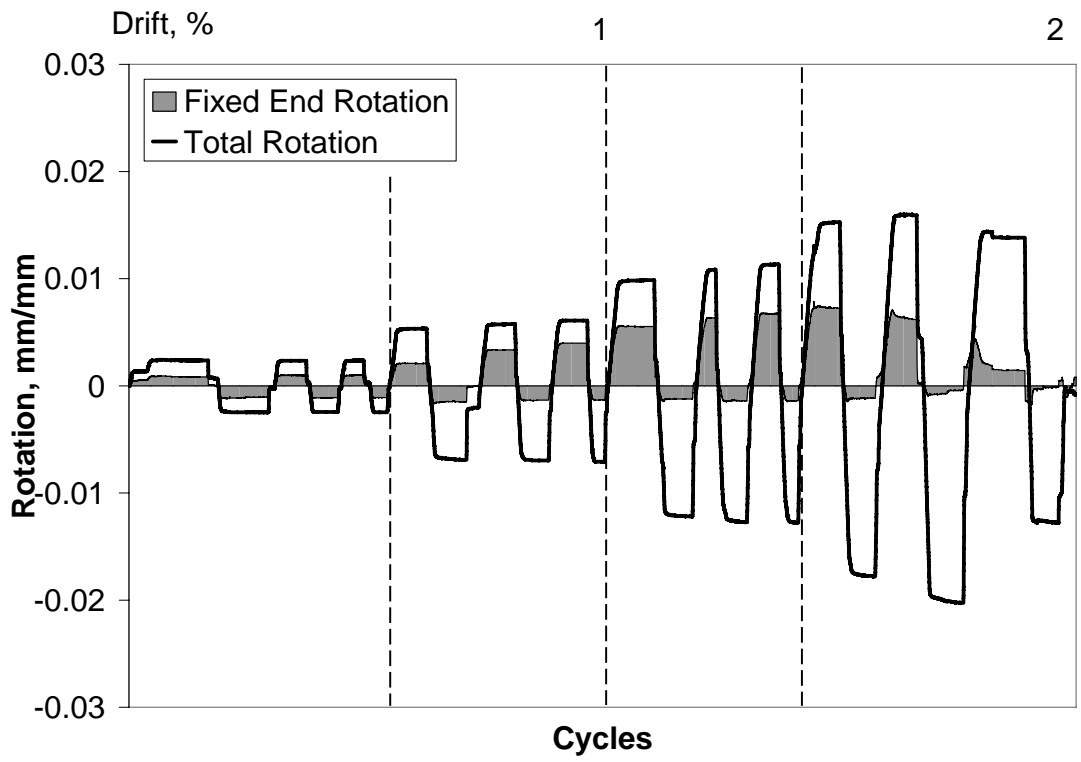


(a)

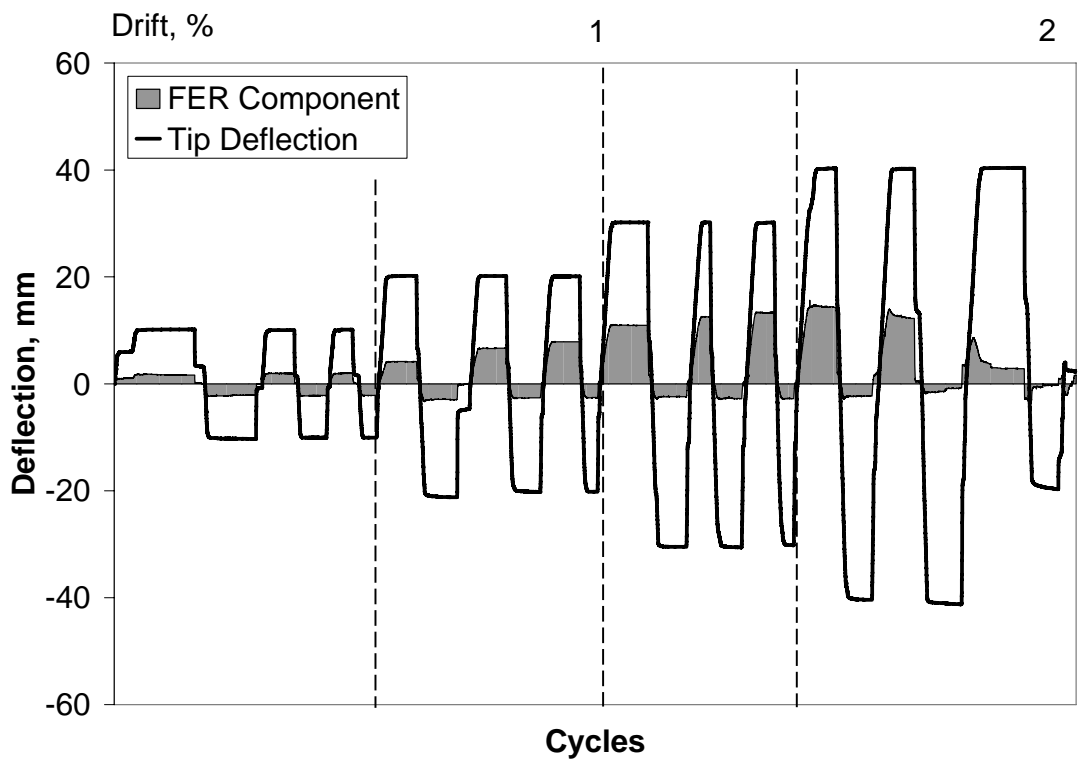


(b)

Figure 2.121 (a) Rotation and (b) Deflection Components for S-HC-1-00

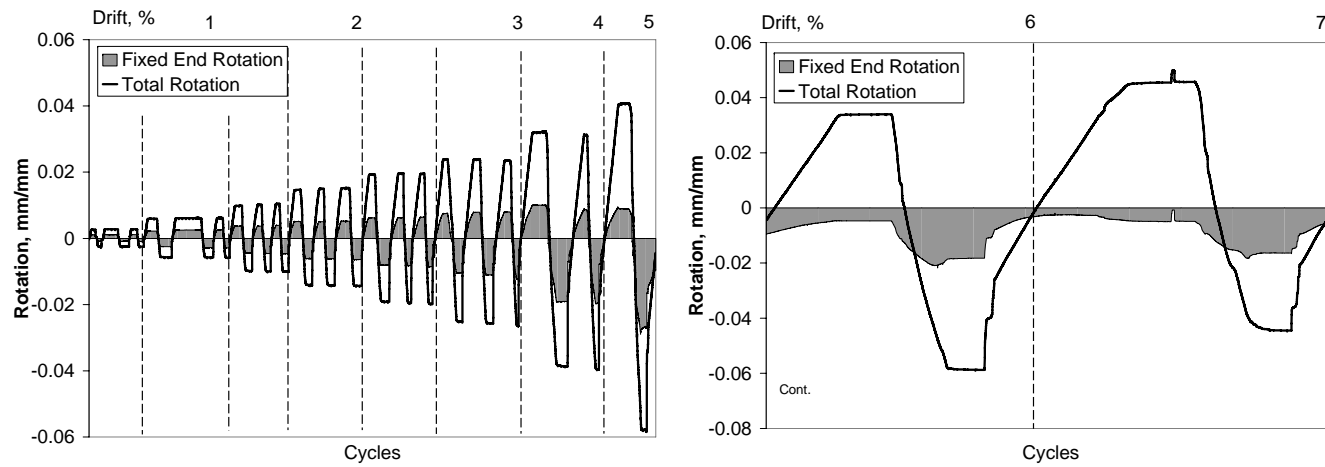


(a)

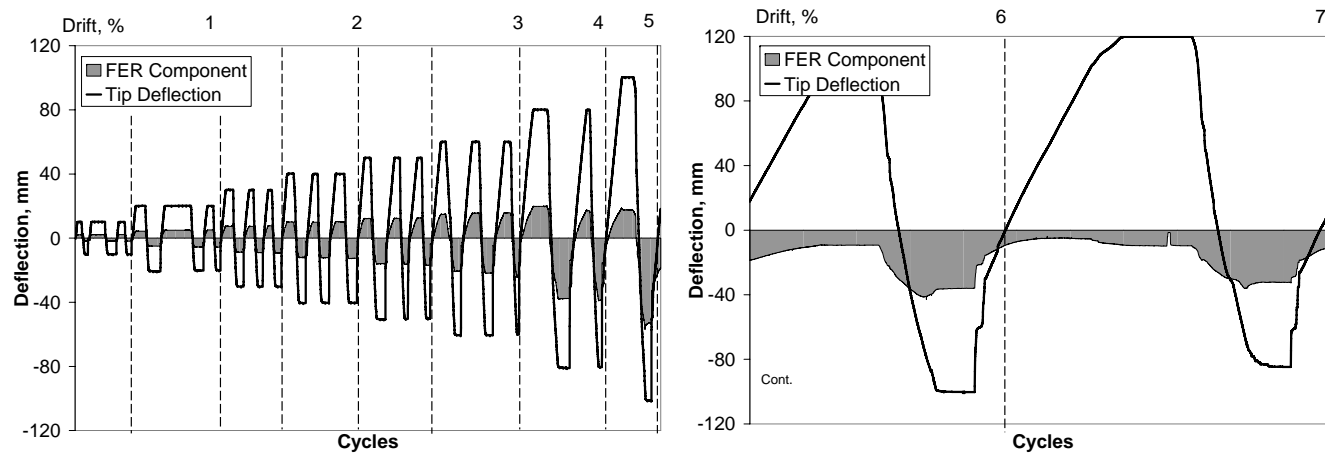


(b)

Figure 2.122 (a) Rotation and (b) Deflection Components for R-NC-0-00

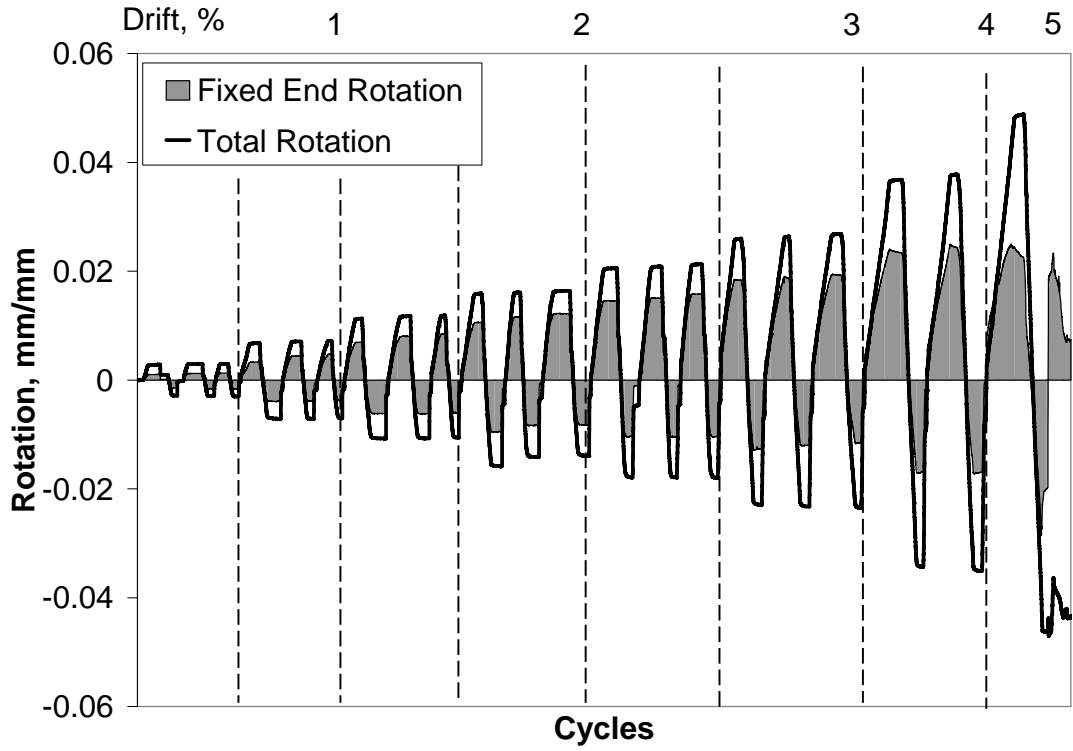


(a)

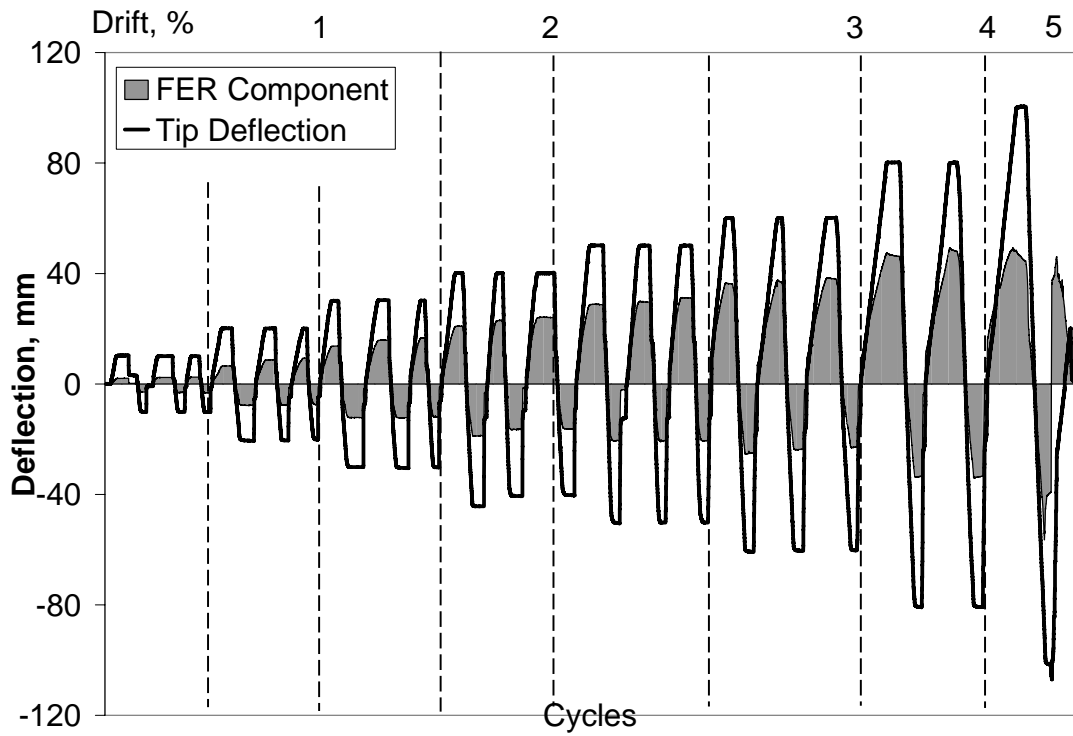


(b)

Figure 2.123 (a) Rotation and (b) Deflection Components for R-MC-1-16P

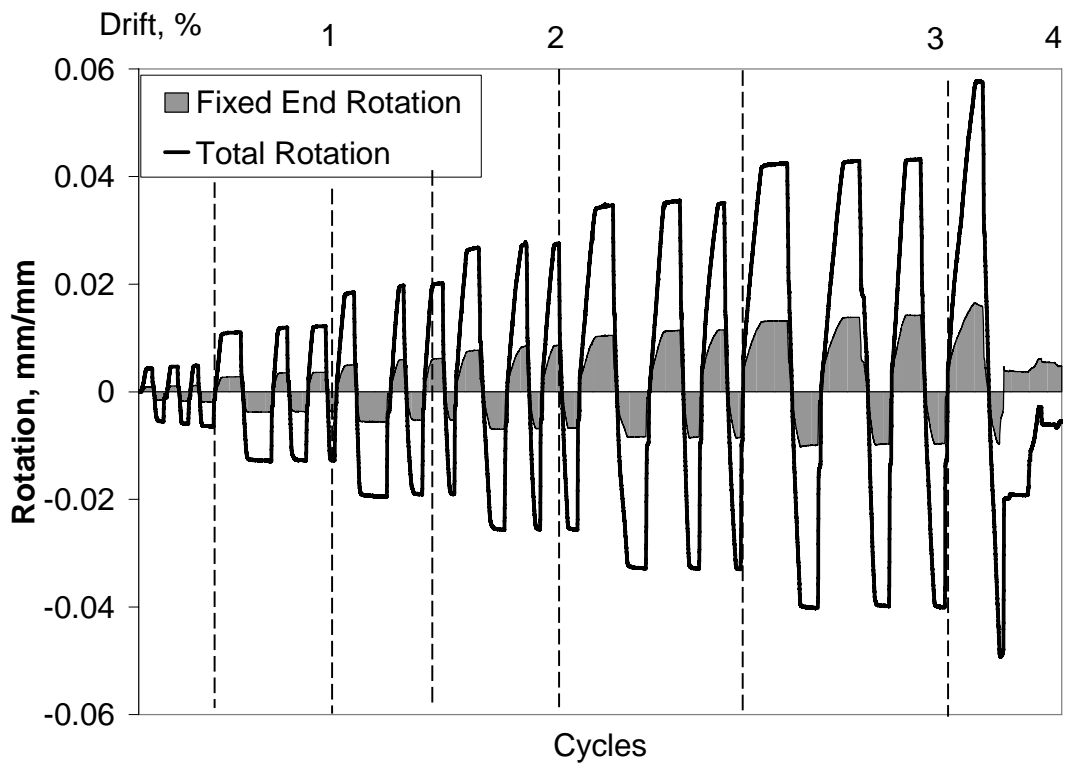


(a)

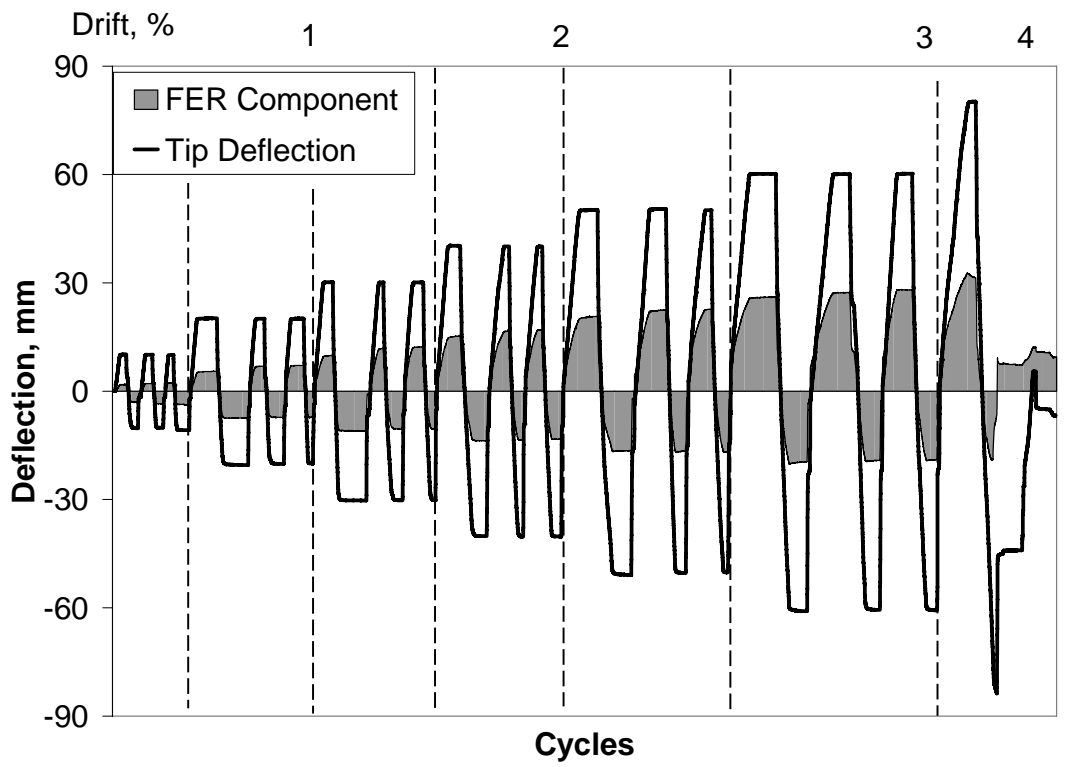


(b)

Figure 2.124 (a) Rotation and (b) Deflection Components for R-MC-1-8P

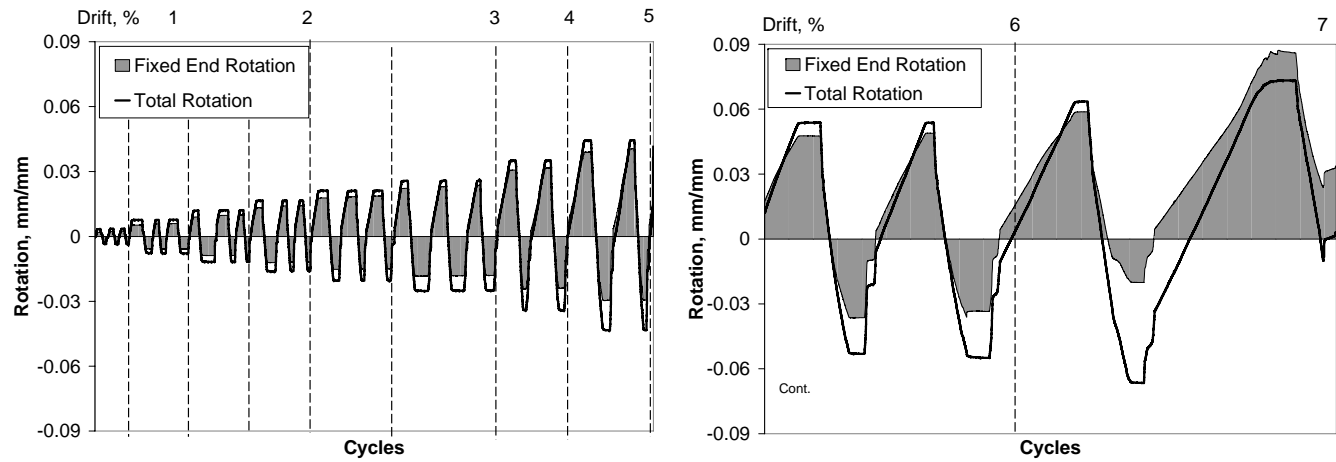


(a)

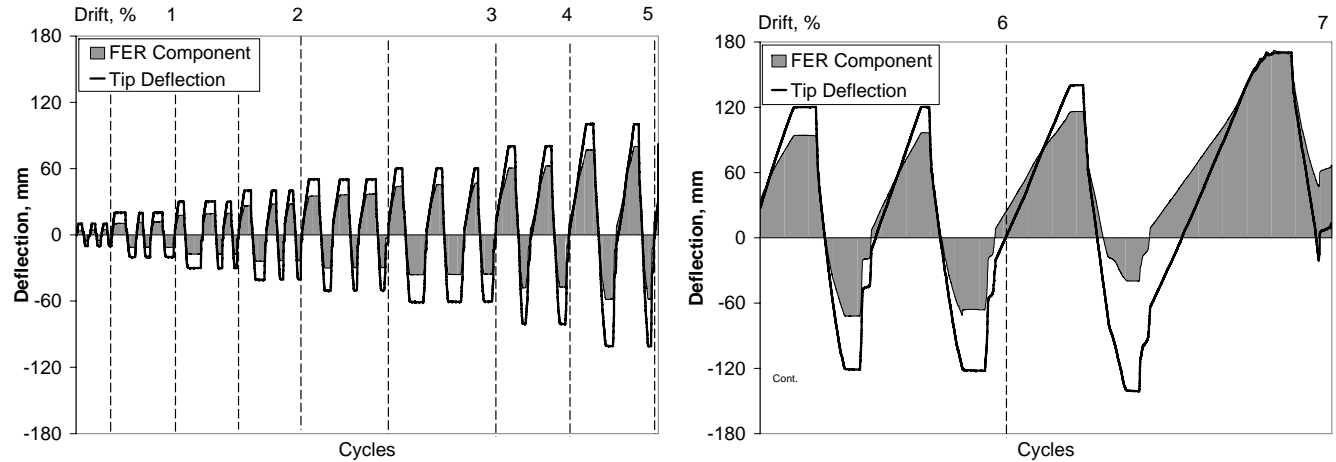


(b)

Figure 2.125 (a) Rotation and (b) Deflection Components for R-MC-1-NP



(a)



(b)

Figure 2.126 (a) Rotation and (b) Deflection Components for R-HC-1-16P

2.7.3. Deflection Profiles

All specimens were instrumented at heights of 350, 1000, 1750 and 2000 mm from the column base using seven LVDTs that recorded lateral deflections during reversed cyclic displacement excursions. The acquired deflection data from the LVDTs were plotted against column height for each level of tip deflection in the Figures 2.127-2.129. All specimens exhibited a flexure dominated response while the number of CFRP wraps increased the fixed-end rotation components. In general, CFRP retrofitting of the columns having plain longitudinal rebars, increased the fixed-end rotations hence, the shape of the deflection profiles was observed to be linear beyond the plastic hinging region ignoring elastic deformations.

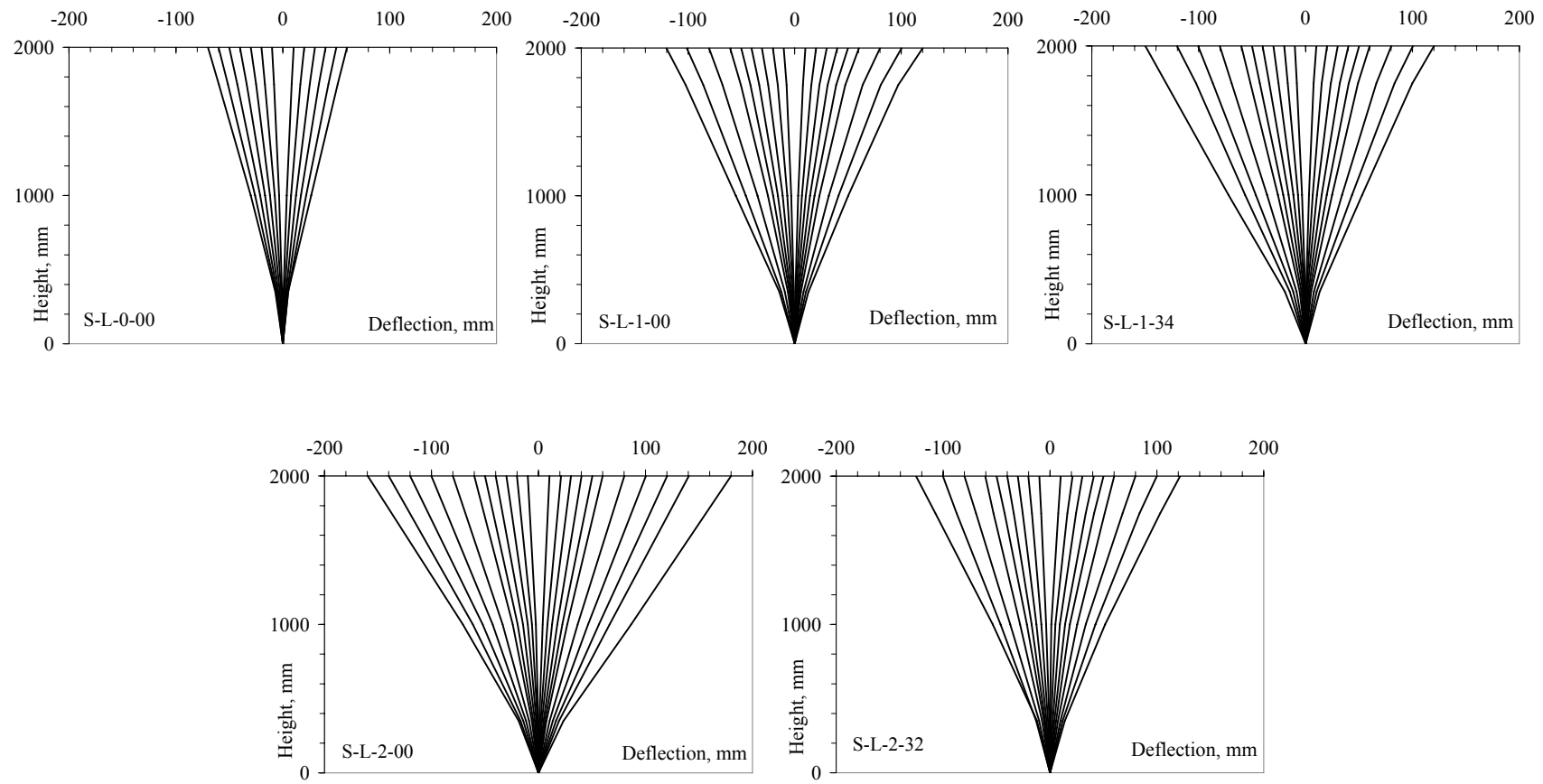


Figure 2.127 Deflection Profiles for Series 1

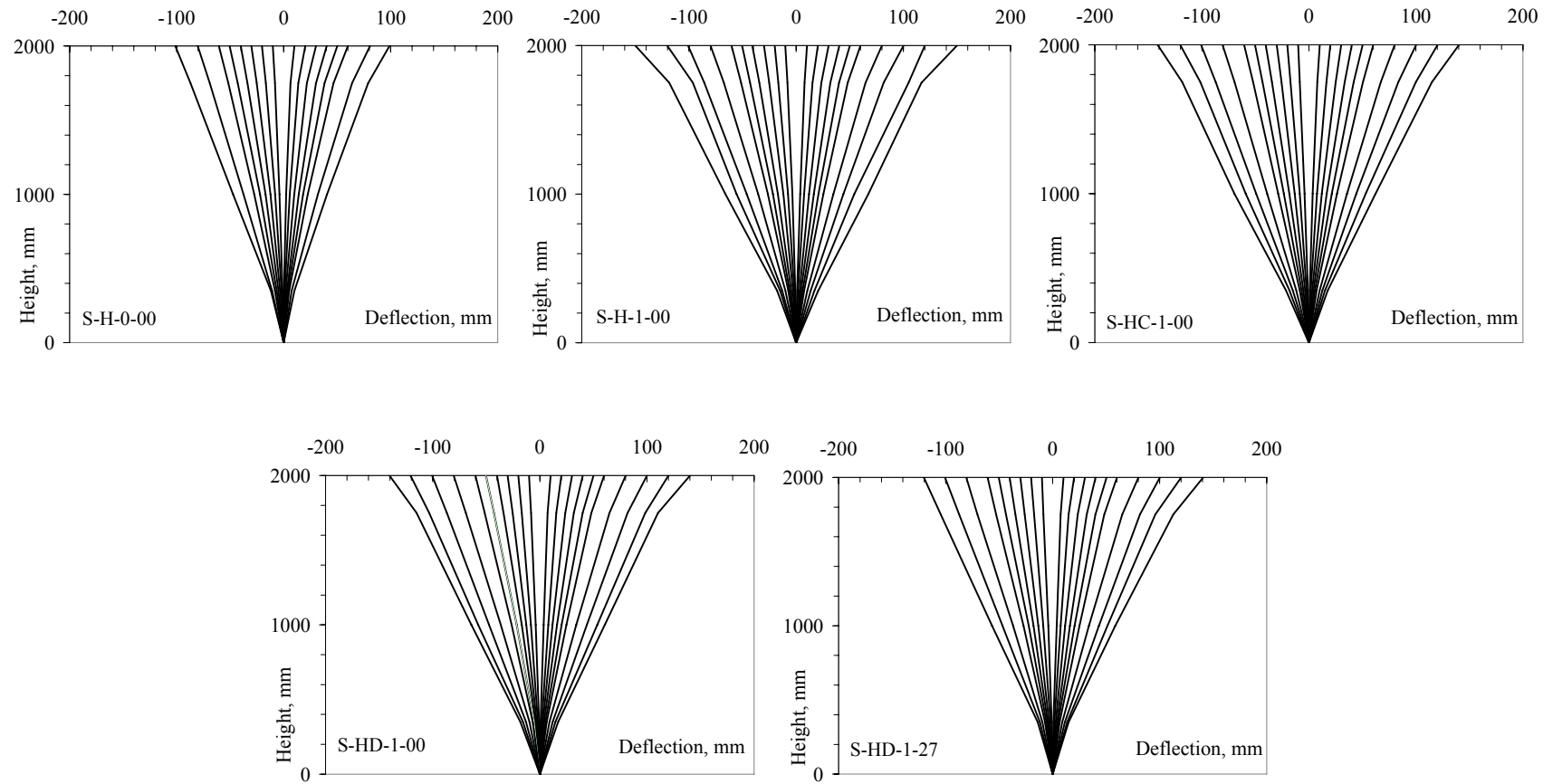


Figure 2.128 Deflection Profiles for Series 2

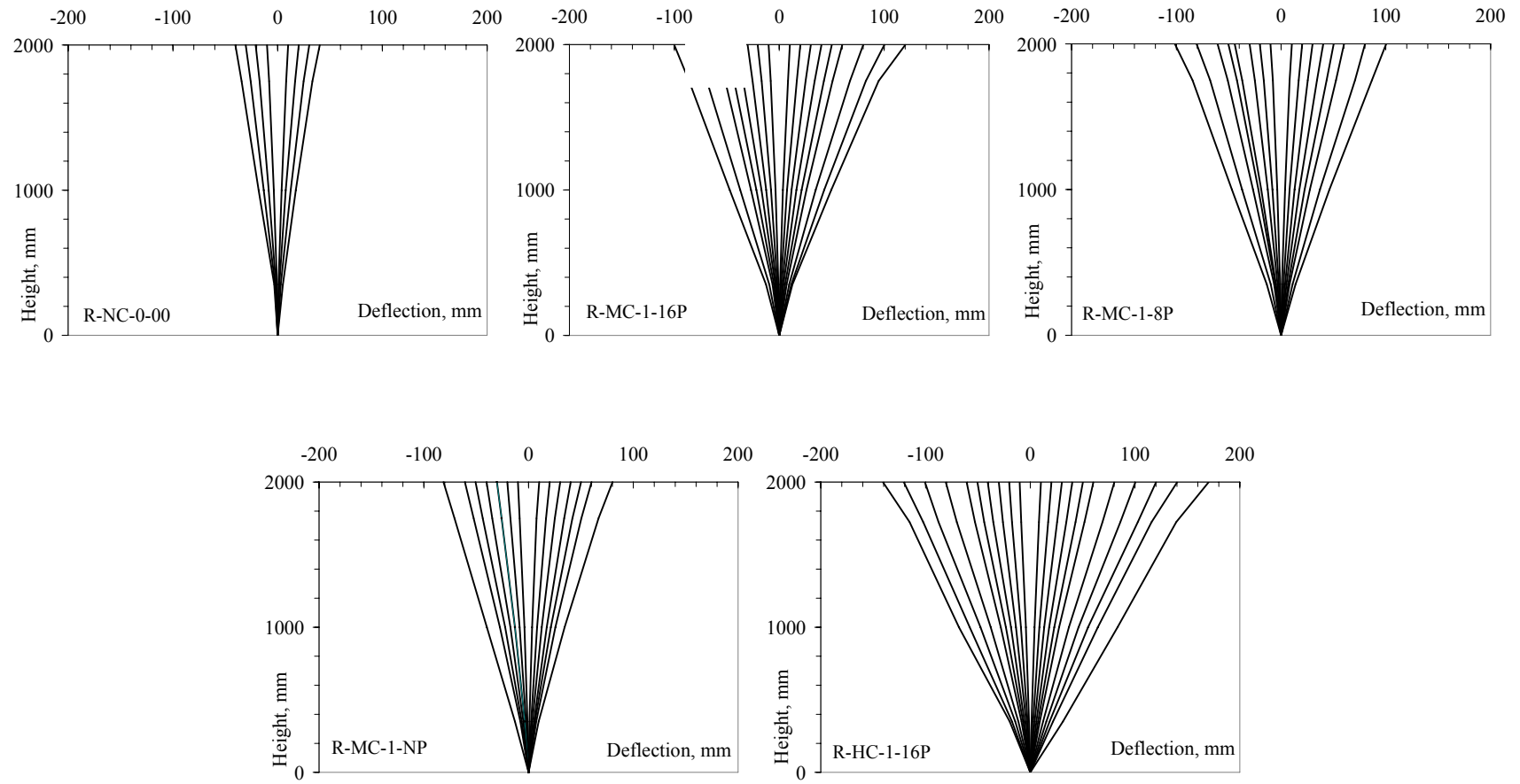


Figure 2.129 Deflection Profiles for Series 3

2.7.4. Energy Dissipation Comparisons

The dissipated energy during each cycle of the loading program was calculated by extracting the area under each displacement-based cycle throughout the loading program. The cycles were extracted regarding a lateral load-based method considering that at the beginning and at the end of each single full hysteretic cycle, lateral load is initialized its zero condition after the column experienced a fully reversed displacement excursion (Figure 2.130). By extracting each single hysteretic loop, the areas under each cycle was calculated and the normalized Cumulative Dissipated Energy (CDE) – Cumulative Drift Ratio (CDR) graphs were obtained regarding the failure of each specimen was at the drift level at which the lateral capacity dropped to 80% of lateral capacity. For the test series having variable concrete compressive strengths, in order to compare the dissipated energy levels, they were normalized by the dividing the dissipated energy amounts into the product of yield forces and yield displacements that were found experimentally (Table 2.5).

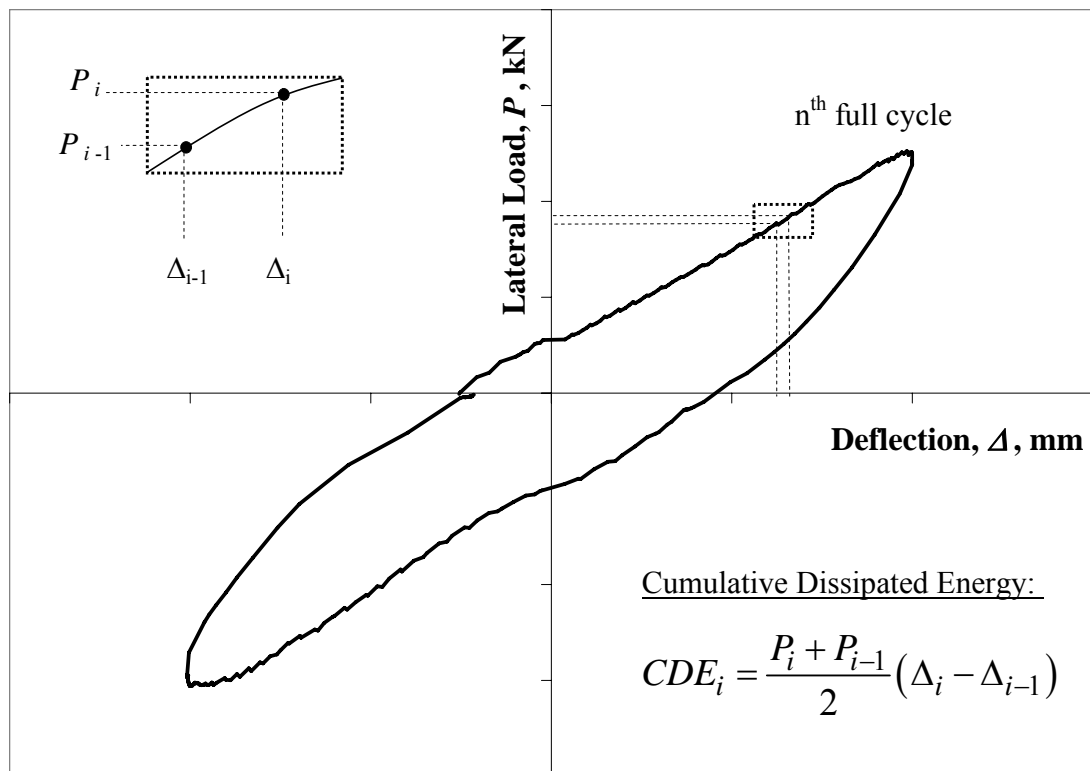


Figure 2.130 Cumulative Dissipated Energy (CDE) calculation method

The normalized dissipated energy responses for the Series 1 implied that wrapping one layer of CFRP doubled the normalized dissipated energy level while increasing the cumulative drift ratio from 20% to 50% approximately. Two-layer CFRP wrapped specimens exhibited a better energy dissipation response since the normalized cumulative energy level improved up to 4 times of the unwrapped specimen with cumulative drift level of about 60% as shown in Figure 2.131. The increase in normalized CDE was directly proportional with the number of CFRP wraps since the increase in normalized CDE was 2 and 4 times of the reference for 1 and 2 layer CFRP wrapped columns, respectively. The direct proportion was not observed in cumulative drift ratios regarding the increase of 2.5 and 3 times of the reference for 1 and 2 layer CFRP wrapped specimens. The effect of strengthening under an axial load of about 35% of axial capacity was investigated to have a trivial effect on the energy dissipation characteristics for the columns in Series 1. For the second series, regarding the reference specimen S-H-0-00 (Figure 2.132), the repaired columns S-HD-1-00 and S-HD-1-27 were able to sustain the same level of normalized dissipated energy level with 50% of cumulative drift ratio. The initial energy levels up to 30% of CDR were observed to be lower than the reference specimen due to the initially imposed lateral cycles on the repaired specimens. The slight reduction in dissipated energy levels can be interpreted due to the reduction in column corner rounding radius considering the specimens S-H-1-00 and S-HC-1-00. Moreover, CFRP repairing under an axial load of 27% of capacity was inspected to have a trivial effect on the energy dissipation responses for the columns in Series 2. For the last series, considering the reference specimen R-NC-0-00, the highly confined column R-HC-1-16P could maintain a normalized energy level and cumulative drift ratio of approximately 6 times of the reference specimen. In addition, R-HC-1-16P exhibited a superior energy dissipation response over the moderately confined specimens having normalized energy dissipation capacities as illustrated in Figure 2.133. The effect of CFRP confinement on the rectangular columns and the CFRP anchor dowel configurations was observed in energy dissipation characteristics of the columns tested in the last series. The moderately confined columns that had no-pinned, 8-pinned and 16-pinned CFRP anchor dowel configurations performed a similar behavior in energy dissipation responses.

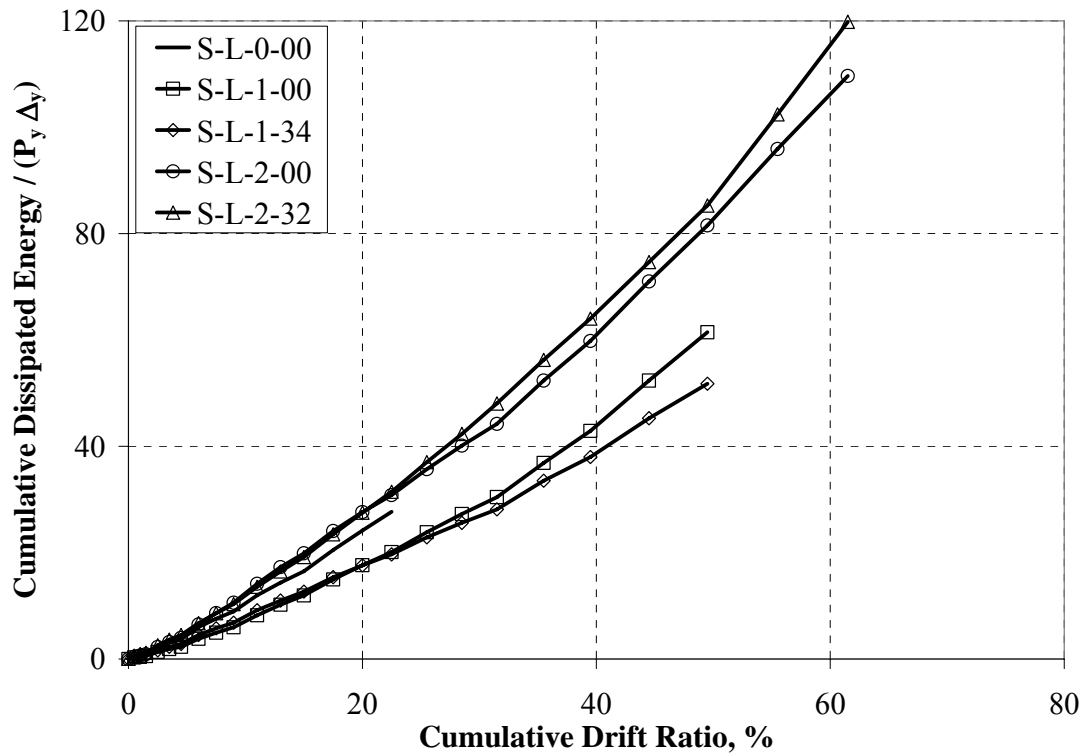


Figure 2.131 Normalized Cumulative Dissipated Energy (CDE) – Cumulative Drift Ratio (CDR) graph for Series 1 columns

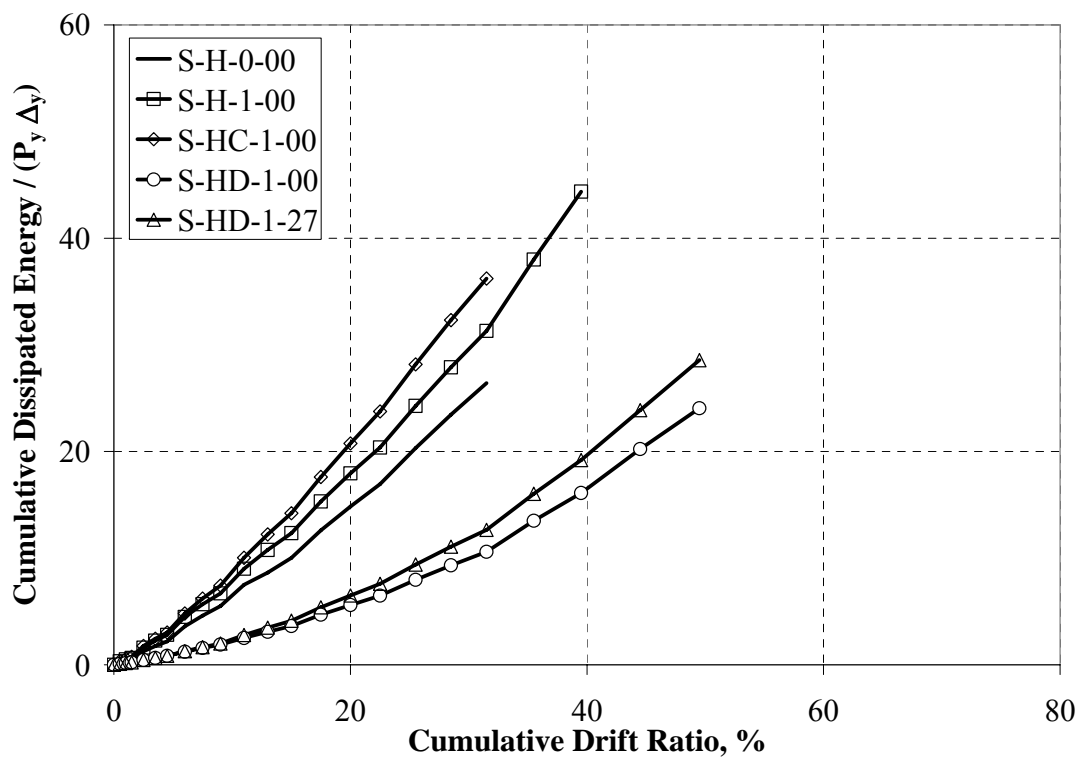


Figure 2.132 Normalized Cumulative Dissipated Energy (CDE) – Cumulative Drift Ratio (CDR) graph for Series 2 columns

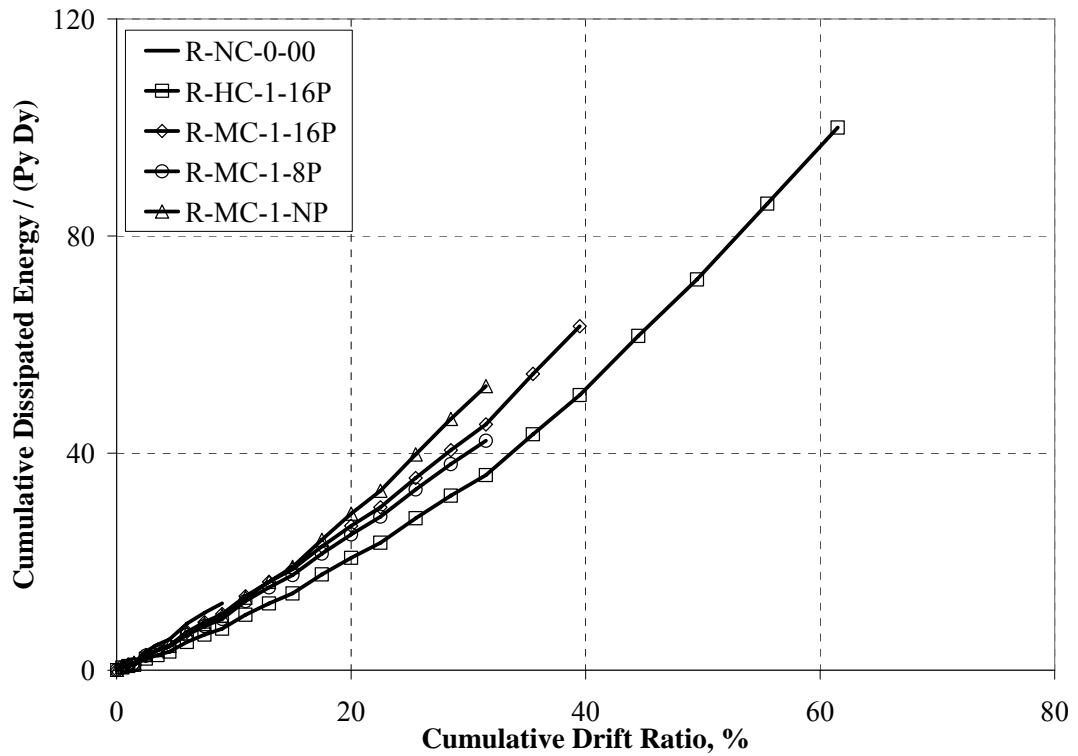


Figure 2.133 Normalized Cumulative Dissipated Energy (CDE) – Cumulative Drift Ratio (CDR) graph for Series 3 columns

2.7.5. Stiffness Degradation Comparisons

The stiffness degradation curves for the specimens were evaluated by using the average secant stiffness in both directions of loading. The slope connecting the origin and the deflection level was considered as the secant stiffness at each hysteretic loop. The normalization process was applied by dividing the average secant stiffness by the ratio of experimental section yield forces to yield displacements. The normalized average secant stiffness values were used regarding all cycles in the loading program and each average stiffness value were plotted against the corresponding drift levels.

For the first series, the reference specimen S-L-0-00 had approximately the same initial normalized secant stiffness similar to all the strengthened columns at the beginning of the test (Figure 2.134). After 2% drift ratio, the normalized stiffness of the reference specimen started to degrade more rapidly than the strengthened specimens. At 3% of drift level, all the CFRP wrapped columns had a normalized

stiffness level of approximately 2 times of the reference specimen. During further lower normalized stiffness levels, the reference specimen was able to maintain a drift level of almost 3% while the strengthened columns could sustain a drift demand of 5%. Since all the strengthened specimens had comparable lateral strengths and consequent lateral stiffness values, approximately the same level of normalized stiffness values were obtained. During the following cycles, the CFRP wrapped columns experienced an improved behavior since the CFRP layers enforced further opening of the interface crack and until the buckling of the longitudinal bars, the CFRP wrapped columns were able to maintain higher stiffness levels up to the failure.

The specimen responses in Series 2 were similar for the strengthened and the reference columns. During further cycles, the secant stiffness of the reference specimen started to degrade after 3% drift ratio and dropped to zero level at 5% of drift. However, for the CFRP strengthened columns S-H-1-00 and S-HC-1-00, the drift level at which zero stiffness was observed, was improved to 7% by the contribution of the CFRP layers (Figure 2.135). At a drift ratio of 5%, the reference column was able to sustain almost no stiffness regarding the repaired and the strengthened columns. The amplified normalized stiffness levels for the repaired columns S-HD-1-00 and S-HD-1-27 were due to increase in the yield deflections by which the stiffness values were normalized. There was no significant effect of repairing under the presence of axial load of 27% of the capacity can be observed as shown in Figure 2.135

The normalized secant stiffness responses for the columns in the last series illustrated that while all the specimens had comparable initial normalized stiffness values. The reference specimen could not maintain any lateral stiffness after 2% drift level as shown in Figure 2.136. For the moderately confined specimens R-MC-1-16P, R-MC-1-8P and R-MC-1-NP, the stiffness degradation characteristics were similar as soon as the secant stiffness for all the columns degraded to zero level about 5% drift ratio. However, the highly confined column R-HC-1-16P had a higher stiffness capacity beyond 7% owing to the enhanced level of confinement among the moderately confined specimens.

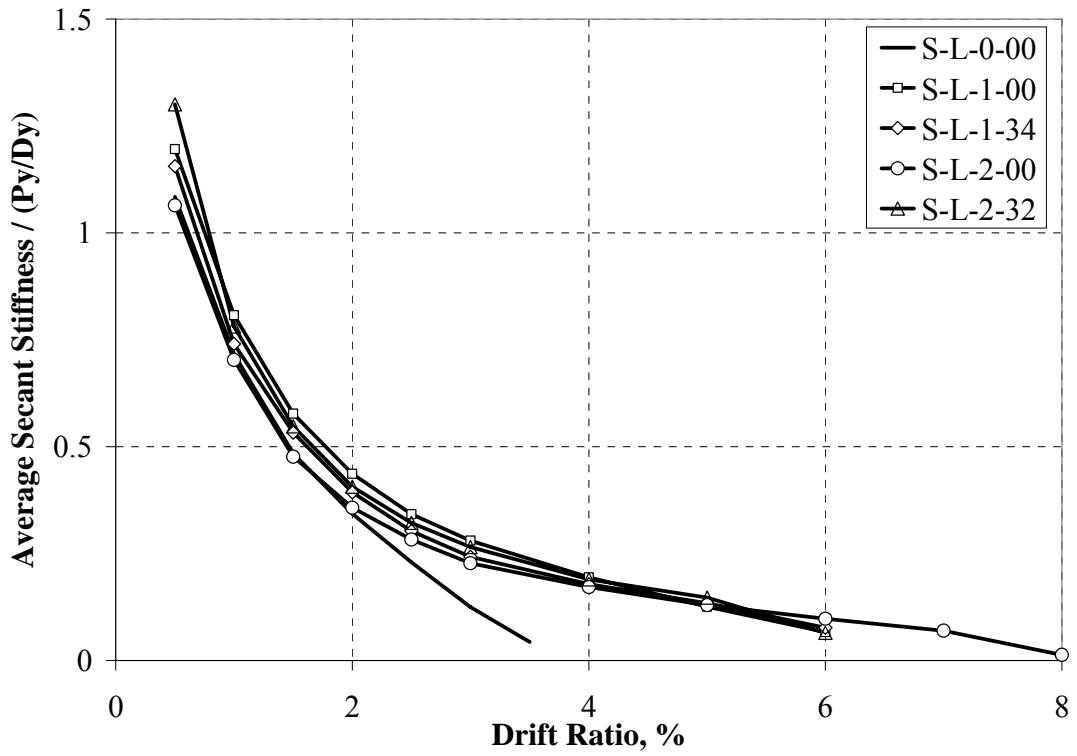


Figure 2.134 Normalized secant stiffness degradation curves for Series 1

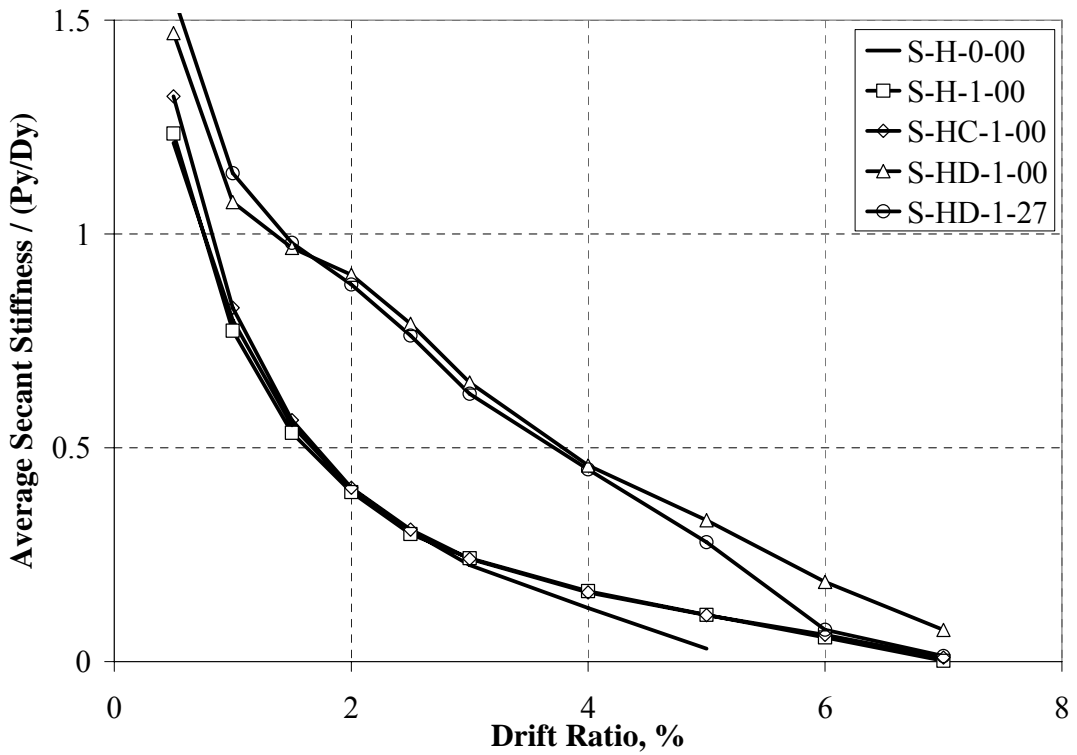


Figure 2.135 Normalized secant stiffness degradation curves for Series 2

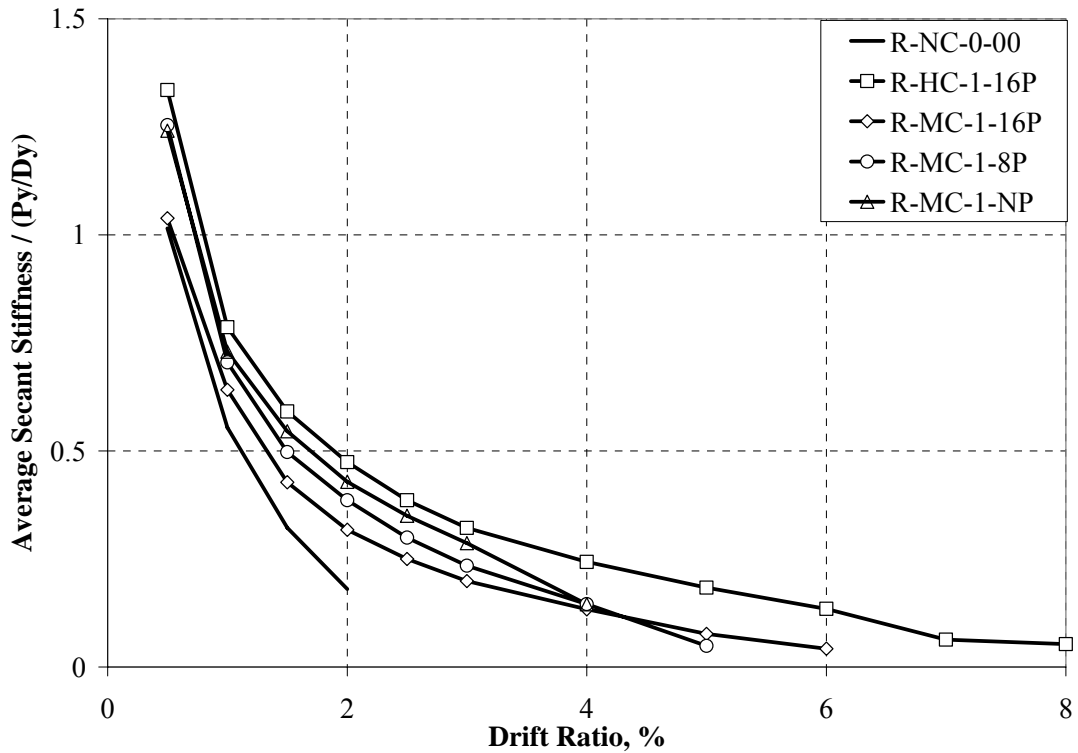


Figure 2.136 Normalized secant stiffness degradation curves for Series 3

2.8. Discussion of Test Results

In the first part of the experimental program, the effects of the number of CFRP layers wrapped around the column and the presence or absence of axial load during strengthening were examined. For the second series of tests, the cases of pre-damage, repairing columns under axial load and the corner radius effects were investigated. The final test series included the investigation of the effects of section aspect ratio and different CFRP anchor dowel configurations on the column behavior.

2.8.1. Effect of CFRP Layers

For the first test series, strengthening square columns with either 1 or 2 plies of CFRP sheets significantly improved the seismic performance (ductility and energy dissipation capacity) of the test specimens. The experiments showed that increasing the number of CFRP sheets wrapped around the column increased the displacement ductility of the specimens. However, negligible strength enhancement was observed

(10 to 15%) compared to the control specimen, showing that multiple layer FRP application result in deformation capacity increase rather than strength increase (Figure 2.83). It was observed that, the enhancement in drift capacity at 20% strength drop was not in linear proportion to the amount of CFRP used. Wrapping 1 layer of CFRP sheet increased the ultimate drift ratio of the specimen S-L-1-34 by a factor of about 1.9 compared to the control specimen. On the other hand, this ratio was about 2.4 for specimen S-L-2-32. This shows that doubling the amount of FRP did not result in twice the deformation capacity enhancement. Similar arguments can be made upon comparing specimens S-L-1-00 and S-L-2-00 (Table 2.5). The fixed-end rotation levels also increased with the increase in the number of CFRP layers wrapped around the column since the confining effect of CFRP layers prevented premature buckling of the longitudinal rebars and made the columns sustain higher levels of fixed-end rotation responses (Figure 2.89). The increase in CFRP layers resulted in the enhancement in confinement level and consequent improvement in energy dissipation characteristics. A higher level of confinement helped the columns maintain a superior level of response through dissipated energy levels and corresponding drift levels. The confining effect of CFRPs also made the columns sustain higher stiffness levels after the formation of the column-stub interface cracking regarding the higher stiffness degradation responses of the reference specimens.

2.8.2. Effect of Axial Load during Strengthening and Repairing

The influence of strengthening under axial load was evaluated by comparing two sets of companion specimens that were wrapped by 1 ply and 2 plies of CFRP sheets (Figures 2.84, 2.85 and Table 2.5). Although there was a slight variation in axial load levels among the specimens, the companion specimens S-L-1-00, S-L-1-34 and S-L-2-00, S-L-2-32 attained similar drift deformations (5% and 6.1% respectively). It can be stated that the presence of axial load corresponding to 34% of axial capacity during FRP wrapping has negligible influence on the ultimate drift ratios. Even the axial load level was 27% instead of 34% for one layer CFRP wrapped columns; the attained ultimate drift levels were similar. A similar argument is also valid upon comparing specimens S-L-2-00 and S-L-2-32. It can be claimed that the effect of

presence of axial load of about 35% of capacity during strengthening is not significant considering the drift demands for structural stability. The effect of axial load during repairing was interpreted by comparing the columns S-HD-1-00 and S-HD-1-27. It was observed that both of the columns performed similar inelastic responses achieving similar ultimate drift deformations. The presence of axial load during the repairing process did not affect the ultimate drift ratios (~5.1%). The drift levels at which the CFRP debonding and rupture took place were also similar (2% and 5%, respectively) for the specimens repaired in the presence and absence of axial load. The only effect of axial load during repairing was the gain in lateral capacity of about 15% as compared to the reference column (Figure 2.93). This difference can be attributed to the high compressive and tensile strength of the epoxy repair mortar (~70 MPa) compared to the concrete compressive strength (about 20MPa) of the original column. The high variation in compressive strength (3.5 times the concrete) forced the repaired column S-HD-1-00 to increase its lateral capacity after the application of the axial load. However, for the repaired column under axial load the section, lateral load carrying capacity was kept constant (i.e. axial load was always carried by the damaged column, not by the epoxy mortar) as the section behavior was not significantly affected by the high compressive strength of the epoxy mortar. Moreover, repairing square columns with 1 ply of CFRP sheet significantly improved the ductility and energy dissipation response of the columns. However, the strength and energy dissipation capacity of the repaired columns, S-HD-1-00 and S-HD-1-27, were lower than the strengthened column, S-H-1-00, which had no prior damage. This can be attributed to cracking and stiffness degradation that occurred in the pre-damage state, i.e. no effort was needed for the reopening of the interface crack at the base and other flexural cracks outside plastic hinge region.

2.8.3. Effect of Plain Bars

The effect of plain bars can be examined by comparing the concentrated rotations that occurred within bottommost 50 mm of the column in Series 1. Thus, the fixed end rotation data monitored in the experiments included bar-slip and inelastic rotation components. For the reference specimen S-L-0-00, the column rotation due to fixed-end rotations reached up to 40% of the ultimate drift ratio. Wrapping 1 layer

of CFRP sheet increased the fixed end rotations to almost 65% of the total rotations in the plastic hinge region and one more additional layer of CFRP increased these rotations to a level of 80% as shown in Figures 2.110-2.114. The columns withstood larger drift demands without any strength degradation due to the confining effect of CFRP sheets preventing premature buckling of the longitudinal bars and helping the specimen to maintain its lateral load resistance. Although the anchorage of plain bars is not affected by the CFRP confinement, CFRP wrapping delays rebar buckling till CFRP rupture takes place. For the second series, in which the longitudinal bar diameter increased to 22 mm, the effect of using plain bars can be observed more significantly since the fixed-end rotation components increased to levels of 65% and 80% for the reference and strengthened columns, respectively (Figures 2.115-2.121). Similar observations can be made upon comparing the last series columns while the fixed-end rotation components of the reference specimen increased from 40% to 50 and 80% by using moderate and high confinement levels as shown in Figures 2.122-2.126. Thus, deficient columns with plain bars could sustain larger deformations compared to columns with deformed bars due to increased deformations regarding the slippage and extension of longitudinal rebars upon CFRP retrofit. This requires the drift control to be much more important for columns with plain bars due to the possibility of having large deformation that may lead to severe stability problems. It is therefore crucial to account for fixed end rotations in seismic assessment and retrofit design of deficient reinforced concrete columns with plain bars.

2.8.4. Effect of Column Corner Rounding Radius

The column corners were rounded to a radius of 30 mm for all the strengthened and repaired columns except the column S-HC-1-00 whose corners were rounded to 10 mm. Considering the one layer CFRP wrapped specimens, decreasing the corner-rounding radius from 30 mm to 10 mm, led to slight degradation in the ultimate drift level from 4.1% to 3.6% while the reference specimen could sustain an ultimate drift of 3.3% (Figure 2.92). This degradation in the seismic behavior of the columns was clarified by virtue of slight reduction in the CFRP confined regions in the cross-section of the column. Energy dissipation capacity and corresponding cumulative drift level of S-HC-1-00 also reduced by 25% regarding its companion specimen S-

H-1-00 in which 10 mm of corner rounding radius was employed (Figure 2.132). In addition, for the specimen S-HC-1-00, no significant variation in normalized stiffness degradation response was observed regarding the other strengthened and repaired columns (Figure 2.135).

2.8.5. Effect of Column Section Aspect Ratio

The section aspect ratio was 2 for the third series, while square cross-section was used for the other test series. Increasing the section aspect ratio from 1 to 2 changed the column behavior dramatically by reducing the section area and increasing the depth. It also decreased the CFRP confined area in retrofitted columns and thus had a detrimental effect on the seismic behavior of the columns. The ultimate drift level for the reference specimens S-L-0-00 and R-NC-0-00 that had comparable concrete compressive strengths (14 and 12 MPa) were 2.6 and 1.8%, respectively (Table 2.5). In addition, the ultimate curvature and fixed-end rotation values for R-NC-0-00 also decreased to half of the square shaped column S-L-0-00 as shown in Table 2.5. The plastic hinging region which was observed at the base of the columns along a height of approximately depth of the section, elongated in the rectangular columns due to the increase in the section depth. In addition, energy dissipation characteristics for R-NC-0-00 deteriorated up to half of S-L-0-00 (Figures 2.131 and 2.133). A similar response was investigated in the normalized stiffness degradation characteristics. At 2% of drift level, the normalized stiffness level deteriorated to 0.2 for R-NC-0-00, while the maintained stiffness level was 0.4 for square shaped column S-L-0-00 as shown in Figures 2.134 and 2.136.

2.8.6. Effect of CFRP Anchor Dowels and Anchor Dowel Configurations

The comparison between the moderately confined specimens was based on the lateral pressure due to CFRP (f_l) and confinement efficiency factor (κ_a) definitions (Equations 2.9-2.11). Herein, confinement ratio (ϕ) was selected as the deterministic comparative parameter that can be calculated by dividing the lateral pressure due to FRP (f_l) by the concrete compressive strength (f_c'). This normalization was crucial since the concrete compressive strengths were different for different test series.

Herein, the moderately confined specimens in Series 3 had approximately the same level of confinement ratio about 0.20. The attainable lateral drift ratio for the columns that had no-pinned or 8-pinned CFRP anchor configurations was approximately 4%. For the specimen R-MC-1-16P, 16-pinned configuration made the column sustain the same drift level of 4% due to the increase in confined area and confinement efficiency factor (Figure 2.8). In other words, in order to sustain an ultimate drift level of 4%, no-pinned or 8-pinned specimens required a confinement ratio of about 0.20 whereas, for the specimen R-MC-1-16P, by using 16-pinned detailing, the increase in confinement efficiency factor (κ_a) made the column sustain the same drift level (Figure 2.137). For R-HC-1-16P, the improvement in confinement ratio was observed, since the column had relatively lower concrete compressive strength than R-MC-1-16P and the CFRP anchor dowels changed the shape of the effectively confined region for both columns (Figure 2.8a). This behavior shows the effectiveness of 16-pinned CFRP anchors. For 8-pinned detailing, due to the placement of the anchors at the middle of the longer side of the column, the CFRP anchors were not clamped to the parabolic borderline of the confining region (Figure 2.8b).

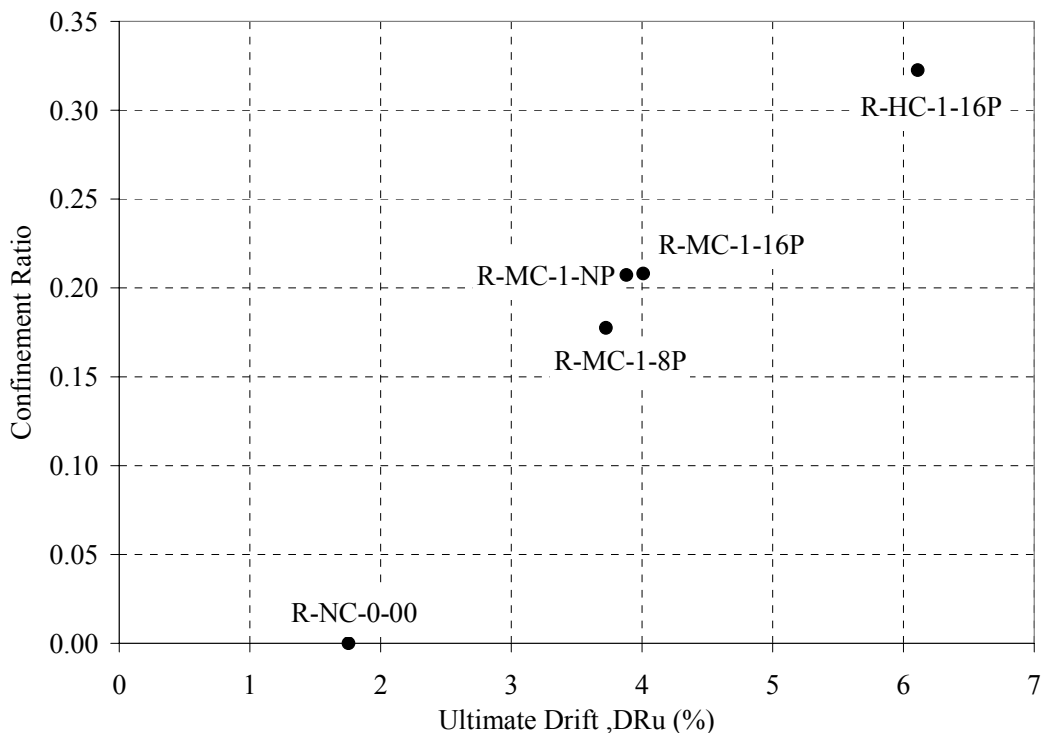


Figure 2.137 Ultimate Drift (DR_u) – Confinement Ratio comparisons for Series 3

CHAPTER 3

ANALYTICAL STUDIES

3.1. General

The tip deflection of the columns is estimated by considering the flexural and the fixed end rotation components. Shear deflections are ignored, as the columns are flexural dominant with section aspect ratios of 5 and 5.7. A Matlab Code was written in order to calculate the column shear (P) versus tip deflection (Δ) by considering the moment (M) vs. curvature (K) and moment (M) vs. fixed end rotation (FER) response of each column. For the repaired columns, this analytical study was implemented directly, however the distribution of high-strength epoxy mortar over the repaired column base sections was not considered.

The analysis was initiated with the computation of two moment-curvature responses of the column cross sections i.e. section without any confinement and FRP confined plastic hinge section (if there is any FRP wrapping). Each analyzed section was divided into a number of concrete layers and the steel reinforcement was defined for given coordinates from the centroid of the section. A curvature increment was imposed on the section, and assuming that plane sections remain plane, a linear strain profile was employed to determine the strain of each layer and steel reinforcement.

3.2. Constitutive Models for Materials

The corresponding stresses at the layers and at the reinforcement are found by using unconfined (Popovics 1978 [55]) and confined concrete models (Doruk 2006 [56]) and the steel model including rebar buckling in compression (Maekawa 2002 [57]) as shown in Figure 3.1.

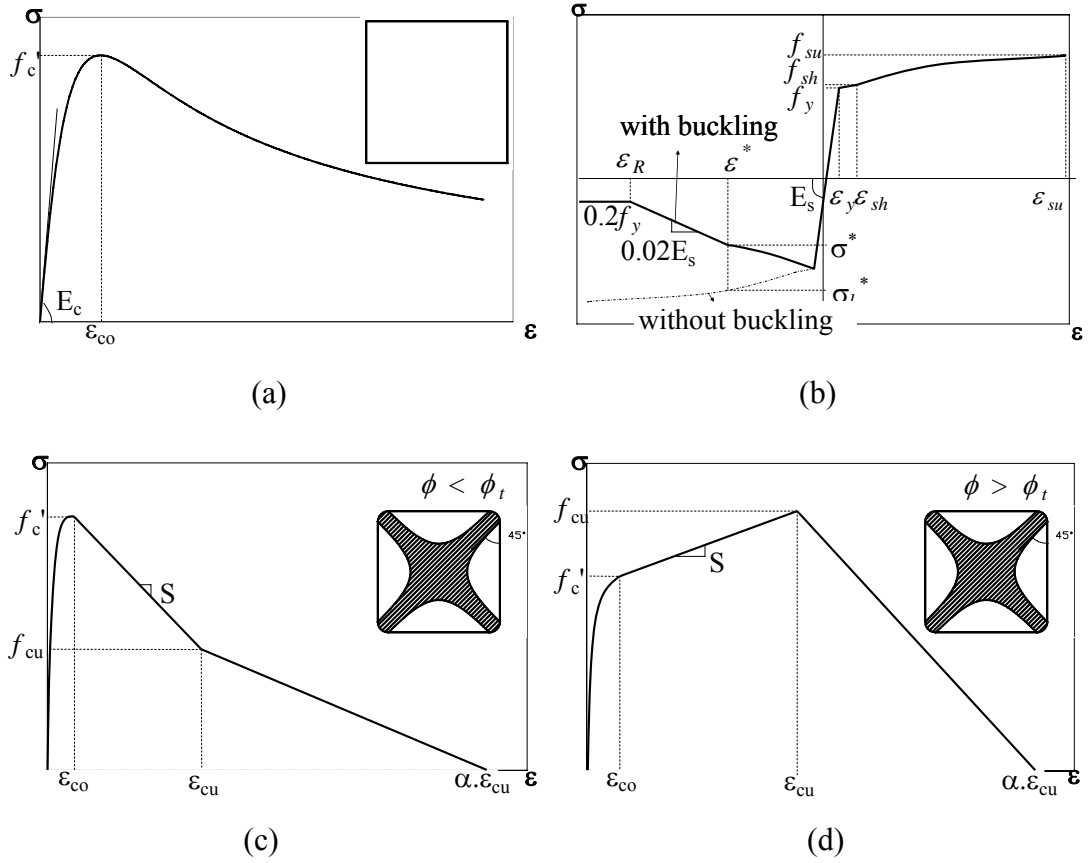


Figure 3.1 The constitutive models for (a) Unconfined concrete, (b) Steel, (c) Confined concrete – softening and (d) Confined concrete – hardening

3.2.1. Unconfined Concrete Model

The unconfined concrete model describes the axial stress strain behavior of unconfined concrete using a single function as shown in Equations 3.1a and b [55].

$$\sigma_c = \frac{nf_c' \left(\frac{\epsilon_{cf}}{\epsilon_{co}} \right)}{n-1 + \left(\frac{\epsilon_{cf}}{\epsilon_{co}} \right)^{nk}} \quad (3.1a)$$

$$n = 0.8 + \frac{f_c'}{17}, \quad k = 0.67 + \frac{f_c'}{62} \text{ for } \frac{\epsilon_{cf}}{\epsilon_{co}} > 1 \text{ else } k = 1 \quad (3.1b)$$

$$\epsilon_{co} = (-0.067 f_c'^2 + 29.9 f_c' + 1053) 10^{-6} \quad (3.1c)$$

where, f_c' is the concrete compressive strength, σ_c and ε_{cf} are the concrete stress and strain respectively and ε_{co} is the strain at f_c' . Equation 3.1c is an expression for the axial strain of unconfined concrete at peak stress proposed by Tasdemir et al. [58] and covers a wide range of concrete strength (between 10 to 100 MPa).

3.2.2. FRP Confined Concrete Model

The FRP confined concrete model, which was previously employed successfully to estimate moment-curvature response of circular columns is used in this study [56]. The model has the capability of simulating FRP confined concrete behavior with a hardening response for high levels of confinement and softening behavior when the confinement is low. The confined concrete model has three functions defining the ascending and descending branches of the stress-strain model. The transition value for confinement ratio ($\phi_t = 0.14$) of concrete determines whether the response will exhibit hardening or softening response. In other words, when the confinement ratio (ϕ) calculated using Equation 3.2 for a given jacket thickness and section, is greater than ϕ_t , response is a hardening type, whereas when it is less than ϕ_t , response exhibits a softening branch (Figure 3.1).

$$\phi = \frac{(b+h)E_j\varepsilon_f t_j}{bhf_c'} K_e \quad (3.2a)$$

$$K_e = 1 - \frac{(h-2r)^2 + (b-2r)^2}{3bh} \quad (3.2b)$$

where b and h are the column width and height, respectively. E_j , ε_f and t_j are the elasticity modulus, rupture strain and the thickness of the CFRP jacket, respectively. K_e is the effectiveness factor of the confinement and it is a function of column dimensions and corner round off radius, r , as given by EC8 [59], f_c' is the concrete compressive strength. The confinement effectiveness factor (K_e) is the ratio between effectively confined area and column gross area. A number of different expressions were proposed for this factor [60-63]. In this study, it is preferred to use a simple code given equation, which can simulate the confinement efficiency for a wide variety of column sizes. For cases where aspect ratio of column dimensions is greater

than 1.5 it may be necessary to provide internal anchors to increase the effectively confined area. For such cases, use of Equation 3.2b is not recommended and more detailed expressions proposed in the literature need to be used [64]. The stress-strain behavior of FRP confined concrete exhibiting softening and hardening responses are given by the Equations 3.3a and b.

$$\sigma_c = \begin{cases} E_c \varepsilon \left[1 - \frac{1}{n} \left(\frac{\varepsilon}{\varepsilon_{co}} \right)^{n-1} \right] & 0 \leq \varepsilon \leq \varepsilon_{co} \\ f_c' + S (\varepsilon - \varepsilon_{co}) & \varepsilon_{co} < \varepsilon < \varepsilon_{cu} \quad \text{when } \phi < \phi_t \quad (3.3a) \\ \frac{f_{cu}}{\alpha - 1} \left(\alpha - \frac{\varepsilon}{\varepsilon_{cu}} \right) & \varepsilon_{cu} \leq \varepsilon \end{cases}$$

$$\sigma_c = \begin{cases} E_c \varepsilon \left[1 - \frac{1}{n} \left(1 - \frac{S}{E_c} \right) \left(\frac{\varepsilon}{\varepsilon_{co}} \right)^{n-1} \right] & 0 \leq \varepsilon \leq \varepsilon_{co} \\ f_c' + S (\varepsilon - \varepsilon_{co}) & \varepsilon_{co} < \varepsilon < \varepsilon_{cu} \quad \text{when } \phi > \phi_t \quad (3.3b) \\ \frac{f_{cu}}{\alpha - 1} \left(\alpha - \frac{\varepsilon}{\varepsilon_{cu}} \right) & \varepsilon_{cu} \leq \varepsilon \end{cases}$$

where E_c is the elasticity modulus of concrete. In Equations 3.3a and 3b, α is used as ultimate strain multiplier for the cases of softening and hardening which is taken as 5 for both cases considering gradual post peak degradation after the ultimate strain as shown in Figures 3.1c and 3.1d. In order to obtain Equations 3.3a and 3b, a linear strength degradation is considered after ultimate strain and the boundary conditions of $\sigma_c = f_{cu}$ at ε_{cu} and $\sigma_c = 0$ at $\alpha \varepsilon_{cu}$ were enforced. In this way, progressive rupture of FRP as observed in the experiments and gradual strength degradation upon CFRP rupture are taken into account. The stress enhancement factor, K_σ for softening and hardening is obtained using a nonlinear curve with boundary conditions of $K_\sigma = 0$ at $\phi = 0$ and $K_\sigma = 1$ at $\phi = \phi_t$ for softening and $K_\sigma = 1$ at $\phi = \phi_t$ for hardening cases. K_ε which is termed as stress enhancement factor is taken as proposed by Lam and Teng [65] obtained from the calibration of 76 confined concrete specimens exhibiting both softening and hardening. These factors (K_σ and K_ε) reflect the effect of confinement on peak stress and strain of FRP confined concrete and given as:

$$K_{\sigma} = 1.8\phi^{0.3}, K_{\varepsilon} = 1.75 + 12\phi\left(\frac{\varepsilon_f}{\varepsilon_{co}}\right)^{0.45} \quad \text{when } \phi < \phi_t \quad (3.4a)$$

$$K_{\sigma} = 1 + 2.6(\phi - 0.14)^{0.7}, K_{\varepsilon} = 1.75 + 12\phi\left(\frac{\varepsilon_f}{\varepsilon_{co}}\right)^{0.45} \quad \text{when } \phi > \phi_t \quad (3.4b)$$

The model parameters S and n are defined as:

$$S = \frac{(K_{\sigma} - 1)f_c'}{(K_{\varepsilon} - 1)\varepsilon_{co}} \text{ and } n = \frac{E_c \varepsilon_{co}}{E_c \varepsilon_{co} - f_c'} \quad \text{when } \phi < \phi_t \quad (3.5a)$$

$$S = \frac{(K_{\sigma} - 1)f_c'}{(K_{\varepsilon} - 1)\varepsilon_{co}} \text{ and } n = \frac{(E_c - S)\varepsilon_{co}}{E_c \varepsilon_{co} - f_c'} \quad \text{when } \phi > \phi_t \quad (3.5b)$$

The stress enhancement factors of hardening and softening are compared with the results presented in Lam and Teng [65], Xiao and Wu [66], Wu et al [67] and Rochette and Labossiere [68]. Binici [69] reported that the test data are well represented by these equations of strength enhancement factor.

3.2.3. Steel Model

The steel constitutive model was selected to include elastoplastic model including linear and a nonlinear hardening regions in tension and bar buckling in compression depending on the unsupported length of transverse ties. For the case of FRP, confined concrete bar buckling was not taken into account as FRPs prevent longitudinal bar buckling. Stress-strain model in tension and compression are given by Equations 3.6 and 7, respectively [57].

$$f_s = \begin{cases} E_s \varepsilon_s & \varepsilon \leq \varepsilon_y \\ f_y + \frac{(f_{sh} - f_y)}{7\varepsilon_y} (\varepsilon_s - \varepsilon_y) & 8\varepsilon_y \geq \varepsilon > \varepsilon_y \\ f_{sh} + 0.03E_s (\varepsilon_s - 8\varepsilon_y) & 40\varepsilon_y \geq \varepsilon > 8\varepsilon_y \\ f_{sh} + 0.96E_s \varepsilon_y & \varepsilon > 40\varepsilon_y \end{cases} \quad (3.6)$$

$$f_s = \begin{cases} E_s \varepsilon_s & \varepsilon \leq \varepsilon_y \\ \sigma_l \left[1 - \left(1 - \frac{\sigma^*}{\sigma_l^*} \right) \left(\frac{\varepsilon_s - \varepsilon_y}{\varepsilon^* - \varepsilon_y} \right) \right] & \varepsilon^* \geq \varepsilon > \varepsilon_y \\ \sigma^* - 0.02 E_s (\varepsilon_s - \varepsilon^*) & \varepsilon_R \geq \varepsilon > \varepsilon^* \\ 0.2 f_y & \varepsilon > \varepsilon_R \end{cases} \quad (3.7)$$

where E_s is the elasticity modulus of steel, f_y and f_{sh} are the stresses at the yield and strain hardening points, ε_y and ε^* are the strains at yield and intermediate point, ε_s and σ are the average strain and stresses. ε_R stands for the strain at which the steel stress decreases to $0.2 f_y$ having the value of $\frac{(\sigma^* - 0.2 f_y)}{0.02 E_s} + \varepsilon^*$. In calculating average steel stress f_s , the compressive and tensile stresses that are σ^* and σ_l^* , respectively and current strain ε^* , are calculated as a function of transverse steel unsupported length L and bar diameter D using Equations 3.8 and 3.9.

$$\frac{\varepsilon^*}{\varepsilon_y} = 55 - 2.3 \sqrt{\frac{f_y}{100}} \frac{L}{D} \quad (3.8)$$

$$\frac{\sigma^*}{\sigma_l^*} = 1.1 - 0.016 \sqrt{\frac{f_y}{100}} \frac{L}{D} \quad (3.9)$$

By multiplying the corresponding stresses by the concrete strip and steel areas, concrete and steel forces were obtained. Afterwards, the location of the neutral axis was established employing the equilibrium of forces at each curvature increment by an iterative process. The moment at the column was then calculated by taking moments of each concrete layer and steel forces. Looping over all curvature increments, the moment-curvature response of FRP confined concrete section including FRP confinement and rebar buckling can be computed.

3.3. Bond Slip Model

The fixed end rotation was obtained for each curvature increment by calculating the outermost bar slip of the reinforcement and dividing it by the effective depth of the section as shown in Figure 3.2. Since the tensile strain at the reinforcement was known, the stress was found by using the steel stress strain model described above.

Mylrea [70] defined the allowable values of bond stress in plain bars for beams until yielding of the reinforcing rebars and under no axial load. The bond stresses for pull-out specimens and beams were stated as non-uniformly distributed along the embedment length. The allowable bond stresses along 10, 20, 30 and 40-bar diameter distances measured from the reaction end should be used as 2.76, 2.07, 1.24 and 0.83 MPa, respectively. For the remaining lengths along the plain bar, the allowable bond stress was suggested as 0.69 MPa. However, for the columns under axial load, the strains in the tension reinforcement should be lower than the case in beams. Thus the bond stresses should be reduced according to the axial load. A simple bond stress formula was used in the analytical program and the calculation of the slip (s) was based on an average uniform bond stress assumption [71, 72] as described in Figure 3.2. Consequently, a constant value for bond stress was used and the maximum bond stress, u that a plain bar can carry can be assumed as:

$$u = 0.4\sqrt{f_c'} \quad (3.10)$$

In Equation 3.10, u and f_c' are both measured in MPa [71]. Considering the test specimens used in this study, the average bond stress developed in rebars was computed as approximately 2.5 MPa regardless of the axial load level on the specimens. For comparison, Equation 3.10 gives relatively lower bond stress values of about 1.8 MPa for columns with a concrete strength of 20 MPa. Since Mylrea considered beams with no axial load, relatively lower levels of bond stresses for the columns under axial load was obtained. Hence, the suggested approach by Equation 3.10 gave reasonable estimations regarding Mylrea's approach.

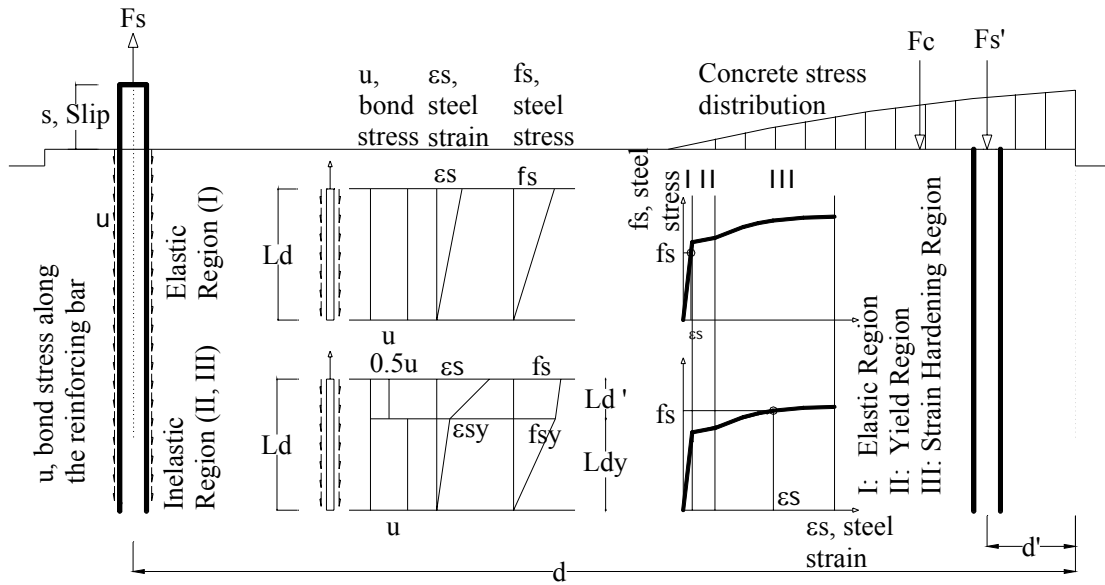


Figure 3.2 The bond-slip model

In Figure 3.2, the calculation method of reinforcement slip deformations for each strain increment is presented. The bond stress, steel stress-strain distribution is shown for elastic and inelastic strains over the reinforcing bar. The bond stress distribution along the development length is assumed uniform for elastic strains and bi-uniform for inelastic strains (Figure 3.2) [71, 72]. The reinforcement strains are linear until the reinforcement reaches the yield point. After yielding, a bilinear form of distribution is assumed. In bond calculations over the longitudinal reinforcing bar, the presence of 90-degree hooks was assumed to have the same behavior of sufficiently embedded straight bars such that both cases have the sufficient development length. Hence, when the rebar has an end hook, this bar can be treated as the hook plus the straight portion [73]. The longitudinal bar and hook at the footing level are therefore treated as a straight bar and the bond calculations are carried out employing this assumption. The equilibrium equations for elastic and inelastic regions are:

$$u \pi d_b L_d = f_s \frac{\pi d_b^2}{4} \quad \varepsilon_s \leq \varepsilon_y \quad (3.11a)$$

$$u \pi d_b L_d' = (f_s - f_y) \frac{\pi d_b^2}{4} \quad \varepsilon_s > \varepsilon_y \quad (3.11b)$$

where ε_s and ε_y is the strain and yield strain of reinforcement, f_s and f_y are the corresponding steel stresses. L_d , L_{dy} and L_d' are the development lengths at elastic and inelastic regions and d_b is the bar diameter as shown in Figure 3.2. The development lengths of elastic and inelastic regions are derived by using Equations 3.11a and 11b. Equation 3.12 shows the development lengths as a function of bond strength u , which is in turn a function of slip, s :

$$L_d = \frac{f_s d_b}{4u} \quad \varepsilon_s \leq \varepsilon_y \quad (3.12a)$$

$$L_d' = \frac{(f_s - f_y) d_b}{4u} \text{ and } L_{dy} = L_d - L_d' \quad \varepsilon_s > \varepsilon_y \quad (3.12b)$$

The slip deformations distributed along the reinforcing bar are calculated by integrating the steel strains over the development length (L_d), which yields the following equations:

$$s = \begin{cases} \frac{\varepsilon_s L_d}{2} & \varepsilon_s \leq \varepsilon_y \\ \frac{\varepsilon_s L_{dy}}{2} + \frac{L_d'}{2} (\varepsilon_s + \varepsilon_y) & \varepsilon_s > \varepsilon_y \end{cases} \quad (3.13)$$

Then substituting L_d and L_d' from Equation 5.12 into Equation 3.13 yields:

$$s = \begin{cases} \frac{\varepsilon_s f_s d_b}{8u} & \varepsilon_s \leq \varepsilon_y \\ \frac{d_b}{8u} \left[\varepsilon_s f_s + 2(\varepsilon_s + \varepsilon_y)(f_s - f_y) \right] & \varepsilon_s > \varepsilon_y \end{cases} \quad (3.14)$$

For prescribed steel strain, ε_s , bar slip, s , is obtained from Equation 3.14 and once s is known fixed end rotation is computed as [71]:

$$\theta_{fe} = \frac{s}{d - d'} \quad (3.15)$$

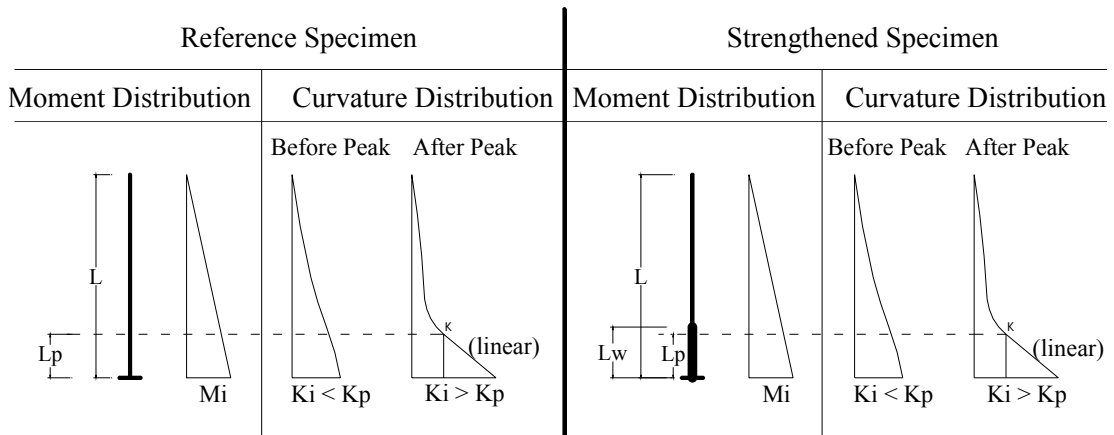
3.4. Tip Displacement Calculations

The tip displacement for a cantilever column can be found using:

$$\Delta = \theta_{fe}L + \int_0^L xK(x)dx \quad (3.16)$$

For each imposed curvature increment at the bottom of the column, base moment was found from the Moment (M) – Curvature (K) response and the corresponding lateral force was determined. The analytically obtained M – K responses are plotted against each series data as shown in Figures 2.24-2.28 for Series 1, Figures 2.45-2.49 for Series 2 and Figures 2.68-2.72 for Series 3. Flexural deformations (second term in Equation 3.16) were then computed by discretizing the column into a number of stations and integrating the curvatures obtained from moments corresponding to a linear bending moment diagram. The fact that stations can be unconfined or FRP confined was taken into account by using the appropriate *M-K* response for each station.

The curvature at each strip was calculated considering two regions: (1) before plastic hinging, (2) after plastic hinging as shown in Figure 3.3. Before the plastic hinge formed, the column does not exceed its peak moment. Therefore, the curvatures were interpolated using the ascending branch of the M vs. K curve. After the formation of the plastic hinge, the base curvature exceeds the curvature corresponding to the peak moment. There are several studies [74, 75] on plastic hinging length assumption for RC members however, for the sake of simplicity and regarding the experimental observations, the length of the plastic hinge was assumed equal to the depth of the section. The curvature distribution for the regions (1) and (2) is shown in Figure 3.3. In the plastic hinge region, the curvature distribution was modeled to be linear and at the end of the hinging region, the curvature corresponding to the interpolated moment was used. Consequently, for each level of incremental curvatures, fixed end rotation components and flexural deflection components were computed and added up in order to find the Lateral force (P) vs. Tip deflection (Δ) response of the columns.



K_i : Incremental curvatures assigned to the base of the column
 K : Curvature at the plastic hinge height
 K_p : Curvature at the peak moment
 M_p : Peak moment
 L_p : Plastic hinge length
 L_w : CFRP wrapped height

Figure 3.3 The plastic hinging model

3.5. Program Outputs and Experimental Comparisons

The program was used to estimate the Lateral Load (P) – Tip Deflection (Δ) behavior of all the columns in the experimental program including the repaired columns (Appendix E). Regarding the program outputs, the used constitutive material models and the bond-slip model were compared with the experimental data.

3.5.1. Series 1

In the reference specimen S-L-0-00, the analytical estimations follow the specimen envelope response well including the pre and post-peak behavior of the specimen. The estimation of the specimen response is in a close agreement until the onset of the bar buckling stage where the capacity degraded nearly to zero as shown in Figure 2.19. A similar behavior can be observed throughout the specimens S-L-1-00 and S-L-1-34. The column shear is underestimated in the post-peak region but the CFRP rupture points are estimated with a reasonably good accuracy for both specimens as shown in Figures 2.20 and 2.21. The specimen responses for S-L-2-00 and S-L-2-32 are overestimated in the post-peak regions but the overall responses are in reasonable agreement especially for the envelopes of negative loading cycles with the

experiments as shown in Figures 2.22 and 2.23. The reason of overestimation of the post-peak behavior of 2 layer CFRP wrapped columns (S-L-2-00 and S-L-2-32) can be due to the fact that FRP confined concrete model possess a hardening type behavior for the uniaxial compression response as the confinement ratio provided by the FRP jacket exceeds the transition value of confinement ratio, ϕ_t . In order to obtain superior estimations of moment capacity and lateral strength, it may be necessary to better estimate the transition value of hardening to softening response for FRP wrapped columns under axial compression by using analysis-oriented models [64, 65 and 69]. The analytical drift values that correspond to the CFRP rupture points are 7% and 6% respectively for S-L-2-00 and S-L-2-32 that are close to the experimental results. The overestimated and underestimated values can be improved by using further modification to the analytical model of the confined concrete and consequently a better response can be attained.

3.5.2. Series 2

The predicted envelope response for the reference specimen of Series 2 was in a good agreement with the monitored Lateral Force (P) – Deflection (Δ) hysteretic loops since the capacity and the ultimate drift levels of the column S-H-0-00 was estimated in a reasonable way as shown in Figure 2.40. The accuracy in estimating the overall response and the ultimate levels of strength and deflection can be interpreted due to the steel model considering the buckling of the longitudinal rebars that dominantly determines the ultimate behavior of the reference columns. For the 1-layer CFRP wrapped column S-H-1-00, the estimated envelope response was also in a reasonable agreement with the experimental data by estimating the drift levels at which the CFRP rupture took place (Figure 2.41). However, the response was overestimated about 10% for the push direction since the hysteretic curves were unsymmetrical. For the repaired columns S-HD-1-00 and S-HD-1-27, the envelope responses were also overestimated since both columns experienced damaging cycles that were not included in the analytical method as stated previously. However, the analytical drift level at which the CFRP ruptured, was predicted in a close agreement with the experimental observations (Figures 2.42 and 2.43). For the specimen S-HC-1-00, the envelope response for Lateral load (P) – Tip Deflection (Δ) was in better

agreement with the monitored data than in the repaired columns concerning the CFRP rupture drift levels and specimen strengths during the test as shown in Figure 2.44.

3.5.3. Series 3

The column performances in the last series were mostly over predicted since the shape of the column was changed to rectangular with a section aspect ratio of two. Considering the estimated Lateral Force (P) – Tip Deflection (Δ) envelope responses for the reference specimen R-NC-0-00, an overestimation regarding the peak lateral load was observed but the ultimate drift level at which the lateral capacity dropped to 80% of the peak was predicted in a reasonable accuracy (Figure 2.63). Whereas, for the strengthened columns R-HC-1-16P and R-MC-1-16P, since the confinement ratio improved by the help of the CFRP anchor dowels that were penetrated successfully into the borderline of the confined region (Figure 2.8b). Thus, the analytically obtained envelope curves were above the experimental envelopes except the specimen R-MC-1-16P as shown in Figures 2.64-2.67. The analytical CFRP rupture levels were predicted in a good accuracy. For the remaining columns R-MC-1-8P and R-MC-1-NP, the confined region of the concrete cross-sections was not changed since the CFRP anchor dowels could not penetrate into the confined borderline (Figure 2.8a), the analytical envelope responses concerned this assumption and the consequent curves overestimated the overall deflection responses as shown in Figures 2.65 and 2.66.

3.6. Parametric Study

The parametric study was conducted to observe the effects of CFRP thickness, column corner-rounding radius, axial load and longitudinal reinforcement buckling on the Lateral Force (P) – Tip Deflection (Δ), Moment (M) – Curvature (K) and Moment (M) – Fixed-End Rotation (FER) responses of the columns. Herein, an analytical reference specimen was selected with dimensions 350×350×2000 mm (width×depth×height) having longitudinal reinforcement of eight 18 mm diameter continuous rebars and transverse reinforcement of 10 mm diameter bars spacing at

200 mm. The concrete compressive strength was employed as 15 MPa. In order to observe the effects of aforementioned parameters on the column performance, each parameter was changed while the other parameters were held constant.

3.6.1. Effect of CFRP Thickness

The effect of CFRP thickness and resultant confinement efficiency was observed upon comparing specimens having constant corner rounding radius (CRR) of 30 mm and axial load (N) of 30% of the axial capacity. The reinforcement buckling was considered for the reference specimen that was regarded as unconfined. For the other cases namely the CFRP confined columns, the reinforcement buckling was not considered since the confining effect of the CFRP layers restrains the longitudinal bars from buckling. In the parametric study, one, two and three layers of CFRP wrapped specimens are compared by the reference specimen having no CFRP layers regarding that each CFRP layer had a thickness of 0.165 mm as used in the experimental program. Figure 3.4 shows the effect of CFRP layer number on column performances in terms of deflection, curvature and fixed-end rotation. The solid line represents the unwrapped specimen and the other dashed lines reflect the effects of wrapping the columns by 1, 2 and 3 layers of CFRP. From all the response data observed in Figure 3.4, it can be interpreted that increasing the number of CFRP layers led to an improvement in the seismic behavior of the CFRP wrapped columns. The confining effect of the CFRP layers resulted in consequent increase in ultimate drift, curvature and fixed-end rotations. The enhancement in seismic responses of the columns was observed more significantly upon observing the 2 and 3 layer CFRP wrapped specimens since the improvement in behavior was higher than the 1-layer wrapped specimen. A similar behavior can be observed with the test results since a comparable improvement in strength and drift capacities was observed in experimental test series. The fixed-end rotations were fixed after the longitudinal strain values started to recede and resulted in lower levels of fixed-end rotation.

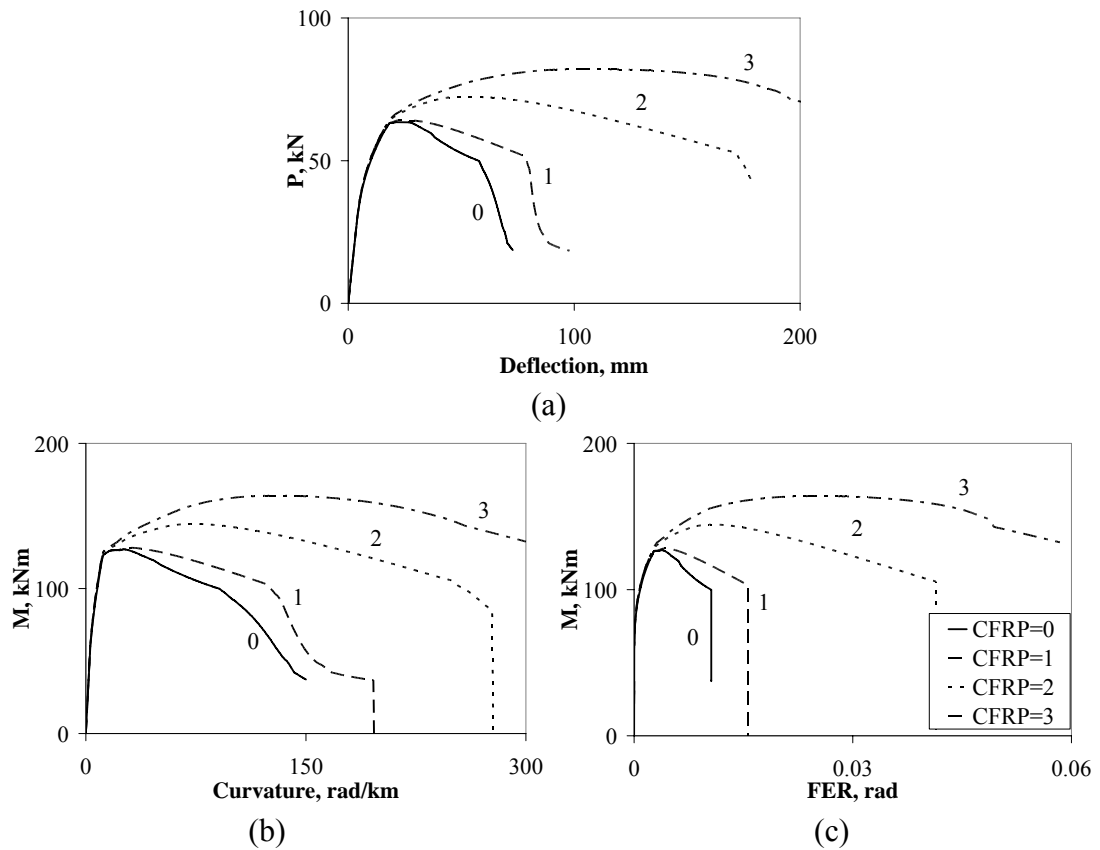


Figure 3.4 Effect of CFRP layers on (a) Lateral Load (P)-Tip Deflection (Δ), (b) Moment (M) - Curvature (K) and (c) Moment (M) - Fixed-end Rotation (FER)

3.6.2. Effect of Column Corner Rounding Radius

The parameter of column corner-rounding radius (CRR) was observed to have a significant effect on the seismic performance of the reinforced concrete columns as shown in Series 2 columns S-H-1-00 and S-HC-1-00 since the column S-HC-1-00 had a reduced corner-rounding radius of 10 mm as compared to its companion specimen having 30 mm of rounding radius. The effects of using 10, 30 and 50 mm of corner-rounding radius was investigated and discussed by comparing their deflection, curvature and fixed-end rotation responses with corresponding lateral load levels. The effect of reinforcement buckling was not concerned since the observed columns were wrapped with CFRP. As can be observed from Figure 3.5, increasing the corner-rounding radius led to a substantial improvement in the seismic

behavior of reinforced concrete columns. The confining effect of CFRP was improved with the increase in corner-rounding radius while the CFRP confined area in the column cross-section enhances. The increase in ultimate deflection, curvature and fixed-end rotation responses had a linear trend with the increase in the corner-rounding radius. The same fixation of the fixed-end rotations was applied before the longitudinal strains started to decrease. Herein, while the corner-rounding radius increased, the fixated rotation values were also enhanced due to the increase in confinement efficiency and consequent confinement ratio.

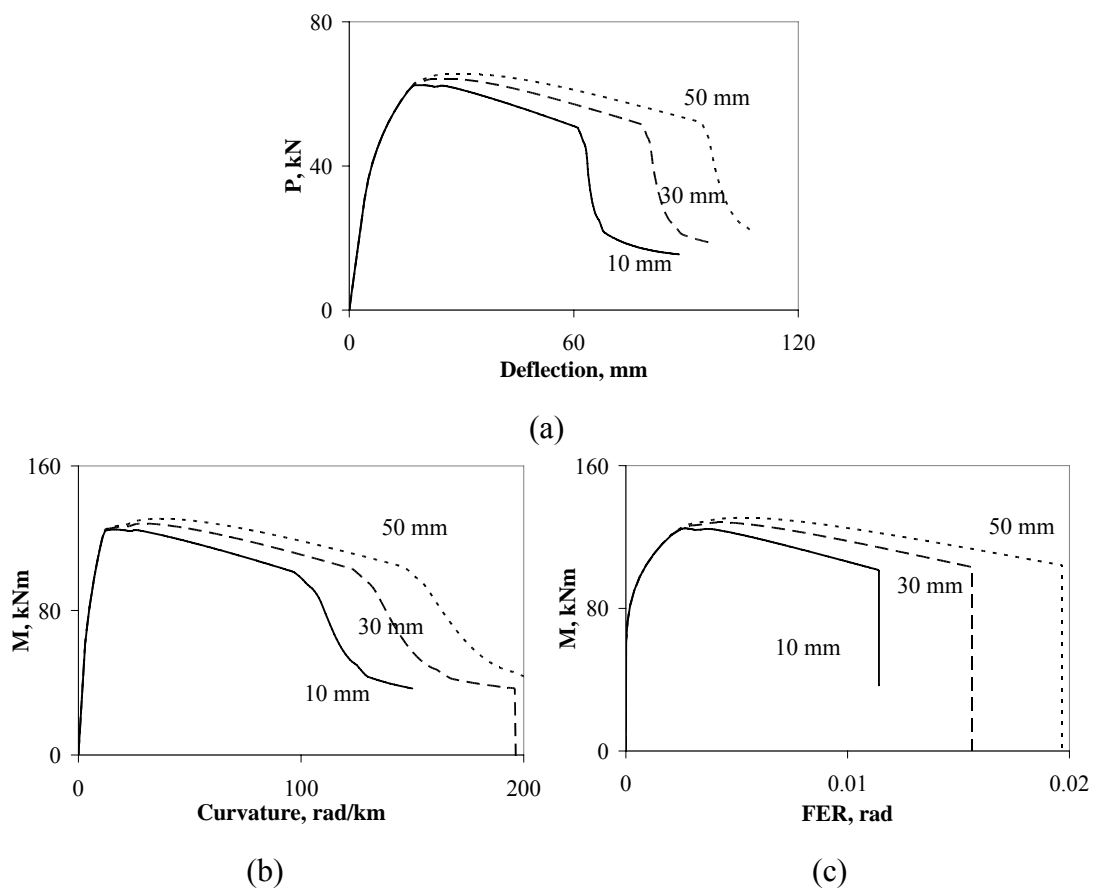


Figure 3.5 Effect of corner-rounding radius on (a) Lateral Load (P) – Tip Deflection (Δ), (b) Moment (M) – Curvature (K) and (c) Moment (M) – Fixed-end Rotation (FER) responses

3.6.3. Effect of Axial Load

The level of axial load was held constant throughout the entire test series with an approximate level of 30% of the axial capacity whereas its effect was not discussed in the experimental part of this study. Herein, by the analytical procedure, the effect of axial load was investigated by applying 1 layer of CFRP and 30 mm of corner-rounding radius to the analytical reference specimen. The influence of longitudinal bar buckling was ignored since all the observed specimens were CFRP confined. The axial load levels of 0%, 30% and 60% of axial capacity were selected regarding the unloaded, moderately loaded and heavily loaded cases, respectively. Figure 3.6 illustrates that the columns having no axial load typically exhibited beam behavior for all cases for deflection, curvature and fixed-end rotation responses.

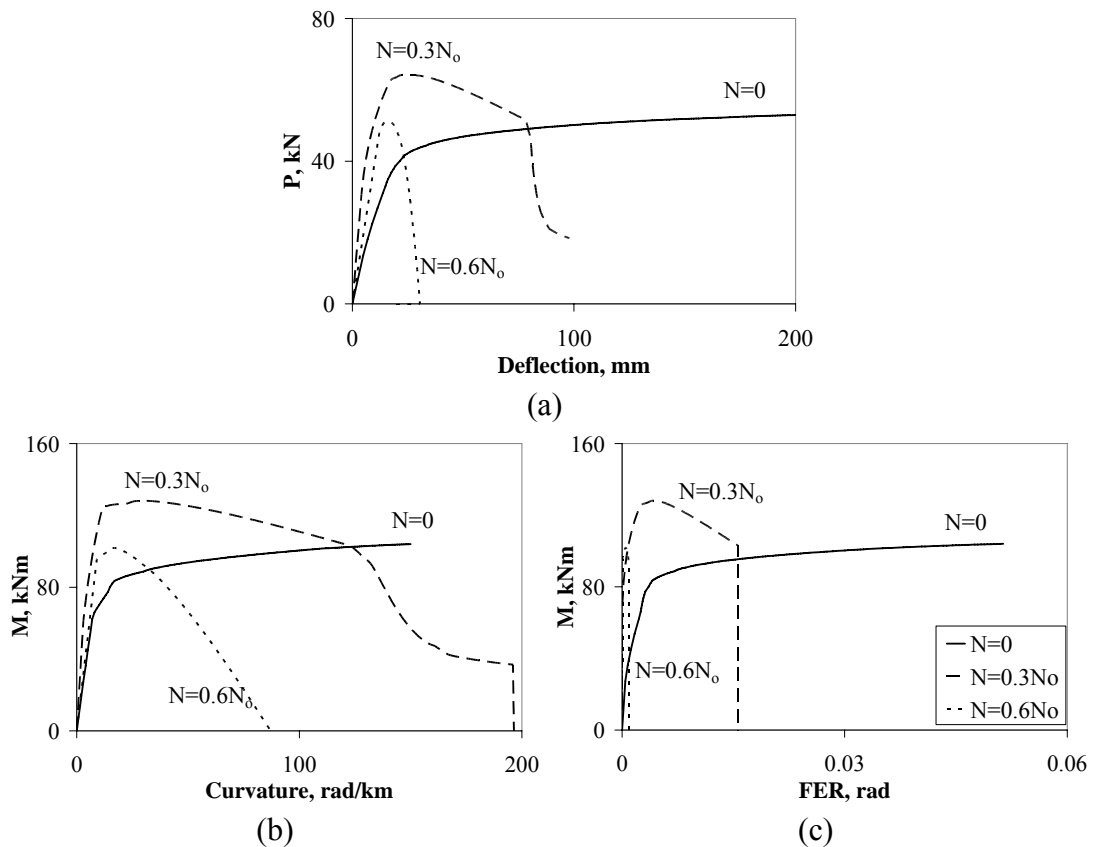


Figure 3.6 Effect of axial load on (a) Lateral Load (P) – Tip Deflection (Δ), (b) Moment (M) – Curvature (K) and (c) Moment (M) – Fixed - End Rotation (FER)

Whereas, increasing the axial load level to 30% of the axial capacity led to an improvement in column strength but a decrease in attained drift levels. The curvature response for the column having an axial load of 30% of axial capacity reduced after approaching to beam response and the axial load enforced the columns to fail at that level. The fixed-end rotation response for the columns having a moderate level of axial load was about one-third of the column having a beam response since the axial load level restrained the longitudinal bars from slipping and extending. For the column having the maximum level of axial load about 60% of its axial capacity, the deflection and curvature responses were the worst among all specimens and this column experienced almost no fixed-end rotation response. Since the axial load on the column was high, no slipping or extension of the longitudinal bars was observed.

3.6.4. Effect of Reinforcement Buckling

The effects of longitudinal bar buckling on the columns were investigated upon comparing one layer CFRP wrapped specimens having a corner rounding radius of 30 mm and an axial load level of 30% of the axial capacity. Since the longitudinal bars in compression could not exhibit a similar response compared to the bars in tension due to premature buckling, the lateral capacity of the columns degrades dramatically. The adverse effect of buckling of longitudinal reinforcement on the deflection, curvature and fixed-end rotation responses of the columns can be observed in Figure 3.7. The buckling of the reinforcement worsened the seismic performance of the columns since it degraded the ultimate drift ratio. Furthermore, the curvatures were also degraded in the case of bar buckling was not considered.

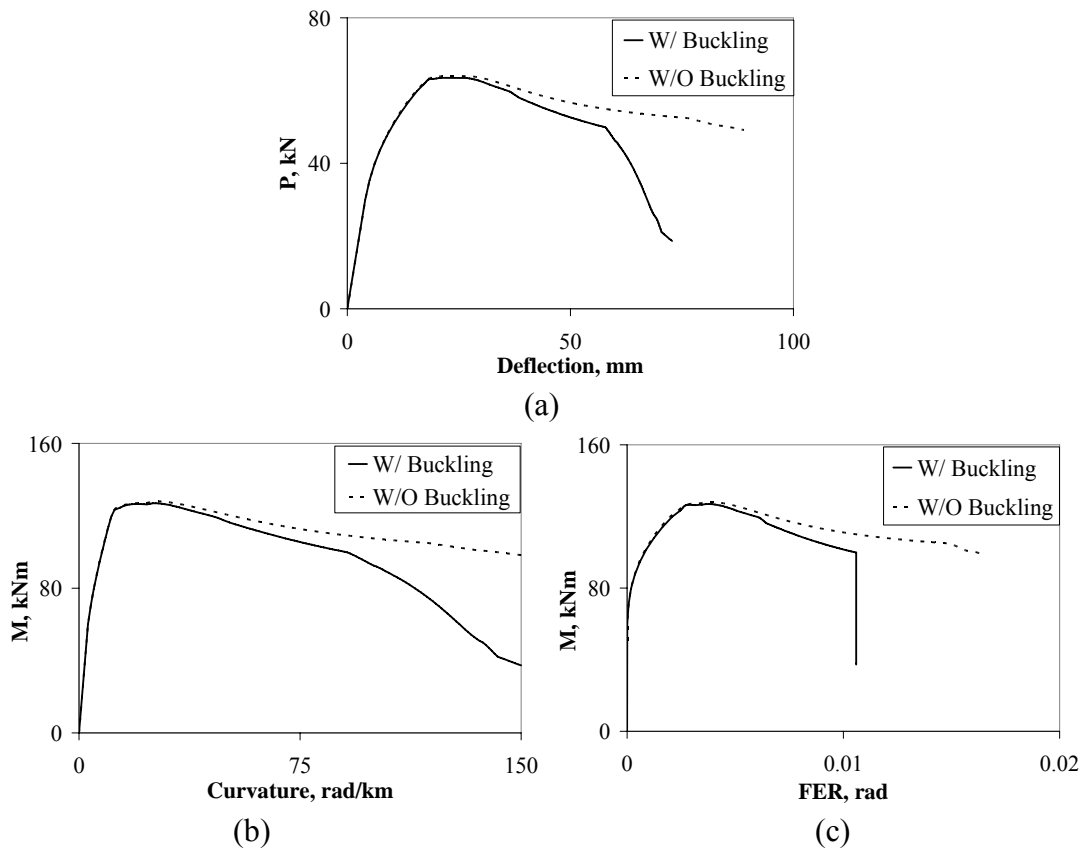


Figure 3.7 Effect of longitudinal bar buckling on (a) Lateral Load (P) – Tip Deflection (Δ), (b) Moment (M) – Curvature (K) and (c) Moment (M) – Fixed-end Rotation (FER) responses

CHAPTER 4

DESIGN-ORIENTED STUDIES

4.1. Introduction

In addition to the analytical based methods that provides estimates of the response envelopes for as-built or FRP strengthened columns, design – oriented methods should also be applied in order to predict the ultimate behavior of RC columns in a simpler way. This study on design – oriented methods focuses on estimating the ultimate drift ratios of as-built and FRP strengthened square or rectangular columns. In addition, some previous methods and design guidelines that are used to predict the ultimate drift ratios and ultimate ductility are also discussed.

4.2. Previous Research

In order to design FRP jackets that confine rectangular or square column sections, proper selection of the column parameters should be made regarding the observed displacement demands for the columns. The design guidelines for steel confined columns given in Canadian Standards Association (CSA S806-02) [76] are based on mainly as proposed by Saatcioglu and Razvi [77] that considers lateral drift as the performance criterion. The lateral drift capacities of RC columns for various section shapes are calculated for different levels of confinement and axial load. The study reported herein does not consider retrofitting for the failures caused by either splicing regions or shear. As shown in Equation 4.1a, based on the strategy of retrofitting for concrete confinement, the transverse confinement in columns is acquired by the parameters of concrete compressive strength (f_c'), transverse steel yield stress (f_{yh}), ratio of unconfined to confined regions ($\frac{A_g}{A_c} - 1$), axial load level ($\frac{P_f}{P_{ro}}$), attained drift demand (δ) and the confinement efficiency factor (k_s). For the cases of which the column does not have a cover concrete, the ratio $\frac{A_g}{A_c} - 1$ approaches zero and hence it

is replaced by a limiting factor of 0.3 as shown in Equation 4.1b. The axial load level $\frac{P_f}{P_{ro}}$ is also factored in order to sustain column design limits used in practice.

$$\rho_c = 14 \frac{f_c'}{f_{yh}} \left[\frac{A_g}{A_c} - 1 \right] \frac{P_f}{P_{ro}} \frac{\delta}{\sqrt{k_s}} \quad (4.1a)$$

$$\frac{A_g}{A_c} - 1 \geq 0.3 \quad \text{and} \quad \frac{P_f}{P_{ro}} \geq 0.2 \quad (4.1b)$$

Equations 4.1a and 4.1b can also be adapted to the FRP confined columns having rectangular [78] or circular cross-sections [79]. For the FRP wrapped sections, the cover concrete is not present hence; the ratio of unconfined to confined region is zero. Thus, this factor is replaced by the minimum value for which the Equations 4.2a and 4.2b were derived. For the case of FRP wrapped sections, the previously affirmed equations for steel confined columns can be written in a similar arrangement with the CSA S806-02.

$$t_j = 2D \frac{f_c'}{f_{Fj}} \frac{P_f}{P_{ro}} \frac{\delta}{\sqrt{k_s}} \quad (4.2a)$$

$$\frac{P_f}{P_{ro}} \geq 0.2 \quad (4.2b)$$

where t_j represents the thickness of the FRP sheet, D is the diameter or the height of the column cross-section and f_{Fj} stands for the rupture stress of FRP. The k_s parameter differs from Equation 4.1a in which the confinement efficiency is evaluated for FRP wrapped sections. In square or rectangular columns, the confinement efficiency factor is equivalent to the columns with perimeter ties only and rounding the column corners will increase the value of k_s . In the calculation of the axial load ratio $\frac{P_f}{P_{ro}}$, the material safety factors should be used (Equation 4.2b) owing to the superiority of nominal lateral drift capacities over design drift levels [76].

For design purposes, the inelastic drift demand of the structure should be evaluated considering the target drift levels for the FRP retrofitted columns. Depending on the column parameters such as confinement efficiency, axial load level and concrete strength, the acquired strength gain was observed to have a degrading behavior beyond a transverse strain of 0.004. Thus, a conservative limit of FRP design strength is employed as $0.004E_f$ for f_{Fj} where E_f represents the elasticity modulus of the FRP jacket as proposed by Elnabelsy et al. Conservative predictions were obtained against the test data that included square and rectangular columns [78].

Sheikh and Li [80] proposed a design based methodology on FRP confined square columns to enhance their seismic resistance, which was an extension of the previous research on design of confining steel in square RC columns by Sheikh and Khoury [81]. Concerning the same design philosophy, the required amount of confining FRP was calculated for a specific ductility performance designated in advance regarding the axial load level and the properties of FRP. The design procedure was developed for columns having continuous longitudinal reinforcement in plastic hinge regions and having the same amount of transverse reinforcement (Iacobucci et al. [45] and Memon et al. [82]). Sheikh and Khoury [81] proposed Equations 4.3a and 4.3b for steel confined columns that were shown below.

$$\rho_c = \frac{A_{sh}}{sh_c} = 0.3\alpha \left[\frac{A_g}{A_{ch}} - 1 \right] \frac{f_c'}{f_{yh}} Y_p Y_\phi \geq 0.09\alpha \frac{f_c'}{f_{yh}} Y_p Y_\phi \quad (4.3a)$$

$$Y_p = 6 \frac{P}{P_0} - 1.4 \geq 1, Y_\phi = \frac{\mu_{\phi 80}}{18} \quad (4.3b)$$

where A_{sh} is the area of transverse reinforcement, α is the confinement efficiency parameter, s is tie spacing and h_c is the dimension of concrete core measured to the outside of perimeter tie. The factor $\frac{A_g}{A_{ch}} - 1$ is the ratio of unconfined area to confined area. The concrete compressive strength and the transverse steel yield strength are termed as f_c' and f_{yh} respectively. The parameters of Y_p and Y_f designate the axial load and ductility parameters in which $\frac{P}{P_0}$ is the axial load level, $\mu_{\phi 80}$ is the curvature

ductility considering 80% of the maximum moment. These equations were modified for FRP confined columns by introducing the parameters of n , f_u and β that were the number of FRP layers, ultimate FRP stress and confinement efficiency factor respectively as shown in Equations 4.4a and 4b.

$$n = h \frac{f_c'}{f_u} \left[6 \frac{P}{P_0} - 1.4 \right] \frac{\mu_{\phi 80, in}}{18} \beta \quad (4.4a)$$

$$\frac{P}{P_0} \geq 0.4 \quad (4.4b)$$

where h is the cross-section dimension of the column and $\mu_{\phi 80, in}$ is the curvature ductility difference between FRP confined and control columns. The similarity between the design equations and the design limits considering the axial load levels can be seen in Equations 4.3a and 4.4a. There are primarily four parameters observed interrelating ultimate behavior of columns and the required amount of FRP that are column dimensions, strength ratio of concrete to FRP, axial load level and confinement efficiency. The product of these parameters with correlated terms predicted the behavior of columns accurately for the used column databases. However, none of the aforementioned design methods concerns designing FRP wrapped rectangular sections regarding longitudinal reinforcement ratios, axial load levels and confinement ratios together. In the light of these pre-specified design parameters, a design equation for FRP retrofitting of rectangular reinforced concrete columns is proposed.

4.3. Proposed Design Procedure

4.3.1. Ultimate Drift Based: Method I

Since this study investigates the behavior of flexural dominant RC columns with rectangular cross-sections, the drift-based design methods need to be generalized for various section aspect ratios, longitudinal reinforcement ratios, axial load levels and confinement ratios. Concerning these inadequacies in predicting ultimate drift levels of flexural columns, a column database containing square and rectangular columns

with various cross-section dimensions, corner rounding radii and transverse reinforcement ratios was acquired. In order to predict the ultimate drift ratios at which the lateral resistance dropped 80% of the peak, three parameters were employed as the ratios of longitudinal reinforcement, axial load and confinement. The column database is shown in Tables 4.1 and 4.2. 21 columns were CFRP wrapped out of 28 FRP strengthened columns and the remaining ones were strengthened with GFRP. In the database, plain and deformed bars were used as longitudinal reinforcement and the FRP wrapped section heights were in a range from 500 to 610 mm. Besides, the cross-section dimensions and the material properties for concrete, steel and FRP were shown. The axial load level, n , was calculated as shown in Equation 4.5.

$$n = \frac{N}{N_0} = \frac{N}{0.85 f_c' A_g + A_{st} f_y} \quad (4.5)$$

where N is the applied axial load on the column and N_0 is the nominal axial capacity of the columns. A_g is the cross-section area of the column, A_{st} is the total steel area and f_y represents the longitudinal steel yield stress. The confinement efficiency factor K_e and the confinement ratio ϕ are evaluated by using Equations 3.2a and b. Knowing these parameters for design purposes, the design drift levels are predicted by using nonlinear regression analysis. The parameters of longitudinal steel ratio (ρ), axial load ratio (n) and confinement ratio (ϕ) are used to obtain ultimate drift levels (DR_u) for the columns at which the lateral resistance dropped to 80% of the peak. According to the regression analysis, the design equation is obtained in the form as shown in Equation 4.6. Besides, this equation is simplified for the ease of usage and presented in Equation 4.7 that predicts the lower bound of the ultimate drift ratio.

$$DR_u = 2.47 + 50 \frac{\phi^{0.64}}{n^{0.35} \rho^{1.29}} \quad (4.6)$$

$$DR_u = 2 + 4.5 \frac{\phi}{n\rho} \quad (4.7)$$

$$\frac{\phi}{n\rho} > 0.05$$

where ρ , ϕ and n are in percents.

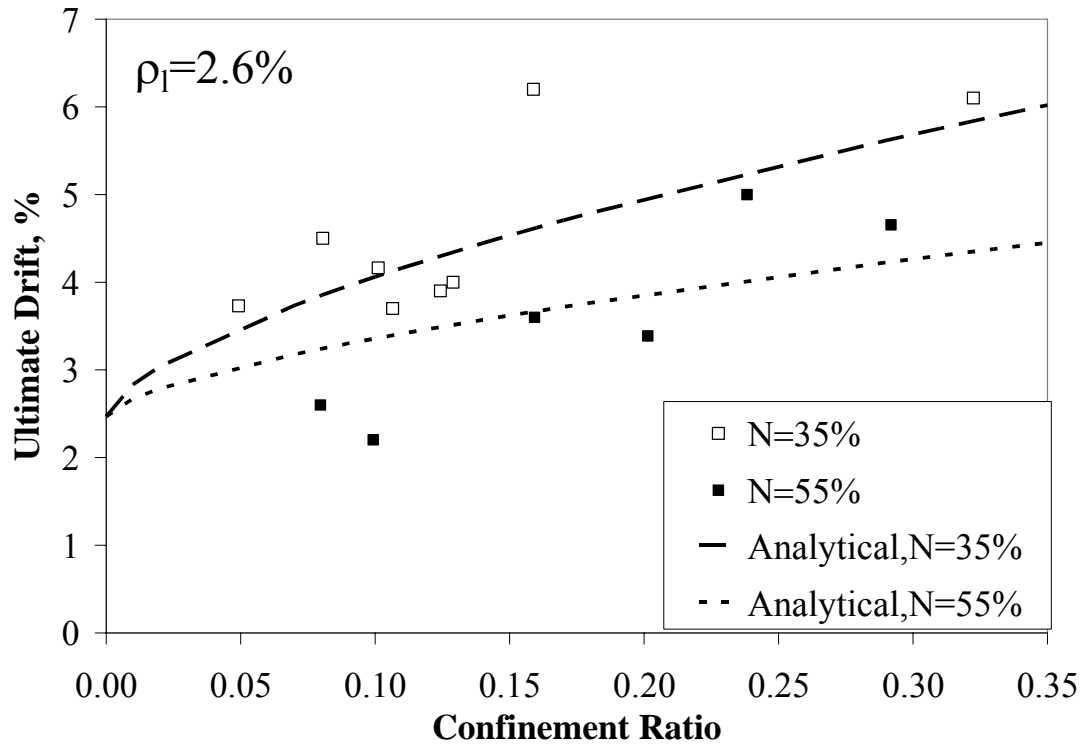
The predicted values of ultimate drift levels are shown in Tables 4.1 and 4.2 with the calculated design parameters of the column database. In Equation 4.6, it can be stated that the ultimate drift level that a column can sustain is proportional to the confinement factor, ϕ that is provided by the amount of FRP. In Figures 4.1a and 4.1b, it is proved that increasing the confinement ratio led to an increase in ultimate drift ratios considering different axial load levels of 35% and 55% and the longitudinal reinforcement ratios ranging from 0.8% to 2.7%. The effect of axial load is investigated throughout the experiments with an adverse influence on sustainable ultimate drift levels. This expected behavior regarding different confinement levels and longitudinal reinforcement ratios is plotted in Figures 4.2a and 4.2b. The confinement levels stated in the mentioned graphical data includes low confinement level ranging from 0 to 0.13, moderate confinement level ranging from 0.13 to 0.29 and high confinement level that has a range from 0.29 to 0.69. Figure 4.2a also illustrates the effect of longitudinal reinforcement ratio for the moderate level of confinement that has a range from 0.13 to 0.29 and the borderlines for different confinement levels. These two couples of lines represent upper and lower limits for moderate confinement level having different longitudinal reinforcement ratio. For both cases, namely the columns having various longitudinal reinforcement ratio and confinement ratio, the attainable ultimate drift ratios tend to reduce for amplified axial load levels. Additionally, the adverse effect of longitudinal reinforcement ratio ρ_l , on ultimate drift ratios can be observed for different levels of axial load and confinement ratios. This fact can be observed in the graphs in Figure 4.3a. For the moderate level of confinement ratio, the attained drift levels have a tendency to degrade as the longitudinal reinforcement ratio increases. This phenomenon was proved for various levels of axial loads ranging from 35% to 55%. In the first graph of Figure 4.3a having moderate confinement level, the curves for the axial loads of 35% and 55% almost coincide since Equation 4.6 gives very close results for both cases. In addition, the same trend can be monitored at a constant level of axial load at 35% with different confinement levels. The boundaries between the confinement levels ranging from low to high are shown in Figure 4.3b and the adverse effect of longitudinal reinforcement ratio can also be observed throughout these tests. The predicted and experimental ultimate drift ratios obtained by using CSA S806-02 [76], Equations 4.6 and 4.7 are illustrated in Figures 4.4 - 4.6, respectively.

Table 4.1 Results for the used database

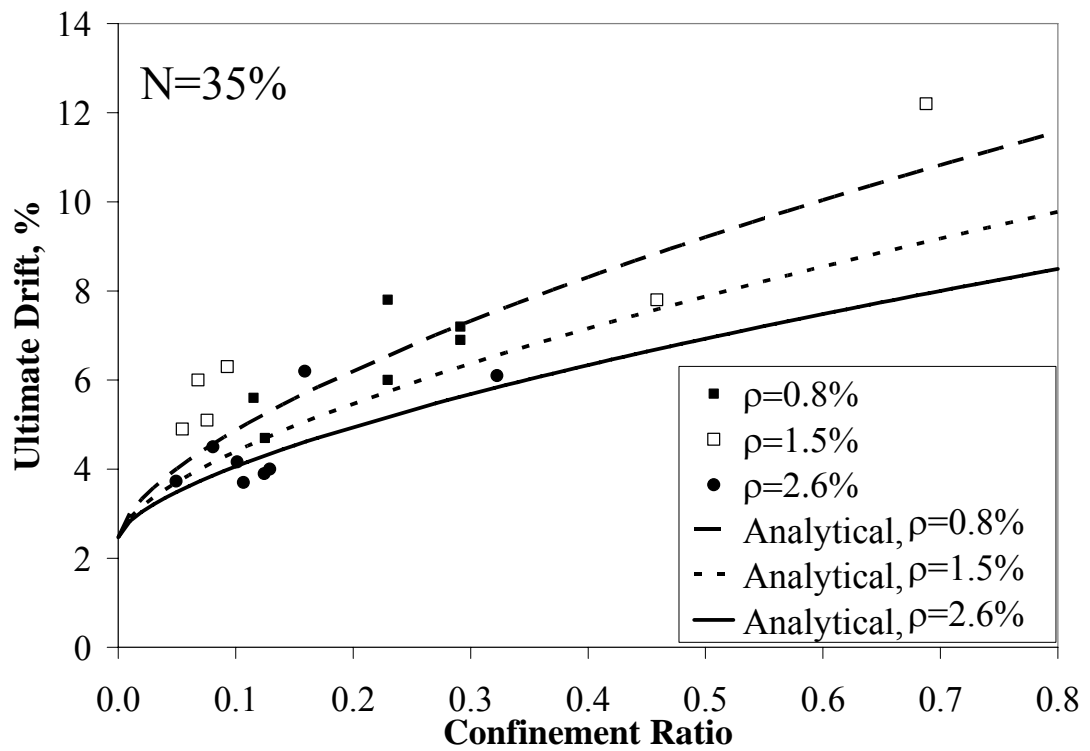
Research	b	h	L	r	f _c '	A _{st}	f _y	E _j	ε _f	t _j	K _e	ρ	n	φ	DR _u	Eq. 4.2		Eq. 4.6		Eq. 4.7	
																DR _{u,p}	DR _u / DR _{u,p}	DR _{u,p}	DR _u / DR _{u,p}	DR _{u,p}	DR _u / DR _{u,p}
	mm	mm	mm	mm	MPa	mm ²	MPa	MPa		mm			%		%	%		%		%	
Bousias et al. [47]	250	500	1600	30	18.1	1017.9	559.5	230000	0.015	0.26	0.387	0.81	34	0.115	5.6	2.45	2.29	5.23	1.07	3.90	1.44
	250	500	1600	30	16.7	1017.9	559.5	230000	0.015	0.26	0.387	0.81	36	0.125	4.7	2.50	1.88	5.16	0.91	3.94	1.19
	250	500	1600	30	17.9	1017.9	559.5	230000	0.015	0.65	0.387	0.81	35	0.291	6.9	5.89	1.17	7.15	0.96	6.56	1.05
	500	250	1600	30	17.9	1017.9	559.5	230000	0.015	0.65	0.387	0.81	35	0.291	7.2	11.78	0.61	7.15	1.01	6.56	1.10
	250	500	1600	30	18.7	1017.9	559.5	70000	0.031	0.85	0.387	0.81	34	0.229	6.0	2.34	2.56	6.72	0.89	5.75	1.04
	500	250	1600	30	18.7	1017.9	559.5	70000	0.031	0.85	0.387	0.81	34	0.229	7.8	4.68	1.67	6.72	1.16	5.75	1.36
Iacobucci et al. [45]	305	305	1473	16	36.5	2513.3	465	76350	0.013	1.00	0.466	2.70	33	0.081	4.5	2.84	1.59	3.94	1.14	2.41	1.87
	305	305	1473	16	36.9	2513.3	465	76350	0.013	2.00	0.466	2.70	56	0.159	3.6	3.31	1.09	3.62	0.99	2.47	1.46
	305	305	1473	16	36.9	2513.3	465	76350	0.013	1.00	0.466	2.70	56	0.080	2.6	1.65	1.57	3.21	0.81	2.24	1.16
	305	305	1473	16	37.0	2513.3	465	76350	0.013	3.00	0.466	2.70	56	0.238	5.0	4.95	1.01	3.96	1.26	2.71	1.85
	305	305	1473	16	37.0	2513.3	465	76350	0.013	2.00	0.466	2.70	33	0.159	6.2	5.60	1.11	4.75	1.31	2.80	2.21
Sause et al. [48]	458	458	2419	45	24.8	3096.6	460	76200	0.015	6.00	0.570	1.48	29	0.688	12.2	20.79	0.59	10.88	1.12	9.18	1.33
	458	458	2419	45	24.8	3096.6	460	76200	0.015	4.00	0.570	1.48	29	0.459	7.8	13.86	0.56	8.96	0.87	6.78	1.15
Memon et al. [82]	305	305	1473	16	42.5	2450.4	465	24693	0.023	2.50	0.466	2.63	33	0.101	4.2	1.96	2.12	4.18	0.99	2.52	1.65
	305	305	1473	16	42.7	2450.4	465	24693	0.023	5.00	0.466	2.63	55	0.201	3.4	2.34	1.45	3.84	0.88	2.62	1.29
	305	305	1473	16	43.3	2450.4	465	24693	0.023	2.50	0.466	2.63	55	0.099	2.2	1.16	1.89	3.35	0.66	2.31	0.95
	305	305	1473	16	43.7	2450.4	465	24693	0.023	1.25	0.466	2.63	32	0.049	3.7	0.97	3.83	3.58	1.04	2.26	1.65
	305	305	1473	16	44.2	2450.4	465	24693	0.023	7.50	0.466	2.63	54	0.292	4.7	3.48	1.34	4.27	1.09	2.92	1.59

Table 4.2 Results for the experimental study

Research	b	h	L	r	f _c '	A _{st}	f _y	E _j	ε _f	t _j	K _e	ρ	n	φ	DR _u	Eq. 4.2		Eq. 4.6		Eq. 4.7	
																DR _{u,p}	DR _u / DR _{u,p}	DR _{u,p}	DR _u / DR _{u,p}	DR _{u,p}	DR _u / DR _{u,p}
	mm	mm	mm	mm	MPa	mm ²	MPa	MPa		mm			%		%	%		%		%	
This Study	350	350	2000	30	19.4	2035.8	287	230000	0.015	0.165	0.542	1.66	27	0.091	4.9	3.06	1.60	4.93	0.99	2.92	1.68
	350	350	2000	30	14.0	2035.8	287	230000	0.015	0.165	0.542	1.66	34	0.126	5.1	3.33	1.53	4.69	1.09	3.00	1.70
	350	350	2000	30	11.4	2035.8	287	230000	0.015	0.33	0.542	1.66	40	0.309	6.3	7.09	0.89	5.75	1.10	4.12	1.53
	350	350	2000	30	15.6	2035.8	287	230000	0.015	0.33	0.542	1.66	32	0.226	6.0	6.46	0.93	6.04	0.99	3.93	1.53
	350	350	2000	30	20.0	3041.1	287	230000	0.015	0.165	0.542	2.48	27	0.088	4.1	2.96	1.39	4.56	0.90	2.59	1.58
	350	350	2000	10	22.0	3041.1	287	230000	0.015	0.165	0.407	2.48	27	0.060	3.6	2.33	1.55	4.10	0.88	2.40	1.50
	200	400	2000	30	10.0	2035.8	287	230000	0.015	0.165	0.755	2.54	35	0.322	6.1	4.71	1.29	5.86	1.04	3.63	1.68
	200	400	2000	30	10.5	2035.8	287	230000	0.015	0.165	0.437	2.54	35	0.178	3.7	3.41	1.08	4.79	0.77	2.90	1.28
	200	400	2000	30	9.0	2035.8	287	230000	0.015	0.165	0.437	2.54	35	0.207	3.9	3.98	0.98	5.03	0.78	3.05	1.28
	200	400	2000	30	15.0	2035.8	287	230000	0.015	0.165	0.755	2.54	35	0.215	4.0	3.14	1.27	5.09	0.79	3.09	1.30

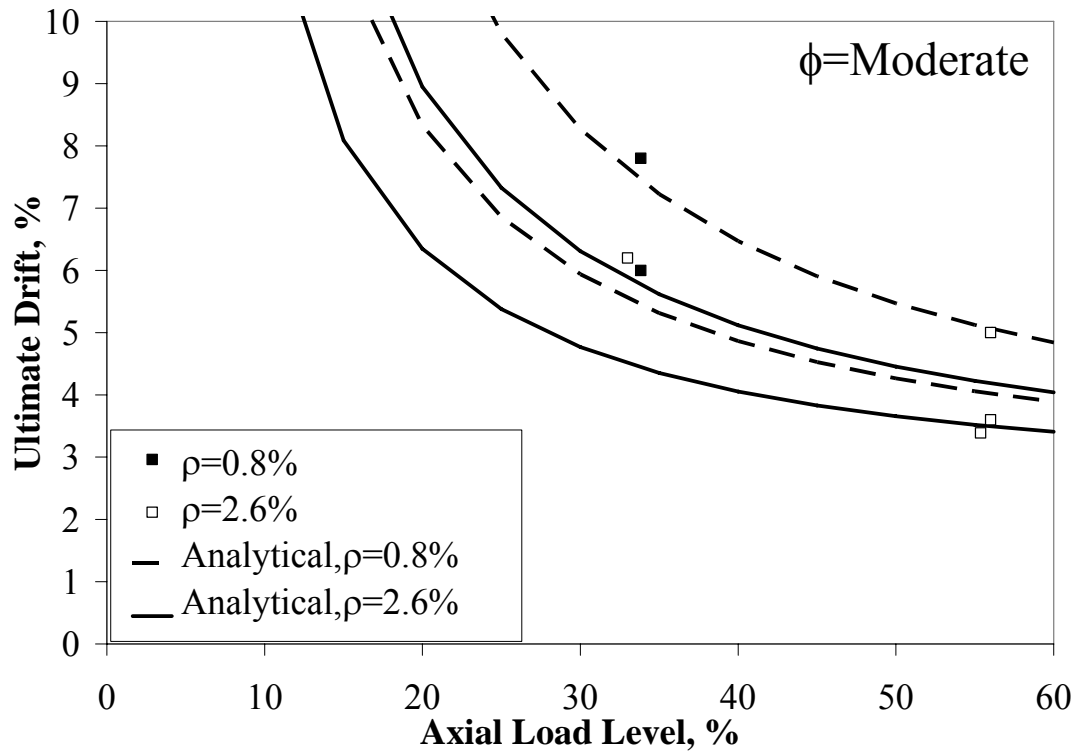


(a)

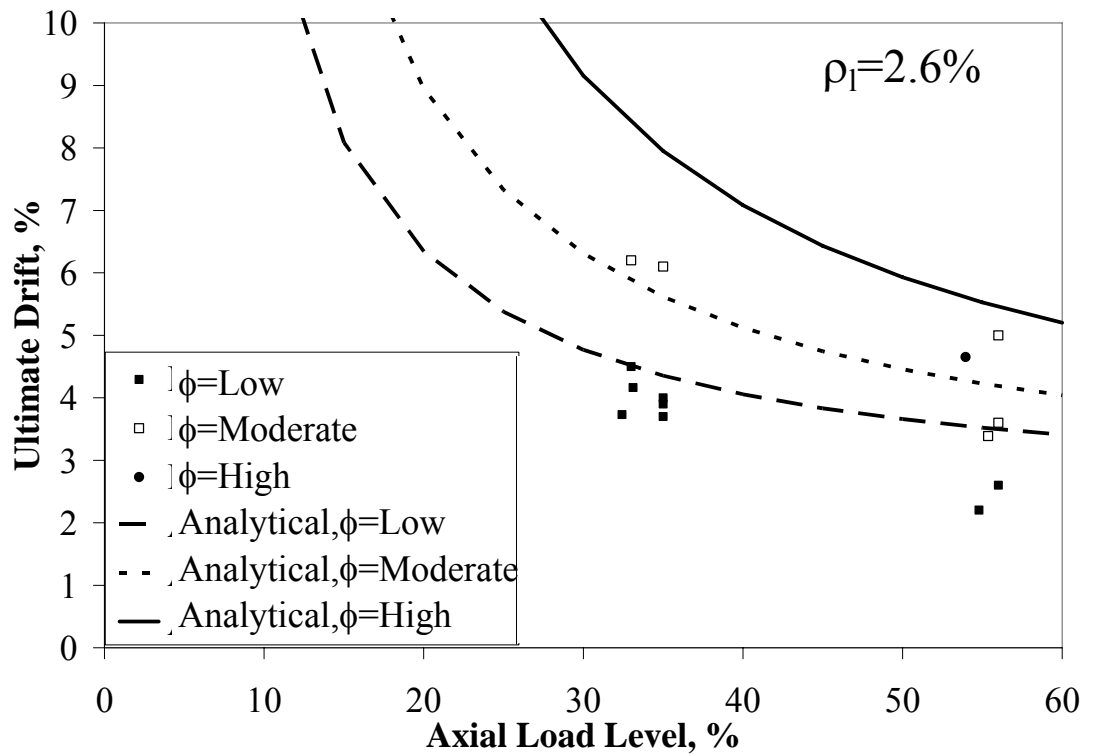


(b)

Figure 4.1 Best-fit drift equation compared with experimental data in confinement ratio basis for constant (a) longitudinal reinforcement ratio and (b) axial load.

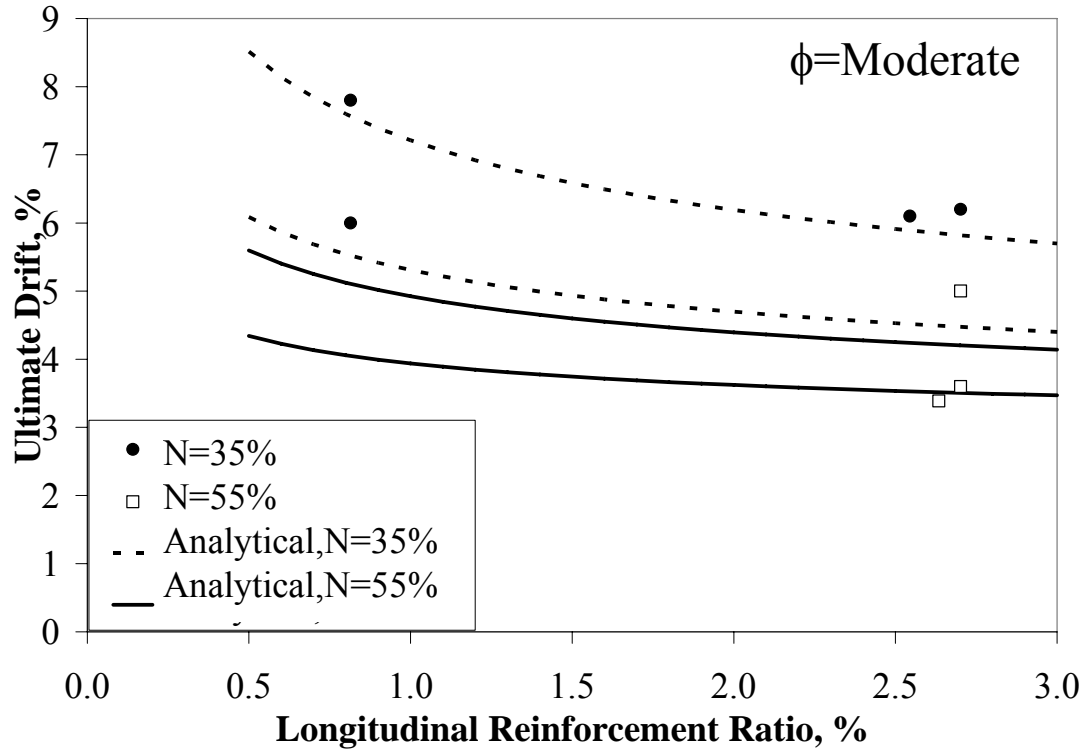


(a)

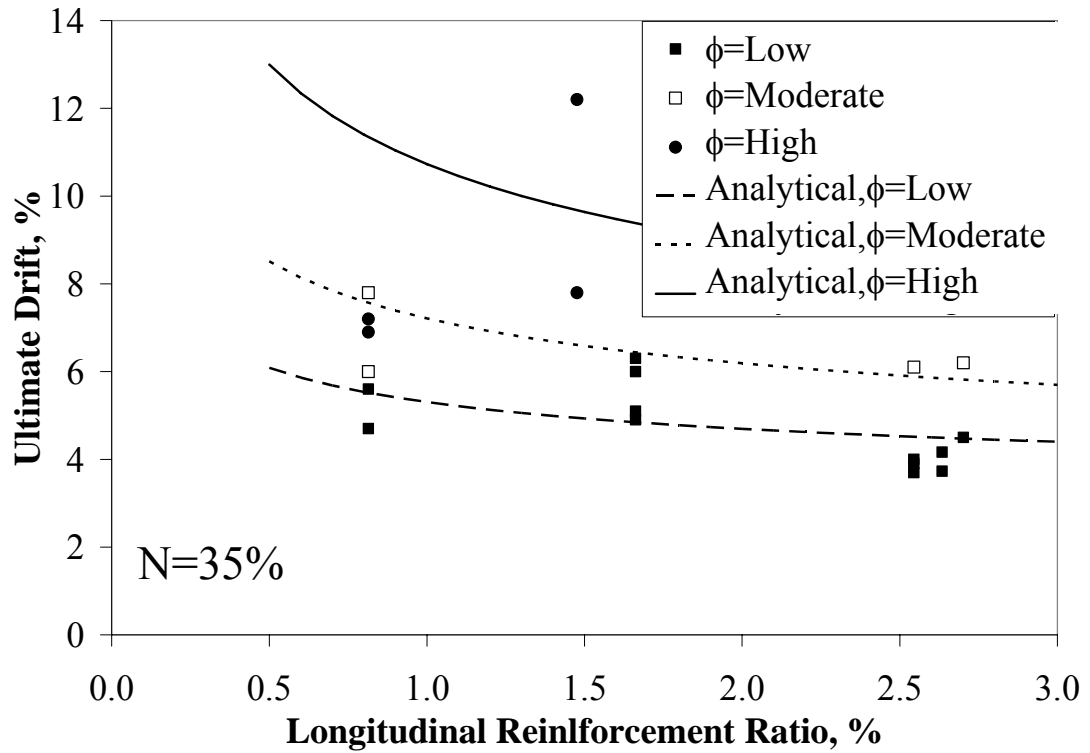


(b)

Figure 4.2 Best-fit drift equation compared with experimental data in axial load basis for constant (a) confinement ratio and (b) longitudinal reinforcement ratio.



(a)



(b)

Figure 4.3 Best-fit drift equation compared with experimental data in longitudinal reinforcement ratio basis for constant (a) confinement ratio and (b) axial load.

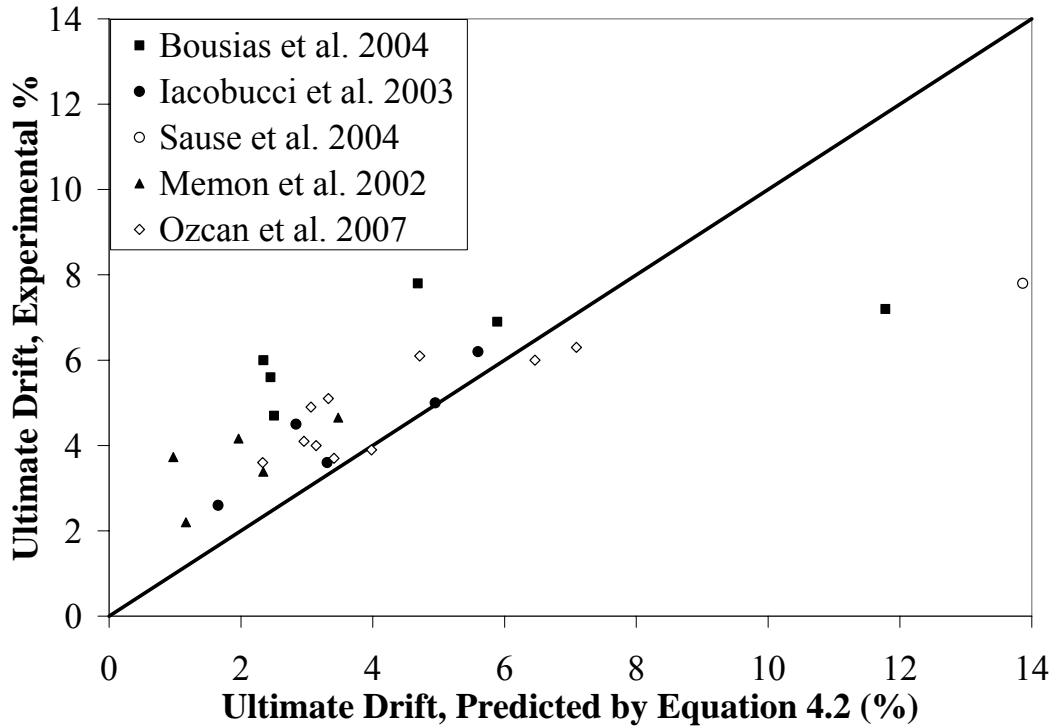


Figure 4.4 Predicted results by nonlinear regression analysis for CSA S806-02 equation

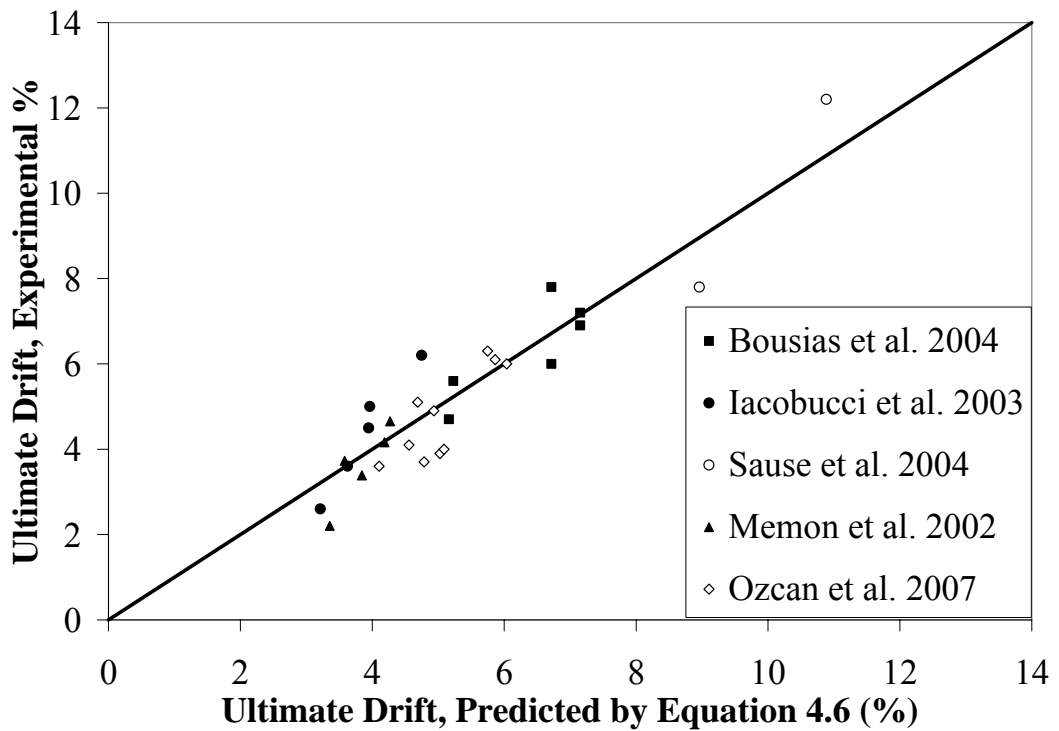


Figure 4.5 Predicted results by nonlinear regression analysis for proposed best-fit equation

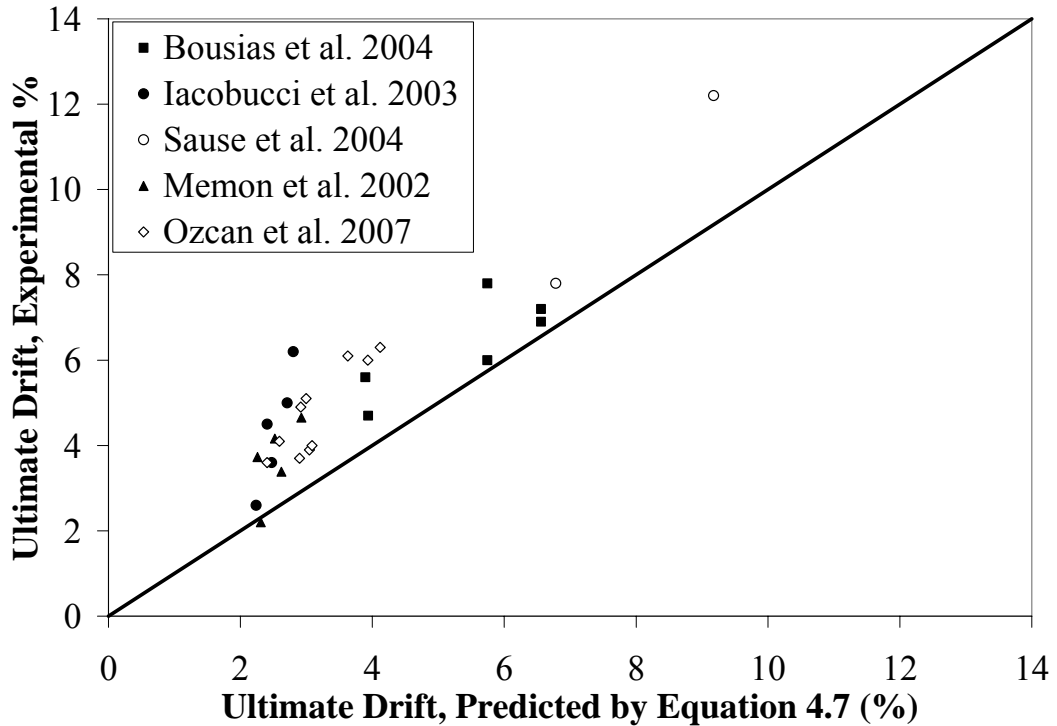


Figure 4.6 Predicted results by nonlinear regression analysis for proposed design equation

The design equation has limitations to longitudinal reinforcement ratio and axial load level regarding the observed behavior of the design equation. The value of longitudinal reinforcement ratio should be between 0.5 and 3% and the axial load level should be in the range from 10 to 60% of the column capacity that were assumed concerning the test database. In addition, the section aspect ratio should be less than two as stated previously by Ozcan et al. [83].

In Table 4.1, the ratio of experimental to analytically predicted drift ratios are shown for the cases of CSA S806-02 equation (Equations 4.2a and b), best-fit and design equations for this study (Equations 4.6 and 4.7). The mean and standard deviations regarding the obtained results are found to be better and more satisfactory as compared to CSA S806-02 predictions. The mean values for the ratio of experimental to analytical predictions of drift levels were 1.00 and 1.52 for Equation 4.6 and CSA S806-02, respectively. Furthermore, a standard deviation having a

reduced degree of 0.18 was attained by using Equation 4.6 as compared to CSA S806-02 equation that has a value of 0.66. The design equation proposed in this study was found to be satisfactory with a mean error ratio of 1.48 and a standard deviation of 0.33. Moreover, the dispersion of the values for ultimate drift ratios obtained from CSA S806-02 equations was monitored to be in elevated levels considering the best-fit and design predictions that were proposed in this study.

4.3.2. Ultimate Compressive Strain Based: Method II

Similar to the methodology used while predicting the ultimate drift ratios for FRP confined RC columns, the ultimate compressive strains compatible with ultimate drift limits for FRP confined concrete were also investigated for columns having different levels of axial load, longitudinal reinforcement ratio and confinement ratio. By using the experimental results in this study, seventh chapter of the current Turkish Earthquake Code (TEC07-7E [54]) was evaluated. Firstly, the Equations 1.8-12 were used to calculate the ultimate compressive strains for the tested columns. The yield moments and ultimate curvatures were calculated by standard section analysis using the concrete and steel models defined in TEC07 as shown in Figures 4.7a and 4.7b. During the analysis, fixed-end rotation and shear components were ignored. The curvatures at yielding (K_y) were obtained by dividing the yield moments (M_y) into the cracked stiffness (EI_{cr}) of the column section. By using Equations 4.8a and b, the yield and ultimate curvatures were converted into column tip deflections while using the plastic hinge length as half of the section depth ($h/2$). A triangular curvature distribution was employed along column length and constant for plastic hinging length (L_p). The obtained results are presented in Table 4.3.

$$\Delta_u = \Delta_y + \Delta_p \quad (4.8a)$$

$$\Delta_u = \frac{K_y L^2}{3} + (K_u - K_y) L_p \left(L - \frac{L_p}{2} \right) \quad (4.8b)$$

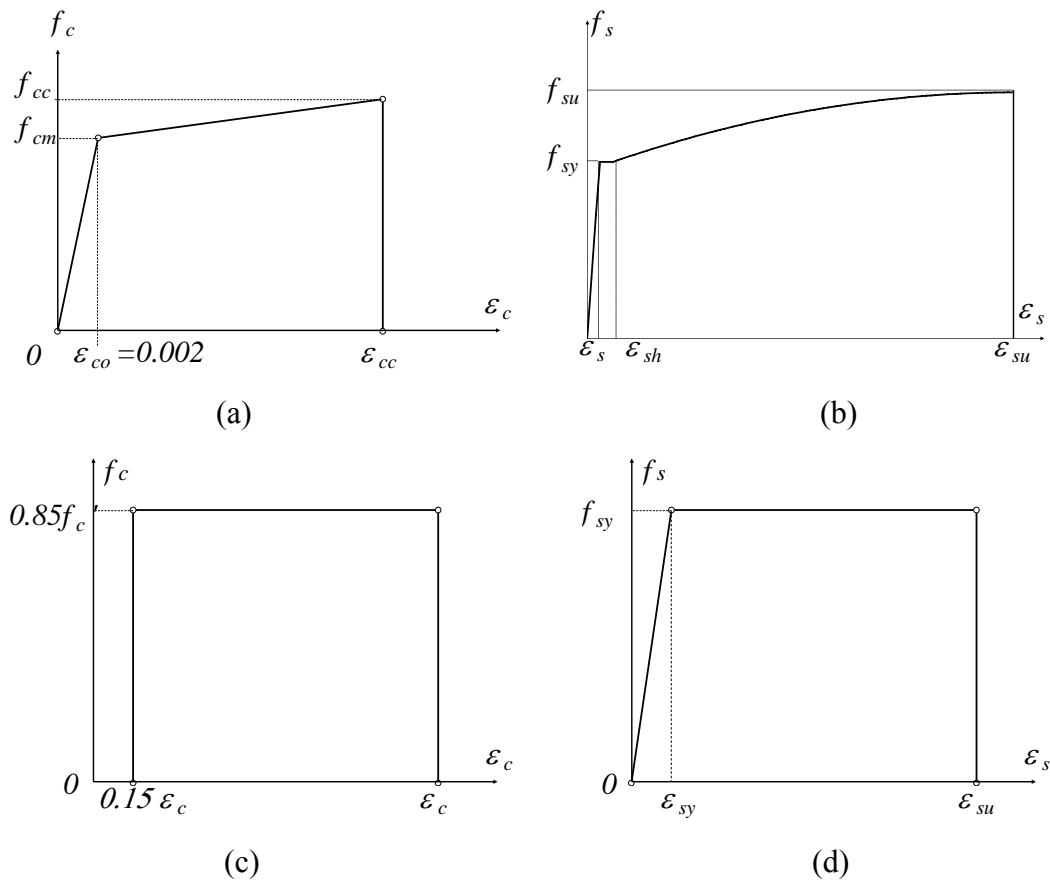


Figure 4.7 TEC07 models for (a) Concrete, (b) Steel and simplified proposed models for (c) Concrete and (d) Steel

The calculated values for ultimate drift ratios of the test specimens could reach at most 1% (20 mm), however very close agreement was obtained regarding the lateral load capacities. Even a good agreement was attained for the lateral load capacities, more realistic and uncomplicated models for FRP confined concrete and steel should be utilized in order to predict the behavior of FRP retrofitted columns in terms of lateral load and drift capacities. In order to achieve this purpose, rectangular stress block and elastoplastic model was employed for FRP confined concrete and steel, respectively (Figures 4.7c and 4.7d).

Table 4.3 The experimental and obtained results using TEC07

	K_y rad/km	M_y kNm	$M_{y,EXP}$ kNm	M_y/EI_{cr} rad/km	K_u rad/km	M_u kNm	Δ_y mm	$\Delta_{y,EXP}$ mm	Δ_u mm	$\Delta_{u,EXP}$ mm
S-L-1-00	9.8	124.6	143.4	7.2	24.7	140.9	9.7	19.1	15.5	98
S-L-1-34	11.6	116.1	132.6	6.9	23.4	122.6	9.1	16.4	14.7	102
S-L-2-00	13.1	110.3	106.6	6.6	34.8	115.7	8.8	15.2	18.2	126
S-L-2-32	10.8	120.2	133.8	7.1	34.2	133.2	9.4	18.8	18.5	120
S-H-1-00	9.9	151.9	172.0	8.7	23.5	169.1	11.6	16.6	16.5	84
S-HC-1-00	9.5	153.9	174.6	8.4	21.4	173.1	11.2	16.1	15.5	72
R-HC-1-16P	10.8	96.6	69.0	7.8	31.6	101.1	10.4	13.6	18.4	122
R-MC-1-16P	10.0	113.9	119.3	7.5	26.1	121.1	10.0	14.7	16.3	80
R-MC-1-8P	10.8	97.2	78.4	7.7	22.4	100.5	10.2	12.8	15.1	74
R-MC-1-NP	11.1	92.2	73.2	7.9	23.8	95.0	10.5	13.1	15.8	78

Initially, the experimental drift ratios were multiplied by the column heights and converted into column tip deflections. Then, standard section analysis was performed to obtain yield moment values considering the proposed FRP confined concrete model and the steel model. Afterwards, yield curvatures were obtained by dividing the yield moments into the cracked stiffness values (EI_{cr}) that were calculated according to the axial load level on the column. The yield deflections were obtained according to the Equations 4.8a and b by virtue of TEC07 consistency. The plastic deflections (Δ_p) were obtained by subtracting the yield deflections (Δ_y) from the ultimate values (Δ_u). The ultimate curvatures (K_u) were acquired presuming that the ultimate curvature has a constant distribution along the plastic hinge length (L_p) that was used as the section depth (h). After obtaining the ultimate curvature values, the ultimate strains for concrete (ϵ_{cc}) were evaluated using the concrete and steel models as shown in Figures 4.7c and 4.7d. In this calculation, the ultimate strain for concrete was obtained by changing the neutral axis depth while iterating the strains (ϵ_{cc}) at the top of the section depth and keeping the ultimate curvature value constant. By applying the same process to all columns in the database, which was used for the ultimate drift based design; the required ultimate strains were obtained. Thus, the ultimate strain values obtained by using the rectangular stress block and elastoplastic steel model are presented in Tables 4.4 and 4.5.

Table 4.4 The obtained results for database using simplified models

Research	b	h	L	r	f _c '	A _{st}	f _y	E _j	ε _f	t _j	K _e	ρ	n	φ	ε _{cc}	Eq. 6.9	ε _{cc} / ε _{cc, p}	Eq.6.10	ε _{cc} / ε _{cc, p}
	mm	mm	mm	mm	MPa	mm ²	MPa	MPa				%	%			ε _{cc, p}		ε _{cc, p}	
Bousias et al. [47]	250	500	1600	30	18.1	1017.9	559.5	230000	0.015	0.26	0.387	0.81	34	0.115	0.03358	0.0282	1.19	0.0192	1.75
	250	500	1600	30	16.7	1017.9	559.5	230000	0.015	0.26	0.387	0.81	36	0.125	0.03041	0.0287	1.06	0.0195	1.56
	250	500	1600	30	17.9	1017.9	559.5	230000	0.015	0.65	0.387	0.81	35	0.291	0.04372	0.0417	1.05	0.0405	1.08
	500	250	1600	30	17.9	1017.9	559.5	230000	0.015	0.65	0.387	0.81	35	0.291	0.04020	0.0417	0.96	0.0405	0.99
	250	500	1600	30	18.7	1017.9	559.5	70000	0.031	0.85	0.387	0.81	34	0.229	0.03601	0.0373	0.97	0.0340	1.06
	500	250	1600	30	18.7	1017.9	559.5	70000	0.031	0.85	0.387	0.81	34	0.229	0.04143	0.0373	1.11	0.0340	1.22
Iacobucci et al. [45]	305	305	1473	16	36.5	2513.3	465	76350	0.013	1.00	0.466	2.70	33	0.081	0.02397	0.0226	1.06	0.0073	3.31
	305	305	1473	16	36.9	2513.3	465	76350	0.013	2.00	0.466	2.70	56	0.159	0.02996	0.0244	1.23	0.0078	3.85
	305	305	1473	16	36.9	2513.3	465	76350	0.013	1.00	0.466	2.70	56	0.080	0.02098	0.0217	0.97	0.0059	3.56
	305	305	1473	16	37.0	2513.3	465	76350	0.013	3.00	0.466	2.70	56	0.238	0.04251	0.0271	1.57	0.0097	4.40
	305	305	1473	16	37.0	2513.3	465	76350	0.013	2.00	0.466	2.70	33	0.159	0.03349	0.0260	1.29	0.0104	3.22
Sause et al. [48]	458	458	2419	45	24.8	3096.6	460	76200	0.015	6.00	0.570	1.48	29	0.688	0.06485	0.0628	1.03	0.0614	1.06
	458	458	2419	45	24.8	3096.6	460	76200	0.015	4.00	0.570	1.48	29	0.459	0.04063	0.0482	0.84	0.0423	0.96
Memon et al. [82]	305	305	1473	16	42.5	2450.4	465	24693	0.023	2.50	0.466	2.63	33	0.101	0.02183	0.0235	0.93	0.0082	2.67
	305	305	1473	16	42.7	2450.4	465	24693	0.023	5.00	0.466	2.63	55	0.201	0.02686	0.0260	1.03	0.0090	2.99
	305	305	1473	16	43.3	2450.4	465	24693	0.023	2.50	0.466	2.63	55	0.099	0.01642	0.0225	0.73	0.0065	2.54
	305	305	1473	16	43.7	2450.4	465	24693	0.023	1.25	0.466	2.63	32	0.049	0.01918	0.0212	0.90	0.0061	3.16
	305	305	1473	16	44.2	2450.4	465	24693	0.023	7.50	0.466	2.63	54	0.292	0.03645	0.0292	1.25	0.0114	3.20

Table 4.5 The obtained results for experimental study using simplified models

Research	b	h	L	r	f _c '	A _{st}	f _y	E _j	ε _f	t _j	K _e	ρ	n	φ	ε _{cc}	Eq. 6.9 ε _{cc} / ε _{cc,}	Eq.6.10 ε _{cc} / ε _{cc,}		
	mm	mm	mm	mm	MPa	mm ²	MPa	MPa				%	%			ε _{cc, p}	p	ε _{cc, p}	p
This Study	350	350	2000	30	19.4	2035.8	287	230000	0.015	0.165	0.542	1.66	27	0.091	0.02419	0.0247	0.98	0.0113	2.14
	350	350	2000	30	14.0	2035.8	287	230000	0.015	0.165	0.542	1.66	34	0.126	0.02721	0.0260	1.05	0.0120	2.27
	350	350	2000	30	11.4	2035.8	287	230000	0.015	0.33	0.542	1.66	40	0.309	0.03649	0.0350	1.04	0.0210	1.74
	350	350	2000	30	15.6	2035.8	287	230000	0.015	0.33	0.542	1.66	32	0.226	0.03153	0.0320	0.98	0.0195	1.62
	350	350	2000	30	20.0	3041.1	287	230000	0.015	0.165	0.542	2.48	27	0.088	0.02015	0.0235	0.86	0.0087	2.30
	350	350	2000	10	22.0	3041.1	287	230000	0.015	0.165	0.407	2.48	27	0.060	0.01730	0.0221	0.78	0.0072	2.39
	200	400	2000	30	10.0	2035.8	287	230000	0.015	0.165	0.755	2.54	35	0.322	0.03380	0.0333	1.02	0.0170	1.98
	200	400	2000	30	10.5	2035.8	287	230000	0.015	0.165	0.437	2.54	35	0.178	0.02037	0.0269	0.76	0.0112	1.82
	200	400	2000	30	9.0	2035.8	287	230000	0.015	0.165	0.437	2.54	35	0.207	0.02154	0.0282	0.76	0.0124	1.74
	200	400	2000	30	15.0	2035.8	287	230000	0.015	0.165	0.755	2.54	35	0.215	0.02188	0.0285	0.77	0.0127	1.72

In addition, the ultimate moment values (M_u) were taken to be equal to the yield moments (M_y) since there was no increase in stresses for the employed models of concrete and steel. Subsequent to obtaining the ultimate strain values, a nonlinear regression analysis was performed in order to represent the ultimate strains in terms of axial load level (n), longitudinal reinforcement ratio (ρ) and confinement ratio (ϕ) for experimental ultimate drift levels. Since the obtained equation represents the average of all data, a simple design equation was proposed in order to predict ultimate strains on the safe side. Thus, the regression analysis was followed by simplifying the regression terms of ϕ , n and ρ instead of using complex exponential expressions. Hence, the exponential equations were simplified into a linear equation in terms of $\phi/n\rho$ ratio and the design equation was obtained. The obtained design equation estimates the ultimate strain of FRP confined concrete by the corresponding $\phi/n\rho$ values while keeping the average inclination angle very close to the experimental data. The obtained equations for best-fit and design are presented in Equations 4.9 and 4.10. The results of the regression analysis are shown in Figures 4.8 and 4.9 for the best fit and design equations, respectively.

$$\varepsilon_{cc} = 0.019 + 0.418 \frac{\phi}{\sqrt{n\rho}} \quad (4.9)$$

$$\varepsilon_{cc} = 0.004 + 3.6 \frac{\phi}{n\rho} \quad (4.10)$$

$$\frac{\phi}{n\rho} > 0.0005$$

where n and ρ are in percents while ϕ has no units. The ultimate concrete strains for the best-fit and design equations are shown in Tables 4.4 and 4.5. In order to obtain the required ultimate curvature values (K_u), the ultimate strain values were determined according to the design equation. By using these values, the ultimate curvatures and consequent ultimate drift ratios (DR_p) were acquired. The ratio of predicted to ultimate drift levels was observed to be around 75% for the model. In order to be consistent with the TEC07, the design equation was modified by using the strain of 0.004 for the unconfined case. The design-oriented data is compared with the experimental hysteretic data in Figures 4.10 – 4.22. Both of the methods gave safer and more economical designs regarding TEC07.

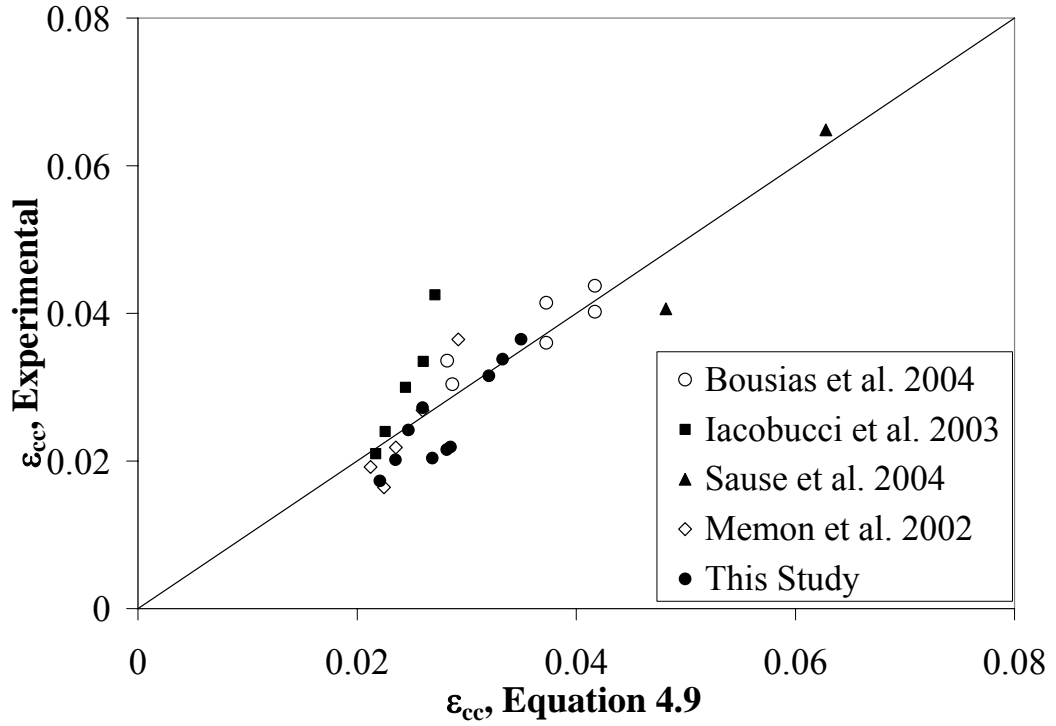


Figure 4.8 Regression results considering best-fit equation

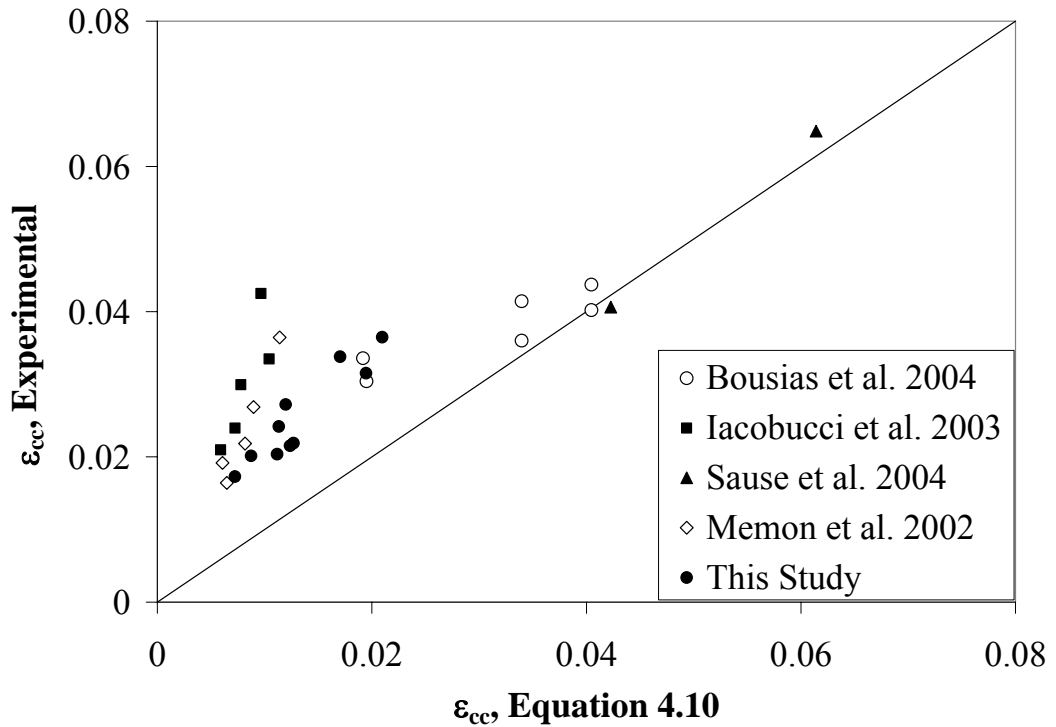


Figure 4.9 Regression results considering design equation

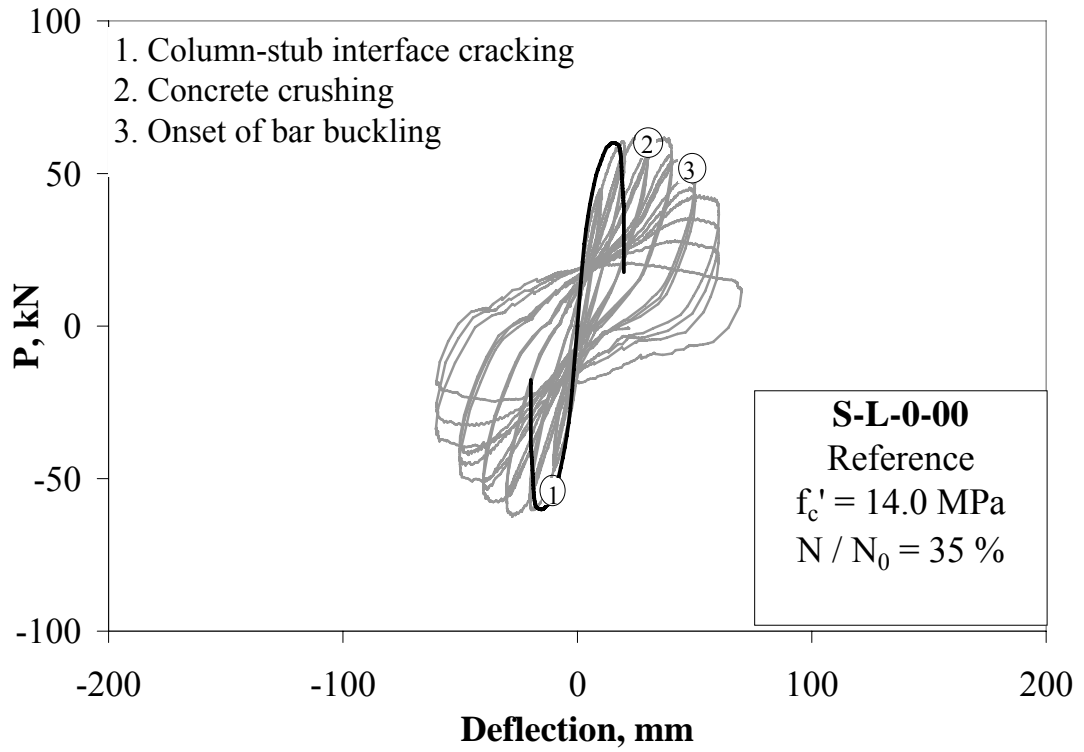


Figure 4.10 Experimental and design comparison for the specimen S-L-0-00

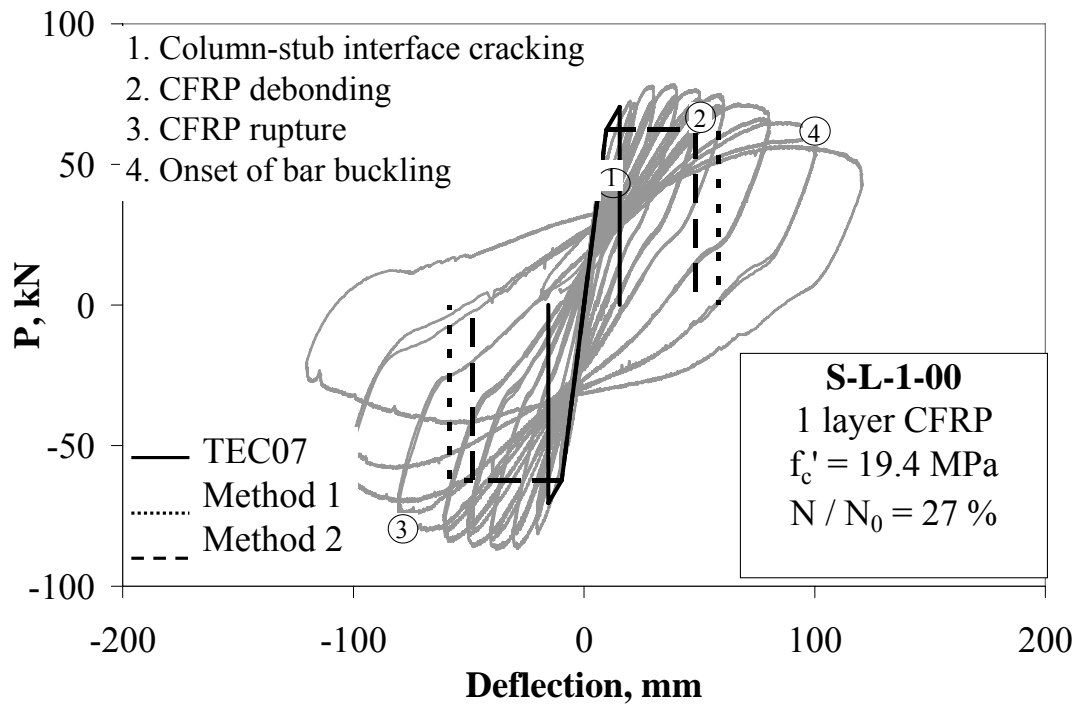


Figure 4.11 Experimental and design comparison for the specimen S-L-1-00

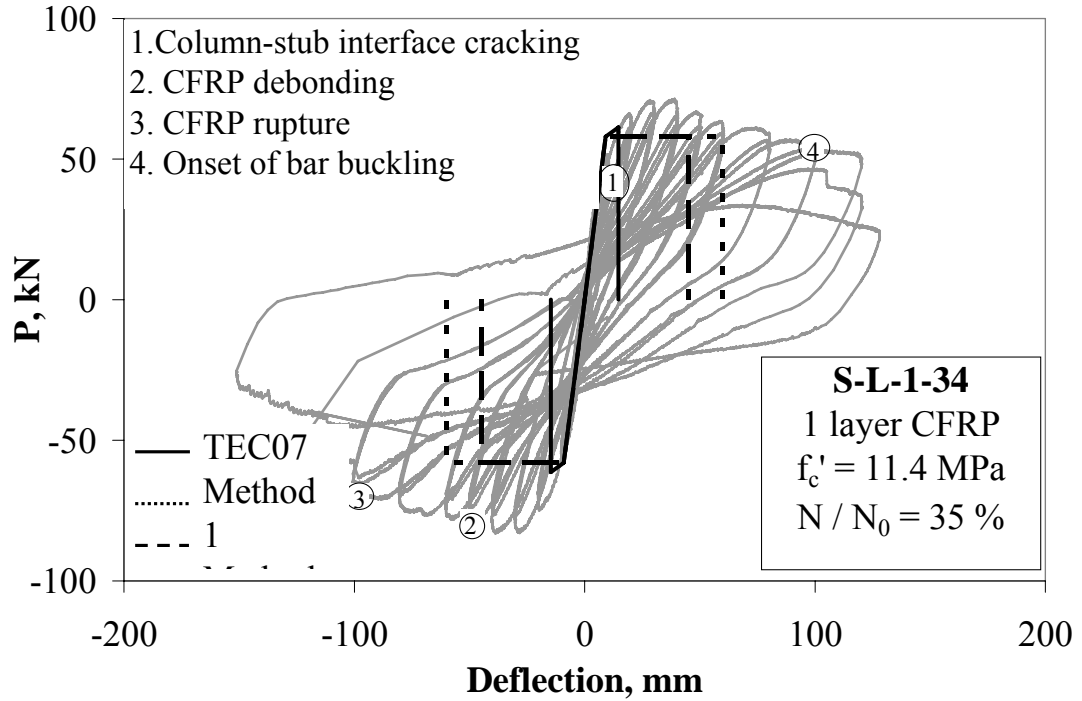


Figure 4.12 Experimental and design comparison for the specimen S-L-1-34

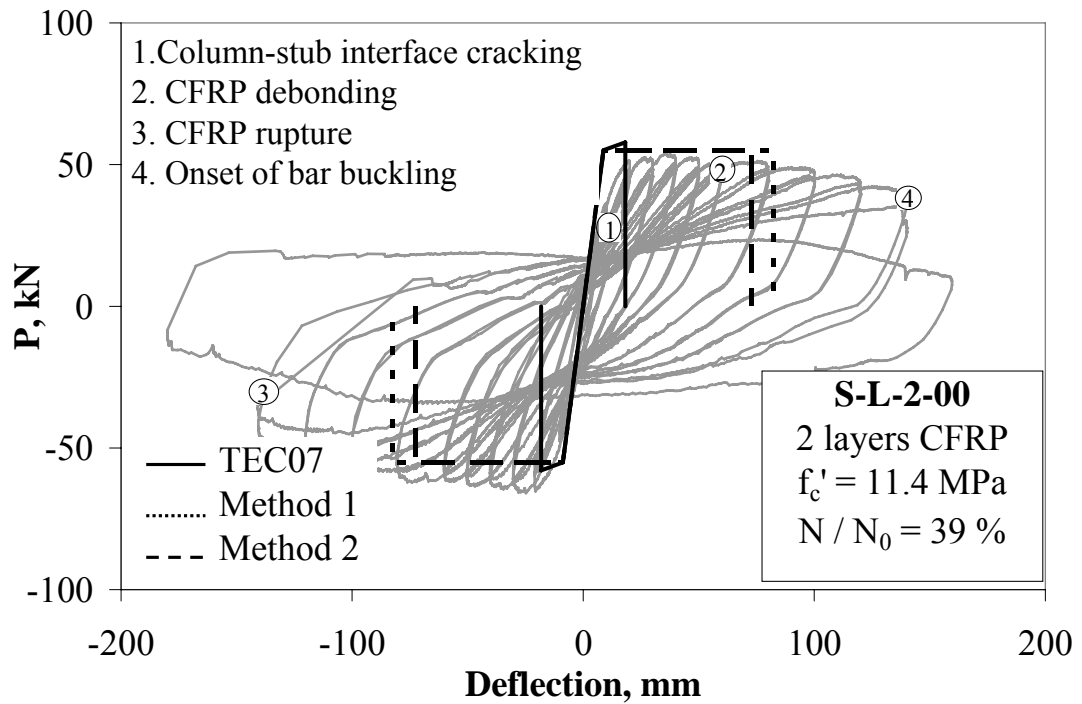


Figure 4.13 Experimental and design comparison for the specimen S-L-2-00

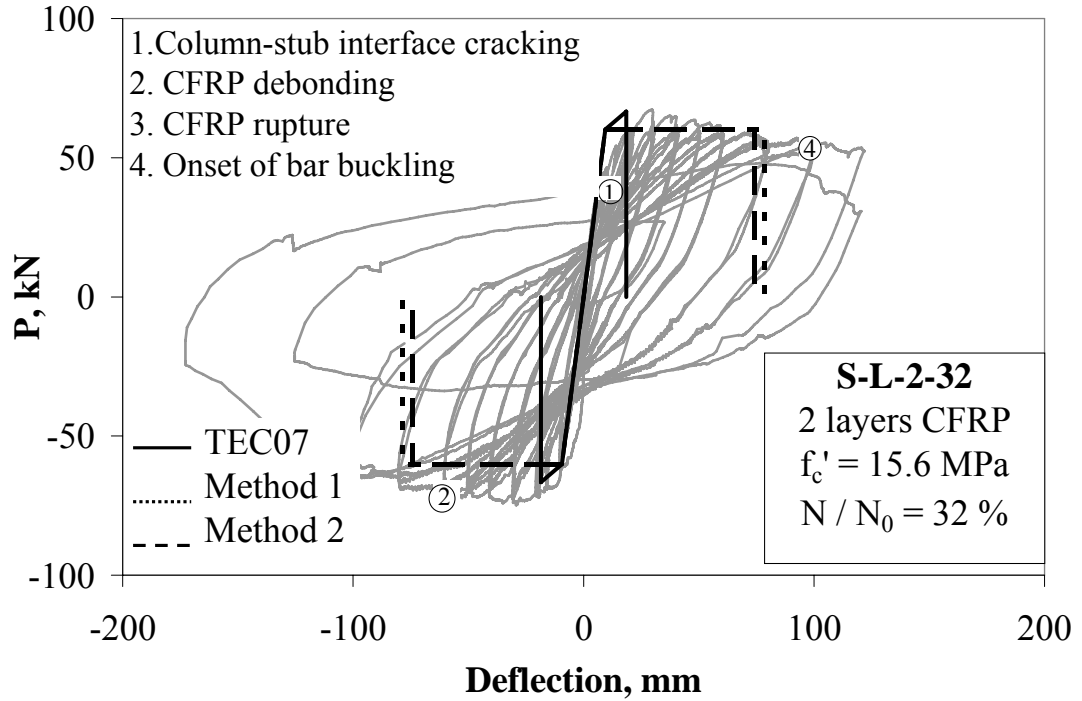


Figure 4.14 Experimental and design comparison for the specimen S-L-2-32

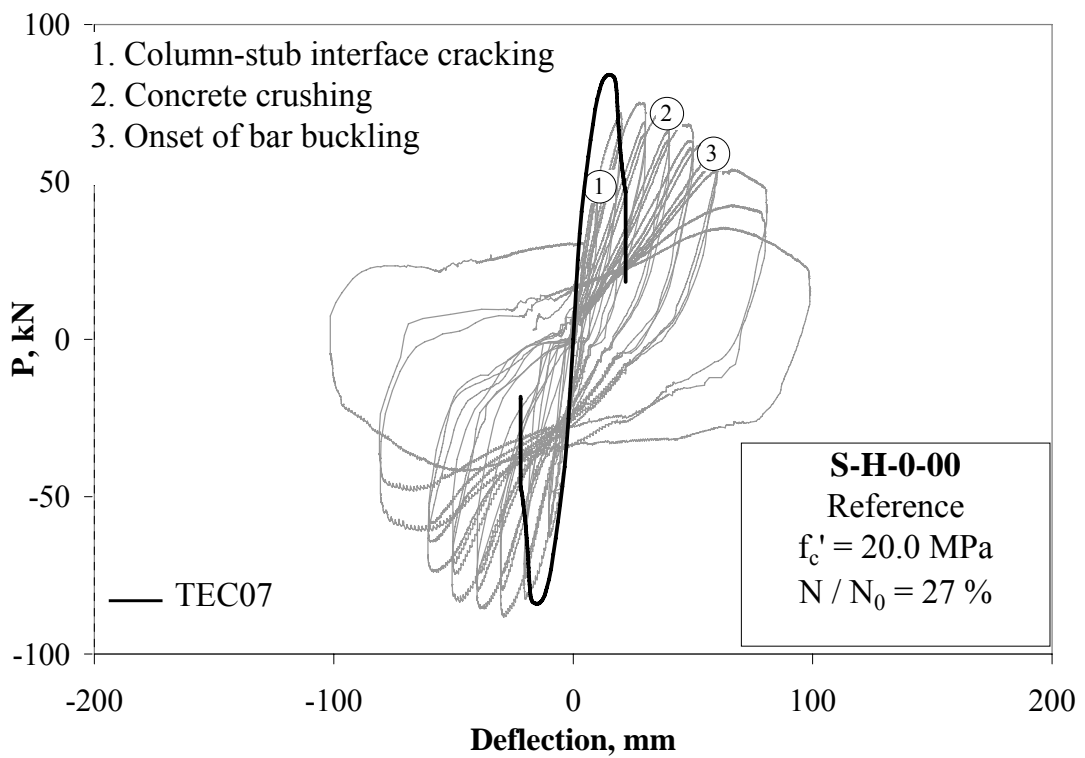


Figure 4.15 Experimental and design comparison for the specimen S-H-0-00

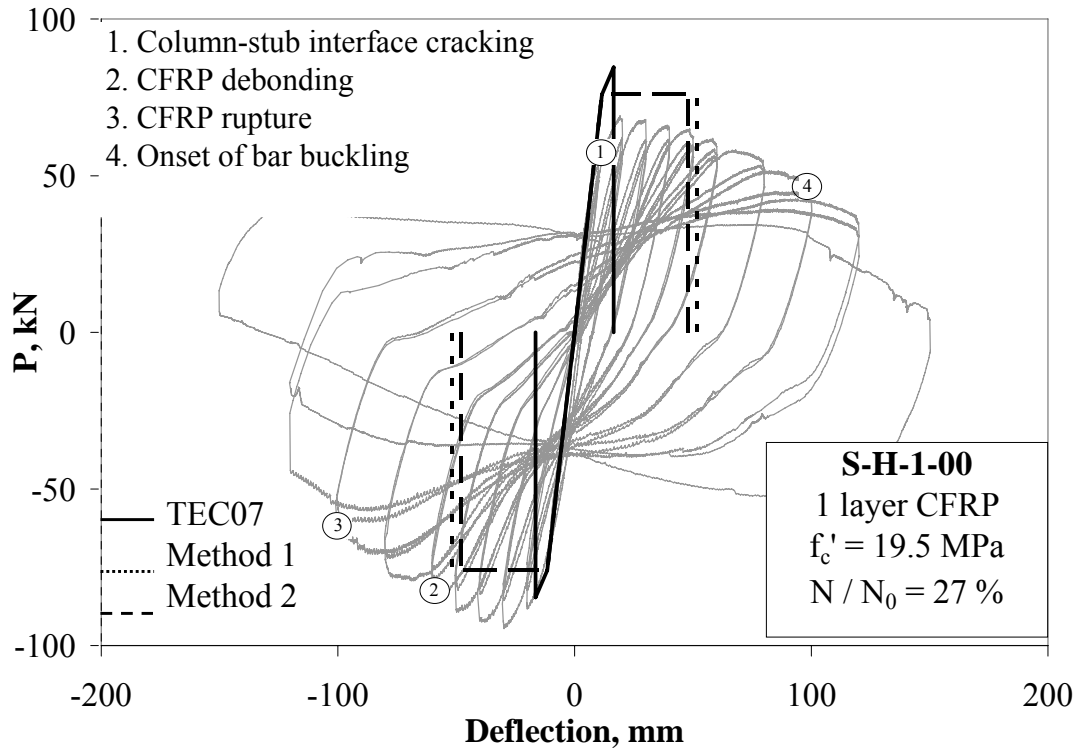


Figure 4.16 Experimental and design comparison for the specimen S-H-1-00

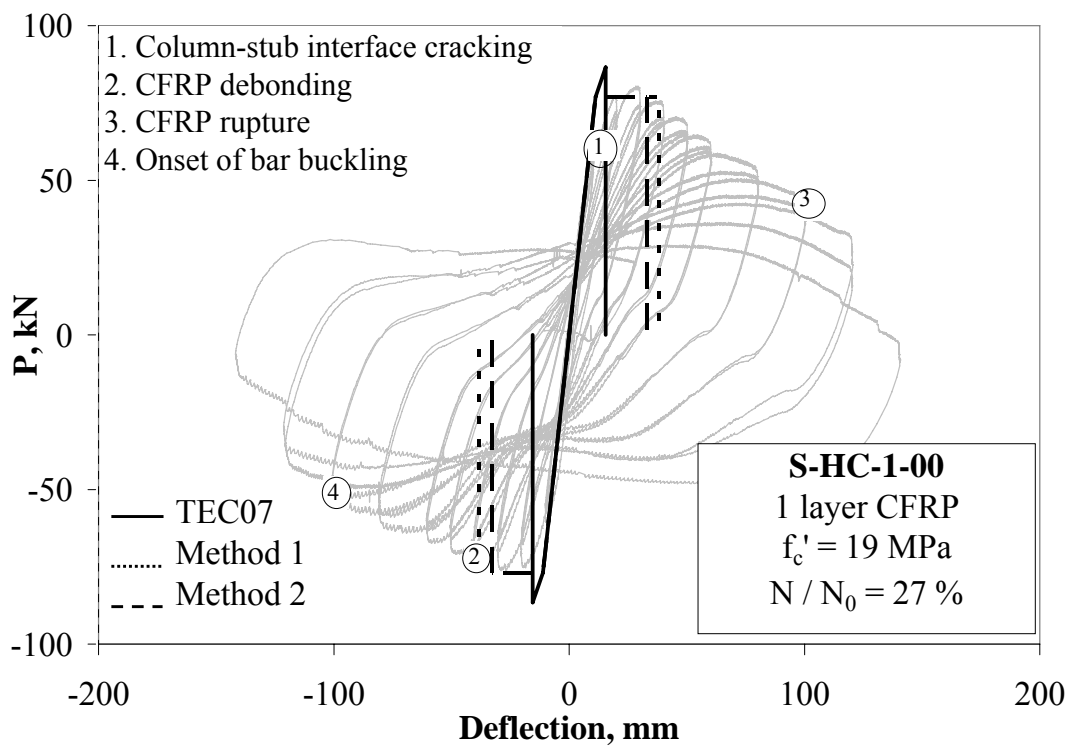


Figure 4.17 Experimental and design comparison for the specimen S-HC-1-00

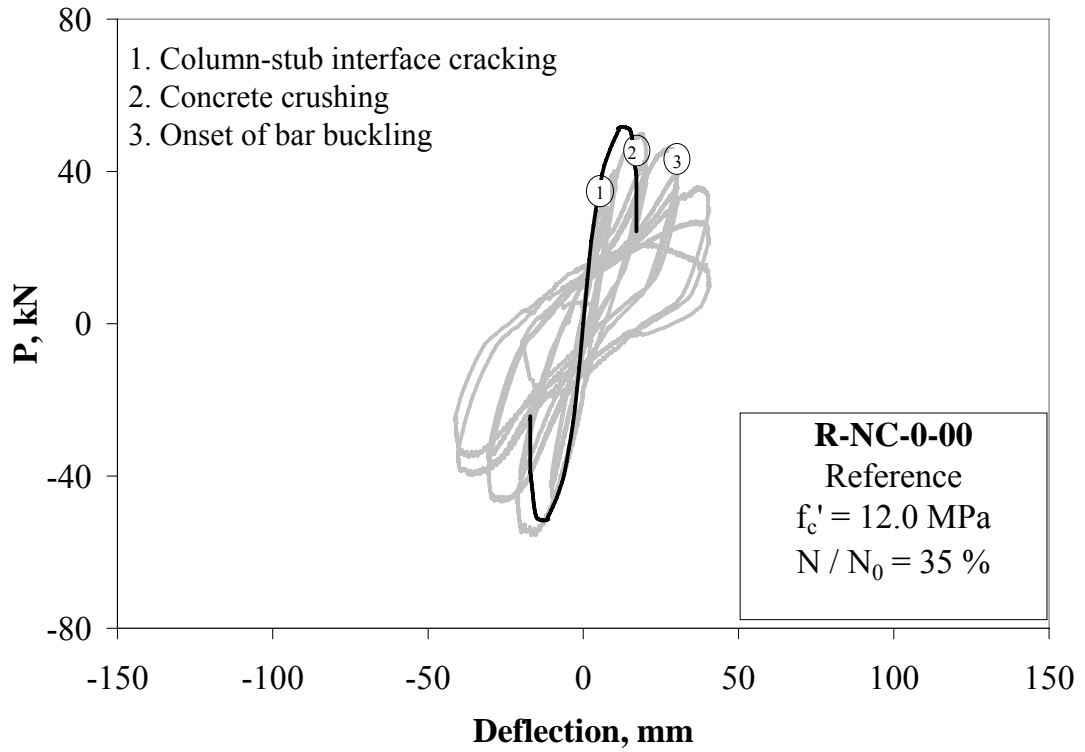


Figure 4.18 Experimental and design comparison for the specimen R-NC-0-00

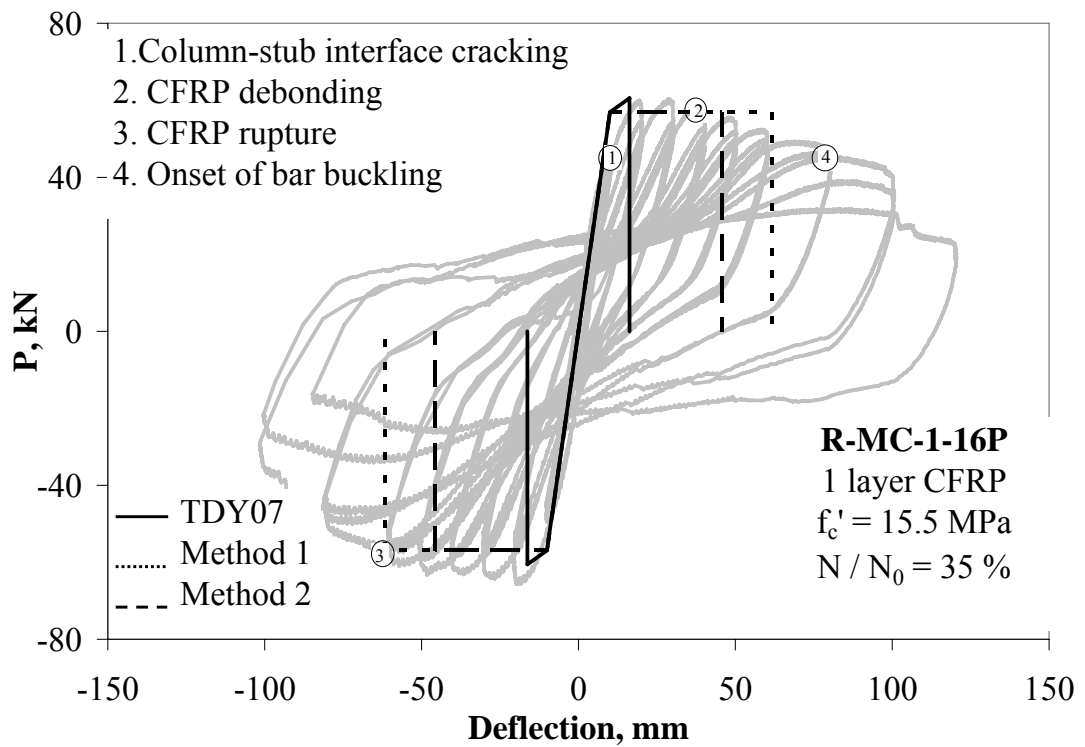


Figure 4.19 Experimental and design comparison for the specimen R-MC-1-16P

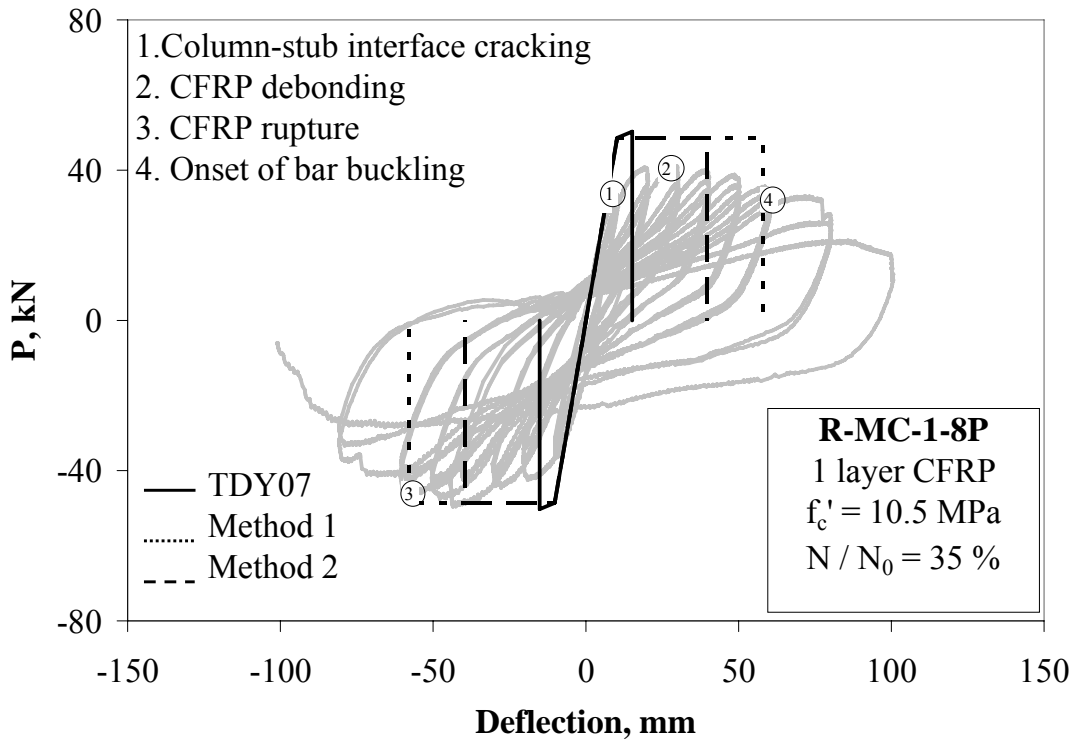


Figure 4.20 Experimental and design comparison for the specimen R-MC-1-8P

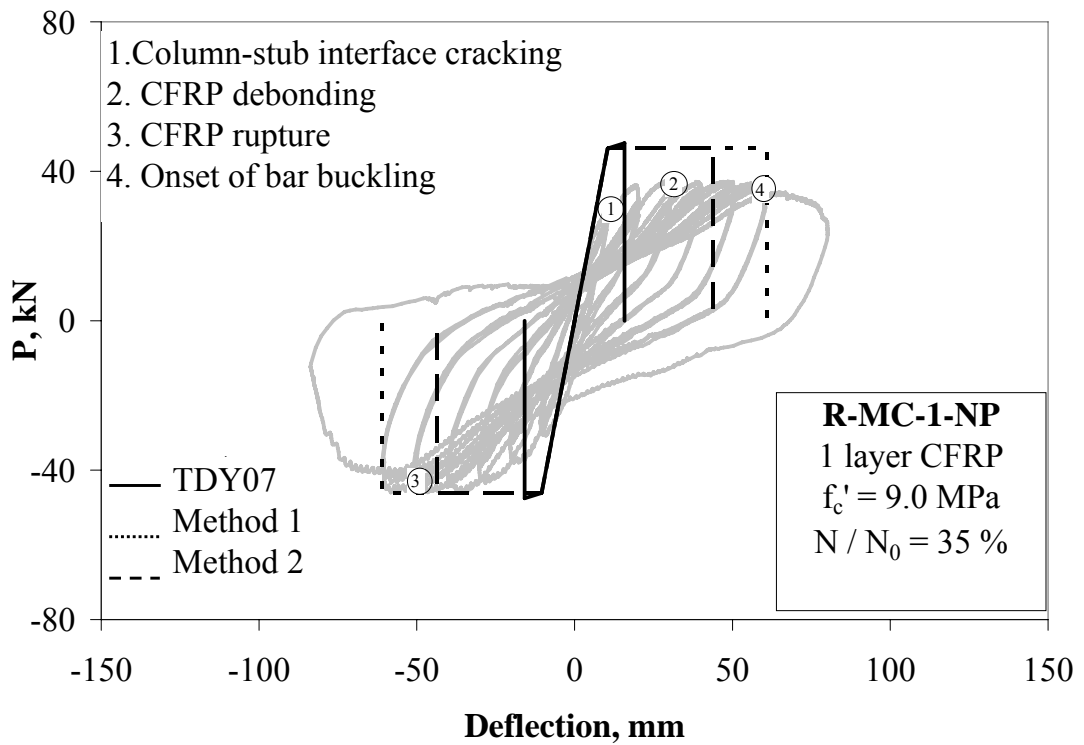


Figure 4.21 Experimental and design comparison for the specimen R-MC-1-NP

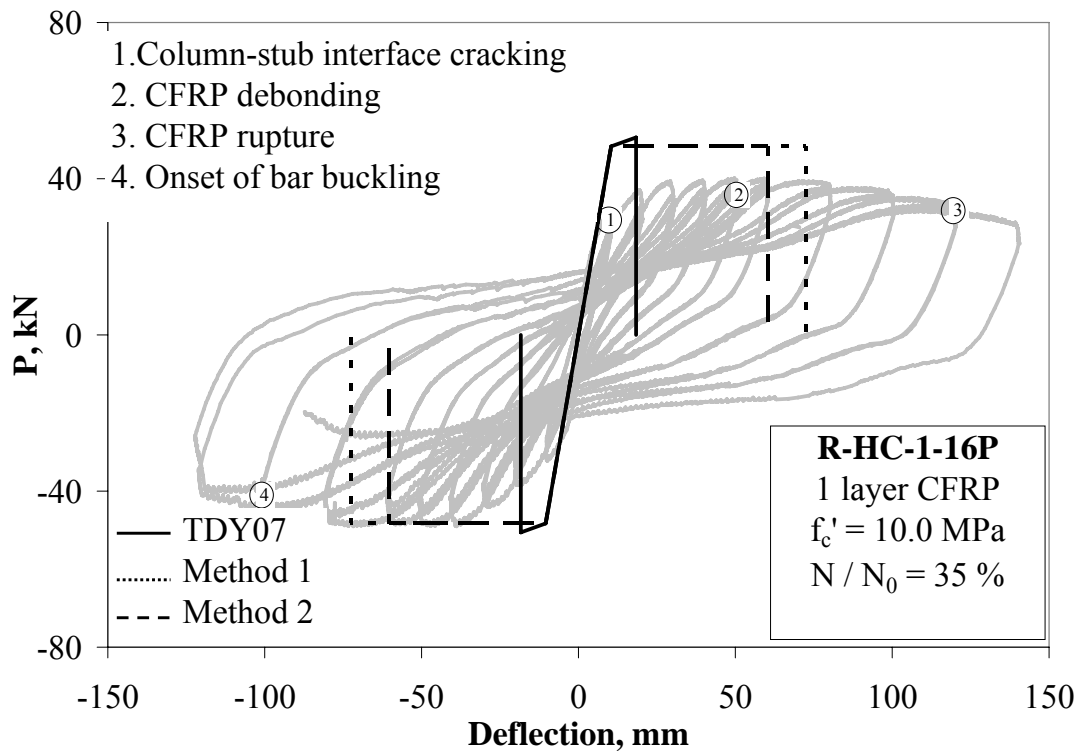


Figure 4.22 Experimental and design comparison for the specimen R-HC-1-16P

For the columns in the first series, the lateral performance of the reference specimen and the FRP retrofitted specimens were highly underestimated by the TEC07 approach (Figures 4.10-4.14). However, the predictions of lateral strength and ultimate drift level for the FRP retrofitted columns were found to be safer and more economical regarding the TEC07 method. Only the lateral strength of S-L-2-00 was overestimated at most 5% regarding the test data that can be considered as a reasonable agreement with the experimental results (Figure 4.13). Both methods gave safe and economical results while predicting the ultimate drift ratios in a reasonable good agreement with each other. In addition, both methods estimated the ultimate drift levels close to onset of rebar buckling at which the specimens could experience successive three lateral cycles without a significant strength drop. Similar observations were made amongst the specimens in Series 2 while TEC07 approach underestimated ultimate drift levels (Figures 4.15-4.17). For the strengthened specimens, the estimated lateral load and deflection capacities were safer and more economical as compared to the TEC07. Lateral load capacity was overestimated

about 10% for S-H-1-00 that can be considered as a reasonable agreement as shown in Figure 4.16. Moreover, both methods gave very close results with each other. For the columns in the last test series, underestimated ultimate drift levels were present for TEC07 approach. However, similar to the other test series, reasonable and safer estimations in terms of lateral load and drift capacity can be observed in Figures 4.18-4.22. Herein, the predictions for Method I and II differed about 10% that can be regarded as a reasonable agreement.

4.3.3. Database Comparison and Code Recommendations

The predicted ultimate drift values for the experimental studies showed a good correlation among the test database for both of the methods. The columns tested by Bousias et al. [47] failed at ultimate drift ratios of about 6% that were tested in strong and weak directions. Irrespective of the loading direction, the columns performed a similar behavior regarding the failure drift levels and ultimate strains that were predicted well by both of the best-fit equations for two models. The overestimated values for ultimate drift and compressive strain can be attributed to the presence of pre-damage on the columns. Besides, the predictions for the test specimens of Iacobucci et al. [45] are in well agreement with the experimental data for the Models I and II. The performance of the columns tested by Sause et al. [48] was approximated well by having close predictions to the tests and the ratio of predicted to experimental drifts and ultimate strains was found to be in permissible limits concerning the attainable drift levels for structures. For the series that were tested by Memon [82], there exist only one outlier specimen and the predicted values of the remaining specimens were found to be close to the experimental data considering the best-fit equations. The predictions of the Models I and II regarding this study were also found to be in admissible limits concerning the experimental data since the estimations concerning the ultimate drift and strain levels were found to be in range of $\pm 20\%$ of error. Additionally, regarding the specimens in this study, the maximum error was obtained from the moderately confined columns in which the effects of CFRP anchor dowels were investigated. However, the design equation predicted the ultimate drift and compressive strain levels in a good correspondence and a safety factor of approximately 2.5 throughout the test database.

Considering TEC07, the utilized models for FRP confined concrete and steel are redundantly complicated and lead to uneconomical FRP design for the columns. Thus, two design methods that were based on ultimate drift and concrete compressive strain were developed. Although the first method is simpler and more practical to implement, detailed analyses are required for Method II that is compatible with the provisions of TEC07. For both of the methods, the FRP retrofitted column performances are estimated by using three parameters of confinement, axial load and longitudinal steel ratio. First method directly estimates the ultimate drift ratio of the columns however; standard section analysis should be implemented for Method II while using rectangular stress block for concrete and elastoplastic model for steel. Hence, it was established that utilizing such simplifications and equating the yield moments and moment capacities to each other would be acceptable for column FRP design. A column design example of FRP retrofitting according to TEC07, Method I and II is presented in Appendix F. Moreover, in accordance with TEC07, the performance levels can be selected as the ultimate drift level, 75% of ultimate drift level and yield point (corresponding to the transition point), for collapse prevention (CP), life safety (LS) and immediate occupancy (IO), respectively.

CHAPTER 5

CONCLUSIONS AND FUTURE RECOMMENDATIONS

Results from an experimental study, in which 15 column specimens in three experimental series were tested under constant axial load and cyclic lateral displacement excursions that simulated seismic forces, are presented in this study. The specimens consisted of a 350×350×2000 mm or 200×400×2000 mm columns cast vertically together with a 1350×500×400 mm stub. Besides the reference specimens for each series simulating a typical deficient building column with insufficient transverse reinforcement and relatively low concrete compressive strength, there were two sets of companion specimens in each test series. For Series 1, the effect of CFRP confinement, presence of axial load during retrofit and plain bars were studied. The second test series consisted of investigating the possible effects of increasing longitudinal bar diameter, repairing under axial load and decreasing the corner-rounding radius while wrapping the column with CFRP on the seismic performance of square reinforced concrete columns. In addition, the specimens tested in the last series were used to observe and monitor the influences of increasing the section aspect ratio (depth/width) of the columns and using different CFRP anchor dowel configurations on the seismic response of the rectangular reinforced concrete columns. The following conclusions were drawn from this study:

1. The number of CFRP sheets used to confine plastic hinge regions of columns significantly improved the seismic behavior of deficient columns by means of enhancing ductility, dissipated energy and ultimate drift levels. However, negligible lateral load carrying capacity enhancement was observed (~10-15%). In addition, increasing number of CFRP layers wrapped around the column improved drift capacities but that was not in proportion with the effect provided by CFRP confinement.
2. Wrapping the column critical region under an axial load level of about 35% of capacity did not have a considerable influence on the behavior of the

columns as the experimental results revealed that axial strain and column lateral expansion due to existing axial load on the column had no significant effect. Additional studies, however, are needed to support this result at higher axial load levels further.

3. Use of plain bars can result in a higher contribution of fixed end rotation component. While strengthening columns with CFRP increased the fixed end rotations up to 2 times of the reference, the plain bars should be considered carefully in the assessment and retrofit design of deficient RC columns.
4. The energy dissipation capacities of the repaired columns were lower than the strengthened columns due to the initial cracks that formed while introducing moderate damage to the specimen.
5. The presence of axial load level of 27% of the capacity during repairing had almost no influence on the ultimate drift and ductility of the columns. The repaired columns behaved in a similar manner with the strengthened column. On the contrary, the lateral load carrying capacity increased by 15% of the reference column in the absence of the axial load during repairing. This fact was due to the higher compressive strength of the epoxy mortar compared to the existing compressive strength of concrete that influenced the section capacity in the absence of axial load. When the axial load was present, there was no gain in the lateral capacity of the column. In this case, the section capacity was not affected since the axial load was not perceived by the epoxy mortar repair section of the column.
6. The energy dissipation and secant-stiffness degradation characteristics of the repaired columns were not as good as the strengthened columns whereas the repaired columns were able to maintain higher levels of dissipated energy than the strengthened columns at further drift ratios. Furthermore, the repaired columns were able to sustain the same level of secant-stiffness at these drift levels.

7. The improvement in the confinement ratio made the columns sustain greater levels of ultimate drift ratios. Since the enhancement in confinement ratio was higher for the columns having low concrete compressive strengths, the drift capacity was also improved concerning the increase in the area of confined region.
8. Using 16-pinned CFRP anchor dowel configuration induced higher confinement ratios than the 8-pinned configuration. In 16-pinned case, the confined region of the columns extended by closely spaced CFRP dowels.
9. A simple analytical model that takes into account FRP confinement, longitudinal rebar buckling and deformations due to slip of plain bar is employed. A good agreement between analytical and experimental results was observed.
10. A drift-based design method was proposed including the parameters of longitudinal reinforcement ratio, axial load level and confinement ratio. The drift capacities of the columns in the experimental database were predicted with a good approximation.
11. The design method was improved in order to predict ultimate compressive strain levels regarding the Turkish Earthquake Code (TEC2007). The ultimate strains were estimated in a good prediction while providing safe design regulations. Lower and upper bounds were determined in order to predict the maximum and minimum ultimate compressive strains, respectively.
12. Since the design – oriented studies did not consider any components of bond-slip and shear components of ultimate deformations, the curvature values and corresponding ultimate concrete strains were calculated to be higher than their actual values.

13. Since two design methods concerning ultimate drift levels and ultimate compressive strains were proposed in this study, the engineer can select the proper design case considering the aim of the project and can use either drift based or ultimate strain based design methods. This selection should be made regarding the stipulated terms for both of the design cases.

The following recommendations should be taken out considering the experimental and analytical shortcomings of this study. Since this research responds to the particular research needs regarding CFRP retrofitting of reinforced concrete columns, additional and further research should be conducted in order to comprehend the behavior of CFRP confining and CFRP confined columns for experimental, analytical and design – oriented considerations.

1. Since the effect of shear was ignored regarding that all the columns were designed to be flexural dominant in this study, additional tests should be conducted investigating the influences of shear failure on CFRP retrofitting. Moreover, the effects of strengthening and repairing can be utilized.
2. The experimental database can be extended by performing new tests considering different transverse reinforcement schemes with plain and deformed bars. The possible influences of double confinement action by transverse reinforcement and CFRP can be monitored by using this type of experimental study.
3. Any interactive models between shear, flexure, axial load and bond-slip can be utilized in the program since the analytical method is only applicable for flexural dominant columns and ignores any interaction models.
4. The column database should be extended and the design equations estimating ultimate drift ratio and ultimate compressive strains should be modified regarding the other parameters such as transverse reinforcement ratio, loading direction and aspect ratio. Since there was no contribution of these parameters for this study, these components should be added and the

equations should be generalized considering all these additional parameters for the columns.

5. The tip displacement components of bond-slip and shear of the columns should be added to the general design equation in terms of ultimate drift ratio and maximum ultimate compressive strain. While regulating these constituents to the main design equations, any interaction relationships should be considered and simplified according to the related code.
6. The proposed design method that estimates the ultimate drift levels and maximum ultimate strains should also cover unconfined cases for columns in details regarding the column and section properties in addition to the FRP confined columns.

REFERENCES

1. Saatçioğlu M, Bruneau M. Performance of Structures during the 1992 Erzincan Earthquake. *Canadian Journal of Civil Engineering*, 1993(20): 305-325.
2. Saatçioğlu M, Bruneau M. The 1992 Erzincan Earthquake. Performance of Reinforced Concrete Structures, *Concrete International*, 1994 September: 51-56.
3. Saatçioğlu M, Bruneau M. Behavior of Unreinforced Masonry Structures During the 1992 Erzincan, Turkey, Earthquake. *TMS Journal*, 1994 February: 79-87.
4. Earthquake Engineering Research Institute (EERI), The Dinar, Turkey, Earthquake of October 1, 1995. EERI Special Earthquake Report, November 1995.
5. Çatal HH. A Report on Dinar Earthquake of 1 October 1995, and Response Spectra. *Engineering Structures*, 1997, 19(7): 594-602.
6. Adalier K, Aydingün O. Structural Engineering Aspects of the June 27, 1998 Adana-Ceyhan (Turkey) Earthquake. *Engineering Structures*, 2001, 23: 343-355.
7. Earthquake Engineering Research Institute (EERI), Turkish Earthquakes: Two Reports, Lessons from the Adana-Ceyhan Quake and the Dinar Aftershock. EERI Special Earthquake Report, September 1998.
8. Saatçioğlu M, Mitchell D, Tinawi R, Gardner NJ, Gillies AG, Ghoborah A, Anderson DL, Lau D. The August 17, 1999, Kocaeli (Turkey) Earthquake – Damage to Structures. *Canadian Journal of Civil Engineering*, 2001, 28(4): 715-737.
9. Sezen H, Whittaker AS, Elwood KJ, Mosalam KM. Performance of Reinforced Concrete Buildings during the August 17, 1999 Kocaeli, Turkey Earthquake, and Seismic Design and Construction Practise in Turkey. *Engineering Structures*, 2003, 25: 103-114.

10. Earthquake Engineering Research Institute (EERI), The Izmit (Kocaeli), Turkey Earthquake of August 17, 1999. EERI Special Earthquake Report, October 1999.
11. Wallace JW. Building Performance in the 17 August 1999 Izmit (Kocaeli), Turkey Earthquake. In: CUREe Open Symposium Sponsored by Kajima, Tokyo, Japan, 1999.
12. Erdik, M. Report on 1999 Kocaeli and Düzce (Turkey) Earthquakes. Reconnaissance Report: Department of Earthquake Engineering, Boğaziçi University, 2000.
13. Bruneau M. Building Damage from the Marmara, Turkey Earthquake of August 17, 1999. Journal of Seismology, Kluwer Academic Publishers, 2002, 6: 357-377.
14. Scawthorn C, Johnson GS. Preliminary Report: Kocaeli (Izmit) Earthquake of 17 August 1999. Engineering Structures, 2000, 22: 727-745.
15. Dönmez C, Pujol S. Spatial Distribution of Damage Caused by the 1999 Earthquakes in Turkey. Earthquake Spectra, 21(1): 53-69.
16. Doğangün A. Performance of Reinforced Concrete Buildings during the May 1, 2003 Bingöl Earthquake in Turkey. Engineering Structures, 2004, 26: 841-856.
17. Kaplan H, Yılmaz S, Binici H, Yazar E, Çetinkaya N. May 1, 2003 – Turkey Bingöl Earthquake: Damage in Reinforced Concrete Structures. Engineering Failure Analysis, 2004, 11: 279-291.
18. Erdik M, Demircioğlu M, Beyen K, Şeşetyan K, Aydınoglu N, Gül M, Siyahi B, Önem G, Tüzün C, Salkın A, Kaya Y. May 01, 2003 Bingöl (Turkey) Earthquake. Department of Earthquake Engineering, Kandilli Observatory and Earthquake Research Institute, Boğaziçi University, 2003.
19. Aydan Ö, Ulusay R, Miyajima M. The Bingöl Earthquake of May 1, 2003. Reconnaissance Report: Japan Society of Civil Engineers, JSCE, 2003.
20. Özcebe G, Ramirez J, Wasti ST, Yakut A. 1 May 2003 Bingöl Earthquake Engineering Report. Turkish Scientific and Technical Research Council Report, 2003.
21. Sugano S. State of Art in Techniques for Rehabilitation of Buildings. In: Proceedings of 11WCCE, Acapulca, Mexico, 1996.

22. Fukuyama H, Sugano S. Japanese Seismic Rehabilitation of Concrete Buildings after the Hyogoken – Nanbu Earthquake. *Cement & Concrete Composites*, 2000, 22, 59-79.
23. ACI Committee 440 Report, Report on Fiber-Reinforced Polymer (FRP) Reinforcement for Concrete Structures, 2006; 440.XR.
24. Demers M, Neale KW. Strengthening of Concrete Columns with Unidirectional Composite Sheets. In: Fourth International Conference on Short and Medium Span Bridges, Halifax, Nova Scotia, 1994.
25. Demers M, Hebert D, Labossiere P, Neale KW. The Strengthening of Structural Concrete with an Aramid Woven Fiber/Epoxy Resin Composite. In: Proceedings of Advanced Composite Materials in Bridges and Structures II, Montreal, 1995.
26. Picher F, Rochette P, Labossiere P. Confinement of Concrete Cylinders with CFRP. In: Proceedings of the First International Conference on Composites in Infrastructure, ICCI'96, Tucson, Arizona, 1996.
27. Mirmiran A, Shahawy M, Samaan M, El Echary H, Mastrapa JC, Pico O. Effect of Column Parameters on FRP-Confined Concrete. *Journal of Composites for Construction*, ASCE, 1998, 2(4): 175-185.
28. Chaallal O, Shahawy M, Al-Saad PEA. Behavior of Axially Loaded Short Rectangular Columns Strengthened with CFRP Composite Wrapping. Technical Report: Structures Research Center, FDOT, 2000.
29. Chaallal O, Shahawy M, Hassan M. Performance of Axially Loaded Short Rectangular Columns with Carbon Fiber-Reinforced Polymer Wrapping. *Journal of Composites for Construction*, ASCE, 2003, 7(3): 200-208.
30. Rochette P, Labossiere P. Axial Testing of Rectangular Column Models Confined with Composites. *Journal of Composites for Construction*, ASCE, 2000, 4(3): 129-136.
31. Pessiki S, Harries KA, Kestner JT, Sause R, Ricles JM. Axial Behavior of Reinforced Concrete Columns Confined with FRP Jackets. *Journal of Composites for Construction*, ASCE, 2001, 5(4): 237-245.
32. Tan KH. Strength Enhancement of Rectangular Reinforced Concrete Columns using Fiber-Reinforced Polymer. *Journal of Composites for Construction*, ASCE, 2002, 6(3): 175-183.

33. Shehata IAEM, Carneiro LAV, Shehata LCD. Strength of Short Concrete Columns Confined with CFRP Sheets. *Materials and Structures*, 2002, 35: 50-58.
34. Lam L, Teng JG. Design-Oriented Stress-Strain Model for FRP-Confined Concrete in Rectangular Columns. *Journal of Reinforced Plastics and Composites*, 2003, 22(13): 1149-1186.
35. Tankut AT, Ersoy U, Aksan B. Repair and Strengthening of Reinforced Concrete Columns. IMO Symposium, CEB, METU, 1989.
36. Suleiman RE. Repair and Strengthening of Reinforced Concrete Columns. PhD Thesis, Middle East Technical University, 1991.
37. Seible F, Priestley MJN, Innamorato D. Earthquake Retrofit of Bridge Columns with Continuous Fiber Jackets. Report: Design Guidelines, Advanced Composite Technology Transfer Consortium, ACTT-95/08, University of San Diego, California, 1995.
38. Seible F, Priestley MJN, Hegemier GA, Innamorato D. Seismic Retrofit of RC Columns with Continuous Carbon Fiber Jackets. *Journal of Composites for Construction*, ASCE, 1997, 1(2): 52-62.
39. Saadatmanesh H, Ehsani MR, Jin L. Repair of Earthquake Damaged RC Columns with FRP Wraps. *ACI Structural Journal*, 1997, 94(2): 206-215.
40. Saadatmanesh H, Ehsani MR, Jin L. Seismic Retrofitting of Rectangular Bridge Columns with Composite Straps. *Earthquake Spectra*, 1997, 13(2): 281-304.
41. Gergely J, Pentelides CP, Nuismer RJ, Reaveley LD. Bridge Pier Retrofit using Fiber-Reinforced Plastic Composites. *Journal of Composites for Construction*, ASCE, 1998, 2(4): 165-174.
42. Pentelides CP, Gergely J, Reaveley LD, Volnyy VA. Retrofit of RC Bridge Pier with CFRP Advanced Composites. *Journal of Structural Engineering*, ASCE, 1999, 125(10): 1094-1099.
43. Ghosh KK. Seismic Upgrade with CFRP of RC Columns Containing Lap Spliced Rebars in Plastic Hinge Regions. MS Thesis, University of Toronto, 2002.

44. Ye LP, Zhang K, Zhao SH, Feng P. Experimental Study on Seismic Strengthening of RC Columns with wrapped CFRP Sheets. *Construction and Building Materials*, 2003, 17: 499-506.
45. Iacobucci RD, Sheikh SA, Bayrak O. Retrofit of Square Concrete Columns with Carbon Fiber-Reinforced Polymer for Seismic Resistance. *ACI Structural Journal*, 2003, 100(6): 785-794.
46. Harajli MH, Rteil AA. Effect of Confinement using Fiber-Reinforced Polymer or Fiber-Reinforced Concrete on Seismic Performance of Gravity Load-Designed Columns. *ACI Structural Journal*, 2004, 101(1): 47-56.
47. Bousias SN, Triantafillou TC, Fardis MN, Spathis L, O'Regan BA. Fiber-Reinforced Polymer Retrofitting of Rectangular Reinforced Columns with or without Corrosion. *ACI Structural Journal*, 2004, 101(4): 512-520.
48. Sause R, Harries KA, Walkup SL, Pessiki S, Ricles JM. Flexural Behavior of Concrete Columns Retrofitted with Carbon Fiber-Reinforced Polymer Jackets. *ACI Structural Journal*, 2004, 101(5): 708-716.
49. Haroun MA, Elsanadedy HM. Fiber-Reinforced Plastic Jackets for Ductility Enhancement of Reinforced Concrete Bridge Columns with Poor Lap-Splice Detailing. *Journal of Bridge Engineering, ASCE*, 2005, 10(6): 749-757.
50. Galal K, Arafa A, Ghobarah A. Retrofit of Square Short Columns. *Engineering Structures*, 2005, 27: 801-813.
51. Chang SY, Tsai I. Experimental Study of As-Built and Composite Materials Retrofitted Reinforced Concrete Columns. *Canadian Journal of Civil Engineering*, 2005, 32: 454-460.
52. Haroun MA, Elsanadedy HM. Behavior of Cyclically Loaded Squat Reinforced Concrete Bridge Columns Upgraded with Advanced Composite-Material Jackets. *Journal of Bridge Engineering, ASCE*, 2005, 10(6): 741-748.
53. ACI Committee 440 Report, Guide for the Design and Construction of Externally Bonded FRP Systems for Strengthening Concrete Structures 2002; 440.2R-02.
54. Turkish Earthquake Resistant Design Code, Ministry and Public Works and Settlement of Turkey, Ankara, Turkey, 2007.

55. Popovics S. A numerical Approach to the Complete Stress Strain Curve for Concrete. *Cement and Concrete Research* 1978; 3(5): 583-599.
56. Doruk K. Fiber Reinforced Polymer Confined RC Circular Columns Subjected to Axial Load and Bending Moment. Master of Science Thesis, Middle East Technical University, 2006.
57. Dhakal RP, Maekawa K. Modeling for Postyield Buckling of Reinforcement. *Journal of Structural Engineering* 2002; 128(9): 1139-1147.
58. Tasdemir MA, Tasdemir C, Jefferson AD, Lydon FD, Barr BIG. Evaluation of Strains at Peak Stresses in Concrete: A Three-Phase Composite Model Approach. *Cement and Concrete Composites* 1998; 20: 301-318.
59. Eurocode 8: Design Provisions for Earthquake Resistance of Structures. ENV 1998-3, CEN, Brussels, 1995.
60. Restrepo JI, DeVino B. Enhancement of Axial Load Carrying Capacity of Reinforced Concrete Columns by means of Fiber-Glass Epoxy Jackets. *Proceedings of Advanced Composite Materials in Bridges and Structures II* 1995; August, Montreal: 547-553.
61. Zou XK, Teng JG, De Lorenzis L, Xia SH. Optimal Performance Based Design of FRP Jackets for Seismic Retrofit of Reinforced Concrete Frames. *Composites Part B: Engineering* 2007; 16(7): 584-597.
62. Mirmiran A, Shahawy M, Samaan M, El Echary H. Effect of Column Parameters on FRP-Confined Concrete. *Journal of Composites for Construction, ASCE* 1998; 2(4): 175-185.
63. ACI Committee 440 Report, Guide for the Design and Construction of Externally Bonded FRP Systems for Strengthening Concrete Structures 2002; 440.2R-02.
64. Lam L, Teng JG. Design Oriented Stress-Strain Model for FRP-Confined Concrete in Rectangular Columns. *Journal of Reinforced Plastics and Composites* 2003; 22(13): 1149-1186.
65. Lam L, Teng JG. Design Oriented Stress – Strain Model for FRP Confined Concrete. *Construction and Building Materials* 2003; 17(6-7): 471-489.
66. Xiao Y, Wu H. Compressive Behavior of Concrete Confined by Carbon Fiber Composite Jackets. *Journal of Materials in Civil Engineering* 2000; 12(2): 139-146.

67. Wu G, Lu ZT, Wu ZS. Strength and Ductility of Concrete Cylinders Confined with FRP Composites. *Construction and Building Materials* 2006; 20(3): 134-148.
68. Rochette P, Labossiere P. Axial Testing of Rectangular Column Models Confined with Composites. *Journal of Composites for Construction* 2000; 4(3): 129-136.
69. Binici B. Design of FRPs in Circular Bridge Column Retrofits for Ductility Enhancement. *Engineering Structures* 2007; 5(12).
70. Mylrea TD. Bond and Anchorage. *Proceedings: Journal of the American Concrete Institute*, 1948, 19(7): 521-552.
71. Sezen H. Seismic Behavior and Modeling of Reinforced Concrete Building Columns. PhD Dissertation, University of California, Berkeley, 2006.
72. Lehman DE, Moehle JP. Seismic Performance of Well-Confined Concrete Bridge Columns. Pacific Earthquake Engineering Research Center, PEER Report 1998/01, Dec2000.
73. Cosenza E, Manfredi G, Verderame GM. A Fibre Model for Push-Over Analysis of Underdesigned Reinforced Concrete Frames. *Computers and Structures* 2006; 84(13-14): 904-916.
74. Corley WG. Rotational Capacity of Reinforced Concrete Beams. *Journal of Structural Division, ASCE* 1966; 92(5): 121-146.
75. Park R, Paulay T. *Reinforced Concrete Structures*. John Wiley & Sons 1996, New York: 769 pages.
76. CSA Standard S806-02, Design and Construction of Building Components with Fibre Reinforced Polymers. Canadian Standards Association, 178 Rexdale Boulevard, Rexdale, On, 2002.
77. Saatcioglu M, Razvi SR. Displacement Based Design of Reinforced Columns for Confinement. *ACI Structural Journal* 2002; 90(1): 3-11.
78. Elnabesy G, Saatcioglu M. Concrete Bridge Columns Retrofitted with Carbon Fibre Reinforced Polymer (CFRP) Sheets. OCEERC Research Report, Dept. of Civil Engineering, Univ. of Ottawa, Ottawa, 2003.
79. Elnabesy G, Saatcioglu M. Design of FRP Jackets for Seismic Retrofit of Circular Concrete Columns. *Emirates Journal for Engineering Research* 2004; 9(2): 65-69.

80. Sheikh SA, Li Y. Design of FRP Confinement for Square Concrete Columns. *Engineering Structures* 2007; 29: 1074-1083.
81. Sheikh SA, Houry SS. A Performance Based Approach for the Design of Confining Steel in Tied Columns. *ACI Structural Journal* 1997; 94(4): 421-431.
82. Memon MS, Sheikh SA. Seismic Behavior of Square Concrete Columns Retrofitted with Glass Fibre-Reinforced Polymers. Research Report, Dept. of Civil Engineering, Univ. of Toronto, On. 2002.
83. Ozcan O, Binici B, Ozcebe G. Improving Seismic Performance of Deficient Reinforced Concrete Columns Using Carbon Fiber Reinforced Polymers. *Engineering Structures*, 30, 1632-1646 (2008).

APPENDIX A

BASE ROTATION CALCULATIONS AND MEMBER STABILITY CHECKS

Since the base rotations were not recorded during the tests, in order to check the levels of base rotations and member stability of the test setup, simple calculations were done regarding the lateral forces and moments. Firstly, the worst condition of lateral and axial loading that led to overturning or sliding of the specimen was determined. In addition, the 48 mm-diameter HS bolts that connected the specimen to the main footing were ignored in order to simulate the worst condition that could happen during the test. Afterwards, overturning and sliding circumstances for the test specimens were checked that will lead to any unintended movement of the specimen. Further, the initial elastic stiffness for the specimens was checked regarding the uncracked moment of inertias.

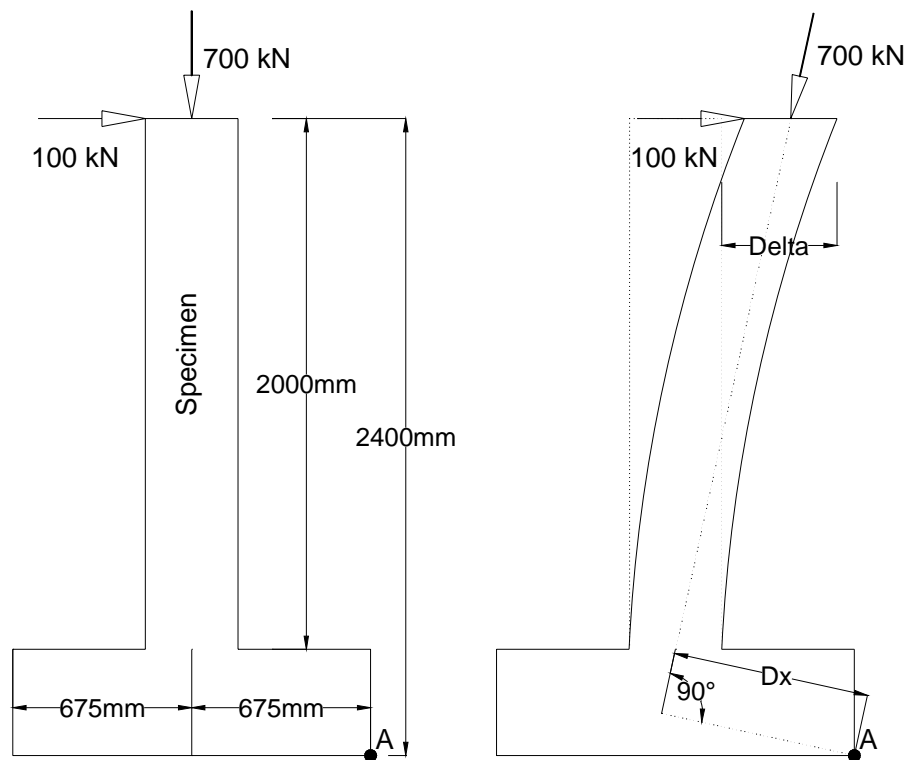


Figure A.1 The forces acting on the specimen for the worst case scenario

As shown in Figure A.1, the worst case scenario that a specimen can experience can be selected as the condition with no lateral displacement under lateral and axial loading. The sliding and overturning checks are stated below.

Sliding and Overturning Checks:

$$\Sigma X = P - \mu N = 100 - 0.2 \times 700 \quad (\mu : \text{Friction coefficient})$$

$$\Sigma X = -40 \text{ kN} \quad (\text{No sliding will occur})$$

$$\Sigma M_A = P \times (L_{\text{specimen}} + h_{\text{footing}}) - N \times \frac{L_{\text{footing}}}{2}$$

$$\Sigma M_A = 100 \times (2.0 + 0.4) - 700 \times \frac{400}{2}$$

$$\Sigma M_A = -232.5 \text{ kNm} \quad (\text{No overturning will occur})$$

Initial elastic stiffness check:

For elastic stiffness checks, the reference specimens were considered. The obtained elastic stiffness values are compared in Figures A.2-A.4. Since the elastic stiffness for the specimens conforms to the calculated stiffness values, it can be stated that the base rotations for the specimen foundation were insignificant during the tests.

$$k_{\text{elastic}} = \frac{3EI}{L^3} = \frac{3 \times 4750 \sqrt{f_c'} \times \frac{bh^3}{12}}{L^3}$$

$$k_{\text{elastic}} = \frac{3 \times 4750 \sqrt{14} \times \frac{350 \times 350^3}{12}}{2000^3} = 8334.5 \text{ N/mm} \quad (\text{S-L-0-00})$$

$$k_{\text{elastic}} = \frac{3 \times 4750 \sqrt{20} \times \frac{350 \times 350^3}{12}}{2000^3} = 9961.6 \text{ N/mm} \quad (\text{S-H-0-00})$$

$$k_{\text{elastic}} = \frac{3 \times 4750 \sqrt{12} \times \frac{200 \times 400^3}{12}}{2000^3} = 6581.8 \text{ N/mm} \quad (\text{R-NC-0-00})$$

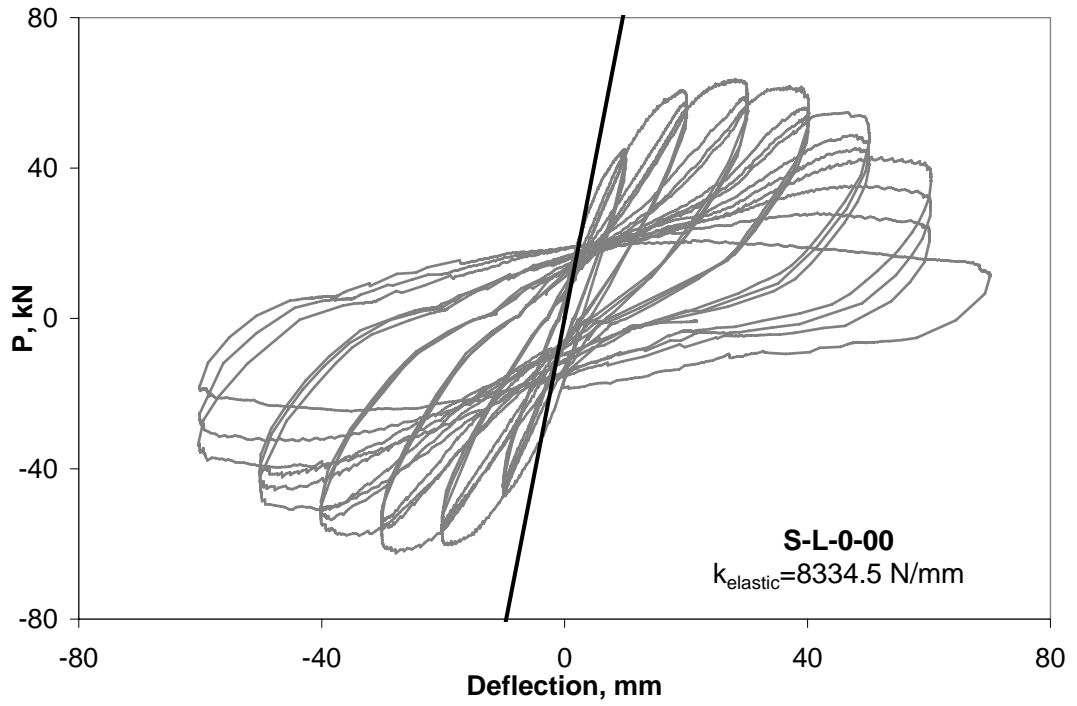


Figure A.2 Elastic Stiffness and member response for specimen S-L-0-00

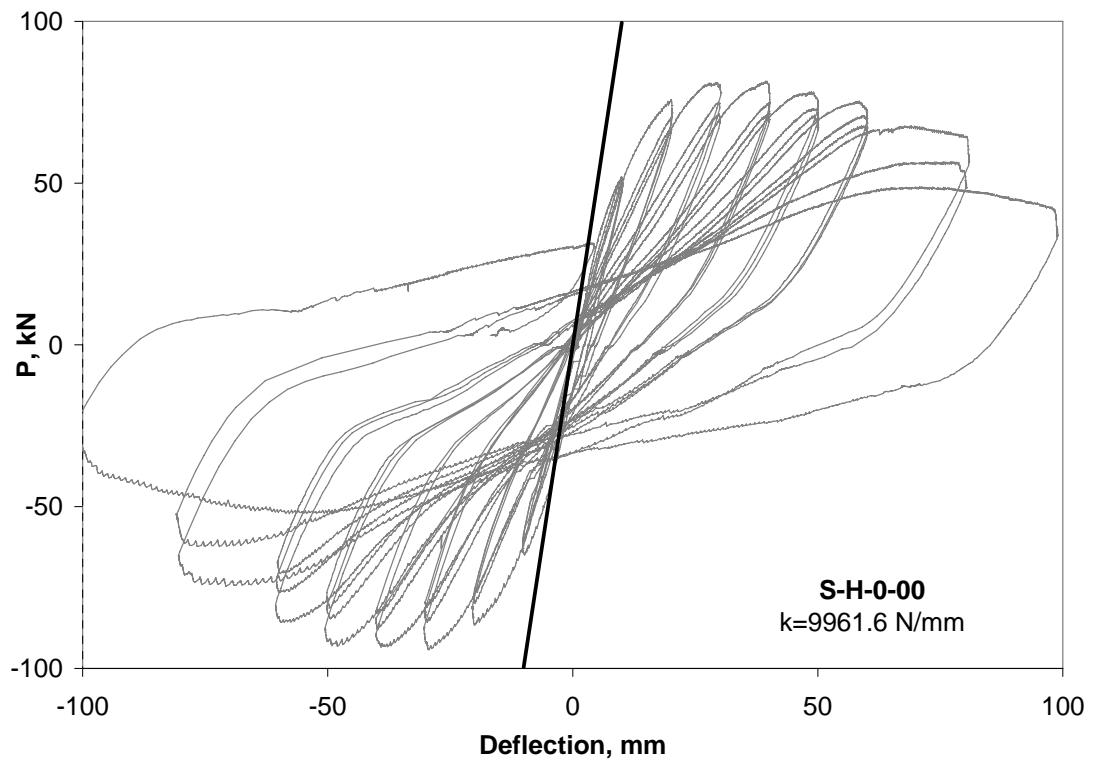


Figure A.3 Elastic Stiffness and member response for specimen S-H-0-00

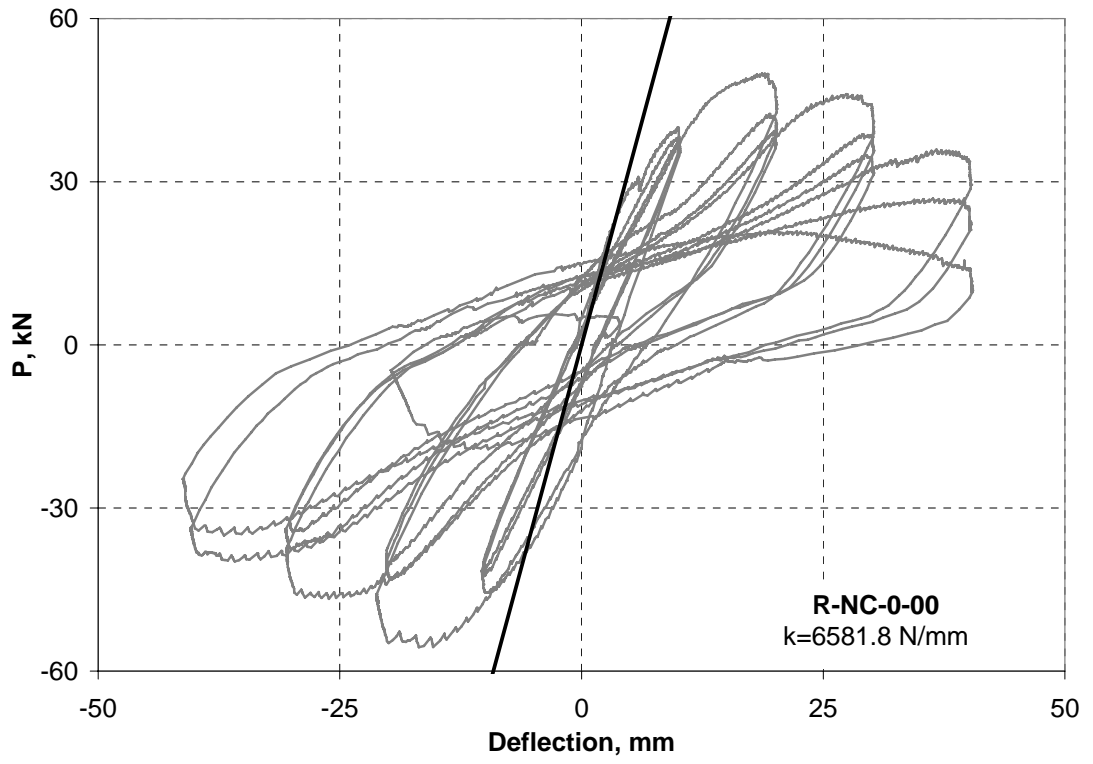


Figure A.4 Elastic Stiffness and member response for specimen R-NC-0-00

APPENDIX B

UNEXPECTED FAILURE MODES

Two of the specimens in Series 1 failed with an unexpected failure mode having plastic hinge formation in the middle part of the columns. One of the columns U1 was the reference column and the other one U2 was the 1-layer CFRP wrapped column. The formation of this failure type was interpreted due to the slipping of the plain reinforcing bars along the height of the column rather than in the footing. In order to prevent this failure type, the longitudinal rebars was welded to the outer transverse bars. Another approach for the formation of this type of failure was the difference in concrete compressive strengths of the three batches of concrete during the casting process. Since one specimen was cast using three batches of concrete, each batch was poured using the same mixture of fine-coarse aggregate, water and cement. Any unexpected variation and reduction in concrete strength in the middle sections of the column might have resulted in the formation of the plastic hinging at this part. Herein, this failure type was investigated by giving the specimens responses in Lateral Force (P) – Tip Deflection (Δ), Moment (M) – Average Curvature (K), Moment (M) – Fixed End Rotation (FER) and Drift – Strain (ϵ) graphs.

For the unwrapped specimen U1, the specimen responses also show the unexpected behavior (Figure B.1) through observing deflection (Figure B.2), curvature (Figure B.3) and fixed-end rotation (Figure B.4) responses. The plastic hinge formation in the middle section of the column enforced the reductions in curvature and fixed-end rotations at the test region. The curvature level of 10 rad/km and 0.3% of fixed-end rotations were monitored during the test. The deflection profile shown in Figure B.5 also illustrates how the column bent by its middle section as opposed to the standard flexural column failure at the base. The rotation and deflection components also reduced considering the unexpected failure type in the middle section of the column as shown in Figure B.6. Strain gage responses proves this fact since the upper bars located at 350 mm from the base yielded before the bottom bars located at 50 mm above the base as shown in Figure B.7.



(a)

(b)

Figure B.1 U1 at the end of test (a) Full view and (b) Close-up view

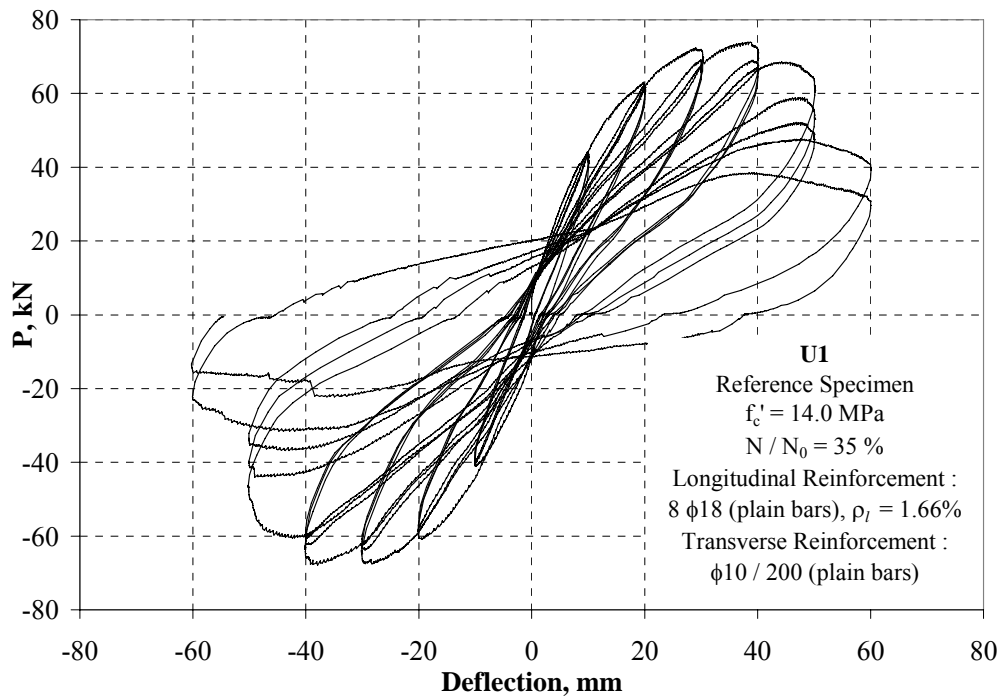
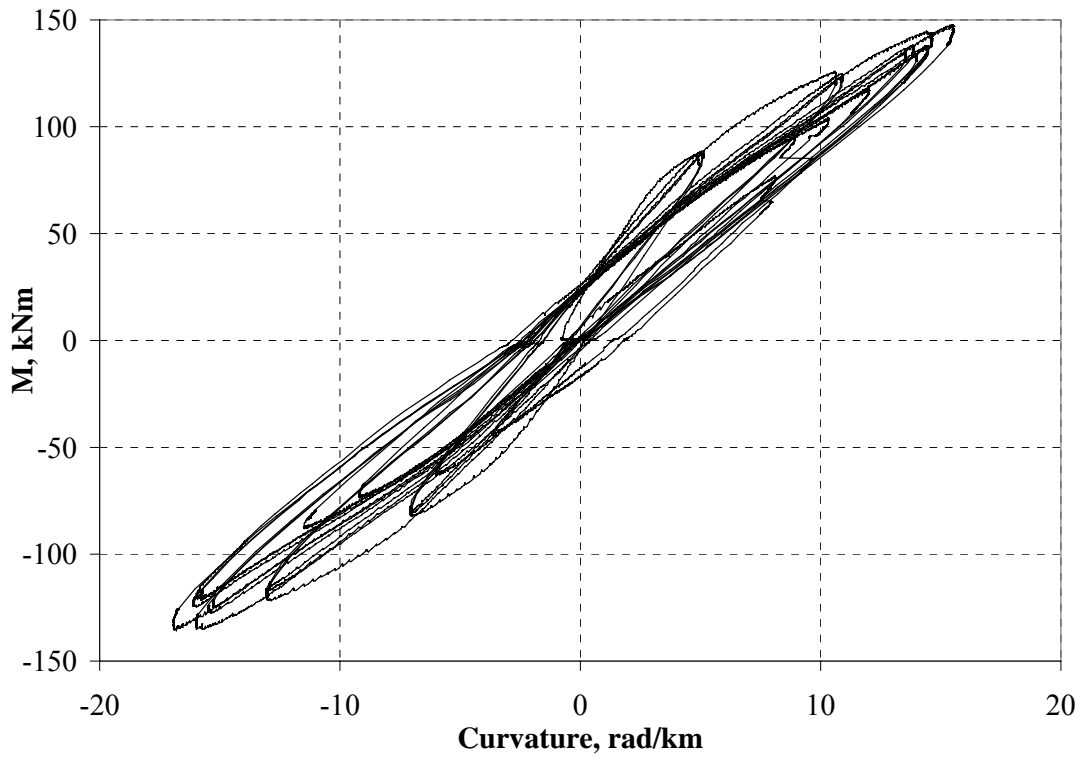
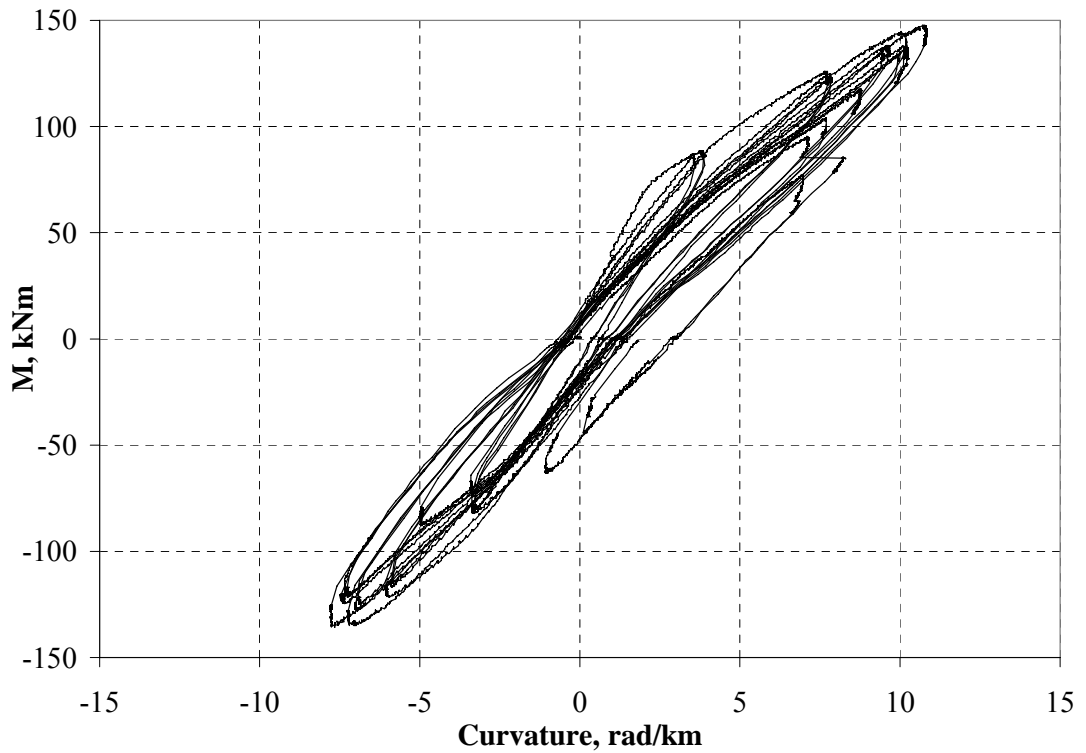


Figure B.2 The Lateral Force (P) – Tip Deflection (Δ) response for U1



(a)



(b)

Figure B.3 Moment-Curvature response for U1: (a) 350-0 and (b) 350-50 mm

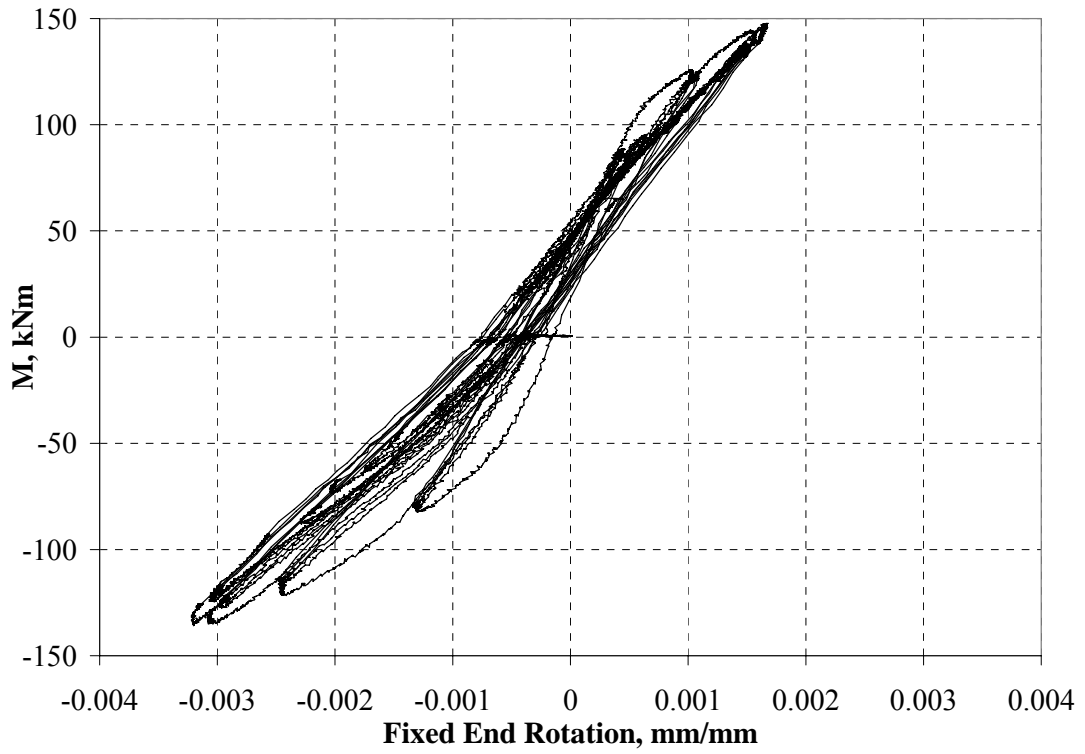


Figure B.4 The Moment (M) – Fixed End Rotation (FER) response for U1

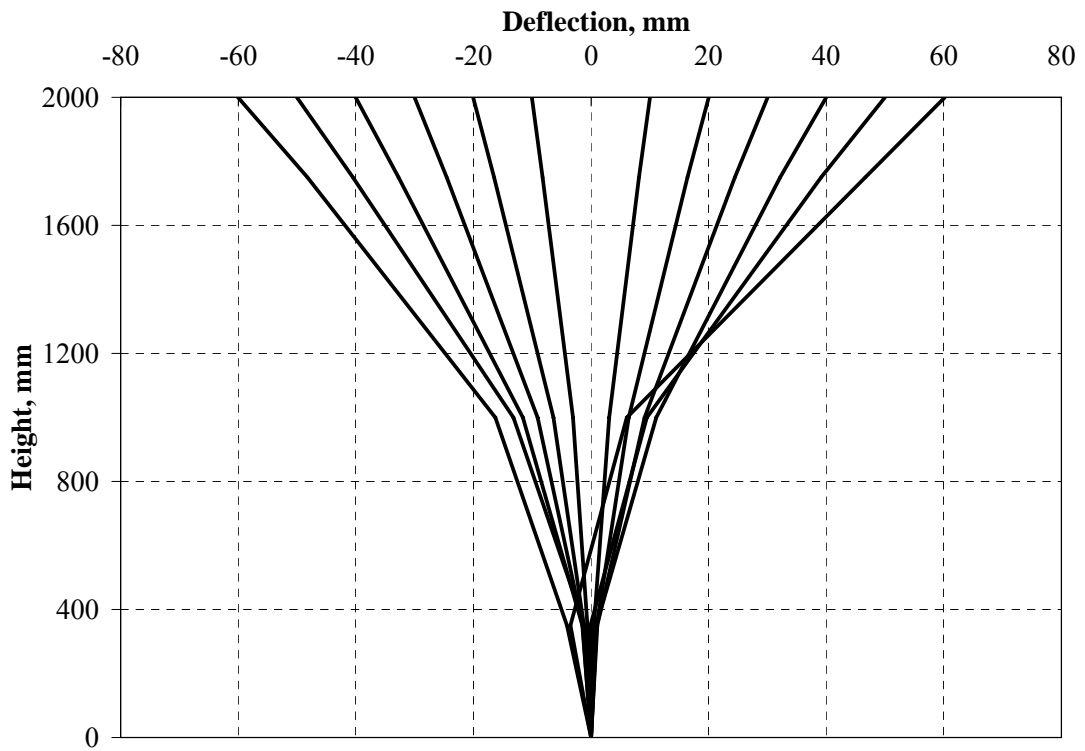
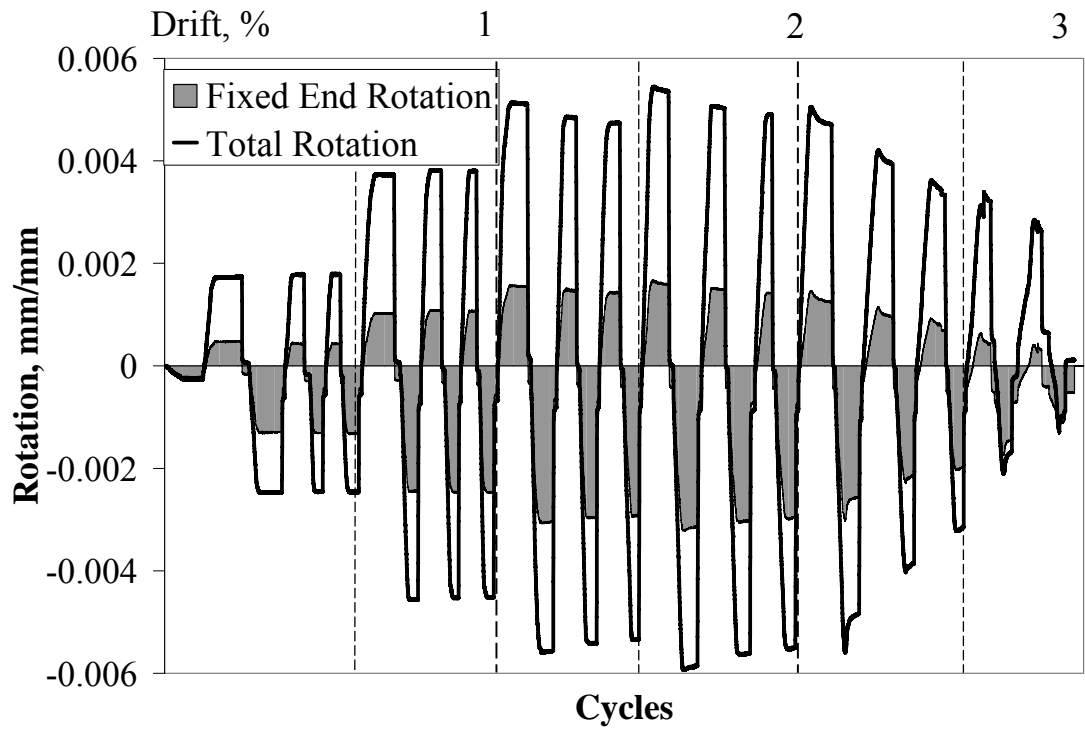
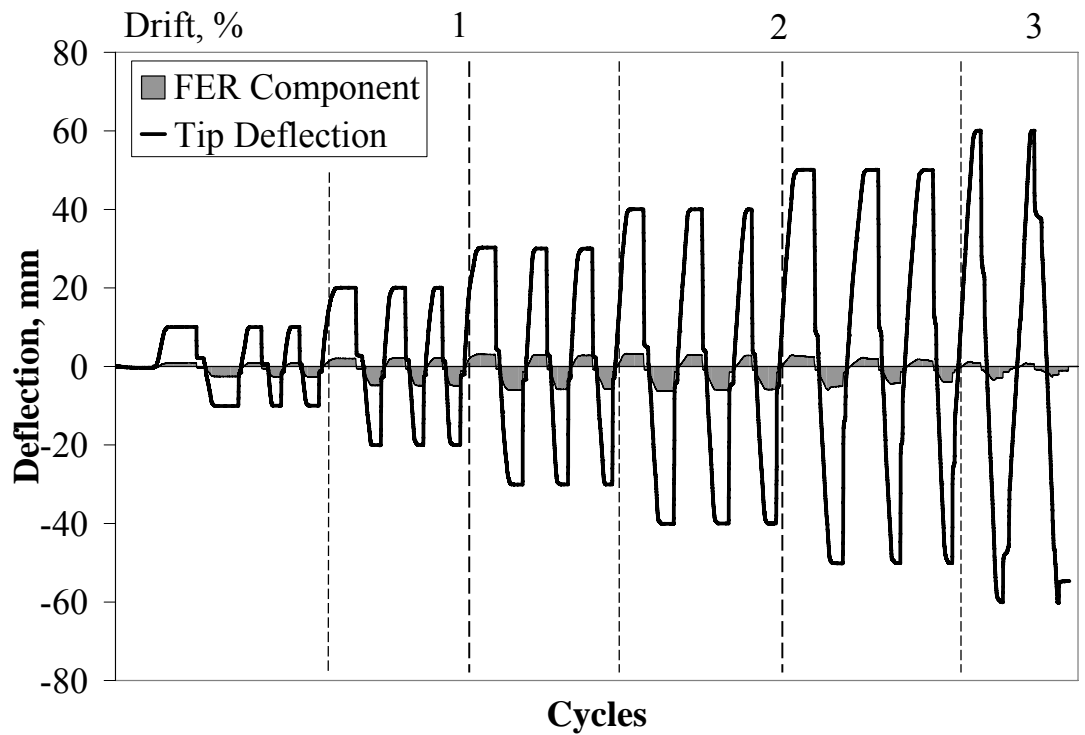


Figure B.5 The Deflection profile for U1



(a)



(b)

Figure B.6 (a) Rotation and (b) Deflection Components for U1

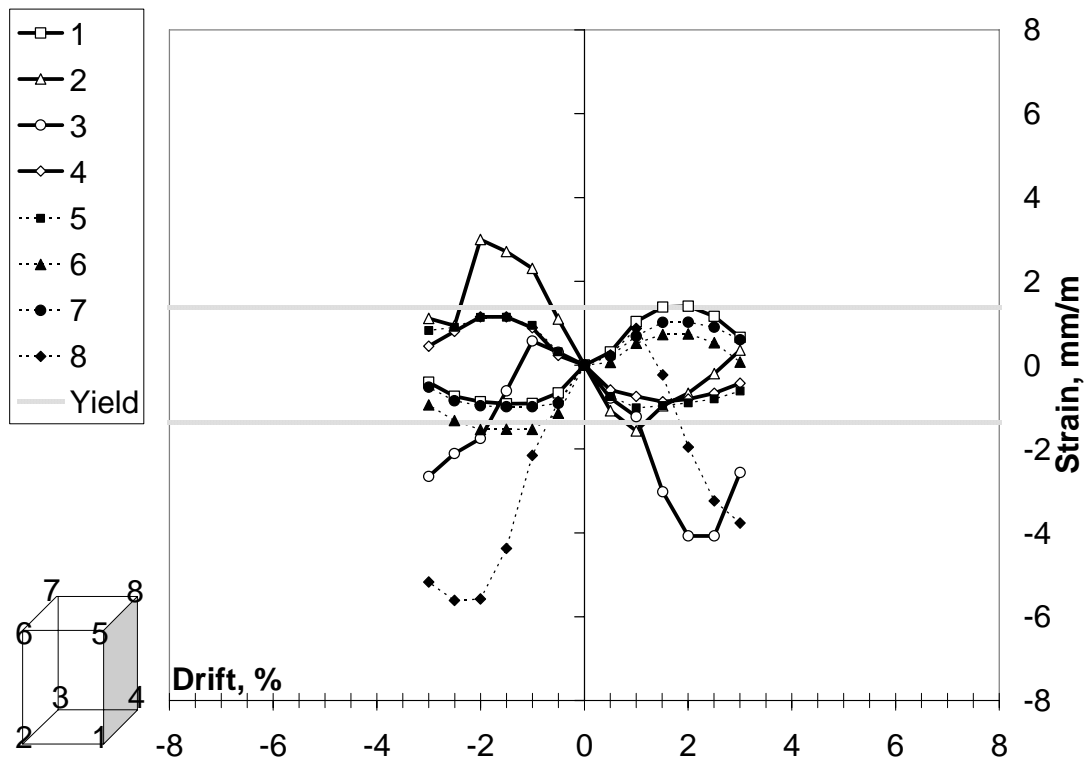


Figure B.7 Drift – Strain (ϵ) response for U1

For the 1-layer CFRP strengthened specimen U2, the specimens exhibited an unexpected behavior as shown in Figure B.8. As shown in Figure B.9, the seismic response for the specimen U2 in lateral loading had a lower initial stiffness as compared to the standard failure type. The curvatures and fixed-end rotations could have the values of maximum 15 rad/km and 0.01 rad, respectively (Figures B.10 and B.11). The deflection profile as shown in Figure B.12 supports that there was no response monitored at the test region that is 350 mm from the column base. The rotation components had the values over the reference specimen U1 since the interface cracking occurred at the base. Whereas, the deflection components proves the formation of plastic hinging in the middle section of the column, owing to the lowered level of fixed-end rotation components (Figure B.13). The strain gage responses as shown in Figure B.14 illustrates that the longitudinal bars at the bottom were yielded.

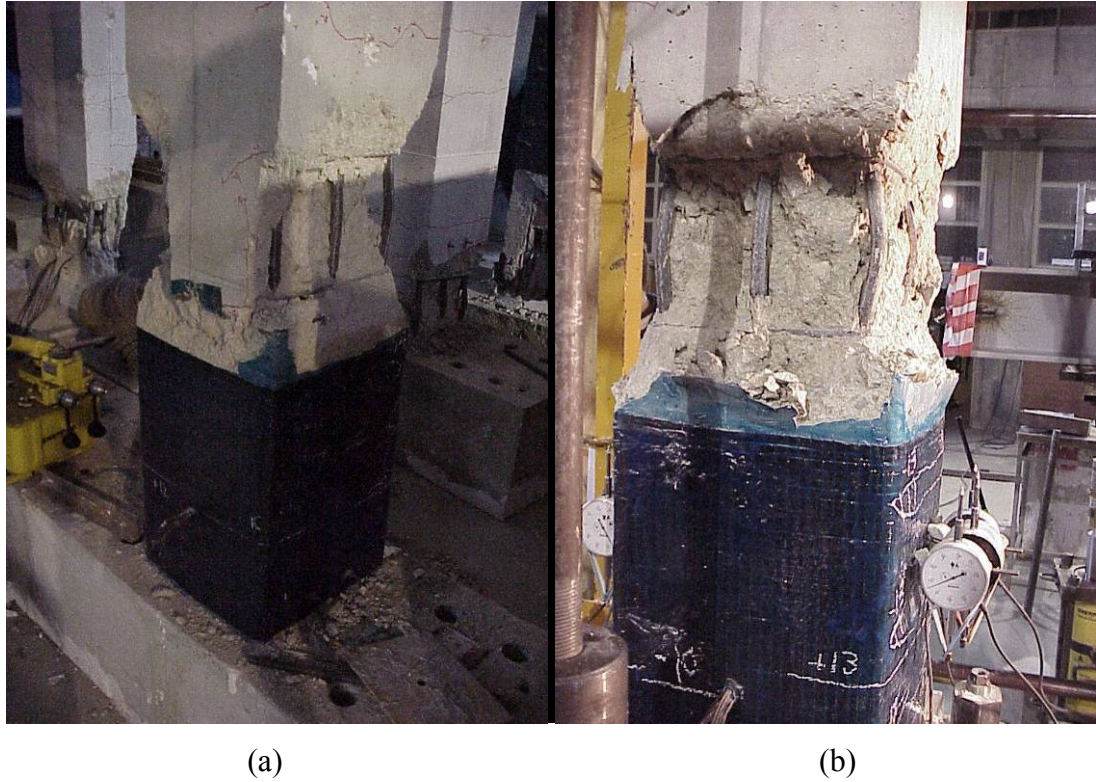


Figure B.8 U2 at the end of test (a) Full view and (b) Close-up view

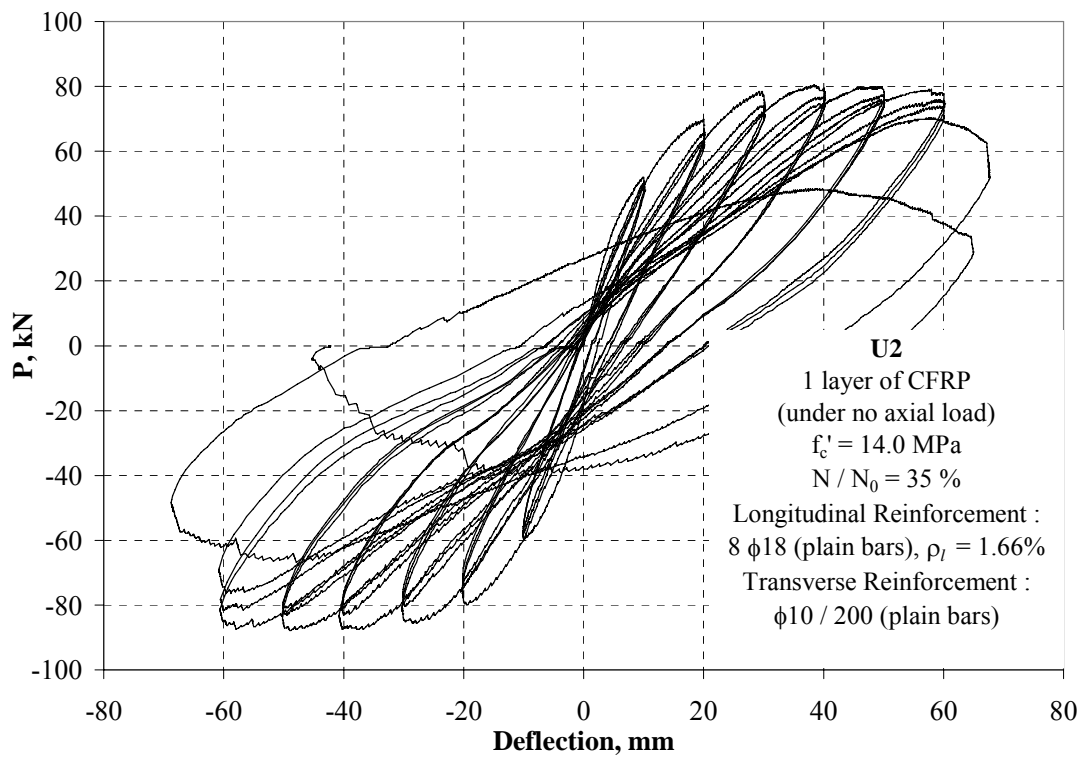
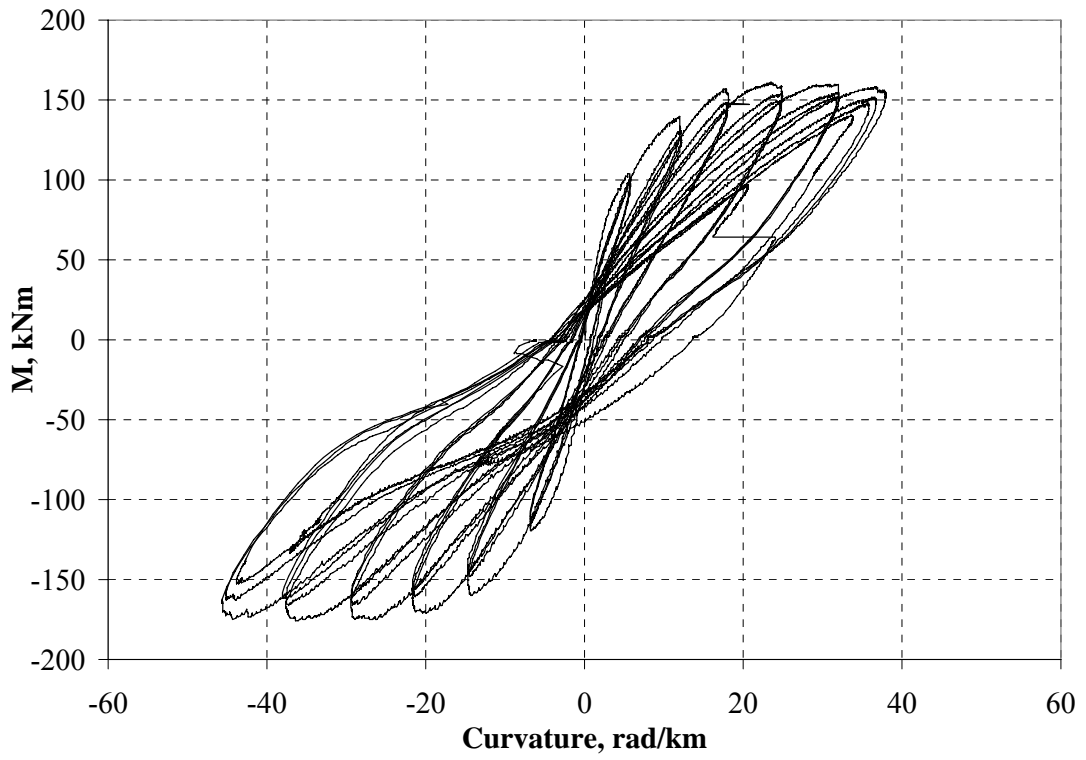
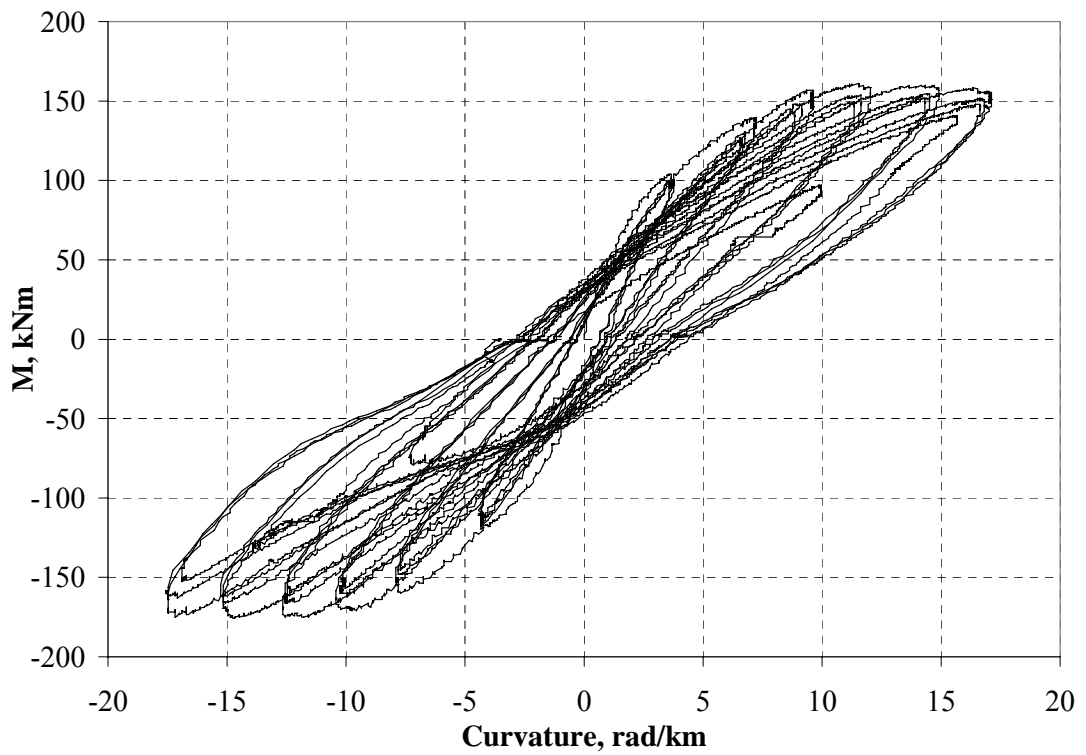


Figure B.9 The Lateral Force (P) – Tip Deflection (Δ) response for U2



(a)



(b)

Figure B.10 Moment-Curvature response for U2: (a) 350-0 and (b) 350-50 mm

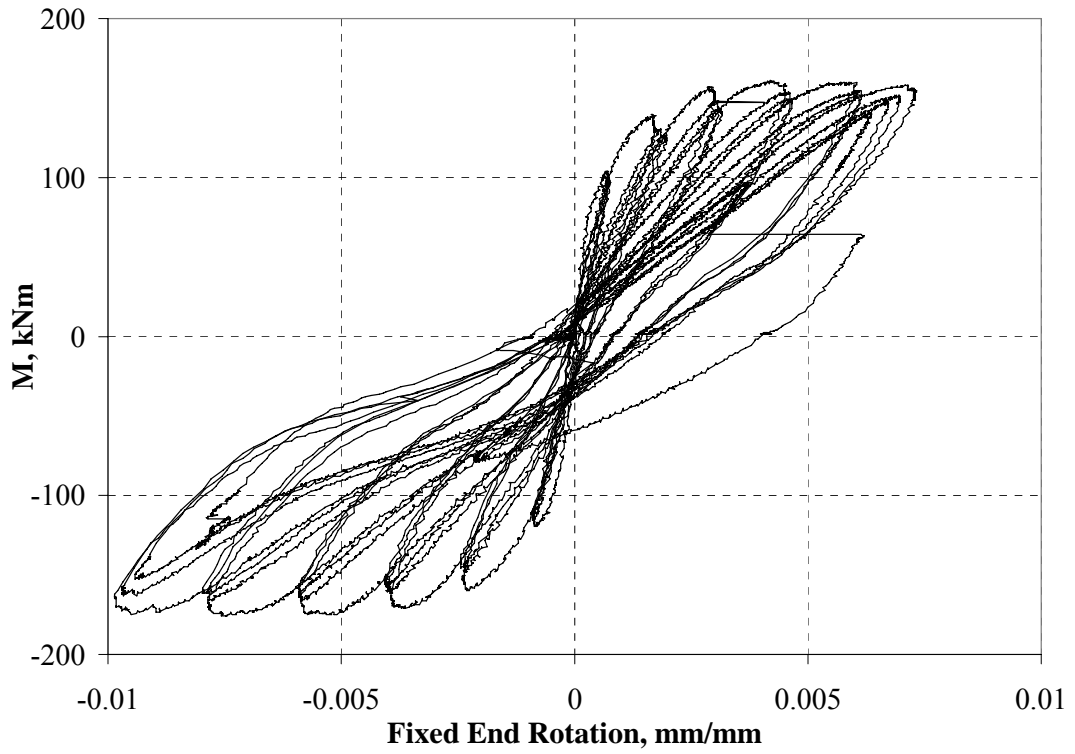


Figure B.11 The Moment (M) – Fixed End Rotation (FER) response for U2

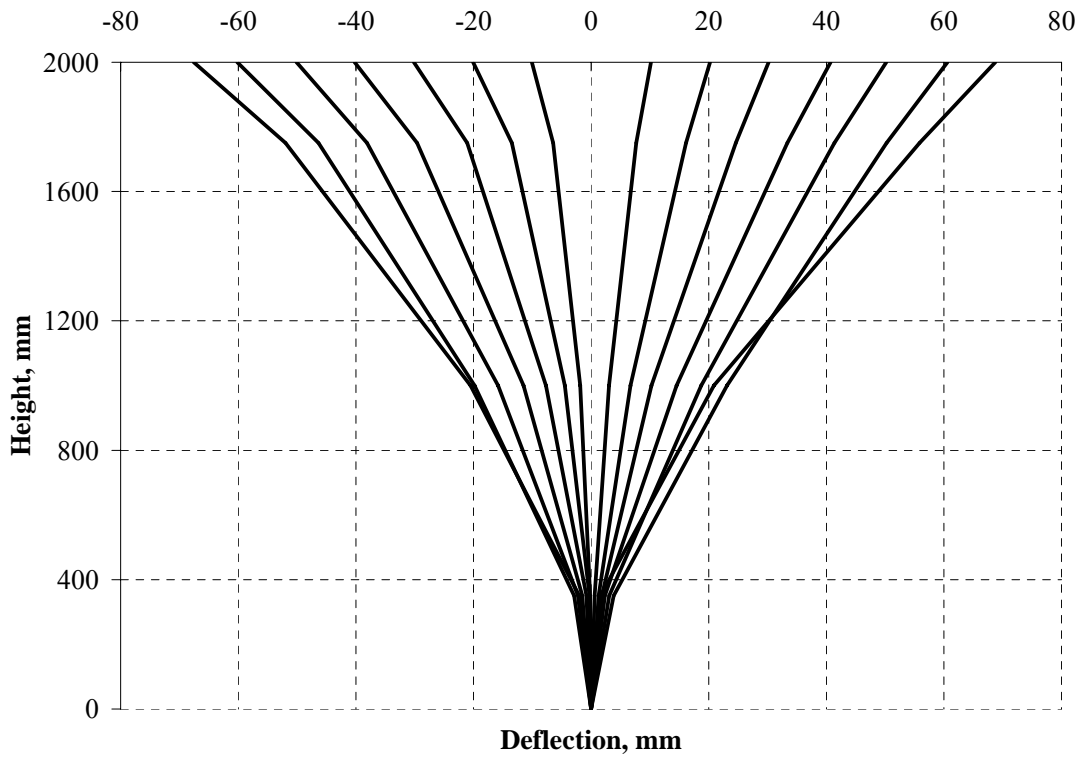
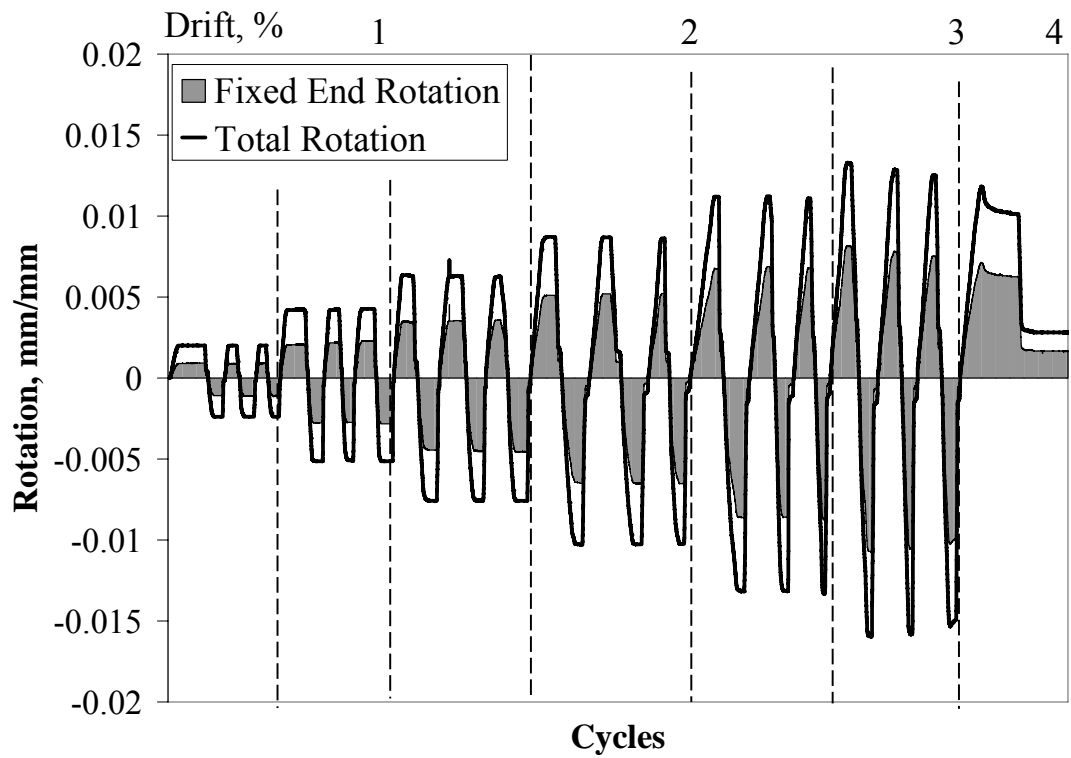
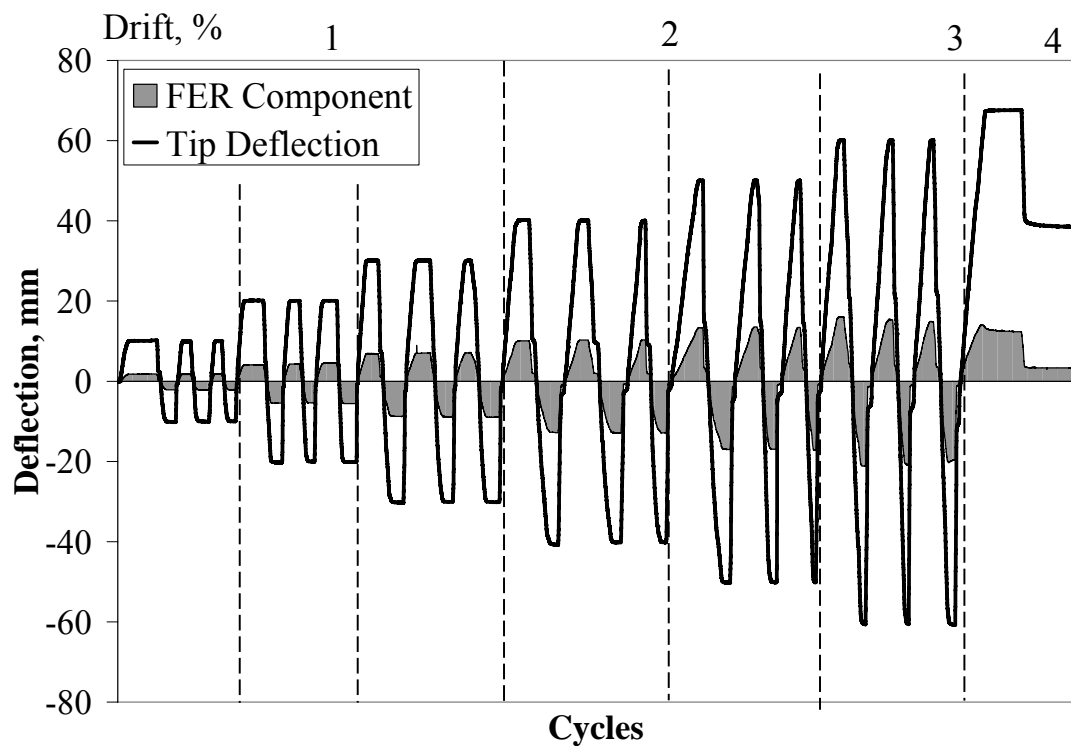


Figure B.12 The Deflection profile for U2



(a)



(b)

Figure B.13 (a) Rotation and (b) Deflection Components for U2

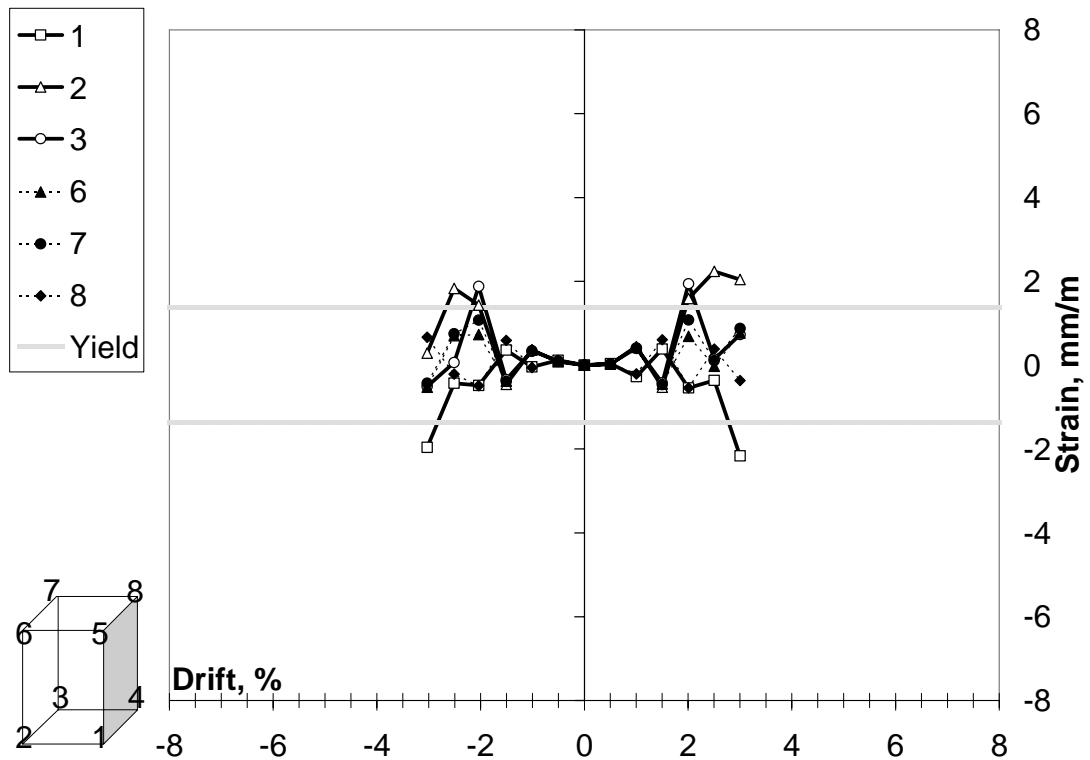


Figure B.14 Drift – Strain (ϵ) response for U2

The specimen C1 was tested for model calibration processes and had the same properties as the reference specimen S-L-0-00 except the concrete compressive strength of 20 MPa. The end-of-test photo of the specimen C1 is shown in Figure B.15. In addition, as shown in Figure B.16, the ultimate drift ratio for C1 is 2.5% sustaining an ultimate curvature of 50 rad/km with the ultimate value of fixed-end rotation level of 0.01 rad (Figures B.17 and B.18). The response of the specimen is very close to the reference specimen S-L-0-00 since the deflection profiles are similar as shown in Figure B.19. The rotation and deflection components presented in Figure B.20 illustrates that about 50% of contribution was attained by the fixed-end rotation responses. Lastly, the strain gage responses implies that the longitudinal bars were yielded and due to buckling of the reinforcing bars the column failed as shown in Figure B.21.

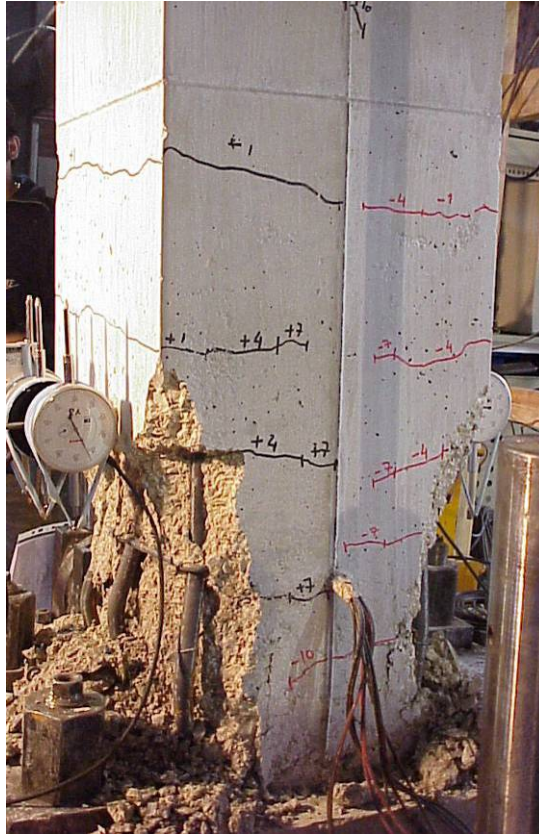


Figure B.15 C1 at the end of test

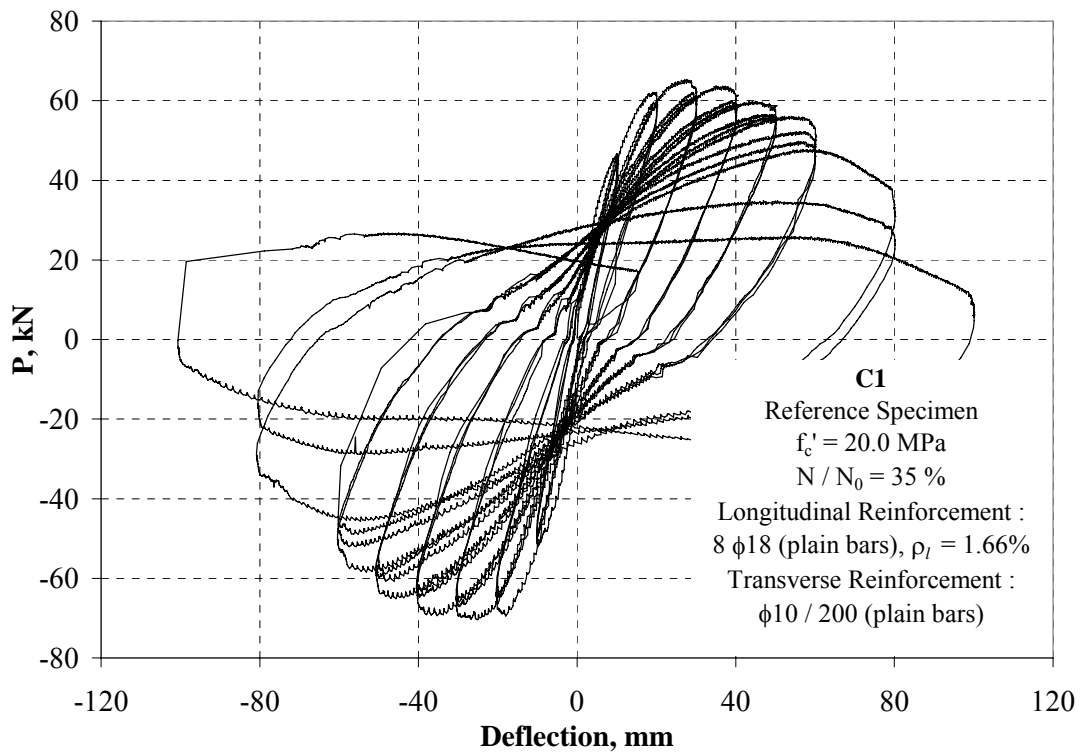
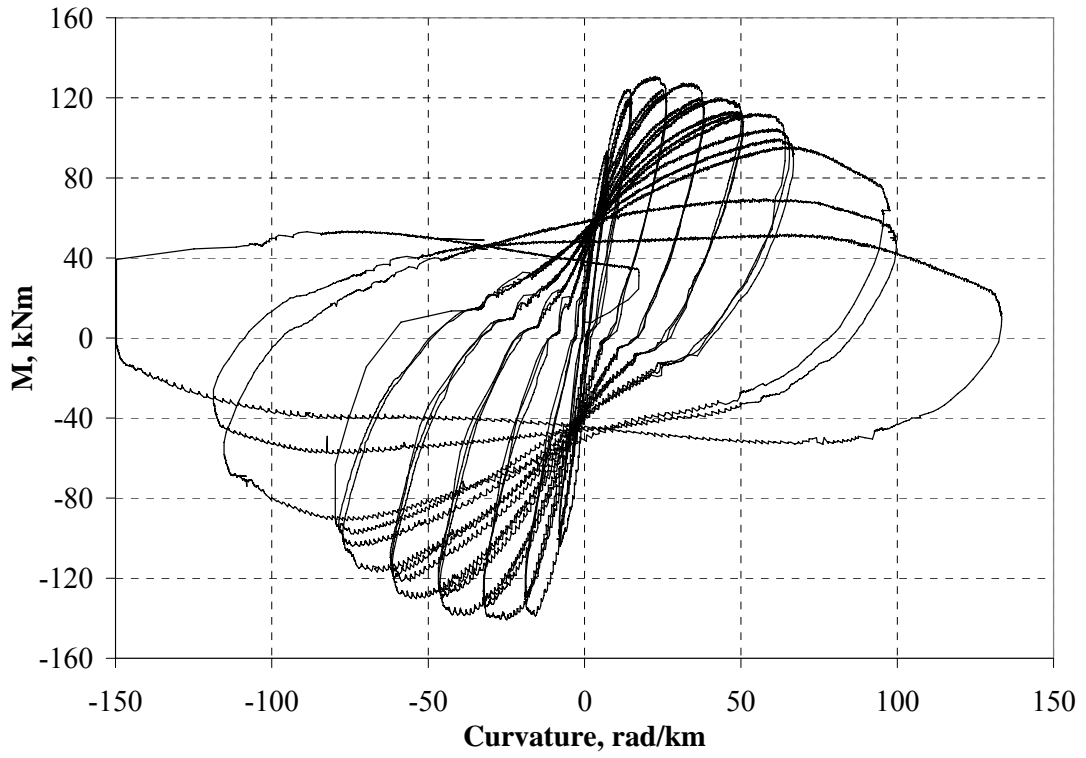
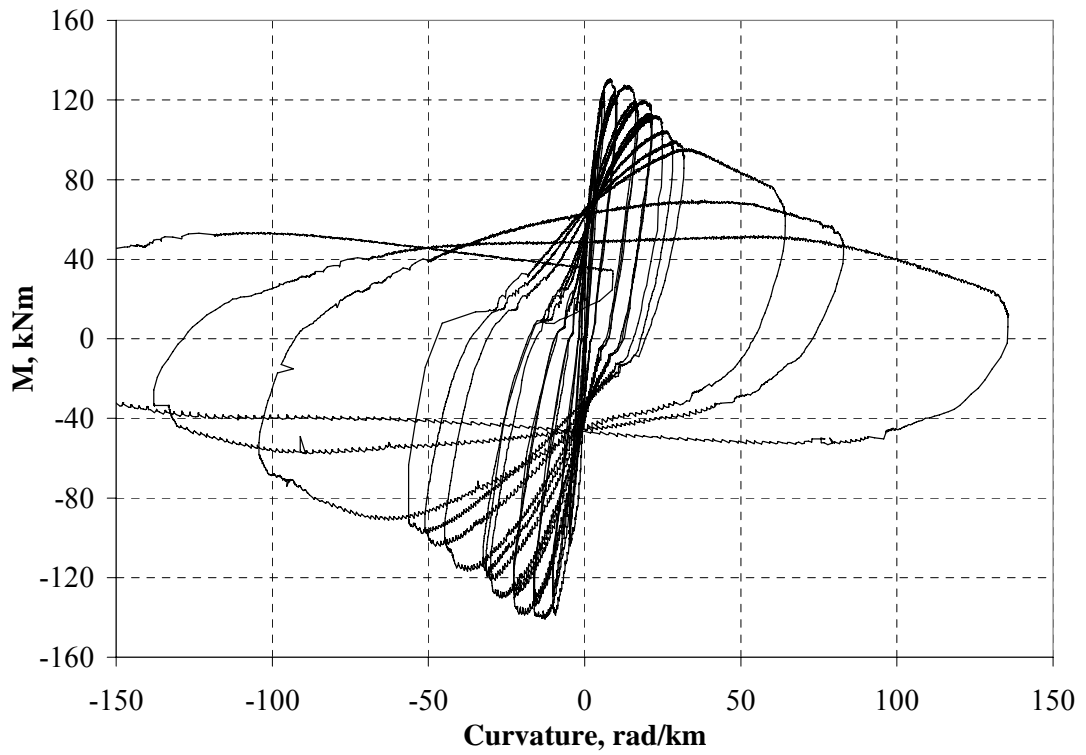


Figure B.16 The Lateral Force (P) – Tip Deflection (Δ) response for C1



(a)



(b)

Figure B.17 Moment-Curvature response for C1: (a) 350-0 and (b) 350-50 mm

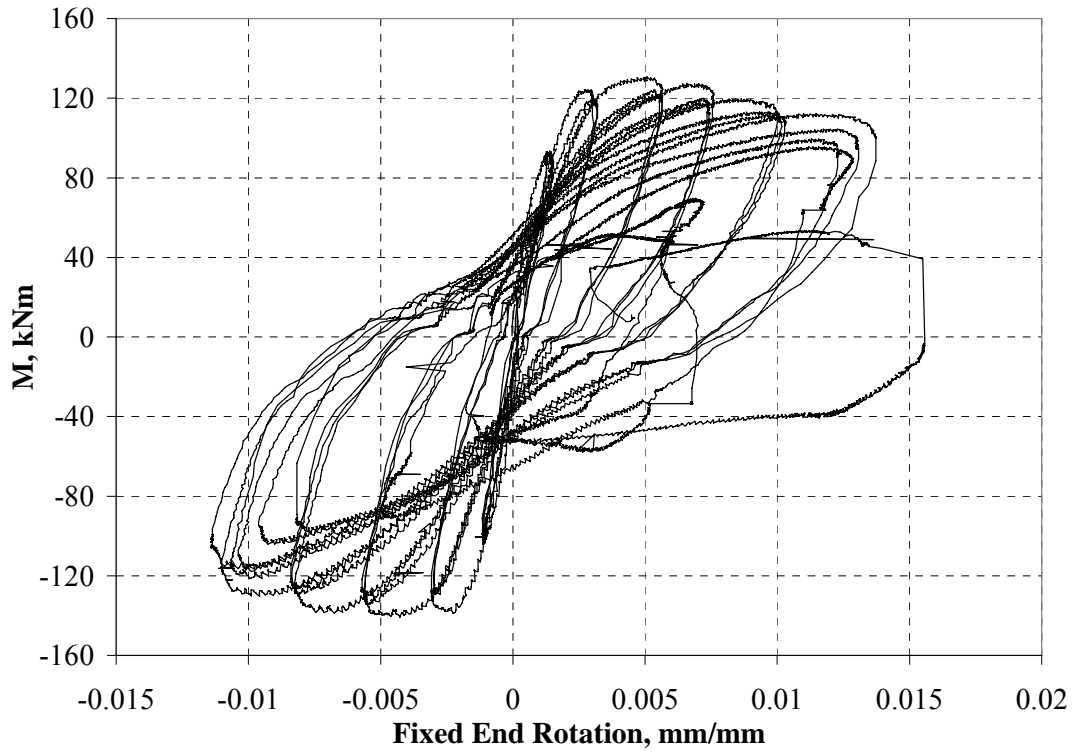


Figure B.18 The Moment (M) – Fixed End Rotation (FER) response for C1

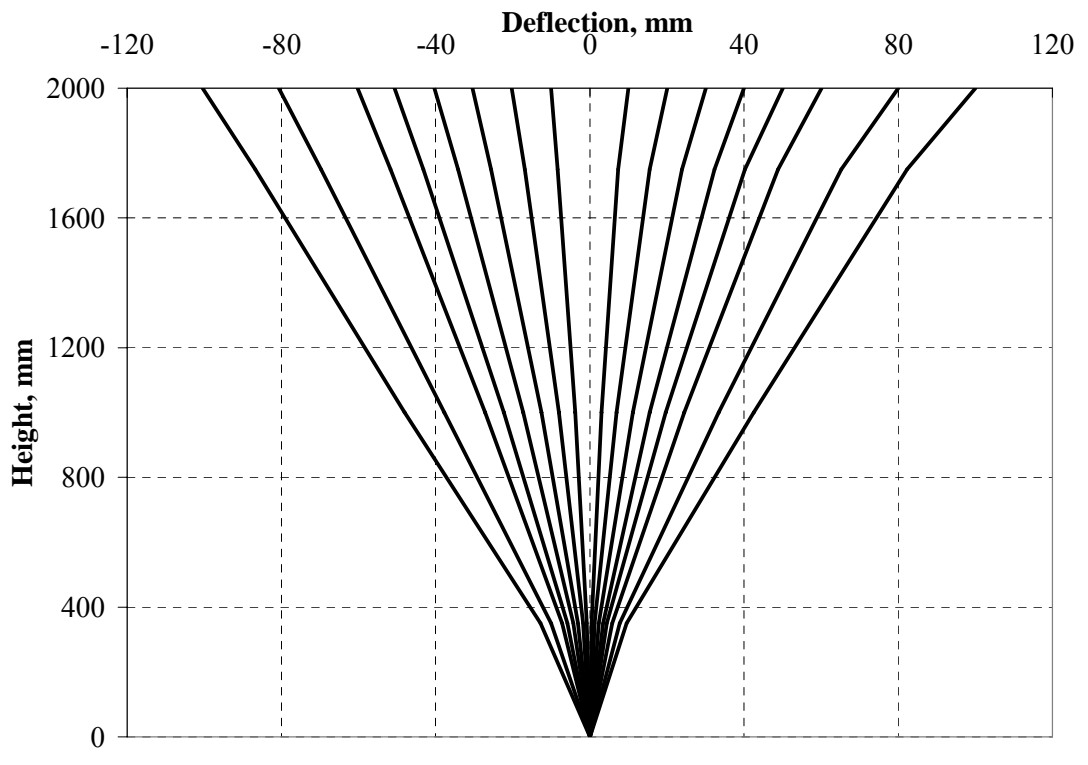
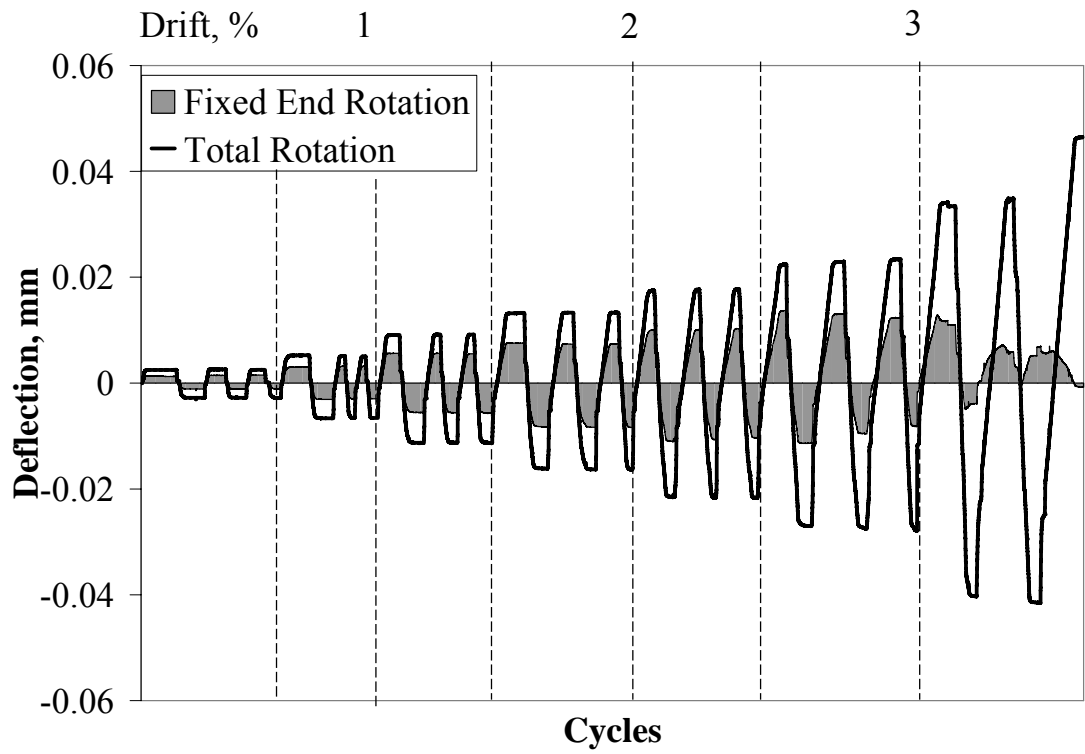
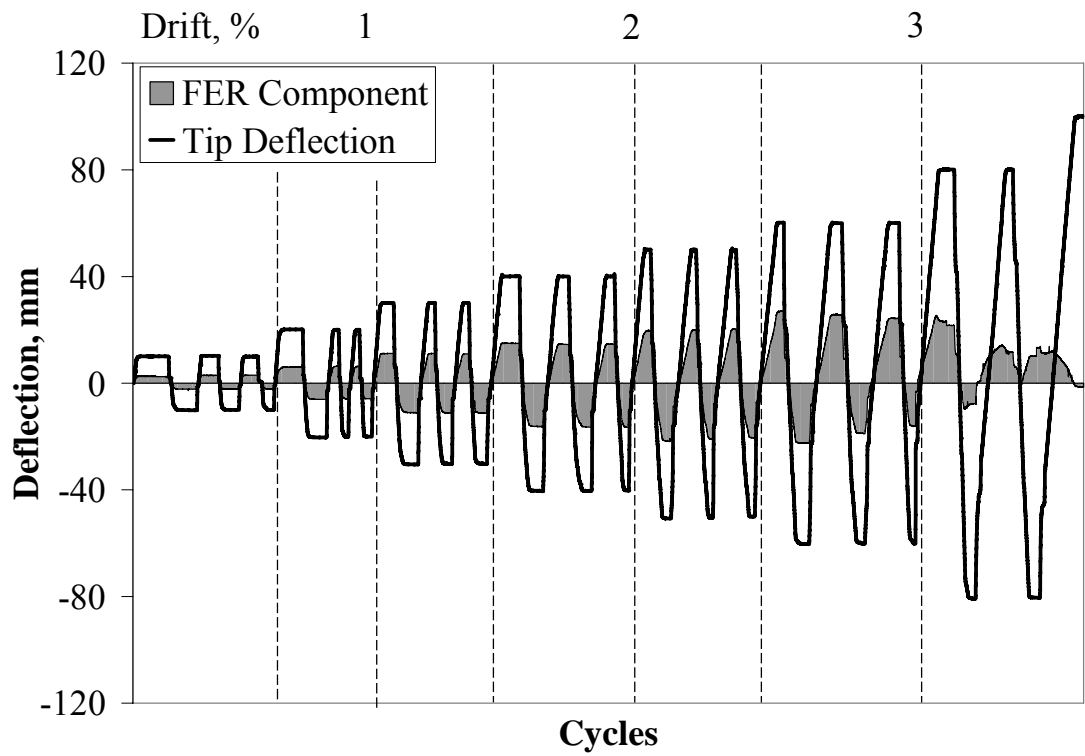


Figure B.19 The Deflection profile for C1



(a)



(b)

Figure B.20 (a) Rotation and (b) Deflection Components for C1

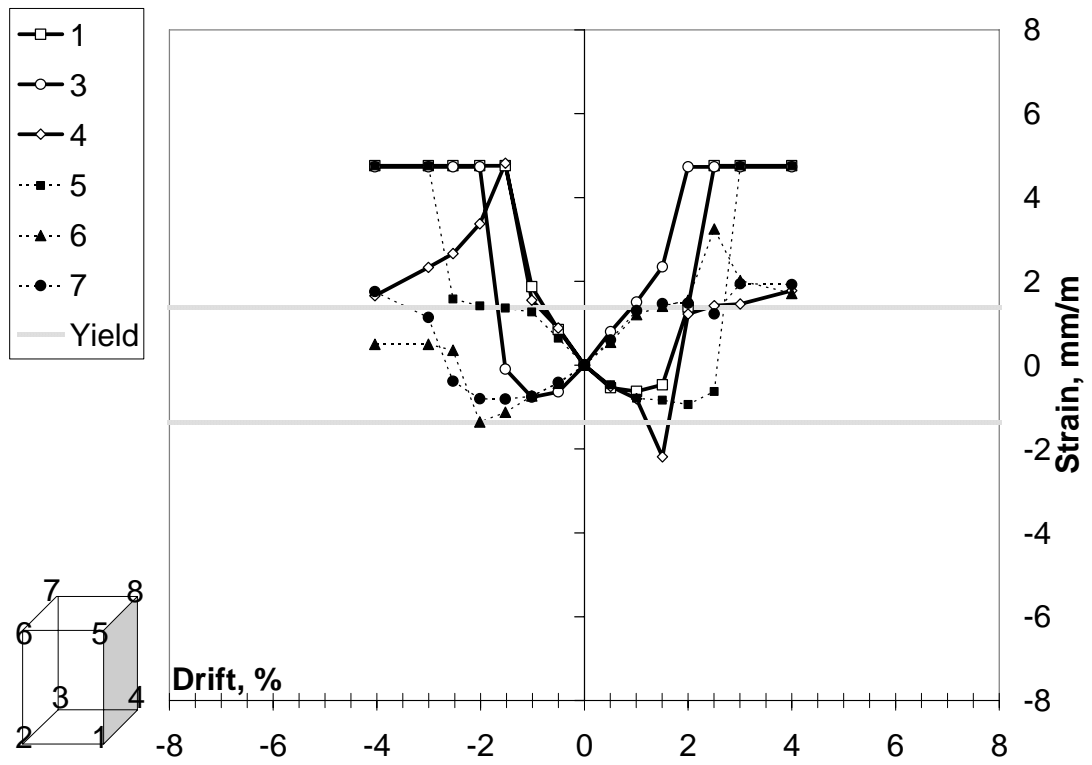


Figure B.21 Drift – Strain (ϵ) response for C1

APPENDIX C

HYSTERETIC STRAIN PLOTS

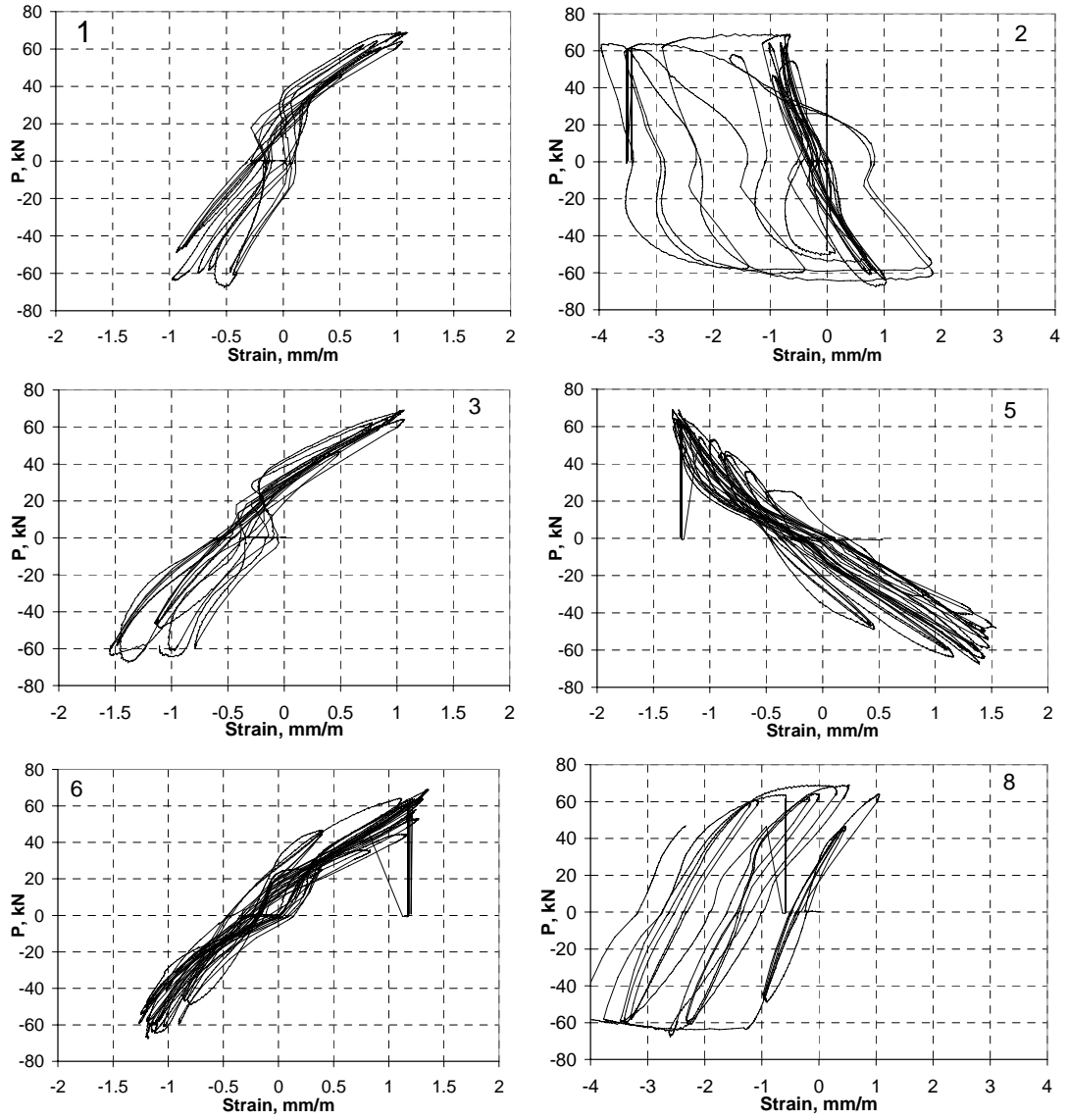


Figure C.1 Strain gage responses for specimen S-L-0-00

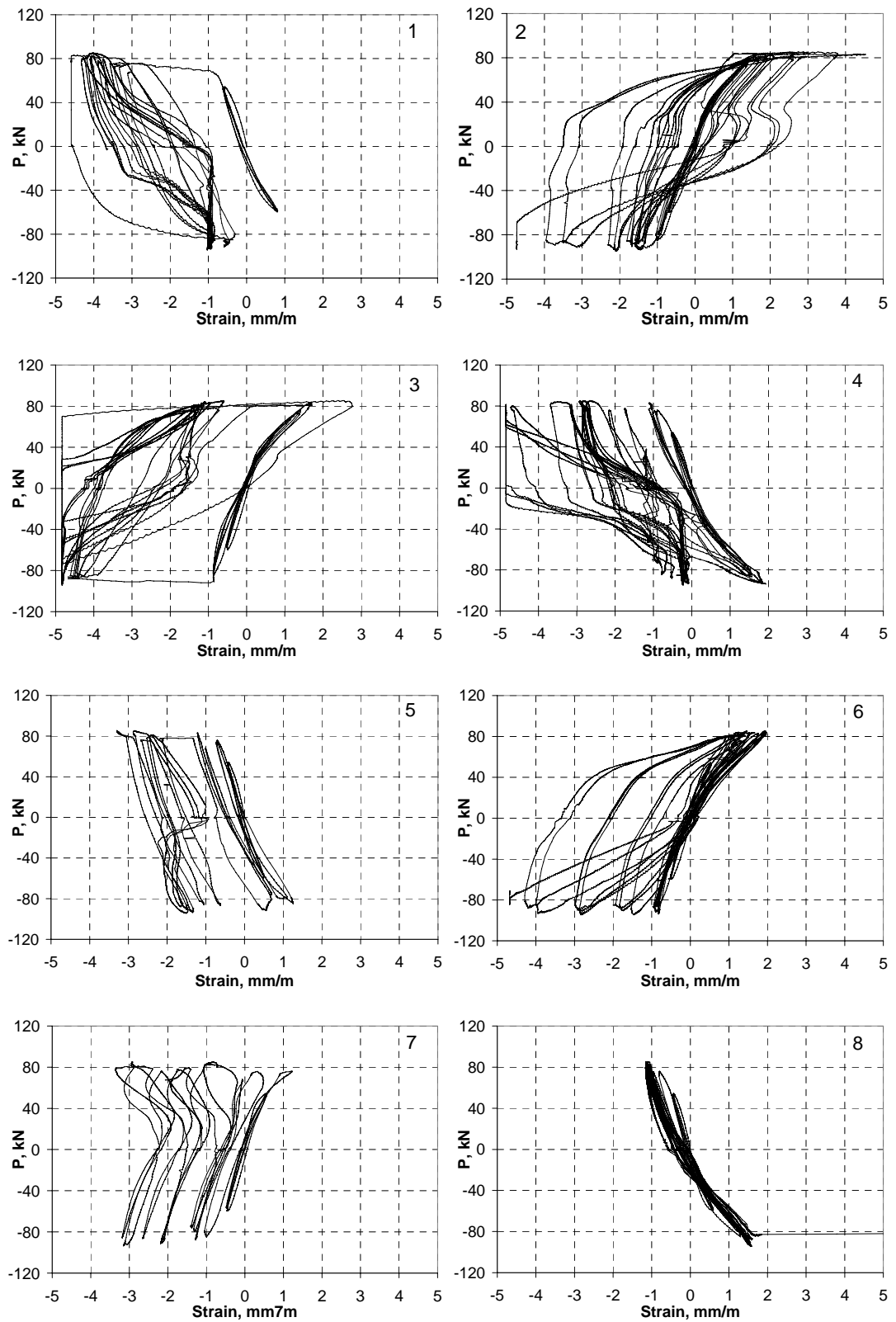


Figure C.2 Strain gage responses for specimen S-L-1-00

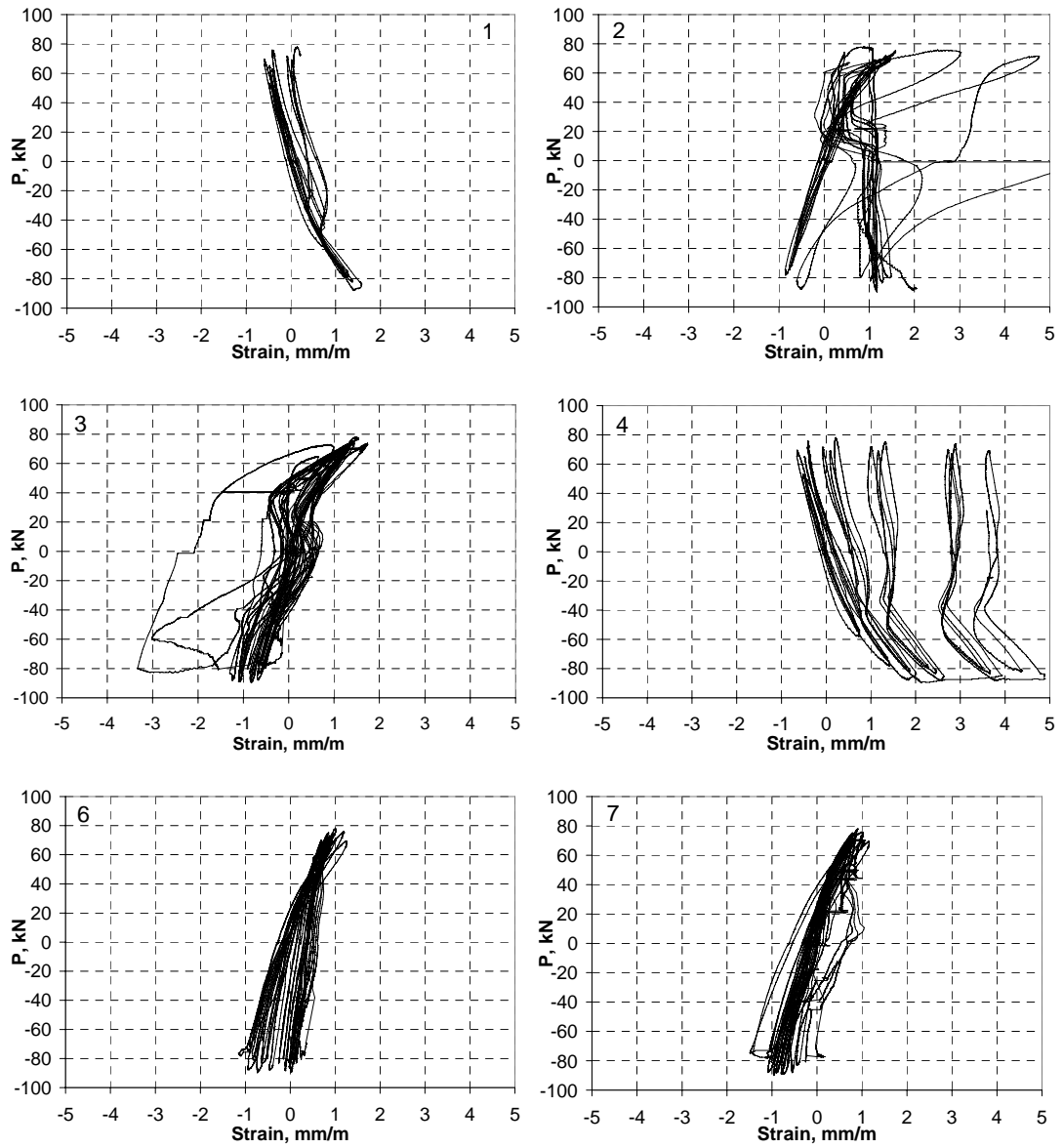


Figure C.3 Strain gage responses for specimen S-L-1-34

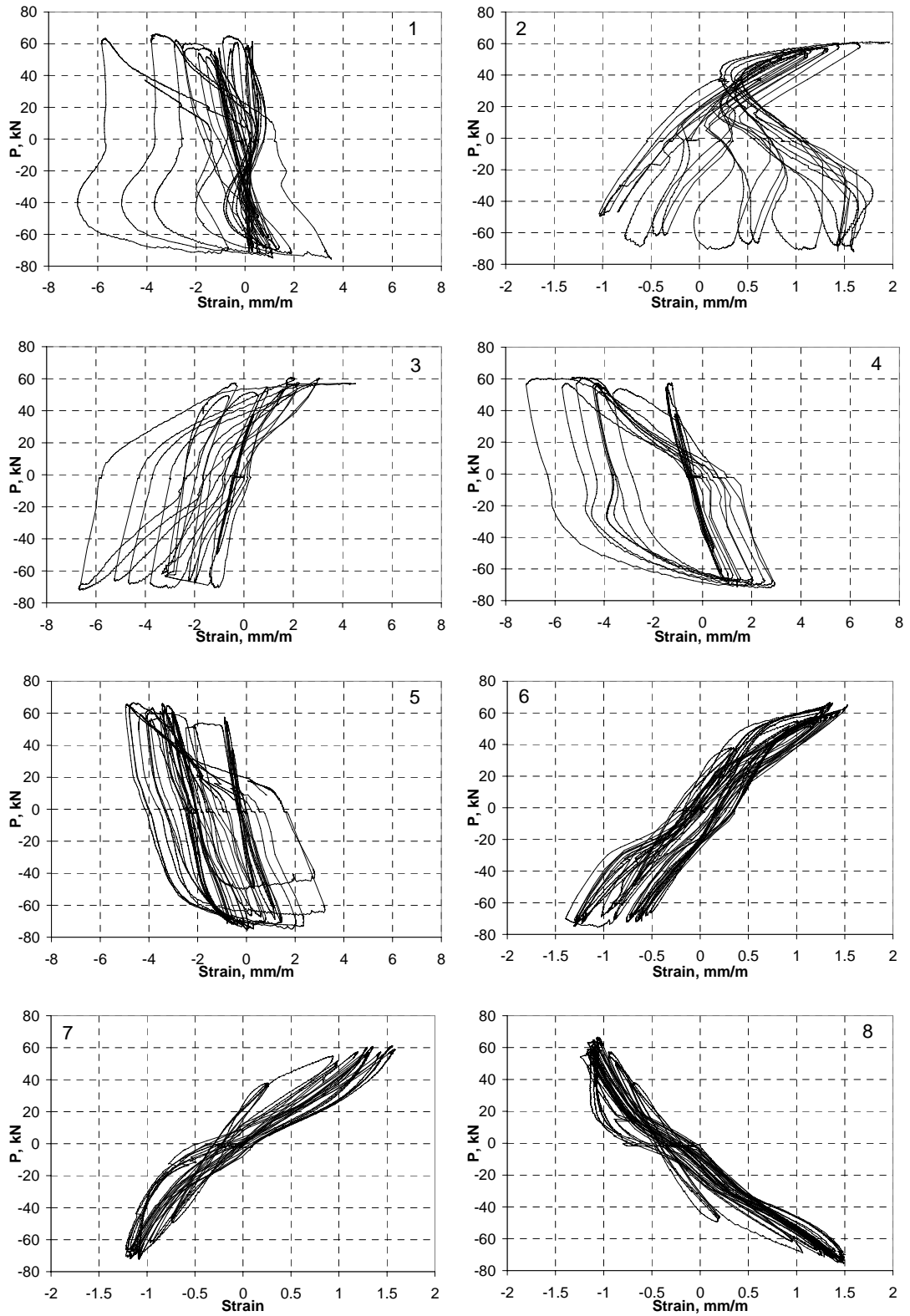


Figure C.4 Strain gage responses for specimen S-L-2-00

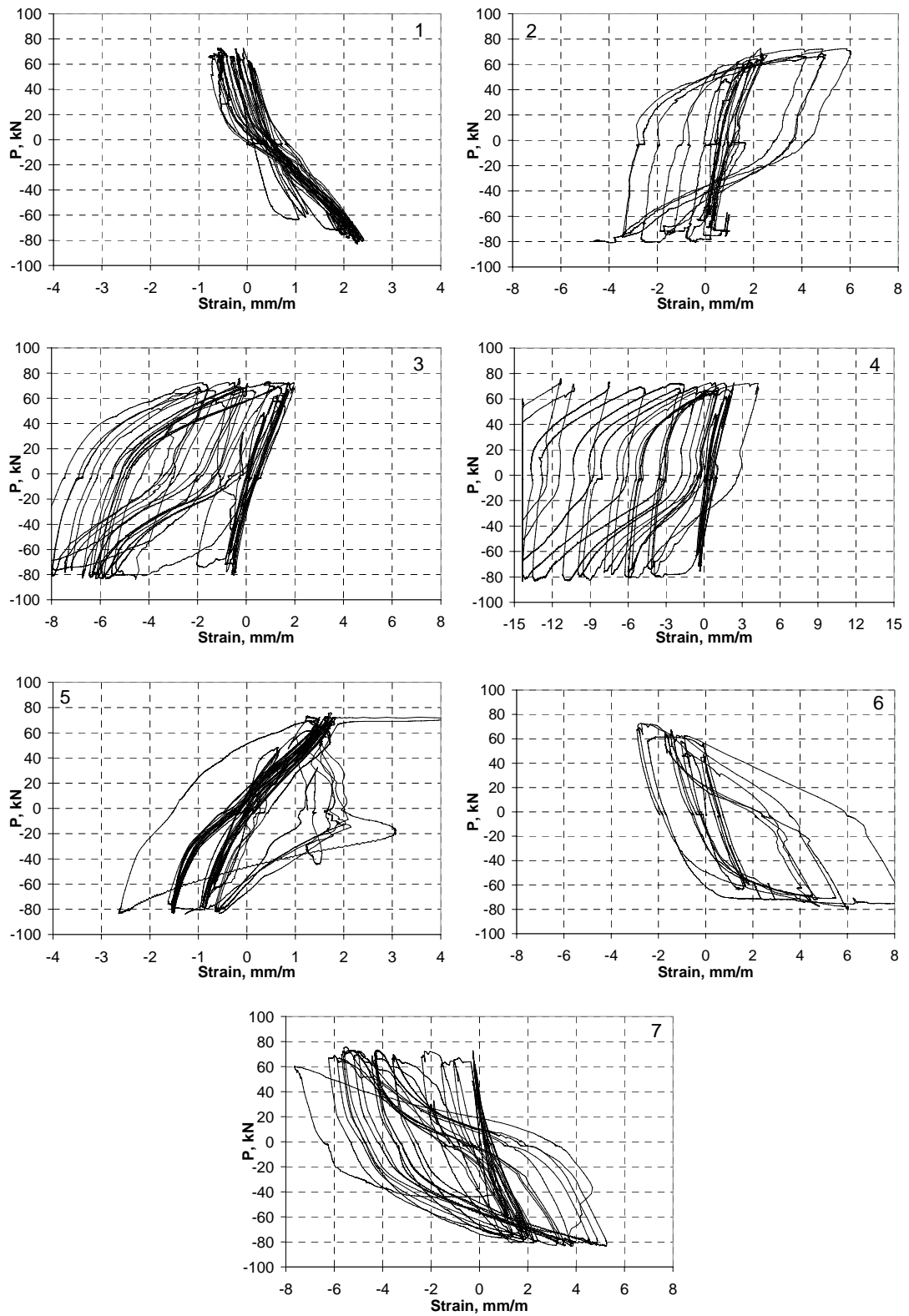


Figure C.5 Strain gage responses for specimen S-L-2-32

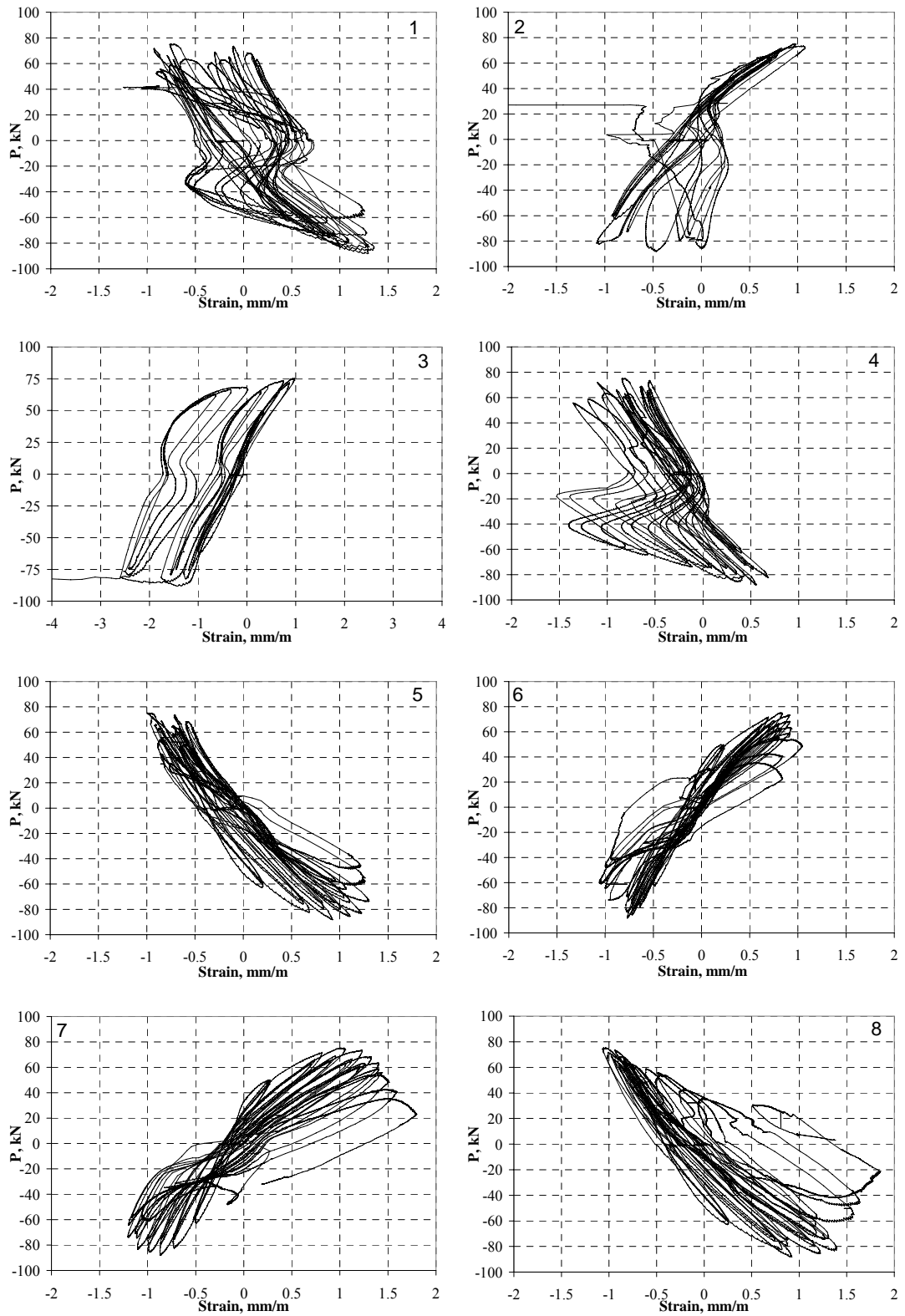


Figure C.6 Strain gage responses for specimen S-H-0-00

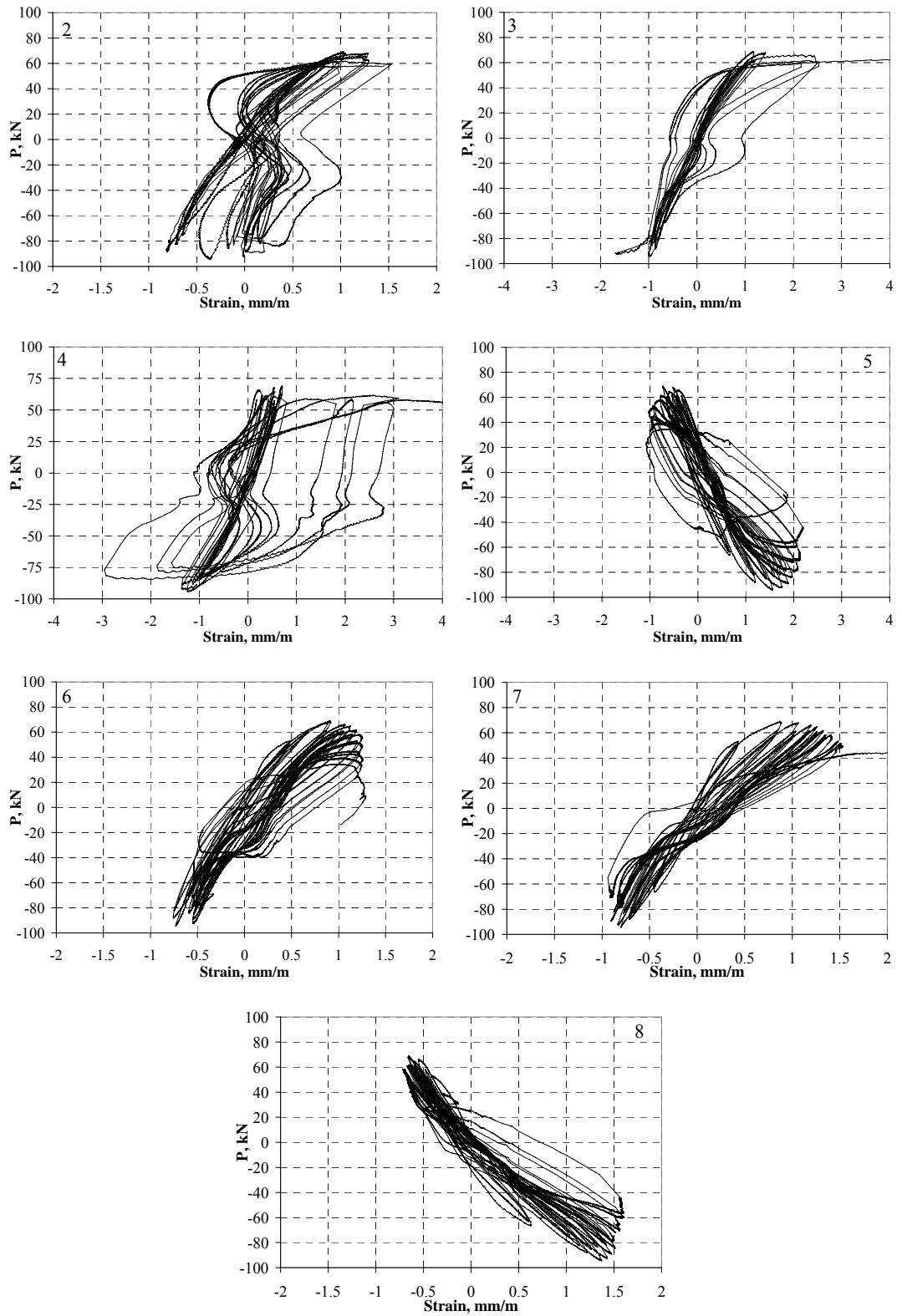


Figure C.7 Strain gage responses for specimen S-H-1-00

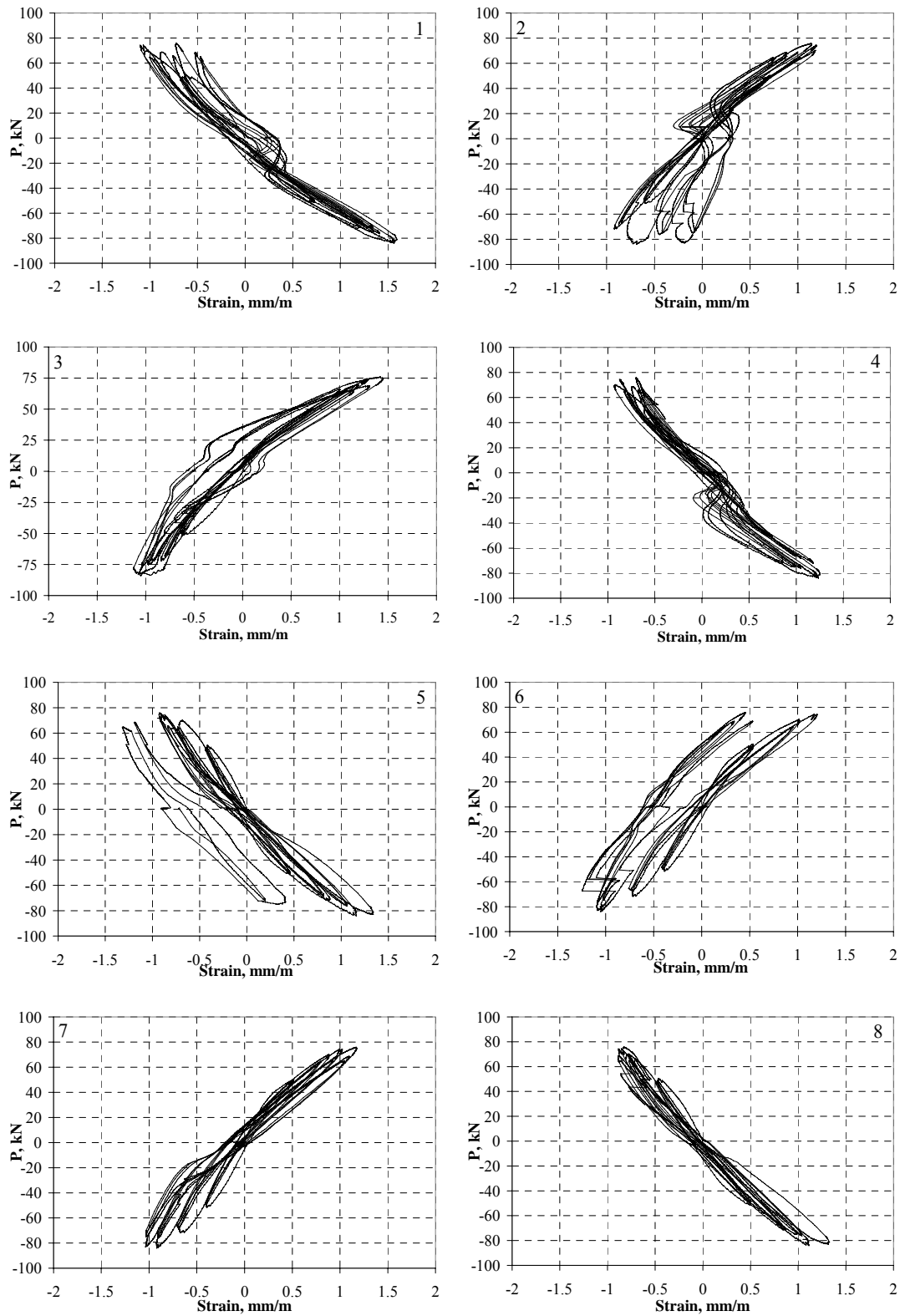


Figure C.8 Strain gage responses for specimen S-HD-1-00: Damage cycles

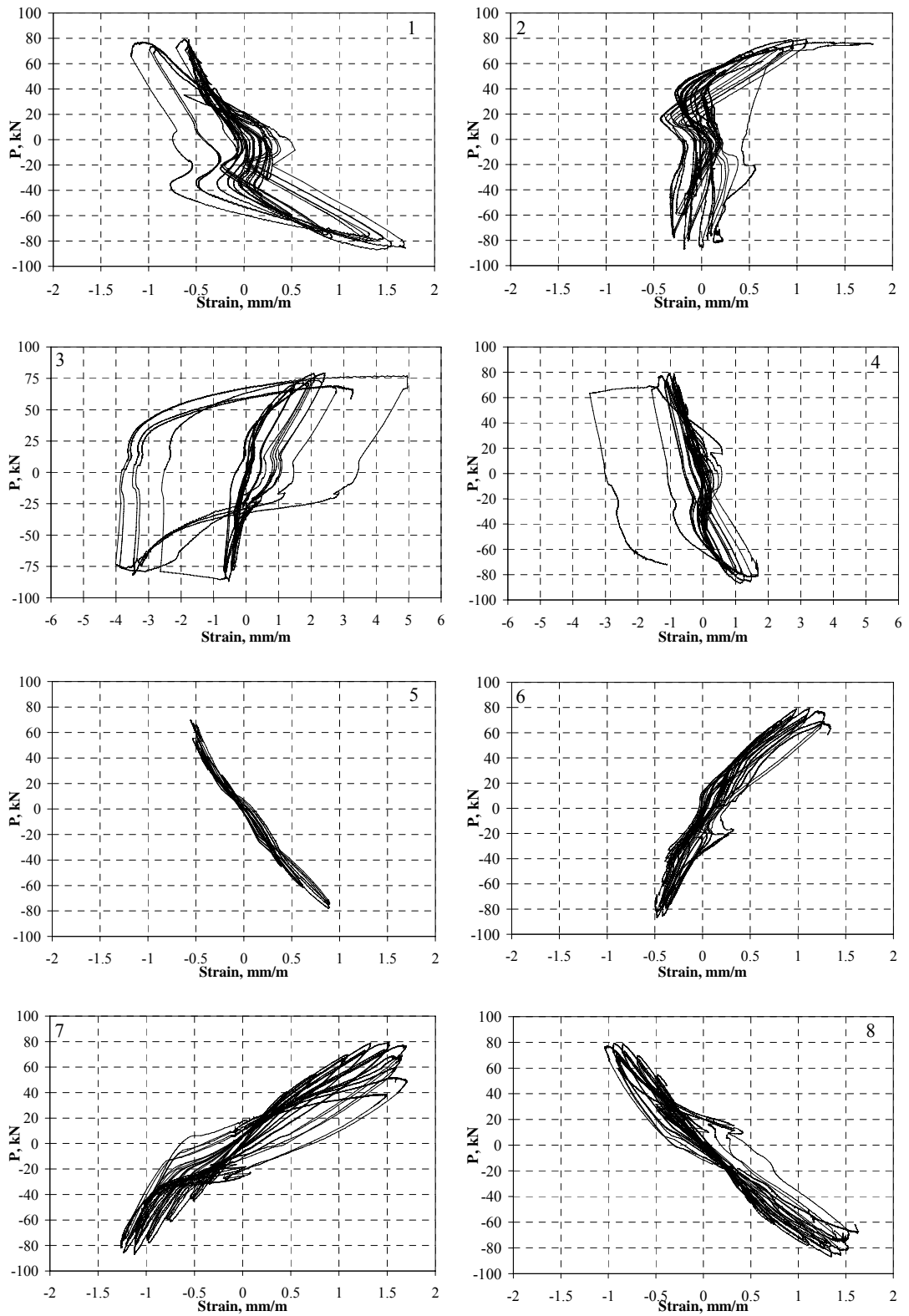


Figure C.9 Strain gage responses for specimen S-HD-1-00: Cycles after repairing

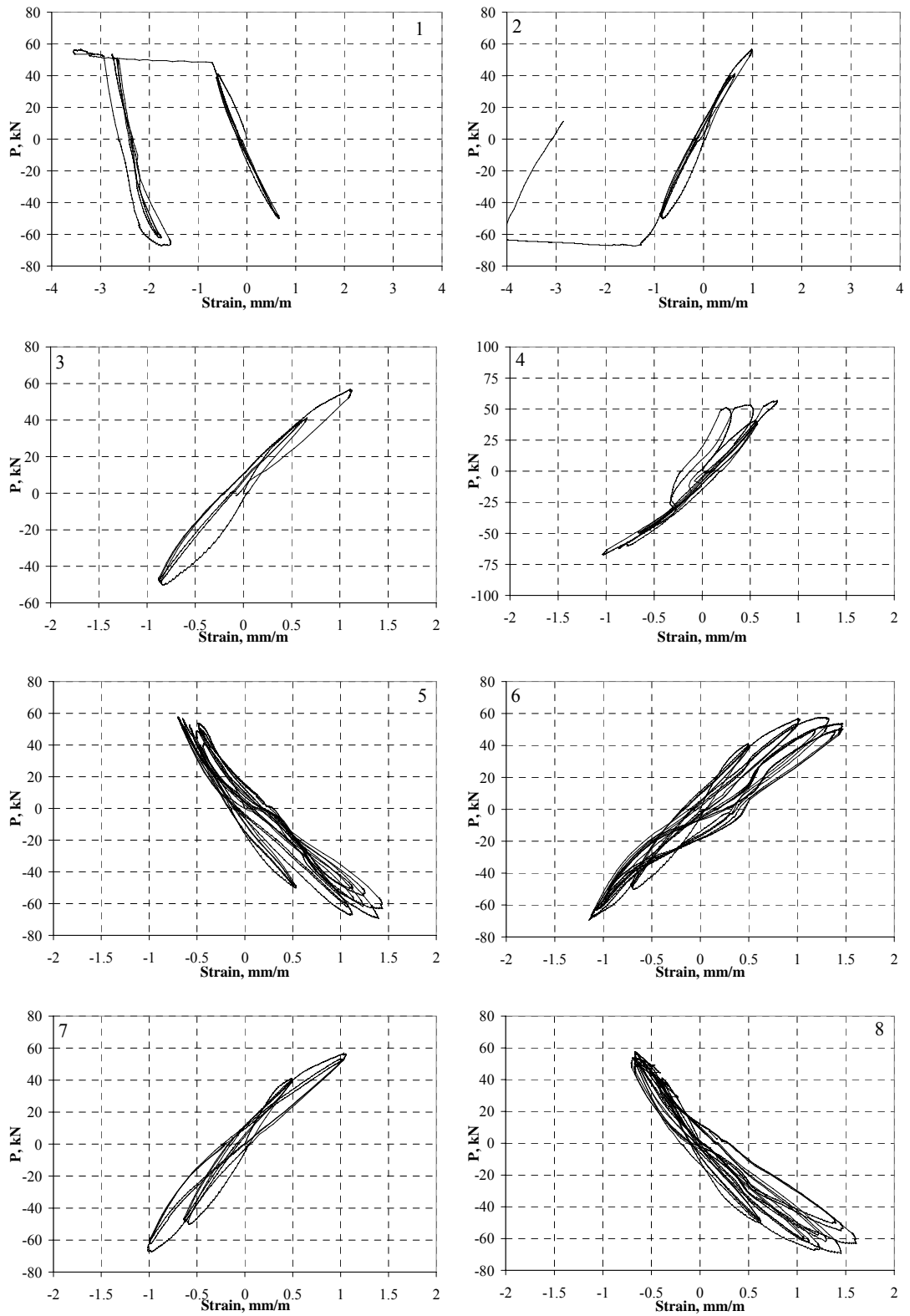


Figure C.10 Strain gage responses for specimen S-HD-1-27: Damage cycles

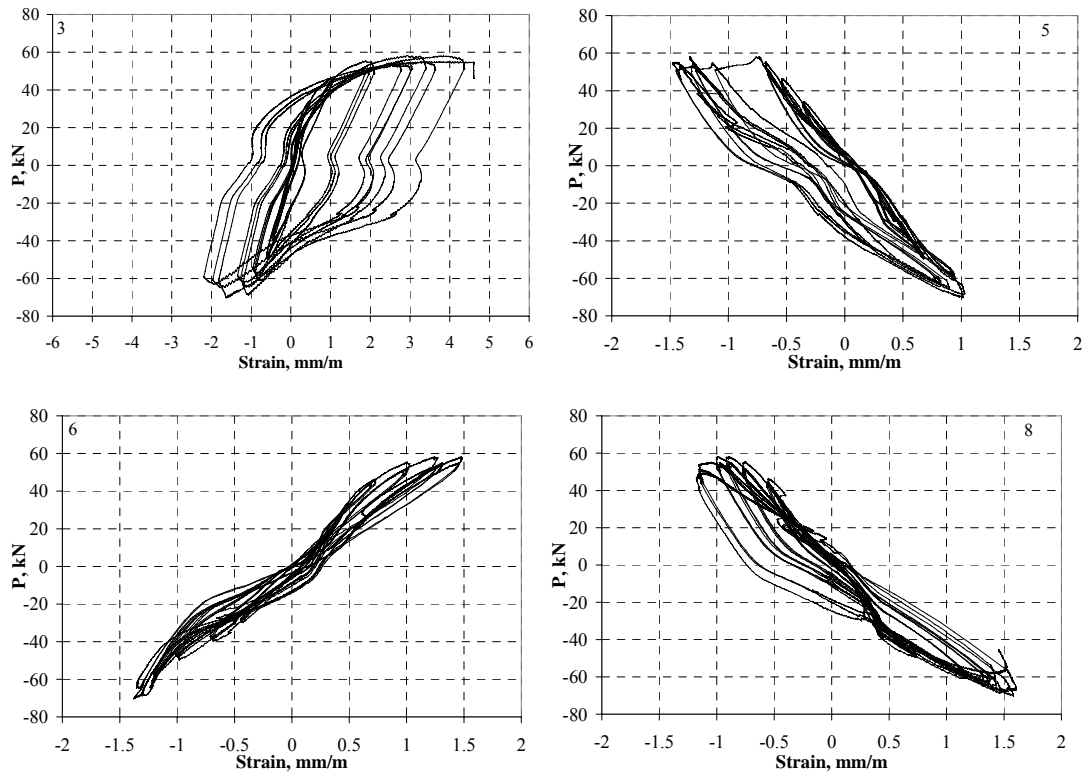


Figure C.11 Strain gage responses for specimen S-HD-1-27: Cycles after repairing

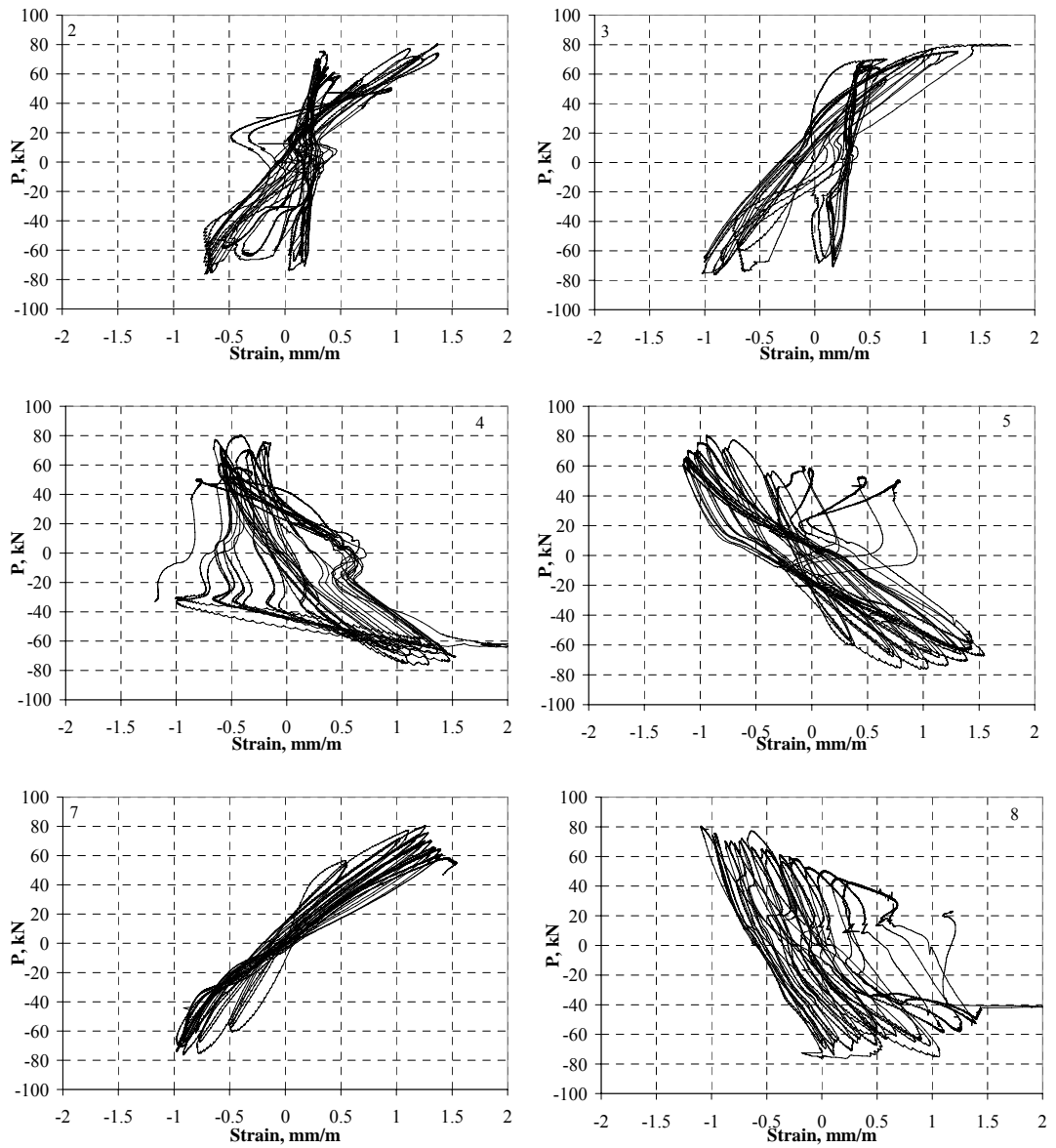


Figure C.12 Strain gage responses for specimen S-HC-1-00

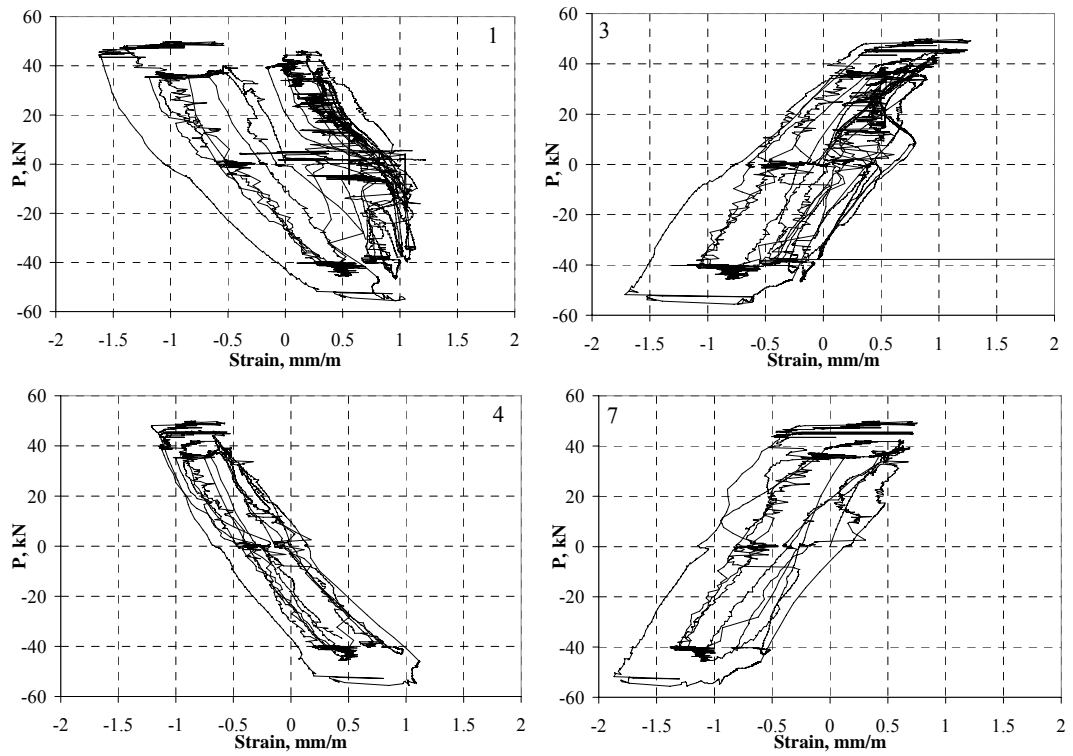


Figure C.13 Strain gage responses for specimen R-NC-0-00

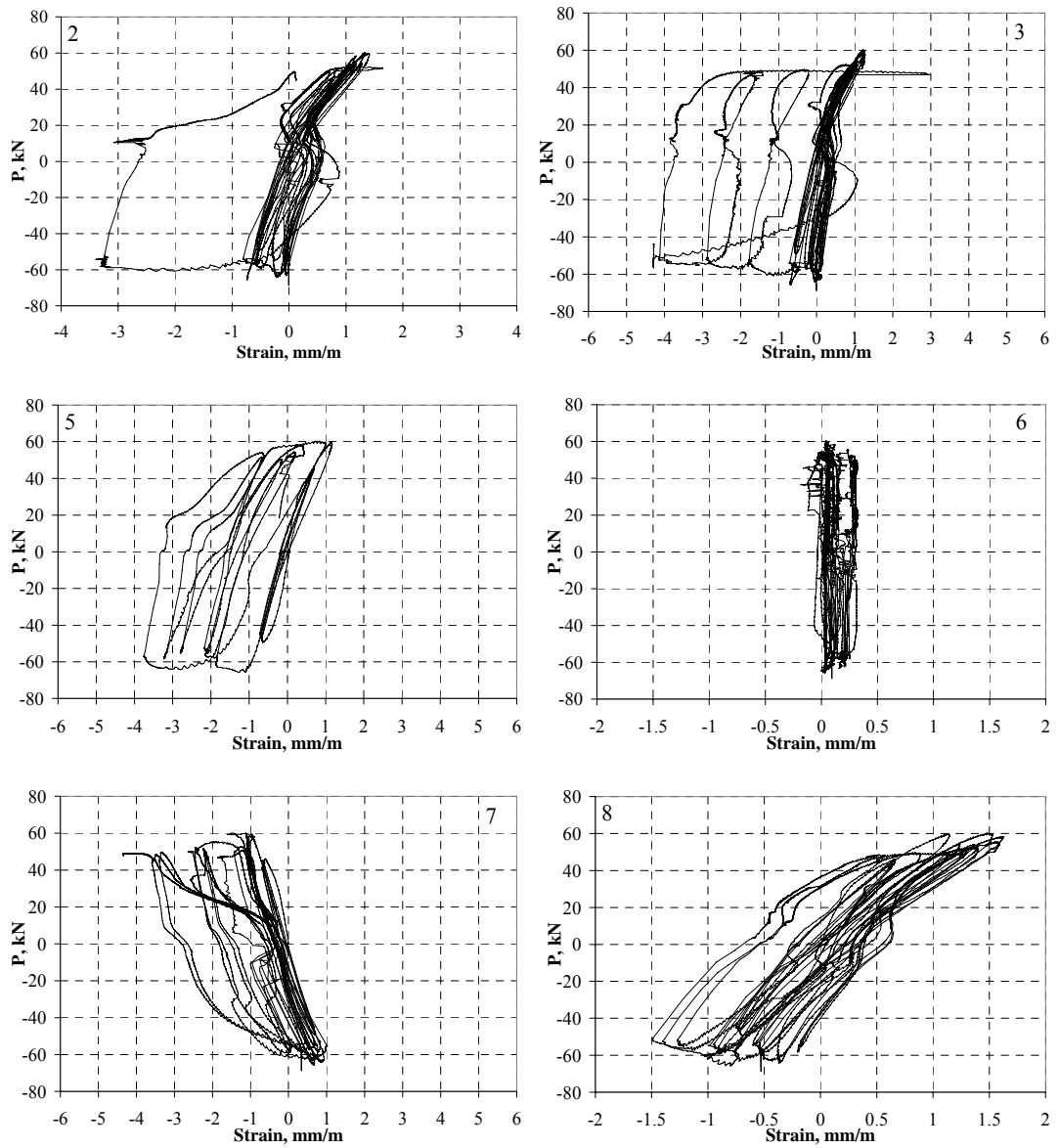


Figure C.14 Strain gage responses for specimen R-MC-1-16P

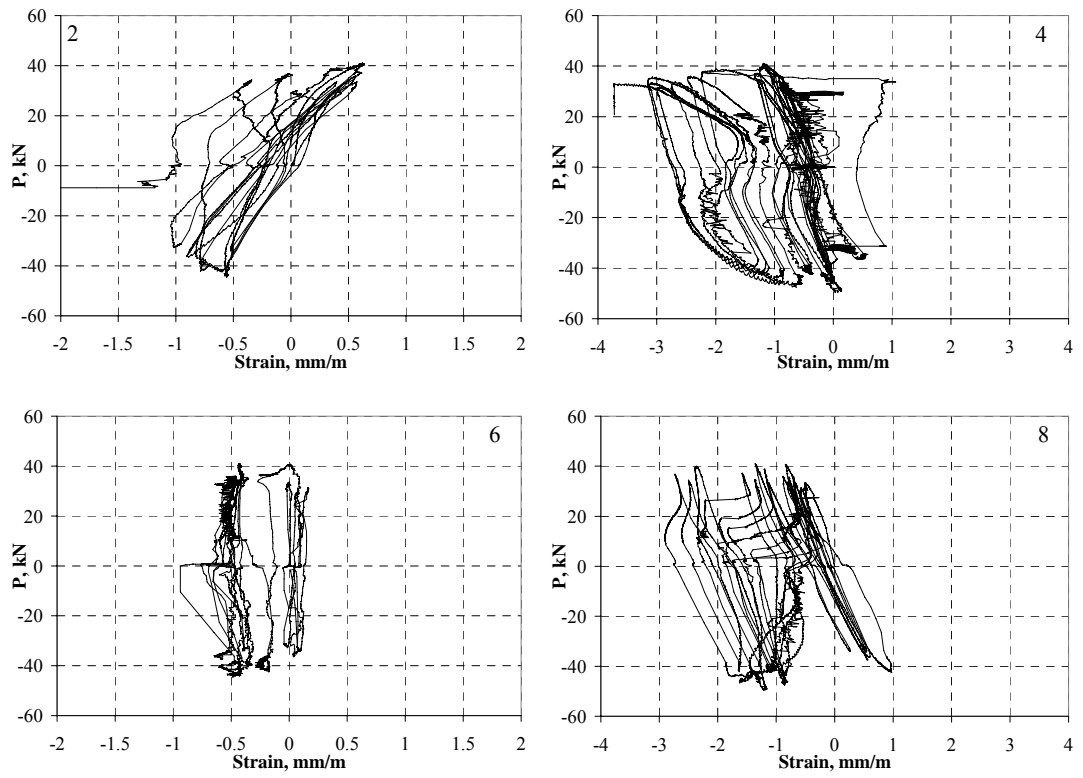


Figure C.15 Strain gage responses for specimen R-MC-1-8P

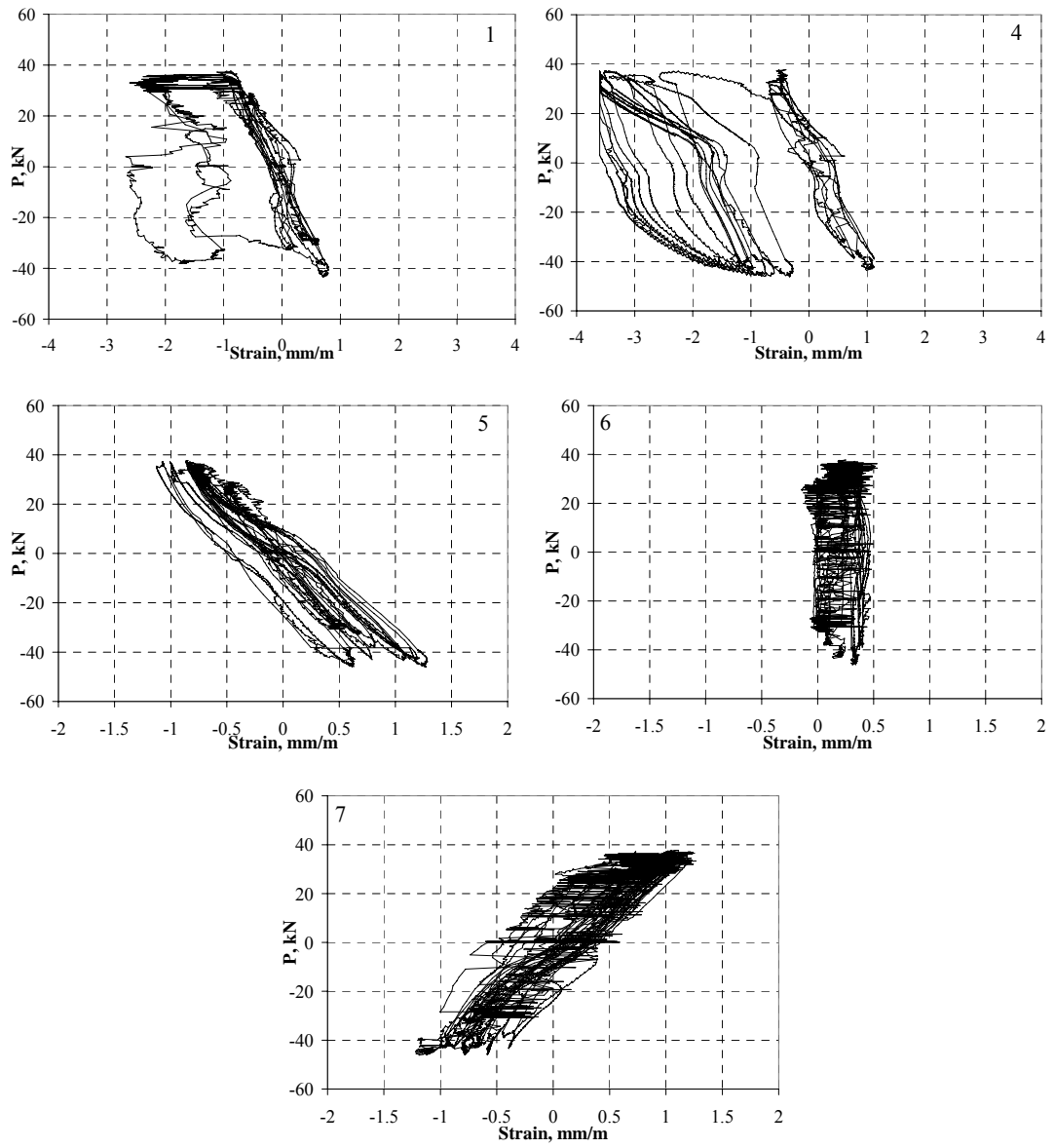


Figure C.16 Strain gage responses for specimen R-MC-1-NP

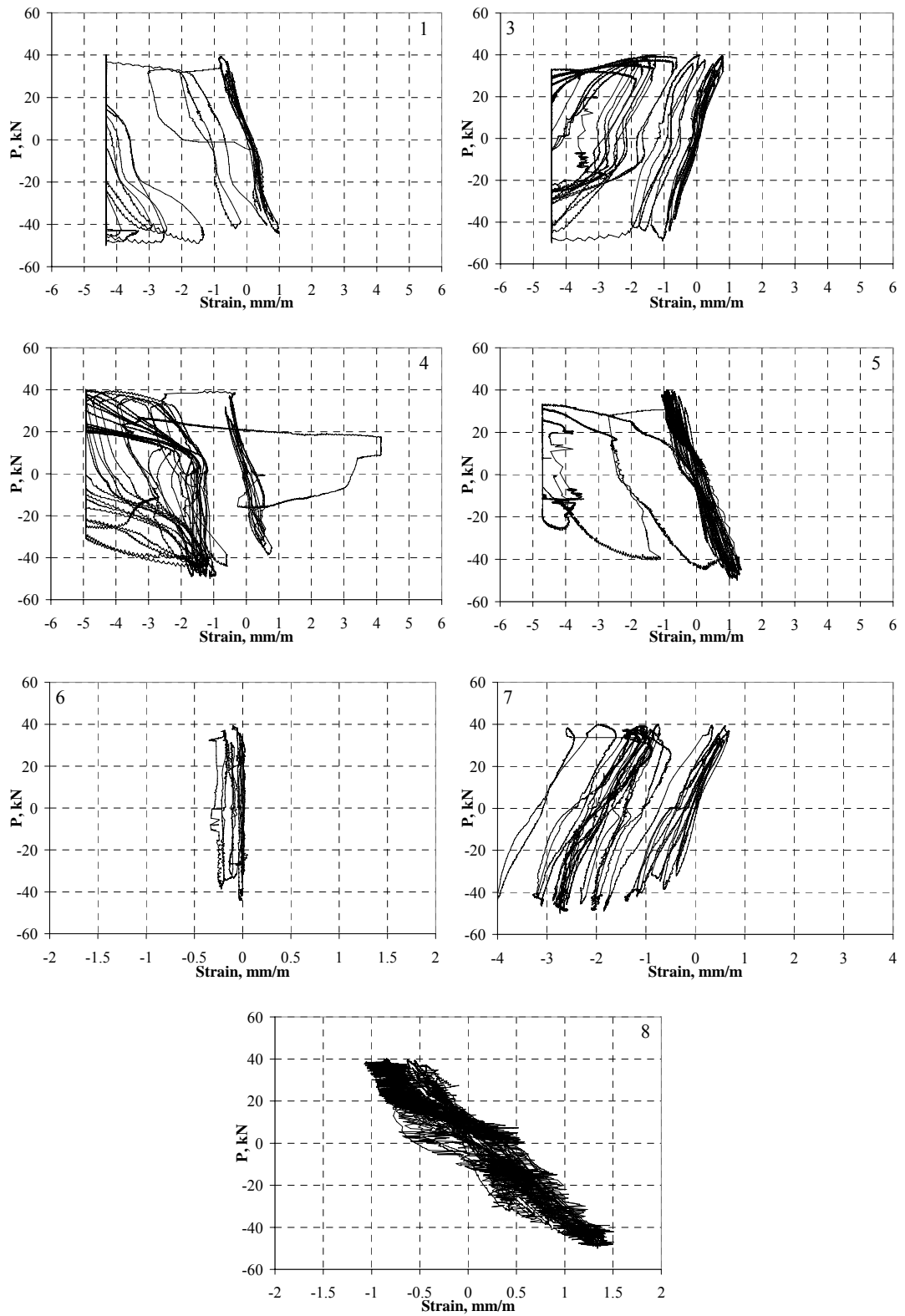


Figure C.17 Strain gage responses for specimen R-HC-1-16P

APPENDIX D

CURVATURE DISTRIBUTION TABLES

DR: Drift Ratio

K₃₅₀₋₅₀: Average curvature measured between 350 and 50 mm height from the base

K_{350-BASE}: Average curvature measured between 350 mm and column base

K₂₅: Average curvature at 25 mm height from the column base

Table D.1 Curvature distribution for S-L-0-00

DR %	K₃₅₀₋₅₀	K_{350-BASE} <i>rad/km</i>	K₂₅	DR %	K₃₅₀₋₅₀	K_{350-BASE} <i>rad/km</i>	K₂₅
0.5	6.2	8.0	18.5	-0.5	-6.4	-9.5	-28.5
1.0	12.3	18.3	54.7	-1.0	-11.6	-20.2	-72.3
1.5	21.0	32.9	104.5	-1.5	-20.1	-35.7	-129.4
2.0	34.9	50.2	142.1	-2.0	-32.0	-53.6	-183.0
2.5	56.2	70.2	154.3	-2.5	-50.9	-73.6	-209.4
3.0	81.7	92.9	160.4	-3.0	-85.7	-93.6	-141.3
3.5	123.7	116.1	70.9				

Table D.2 Curvature distribution for S-L-1-00

DR %	K₃₅₀₋₅₀	K_{350-BASE} <i>rad/km</i>	K₂₅	DR %	K₃₅₀₋₅₀	K_{350-BASE} <i>rad/km</i>	K₂₅
0.5	5.2	7.1	18.5	-0.5	-5.5	-7.5	-19.7
1.0	11.1	16.1	46.3	-1.0	-11.5	-17.2	-51.6
1.5	15.0	26.2	93.5	-1.5	-16.3	-30.0	-112.2
2.0	18.7	38.0	153.3	-2.0	-22.5	-42.7	-164.0
2.5	23.0	50.0	211.5	-2.5	-30.0	-56.0	-211.7
3.0	26.4	63.3	284.8	-3.0	-40.7	-71.4	-255.9
4.0	35.0	91.5	430.4	-4.0	-77.2	-102.2	-252.6
5.0	39.7	124.0	630.0	-5.0	-156.0	-127.7	42.2
6.0	18.9	163.0	1027.6	-6.0	-344.7	-244.5	357.1

Table D.3 Curvature distribution for S-L-1-34

DR %	K₃₅₀₋₅₀	K_{350-BASE} <i>rad/km</i>	K₂₅	DR %	K₃₅₀₋₅₀	K_{350-BASE} <i>rad/km</i>	K₂₅
0.5	4.1	7.3	26.6	-0.5	-3.5	-7.3	-30.1
1.0	10.9	15.8	45.4	-1.0	-8.1	-16.1	-64.1
1.5	19.3	25.4	61.9	-1.5	-12.6	-26.4	-109.3
2.0	30.9	38.2	81.8	-2.0	-18.4	-40.0	-170.0
2.5	43.3	54.6	122.5	-2.5	-23.0	-58.3	-269.9
3.0	55.0	73.5	184.5	-3.0	-19.0	-77.1	-425.3
4.0	81.2	111.0	290.2	-4.0	-27.1	-112.3	-623.1
5.0	83.6	151.5	558.6	-5.0	-37.9	-148.4	-811.3
6.0	97.2	188.5	736.5	-6.0	-72.1	-191.5	-908.0
				-7.6	-235.3	78.4	1961.1

Table D.4 Curvature distribution for S-L-2-00

DR %	K₃₅₀₋₅₀	K_{350-BASE} <i>rad/km</i>	K₂₅	DR %	K₃₅₀₋₅₀	K_{350-BASE} <i>rad/km</i>	K₂₅
0.5	4.8	9.0	34.8	-0.5	-3.8	-8.8	-38.8
1.0	10.5	21.7	88.7	-1.0	-6.8	-21.7	-111.5
1.5	14.2	37.2	174.8	-1.5	-10.8	-36.4	-189.8
2.0	14.1	53.5	289.9	-2.0	-13.9	-52.4	-283.3
2.5	15.0	70.4	402.5	-2.5	-13.1	-69.5	-408.0
3.0	19.0	87.5	498.5	-3.0	-11.5	-86.1	-534.0
4.0	28.7	120.0	668.1	-4.0	-4.5	-122.3	-828.7
5.0	30.0	153.9	897.1	-5.0	-9.0	-157.7	-1050.3
6.0	30.1	186.5	1124.8	-6.0	-17.2	-194.0	-1254.4
7.0	26.7	221.0	1386.8	-7.0	-46.3	-229.0	-1325.2
8.0	134.2	268.0	1070.8	-8.0	-129.2	-282.6	-1202.8

Table D.5 Curvature distribution for S-L-2-32

DR %	K₃₅₀₋₅₀ <i>rad/km</i>	K_{350-BASE} %	K₂₅ <i>rad/km</i>	DR	K₃₅₀₋₅₀	K_{350-BASE}	K₂₅
0.5	4.3	10.2	45.9	-0.5	-6.3	-15.1	-68.4
1.0	8.0	22.7	111.2	-1.0	-12.9	-31.4	-142.6
1.5	12.5	37.2	185.4	-1.5	-13.1	-45.6	-241.0
2.0	12.6	53.6	299.6	-2.0	-15.6	-61.6	-337.6
2.5	11.3	70.1	422.6	-2.5	-24.5	-79.1	-406.3
3.0	9.7	92.0	586.2	-3.0	-42.3	-95.8	-417.0
4.0	20.4	121.9	730.9	-4.0	-72.3	-139.1	-539.9
5.0	37.5	153.1	846.9	-5.0	-94.0	-175.5	-665.0
6.0	54.3	179.9	933.6	-6.3	-118.2	-199.4	-686.0

Table D.6 Curvature distribution for S-H-0-00

DR %	K₃₅₀₋₅₀	K_{350-BASE} <i>rad/km</i>	K₂₅	DR %	K₃₅₀₋₅₀	K_{350-BASE} <i>rad/km</i>	K₂₅
0.5	4.9	9.4	36.0	-0.5	-3.9	-8.8	-38.0
1.0	10.3	20.1	79.5	-1.0	-8.1	-21.0	-98.6
1.5	15.3	33.2	140.5	-1.5	-10.0	-36.0	-192.2
2.0	24.4	47.7	187.5	-2.0	-14.1	-52.8	-285.2
2.5	33.3	61.6	231.7	-2.5	-22.7	-72.8	-373.4
3.0	44.6	76.3	266.3	-3.0	-30.1	-94.0	-477.5
4.0	81.9	116.6	324.5	-4.0	-64.5	-135.0	-557.9
4.9	119.0	159.7	403.9	-5.0	-152.9	-178.6	-332.3

Table D.7 Curvature distribution for S-H-1-00

DR %	K₃₅₀₋₅₀	K_{350-BASE} <i>rad/km</i>	K₂₅	DR %	K₃₅₀₋₅₀	K_{350-BASE} <i>rad/km</i>	K₂₅
0.5	5.0	9.0	33.1	-0.5	-4.5	-8.7	-33.6
1.0	10.4	20.5	80.8	-1.0	-7.7	-18.2	-81.0
1.5	12.1	34.2	166.7	-1.5	-11.6	-30.2	-141.8
2.0	15.0	48.0	245.9	-2.0	-12.6	-43.4	-228.0
2.5	11.2	61.6	363.8	-2.5	-11.9	-57.1	-328.3
3.0	5.1	75.5	497.9	-3.0	-12.0	-71.5	-428.4
4.0	-3.5	103.9	748.6	-4.0	-10.1	-100.0	-639.4
5.0	-0.2	132.9	931.9	-5.0	-18.7	-132.7	-816.6
6.0	35.3	162.3	924.8	-6.0	-95.4	-165.2	-583.9
7.0	-35.7	241.9	1907.4	-7.2	-129.5	-241.7	-914.7

Table D.8 Curvature distribution for S-HC-1-00

DR %	K₃₅₀₋₅₀	K_{350-BASE} <i>rad/km</i>	K₂₅	DR %	K₃₅₀₋₅₀	K_{350-BASE} <i>rad/km</i>	K₂₅
0.5	4.4	7.7	27.6	-0.5	-5.1	-8.6	-29.7
1.0	8.3	17.5	73.0	-1.0	-10.8	-19.1	-69.0
1.5	10.7	30.2	146.7	-1.5	-13.1	-31.8	-143.5
2.0	7.3	44.0	263.9	-2.0	-11.5	-45.0	-246.5
2.5	2.3	58.9	398.7	-2.5	-11.5	-56.2	-324.2
3.0	0.1	75.3	526.1	-3.0	-9.7	-70.5	-434.8
4.0	-2.7	106.3	760.2	-4.0	-26.4	-98.4	-530.1
5.0	25.6	136.4	801.1	-5.0	-61.3	-126.1	-514.7
6.0	90.5	168.3	635.0	-6.0	-58.2	-153.5	-725.3
7.0	128.2	198.4	620.1	-7.1	-41.6	-186.1	-1053.1

Table D.9 Curvature distribution for S-HD-1-00

DR %	K₃₅₀₋₅₀	K_{350-BASE} <i>rad/km</i>	K₂₅	DR %	K₃₅₀₋₅₀	K_{350-BASE} <i>rad/km</i>	K₂₅
0.5	6.6	9.3	25.2	-0.5	-8.9	-10.3	-18.8
1.0	11.8	20.3	71.6	-1.0	-19.8	-22.1	-35.4
1.5	16.1	30.5	117.0	-1.5	-30.1	-32.7	-48.3
2.0	20.8	41.0	162.4	-2.0	-40.5	-43.3	-60.2
2.5	25.3	52.7	216.7	-2.5	-52.5	-55.8	-75.7
3.0	31.2	65.3	269.5	-3.0	-66.3	-69.7	-90.4
4.0	47.1	93.5	371.9	-4.0	-96.1	-98.7	-114.1
5.0	69.3	125.6	463.4	-5.0	-128.6	-128.4	-127.1
6.0	98.3	162.3	546.1	-6.0	-184.7	-162.5	-29.1
7.0	142.8	201.9	556.9	-7.0	-273.0	-195.2	271.5

Table D.10 Curvature distribution for S-HD-1-27

S-HD-1-27							
DR	K₃₅₀₋₅₀	K_{350-BASE}	K₂₅	DR	K₃₅₀₋₅₀	K_{350-BASE}	K₂₅
<i>%</i>		<i>rad/km</i>		<i>%</i>		<i>rad/km</i>	
0.5	5.6	10.6	40.8	-0.5	-4.1	-11.7	-57.6
1.0	9.7	22.3	97.3	-1.0	-7.3	-24.8	-129.6
1.5	14.0	34.1	155.1	-1.5	-12.4	-37.9	-190.9
2.0	18.9	46.3	210.5	-2.0	-16.5	-50.6	-255.4
2.5	24.8	59.5	267.5	-2.5	-25.6	-64.4	-297.1
3.0	30.9	72.8	324.4	-3.0	-40.9	-79.7	-312.0
4.0	47.1	101.3	426.7	-4.0	-70.3	-104.0	-306.0
5.0	60.6	142.6	634.8	-5.0	-105.7	-134.0	-304.0
6.0	103.3	173.5	594.9	-6.0	-151.5	-171.1	-288.6
7.0	226.0	138.6	-386.0				

Table D.11 Curvature distribution for R-NC-0-00

R-NC-0-00							
DR	K₃₅₀₋₅₀	K_{350-BASE}	K₂₅	DR	K₃₅₀₋₅₀	K_{350-BASE}	K₂₅
<i>%</i>		<i>rad/km</i>		<i>%</i>		<i>rad/km</i>	
0.5	4.2	6.8	22.0	-0.5	-3.6	-6.9	-27.1
1.0	9.2	15.2	50.9	-1.1	-15.0	-19.2	-44.3
1.5	12.1	27.9	122.5	-1.5	-31.0	-34.5	-55.8
2.0	22.4	43.4	169.3	-2.0	-46.9	-50.3	-70.3

Table D.12 Curvature distribution for R-HC-1-16P

DR	K₃₅₀₋₅₀	K_{350-BASE}	K₂₅	DR	K₃₅₀₋₅₀	K_{350-BASE}	K₂₅
<i>%</i>		<i>rad/km</i>		<i>%</i>		<i>rad/km</i>	
0.5	4.3	9.6	41.5	-0.5	-2.7	-10.0	-53.7
1.0	6.8	21.8	111.6	-1.0	-5.5	-21.8	-120.2
1.5	8.4	34.1	188.3	-1.5	-8.2	-33.5	-184.9
2.0	9.1	47.2	275.3	-2.0	-11.4	-45.9	-252.4
2.5	9.5	59.9	362.5	-2.5	-15.1	-58.6	-319.5
3.0	9.9	73.4	454.0	-3.0	-18.8	-70.7	-382.2
4.0	12.7	100.3	625.7	-4.0	-28.0	-97.5	-514.3
5.0	15.5	126.6	793.7	-5.0	-39.8	-124.1	-630.2
6.0	17.6	153.7	970.2	-6.1	-47.8	-151.7	-775.2
7.0	13.7	181.8	1190.0	-7.0	-132.6	-190.0	-534.5
8.4	-36.8	208.3	1678.9				

Table D.13 Curvature distribution for R-MC-1-16P

DR %	K₃₅₀₋₅₀	K_{350-BASE} <i>rad/km</i>	K₂₅	DR %	K₃₅₀₋₅₀	K_{350-BASE} <i>rad/km</i>	K₂₅
0.5	4.4	7.4	25.6	-0.5	-4.8	-7.4	-23.0
1.0	10.8	17.0	54.2	-1.0	-9.1	-16.3	-59.5
1.5	17.6	28.1	91.3	-1.5	-15.2	-28.0	-104.7
2.0	27.3	41.8	128.3	-2.0	-23.0	-40.3	-144.5
2.5	37.7	55.4	161.8	-2.5	-31.3	-54.4	-193.1
3.0	46.8	68.3	197.6	-3.0	-41.9	-71.7	-250.5
4.0	62.9	91.5	263.6	-4.0	-55.4	-110.0	-437.6
5.0	90.6	116.1	268.8	-5.1	-88.7	-165.1	-623.7
6.0	143.0	129.2	46.3				

Table D.14 Curvature distribution for R-MC-1-8P

DR %	K₃₅₀₋₅₀	K_{350-BASE} <i>rad/km</i>	K₂₅	DR %	K₃₅₀₋₅₀	K_{350-BASE} <i>rad/km</i>	K₂₅
0.5	5.1	8.0	25.2	-0.5	-4.0	-8.2	-33.3
1.0	9.9	19.3	76.1	-1.0	-9.0	-20.2	-87.6
1.5	12.3	32.0	149.8	-1.5	-13.0	-30.5	-136.0
2.0	15.2	45.5	227.3	-2.2	-18.2	-45.2	-207.1
2.5	16.8	58.6	309.1	-2.5	-21.6	-51.1	-228.1
3.0	21.7	74.2	389.0	-3.0	-29.4	-65.6	-282.8
4.0	36.7	104.7	512.9	-4.0	-48.8	-97.7	-391.2
5.0	69.6	138.3	550.3	-5.0	-188.1	-133.4	195.0

Table D.15 Curvature distribution for R-MC-1-NP

DR %	K₃₅₀₋₅₀	K_{350-BASE} <i>rad/km</i>	K₂₅	DR %	K₃₅₀₋₅₀	K_{350-BASE} <i>rad/km</i>	K₂₅
0.5	9.7	8.3	12.1	-0.5	-11.2	-9.6	-34.1
1.0	23.4	20.1	88.7	-1.0	-25.5	-21.9	-32.3
1.5	38.0	32.6	181.2	-1.5	-39.4	-33.8	-41.4
2.0	54.1	46.3	211.5	-2.0	-53.4	-45.7	-65.5
2.5	68.7	58.9	411.6	-2.5	-69.3	-59.4	-89.7
3.0	82.8	71.0	499.2	-3.0	-85.3	-73.2	140.0
4.0	119.0	102.0	501.4				

APPENDIX E

THE PROGRAM NAKO

The seismic behavior of all the columns tested in the experimental program was estimated by using the program NAKO. It can predict the seismic performance of unconfined and CFRP confined rectangular columns by using models for concrete, steel, bond-slip and plastic hinging. The code was written in MATLAB language and the data was transferred to excel for editing and graphing purposes. The program uses a primary routine for the analysis options and after running, the column envelope response was predicted according to the selected parameters by using different subroutines. The main program initiates with the input parameters defining all properties of the reinforced concrete section. For unconfined columns, after the input phase, the moment – curvature response of the column was attained using concrete and steel models. By using the bond-slip model, the fixed-end rotations were estimated for each incremental steel strain value in tension. In the following step, for each incremental curvature located at the base section of the column, the flexural deflections were calculated by dividing the column height into numerous stations. By multiplying the fixed-end rotations with the column length, the FER components of the tip deflection were calculated for each incremental steel strain value. The total tip deflection was attained by adding the FER components to the flexural components. The parameters used in the program and the source code are indicated below.

Source Code - Starter Routine for Unconfined Columns

```
% STARTER ROUTINE.....
% PARAMETERS - UNCONFINED COLUMNS%

% cslnum: Number of strips for the column cross-section
% concid: Concrete id: 1.Hognestad, 2.Popovivcs-Thorenfeldt-Collins 1978,
%3.Modified Binici FRP Confined Concrete Model
% fck: Concrete compressive strength in MPa
% Ec: Elasticity modulus for concrete in MPa
% b: Section width in mm
% h: Section depth in mm
% ax: Axial load in N
% scoord1, scoord2, scoord3: Reinforcing bar locations measured from the
% mid-point of the section in mm
% a1, a2, a3: Reinforcing bar areas at specified locations in mm2
% stnum: Number of reinforcing bar layers
% stid: Steel id: 1.Buckling ignored, 2. Buckling included
% Es: Steel elasticity modulus in MPa
% fsy, fsh, fsu: Yield, strain hardening and ultimate stresses for steel in
% MPa
% esy, esh, esu: Yield, strain hardening and ultimate strains for steel
% Ki: Incremental curvature value in rad/mm
% L: Column length in mm
% Lt: Transverse reinforcement spacing in mm
% db: Longitudinal bar diameter in mm
% eso: Strain at the reinforcing bars after axial loading
% fso: Stress at the reinforcing bars after axial loading in MPa
% incr: curvature increment in rad/km
% a: Dummy variable for curvature and moment evaluation
% err: Error in axial load during curvature calculations in N
% mom: Moment in Nmm
% ess, fss: incremental steel stress and strain in tension in MPa
% res: Resultant matrix with [[Moment] [Curvature] [Steel strain] [Steel
% Stress] [Fixed end rotation] [Flexural deflection] [FER Cmpnent]
% [Tip deflection]
% s: Displacement at the bar in tension due to FER in mm
% zero: Initial matrix after the axial load application
% delta: Tip deflection vector in mm

clear;clc;
global cslnum concid fck Ec n b h ax scoord1 scoord2 scoord3 a1 a2 a3
global stnum stid Es fsy fsh fsu esy esh esu ess fs Ki L Lt db
%res=[M K es fs BSR FD BSD DELTA]
%Section [N,mm].
b=350;h=350;L=2000;ax=689000;
%Concrete: concid = 1 for Hognestad, 2 for PTC, 3 for Binici FRP Confined.
cslnum=200;fck=14;concid=2;Ec=4750*fck^.5;
```

```

%Steel:stid=1 (default), 2(Maekawa-including buckling)
stnum=3;stid=1;Es=200000;fsy=287;fsh=300;fsu=420;esy=fsy/Es;esh=0.003;esu=0.05;
scoord1=126;a1=763.4;scoord2=0;a2=508.9;scoord3=-126;a3=763.4;db=18;Lt=200;
eso=ax/(Es*(a1+a2+a3)+Ec*b*h);fso=eso*Es; %initial steel strain, stress assumed elastic initially
%MAIN
incr=.000001;j=1;
for Ki=incr*3:incr:150*incr;
a=fzero(@mk,h/2);
[err,mom,ess,fs]=mk(a);
res(j,1)=mom/1000000;res(j,2)=Ki*1000000;res(j,3)=ess;res(j,4)=fs;
s=slip(ess,fs);res(j,5)=s/(scoord1-scoord3);j=j+1;
end
zero=[0,0,eso,fso,0];res=cat(1,zero,res); %adding initial values
%FD
mom=res(:,1);curv=res(:,2)*1/1000000;
[delta]=flexDisp(mom,curv);
res(:,6)=delta;
%BSD
res(:,7)=res(:,5)*L;
%DELTA
res(:,8)=res(:,6)+res(:,7);

```

Source Code - Starter Routine for FRP-Confined Columns

```

%STARTER ROUTINE.....
%PARAMETERS - CFRP CONFINED COLUMNS%
%%%%%%%%%%%%%%%%%%%%%%%%%%%%%%%%%%%%%%%%%%%%%%%%%%%%%%%%%%%%%%%%%%%%%%%%
%cslnum: Number of strips for the column cross-section
%concid: Concrete id: 1.Hognestad, 2.Popovics-Thorenfeldt-Collins 1978,
    %3.Modified Binici FRP Confined Concrete Model
%fck: Concrete compressive strength in MPa
%Ec: Elasticity modulus for concrete in MPa
%b: Section width in mm
%h: Section depth in mm
%ax: Axial load in N
%scoord1, scoord2, scoord3: Reinforcing bar locations measured from the
    %mid-point of the section in mm
%a1, a2, a3: Reinforcing bar areas at specified locations in mm2
%stnum: Number of reinforcing bar layers
%stid: Steel id: 1.Buckling ignored, 2. Buckling included
%Es: Steel elasticity modulus in MPa
%fsy,fsh,fsu: Yield, strain hardening and ultimate stresses for steel in
    %MPa
%esy,esh,esu: Yield, strain hardening and ultimate strains for steel
%Ki: Incremental curvature value in rad/mm
%L: Column length in mm
%Lt: Transverse reinforcement spacing in mm

```

```

%db: Longitudinal bar diameter in mm
%Ej: FRP jacket elasticity modulus in MPa
%ef: FRP jacket rupture strain
%tj: FRP jacket thickness in mm
%cr: Corner rounding radius in mm
%Lw: FRP wrapped height from the base of the column in mm
%eso: Strain at the reinforcing bars after axial loading
%fso: Stress at the reinforcing bars after axial loading in MPa
%incr: curvature increment in rad/km
%a: Dummy variable for curvature and moment evaluation
%err: Error in axial load during curvature calculations in N
%mom: Moment in Nmm
%ess, fss: incremental steel stress and strain in tension in MPa
%res: Resultant matrix with [[Moment] [Curvature] [Steel strain] [Steel
    %Stress] [Fixed end rotation] [Flexural deflection] [FER Component]
    % [Tip deflection]
%s: Displacement at the bar in tension due to FER in mm
%zero: Initial matrix after the axial load application
%delta: Tip deflection vector in mm

clear,clc
global cslnum concid fck Ec n b h ax scoord1 scoord2 scoord3 a1 a2 a3
global stnum stid Es fsy fsh fsu esy esh esu ess fs Ki L Lt db
global Ej ef tj cr Lw
%res=[M_unc K_unc M_conf K_conf es_conf fs_conf BSR_conf FD BSD DELTA]
%Section [N,mm].
b=350;h=350;L=2000;ax=689000;
%Concrete: concid = 1 for Hognestad, 2 for PTC, 3 for Binici FRP Confined.
cslnum=100;fck=14;Ec=4750*fck^.5;
%Steel:stid=1 (default), 2(Maekawa)
stnum=3;stid=1;Es=200000;fsy=287;fsh=300;fsu=420;esy=fsy/Es;esh=0.003;esu=0.
05;
scoord1=126;a1=763.4;scoord2=0;a2=508.9;scoord3=-126;a3=763.4;db=18;Lt=200;
eso=ax/(Es*(a1+a2+a3)+Ec*b*h);fso=eso*Es; %initial steel strain, stress assumed
elastic initially
%FRP
Ej=230000;ef=0.009;tj=0.165;cr=30;Lw=500;
%MAIN
concid=2; %unwrapped section
incr=.000001;j=1;opt=optimset('TolX',1e-10,'MaxFunEvals',1e7,'MaxIter',1e7);
for Ki=incr*3:incr:300*incr;
    a=fzero(@mk,h/2,opt);
    [err,mom,ess,fs]=mk(a);
    res(j,1)=mom/1000000;res(j,2)=Ki*1000000;
    j=j+1;
end
concid=3;j=1; %wrapped section
for Ki=incr*3:incr:300*incr;
    a=fzero(@mk,h/2,opt);

```

```

[err,mom,ess,fs,ec,ecu]=mk(a);

res(j,3)=mom/1000000;res(j,4)=Ki*1000000;res(j,5)=ess;res(j,6)=fs;eps(j,1)=ec;eps
c(j,2)=mom/1e6;
    ex=5*ecu;
    s=slip(ess,fs);res(j,7)=s/(scoord1-scoord3);j=j+1;
end
zero=[0,0,0,0,eso,fso,0];res=cat(1,zero,res); %adding initial values
%FD
momunc=res(:,1);curvunc=res(:,2)*1/1000000;momconf=res(:,3);curvunc=res(:,4)*1
/1000000;
[delta]=flexDisp1(momunc,curvunc,momconf,curvunc);
res(:,8)=delta;
%BSD
res(:,9)=res(:,7)*L;
%DELTA
res(:,10)=res(:,8)+res(:,9);

```

Source Code - Moment-Curvature Function

```

function [ferror,M,ess,fs,ec,ecu] = mk(a)
global cslnum concid fck Ec n b h ax scoord1 scoord2 scoord3 a1 a2 a3
global stnum stid Es fsy fsh fsu esy esh esu ess fs Ki Lt db
global Ej ef tj cr
eci=Ki*a;
%Concrete Matrix
c(:,1)=1:cslnum; %slice no
c(:,2)=(2*c(:,1)-1)/2*a/cslnum; %slice midpoint coordinate
c(:,3)=eci/a*c(:,2); %slice midpoint strain

for i=1:cslnum; %slice midpoint stress
ec=c(i,3);

    if concid==1; %Hognestad
        eco=2*fck/Ec;ecu=0.0038;
        if ec<eco;
            c(i,4)=fck*(2*ec/eco-(ec/eco)^2);
        elseif (ec>eco && ec<ecu);
            c(i,4)=fck*(1-0.15*(ec-eco)/(ecu-eco));
        else
            c(i,4)=0;
        end

    elseif concid==2; %PTC
        n=0.8+fck/17;eco=fck/Ec*n/(n-1);
        if fck>20
            if (ec<eco)
                k=1;
            else

```

```

        k=0.67+fck/62;
    end
else
    n=1.55+(fck/32.4)^3;k=1;
end
c(i,4)=fck*n*ec/eco/(n-1+(ec/eco)^(n*k));
if c(i,4)<0
    c(i,4)=0;
end

elseif concid==3;          %FRP Confined Concrete
    Ke=1-((h-2*cr)^2+(b-2*cr)^2)/(3*b*h);
    %Ke=0.756;
    phi=(b+h)*Ej*ef*tj/(b*h*fck)*Ke;phit=0.14;
    eco=(-0.067*fck^2+29.9*fck+1053)*10^-6;alpha=5;

    if (phi<=phit);        %Softening
        Ksig=1.8*phi^0.3;Keps=1.75+12*phi*(ef/eco)^0.45;
        fcu=Ksig*fck;ecu=Keps*eco;
        if (ec>=0 && ec<eco);
            nn=Ec*eco/(Ec*eco-fck);
            c(i,4)=Ec*ec*(1-1/nn*(ec/eco)^(nn-1));
        elseif (ec>=eco && ec<=ecu)
            c(i,4)=fck+(Ksig-1)/(Keps-1)*fck/eco*(ec-eco);
        elseif ec>ecu
            c(i,4)=fcu/(1-alpha)*(ec/ecu-alpha);
        end
        if c(i,4)<0
            c(i,4)=0;
        end
    elseif (phi>phit)      %Hardening
        Ksig=2.6*(phi-0.14)^0.7+1;Keps=1.75+12*phi*(ef/eco)^0.45;
        fcu=Ksig*fck;ecu=Keps*eco;
        if (ec>=0 && ec<=eco);
            S=(Ksig-1)/(Keps-1)*fck/eco;nn=(Ec-S)*eco/(Ec*eco-fck);
            c(i,4)=Ec*ec*(1-1/nn*(1-S/Ec)*(ec/eco)^(nn-1));
        elseif (ec>eco && ec<ecu);
            c(i,4)=fck+(Ksig-1)/(Keps-1)*fck/eco*(ec-eco);
        else
            c(i,4)=fcu/(1-alpha)*(ec/ecu-alpha);
            %c(i,4)=0;
        end
        if c(i,4)<0
            c(i,4)=0;
        end
    end
end
elseif concid==4          %Kent&Park Unconfined Mod.
    eco=0.0016;ecu=0.02;
    if (ec>0 && ec<=eco)

```

```

        c(i,4)=fck*(2*ec/eco-(ec/eco)^2);
    elseif ec>eco
        c(i,4)=fck*(ecu-ec)/(ecu-eco);
    end
    if c(i,4)<0.2*fck
        c(i,4)=0.2*fck;
    end
end
end
end

c(:,5)=a/cslnum*b*c(:,4);    %slice force

for i=1:cslnum
c(i,6)=c(i,5)*(h/2-a+c(i,2));    %slice moment
end

Fc=sum(c(:,5));Mc=sum(c(:,6));

%Steel Matrix
s=[scoord1,a1;scoord2,a2;scoord3,a3]; %coordinate from midheight,area
s(:,3)=eci/a*(a-h/2+s(:,1));    %steel strain +.comp, -.tens
ess=s(3,3);    %bottom steel strain (bond calc.)

if stid==1; %No buckling

    for i=1:stnum;    %steel stress: +.compression, -.tension
        es=abs(s(i,3));
        if es<esy;
            s(i,4)=es*Es;
        elseif (es>esy && es<esh);
            s(i,4)=fsy+(fsh-fsy)/(esh-esy)*(es-esy);
        elseif (es>esh && es<esu);
            s(i,4)=fsh+(fsu-fsh)*((es-esh)/(esu-esh))^0.5;
        else
            s(i,4)=0;
        end
        if s(i,3)<0;
            s(i,4)=-s(i,4); %convert (-) for tension steel
        end
    end
    fs=s(3,4);    %bottom steel stress, tension

elseif stid==2; %Maekawa, with buckling

    estar=esy*(55-2.3*(fsy/100)^0.5*Lt/db);    %es* for buckling analysis
    if (estar<7*esy)
        estar=7*esy;
    end;
end;

```

```

if estar<=esy;                                %f* local
    fstarl=estar*Es;
elseif (estar>esy && estar<=esh);
    fstarl=fsy+(fsh-fsy)/(esh-esy)*(estar-esy);
elseif (estar>esh && estar<esu);
    fstarl=fsh+(fsu-fsh)*((estar-esh)/(esu-esh))^0.5;
else
    fstarl=0;
end

salfa=0.75+(esu-esh)/(300*esy);
if salfa>=fsu/(1.5*fsy)
    salfa=fsu/(1.5*fsy);
end

fstar=fstarl*salfa*(1.1-0.016*(fsy/100)^0.5*Lt/db); %fs*
if (fstar<0.2*fsy)
    fstar=0.2*fsy;
end

for i=1:stnum;
es=abs(s(i,3));
    if es<=esy;                                %default: Consider as Tension
        s(i,4)=es*Es;
    elseif (es>esy && es<=esh);
        s(i,4)=fsy+(fsh-fsy)/(esh-esy)*(es-esy);
    elseif (es>esh && es<esu);
        s(i,4)=fsh+(fsu-fsh)*((es-esh)/(esu-esh))^0.5;
    else
        s(i,4)=0;
    end

    if s(i,3)>0;                                %if Compression,=>> buckling model
        if es<=esy;
            s(i,4)=es*Es;
        elseif (es>esy && es<=estar);
            s(i,4)=s(i,4)*(1-(1-fstar/fstarl)*((es-esy)/(estar-esy)));
        elseif (es>estar);
            s(i,4)=fstar-0.02*Es*(es-estar);
        end
        if (s(i,4)<0.2*fsy)
            s(i,4)=0.2*fsy;
        end
    end
    if (s(i,3)<0)    %convert (-) for tension steel
        s(i,4)=-s(i,4);
    end
end
fs=s(3,4); %bottom steel stress, tension

```

```

end

for i=1:stnum
s(i,5)=s(i,2)*s(i,4);           %steel force
s(i,6)=s(i,5)*s(i,1);         %steel moment: +.compression at top, -.compression
at bottom
end

Fs=sum(s(:,5));Ms=sum(s(:,6));
F=Fc+Fs;ferror=F-ax;M=Mc+Ms;

```

Source Code - Bond Slip Function

```

function [s] = slip(ess,fs)
global fsy esy fck db
u=.4*fck^.5;ess=abs(ess);fs=abs(fs);
if ess<esy
    s=ess*fs*db/(8*u);
else
    s=db/(8*u)*(esy*fsy+2*(ess+esy)*(fs-fsy));
end

```

Source Code - Flexural Deflection Function for Unconfined Columns

```

function [delta] = flexDisp(mom,curv)
global L h

%Displacement Component: Flexural Displacements
nh=100;len=length(mom);momp=max(mom);kp=interp1(mom,curv,momp); %peak
moment,curvature at peak

for i=1:len;if
(mom(i)==momp);break;break;else;momr(i)=mom(i);end;end;momr=[momr,momp];
for i=1:len;if
(curv(i)==kp);break;break;else;curvr(i)=curv(i);end;end;curvr=[curvr,kp];
Lp=h;

for i=1:len;
    m=mom(i);k=curv(i);

    if k<kp %before peak
        for j=1:nh;
            flexD(j,1)=(2*j-1)/(2*nh)*L; %slice midpoint coordinates over L
            flexD(j,2)=(2*nh-(2*j-1))/(2*nh)*m; %moments over L
            flexD(j,3)=interp1(momr,curvr,flexD(j,2)); %curvatures over L
            flexD(j,4)=flexD(j,3)*L/nh*(L-flexD(j,1)); %local displacements over L
        end
    elseif k>kp %after peak
        t=1;
    end
end

```

```

for j=1:nh;
    if j==1
        flexD(j,1)=0;flexD(j,2)=m;flexD(j,3)=k;flexD(j,4)=0; %hcor,m,k,del of
base, total moment at second
    elseif j==2;
        flexD(j,1)=Lp;flexD(j,2)=m*(1-Lp/L); %coordinate of Lp,moment at Lp
        flexD(j,3)=interp1(momr,curvr,flexD(j,2)); %curvature at Lp
        flexD(j,4)=flexD(j,3)*Lp*(L-Lp/2)+(k-flexD(j,3))*Lp/2*(L-Lp/3);
%plastic hinge delta
    else
        flexD(j,1)=Lp+t/(2*nh)*(L-Lp);flexD(j,2)=(2*nh-t)/(2*nh)*flexD(2,2);
%coordinates & moments over (L-Lp)

flexD(j,3)=interp1(momr,curvr,flexD(j,2));flexD(j,4)=flexD(j,3)*L/nh*(L-
flexD(j,1)); %curvatures,deltas over Lp
        t=t+2;
    end
end
end
end
delta(i)=sum(flexD(:,4)); %total delta at Mi
end

```

Source Code - Flexural Deflection Function for FRP-Confined Columns

```

function [delta] = flexDisp1(momunc,curvunc,momconf,curvconf)
global L Lw h
%Displacement Component: Flexural Displacements
nh=100;
lenunc=length(momunc);mompunc=max(momunc);kpunc=interp1(momunc,curvunc
,mompunc); %peak moment,curvature at peak, unconfined
lenconf=length(momconf);mompconf=max(momconf);kpconf=interp1(momconf,cur
vconf,mompconf); %peak moment,curvature at peak, confined
Lwmin=L*(1-mompunc/mompconf);if (Lw<Lwmin);disp 'Lw<Lwmin: increase Lw
length!';end
Lp=h;

for i=1:lenunc;if
(momunc(i)==mompunc);break;break;else;momrunc(i)=momunc(i);end;end;momrunc
c=[momrunc,mompunc];
for i=1:lenunc;if
(curvunc(i)==kpunc);break;break;else;curvrunc(i)=curvunc(i);end;end;curvrunc=[cur
vrunc,kpunc];
for i=1:lenconf;if
(momconf(i)==mompconf);break;break;else;momrconf(i)=momconf(i);end;end;mom
rconf=[momrconf,mompconf];
for i=1:lenconf;if
(curvconf(i)==kpconf);break;break;else;curvrconf(i)=curvconf(i);end;end;curvrconf=
[curvrconf,kpconf];

```

```

len=lenunc;

for i=1:len;
    mu=momunc(i);mc=momconf(i);k=curvconf(i);

    %1st region: k<kp_unc and k<kp_conf: both before peak moment

    if (k<=kpconf);
        for j=1:nh;
            flexD(j,1)=(2*j-1)/(2*nh)*L; %slice midpoint coordinates over L
            flexD(j,2)=(2*nh-(2*j-1))/(2*nh)*mc; %moments over L
            if flexD(j,1)<Lw;
                flexD(j,3)=interp1(momrconf,curvrconf,flexD(j,2)); %curvatures over
Lw, confined
            elseif flexD(j,1)>=Lw;
                flexD(j,3)=interp1(momrunc,curvrunc,flexD(j,2)); %curvatures over L-
Lw, unconfined
            end
            flexD(j,4)=flexD(j,3)*L/nh*(L-flexD(j,1)); %local displacements over L
        end

    elseif (k>kpconf); %Plastic hinging over Lp
        t=1;
        for j=1:nh;
            if j==1
                flexD(j,1)=0;flexD(j,2)=mc;flexD(j,3)=k;flexD(j,4)=0; %hcor,m,k,delta
of base, total moment at second
            elseif j==2;
                flexD(j,1)=Lp;flexD(j,2)=mc*(1-Lp/L); %Lp,moment at Lp
                flexD(j,3)=interp1(momrconf,curvrconf,flexD(j,2)); %curvature at Lp
                flexD(j,4)=flexD(j,3)*Lp*(L-Lp/2)+(k-flexD(j,3))*Lp/2*(L-Lp/3);
            %plastic hinge delta
            else
                flexD(j,1)=Lp+t/(2*nh)*(L-Lp);flexD(j,2)=(2*nh-
t)/(2*nh)*flexD(2,2); %coordinates & moments over (L-Lp)
                if flexD(j,1)<=Lw; %Confined, inside Lw
                    flexD(j,3)=interp1(momrconf,curvrconf,flexD(j,2));
                elseif flexD(j,1)>Lw; %Unconfined, outside Lw
                    flexD(j,3)=interp1(momrunc,curvrunc,flexD(j,2));
                end
                flexD(j,4)=flexD(j,3)*L/nh*(L-flexD(j,1)); %curvatures, over Lp
            end
            t=t+2;
        end
    end
    delta(i)=sum(flexD(:,4)); %total delta at Mi
end

```

APPENDIX F

DESIGN EXAMPLE OF CFRP COLUMN RETROFITTING

The design example represents CFRP retrofitting of a typical flexure dominated building column according to TEC07, Method I and Method II as presented in Chapter 4. Herein, the drift demand of an unconfined column was calculated by using a single degree of freedom column model according to the 7th Chapter of TEC07. The lateral displacement demand of the column was determined by using the design spectrum and presumed soil class. Further, the design steps are explained in details below.

Column Properties:

- $350 \times 350 \times 2000$ mm
- $f_c=20$ MPa, clear cover: 30 mm
- Corner rounding radius: 30 mm
- Axial load: $N=700$ kN,
- Longitudinal reinforcement: $8\phi 18$ mm
- Transverse reinforcement: $\phi 10/200$ mm
- $f_y=287$ MPa, $\epsilon_{su}=0.05$, $\epsilon_{sy}=0.001435$ (Elastoplastic)
- By standard section analysis:
Column yield force: 65 kN, yield curvature: 7.1×10^{-6} rad/mm
- Soil: Z1, $T_A=0.2$ s, $T_B=0.9$ s

$$m = \frac{700 \text{ kN}}{9.81 \text{ m/s}^2} = 71.36 \text{ kNs}^2 / \text{m} \text{ (mass consistent with the axial load)}$$

$$I_{cr} = 0.73I = 0.73 \left(\frac{350^4}{12} \right) = 912.88 \times 10^6 \text{ mm}^4 \text{ (Cracked moment of inertia)}$$

$$k = \frac{3EI_{cr}}{L^3} = \frac{3 \times 28000 \times 912.88 \times 10^6}{2000^3} = 9585.2 \text{ kN/m}$$

$$T = 2\pi \sqrt{\frac{m}{k}} = 2\pi \sqrt{\frac{71.36}{9585.2}} = 0.542 \text{ s}, w^2 = \frac{k}{m} = 134.3 \text{ s}^{-2} \rightarrow w = 11.6 \text{ s}^{-1}$$

$$S_{De} = \frac{S_{ae}}{w^2} = \frac{1 \times 9.81}{134.3} = 73.1 \text{ mm}$$

$$a_y = \frac{65\text{kN}}{700\text{kN}} = 0.093 \text{ (acceleration coefficient concerning yield)}$$

$$R_y = \frac{S_{ae}}{a_y} = \frac{1}{0.093} = 10.75$$

$$C_{R1} = \frac{1 + (R_y - 1)T_B / T_n}{R_y} = \frac{1 + (10.75 - 1)0.9 / 0.542}{10.75} = 1.6$$

$$S_d = C_{R1}S_{De} = 1.6 \times 73.1 = 117.0\text{mm} \approx 120\text{mm} \rightarrow DR_u \approx 6\%$$

Thus, approximately 6% of drift demand was acquired for the design example. The calculation results are presented in Figure F.1. The CFRP layer numbers was calculated according to the acquired drift demand considering TEC07, Method I and II.

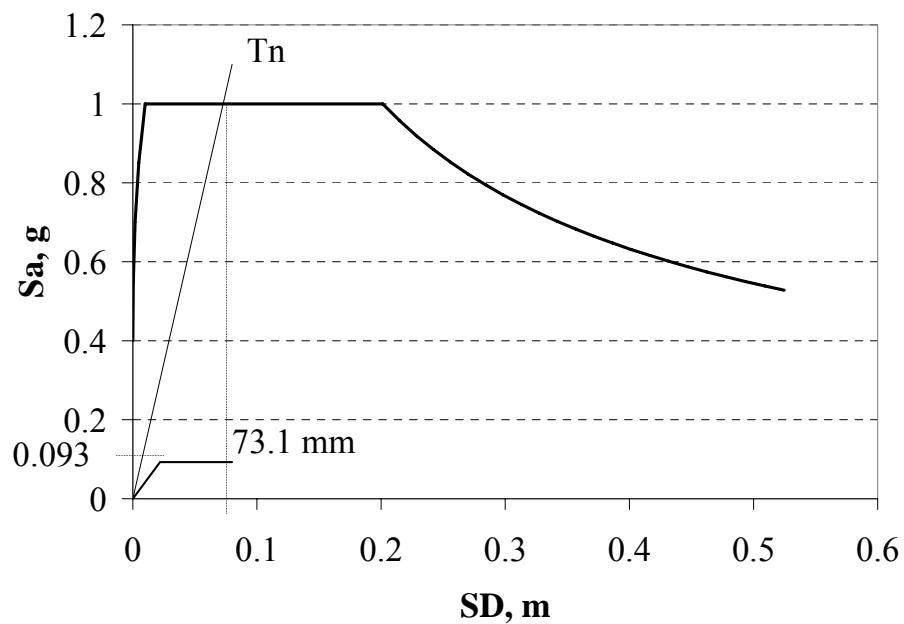


Figure F.1 Determining the spectral acceleration and displacement values for the design example

FRP design according to TEC07:

$$\Delta_u = \frac{\kappa_y L^2}{3} + (\kappa_u - \kappa_y) L_p \left(h - \frac{L_p}{2} \right)$$

$$\Delta_u = \frac{7.1 \times 10^{-6} \times 2000^2}{3} + (\kappa_u - 7.1 \times 10^{-6}) \frac{350}{2} \left(2000 - \frac{350}{4} \right) = 120 \text{ mm}$$

$$\kappa_u = 337.4 \text{ rad / km} \rightarrow \varepsilon_{cc} = 0.064$$

$$\varepsilon_{cc} = 0.002 \left(1 + 15 \left(\frac{f_1}{f_c} \right)^{0.75} \right) = 0.002 \left(1 + 15 \left(\frac{f_1}{20} \right)^{0.75} \right) = 0.064 \rightarrow f_1 = 52.47 \text{ MPa}$$

$$f_1 = \frac{(b+h) E_j \varepsilon_f t_j}{bh} K_e = \frac{(350+350) 230000 \times 0.015 \times t_j}{350 \times 350} \cdot \left(1 - \frac{2(350-2 \times 30)^2}{3.350^2} \right)$$

$$t_j = 4.91 \text{ mm} \rightarrow \frac{4.91}{0.165} = 29.7 = 30 \text{ layers (FRP thickness was selected as 0.165 mm)}$$

FRP design according to Method I:

$$DR_u = 2 + 4.5 \frac{\phi}{n_p} = 2 + 4.5 \frac{\phi}{26 \times 1.66} = 6 \rightarrow \phi = 0.384$$

$$\phi = \frac{(b+h) E_j \varepsilon_f t_j}{bh f_c} K_e = \frac{(350+350) 230000 \times 0.015 \times t_j}{350 \times 350 \times 20} \cdot \left(1 - \frac{2(350-2 \times 30)^2}{3.350^2} \right)$$

$$t_j = 0.719 \text{ mm} \rightarrow \frac{0.719}{0.165} = 4.4 = 5 \text{ layers of CFRP}$$

FRP design according to Method II:

$\kappa_y = 10 \text{ rad / km}$ (by using rectangular stress block and elastoplastic steel model)

$$\Delta_u = 120 \text{ mm} = \kappa_y \frac{L^2}{3} + (\kappa_u - \kappa_y) L_p \left(L - \frac{L_p}{2} \right), L_p = h = 350 \text{ mm}$$

$$120 = 10 \times 10^{-6} \frac{2000^2}{3} + (\kappa_u - 10) \times 10^{-6} \times 350 \times \left(2000 - \frac{350}{2} \right) \rightarrow \kappa_u = 177 \text{ rad / km}$$

$$\frac{\varepsilon_{cc}}{c} = \frac{\varepsilon_{s1}}{c - pp} = \frac{\varepsilon_{s2}}{h/2 - c} = \frac{\varepsilon_{s3}}{h - c - pp} \text{ (pp: clear cover)}$$

$$N = 0.85f_c'0.85cb_w + A_{s1}f_{s1} + A_{s2}f_{s2} - A_{s3}f_{s3} = 700000N$$

$$N = 0.85^2 \times 20c \times 350 + 3\pi 9^2 \times 287 - 2\pi 9^2 \times 177 \times 10^{-6} \times (175 - c) 2 \times 10^5 - 3\pi 9^2 \times 287$$

$$c = 167\text{mm} \rightarrow \epsilon_{cc} = \kappa_u \cdot c = 177 \times 10^{-6} \times 167 = 0.0296$$

$$\frac{0.0296}{167} = \frac{\epsilon_{s1}}{167-30} = \frac{\epsilon_{s2}}{350/2-167} = \frac{\epsilon_{s3}}{350-167-30}$$

$$\left. \begin{array}{l} \epsilon_{s1} = 0.0242 \\ \epsilon_{s2} = 0.00142 \\ \epsilon_{s3} = 0.0271 \end{array} \right\} \text{yield observed except at the middle rebars}$$

$$\epsilon_{cc} = 0.004 + 3.6 \frac{\phi}{n\rho} = 0.004 + 3.6 \frac{\phi}{26 \times 1.66} = 0.0296 \rightarrow \phi = 0.307$$

$$\phi = \frac{(b+h)E_j\epsilon_f t_j}{bhf_c'} K_e = \frac{(350+350)230000 \times 0.015 \times t_j}{350 \times 350 \times 20} \cdot \left(1 - \frac{2(350-2 \times 30)^2}{3 \times 350^2} \right)$$

$$t_j = 0.575\text{mm} \rightarrow \frac{0.575}{0.165} = 3.5 = 4 \text{ layers of CFRP}$$

As presented in calculations, both of the methods lead to approximately 6 times more economical FRP design schemes.

CURRICULUM VITAE

PERSONAL INFORMATION

Surname, Name: Özcan, Okan

Nationality: Turkish (TC)

Date and Place of Birth: 1 Nov 1981, Gölçük

Marital Status: Single

Phone: +90 5327310764

Email: ookan@metu.edu.tr

EDUCATION

Degree	Institution	Year of Graduation
PhD	Middle East Technical University	2002 – Present (3.33/4)
BS	Istanbul Technical University	2002 (3.38/4.00)
High School	TED Ankara College	1998

WORK EXPERIENCE

Year	Place	Enrollment
2002-Present	METU Civil Eng. Dept.	Research Assistant
Jan. 2008 - Feb.2009	University of Ottawa	Visiting Researcher
June 2001	Kipman İnşaat	Intern Student
June 2000	EKO İnşaat	Intern Student

FOREIGN LANGUAGES

English and German

PUBLICATIONS

1. Özcan O, Binici B, Özcebe G. “Improving Seismic Performance of Deficient Reinforced Concrete Columns using Carbon Fiber-Reinforced Polymers” *Engineering Structures*, 30, 1632-1646 (2008)
2. Özcan O, Binici B, Özcebe G. “Seismic Strengthening of Rectangular Reinforced Concrete Columns Using Fiber Reinforced Polymers” *Engineering Structures*, accepted for publication.
3. Özcan O, Binici B, Özcebe G. “Yetersiz Betonarme Kolonlar için Lifli Polimer Güçlendirme Tasarım Kurallarının İrdelenmesi” *İMO Teknik Dergi*, İnşaat Mühendisleri Odası, in review.
4. Özcan O, Binici B, Özcebe G. “Improving Strength and Ductility of Reinforced Concrete Columns Using Carbon Fiber Reinforced Polymer (CFRP)” In: *Proceedings of Ninth Canadian Conference on Earthquake Engineering*, Ottawa, ON, Canada, 2007.
5. Özcan O, Binici B, Özcebe G. “Seismic Retrofitting of Reinforced Concrete Columns Using Carbon Fiber Reinforced Polymer (CFRP)” In: *Proceedings of Asia-Pacific Conference on FRP in Structures (APFIS-2007)*, IIFC, Hong Kong, 2007.
6. Özcan O, Binici B. “Modeling of Fiber Reinforced Polymer Confined Reinforced Concrete Columns with Plain Reinforcing Bars” In: *Proceedings of 8th International Conference on Advances in Civil Engineering (ACE2008)*, Eastern Mediterranean Univ., Famagusta, North Cyprus, 2008.
7. Özcan O, Binici B, Özcebe G. “Seismic Strengthening of Rectangular RC Columns with CFRPs” In: *9th International Symposium on Fiber Reinforced Polymer Reinforcement for Concrete Structures (FRPRCS9)*, Four Points Darling Harbor, Sydney, Australia, 2009.
8. Özcan O, Binici B, Özcebe G. “Design-Oriented Approaches for FRP Retrofitted RC Columns and Case Study of TEC2007 Example” In: *Asia Pacific Conference on FRP in Structures (APFIS2009)*, Seoul, Korea, 2009.
9. Özcan O, Saatçioğlu M. “Reinforced Concrete Coupling Beams with Welded Grids” *Research Report*, Department of Civil Engineering, University of Ottawa, Ottawa, ON, Canada, 2009.